



**TELLURIUM AND SELENIUM IN MAFIC  
VOLCANOGENIC MASSIVE SULFIDE  
HYDROTHERMAL SYSTEMS: EVIDENCE FROM  
THE TROODOS OPHIOLITE, CYPRUS**

**Andrew J. Martin**

Submitted in partial fulfilment of the requirements for  
the degree of

*Doctor of Philosophy*

**May 2019**



---

## Declaration

This work has not previously been accepted in substance for any degree and is not concurrently submitted in candidature for any degree.

Signed.......... (candidate)                      Date.....13.05.2019.....

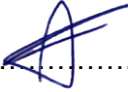
### Statement 1

This thesis is being submitted in partial fulfilment of the requirements for the degree of Doctor of Philosophy (PhD).

Signed.......... (candidate)                      Date.....13.05.2019.....

### Statement 2

This thesis is a result of my own independent work and investigation, except where otherwise stated, and the thesis has not been edited by a third party beyond what is permitted by Cardiff University's policy on the Use of Third Party Editors by Research Degree Students. Other sources are acknowledged by explicit references. Views expressed here are my own.

Signed.......... (candidate)                      Date.....13.05.2019.....

### Statement 3

I hereby give consent for my thesis, if accepted, to be available online in the University's Open Access repository and for inter library loan, and for the title and summary to be made available to outside organisations.

Signed.......... (candidate)                      Date.....13.05.2019.....

### Statement 4

I hereby give consent for my thesis, if accepted, to be available online in the University's Open Access repository and for inter library loan, and for the title and summary to be made available to outside organisations after expiry of a bar on access previously approved by the Graduate Development Committee.

Signed.......... (candidate)                      Date.....13.05.2019.....



---

## ACKNOWLEDGMENTS

There are so many people to thank for their contribution towards this thesis over the past three and a half years. I couldn't have done it without you all!

I'd like to extend my sincerest thanks to my friends and colleagues in Cyprus, especially Iphigenia, Marinos, Apostolus and Eleni for your warm welcome to Cyprus and generally being so lovely! My gratitude to all at the Geological Survey Department of Cyprus, especially Andreas Zissimos, I have fond memories of our cheeky frappes in your office, I'll make a geologist of you yet! I also thank the Director of the Geological Survey Department, Costas Constantinou, for his warm welcome and ongoing support and enthusiasm throughout this study. Thanks to my occasional field partner Michael Green for his support and advice in the field. I'll always remember how you rescued the hire car from certain death at Laxia tou Mavro. Finally, thanks to Lazarus Georgiou for chauffeuring me around the beautiful Skouriotissa mine. Cyprus, it's been amazing. A truly beautiful island with such generous and welcoming people... until next time!

Thanks to past and present Earth and Ocean PhD cohorts for your friendship and encouragement. A special shout out to the 'Staging Chamber' office for putting up with the better half of Cyprus and the occasional swear word. I wouldn't be where I am today without my partners in crime, Emma Bennett(e), Bianca Kennedy and Jamie Price... you guys probably deserve a medal, but it's been the best three years ever, thanks. Special thank you to the 106 Tewkesbury gang past and present, not sure what I did to deserve such amazing housemates but I'm not complaining. My colleagues and friends in the Earth and Ocean department are too numerous to thank but I'd like to give a special shout out to Katie Dobbie, Tony Oldroyd and Duncan Muir. You guys have been amazing, always there for a chat and offering advice and support. I also can't thank team TeaSe enough for their banter, dodgy graphics and guidance, especially Dan Smith, Dave Holwell, Liam Bullock and Joe Armstrong; we've had a great laugh!

Now for my amazing supervisors. Iain McDonald, Chris MacLeod, Katie McFall, and Gawen Jenkin. You have all been beyond brilliant. I have learnt so much from each of you over the past few years, not just knowledge but how to become a good researcher. Words can't express how grateful I am for your banter and support, but most of all for your endless effort and enthusiasm guiding me through my PhD. I'd also like to give a special mention to Manuel Keith and Dom Tanner, you have both been huge sources of support and encouragement throughout my PhD. I will look back on this time with the fondest of memories because of you guys!

Lastly to my family. I'm lucky to have such amazing, caring, loving, and generous parents. Simply without you I wouldn't be where I am today. I'm sure I don't say it often enough but thank you for everything you've done and continue to do for me. Neil, Emma, Harriet and Phoebe, you've kept me sane over the past three years. Neil, you've always got my back, you always encourage me to achieve my dreams, simply the best brother ever!

This thesis is dedicated to the memory of my late supervisor Professor Hazel M. Prichard.

---

## ABSTRACT

Tellurium (Te) and Selenium (Se) are identified as elements critical to the European Union's Strategic Energy Plan: both essential components in the manufacture of thin-film photovoltaic solar cells. Their strategic importance is however paralleled by a poor understanding of their distribution and enrichment in a range of ore-forming environments. The significance of Te and Se in green energy production, their rapidly increasing demand and by-product nature of supply has led to their classification as critical elements by the EU and rest of the world. To address concerns over the supply of Te and Se, the UK National Environmental Research Council established the SoS Minerals (Security of Supply) initiative, within which the 'TeaSe' consortium aimed to characterise Te and Se in a range of ore-forming environments.

This current study, which forms part of the larger TeaSe project, focuses on the distribution and enrichment of Te and Se and associated elements in mafic, Cyprus-type or Cu-Zn Volcanogenic Massive Sulfide (VMS) deposits in one of their principal on-land analogues; the Troodos ophiolite of Cyprus. Exceptional exposure, preservation of original seafloor spreading structures and the lack of any apparent metamorphic overprint in this Late Cretaceous (92 Ma) fragment of Tethyan spreading ridge make the Troodos ophiolite the ideal natural laboratory to investigate processes associated with mafic VMS deposits. VMS deposits occur within the extrusive sequence of the Troodos ophiolite, at the periphery of the complex, within a suite of basaltic to andesitic lavas that once formed the palaeo-seafloor. In this study new geochemical, isotopic and mineralogical data from more than 25 VMS and other mineralised localities spanning the entire Troodos ophiolite is presented, thereby ensuring a representative range of ore-forming processes that control the distribution of Te and Se in Troodos VMS deposits are characterised.

Because of a lack of historic data the concentration of Te and Se in mafic VMS deposits has never previously been characterised. This is especially true in the case of Troodos VMS deposits. This study finds that both Te and Se are enriched in Troodos VMS to levels comparable to actively-forming back-arc and intra-oceanic arc-related hydrothermal systems. Furthermore, data highlights the highest Se concentration in pyrite (9565 ppm; n=1514) yet recorded in any VMS deposit regardless of tectonic environment. Additionally, the mineral-scale distribution of Te and Se between different sulfide minerals is not uniform: Se preferentially partitions into chalcopyrite (n=195) whilst Te partitions into pyrite (n=1514). Selenium is most likely incorporated in pyrite and chalcopyrite in a lattice bound substitution whilst Te can occur as either nano to micro-scale inclusions or as a lattice bound substitution. A correlation between Bi and Te in some Troodos VMS (e.g. the Skouriotissa deposit:  $R^2=0.35$ ) suggests Bi-Te inclusions may host appreciable Te.

On a deposit scale, localised seafloor oxidisation leads to the extreme enrichment of Se. In the Apliki VMS deposit, a hematite-pyrite-chalcopyrite-rich zone termed the South Apliki Breccia Zone (SABZ) was identified via regional geochemical screening as containing high Se (>1000 ppm). The paragenesis of sulfides and oxides in the SABZ suggest the remobilisation of Se during hematite formation and its incorporation in late-stage euhedral pyrite. This demonstrates the significance of fluctuating redox in leading to the extreme, albeit localised, enrichment of Se. Furthermore, whole-rock geochemical data shows that Te and Se may be enriched through supergene oxidation-related processes, leading to the concentration of Te and Se in Fe (oxy)hydroxide crusts.

The distribution of Te and Se between individual VMS deposits on a regional scale (10's of km) across the Troodos ophiolite is extremely variable. Selenium/sulfur ratio, magmatophile trace-element signature and sulfur isotopes have been used to assess variation in magmatic volatile

---

influx and source-rock composition between different VMS deposits. Two processes are proposed that explain the observed distribution of metals and sulfur isotope values in Troodos VMS: i) The leaching of igneous lithologies; or ii) a magmatic volatile influx. The VMS deposits of the Troodos ophiolite occur at different stratigraphic levels within the extrusive sequence: either within the Lower Pillow Lava (LPL), or overlying the Upper Pillow Lava (UPL). Lava geochemistry between the 'UPL' and 'LPL' is markedly different with the UPL distinctly more primitive in composition, and enriched in Cu+Se+Au relative to the LPL suite. Therefore, assuming that the leaching of igneous lithologies provided the only source of metal in the VMS hydrothermal system, those VMS that postdate the accretion of the UPL can be expected to show an enrichment in Cu+Se+Au (e.g., Skouriotissa, Phoucasa) relative to those that predate them (e.g. Agrokippia). However, some LPL hosted VMS deposits exhibit an unusual enrichment in Cu, Se and Au (e.g. Mala); this could indicate the addition of a magmatic volatile phase.

Sulfur isotope ( $\delta^{34}\text{S}$ ) measurements of hydrothermal sulfides indicate that the majority of sulfur in the hydrothermal system for a 'typical' Troodos VMS is sourced through the thermochemical reduction of seawater sulfate and the leaching of primary igneous lithologies and formation of epidiosites in the sheeted dykes underlying the VMS deposits. Consequently,  $\delta^{34}\text{S}$  values for all Troodos sulfides average +4.7‰ (n=180). However, this study identifies, for the first time, an immature magmatic-dominated sulfur isotope signature in an ancient VMS deposit: the exceptionally preserved Mala VMS. This deposit exhibits a light sulfur isotope signature in pyrite averaging -3.4‰ (n=7), a value significantly less than the Troodos magmatic mean (<0-1‰). Considered together with its stratigraphic position, deep within the LPL, geochemical and isotopic data suggest that Mala was preserved – probably through rapid burial by subsequent lava flows – during the immature stages of sulfide accumulation, and therefore retains a distinct magmatic volatile-dominated signature that would normally be overprinted and modified during VMS maturation and off axis fluid flow.

Evidence strongly suggests that metals in immature VMS deposits, even in the relatively volatile-poor mafic VMS system, are sourced from a magmatic volatile phase during the initial stage of VMS formation. Immature or magmatic end-member VMS deposits (e.g. Mala) are characterised by fluids that probably underwent  $\text{SO}_2$  disproportionation (leading to  $\delta^{34}\text{S}$  values of <0‰ in sulfides), an enrichment in magmatophile elements, and apparent lack of zone-refining in the VMS mound. Consequently, Immature VMS deposits exhibit an enrichment in Te, Se and Au, demonstrating a robust link between magmatic volatile influx and the enrichment of Te and Se. In contrast, a 'typical' Troodos VMS deposit exhibits a  $\delta^{34}\text{S}$  signature that is consistent with sulfur derived from the leaching of primary igneous lithologies and the thermochemical reduction of seawater sulfate ( $\delta^{34}\text{S}$  +4.7‰, n=180). The preservation of an immature magmatic signature has only previously been observed in actively forming seafloor massive sulfide deposits in arc-related environments.

---

# CONTENTS

<b>Chapter 1: Introduction .....</b>	<b>1</b>
1. Introduction .....	2
1.1 Aims and Objectives .....	4
1.2 Thesis structure .....	5
<b>Chapter 2: The Troodos Ophiolite, Cyprus .....</b>	<b>7</b>
2. The Troodos ophiolite .....	8
2.1 Tectonics of the Eastern Mediterranean .....	10
2.2 Geological evolution of Cyprus .....	13
2.2.1. The Kyrenia Range .....	13
2.2.2. The Mamonia Complex .....	13
2.2.3. The Troodos ophiolite .....	14
2.3 Troodos crustal stratigraphy .....	16
2.3.1. The Extrusive Sequence .....	17
2.3.1.1. Early subdivisions .....	17
2.3.1.2. Classification based on alteration .....	18
2.3.1.3. Geochemical subdivisions .....	19
2.4 The Sheeted Dykes .....	19
2.5 The Plutonic Sequence .....	20
2.6 The Mantle Sequence .....	21
2.7 Spreading Structure .....	23
2.7.1. Fossil ridge axes .....	24
2.7.2. Off axis graben formation .....	25
2.8 Crustal accretion .....	27
2.8.1. Non-steady state accretion .....	28
2.8.2. Localised eruptive centres .....	29
2.8.3. Melt viscosity .....	30
2.8.4. Core complex formation .....	31
2.8.5. A new perspective on graben formation .....	33
2.9 Faulting and hydrothermal alteration .....	35
2.10 Suprasubduction zone origin .....	36
2.11 Metallogenesis .....	36

---

2.11.1. Asbestos .....	36
2.11.2. Chromite .....	37
2.11.3. Volcanogenic Massive Sulfide deposits .....	37
2.11.4. Pseudo epithermal 'T type' mineralisation .....	37
2.11.5. Umbers .....	38
2.12 Synthesis of ophiolite structure and VMS formation .....	40
<b>Chapter 3: Volcanogenic Massive Sulfide (VMS) deposits: Formation, mineralogy and geochemistry.....</b>	<b>41</b>
3. Introduction .....	42
3.0 VMS classification .....	43
3.1 VMS formation .....	44
3.1.1. Seawater-basalt modelling .....	45
3.1.2. Key ligand species .....	47
3.2 The source of metals in the VMS hydrothermal system .....	48
3.2.1. Epidosites .....	48
3.2.2. Magmatic volatile contribution .....	50
3.3 Modern VMS analogues: Seafloor Massive Sulfides .....	54
3.4 VMS mineralogy and geochemistry .....	56
3.4.1. Zone refining .....	56
3.4.2. VMS mineralogy .....	57
3.4.3. Fluid boiling and phase separation .....	59
3.4.4. Trace element incorporation in sulfide minerals .....	61
3.5 Te and Se in the VMS hydrothermal system .....	62
3.5.1. Te and Se incorporation in sulfide and discrete mineral phases .....	62
3.5.2. Physicochemical fluid factors .....	63
3.5.3. Concentrations of Te and Se in VMS .....	67
3.6 Introducing Troodos VMS .....	68
3.6.1. VMS distribution .....	69
3.6.2. Troodos VMS in the field .....	69
<b>Chapter 4: Methodology.....</b>	<b>73</b>
4. Sample preparation .....	74
4.1 Whole rock geochemistry.....	74

---

---

4.1.1. Portable X-ray Fluorescence analysis .....	74
4.1.2. Aqua regia digestion .....	74
4.1.3. Solution ICP-MS analysis .....	74
4.2 In situ mineral analysis .....	75
4.2.1. Laser ablation ICP-MS spot analysis .....	75
4.2.2. Laser ablation ICP-MS line analysis .....	76
4.3 Scanning electron microscope analysis .....	77
4.3.1. Automated mineral identification .....	77
4.3.2. Element-Mineral mapping .....	77
4.4 X-ray diffraction analysis .....	78
4.5 Sulfur isotope analysis .....	78
4.5.1. Conventional sulfur isotope analysis .....	78
4.5.2. In situ sulfur isotope analysis .....	78

**Chapter 5: Trace element systematics and ore-forming processes in mafic VMS deposits: Evidence from the Troodos ophiolite, Cyprus.....81**

5. Abstract .....	82
5.1 Introduction .....	83
5.2 Sample localities .....	84
5.3 Method Summary .....	85
5.4 Results .....	86
5.4.1. Ore petrography .....	86
5.4.1.1. Pyrite .....	86
5.4.1.2. Chalcopyrite .....	86
5.4.1.3. Sphalerite .....	88
5.4.2. Mineral chemistry .....	88
5.4.3. Time Resolved Analysis .....	93
5.5 Discussion .....	99
5.5.1. Mineral scale metal incorporation and distribution .....	99
5.5.2. Physicochemical conditions of ore-formation .....	106
5.5.3. Source rock variation and trace element composition .....	110
5.6.3. Magmatic volatile fluid flux to the hydrothermal system .....	113
5.6 Summary .....	116

---

<b>Chapter 6: Extreme enrichment of selenium in the Apliki Cyprus-type VMS deposit, Troodos, Cyprus.....</b>	<b>119</b>
6. Abstract .....	120
6.1 Introduction .....	120
6.2 Sampling and Methodology .....	122
6.3 Results .....	123
6.3.1. P-XRF anomaly identification .....	123
6.3.2. The Apliki VMS .....	125
6.3.3. Mineralogy of the South Apliki Breccia Zone .....	129
6.3.4. LA-ICP-MS of sulfides .....	134
6.3.5. Sulfur Isotope Analysis .....	137
6.3.6. Time Resolved Analysis (TRA) .....	137
6.4 Discussion .....	139
6.4.1. Se concentrations in VMS .....	139
6.4.2. The source of Se in VMS deposits .....	140
6.4.3. Mineral scale distribution of Te and Se in the South Apliki Breccia Zone .....	143
6.4.4. Physicochemical factors effecting the incorporation of Te and Se .....	146
6.4.5. Paragenesis and mechanisms of Se enrichment .....	147
6.4.6. The extreme enrichment of Se at the South Apliki Breccia Zone .....	149
6.4.7. An additional magmatic volatile source of Se in the Apliki VMS? .....	152
6.5 Summary .....	153
<b>Chapter 7: Low temperature silica-rich Au mineralisation in the Troodos ophiolite, Cyprus .....</b>	<b>155</b>
7. Abstract .....	156
7.1 Introduction .....	157
7.1.1. Gold geochemistry in hydrothermal systems .....	158
7.1.2. Off axis silicification in Troodos .....	159
7.2 Sample localities .....	160
7.3 Description of localities .....	162
7.3.1. Alpen Rose .....	162
7.3.2. Mathiatis South .....	166
7.3.3. Kokkinovounaros .....	166

---

7.3.4. Touronjia .....	171
7.3.5. VMS: The on axis hydrothermal system .....	174
7.4 Method Summary .....	175
7.5 Sample characterisation .....	176
7.5.1. Mineralogy .....	176
7.5.2. Geochemistry .....	176
7.6 Discussion .....	183
7.6.1. Gold in VMS .....	183
7.6.2. Low temperature venting .....	184
7.6.3. Touronjia .....	185
7.6.4. Kokkinovounaros .....	187
7.6.5. Mathiatis South .....	190
7.6.6. Alpen Rose .....	192
7.6.7. Models for gold enrichment .....	194
7.6.8. Gold transport In the Troodos hydrothermal system .....	196
7.6.9. Structural implications .....	198
7.7 Summary .....	198
<b>Chapter 8: Assessing variable magmatic volatile influx in mafic VMS hydrothermal systems: Evidence from the Troodos ophiolite, Cyprus .....</b>	<b>201</b>
8. Abstract .....	202
8.1 Introduction .....	203
8.2 Sample localities .....	204
8.3 Methods summary .....	206
8.3.1. Trace element geochemistry .....	206
8.3.2. Sulfur isotope analysis .....	207
8.4 Results .....	207
8.4.1. Ore mineralogy and petrography .....	207
8.4.2. Trace element geochemistry .....	208
8.4.3. Sulfur isotope analysis .....	210
8.5 Discussion .....	217
8.5.1. Trace element variation .....	217
8.5.2. Selenium/sulfur ratios in Troodos VMS .....	220

---

---

8.5.3. Variation in sulfur isotopes .....	221
8.5.4. Linking source rock and VMS composition .....	227
8.5.5. Magmatic volatile influx .....	229
8.5.6. Implications for trace element distribution .....	233
8.6 Summary .....	235
<b>Chapter 9: Pulsed magmatic volatile influx: A true magmatic end member deposit, the Mala VMS, Troodos .....</b>	<b>237</b>
9. Abstract .....	238
9.1 Introduction .....	239
9.2 Sample location .....	239
9.3 Results .....	242
9.3.1. Mineralogy .....	242
9.3.2. Geochemistry .....	244
9.3.3. Sulfur isotope analysis .....	247
9.4 Discussion .....	247
9.4.1. Enrichment of magmatophile elements .....	247
9.4.2. Sulfur isotope signature .....	249
9.4.3. The origin of gypsum .....	252
9.4.4. Pulsed magmatic influx .....	256
9.4.5. A true magmatic end member VMS .....	259
9.4.6. The significance of epidiosites in immature VMS .....	260
9.5 Summary .....	261
<b>Chapter 10: Synthesis .....</b>	<b>263</b>
10.1 Introduction .....	264
10.2 Mineral and deposit scale variation .....	266
10.3 Metal source .....	269
10.4 Magmatic volatile influx .....	269
10.5 Comparison with modern analogues .....	274
10.5.1. An updated comparison with TAG .....	274
10.5.2. An analogue for the Troodos VMS hydrothermal system .....	274
10.6 The off axis hydrothermal system .....	277
10.7 Concluding statement .....	278

---

---

<b>Reference List .....</b>	<b>281</b>
<b>Appendix 3 (relating to all Chapters) .....</b>	<b>311</b>
<b>Appendix 4 (relating to all Chapters) .....</b>	<b>415</b>
<b>Appendix 5 (relating to Chapter 5) .....</b>	<b>423</b>
<b>Appendix 6 (relating to Chapter 6) .....</b>	<b>429</b>
<b>Appendix 7 (relating to Chapter 7) .....</b>	<b>441</b>
<b>Appendix 8 (relating to Chapter 8) .....</b>	<b>445</b>
<b>Appendix 9 (relating to Chapter 9) .....</b>	<b>447</b>
<b>Digital Appendix .....</b>	<b>back cover</b>

---

# LIST OF FIGURES

## Chapter 1:

---

**Figure 1.1** – The concentration of Te and Se in different geological environments .....3

## Chapter 2:

---

**Figure 2.1** – Simplified geological map of the Troodos ophiolite .....8

**Figure 2.2** – Simplified schematic of the Troodos hydrothermal system .....10

**Figure 2.3** – Tectonic setting of Cyprus and the eastern Mediterranean .....11

**Figure 2.4** – Tectonic evolution of Cyprus through time .....12

**Figure 2.5** – Troodos crustal stratigraphy .....16

**Figure 2.6** – Alteration mineralogy vs. lava composition .....18

**Figure 2.7** – Lower vs. Upper affinity dykes (SiO<sub>2</sub> vs. MgO) .....20

**Figure 2.8** – Examples of Troodos mineralisation and lithologies .....22

**Figure 2.9** – Structural classification map of Troodos .....24

**Figure 2.10** – The ‘Kakopetira’ detachment .....25

**Figure 2.11** – Formation of the Solea graben off axis .....26

**Figure 2.12** – Non steady state spreading in Troodos .....29

**Figure 2.13** – Oceanic core complex formation .....32

**Figure 2.14** – Schematic evolution of crustal accretion in Troodos .....34

**Figure 2.15** – Timing of epidotisation .....35

**Figure 2.16** – Examples of VMS and hydrothermal mineralisation, Troodos .....39

## Chapter 3:

---

**Figure 3.1** – Classification of VMS .....43

**Figure 3.2** – Simplified schematic of the VMS hydrothermal system .....45

**Figure 3.3** – Initial generation of acidity in oceanic crust .....46

**Figure 3.4** – Metal and major ion solubility with time and temperature .....47

**Figure 3.5** – Epidosite formation and metal depletion .....49

**Figure 3.6** – Sulfur isotope systematics .....52

**Figure 3.7** – Sulfur isotope values of modern vent sites .....53

**Figure 3.8** – Global distribution of active vent sites .....54

**Figure 3.9** – Zone refining in VMS vs. temperature .....57

**Figure 3.10** – Ore morphologies in mafic VMS: a summary .....58

---

<b>Figure 3.11</b> – Depth vs. temperature phase separation .....	60
<b>Figure 3.12</b> – Average water depth with tectonic setting .....	60
<b>Figure 3.13</b> – Selenium concentration through a VMS chimney .....	63
<b>Figure 3.14</b> – pH vs. $fS_2$ vs. Se incorporation in pyrite .....	64
<b>Figure 3.15</b> – $fS_2$ vs. $fTe_2$ transport vs. Ore forming environment vs. tellurides .....	65
<b>Figure 3.16</b> – Selenium species in solution vs. pH and $fO_2$ .....	66
<b>Figure 3.17</b> – Selenium incorporation in pyrite .....	66
<b>Figure 3.18</b> – Concentrations of Te and Se in ore deposits and Troodos VMS .....	67
<b>Figure 3.19</b> – Summary of all locations sampled in this study .....	68
<b>Figure 3.20</b> – Key field photographs of Troodos VMS .....	70
<b>Chapter 5:</b>	
<b>Figure 5.1</b> – Simplified structural domain map of Troodos .....	84
<b>Figure 5.2</b> – Reflected light photomicrographs of Troodos sulfides .....	87
<b>Figure 5.3</b> – Concentration of elements in chalcopyrite, sphalerite and pyrite .....	93
<b>Figure 5.4</b> – Time resolved analysis profiles of sulfide minerals .....	97
<b>Figure 5.5</b> – Bivariate plots of trace elements in pyrite .....	101
<b>Figure 5.6</b> – Bivariate plot of Te vs. Bi and telluride SEM image .....	103
<b>Figure 5.7</b> – Partitioning of Se between different sulfide phases .....	109
<b>Figure 5.8</b> – Incorporation of Au in Troodos and modern vent pyrite .....	112
<b>Figure 5.9</b> – Selenium/Sulfur ratios for Mitsero and Solea VMS .....	113
<b>Figure 5.10</b> – Source rock variation vs. volatile influx for Troodos VMS .....	116
<b>Chapter 6:</b>	
<b>Figure 6.1 A</b> – Location map of the Apliki VMS .....	121
<b>Figure 6.1 B</b> – Schematic cross-section through N Troodos .....	121
<b>Figure 6.2</b> – Distribution of Te and Se in Troodos soils .....	124
<b>Figure 6.3 A</b> – Location map of the Apliki deposit .....	126
<b>Figure 6.3 B</b> – Map of the Apliki open pit .....	127
<b>Figure 6.4</b> – Annotated photograph of the Apliki VMS deposit .....	128
<b>Figure 6.5</b> – Cross section through the South Apliki Breccia Zone .....	128
<b>Figure 6.6</b> – Reflected light photomicrographs of South Apliki Breccia Zone samples .....	131
<b>Figure 6.7</b> – SEM-BSE images of South Apliki Breccia Zone samples .....	132
<b>Figure 6.8</b> – Paragenesis of the South Apliki Breccia Zone .....	133

---

---

<b>Figure 6.9</b> – Summary of South Apliki Breccia Zone paragenesis .....	134
<b>Figure 6.10</b> – Bivariate plots of trace elements in Apliki sulfides .....	136
<b>Figure 6.11</b> – Sulfur isotopes of SABZ pyrite and chalcopyrite .....	137
<b>Figure 6.12</b> – Times Resolved Analysis SABZ sulfides .....	138
<b>Figure 6.13</b> – Selenium/Sulfur ratios for Apliki sulfides by alteration stage .....	141
<b>Figure 6.14</b> – Laser Ablation time resolved analysis of Apliki sulfides .....	144
<b>Figure 6.15</b> – $fO_2$ vs. temperature and corresponding alteration stage .....	147
<b>Figure 6.16</b> – Remobilisation of Se during oxidation of pyrite .....	150
<b>Figure 6.17</b> – Comparison of South Apliki Breccia Zone stage I and III pyrite .....	151
<b>Figure 6.18</b> – Sulfur isotope analysis of South Apliki Breccia Zone sulfides .....	153
<b>Chapter 7:</b>	
<hr/>	
<b>Figure 7.1</b> – Solubility and major ligand species of Au vs. temperature .....	158
<b>Figure 7.2</b> – The effect of pH on chloride and sulfide Au complexes .....	158
<b>Figure 7.3</b> – Summary map of sample localities .....	161
<b>Figure 7.4</b> – Simplified field map of Alpen Rose .....	163
<b>Figure 7.5</b> – Key field observations Alpen Rose .....	164
<b>Figure 7.6</b> – Key field observations Mathiatis South .....	167
<b>Figure 7.7</b> – Simplified field map of Kokkinovounaros .....	169
<b>Figure 7.8</b> – Key field observations Kokkinovounaros .....	170
<b>Figure 7.9</b> – Reflected light photomicrographs of Touronjia sulfides .....	171
<b>Figure 7.10</b> - Simplified field map of Touronjia .....	172
<b>Figure 7.11</b> – Key field observations Touronjia .....	173
<b>Figure 7.12</b> – Examples of Troodos VMS mineralisation in hand specimen .....	174
<b>Figure 7.13</b> – Mineralogical summary of Au-rich localities (XRD) .....	177
<b>Figure 7.14</b> – Bivariate plots of whole rock geochemistry for VMS and Au rich localities .....	181
<b>Figure 7.15</b> – Linear R value correlation plots for Au localities .....	182
<b>Figure 7.16</b> – Linear R values for VMS classified my sample type .....	182
<b>Figure 7.17</b> – Histogram of all whole rock Au data for Troodos .....	183
<b>Figure 7.18</b> – Sphalerite geothermometer applied to Troodos .....	185
<b>Figure 7.19</b> – Supergene vs. hypogene Au enrichment schematic for Kokkinovounaros .....	189
<b>Figure 7.20</b> – Spider plot showing the enrichment of elements in supergene samples .....	189
<b>Figure 7.21</b> – Unaltered lava pile at Kokkinovounaros .....	190

---

---

<b>Figure 7.22</b> – Schematic summary of Alpen Rose formation .....	193
<b>Figure 7.23</b> – Solubility of Au: Temperature vs. $fO_2$ for the Troodos hydrothermal system .....	197
<b>Chapter 8:</b>	
<b>Figure 8.1</b> – Structural domain map of the Troodos ophiolite .....	205
<b>Figure 8.2</b> – Key field photographs of Troodos VMS .....	205
<b>Figure 8.3</b> – Reflected light photographs of Troodos sulfides .....	208
<b>Figure 8.4</b> – Box and whisker plots of trace elements by structural domain .....	209
<b>Figure 8.5</b> – Selenium/Sulfur ratios classified by structural domain .....	210
<b>Figure 8.6</b> – Histogram of sulfur isotope analysis for Troodos sulfides .....	216
<b>Figure 8.7</b> – Sulfur isotopes classified by structural domain .....	216
<b>Figure 8.8</b> – Troodos VMS location with stratigraphic depth.....	219
<b>Figure 8.9</b> – Troodos sulfur isotopes vs. other active vent sites .....	222
<b>Figure 8.10</b> – Proportion of seawater and igneous sourced sulfur in Troodos VMS .....	226
<b>Figure 8.11</b> – Influence of source rock on contained metal in VMS .....	229
<b>Figure 8.12</b> – Exsolution of a magmatic volatile phase from the upper plutonics .....	232
<b>Figure 8.13</b> – Summary schematic for hydrothermal and magmatic end member VMS .....	233
<b>Chapter 9:</b>	
<b>Figure 9.1</b> – Locality map of the Mala VMS deposit .....	240
<b>Figure 9.2A</b> – Key field observation from the Mala VMS .....	240
<b>Figure 9.2B</b> – Gypsum-pyrite relationships .....	241
<b>Figure 9.2C</b> – Location of samples in the Mala VMS mound.....	241
<b>Figure 9.3</b> – Mineralogy summary for Mala wall rock samples .....	242
<b>Figure 9.4</b> – Mineralogy of Mala sulfides (SEM-BSE and reflected light) .....	243
<b>Figure 9.5</b> – Box and whisker plot of trace elements in the Mala VMS .....	244
<b>Figure 9.6</b> – Bivariate plots of sulfide geochemistry .....	245
<b>Figure 9.7</b> – Time resolved LA-ICP-MS analysis of Mala pyrite .....	246
<b>Figure 9.8</b> – Comparison of Mala geochemistry vs. All Troodos VMS .....	248
<b>Figure 9.9 A</b> – Sulfur isotope values for Mala vs. all Troodos VMS .....	250
<b>Figure 9.9 B</b> – Sulfur isotope comparison with other arc/back arc vent sites .....	250
<b>Figure 9.10</b> – Sulfide and sulfate sulfur isotope values from Mala .....	253
<b>Figure 9.11</b> – Schematic of mound growth at Mala .....	255
<b>Figure 9.12</b> – Pulsed magmatic influx vs. time .....	257

---

---

<b>Figure 9.13</b> – Magmatic volatile influx vs. pyrite chemistry at Mala .....	258
<b>Figure 9.14</b> – Magmatic and hydrothermal end member VMS .....	261
<b>Chapter 10:</b>	
<hr/>	
<b>Figure 10.1</b> – Incorporation of Te and Se .....	265
<b>Figure 10.2</b> – Mineral scale distribution of Te and Se .....	266
<b>Figure 10.3</b> – The effect of co-precipitating sulfide phases on Te and Se distribution .....	268
<b>Figure 10.4</b> – The extreme enrichment of Se .....	268
<b>Figure 10.5</b> – Variable magmatic volatile influx in mafic VMS .....	271
<b>Figure 10.6</b> – A summary of magmatic and hydrothermal end member VMS deposits .....	273
<b>Figure 10.7</b> – Troodos vs. TAG .....	274
<b>Figure 10.8</b> – A new modern analogue for Troodos .....	276
<b>Figure 10.9</b> – Te, Se and Au in the off axis hydrothermal system .....	277
<b>Figure 10.10</b> – A new model for the Troodos VMS hydrothermal system .....	279

---

## LIST OF TABLES

### **Chapter 3:**

---

<b>Table 3.1</b> – Average grade and tonnage of VMS types .....	44
---	----

### **Chapter 5:**

---

<b>Table 5.1</b> – Summary of VMS sample localities .....	85
---	----

<b>Table 5.2</b> – LA-ICP-MS pyrite geochemistry .....	89
--	----

<b>Table 5.3</b> – Linear R values for trace elements in pyrite .....	93
---	----

<b>Table 5.4</b> – LA-ICP-MS chalcopyrite geochemistry .....	94
--	----

<b>Table 5.5</b> – LA-ICP-MS sphalerite geochemistry .....	96
--	----

<b>Table 5.6</b> – Trace element concentration: Solea vs. Mitsero .....	111
---	-----

### **Chapter 6:**

---

<b>Table 6.1</b> – Summary of Te and Se concentration by alteration stage at Apliki .....	129
---	-----

<b>Table 6.2</b> – Te and Se concentration in chalcopyrite and pyrite .....	134
---	-----

<b>Table 6.3</b> – Summary of LA-ICP-MS spot data for Apliki .....	135
--	-----

<b>Table 6.4</b> – Summary of sulfur isotopes .....	137
---	-----

### **Chapter 7:**

---

<b>Table 7.1</b> – Summary of sample localities .....	161
---	-----

<b>Table 7.2</b> – Whole rock geochemistry for low temperature Au deposits .....	178
--	-----

<b>Table 7.3</b> – Whole rock geochemistry for VMS samples .....	179
--	-----

<b>Table 7.4</b> – LA-ICP-MS of Kokkinovounraos pyrite .....	188
--	-----

### **Chapter 8:**

---

<b>Table 8.1</b> – Location of samples analysed .....	206
---	-----

<b>Table 8.2</b> – Pyrite geochemistry (LA-ICP-MS) .....	211
--	-----

<b>Table 8.3</b> – Chalcopyrite geochemistry (LA-ICP-MS) .....	213
--	-----

<b>Table 8.4</b> – Covellite geochemistry (LA-ICP-MS) .....	214
---	-----

<b>Table 8.5</b> – Summary of sulfur isotopes ( $\delta^{34}\text{S}$ ) .....	215
---	-----

<b>Table 8.6 A</b> – The ratio of UPL to LPL elements in Troodos VMS .....	220
--	-----

<b>Table 8.6 B</b> – Summary of UPL vs. LPL elements with stratigraphic depth .....	220
---	-----

<b>Table 8.7</b> – Summary of lava geochemistry between MOR/BAB setting .....	230
---	-----

<b>Table 8.8</b> – Summary of Se/S, Se concentrations and sulfur isotopes .....	234
---	-----

### **Chapter 9:**

---

<b>Table 9.1</b> – Sulfur isotope composition of samples from Mala .....	247
--	-----

# CHAPTER 1

## Introduction

## 1.1 Introduction

Tellurium (Te) and selenium (Se) are identified as critical in low carbon energy technologies under the European Union's Strategic Energy Technology Plan (SET-Plan) (Moss *et al.*, 2013). The use of Te and Se within photovoltaic cells (CdTe and Cadmium Indium Gallium di-Selenide (CIGS)) underpins their strategic importance within the EU and rest of the World. The criticality of these metals stems from the potential for significant growth in demand due to a transition to low carbon, solar dominated energy production (38 GW in 2010 and projected to form 630 GW in 2030: Moss *et al.*, 2013), low crustal abundance (0.002 mg/kg Te and 0.05 mg/kg Se- Perkins, 2011) and their secondary (by-product) nature of production through the refining of copper (approximately 90%, Lu *et al.*, 2015). Global Te production in 2010 was 0.50 Kt and projections by Moss *et al.* (2013) suggest that by 2030 the EU alone will consume over 50% of global Te production. It is clear that Te and Se will play a crucial role in the future transition to a low carbon economy; both currently lack recycling potential (Redlinger *et al.*, 2015) and have little potential for substitution within photovoltaics (Lu *et al.*, 2015). At present they are recovered solely as by-products through the electrolytic refining of copper which will decline in the future as Cu grades decrease globally favouring the use of heap leach extraction methods which are not amenable to Te-Se recovery (Moss *et al.*, 2013).

The future economic importance and significance of Te and Se in emerging technologies is paralleled by a poor understanding of the source, mobilisation and concentration of Te and Se within ore deposits. Tellurium and Se have been of relatively little interest in the recent past as production from copper refining has kept pace with global demand but it is evident this will not suffice in the future with demand set to significantly outstrip supply. To mitigate projected shortages and ensure security of supply, research on all aspects of Te and Se is needed. It has been shown that sulfide ores in a range of ore forming environments (Figure 1.1- overleaf) may concentrate Te and Se to potentially economic, extractable levels (e.g. Känkberg Te-Au mine, Sweden). Dependant on the scale of extraction these cut off grades for Te and Se vary from a few ppm in porphyry Cu deposits to several thousands of ppm at the Känkberg Te-Au mine; ultimately the extraction of Te and Se depends on the extraction of economic co-products e.g., Au or Cu. In combination, these factors above lead to a lack of comprehensive, accurate data which now needs to be implemented to mitigate future risks.

In hydrothermal ore deposits we do not understand the conditions that concentrate Se, for example fluid temperature studies indicate that Se enrichment occurs in both high and low temperature environments (Butler and Nesbitt, 1999; Huston *et al.*, 1995). The physical incorporation of Te and Se in hydrothermal ore deposits is poorly constrained. We do not know

conclusively how they are hosted in the sulfide lattice via a solid solution (e.g., Cook *et al.*, 2009; Huston *et al.*, 1995) or as mineral-nano scale inclusions (e.g. Deditius *et al.*, 2011; Keith *et al.*, 2018a); this has important implications for processing of ore.

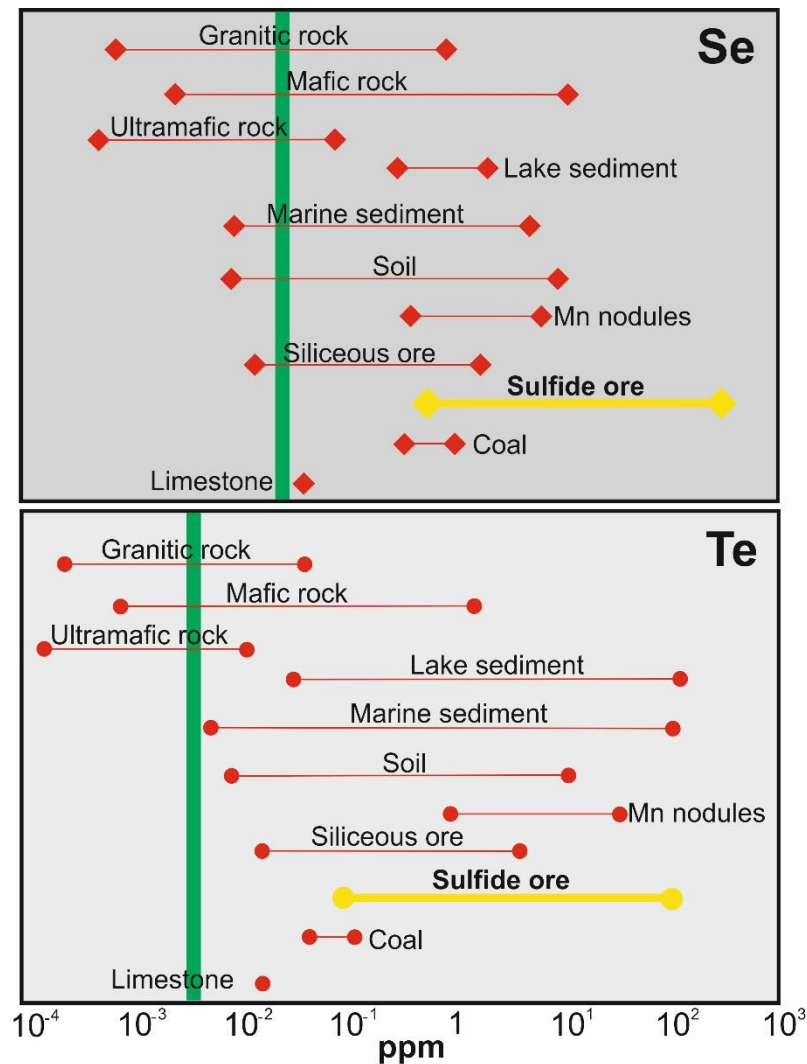


**Figure 1.1:** Concentration of Te and Se in geological environments. Sulfide ore (yellow bar) may be enriched in both Te and Se to 100's or 1000's of ppm. Green line is approximate average crustal abundance (after Schirmer *et al.*, 2014).

This study has been designed to investigate the distribution, behaviour and enrichment of Te and Se in mafic VMS hydrothermal systems with the Troodos ophiolite (Cyprus) selected for detailed study. Furthermore, actively forming submarine mineral deposits, termed Seafloor Massive Sulfide (SMS), are now being assessed as potential mineral resources (e.g. Solowara-1; Boshcen *et al.*, 2013). This study investigates a sub-type of VMS deposits; namely Cyprus-type or mafic VMS. These deposits are often small but high grade (average 3.2 wt.% Cu) and represent important global Cu resources (Galley *et al.*, 2007).

The Troodos ophiolite hosts the type locality for Cyprus-type, mafic or Cu-Zn VMS deposits (Cox and Singer, 1986; Franklin *et al.*, 2005; Galley *et al.*, 2007). The exceptional perseverance of

primary sulfide textures and seafloor structures (i.e. spreading rifts) makes Troodos an excellent ancient analogue to compare with actively forming seafloor massive sulfide deposits (e.g., Hannington *et al.*, 1998). The domical uplift of the Troodos Massif has led to the exposure of a complete section of oceanic crust making it possible to investigate not only shallow surface processes but, to obtain a cross-section through the entire oceanic crust allowing the metal budget of the VMS hydrothermal system to be assessed (Jowitt *et al.*, 2012; Kelley *et al.*, 1992). Furthermore, the Troodos ophiolite has been the subject of intense study in a range of geological disciplines since the 1950's, hence wider magmatic and spreading related processes are debated but well characterised (e.g. Gass, 1968; Miyashiro, 1973; Varga and Moores, 1985). This makes the Troodos ophiolite an ideal natural laboratory to investigate mafic VMS hydrothermal systems and the processes that effect Se and Te in ocean crust.

## 1.2 Aims and Objectives

The aim of this thesis is to characterise **the distribution and nature of Te and Se in mafic VMS deposits on Cyprus** to better understand the spatial distribution, abundance and processes that control their distribution and enrichment in mafic VMS deposits. This will be achieved through the following objectives:

- Ascertain the concentration of Te and Se in VMS deposits and associated host rocks that are representative of a range of physicochemical ore forming processes.
- Understand the mineral scale distribution of Te and Se. How these elements are hosted and their partitioning behaviour between different sulfide minerals will be key in understanding their distribution and future mineral extraction.
- Constrain the factors that affect the enrichment (and especially the extreme enrichment) of Te and Se in VMS. Establish whether these relate to source heterogeneity, physicochemical processes of or a combination of these?
- Characterise Te and Se distribution and their concentrations away from high temperature VMS deposits and compare and contrast with sites of low temperature venting to determine the total Te and Se budget of mafic hosted hydrothermal systems.
- Test current understanding of magmatophile elements, volatile transfer and the significance of epidosite formation in the mafic VMS system.

## 1.3 Thesis structure

The remainder of this thesis is subdivided into 9 Chapters each addressing background information, a different aspect of Te and Se enrichment or a specific characteristic of the Troodos hydrothermal system. Given the diversity of processes in the Troodos hydrothermal system and their apparent control on the distribution and enrichment of Te and Se, Chapters progress broadly from mineral-scale to ophiolite wide processes.

**Chapter 2: The Troodos ophiolite.** This Chapter reviews current understanding of the Troodos ophiolite, Cyprus. Knowledge of the geochemical, structural and tectonic environment of Troodos is vital in understanding how the Troodos hydrothermal system is different from, for example Mid Ocean Ridge (MOR) hosted hydrothermal systems.

**Chapter 3: Volcanogenic Massive Sulfide deposits.** This Chapter reviews our current understanding of modern VMS hydrothermal systems and how these systems are preserved in fossil analogues. Key comparisons are drawn between Troodos and modern submarine vent sites. Current knowledge on the transport of Te and Se is also reviewed.

**Chapter 4: Methodology.** Outline of the analytical methods used in this thesis, specific reference or a method summary are provided in each subsequent Chapter.

**Chapter 5: Trace element systematics and ore forming processes in mafic VMS systems: Evidence from the Troodos ophiolite, Cyprus.** In this Chapter extensive in situ geochemical analyses are presented and synthesised in a bid to understand the enrichment of Te and Se in mafic VMS, their partitioning between different sulfide phases, their incorporation mechanism (lattice bound or inclusions) and factors that may influence their wider distribution. This chapter is a modified version of the paper co-authored by the writer:

- Martin, A.J., Keith, M., McDonald, I., Haase, K.M., McFall, K.A., Klemd, R., MacLeod, C.J., 2019. Trace element systematics and ore-forming processes in mafic VMS deposits: Evidence from the Troodos ophiolite, Cyprus. *Ore Geol. Rev.* 106, 205–225. <https://doi.org/10.1016/j.oregeorev.2019.01.024>

**Chapter 6: The extreme enrichment of Se in the Apliki Cyprus-type VMS.** The Apliki VMS is enriched in Se to levels that have never been reported in mafic VMS until this study. A complex paragenesis leads to the mobilisation and concentration of Se in late euhedral pyrite on the seafloor. Sulfur isotope and in situ trace element data suggests a paragenesis of remobilisation and not an additional Se source. This chapter is a modified version of the paper co-authored by the writer:

- Martin, A.J., McDonald, I., MacLeod, C.J., Prichard, H.M., McFall, K., 2018. Extreme enrichment of selenium in the Apliki Cyprus-type VMS deposit, Troodos, Cyprus. *Mineral. Mag.* 82, 697–724. <https://doi.org/10.1180/mgm.2018.81>

**Chapter 7: Low temperature silica-rich Au mineralisation in the Troodos ophiolite, Cyprus.**

Tellurium is often used a pathfinder element for Au. This Chapter focuses on understanding the distribution of Au using whole rock geochemistry and mineralogy of low temperature vent sites that are enriched to 10's of ppm Au, Te and Se. Additionally, Te and Se may be significantly enriched in residual supergene Fe-(oxy)hydroxide phases.

**Chapter 8: Assessing variable magmatic volatile influx in mafic VMS hydrothermal systems: evidence from the Troodos ophiolite, Cyprus.**

As shown in previous Chapters (Chapter 5 and 6), magmatic volatile influx into the VMS hydrothermal system is variable across Troodos. This Chapter presents the first extensive sulfur isotope study ( $\delta^{34}\text{S}$ ) of VMS spanning the entire ophiolite to assess the influence of variable magmatic volatile influx and protolith composition on VMS geochemistry. This chapter is a modified version of the submitted paper co-authored by the writer:

- Martin, A.J., Keith, M., Parvaz D.B., McDonald, I., Boyce A.J., McFall, K.A., Jenkin G.R.T., MacLeod, C.J., Strauss H. (**Submitted**). Assessing variable magmatic volatile influx in mafic VMS hydrothermal systems: evidence from the Troodos ophiolite, Cyprus. Chem. Geol.

**Chapter 9: Pulsed magmatic volatile influx: A true magmatic end member deposit, the Mala**

**VMS, Troodos.** The Mala VMS is unique, it contains the highest Se of any known VMS/SMS, it is enriched in Au and Te and yields extremely light sulfur isotope values. This study uses Mala as an analogue to highlight complexities in ancient hydrothermal systems and, in combination with previous Chapters to redefine the ore forming model for Troodos.

**Chapter 10: Synthesis and Conclusion.** A new model for ore formation and the enrichment of magamtophile elements in mafic VMS hydrothermal systems.

# **CHAPTER 2**

## **The Troodos Ophiolite, Cyprus**

## 2. The Troodos Ophiolite: Overview

The Troodos ophiolite (Cyprus) has played a fundamental role in our understanding of plate tectonics. Only in 1959 did Wilson realise that the area we now refer to as the sheeted dyke complex (SDC) was actually a swarm of vertical dykes intruding dykes. It wasn't until later when Vine and Matthews (1963) discovered the characteristic 'magnetic stripes' on the seafloor that seafloor spreading was recognised and the theory of plate tectonics established. Ian Gass and the Geological Survey of Cyprus then made the conceptual link between seafloor spreading and ophiolite formation and the true significance of Troodos was realised: The preservation of a complete and undeformed oceanic pseudostratigraphy (Gass, 1968).

Cyprus is located in the Eastern Mediterranean and consists of four main geological terranes: the Kyrenia Range, Mesaoria plain, Troodos Massif and the Mamonía Complex (e.g. Robertson and Xenophontos, 1993). The Troodos Massif is an ophiolite (Figure 2.1) that represents a fragment of Turonian age (~92 Ma; Mukasa and Ludden, 1987) oceanic lithosphere formed during the closure of the Tethys ocean (e.g. Gass, 1968; Robertson, 1977). Initially Troodos was considered to have formed in a typical (open-ocean) mid-ocean ridge (MOR) environment (Gass, 1968, 1980); however geochemical studies of the extrusive section demonstrate a geochemical affinity different from that of N-MORB, instead dominated by arc tholeiites and boninites (e.g. Miyashiro, 1973; Pearce *et al.*, 1984; Rautenschlein *et al.*, 1985; Robinson *et al.*, 1983). Whereas it is now widely accepted that Troodos formed in a supra-subduction type setting, the exact nature of its geodynamic setting remains debated (Gass *et al.*, 1975; Moores *et al.*, 1975; Hynes 1975).

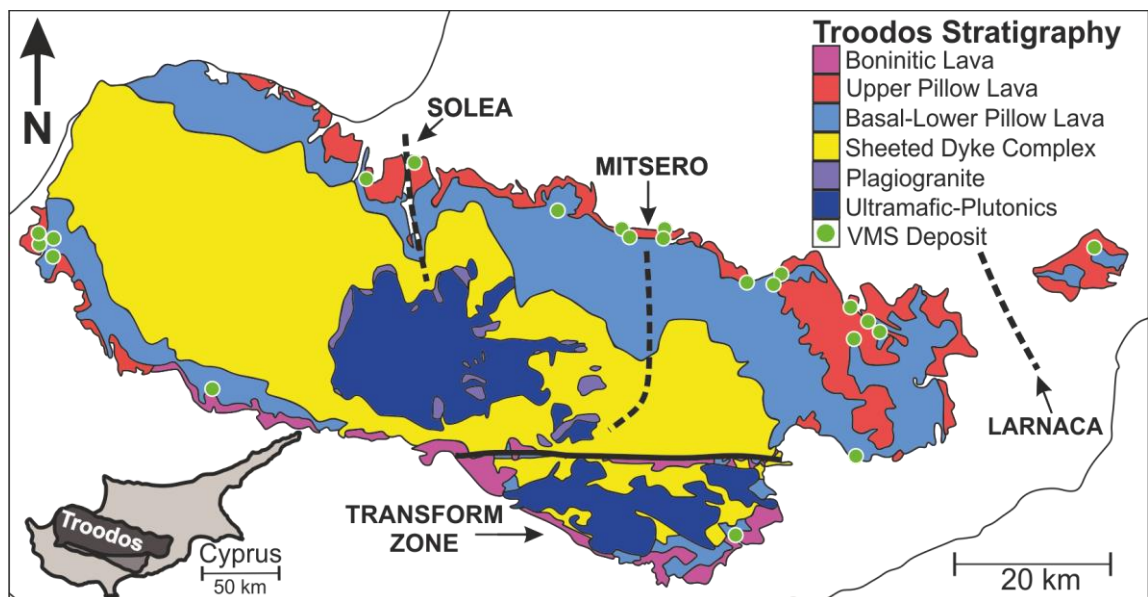


**Figure 2.1:** Simplified geological map of the Troodos Ophiolite. Inset: image showing the location of Troodos within the island of Cyprus (after Martin *et al.*, 2018).

Uplift of the Massif during the Pleistocene was driven by serpentinisation of the mantle sequence (e.g. Robertson, 1977; Robertson & Xenophontos, 1993) leading to diapirism and differential uplift centred on Mt Olympus (1950 m). This led to the exposure of a complete ophiolitic stratigraphy with relatively little deformation (Figure 2.1). Mantle dunites, lherzolites and harzburgites are located at the geographically highest point, surrounded radially by the plutonic sequence – gabbros, wehrlites and plagiogranites. These are overlain by the sheeted dyke complex (SDC) and, at the periphery of the ophiolite and stratigraphically above the SDC, the extrusive sequence consisting of a 'Basal Group' transitional horizon, 'Lower Pillow Lava' (LPL) suite and a more primitive 'Upper Pillow Lava' (UPL) suite (e.g. Gass *et al.*, 1994) (Figure 2.1).

In-depth studies of the internal structure and spreading history of the Troodos ophiolite have revealed complexities in the mechanism of crustal accretion akin to processes recognised at modern slower-spreading mid-ocean ridges (e.g. Escartin and Canales, 2011). In particular, it is evident that tectonic stretching accompanied plate separation, such that normal faulting and tilting of upper crustal blocks occurred above large-offset detachment faults (Varga and Moores, 1985; Nuriel *et al.*, 2009). From W to E regional graben structures are identified comprising the Solea, Mitsero and Larnaca grabens respectively (see section 2.8). Grabens formed during periods of magmatic quiescence and led to the stretching of the SDC and formation of regional scale structures defined by the 'bookshelf' faulting and tilting of SDC and lavas away from each other (Varga and Moores, 1985; Moores *et al.* 1990).

Evidence of hydrothermal alteration is abundant in Troodos; the UPL, LPL and upper Basal Group lithologies are extensively altered to zeolite facies (~150°C) metamorphic assemblages (e.g. Gass and Smewing, 1973). The lower Basal Group marks a transition to greenschist facies metamorphic conditions (Gillis and Robinson, 1980). As fluids descend to the base of the SDC they became heated to upper greenschist temperatures of ~350°C (Figure 2.2); at this point original mafic mineral assemblages are altered to epidote-quartz ± titanite. Fluid inclusion (Bednarz and Schmincke, 1990) and isotopic studies (Bickle and Teagle, 1992; Yamaoka *et al.*, 2015) support the pervasive and high temperature nature of hydrothermal alteration in the SDC.

Volcanogenic massive sulfide deposits outcrop at the periphery of the ophiolite, forming within the extrusive sequence that once represented the palaeo seafloor. These deposits formed through the channelling and exhalation of metal laden evolved seawater at the seafloor. Upon exhalation at or near the seafloor massive sulfide (Figure 2.2; cf. Chapter 3), usually pyrite with minor chalcopyrite, is precipitated (e.g. Constantinou 1980; Spooner, 1977: Chapter 3). The relatively undeformed nature of the Troodos ophiolite, with exceptional exposure, preservation

of original seafloor structures and sulfide textures make it an excellent location to investigate geochemical processes associated with mafic VMS hydrothermal systems (see Chapter 3).

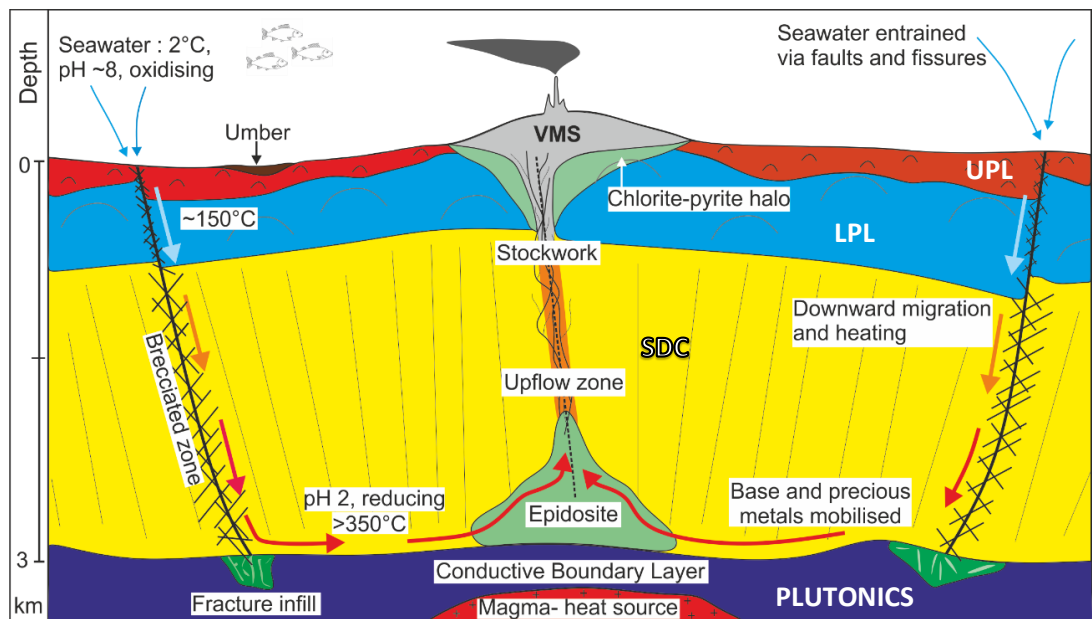


**Figure 2.2:** Schematic cross-section through the Troodos ophiolite hydrothermal system. Metals are sourced primarily from the SDC with a possible magmatic component (Martin *et al.*, 2018). UPL= Upper Pillow Lava, LPL = Lower Pillow Lava/Basal group, SDC = Sheeted Dyke Complex.

## 2.1 Tectonics of the Eastern Mediterranean

The tectonics of the Eastern Mediterranean and its associated ophiolite terrains have played a fundamental role in our understanding of plate tectonics (Robertson and Mountrakis, 2006). Ophiolites are located throughout Croatia, Albania, Greece, Turkey and Cyprus (Figure 2.3 and 2.4). Tectonically the Eastern Mediterranean is a complex region than has been likened in structural complexity to active spreading in the Adaman Sea region (Moore *et al.*, 1984; Morris and Maffione, 2016).

It is widely accepted that the Eastern Mediterranean regions once formed part of a much larger ocean separating Africa and Eurasia: the Palaeotethys (e.g. Moore *et al.*, 1984; Robertson and Mountrakis, 2006). The closure of the Palaeotethys was driven by northward subduction of the African plate below the Eurasian plate throughout the Mesozoic-Cenozoic (Figure 2.4) (Robertson *et al.*, 2012). During the Mesozoic (~260 Ma) rifting of northern Gondwana led to the opening of several small oceanic basins with localised slivers of rifted continental crust (e.g. Mamonnia) (Robertson, 1990). Further N toward the Arabian foreland within the Izmir-Ankara-Erzincan Ocean (Robertson *et al.*, 2006; Figure 2.4) subduction was ongoing leading to the obduction of neotethyan ophiolites onto the Arabian foreland (e.g. the Pontides; Figure 2.4) (Robertson *et al.*, 2006; Robertson, 2002). The late Cretaceous was marked by seafloor

spreading (Troodos formation) in a supra-subduction zone environment within the Southern Tethys Ocean, the continued obduction of ophiolites onto the Arabian foreland and formation of intra-continental basins (Figure 2.3) (Robertson *et al.*, 2012; Robertson and Mountrakis, 2006; Robertson *et al.*, 2002). During the Mid Eocene the closure of the Izmir-Ankara-Erzincan Ocean was complete, driven by the continued northward subduction of Africa beneath Eurasia (Figure 2.4). Continued regional compression throughout the Eocene to mid Miocene led to the closure of the Southern Neotethys to form the modern day Mediterranean Sea (Figure 2.4; Robertson *et al.*, 2012).

The modern day tectonics of the eastern Mediterranean are influenced by the continued convergence of Africa with Eurasia (Robertson, 1990). Subduction along the Cyprean Arc remains active as delineated by the occurrence and focal depth of earthquakes along the Arc (Jackson and McKenzie, 1984). During the Pleistocene Troodos underwent rapid uplift caused by both under-thrusting due to the attempted subduction of the Eratosthenes Seamount/microcontinent to the S of Cyprus at the Cyprean arc (Figure 2.3) (Robertson *et al.*, 2012) and the continued serpentinisation of mantle peridotites that led to the diapiric uplift of the Massif (cf. section 2.2.3).

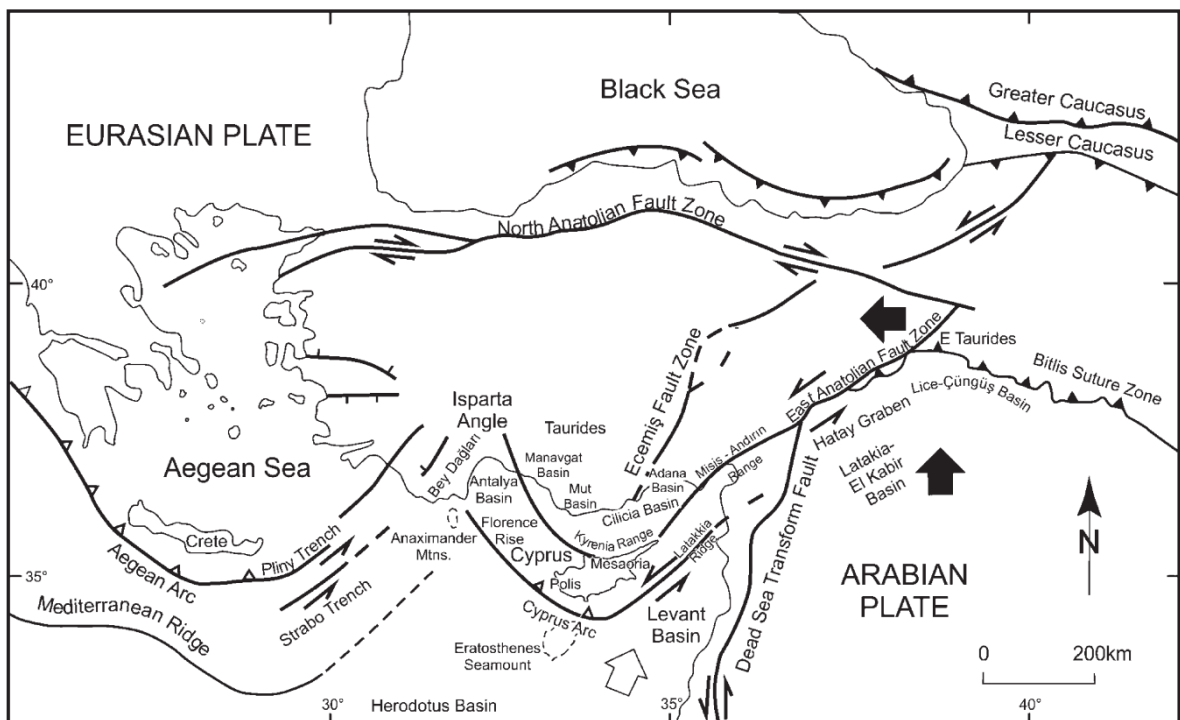


**Figure 2.3:** Present day tectonic setting of the Eastern Mediterranean and Cyprus. The region is dominated by compressional tectonics due to continued convergence between Africa and Eurasia (arrows indicate plate motion). Cyprus is located along the active Cyprean Arc or 'Cyprus Arc' (S of Cyprus) (From Robertson *et al.*, 2012).

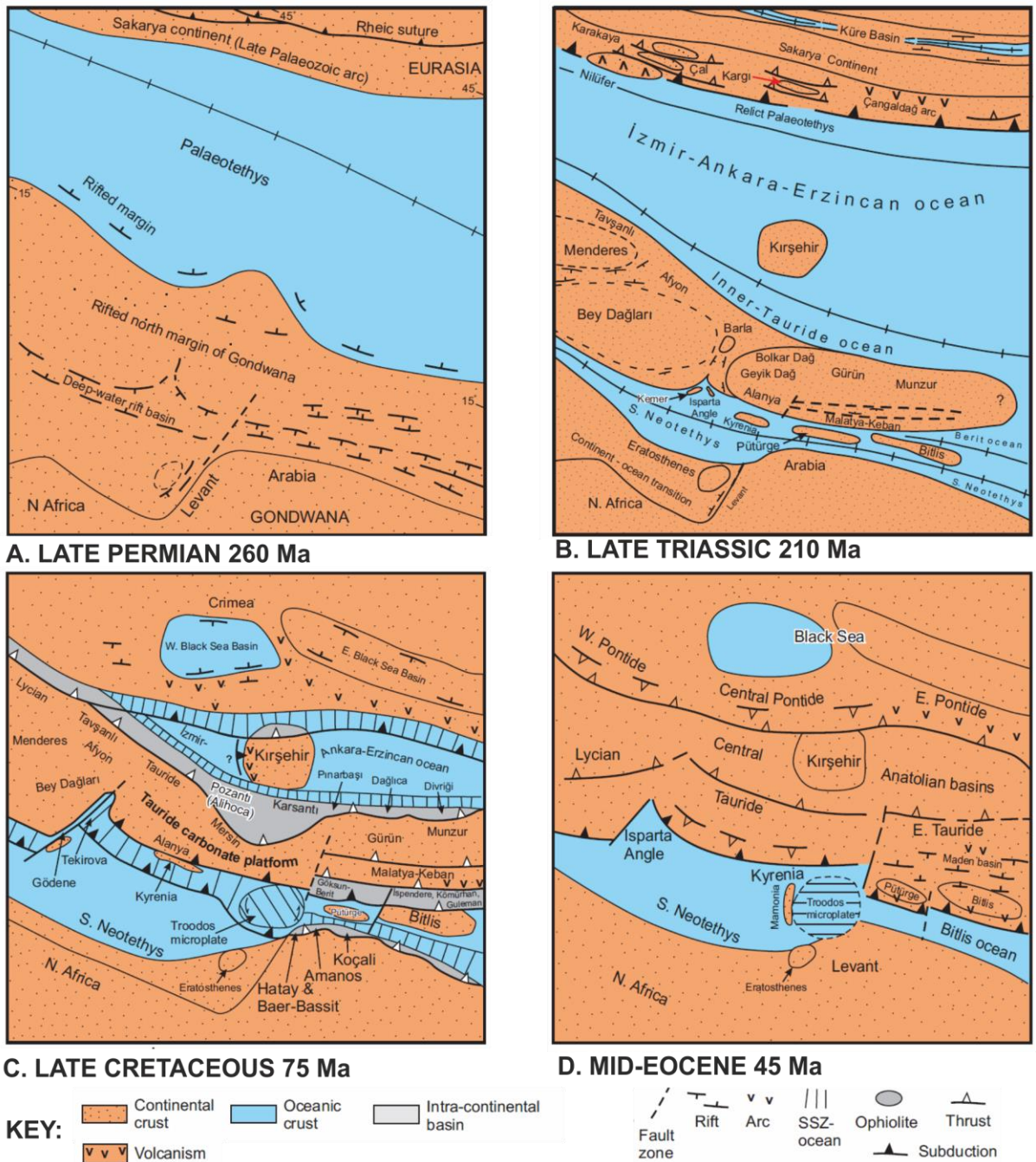


**Figure 2.4:** The tectonic evolution of the Eastern Mediterranean and Troodos microplate (Permian to Eocene). **A)** Permian: Palaeotethys ocean to the N and initial rifting of Gondwana. **B)** Rifting of the Anatolides from northern Gondwana and the formation of the South Neotethys and Izmir-Ankara-Erzincan ocean, microcontinents appear in the South Neotethys. **C)** Continued closure of the Izmir-Ankara-Erzincan ocean and southward subduction along the Arabian continental margin (ophiolite obducted, e.g. Pontides). Northerly dipping subduction to the S of Troodos leads to localised spreading. **D)** Closure of Izmir-Ankara-Erzincan ocean and narrowing of the South Neotethys due to the continued northward subduction of the South Neotethys beneath SE Turkey and localised volcanism (see Figure 2.3 for modern day tectonics) (from Robertson *et al.*, 2012).

## 2.2 Geological evolution of Cyprus

The three main tectonic terranes of Cyprus: the Troodos ophiolite, Mamonia Complex and the Kyrenia range were juxtaposed over a long and complex tectonic history to form the modern-day island of Cyprus. This section outlines key characteristics of each terrane and provides a brief summary of its geological evolution.

### 2.2.1 The Kyrenia Range

The Kyrenia range is located in Northern Cyprus forming the distinctive 'spine' of Cyprus as we know it today. Rocks exposed in Kyrenia are the oldest in Cyprus consisting predominantly of Mesozoic (Permian) and Tertiary sedimentary and subordinate volcanic and metamorphic units (Robertson and Woodcock, 1986). The Kyrenia lineament is approximately 160 km long and 10 km wide, the lineament consists of a steeply dipping composite thrust pile (Robertson and Woodcock, 1986). Lithologies include thinly bedded micaceous marbles, massive brecciated dolomitic limestones, greywackes, conglomerates and volcanoclastic units (Robertson and Woodcock, 1986).

The formation and amalgamation of Kyrenia is long and complex. Initially Kyrenia was rifted off Gondwana in the Triassic where it formed a gently subsiding carbonate platform. The preservation of volcanics and rhyolites dated to the Cretaceous suggests that subduction initiation occurred to the N of present-day Cyprus (Robertson *et al.*, 2012). During this period compression due to the rotation of the Troodos microplate led to localised metamorphism and marble formation. Shortly after rotation of the Troodos microplate, intraplate volcanism is recorded as bimodal volcanic facies (Robertson *et al.*, 2012). Ongoing compression and possible subduction initiation to the S of Cyprus (the Cyprean Arc) led to the juxtaposition and southward thrusting of Kyrenia with Troodos and further localised metamorphism (i.e. marble formation).

### 2.2.2 The Mamonia Complex

The Mamonia Complex is located in southwest Cyprus and comprises an assemblage of Upper Triassic to Lower Cretaceous sedimentary units, Upper Triassic mafic igneous units and minor metamorphic rocks (Robertson and Woodcock, 1980). Lithologies of the Mamonia Complex are sub-divided into two main tectono-stratigraphic units: the Petra tou Romiou formation (Lapierre, 1975) and Ayios Photios Group (Swarbrick and Robertson, 1979). The Petra tou Romiou formation is the lowermost unit comprising of felsic to mafic igneous rocks associated with Late Triassic reef and pelagic sediments (Lapierre *et al.*, 2007). These are overlain by the Ayios Photios Group; a sedimentary succession of marls and limestones recording the

progressive shallowing of a marine basin in a passive continental margin setting (Lapierre *et al.*, 2007).

Lavas preserved in the Mamonia Complex are geochemically and morphologically distinct compared to Troodos lavas. They are described as tholeiitic with N-MORB affinities (Malpas, 1990) and are commonly amygdaloidal. Lavas formed during intra-plate volcanism dated to Late Triassic (Lapierre *et al.*, 2007). The attempted subduction of the Eratosthenes block (to the S of Cyprus; Figure 2.4) led to the imbrication of Mamonia and Troodos terrains. Mamonia sedimentary rocks are now arranged in sub-horizontal extensively deformed thrust sheets and separated from the main Troodos terrane by a series of serpentinite slivers and amphibolites (Robertson and Woodcock, 1979; Clube and Robertson, 1986).

### 2.2.3 The Troodos ophiolite

The Troodos ophiolite represents a complete penrose stratigraphy of oceanic lithosphere (e.g. Gass, 1968). The Troodos Massif formed in the Palaeotethys Ocean approximately ~92 Myr ago (Mukasa and Ludden, 1987). Compression caused by the convergence of Africa with Eurasia initiated subduction somewhere in the Palaeotethys Ocean (refer to Figure 2.4). After the initial subduction of Cretaceous aged oceanic crust, dense Triassic crust entered the trench causing melting, magma upwelling and slab-rollback that probably initiated spreading in the Late Cretaceous ~92-90 Ma (approximately 200 km wide) (Dilek *et al.*, 1990; Pearce and Robinson, 2010). During this time the Troodos and 'anti-Troodos' terrains formed. At approximately 80 Ma the Troodos microplate began to rotate, some ~60° through the Upper Campanian to Maastrichtian (Morris *et al.*, 1990; Robertson and Xenophontos, 1993). It is generally accepted that the area of rotation was small, i.e. a microplate (Robertson and Woodcock, 1980). Several scenarios have been suggested explaining the rotation of the Troodos microplate including oblique subduction (Clube *et al.*, 1985), the collision of Troodos with a 'Mamonia Seamount' (Moores *et al.*, 1984; Murton, 1990), passive rotation in response to collision with the Arabian foreland during the continued convergence between Africa and Eurasia (Clube and Robertson, 1986; Robertson 1990; Robertson *et al.*, 2006) or in response to the attempted subduction of the Eratosthenes seamount (see Figure 2.3 and 2.4). Rotation corresponds to the first evidence of the amalgamation of Troodos with Mamonia and by this time spreading had ceased. The remaining ~30° rotation of the Troodos microplate occurred over a 20 Myr period from the Maastrichtian to early Eocene. All volcanism had ceased in Troodos by the early Eocene (Robertson, 1990). Hence, structures that now trend N-S originally trended E-W on the Cretaceous seafloor due to the rotation of the entire ophiolite terrain.

Troodos was gradually uplifted whilst Mesaoria underwent subsidence (e.g. along the Ovgos fault). Mesaoria was progressively infilled by some 700 m of ophiolite derived debris (e.g. fanglomerates; Robertson, 1990). Regional uplift was focused under Mt. Olympus due to a combination of serpentinite diapirism and continued underplating along the Cyprean arc (Kinnaird *et al.*, 2011). Compression occurred locally along the northern margin of Troodos leading to the thrusting of Kyrenia to near vertical. Fanglomerates formed, and continue to form radially centred around Mt. Olympus (Robertson and Woodcock, 1980; Robertson, 1990).

The progressive emergence of Cyprus is preserved in the sedimentary succession that overlies the Troodos ophiolite. Sediments indicate a transition in water depth from a deep to shallow marine environment followed by the subaerial emergence of Troodos (e.g. Clube and Robertson, 1986; Robertson and Xenophontos, 1993). The ophiolite is directly overlain by Turonian aged chemical sediments of the Peraphedi formation that are in turn overlain by Campanian-Maastrichtian aged bedded radiolarian cherts, bentonites and volcanoclastic sandstones of the Kannaviou formation (Robertson 1975; Clube and Robertson, 1986). The absence of carbonate-rich sediments in both the Peraphedi and Kannaviou formation indicates their formation in deep water below the carbon compensation depth (CCD) (Robertson and Hudson, 1973). This suggests that during the Late Cretaceous that Troodos remained in a deep-water environment approximately 3500 m deep.

### 2.3 Troodos Crustal Stratigraphy

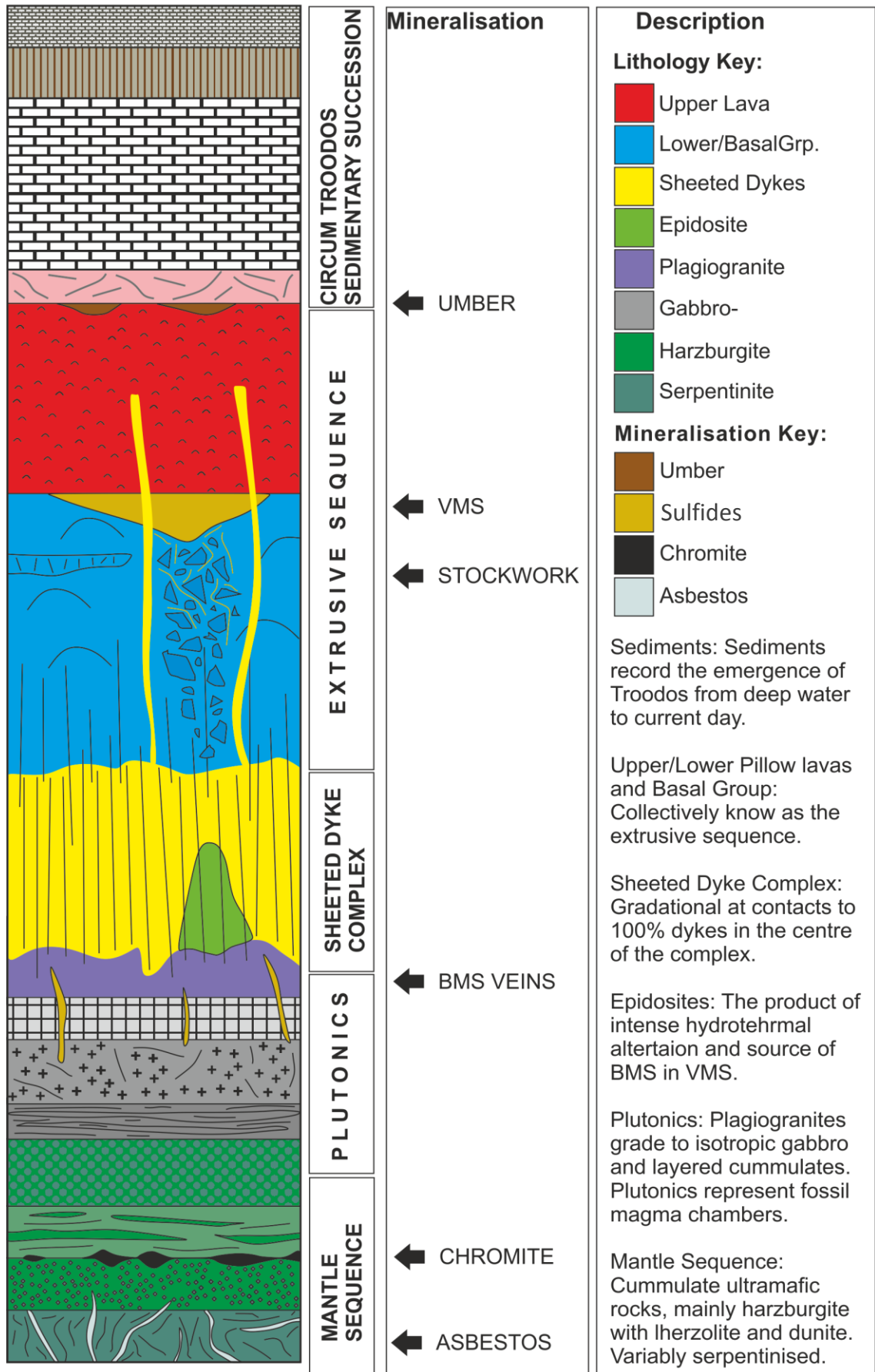


**Figure 2.5:** Simplified stratigraphic section of the Troodos oceanic lithosphere and sediments (\*not to scale\*).

The aim of the forthcoming section is to outline the main lithological units of the Troodos ophiolite. Various classification schemes have been proposed for each unit based on different attributes over many years of research, a summary is provided in the subsequent section. The section progresses in stratigraphic succession from the extrusive sequence to mantle lithologies.

### 2.3.1 The Extrusive Sequence

Collectively the extrusive sequence incorporates three main lithological units: Upper Pillow Lavas (UPL), Lower Pillow Lavas (LPL) and Basal Group (BG) lithologies (Wilson, 1959). The extrusive sequence is exposed at the periphery of the ophiolite, most extensively in the eastern area (Figure 2.1). Classification of the extrusive sequence includes: field observations (Wilson and Ingham, 1959), metamorphic grade (Gass and Smewing, 1973) and lava geochemistry (Robinson and Malpas, 1990), but no single classification has been wholly adopted. The author acknowledges that the UPL/LPL division is arbitrary and that the boundary between the two lithologies is discrete and in some areas continuous. However, these issues notwithstanding the author retains the use of the original classification into UPL/LPL and BG lithologies for the remainder of this thesis (Chapters 5-10). A brief rationale for each classification is outline below.

#### 2.3.1.1 Early subdivision based on field evidence

The Geological Survey Department (GSD) of Cyprus originally classified the extrusive sequence of the Troodos ophiolite into the Upper Pillow Lavas (UPL), Lower Pillow Lavas (LPL) and the transitional Basal Group (BG) horizon between the Sheeted Dyke Complex (SDC) and LPL. The pillow lavas are extensively exposed around the periphery of the ophiolite (Figure 2.8 A and G); most extensively and continuously on the northern and southern flanks of Troodos (Carr and Bear 1960; Gass 1960). These early classifications were based on field observations that appeared, at the time, continuous across the entire ophiolite.

The UPL are described as black to earthy brown, occurring as pillows that are generally small <1 m wide with rare sheet flows and dyke intrusions. Typically, the UPL are olivine phyric with phenocrysts commonly argillised to clay minerals (Carr and Bear, 1960; Gass, 1960).

The lower pillow lavas are blue-grey in colour (Figure 2.8A), aphyric and silica over-saturated. The dominant lava morphology is pillows >1 m wide, lava domes, hyaloclastites and sheet flows exhibiting well-developed columnar jointing. Dyke abundance increases to 30-50% in deeper regions as the basal group transition is approached. Alteration mineralogy is largely celadonite and chalcedony dominated (Figure 2.6; Gass, 1960).

The Basal Group is a transitional horizon between the extrusive sequence and the SDC. The boundary is marked by increased dyke abundance (Figure 2.5; 80-90 %) and the transition to

greenschist facies metamorphic conditions (Gass and Smewing, 1973; Gillis and Robinson, 1990). Pillow screens locally occur accounting for approximately 10% of surface outcrops but diminish to zero at depth (Gass and Smewing, 1973). The transition between BG and SDC lithologies is variable over a depth of several hundred metres (Schouten and Kelemen, 2002).

### 2.3.1.2 Extrusive rocks divided by alteration facies

Gass and Smewing (1973) base their classification of the extrusive sequence on alteration minerals, they noted that the boundary between the UPL and LPL was marked by a discontinuity in metamorphic grade (Figure 2.6). This led them to suggest that the UPL and LPL could have been erupted at different times, with the least altered UPL post-dating the eruption of the altered LPL. However, later studies have shown that the metamorphic boundary between the UPL and LPL is gradational and laterally discontinuous, varying spatially with lava morphology and thickness (Gillis and Robinson, 1990). Both upper and lower pillow lava units contain minerals indicating zeolite facies metamorphic grade (<200°C – Figure 2.6). The UPL stratigraphy is dominated by natrolite, gmelinite and smectite grading to heulandite, stilbite, celadonite and chalcedony in the LPL (Figure 2.6). The transition to BG lithologies marks the onset of greenschist facies metamorphic conditions. The boundary is sharp transitioning over 10-50 m (Gass and Smewing, 1973). Mineralogically the transition from the BG to dykes is marked by the appearance of titanite, quartz, pyrite and epidote (Gass and Smewing, 1973; Gillis and Robinson, 1990).

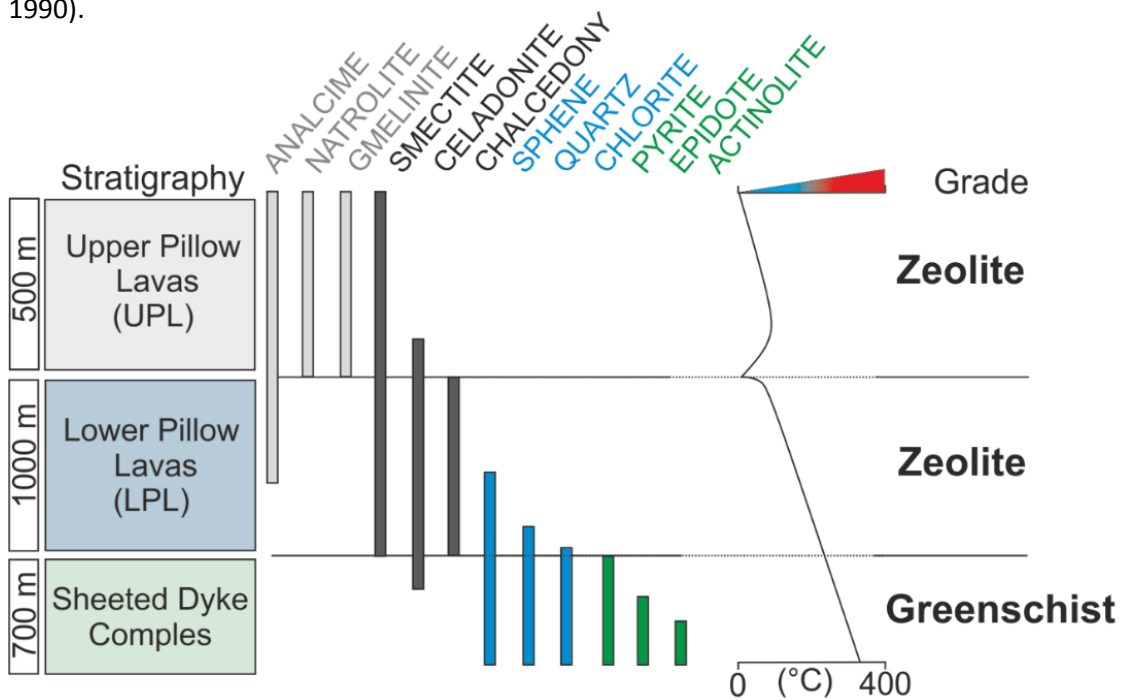


**Figure 2.6:** Common mineral assemblage associated with hydrothermal alteration throughout the Troodos upper crustal stratigraphy (after Gass and Smewing, 1973).

### 2.3.1.3 Subdivisions based on lava geochemistry

Later geochemical investigation of the extrusive sequence focused on the Akaki River section and redefined the classification of the extrusive sequence based on TiO<sub>2</sub> content of volcanic glass (e.g. Robinson *et al.*, 1983; Schmincke *et al.*, 1983). Subsequently, lavas were classified into the high and low TiO<sub>2</sub> suites. Schmincke *et al.* (1983) found no consistent relationship between either metamorphic grade (Gass and Smewing, 1973) or the UPL and LPL classification (e.g. Gass, 1960) of the lavas. Whilst geochemically continuous, the UPL can be broadly classified as the 'low Ti suite' with TiO<sub>2</sub> contents <0.4 wt.% and the LPL as the 'high Ti suite' with TiO<sub>2</sub> contents >0.8 wt.% (Robinson and Malpas, 1990).

## 2.4 The Sheeted Dyke Complex

The Sheeted Dyke Complex (SDC) is extensively exposed for over 70 km perpendicular to strike (Gass, 1968). Dyke abundance increases from 30-50% in the lower BG to 100% in the centre of the SDC (Figure 2.5: Gass, 1990). Individual dykes range from 0.1-3 m wide, are fine-grained and aphyric (Figure 2.8D; Gass, 1990). Chilled margins are ubiquitous in the SDC and locally preserve one-way chilling reflecting the intrusion of dykes around a central loci (Kidd and Cann, 1974). Ultimately the one-way chilling preserved within the sheeted dykes is flawed as we now understand crustal accretion to be much more complex with local eruptive centres. Furthermore, the sample size analysed by Kidd and Cann (1974) was probably inadequate to represent ophiolite wide processes. The transition between the SDC and upper plutonics is gradational over several metres; a small number of dykes are observed cross-cutting gabbroic bodies indicating that dyke formation was not mutually exclusive with the formation of the upper plutonics (Gass, 1990).

Dykes act as a conduit for the ascent of magma from the plutonics to the seafloor feeding the extrusive sequence stratigraphically above. The now rotated SDC would have originally been intruded vertically during seafloor spreading (Cooke *et al.*, 2014; Varga, 1991). The SDC has subsequently been divided into nine structural domains based on average dyke strike and dip (Varga, 1991- see Chapter 5). The dominant strike direction of dykes is NNE-SSW with the exception of the Arakapas, Polis and south Mitsero domains where, for example, the transform terrain is intersected (Varga, 1991; Varga and Moores, 1990).

The geochemistry of the dykes, as with the pillow lavas can be divided into two discrete, but in some instances continuous groups based on TiO<sub>2</sub> content; the high and low Ti series (Staudigel *et al.*, 2000: Figure 2.7). Two discrete trends within the sheeted dyke complex are identified, broadly correlating with those suggested by Schmincke *et al.* (1983) for overlying lava units

(Figure 2.7). The low TiO<sub>2</sub> series (corresponding to the UPL; <0.8% TiO<sub>2</sub>) are basaltic to basaltic andesites in composition and depleted in compatible elements whilst the high Ti suite comprises basaltic andesites to rhyolites (Staudigel *et al.*, 2000). Approximately 20% of dykes correspond to the low TiO<sub>2</sub> 'UPL' series (Figure 2.7; Baragar *et al.*, 1990; Schouten and Kelemen, 2002).

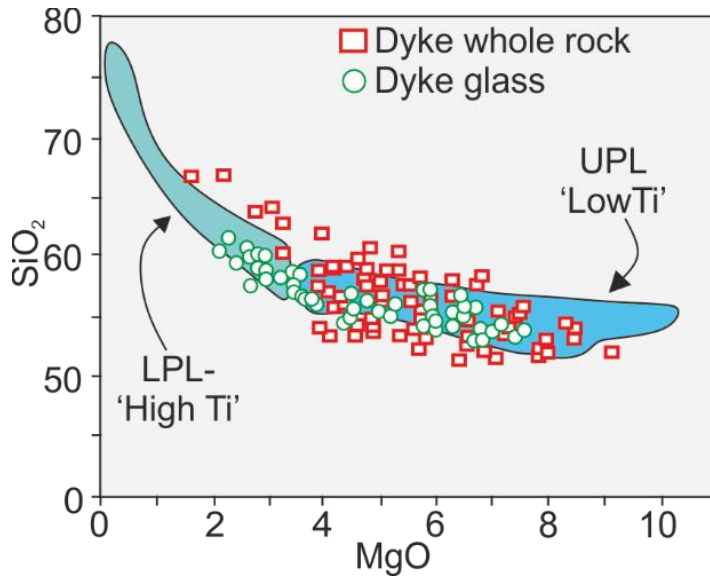


**Figure 2.7:** Comparison between dyke and lava geochemistry. The UPL and LPL suites are definable within the SDC. MgO and SiO<sub>2</sub> are in % (after Staudigel *et al.*, 2000).

## 2.5 The Plutonic Sequence

The Plutonic complex of Troodos is broadly subdivided into high-level intrusives (e.g. plagiogranites), isotropic gabbros and the cumulate sequence (Gass, 1980). Plagiogranites are tonalitic to trondhjemitic in composition and are interpreted to represent differentiated (through fractional crystallisation) shallow melt lenses that directly underlie the SDC (Freund *et al.*, 2014). Alternatively, they formed through the assimilation of hydrated SDC material by an originally gabbroic body during magma ascent (Grimes *et al.*, 2013). Plagiogranites outcrop irregularly between gabbros and the SDC at several localities (Freund *et al.*, 2014; Gass, 1980: Figure 2.1). Plagiogranites are equigranular, fine to medium grained with a mineralogy consisting of quartz, plagioclase, amphibole ± titanite, epidote, clinopyroxene, magnetite, zircon and apatite (Freund *et al.*, 2014). Plagiogranites located at fracture fronts between the SDC and gabbros exhibit evidence of hydrothermal alteration with secondary quartz, epidote and amphibole indicating upper greenschist to amphibolite facies metamorphism associated with >350°C hydrothermal fluids (Freund *et al.*, 2014; Gillis and Roberts, 1999). Highly saline brine inclusions are preserved in plagiogranites attesting to deep seated hydrothermal fluid circulation and volatile phase exsolution (Gillis and Roberts, 1999).

The majority of the plutonic sequence is medium to coarse grained gabbro and olivine gabbro. Mineralogy is dominated by plagioclase, enstatite and pyroxene (Thy, 1987; Vine and Smith,

1990). The homogenous nature of the gabbros and inter-fingering between olivine-rich gabbros suggests melts were generated by multiple magma influxes intruded at different levels of the lower crust (Abelson *et al.*, 2001).

The cumulate sequence is located at the complex boundary between homogenous gabbro and tectonised harzburgite delineating the transition to mantle lithologies (the 'petrological Moho'). Cumulates of the lower crust are extremely heterogeneous ranging from dunite at the base through wehrlite and pyroxenite to gabbro (Figure 2.5) (George, 1978; Thy, 1987). Cumulates exhibit laminar fabrics formed by crystal segregation during fractional crystallisation or mush segregation (Gass, 1980; Greenbaum, 1977). The early cumulate sequence comprises gabbros and pyroxenites exhibiting a well-developed tectonite fabric and small-scale isoclinal folds (Figure 2.8D) (Banks, 2004). The strong tectonite fabric in the early cumulate suite is interpreted to have formed during seafloor spreading (Abelson *et al.*, 2001; Banks, 2004; George, 1978; Thy, 1987). The late cumulate sequence comprises poikilitic wehrlites and gabbro-norites with rare layering and no evidence of high temperature ductile foliation; thus, they formed late (Banks, 2004). The occurrence of wehrlite indicates a hydrous melt source and provides further evidence for the supra-subduction zone origin for the Troodos ophiolite (George, 1978) (cf. section 2.11).

## 2.6 The Mantle Sequence

The mantle section of Troodos outcrops at the topographically highest point; Mt. Olympus (1950 m). Harzburgites make up around 80% of the total mantle outcrop and are suggested to have formed from a plagioclase lherzolite melt from which basaltic melts have been extracted; a depleted mantle source (Gass, 1980; George, 1978; Greenbaum, 1972). This is supported by the occurrence of discrete plagioclase lherzolite pods within harzburgite. The remaining 20% of outcrop is dunite, lherzolite and gabbro-pyroxenite occurring as subordinate bodies most notably in the W of the Troodos Mantle Sequence (Gass, 1980).

The central eastern Mantle Sequence has undergone pervasive serpentinisation centred on the Amiandos Fault, while the western portion remains largely un-serpentinised comprising discrete dunite, lherzolite and harzburgite with associated podiform chromites (Gass, 1980). Chrysotile is typically mesh textured suggesting lizardite is the dominant serpentine mineral (Nuriel *et al.*, 2009).

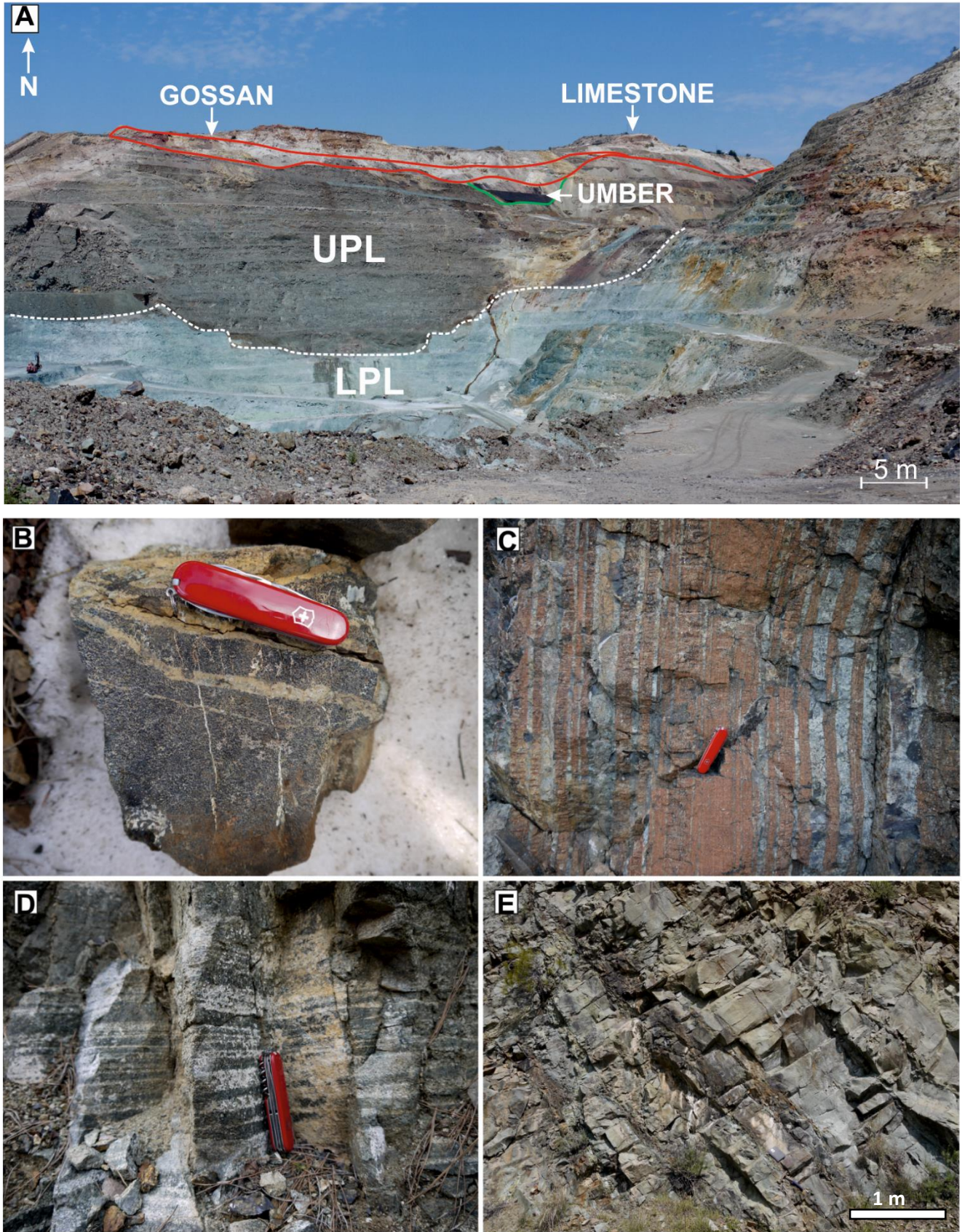


**Figure 2.8:** Examples of Troodos stratigraphy (explanation overleaf).

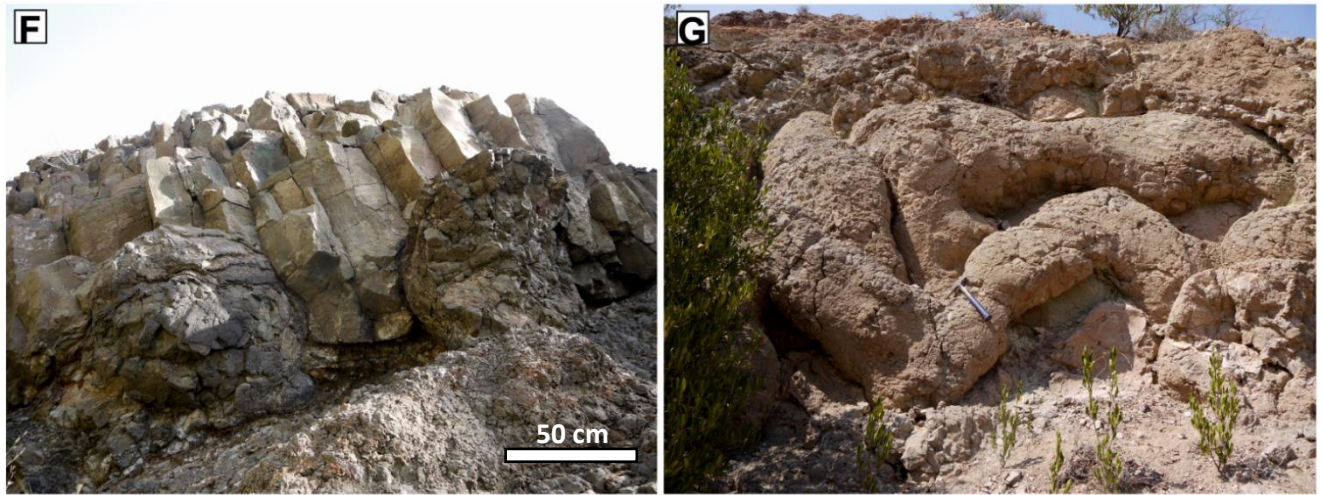


**Figure 2.8:** Examples of Troodos stratigraphy

- A. Sediment-UPL-LPL at Skouriotissa mine. UPL are dark grey and separated from LPL by Phoucasa fault.
  - B. Example of semi-massive chromite from Kokkinorostos cross-cut by serpentinite veins.
  - C. Layered cumulate harzburgites and dunite, E of Mt. Olympus, near Amiandos.
  - D. Cumulate layered mafic-ultramafics with foliation and folding. Platres, central Troodos.
  - E. Sheeted dyke complex, massive dolerite dykes with minor disseminated pyrite and epidote.
  - F. Lower pillow lava, Apliki Mine. Flow engulfs pillows.
  - G. Upper pillow lava Troulloi; small well-formed lava tubes.
- (\*pen knife is 8 cm long, hammer is 40 cm long)

## 2.7 Spreading Structure

Sheeted dykes were originally intruded vertically at the fossil spreading axes with dykes exploiting planes in the direction of least stress i.e. parallel to the spreading axis ( $\sigma_2$ ). Present day dykes trend approximately N-S indicating an E-W palaeo spreading orientation (Figure 2.9). Using the structural orientation of the dykes, nine structural domains have been recognised in Troodos (Figure 2.9; Moores *et al.*, 2000). Opposing dyke dips delineate three major graben structures as defined by regions of sheeted dykes with consistent dip directions dipping away from each other, abruptly flipping polarity to the opposing dip direction across a discrete graben 'axis' (Varga and Moores, 1985; Varga, 1991; Moores *et al.*, 2000). Dietrich and Spencer (1993) note that extension in Troodos is accommodated via a network of small-scale normal faults that formed in close proximity to the ridge axis. These small-scale faults often truncate along larger low angle planar faults (i.e. detachments) that accommodate rotation of upper crustal blocks (Dietrich and Spencer, 1993). On the northern flank of Troodos three grabens are distinguishable, from W-E these are; the Solea, Mitsero and Larnaca grabens (e.g. Varga and Moores, 1985; Dietrich and Spencer 1993).

Troodos exhibits structural characteristics akin to modern intermediate to slow spreading centres (e.g. Varga and Moores, 1985; Allerton and Vine, 1987). In particular characteristics such as detachment faulting (e.g. the Kakopetria detachment) and rotation of upper crustal blocks suggest spreading was not solely accomplished by magmatism but also by crustal thinning and extension via faulting (Dietrich and Spencer, 1993; Nuriel *et al.*, 2009; Varga and Moores, 1990). However, several possible scenarios have been proposed in an attempt to reconstruct the spreading environment of Troodos. These are discussed in sections 2.7.1 and 2.8.

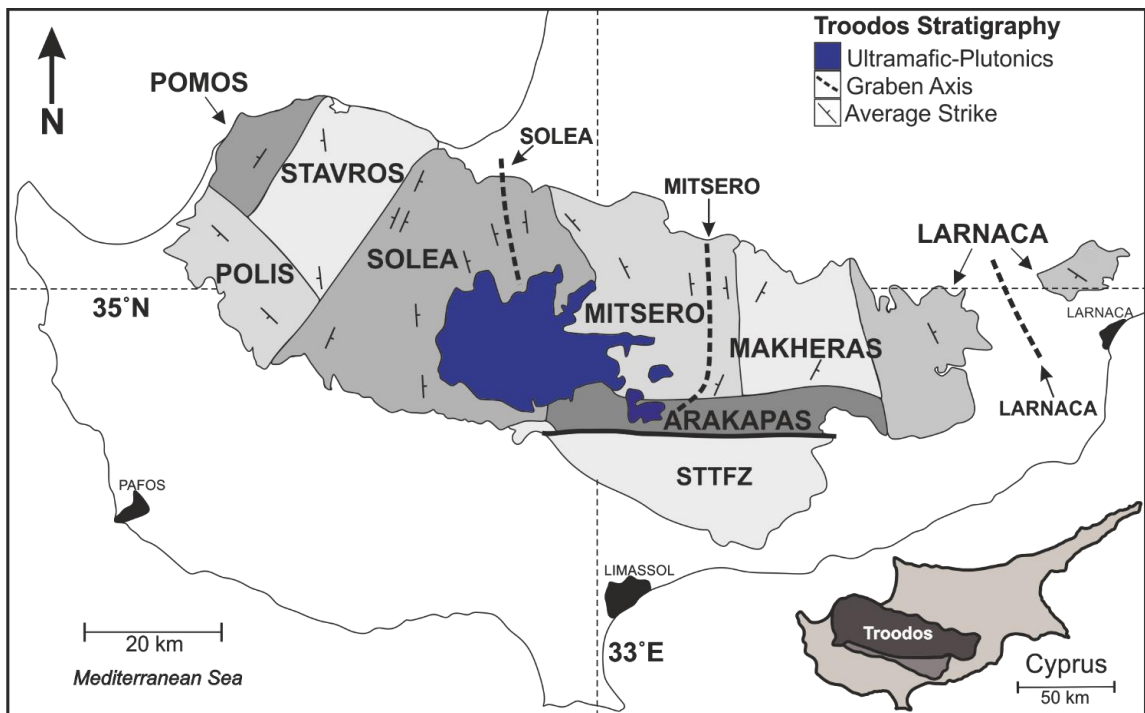


**Figure 2.9:** Summary of structural domains classified by dyke dip and strike for the Troodos ophiolite (after Varga and Moores, 1985).

### 2.7.1 Fossil ridge axes

Early interpretations on the origin of grabens made by Varga and Moores (1985) proposed that the three grabens represented fossil ridge axes that formed during active seafloor spreading. Cross-cutting relationships where low-angle rotated dykes are cross-cut by later vertical dykes support an on axis origin for graben formation. Varga and Moores (1985) propose successive ridge jump events from W to E explaining the migration of spreading between different ridge axes. This assumption is based primarily on the asymmetrical nature of the grabens; they are significantly wider on the western margin than the east (Hurst *et al.*, 1994). Varga and Moores (1985) suggest that all three grabens formed on axis and that the spreading axes progressively young toward the E. This is supported by intrusive relationships at the graben boundary between the Solea and Mitsero domains where Mitsero dykes are cross-cut by younger Solea dykes. Hurst

*et al.* (1994) also suggest an on-axis origin for the Solea graben. They note the significance of detachment faulting to the W of the Solea axis where normal dykes are rotated along axial parallel normal faults that sole along detachment faults at depth (e.g. The ‘Kakopetria’ detachment- Figure 2.10). This leads to the rafting of blocks of sheeted dyke material as they progressively move away from the ridge axis (e.g. Young, 2014). Crucially these axial parallel normal faults have been shown to host volcanogenic massive sulfide deposits (Varga and Moores, 1985). The on axis origin for both Mitsero and Solea grabens is, however, controversial with later work by Allerton and Vine (1987) and Everdingen *et al.* (1995) suggesting an ‘off axis’ origin for the Solea and Mitsero grabens respectively (cf. section 2.7.2).

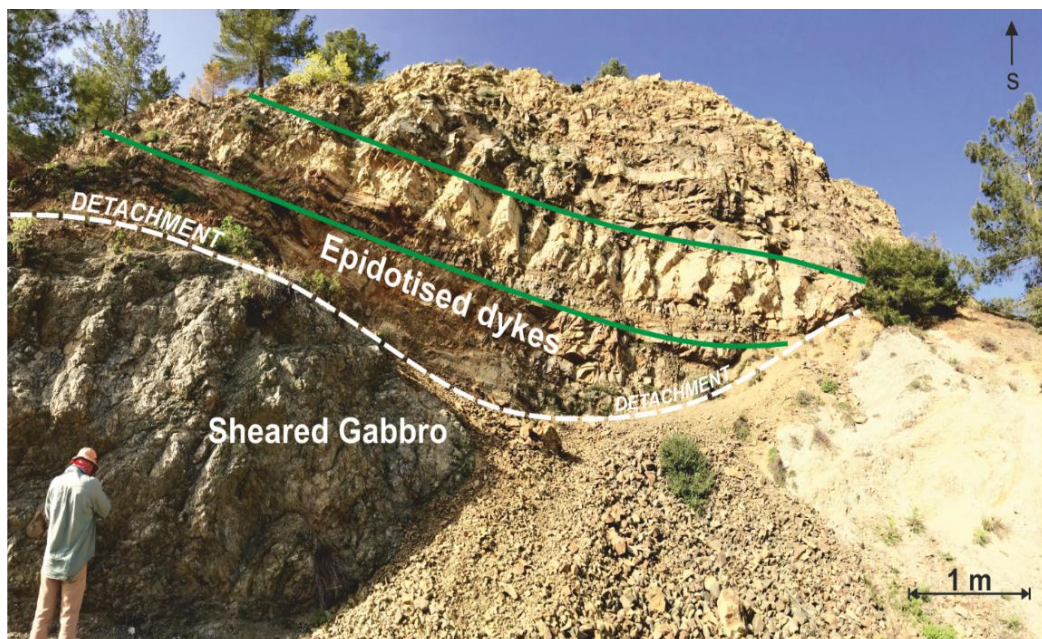


**Figure 2.10:** The ‘Kakopetria’ detachment. Sub-horizontal epidotised dykes above gabbro mylonites. Detachment surface is marked by dashed white line (Village of Kakopetria, Solea domain, Troodos).

### 2.7.2 Off axis graben formation

An alternate hypothesis for the formation of grabens off axis was proposed by Allerton and Vine (1987) for Solea and Everdingen *et al.* (1995) for Mitsero. Allerton and Vine (1987) prefer the formation of the Solea graben on the flank of a ridge (Figure 2.11). Palaeomagnetic investigation of the sheeted dyke complex demonstrate that rotation of the sheeted dykes was consistent with axial tectonics that were later reactivated to accommodate stretching as the crust moved away from the spreading axis. Asymmetrical grabens are expected to develop as antithetic structures to the main ridge (Young, 2014; Figure 2.11).

Everdingen *et al.* (1995) also propose an off axis origin for the Mitsero graben. Graben boundaries are defined based on spatial variations in dyke attitude. In contrast to earlier work by Varga and Moores (1985) who find the eastern boundary between the Mitsero and Makheras

domains to be sharp (i.e. a change in dip and strike), Everdingen *et al.* (1995) state that strike direction remains consistent across the boundary to the neighbouring Makheras domain.

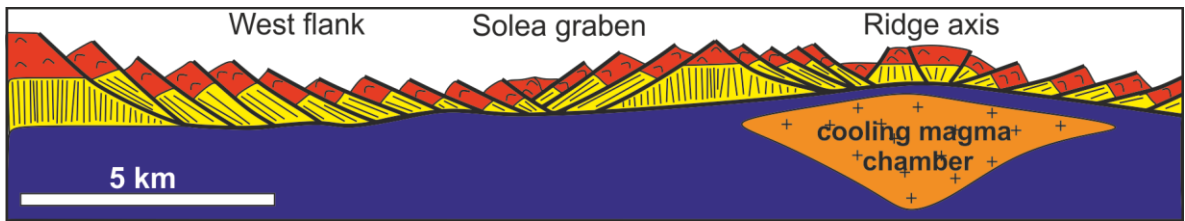


**Figure 2.11:** Interpretation of the Solea graben as an antithetic off axis structure from the main ridge (i.e. Mitsero) to the east of Solea. Fault = thick black line, red = pillow lava, yellow = SDC, blue = plutonics-mantle (after Allerton and Vine, 1987).

This led Everdingen *et al.* (1995) to suggest that the change in dyke attitude between the Mitsero and Makheras domains is a function of off axis graben formation, i.e. dyke rotation in response to stretching, accounting for the uniform strike but variable dyke dip direction across the Mitsero -Makheras domain boundary. This implies that the Mitsero-Makheras domain formed contemporaneously and that the Mitsero graben was superimposed in older 'off axis' crust. This contradicts the earlier findings of Varga and Moores (1985) where the margin of the Mitsero domain should demonstrate a cross-cutting intrusive relationship consistent with later magmatism associated with the Larnaca graben if the graben structures progressively young toward the E.

The pattern of epidote formation, the highly leached source rocks that provide a possible metal source for VMS deposits (cf. Chapter 3), are expected to be symmetrical in relation to the graben axis and underlying heat source. In Mitsero epidotes appear asymmetric in relation to the graben axis (Everdingen *et al.*, 1995). However, Troodos is fed by multiple small magma chambers and not one single melt lens, therefore the pattern of epidotisation is unlikely to be uniform as suggested by Everdigen *et al.* (1995) but instead should vary spatially in response to localised intrusions as epidotes only form in areas of high heat flux. Therefore, it is questionable if the symmetry of epidotes is a reliable proxy for assessing the origin of graben formation.

Whilst there is no visible evidence of detachment faulting in Mitsero, Everdingen *et al.* (1995) and Agar and Klitgord (1995) infer the probable location of a detachment surface at Mitsero to be deep in the crust i.e. below the sheeted dyke-plutonic boundary as observed by Hurst *et al.* (1994) for Solea. The location of a detachment surface deeper in the stratigraphy, possibly within the plutonics suggests that the underlying rocks had cooled prior to graben formation, further supporting an off axis origin for Mitsero. However, the nature of this boundary and indeed the

occurrence of a detachment surface remains unclear, with Gillis (2002) reporting an intrusive and not faulted relationship between the plutonics and dykes at the base of the Mitsero crust.

The rate and migration of spreading between grabens remains poorly constrained. Allerton and Vine (1987) prefer an intermediate to slow spreading rate as seafloor topography is subdued and does not show signs of extensive faulting (i.e. scarps), whereas Varga and Moores (1990) prefer a slow-spreading rate due to well defined graben structures that indicate clear periods of crustal thinning that are subsequently infilled by late 'off axis' lavas (see section 2.8).

The absence of high-precision dating makes the exact evolution of spreading in Troodos hard to assess; this has important implications for our understanding of metal mobilisation. For example, renewed magmatism in 'old' crust has been shown to be important in ore formation. Eddy *et al.* (1998) link the late intrusion of gabbro into older 'off axis' crust in the inter graben zone between Solea and Mitsero with the formation of the Memi and Alestos ore deposits (Appendix 3.1). Whilst this process was localised over an area a few km<sup>2</sup> it highlights the significance of intrusive relationships at the margins of individual graben domains. For example, the overprinting of old, cold, permeable Mitsero crust by newly formed Larnaca crust (?) would probably have led to renewed hydrothermal activity in discrete corridors along the graben boundary.

The exact nature of spreading at Troodos remains unclear. From the author's field experience, the formation of grabens in an on axis position after Varga and Moores (1985) seems more likely. All models that hypothesise an off axis origin for grabens fail to adequately account for VMS mineralisation that must have formed on axis as the heat flow off axis would not have been sufficient to drive VMS formation (e.g. Everdingen *et al.*, 1995). Therefore, the off axis model for the formation of Mitsero fails to explain the occurrence of major VMS that demonstrate a clear spatial relationship to graben bounding faults.

## 2.8 Crustal accretion

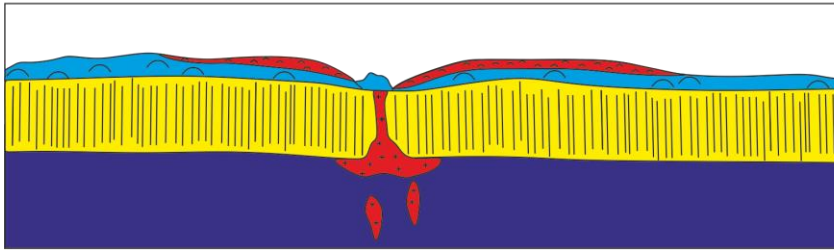
Several competing hypotheses have been developed to unify field observations, metamorphic grade and geochemical stratification related to crustal accretion and spreading dynamics of the Troodos extrusive sequence (section 2.3 and 2.9). These include; Non-steady state accretion (Varga and Moores, 1990), localised eruptive centres (Gass and Smewing, 1973), melt viscosity (Schouten and Kelemen, 2002) and oceanic core complex formation (Nuriel *et al.*, 2009). Additionally, this study summarises a recent holistic study by Young (2014) utilising geochemistry, volcanology and structural observations of the Troodos extrusive sequence.

### 2.8.1 Non-steady state accretion

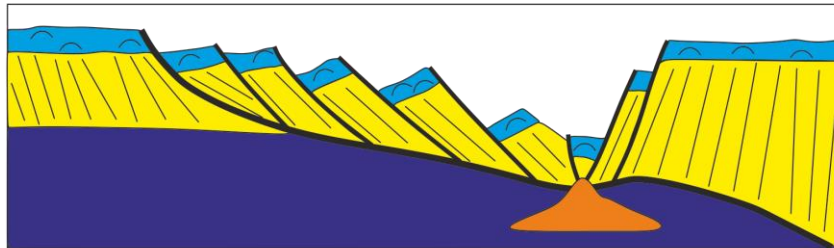
Varga and Moores (1990) proposed a “non-steady state” accretion model for the Solea graben. This style of magmatism interspersed with tectonic stretching and thinning is commonly observed in slow spreading environments where magma supply is sporadic. This model accounts for the cross-cutting relationships observed in the Solea graben where vertical dykes cross-cut steeply rotated dykes, signifying periods of faulting and tectonism followed by renewed magmatism (Varga and Moores, 1985). This model has merit as it effectively explains the location of VMS along major faults. For example, VMS located distally to the inferred ridge axis such as Apliki (Appendix 3.1; Chapter 6) are dissected by later faults that probably formed during crustal thinning. This led to the progressive fragmentation of VMS as they migrated away from the spreading axis (Figure 2.11).

This model is summarised into the following three stages (Figure 2.12 overleaf):

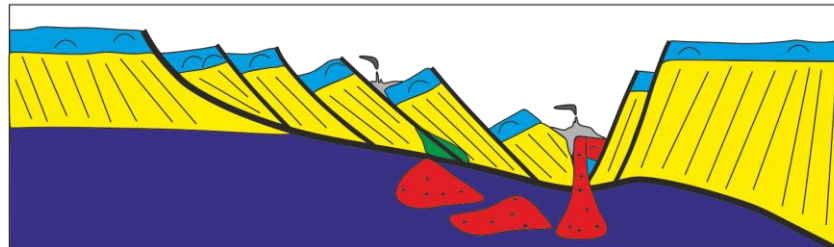
1. **Magmatic spreading.** Crustal accretion accomplished through plutonism and dyke injection. Cross-cutting dykes and normal fault development is absent; magmatism keeps pace with spreading (Figure 2.12A).
2. **Tectonic extension.** Formation of the Solea graben during cessation of magmatism. Crustal extension and thinning accommodated via normal axial parallel faults and development of ‘bookshelf faulting’ (e.g. Varga *et al.*, 1999); rotation of SDC away from vertical (Figure 2.12B).
3. **Renewed magmatism, hydrothermal alteration and ore deposition.** Normal faults provide deep seated permeability pathways whilst renewed magmatism provides a heat source driving hydrothermal circulation and VMS formation. Late vertical dykes are observed cross-cutting early, rotated, epidotised dykes (Figure 2.12C).

**A. Magmatic spreading**

Magmatism keeps pace with extension at Solea (1-1.5 cm/yr). VMS formation potential is low as normal fault systems are not developed

**B. Graben formation**

Magmatism decreases and extension is achieved through graben formation and tectonic stretching. Sheeted dykes undergo 'bookshelf' rotation. Normal faults dip away from ridge axis.

**C. Renewed magmatism**

Renewed magmatism and VMS formation. Hydrothermal fluids exploit graben bounding faults forming VMS deposits driven by renewed magmatic heat source. Epidosites form in SDC.



**Figure 2.12:** Non steady state spreading in Troodos (after Varga and Moores, 1990)

This model does not adequately explain the subdued seafloor topography observed in Troodos. At modern slow spreading centres e.g. the Mid Atlantic Ridge, significant seafloor topography dominated by fault scarp formation is common. The model fails to explain why most areas are infilled with 'off axis' UPL lavas (see section 2.8.4). Furthermore, the absence of any evidence of large-scale fault scarps on the seafloor, i.e. talus piles, is a key flaw.

## 2.8.2 Localised eruptive centres

Crustal accretion of the extrusive sequence is complex and divided into on axis and off axis lava suites that are broadly equivalent to the LPL and UPL classification outlined previously (Gass and Smewing, 1973). The distinctive, sharp nature of the contact between the UPL and LPL has been interpreted as an unconformity by Gass and Smewing (1973). Upper pillow lavas that occur overlying basal and LPL lithologies have been metamorphosed to greenschist facies metamorphic grades whilst the overlying UPL are un-metamorphosed (Gass and Smewing, 1973). Additionally, feeder dykes often truncate at the UPL/LPL boundary and sulfide conglomerates occur at the contact; hence the interpretation of the UPL-LPL boundary as an unconformity (Gass and Smewing, 1973).

Gass and Smewing (1973) viewed the LPL and the underlying SDC as cogenetic; they formed in close proximity to the ridge axis. According to Gass and Smewing (1973) the UPL formed away from the ridge axis and are unrelated to the main 'on axis' crustal accretion phase. The abrupt nature of the contact and, in some instances, presence of conglomerate at this boundary suggests that a period of submarine erosion occurred between the accretion of the 'on axis' LPL-BG and the 'off axis' UPL.

Gass and Smewing (1973) proposed that the UPL may represent off axis seamounts; however, their morphology is inconsistent with this observation. Instead the UPL infill and blanket the LPL and lack evidence of clear eruptive centres in the form of pillow mounds. Furthermore, the boundary between the off and on axis lava suites is diffuse in some areas (e.g. Schminke *et al.*, 1983). Eruption of the UPL 'off axis' is inferred to have occurred relatively near to the axis as no sediment, including the metalliferous sediments of the Peraphedi formation (umbers) are preserved along the contact (Gass and Smewing, 1973).

The UPL (low Ti) are suggested to have formed temporally later than the on axis LPL (high Ti) suite (e.g. Pearce and Robinson, 2010). The progressive enrichment in LREE in the low Ti suite is interpreted to represent the initiation of subduction and the subsequent transition in lava geochemistry from an early tholeiitic trend towards a boninitic trend (Pearce and Robinson, 2010). If this scenario was true then low Ti dykes would exclusively cross-cut high Ti dykes and this is not observed (e.g. Baragar *et al.*, 1990; Staudigel *et al.*, 2000; Young, 2014). Additionally, Young (2014) report syn-tectonic tilting of the entire lava stratigraphy suggesting that both lava suites were erupted contemporaneously at or near the spreading axis and subsequently rotated as one unit during migration of crust away from the spreading axis (see section 2.8.4).

### 2.8.3 Melt viscosity

The physical characteristics of lava are attributed to the varied but different geochemical composition of the UPL and LPL; this effects eruption temperature and melt viscosity (Schouten and Kelemen, 2002). Melt viscosity has been proposed as an alternative mechanism explaining the stratification between the UPL and LPL suites. Geochemical studies of the SDC complex have identified dykes with both UPL (low Ti) and LPL (high Ti) affinities (Jowitt *et al.*, 2012; Schouten and Kelemen, 2002). Twenty percent of dykes correspond to the UPL classification with no clear age relationship between dyke geochemistry i.e. low Ti dykes do not exclusively cross-cut high Ti dykes. This evidence suggests that low and high Ti dykes are co-magmatic and were erupted by penecontemporaneous eruptions from adjacent fissures (Baragar *et al.*, 1990; Schouten and Kelemen, 2002). Conversely, it was not necessary, as suggested by Gass and Smewing (1973), for the eruption of the UPL (low Ti suite) to occur off axis. Instead both lava types could be

erupted on, or very close to the ridge axis but the UPL simply flowed further which led to the interpretation that they formed further off axis to begin with.

The physical evidence based on major element geochemistry of the lava suggest a pronounced difference in lava viscosity between the UPL and LPL. Upper Pillow Lavas had a viscosity of  $10^{1-2}$  Pa s (viscosity of warm corn syrup) whilst LPL were much more viscous at  $10^{3-4}$  Pa s (cold honey) (Schouten and Kelemen, 2002). In this model the eruption of the LPL was low volume but frequent and sourced from shallow, more highly fractionated crustal reservoirs. In contrast the UPL were formed from high volume (~6 times greater than LPL), infrequent eruptions derived from deep conduits of primitive cumulate lithologies (Schouten and Kelemen, 2002). The UPL may have been erupted on axis but due to their low viscosity and high-volume eruption meant they travelled further from the axial ridge. This led to the blanketing of LPL that previously formed on axis. In contrast, the LPL were erupted on axis but due to their high viscosity did not migrate to distal off axis regions (Schouten and Kelemen, 2002). This provides an effective argument explaining I) the sharp but in some areas transitional boundary between the UPL and LPL, II) the inclusion of erosional horizons and, c) geochemical and co-magmatic trends.

#### 2.8.4 Core complex formation

Serpentinisation played an important role in the emergence of Troodos but the timing and conditions under which serpentinisation occurred remain debated (Magaritz and Taylor, 1974; Nuriel *et al.*, 2009). The exhumation and serpentinisation of ultramafic lithologies on the seafloor at oceanic core complexes is documented at slow spreading ridge transform intersections (<80 km/Myr) (Cann *et al.*, 1997; Escartín *et al.*, 2008; Püthe and Gerya, 2014). Evidence for seafloor hydrothermal alteration along detachment faults bounding oceanic core complexes is widespread (Figure 2.13- Nuriel *et al.*, 2009). Troodos is no exception exhibiting widespread, possibly seafloor related serpentinisation of mantle lithologies. Serpentinisation is focused around the Amiandos Fault; a major axis parallel (Solea) detachment surface that juxtaposes gabbro and serpentinite (Magaritz and Taylor, 1974; Nuriel *et al.*, 2009).

The timing and source of serpentinising fluid remains debated; was serpentinisation seafloor or meteoric and uplift related? Nuriel *et al.* (2009) identify two distinct serpentinisation events: 'oceanic-type' hydrothermal (100-200°C) alteration initiated on the seafloor by the penetration of seawater during spreading, followed by a later pervasive low temperature 'ophiolite-type' serpentinisation event (50-80°C). Isotopic evidence supports this hypothesis as  $\delta^{18}\text{O}$  and  $\delta\text{D}$  (oxygen and hydrogen) exhibit bimodal distributions (Figure 2.13).

While it is accepted that subsurface serpentinisation occurs at the seafloor (e.g. Alt and Shanks 2003) and in extreme, usually slow spreading environments mantle rocks may be exhumed

forming oceanic core complexes (e.g. Smith *et al.*, 2006), there is little evidence of oceanic core complex formation in Troodos. It seems likely that given the scale of the Amiandos fault and the concentric pattern of serpentinisation radiating from the fault, with the western portion of the ultramafic sequence remaining relatively unaltered, that some serpentinisation occurred at the seafloor. However, if an oceanic core complex formed, as depicted schematically in Figure 2.13, then later sediments that overly the ophiolite would rest unconformably directly on serpentinite. Instead it seems more reasonable to assume the serpentinisation acted as a primer for later uplift that was facilitated by meteoric water ingress and that serpentinite was not exposed on the Cretaceous seafloor (Kinnaird *et al.*, 2011; Morag *et al.*, 2016; Robertson, 1977).

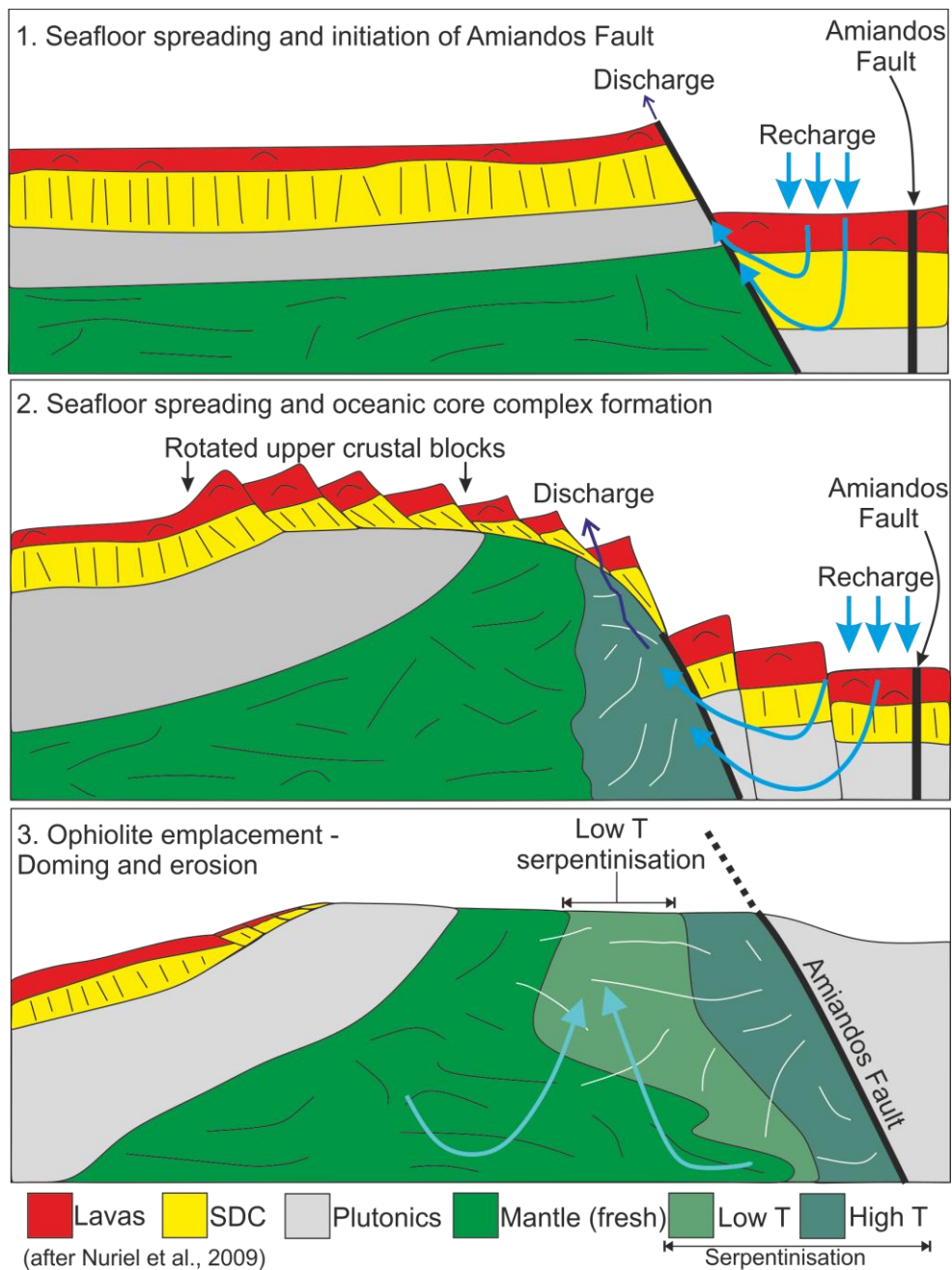


**Figure 2.13:** Oceanic core complex formation related to seafloor serpentinisation in Troodos. Not to scale (after Nuriel *et al.*, 2009).

### 2.8.5 A new perspective on graben formation

Recent studies combining detailed structural investigation, physical volcanology and lava geochemistry have advanced our understanding of the relationship between crustal accretion and spreading structure of the Troodos ophiolite (Young, 2014). New evidence suggests that the Troodos lava-sediment contact was significantly more subdued on the seafloor than initially thought (Figure 2.14); indicating seafloor topography that was formed during graben formation (i.e. fault scarps) was rapidly infilled as new crust was rafted off axis (Young, 2014).

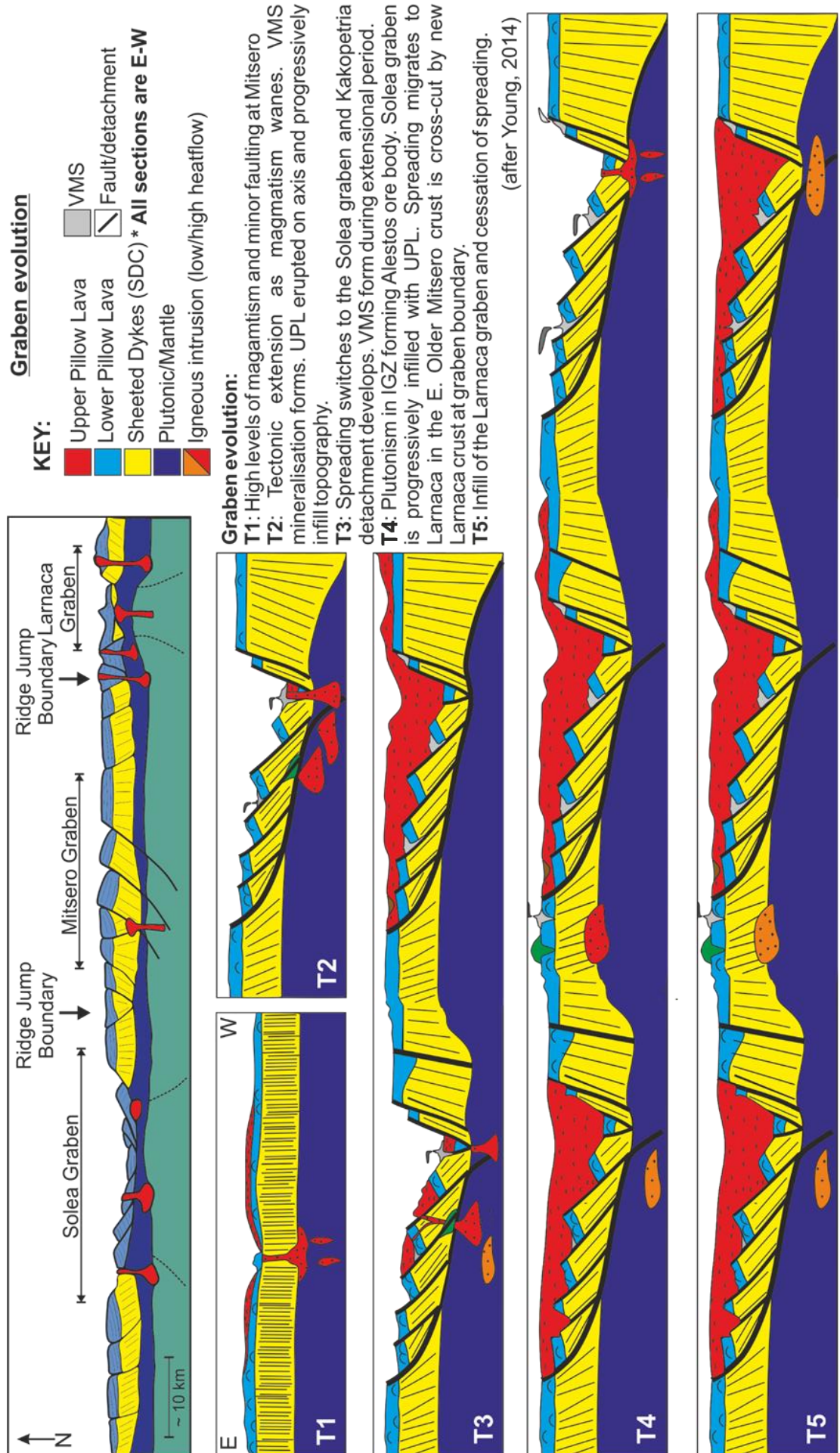
The UPL or low Ti lava suite most likely formed from ascending melt that by-passed the axial melt lens during ascent to the seafloor; Young (2014) suggest that these lavas were erupted in a 'near axis' position. This near but not on axis position adequately explains how these melts by-passed the axial melt lens, and are hence more primitive in composition, but in places exhibit a transitional geochemical signature with the on axis LPL suite (Young, 2014). Furthermore, a series of progressive angular unconformities within the extrusive sequence suggest the eruption of the UPL within the active fault terrain (i.e. close to the axis) and not 'off axis' as proposed by Gass and Smewing (1973) (Figure 2.14). In essence this study is a hybrid between previous studies by Schmincke *et al.* (1983) and Schouten and Kelemen (2002) as Young (2014) find no clear geochemical distinction between the two lava series but suggest melt geochemistry would have influenced their viscosity as previously suggested.

Large variations in the thickness and the progressive rotation of lower lava units in the Troodos extrusive sequence suggests the existence of large growth faults (Young, 2014). The topography of these seafloor near axis or valley wall faults has been shown to cause damming and ponding (thickening) of the lava stratigraphy. This explains the original classification of the lavas into UPL and LPL and the location of VMS exclusively (albeit wrongly) at the contact between UPL and LPL horizons (Constantinou, 1980). Instead, VMS formed along bounding faults and then were later covered by low viscosity UPL eruptions within the axial valley during the infilling of seafloor topography (e.g. Agrokippia VMS deposit) (Young, 2014).

The following model has been proposed by Young (2014) explaining the graben evolution of the Troodos ophiolite in Figure 2.14 overleaf.

**Figure 2.14 (overleaf):** Schematic summary of the evolution of spreading/crustal accretion of Troodos (after Young, 2014). Explanation in caption.

**T1:** Magmatic spreading at Mitsero, **T2:** Magmatism wanes and spreading is accommodated via normal faulting, **T3:** Spreading migrates to Solea and Kakopetria detachment forms, intrusion in IGZ and Alestos/Memi formation, **T4:** Migration of spreading to Larnaca, **T5:** Infill of Larnaca graben by UPL (further detail overleaf).



## 2.9 Faulting and hydrothermal alteration

Palaeomagnetism has been used in an attempt to constrain the timing of faulting relative to hydrothermal circulation and thus the timing of VMS formation. Progressive overprinting by hydrothermal fluid resets the original magmatic magnetic vector of dykes leading to the preservation of the magnetic inclination at the time of alteration (Allerton and Vine, 1987; Varga *et al.*, 1999). Dykes initially formed near vertical with a N-NNW strike and subsequently underwent rotation in the hanging wall of listric normal faults (see section 2.8.5) (Varga *et al.*, 1999; Varga and Moores, 1985). Two scenarios allow the relative timing of hydrothermal alteration to be established (Figure 2.15); scenario (A) is correct if epidiosites (and therefore VMS) formed prior to graben formation whilst (B) indicates epidiosite formation postdating extension and rotation (Varga *et al.*, 1999).

Palaeomagnetic data suggests that scenario A is most likely; all dykes exhibit the same demagnetisation vectors signifying epidiotisation occurred when dykes were vertical (Richardson *et al.*, 1987; Varga *et al.*, 1999). However, Varga *et al.* (1999) prefer a model whereby epidiosites did not form completely contemporaneously with dyke rotation but instead formed during the very early stages of graben formation. This would have been early enough that the magnetic vector of epidiosites is not noticeably different from surrounding dykes but not so late that dykes were completely rotated; i.e. somewhere between scenarios (Figure 2.15). When considering VMS formation, multiple authors have demonstrated the link between normal faulting and VMS mineralisation (e.g. Adamides, 2010a; Constantinou, 1980; Richardson *et al.*, 1987). Consequently, normal faulting and hydrothermal alteration must be at least coeval otherwise VMS would not exhibit an intimate relationship with spreading structure.

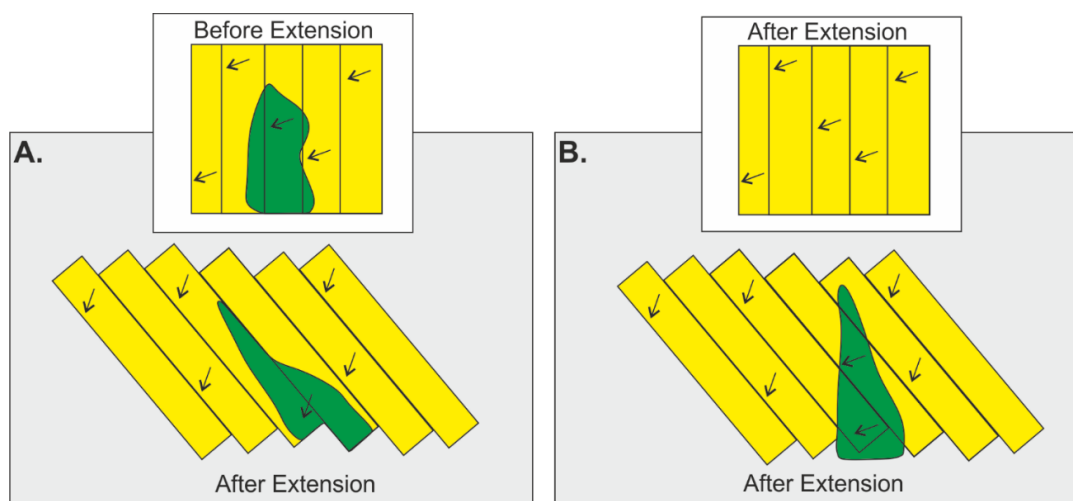


**Figure 2.15:** Timing of epidiotisation (and VMS formation) relative to crustal extension, graben formation and block rotation using palaeomagnetism. A) Epidiotisation before rotation B) Epidiotisation post fault rotation (after Varga *et al.*, 1999).

## 2.10 Supra-subduction zone origin

The Troodos ophiolite is generally regarded as having formed in a supra-subduction zone environment because of the unequivocal geochemical evidence for a fluid-enriched magmatic source (e.g. Fonseca *et al.*, 2017; Malpas, 1990; Miyashiro, 1973; Robinson *et al.*, 1983; Pearce *et al.*, 1984; Pearce and Robinson, 2010; Rautenschlein *et al.* 1985). This comes from several lines of evidence; for example the occurrence of 'ultra-depleted' boninites (e.g. Cameron *et al.*, 1979), the inclusion of calc-alkaline trend lavas (Miyashiro, 1973), the hydrous nature of Troodos glass (2-4 wt.% H<sub>2</sub>O), occurrence of wehrlite (e.g. Benn and Laurent, 1987; Muenow *et al.*, 1990), lava geochemistry (e.g. Rautenschlein *et al.*, 1985), isotopic evidence (e.g. Rautenschlein *et al.*, 1985; Rogers *et al.*, 1989; Yamaoka *et al.*, 2015), high oxygen fugacity magmas (Coogan *et al.*, 2003) and tectonic setting (e.g. Pearce *et al.*, 1984; Pearce and Robinson, 2010). While the exact configuration of subduction in late Cretaceous Neotethys remains unknown and is controversial (e.g. Robertson *et al.*, 2012; Maffione *et al.*, 2017), the crucial observation remains that the Troodos spreading centre formed above a subduction zone and not at an open-ocean MOR. Our best approximation of geodynamic setting is that Troodos formed in a nascent arc setting most likely during subduction initiation in a slab edge setting (Pearce and Robinson, 2010). As discussed in subsequent chapters this has important implications for the mineralising system.

## 2.11 Metallogensis

Ore deposits occur at different stratigraphic levels throughout the Troodos ophiolite (Figure 2.5). This section provides a brief outline of the mineral endowment of Troodos with VMS discussed in considerable detail in Chapter 3. In addition to hosting the type locality for mafic VMS, Troodos also hosts considerable asbestos, gypsum, industrial stone, chromite and minor gold mineralisation. The section progresses in stratigraphic order from mantle lithologies to the seafloor.

### 2.11.1 Asbestos

Asbestos mining started in Cyprus in 1904 and continued for over 80 years at the Amiandos asbestos mine located east of Mt. Olympus (Constantinou, 1980). Asbestos formed within the serpentinised portion of the ultramafic mantle sequence occurring primarily as veined chrysotile (Nuriel *et al.*, 2009). At its peak, over 40,000 tonnes of asbestos was exported from Amiandos per year (Figure 2.16) (Constantinou, 1980). In addition to its economic significance, serpentinisation of the Mantle sequence also played a fundamental role in the uplift and emergence of Troodos to its current elevation of 1950 m (Mt. Olympus) (section 2.2).

### 2.11.2 Chromite

Podiform chromite ( $\text{Cr}_2\text{O}_3$ ) is associated with dunite (Kannoures mine) and harzburgite (Kokkinorostos mine) in the mantle sequence of Troodos (Figure 2.16). Chromites outcrop in the least serpentinised lithologies west of Mt. Olympus. Chromite forms in four main phases: as an accessory in dunite (<5%  $\text{Cr}_2\text{O}_3$ ), as chromitiferous dunite (5-50%  $\text{Cr}_2\text{O}_3$ ), olivine chromite (51-90 %  $\text{Cr}_2\text{O}_3$ ) or massive chromite (>90%  $\text{Cr}_2\text{O}_3$ ) (Greenbaum, 1977; McElduff and Stumpfl, 1991) (Figure 2.16). Chromite has been historically mined in Troodos, for example at Kokkinorostos, which produced >1 Mt of chromite ore at 47%  $\text{Cr}_2\text{O}_3$  (Greenbaum, 1977). In total 64 deposits are known but many are sub-economic (Greenbaum, 1977).

### 2.11.3. Volcanogenic Massive Sulfide (VMS) deposits

Troodos is widely accepted as hosting the type locality for mafic or Cyprus-type VMS (e.g. Barrie and Hannington, 1999; Hannington *et al.*, 1998). There are over 90 known VMS occurrences in Troodos ranging in size from <0.05 Mt to >16 Mt (Adamides, 2010a). Grades vary substantially from barren to >4 wt.% Cu with average Cu grades of 2 wt.% (Hannington *et al.*, 1998). Ore bodies have been historically mined for base metals, most notably Cu and Zn. Supergene gossans occur at the surface and have been historically mined for thousands of years for the Au and Cu that are preferentially enriched in these environments. The last working Cu mine in Cyprus, Skouriotissa, is located in north-west Troodos (Figure 2.16). Ore is processed using heap leaching followed by solvent extraction electro-winning (SXEW) (Figure 2.16, cf. Chapter 3).

The Limassol Forest Complex (LFC; i.e. transform terrain) hosts some unusual mineralisation, sometimes referred to as Outokumpu VMS (e.g. Peltonen *et al.*, 2008). Located within sheared, structurally complex serpentinite bodies within the LFC are pyrrhotite dominated massive sulfide lenses (Thalhammer *et al.*, 1986). The deposits are pyrite poor and contain pentlandite, chalcopyrite and secondary löllingite. The occurrence of this unusual mineralisation highlights the diverse range of ore forming environments in Troodos.

### 2.11.4 Pseudo-epithermal 'T type' Au mineralisation

Pseudo epithermal mineralisation exhibits distinct alteration mineralogy supposedly produced from fluid boiling on the seafloor (Jowitt *et al.*, 2005). Examples of 'epithermal' mineralisation include Touronjia located in south-east Troodos and Alestos, central Troodos (Appendix 3.1). As a consequence of fluid boiling deposits are often enriched in Au and exhibit alteration assemblages such as dickite that indicate the presence of low pH fluids. These deposits are proposed to be similar to subaerial epithermal deposits as they both experienced a more direct contribution of magmatic volatiles, however deposits in Troodos must have formed in a subaqueous environment (Jowitt *et al.*, 2005).

#### 2.11.5 Umbers

Umbers are hydrothermal trace element-rich muds of exhalative origin (Robertson, 1975). They form part of the Perapedhi Formation and occur infilling seafloor depressions (Pyrga, Marki; Appendix 3.1). Umbers are several 10's to 100's of meters thick (e.g. Maghelani, Figure 2.16). Umber is typically dark brown to black in colour, fine grained and highly porous (Robertson, 1975). Mineralogy is predominantly goethite and poorly crystalline manganese (pyrolusite- $MnO_2$ ) with trace amounts of REE, Co, Ni, Pb, V, Zn and Zr (Josso et al., 2018; Robertson, 1975). Umbers are extracted from several localities around Cyprus for their use as a pigment in traditional paints.

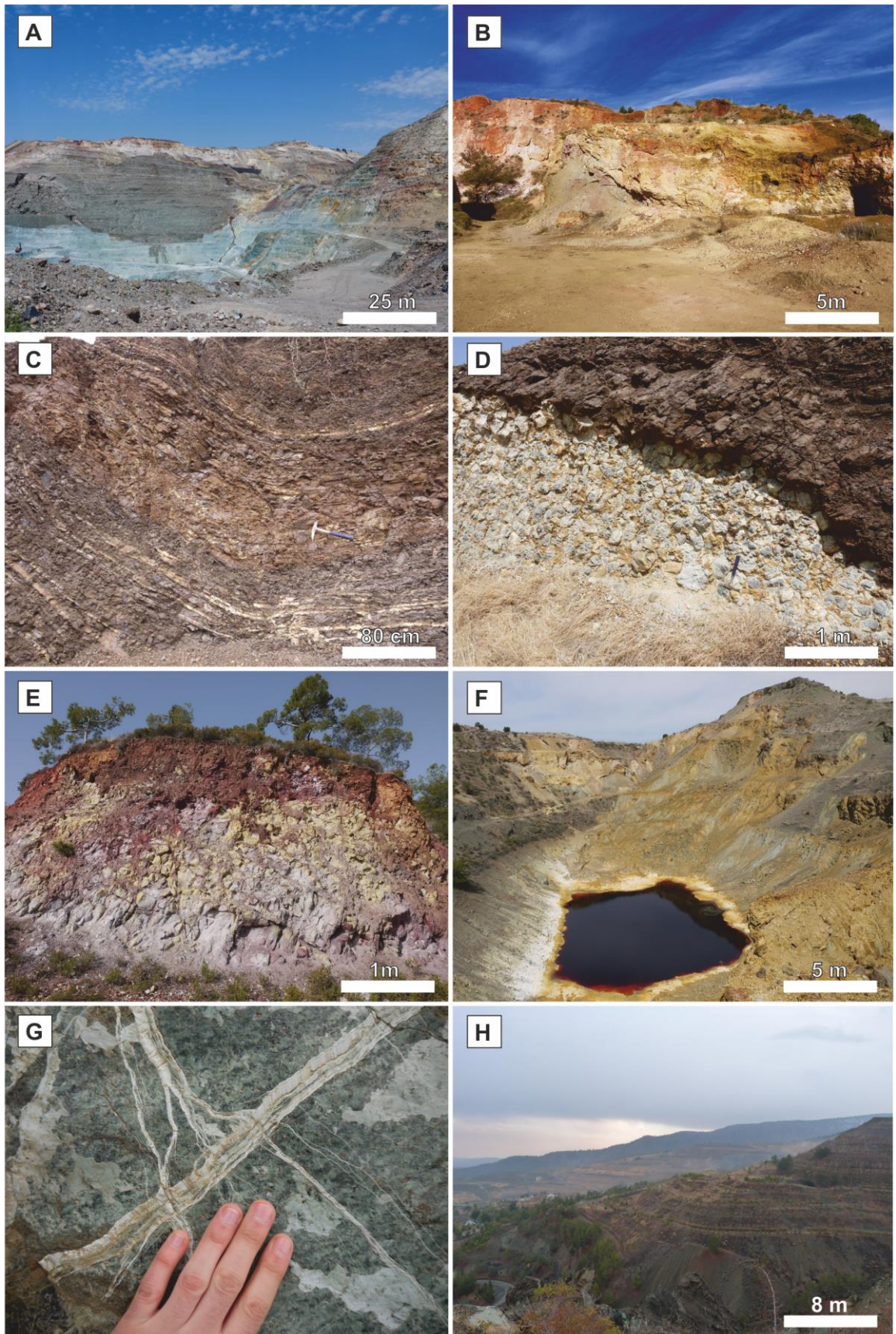


**Figure 2.16:** (A) Skouriotissa VMS, B) Kokkinovounaros Au mineralisation, Analiontas, C) Massive bedded amber, Maghelani, D) UMBER-tectonite contact, Asgata, E) Stockwork supergene alteration, Apliki West, F) Kambia VMS well-developed acid mine drainage, G) Chrysotile asbestos in serpentinite from Amiandos, H) Amiandos asbestos open pit, central Troodos.

## 2.12 Synthesis of ophiolite structure and VMS formation

The accretionary history of Troodos is complex and remains controversial, with a lava affinity distinctly different from N-MORB requiring formation by seafloor spreading in some sort of supra-subduction zone environment (potentially soon after subduction initiation) rather than an open-ocean MOR setting. The development of three major grabens, interpreted most likely as fossil axial ridges, suggests 'non steady-state' spreading and ephemeral magmatism. During periods of diminished magmatic influx, low-angle detachment faults formed at or near the plutonic-dyke boundary. Upper crustal units were rotated through listric normal faulting in a 'bookshelf' manner. Where extension was extreme (i.e. Amiandos Fault or LFC) seafloor serpentinisation may have occurred but did not lead to oceanic core complex formation.

Inversely dipping dyke domains forming grabens could represent fossil seafloor spreading axes. Graben bounding faults are spatially associated with VMS mineralisation. Of importance is the migration of spreading between the grabens and the order in which this occurred. As previously eluded to, this has important implications for the mobilisation of metals along graben boundaries due to renewed magmatic activity in older off axis crust. Further high-resolution geochronology data is needed to constrain graben evolution.

Despite the fact Troodos is considered a modern analogue for VMS actively forming at the Mid Atlantic Ridge (e.g. TAG hydrothermal field, see Chapter 3), a typical MORB-MOR environment; the hydrothermal system preserved on Troodos is likely to be more similar to those encountered in subduction-dominated spreading environments (e.g. the Lau Basin). Therefore, the following important distinctions between a typical MOR type setting and that of Troodos are emphasised: a) the possibility of an additional metal source derived from the subducting slab through a magmatic volatile contribution; b) the effect of non-steady state magmatism and multiple small magma injections vs. one large axial melt lens; c) the significance of epidotes as a source of metal in a supra-subduction zone settings vs. MOR and; d) the difference in lava/parental magma composition (trace elements and H<sub>2</sub>O content) that may strongly influence metal transfer in the hydrothermal system and therefore the contained Te and Se in VMS.

# CHAPTER 3

## **Volcanogenic Massive Sulfide (VMS) deposits: Formation, mineralogy and geochemistry**

### 3. Introduction

Volcanogenic Massive Sulfide (VMS) deposits are important sources of base and trace metals, supplying 22% of the world's Zn, 6% Cu, 9.7% Pb, 2.2% Au, 8.7% Ag, and significant amounts of trace metals Co, Sn, Se, Mn, Cd, In, Bi, Te, Ga, and Ge (Franklin *et al.*, 2005; Galley *et al.*, 2007). Despite their economic significance, the distribution and concentration of trace elements remains poorly constrained; this is especially true for critical elements Tellurium (Te) and Selenium (Se).

The Troodos ophiolite hosts the type locality for Cyprus-type, mafic (Galley *et al.*, 2007) or Cu-(Zn) VMS (Franklin *et al.*, 2005). Cyprus-type VMS are hydrothermal ore deposits derived from the interaction of evolved seawater with mafic country rocks under greenschist facies metamorphic conditions (>350°C). Oxidised seawater reacts with volcanic glass in the pillow lavas that lowers the fluid pH as it enters the subsurface through cracks and fissures (Seyfried Jr. and Mottl, 1982). The fluid continues to migrate downwards into the SDC and becomes superheated to 350-400°C with a pH of around 2; at this point exchange occurs between the fluid and host rock forming epidiosites (Gillis and Robinson, 1980; Jowitt *et al.*, 2012). Epidiosites are widely accepted as a source of base metal in Cyprus-type VMS deposits of Troodos (Jowitt *et al.*, 2012; Schiffman *et al.*, 1990; Seyfried and Bischoff, 1977). Metal-laden hydrothermal fluid then rises through normal faults that provide a permeability pathway and focal mechanism channelling fluids to the seafloor. Upon exhalation, hot reduced fluid mixes with seawater leading to ligand disassociation, the precipitation of sulfides and VMS formation (Humphris and Cann, 2000).

Cyprus-type VMS are relatively low tonnage averaging 2.8 Mt (n=62) but high grade with >2 wt.% Cu (Barrie, 1999; Hannington *et al.*, 1998). Deposits are typically Zn and Pb poor with average grades of <0.7 wt.% and <0.1 wt.% respectively (e.g. Adamides, 2010a); this reflects the Cu-rich mafic host rocks, absence of sediments and minor felsic volcanics in the metal source region that leads to the depletion of Pb relative to Cu (Tornos *et al.*, 2015).

Exhalative ore bodies are characterised by a strataform lens of cupriferous pyrite with a typical mound like morphology. For some deposits no clear evidence of exhalation is preserved as they do not contain colloform textures, chimney fragments or vent fauna (Little *et al.*, 1999; Oudin and Constantinou, 1984), this suggests some VMS may have formed via sub-seafloor replacement (Doyle and Allen, 2003). Mineralogy is predominantly pyrite (euhedral to colloform), chalcopyrite and sphalerite with inclusions of galena (Adamides, 2010a,b; Hannington *et al.*, 1998). Alteration surrounding the VMS is characteristically silica and chlorite dominated with disseminated pyrite (Constantinou and Govett, 1973).

### 3.0 VMS Classification

VMS deposits are classified based on a wide range of attributes including host rock lithology, Au content and base metal ratios; readers are directed to Barrie (1999), Cox and Singer (1986), Galley *et al.* (2007), Herrington *et al.* (2005), Tornos *et al.* (2015) and references therein for further detail. The most widely adopted scheme classifies VMS based on their host lithology as this is thought to control the metal budget of the hydrothermal system (Figure 3.1, Table 3.1).

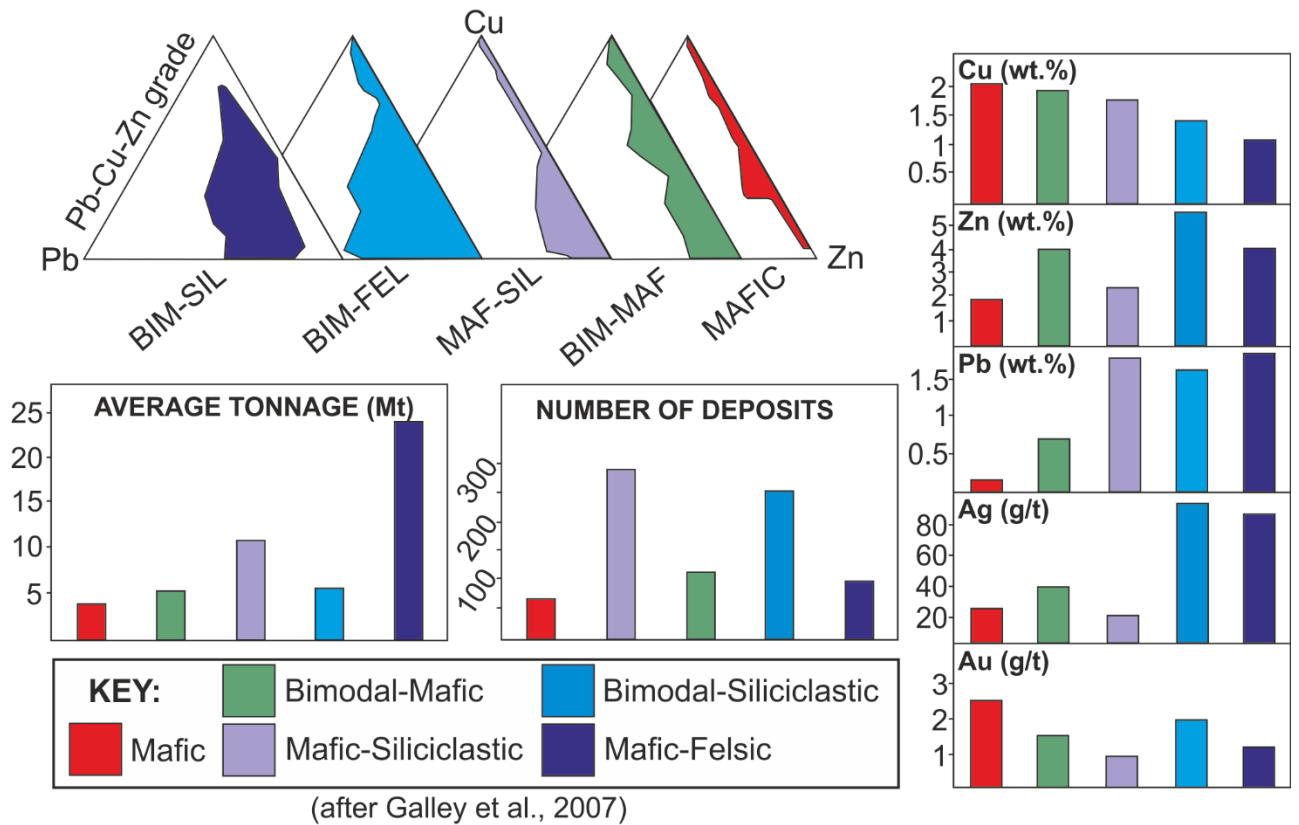


**Figure 3.1:** VMS classification based on host rock composition (after Galley *et al.*, 2007). (BIM-SIL= Bimodal-Siliciclastic, BIM-FEL= Bimodal-Felsic, MAF-SIL=Mafic Siliciclastic).

Type	<i>n</i>	Size (Bt)	Av. (Mt)	Av. Cu (wt.%)	Av. Pb (wt.%)	Av. Zn (wt.%)	Av. Au (ppm)	Av. Ag (ppm)	Deposits > 100Mt
<b>Mafic</b>	62	0.18	2.8	2.04	0.10	1.82	2.56	20.0	0
<b>Bimodal-mafic</b>	284	1.45	5.1	1.88	0.75	4.22	1.52	36.5	1
<b>Mafic-siliciclastic</b>	113	1.24	11.0	1.74	1.83	2.43	0.84	19.8	3
<b>Bimodal-felsic</b>	255	1.29	5.2	1.44	1.64	5.63	2.06	92.8	0
<b>Bimodal-siliciclastic</b>	97	2.50	23.7	1.10	1.84	4.16	1.13	84.4	9

**Table 3.1:** Average VMS deposit contained metal, tonnage and number of known deposits (after Galley *et al.*, 2007). Note variation in size and contained metal with host lithology. Av.= average.

### 3.1 VMS formation

Volcanogenic Massive Sulfide deposits form through the exhalation of highly evolved seawater at or near the seafloor (Doyle and Allen, 2003). The mixing of hot ~350°C metal-laden hydrothermal fluid with cold oxidised seawater leads to the disassociation of metal bearing ligands and sulfide precipitation (e.g. Allen *et al.*, 2002; Barrie and Hannington, 1999; Franklin *et al.*, 2005). In some tectonic settings metal is sourced from footwall lithologies through mass ion exchange between the hydrothermal fluid and igneous rock, however in subduction zone environments an additional magmatic volatile component may be contributed to the hydrothermal system (Berkenbosch *et al.*, 2012; de Ronde *et al.*, 2005; Herzig *et al.*, 1998a; Sun *et al.*, 2004). Moreover, host rock composition has been shown to influence the metal budget of VMS deposits (Tornos *et al.*, 2015; Franklin *et al.*, 2005). Footwall assemblages containing sediments or felsic volcanics are typically Pb-rich whilst mafic, or sediment starved systems are Cu-rich (Galley *et al.*, 2007: Table 3.1). The size of VMS deposits is controlled by many factors including the longevity of hydrothermal circulation and host rock permeability; a longer lived and more permeable system favouring the formation of high tonnage VMS deposits (Barrie, 1999).

Seawater enters the upper lava stratigraphy through cracks, fissures and faults and as it descends through the upper oceanic crust reacts with hot country rock (>150°C) becoming distinctly acidic with a pH of ~2 (Bickle *et al.*, 1998: Figure 3.2). Continuing to migrate downwards seawater becomes super-heated to >350°C towards the base of the SDC. At upper greenschist temperatures the hydrothermal fluid is highly reactive and mass ion exchange occurs between rock and fluid (e.g. Humphris and Cann, 2000). Metals (e.g. Cu, Zn etc.) are stripped from the host rock whilst Na and K may be added (Seyfried Jr. and Mottl, 1982). The thermally buoyant metal-rich fluid begins to ascend along faults that provide a permeable conduit and focal mechanism channelling fluid to the seafloor (Schiffman *et al.*, 1990- Figure 3.2). Focused fluid,

if it reaches the seafloor, is exhaled forming Seafloor Massive Sulfide deposits (SMS) that may subsequently be preserved as VMS deposits in ancient ophiolite terranes (Humphris and Cann, 2000; Von Damm *et al.*, 1997).

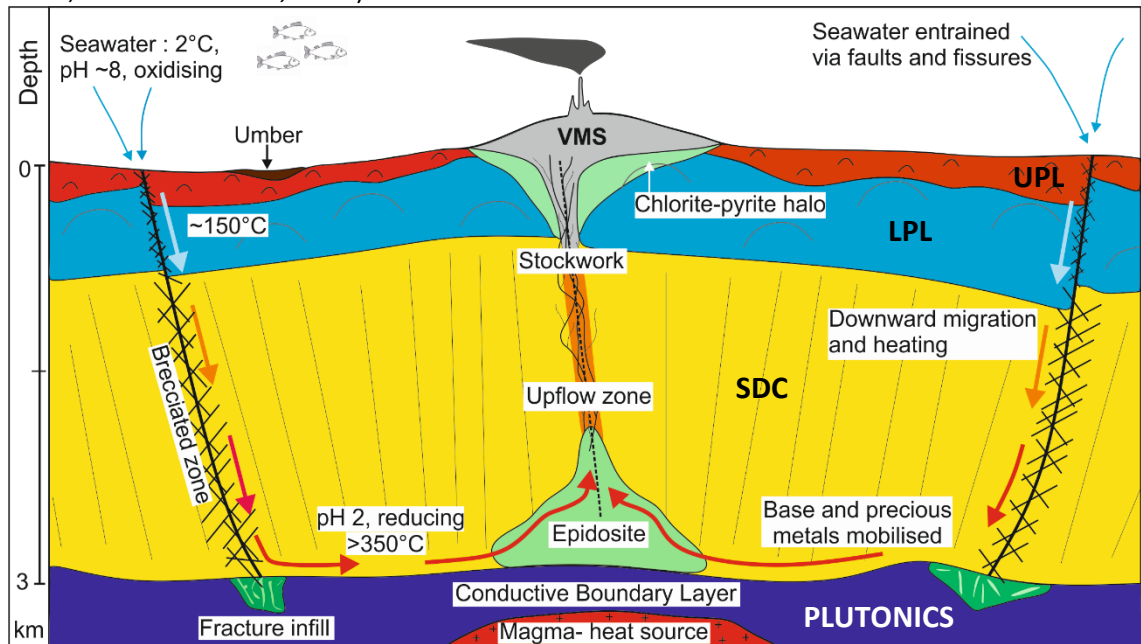


**Figure 3.2:** Simplified schematic cross-section through the VMS hydrothermal system (Martin *et al.*, 2018; Chapter 6).

### 3.1.1 Seawater-basalt modelling

The capacity of a hydrothermal fluid to transport metal relies on a low pH, high temperature and presence of key ligand species  $\text{Cl}^-$  and  $\text{HS}^-$  (e.g. Seewald and Seyfried Jr., 1990; Seyfried and Bischoff, 1977; Seyfried Jr. and Ding, 1993; Seyfried Jr. and Janecky, 1985; Seyfried Jr. and Mottl, 1982). The potential for seawater to dissolve and transport metals is low as it is near neutral pH, cold  $\sim 2^\circ\text{C}$  and oxidising (Banerjee and Gillis, 2001). Modification of seawater begins in the upper lava stratigraphy and relies critically upon the presence of glassy pillow rims and high water:rock ratios. It should be noted that water:rock ratio refers to the total mass of fluid that passed through a point divided by the total rock mass that it altered (Seyfried Jr. and Mottl, 1982). This initial reaction takes place under zeolite facies metamorphic temperatures ( $<250^\circ\text{C}$ ) and lowers fluid pH from  $\sim 7.8$  toward 2.

The modification of seawater is facilitated by the quantitative removal of Mg through the alteration of glassy pillow rims to form secondary Mg bearing silicates (e.g. clinocllore ( $\text{Mg,Fe}^{2+})_5\text{Al}(\text{Si}_3\text{Al})\text{O}_{10}(\text{OH})_8$ )), a reaction that generates  $\text{H}^+$  and lowers fluid pH (Seyfried Jr. and Mottl, 1982). Seawater contains  $\sim 1290$  ppm Mg, however at high water:rock ratios Mg is quantitatively removed from the hydrothermal fluid (Figure 3.3). In order to maintain the effective buffering capacity of the solution, Mg saturation must be achieved and this is only possible at water:rock ratios  $>125$  (Figure 3.3) (Seyfried and Bischoff, 1977). If water:rock ratios

decrease, silicate hydrolysis consumes all available  $H^+$  causing the fluid pH to increase (Figure 3.3). Increasing pH will reduce metal solubility in the hydrothermal system (Figure 3.4).

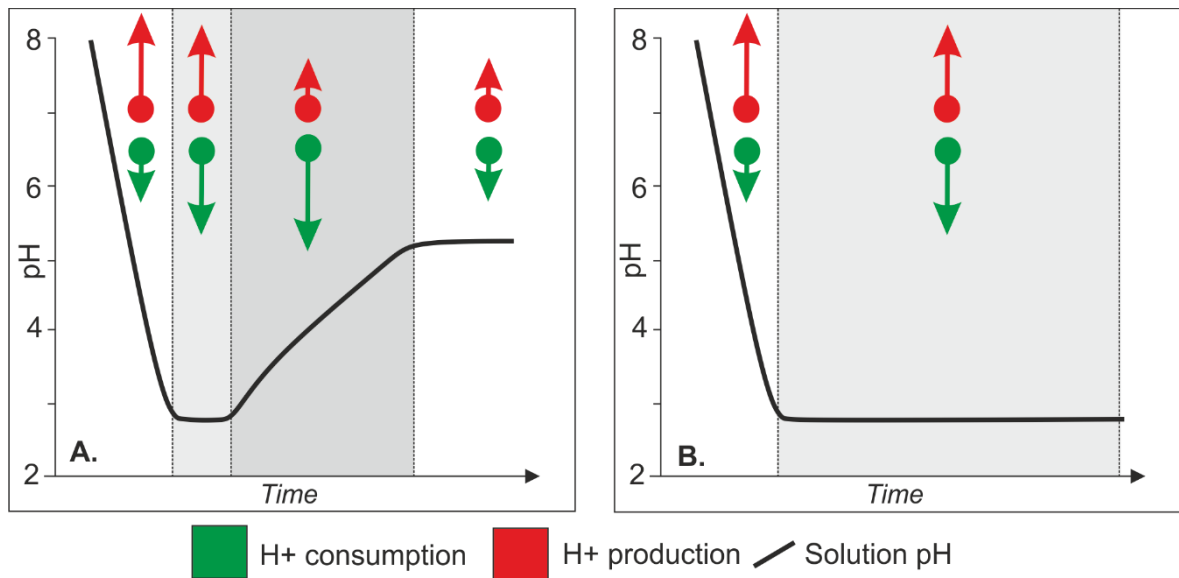


**Figure 3.3:**  $H^+$  kinetics of rock dominated (A) and seawater dominated (B) hydrothermal system. Low pH is only maintained in at high water:rock ratios >125 (after Seyfried and Mottle, 1982).

Fluid-rock exchange is experimentally modelled (at  $300^\circ C$ ) by Seyfried Jr. and Mottl (1982) who demonstrate the importance of water:rock ratios in achieving a low fluid pH. At water:rock ratios <50 (rock dominated) a low pH cannot be maintained (Figure 3.3A). Magnesium removal initially leads to a decrease in pH from 8 to 4.2 but as Mg is quantitatively removed from seawater (Figure 3.3A) through silicate hydrolysis, fluid pH begins to increase from 3 to 6 (after 576 hours- Seyfried Jr. and Mottl, 1982). Using identical parameters but at higher water:rock ratios (>125), pH decreases to 3.7 and is maintained by Mg saturation. In scenario B (Figure 3.3)  $H^+$  generation is in equilibrium with silicate hydrolysis, pH is buffered and metals remain soluble.

Experimental data from Seewald and Seyfried Jr. (1990) demonstrate the effect of temperature variations on ligand, metal and major ion species in solution (Figure 3.4). Manganese, Fe, Zn and Cu are most soluble at temperatures > $400^\circ C$  and cooling the fluid to  $350^\circ C$  leads to a decrease in solubility for all metals considered. Copper concentration in solution decreases from 30 ppm to <5 ppm (Figure 3.4) (Seewald and Seyfried Jr., 1990). Key ligand species  $HS^-$  and  $Cl^-$  exhibit different solubility trends with temperature;  $HS^-$  is stable at low temperature (< $250^\circ C$ ) and  $Cl^-$  at high temperature (> $350^\circ C$ ) (Figure 3.4- Chapter 7). This suggests low temperature off axis mineralisation could contain appreciable metal concentrations (Chapter 7). Seewald and Seyfried Jr. (1990) also consider the temporal response of metals to changing temperature; Cu responds rapidly to decreasing temperature followed by Fe, Zn and Mn (Seewald and Seyfried Jr., 1990). Copper will be precipitated rapidly as the hydrothermal system cools with Zn and Mn deposited distally (i.e. as umbers).

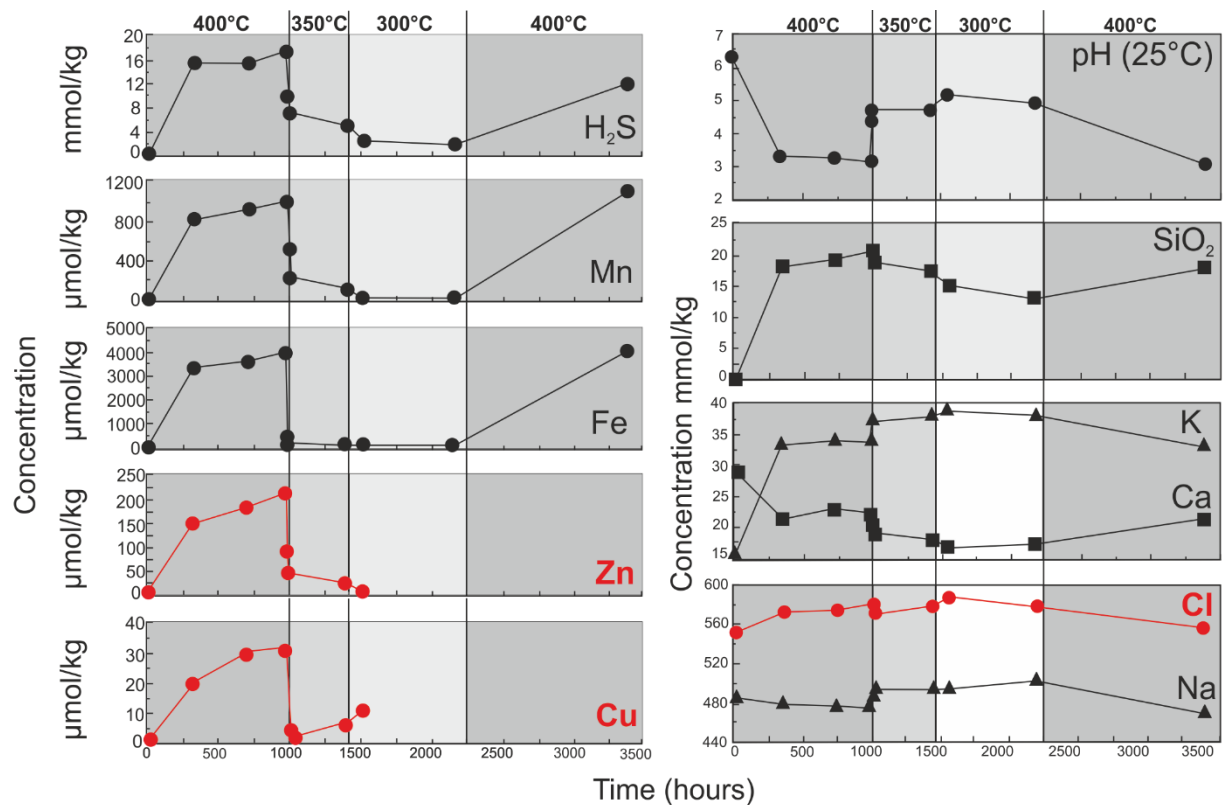


**Figure 3.4:** Metal and major ion solubility in response to temperature variation. All metals exhibit increased solubility at temperatures  $>400^{\circ}\text{C}$  (400 bar, fluid/rock mass ratio of 1). Copper and Fe exhibit a rapid response to temperature change whilst Mn and Zn respond more slowly. Note that after 1536 hours Cu and Zn were not quantifiable (after Seewald and Seyfried Jr., 1990).

### 3.1.2 Key ligand species

The dominant ligand species is dictated by the composition of the source fluid that may evolve during fluid-rock reaction. In hydrothermal fluids of seawater origin, such as those present in VMS hydrothermal systems,  $\text{Cl}^-$  is derived from the disassociation of  $\text{Na}^+$  and  $\text{Cl}^-$  in seawater (e.g. Seyfried Jr. and Ding, 1993). In addition to  $\text{Cl}^-$ ,  $\text{HS}^-$  or  $\text{H}_2\text{S}$  ligands and associated metal complexes (e.g.  $\text{Zn}(\text{HS})_2$ ) are a minor component, they are primarily derived through the leaching of primary igneous sulfides and igneous rocks or through the direct addition of a magmatic volatile phase to the hydrothermal system (e.g. Butterfield *et al.*, 1997).  $\text{Cl}^-$  is present in much higher concentrations than  $\text{HS}^-$  for example, in active systems the analysis of vent fluid contained 328 mmol/kg Cl but only 7 mmol/kg  $\text{H}_2\text{S}$  (Inferno, Axial Seamount; Butterfield *et al.*, 1997); it should be noted that volatile-rich arc related environments contain elevated concentrations of  $\text{H}_2\text{S}$  due to an increased magmatic volatile influx (e.g. Brothers caldera, de Ronde *et al.*, 2005). This has important implications for metal transport as, for example, Cu and Au will preferentially complex with  $\text{HS}^-$  or  $\text{H}_2\text{S}$  ligands. In most cases the ability of ligands to transport metals depends upon the fluid physicochemistry, for example Au( $\text{HS}$ ) complexes prevail at low temperatures  $<300^{\circ}\text{C}$  whilst  $\text{AuCl}_2^-$  form at high temperatures  $>500^{\circ}\text{C}$  (Pokrovski *et al.*, 2014; Robb, 2005; Ruaya, 1988; Seyfried Jr. and Ding, 1993).

## 3.2 The source of metals in the VMS hydrothermal system

The source of metals in the VMS hydrothermal system is poorly constrained and probably varies depending on the tectonic environment i.e. back-arc vs. MOR (e.g. Humphris and Cann, 2000; Huston and Large, 1989; Keith *et al.*, 2018a; Ronde *et al.*, 2005; Sun *et al.*, 2004). Our current understanding suggests that metals are sourced primarily from wall-rock interactions where primary igneous lithologies are leached by hydrothermal fluids, and, in extreme cases like Troodos, fossil hydrothermal reaction zones are preserved as epidiosites (section 3.2.1- Jowitt *et al.*, 2012; Patten *et al.*, 2016; Richardson *et al.*, 1987). Metals can also be contributed through the direct exsolution of a magmatic volatile-rich brine or vapour phase (Keith *et al.*, 2018a; Kelley *et al.*, 1992; Sun *et al.*, 2004). In reality the author prefers a scenario where both of these sources contribute to the metal budget of the VMS hydrothermal system, and the relative proportion of each component has important implications for trace element enrichment, especially magmatic volatile elements e.g. Se, Te, Au, Cu etc. (de Ronde *et al.*, 2011; see Chapters 8 and 9).

### 3.2.1 Epidiosites

Epidiosites form through the hydrothermal alteration of igneous rocks at greenschist facies temperatures  $>350^{\circ}\text{C}$  within the sheeted dyke complex. Epidiosites contain almost entirely epidote + quartz  $\pm$  titanite (Jowitt *et al.*, 2012). These rocks have long been hypothesised as a source region for metals contained within VMS deposits of the Troodos ophiolite (e.g. Bendnarz and Schmincke, 1990; Jowitt *et al.*, 2012; Schiffman *et al.*, 1990). It must be stressed that despite the discovery of epidiosites in modern subduction related tectonic settings (e.g. Tonga fore-arc; Banerjee and Gillis, 2001) the significance and even occurrence of epidiosites in MOR environments remains unknown.

Epidiosite zones are well-developed in the SDC of Troodos (Figure 3.5). The volume and alteration intensity of epidiosite zones varies spatially and is localised over several hundred meters perpendicular to dyke strike. Epidiosite zones are often characterised by an intricately woven mesh of variably epidotised dykes (Jowitt *et al.*, 2012). Individual dykes exhibit a striped zonation with intense epidotisation limited to the centre of individual dykes (Figure 3.5) (Cann *et al.*, 2015). Primary minerals (e.g. clinopyroxene + plagioclase) are replaced by epidote + quartz + chlorite  $\pm$  titanite and the primary ophitic texture destroyed (Jowitt *et al.*, 2012). The progressive replacement of a dyke may be classified into four stages (overleaf- Figure 3.5):

**Stage I: Diabase** with a modal mineralogy of clinopyroxene + amphibole + chlorite + albite ± epidote ± quartz with retention of primary ophitic texture. Epidote and quartz are minor or accessory phases (<10%).

**Stage II: Transitional-diabase** has a similar modal mineralogy to diabase but higher concentrations of chlorite (<30%), epidote (15-30%) and quartz (15-30%); the igneous texture is destroyed.

**Stage III: Intermediate epidosite** is marked by the absence of plagioclase and increased abundance of epidote (>30%) and quartz (>30%) with variable chlorite from 15-30%.

**Stage IV: End-member epidosite** is entirely composed of quartz + epidote ± titanite (up to 63%: Schiffman *et al.*, 1990). Epidosites are pistachio green in colour with a 'sandy' granoblastic texture.

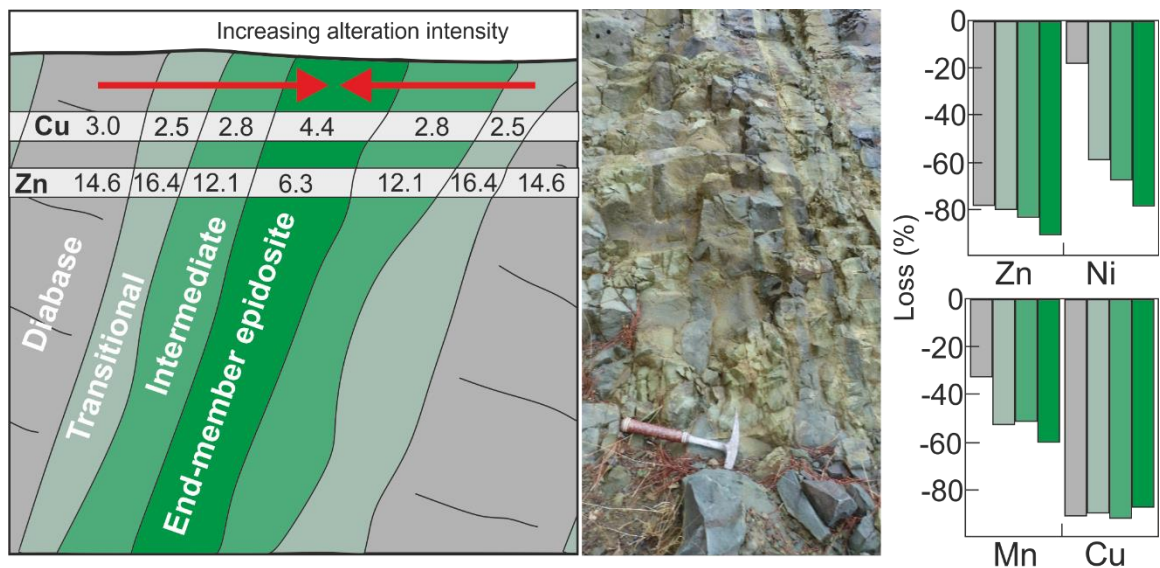


**Figure 3.5:** Schematic cross-section of epidosite zone with average metal content of Cu and Zn in ppm. Epidosites are depleted in Zn relative to unaltered protoliths. Cu shows a minor enrichment due to sulfide precipitation (generally pyrite-chalcopyrite) (after Jowitt *et al.*, 2012).

The cogenetic nature of the Troodos crust allows a mass balance to be calculated using fresh volcanic glass and epidotised samples (Jowitt *et al.*, 2012; Patten *et al.*, 2017). Troodos glass originally contained 47-99 ppm Zn, 1030-1390 ppm Mn, 19-28 ppm Co, 19-57 ppm Cu and 7-50 ppm Ni. Comparatively, end-member epidosite contain 6.3 ppm Zn, 485 ppm Mn, 15.9 ppm Co and 4.4 ppm Cu. This leads to an average depletion of 91, 60, 29, 87% for Zn, Mn, Co and Cu respectively (Jowitt *et al.*, 2012- summarised Figure 3.5). Assuming a volume of 2 km<sup>3</sup>, fluids leached 369 Kt of Zn, 52 Kt of Ni, 3647 Kt of Mn and 162 Kt of Cu (Jowitt *et al.*, 2012). This mass balance suggests that the amount of metal leached is enough to form a medium sized VMS deposit. Theoretically a larger volume of epidotised dykes would be required than the 2 km<sup>3</sup> envisaged by Jowitt *et al.* (2012) as they assume a 100% precipitation efficiency, realistically this is significantly lower.

The same method as outlined above has been applied to trace elements by Patten *et al.* (2017). Troodos glass is enriched in Sb, As and Pb relative to N-MORB (Patten *et al.*, 2017- See Chapter 8). During magnetite crystallisation (<3.5 wt.% MgO- Jenner *et al.*, 2010) sulfide segregation leads to the enrichment of chalcophile elements Au, Cu and Se in the most primitive lithologies (the UPL) whilst incompatible Zn, Sb, As and Pb are concentrated in the more evolved lithologies (e.g. LPL) (Patten *et al.*, 2017).

Trace element geochemistry of Troodos glass exhibits a systematic enrichment in Zn, As and Sb with increasing differentiation from basalt to andesite. Basaltic lavas originally contained  $96 \pm 36$  ppm Cu, 69 ppb Se and 0.77 ppb Au. Epidosites exhibit a depletion relative to Troodos glass for all trace elements considered by Patten *et al.* (2017) with concentrations of 0.18 ppb Au and 7.8 ppb Se (Patten *et al.*, 2017). This demonstrates that both base and trace metals are mobilised from epidosite zones during hydrothermal alteration. Assuming 24% 'diabase', 24% transitional diabase, 39% intermediate epidosite and 13% end member epidosite (Figure 3.5) in a given epidosite zone  $88 \pm 16\%$  Au,  $89 \pm 23\%$  As,  $60 \pm 12\%$  Sb and  $91\% \pm 20\%$  Se were mobilised during epidosite formation (Patten *et al.*, 2017).

With a theoretical volume of  $10.9 \text{ km}^3$ ,  $5.9 \text{ km}^3$  epidosite and  $5 \text{ km}^3$  'diabase' the epidosite zone(s) of the Solea graben mobilised  $47 \pm 9 \text{ t Au}$ ,  $21,000 \pm 5,000 \text{ t As}$ ,  $1200 \pm 200 \text{ t Sb}$  and  $3100 \pm 700 \text{ t Se}$ . Deposits of the Solea graben (Skouriotissa, Apliki and Mavrovouni) contain approximately 6.8 t Au, 2.95 t As, 16.2 t Sb and 836 t Se (based on historic whole rock data). This is significantly less metal than the amount mobilised during epidosite formation. Low trapping efficiencies of metals in the VMS mound are proposed to explain the deficit of metals in VMS relative to the amount leached during epidosite formation (Patten *et al.*, 2017). Trapping efficiencies reported by Patten *et al.* (2017) are low and range from 1% for Sb to 27% for Se (see Chapter 6). These values probably underestimate trapping efficiencies as the trace element composition of Troodos VMS are highly variable (cf. Chapter 5, 6 and 9).

### 3.2.2 Magmatic volatile contribution

Multiple sources of sulfur have been identified in VMS hydrothermal systems. The relative contribution of sulfur from each isotopically distinct reservoir dictates the sulfur isotope composition of precipitated sulfate and sulfide bearing minerals that can act as a proxy for the source of metals in the VMS hydrothermal system. Sulfur is principally sourced from, A) seawater sulfate with  $\delta^{34}\text{S}$  between 18-19‰ (Cretaceous) or 21-22‰ (modern day) (Kampschulte and Strauss, 2004) in sulfate minerals or through thermochemical seawater sulfate reduction (TSR) in sulfides, B) the leaching of magmatic rocks (0-1‰ in MORB and 0-7‰

in back-arc basin (BAB); Herzig *et al.*, 1998a), C) the direct contribution of a magmatic volatile phase ( $\delta^{34}\text{S} \approx 0\text{‰}$ ) or, D) Microbial activity and bacterial sulfate reduction (BSR) (e.g. de Ronde *et al.*, 2003, 2005; Ohmoto and Lasaga, 1982; Ohmoto *et al.*, 1983; Ono *et al.*, 2007; Pederson *et al.*, 2017; Shanks and Seyfried, 1987).

In active sediment free MOR hosted vent sites the  $\delta^{34}\text{S}$  of VMS sulfides average around +4‰ with a range generally between 0 and 10‰ (Figure 3.6). This suggests that the primary source of sulfur in SMS hydrothermal systems and by inference VMS deposits is the thermochemical reduction of seawater sulfate (+21‰) and the leaching of igneous lithologies (0-1‰). Two hypotheses exist explaining the observed distribution of  $\delta^{34}\text{S}$  in sulfide minerals; the *two phase mixing model* (Ono *et al.*, 2007) and the *anhydrite buffer model* (Ohmoto *et al.*, 1983).

Seawater contains 28 mmol/kg of sulfate, during hydrothermal circulation most sulfate is precipitated as anhydrite in the subsurface as fluids become heated to temperatures >150°C (Ono *et al.*, 2007- Figure 3.6). The precipitation of anhydrite depletes the down going fluid in sulfate (<1mmol/kg). In the high temperature reaction zone (the sheeted dykes) hydrothermal fluids gains  $\text{H}_2\text{S}$  through i) the quantitative reduction of seawater sulfate (>250°C) through interaction with  $\text{Fe}^{2+}$  bearing minerals (e.g. olivine, pyroxene etc.) or, ii) the leaching of primary igneous sulfides (Ono *et al.*, 2007; Shanks, 2001). This model predicts that sulfur in the hydrothermal system must be sourced from the two component mixing between seawater sulfate  $\delta^{34}\text{S} \approx 21\text{‰}$  and igneous derived sulfur  $\delta^{34}\text{S} \approx 0\text{‰}$  (Ono *et al.*, 2007). Based on the two component mixing model the  $\delta^{34}\text{S}$  of precipitated sulfides in VMS should fall between 1-5‰; this indicates that the leaching of igneous rocks provides the principal source of sulfur in the VMS hydrothermal system (>75%) (Ono *et al.*, 2007; Shanks, 2001).

An opposing model developed principally from the study of ancient VMS systems is the anhydrite buffer model (Ohmoto *et al.*, 1983; Shanks, 2001). This model is based on the temperature dependent fractionation between  $\text{H}_2\text{S}$  and  $\text{SO}_4^{2-}$  and the buffering of sulfides by anhydrite (Ohmoto *et al.*, 1983). In the expected temperature range for the VMS hydrothermal system (300-400°C) fractionation factors between sulfate and sulfide are 15.8‰ and 21.5‰ at 300 and 400°C respectively (Ono *et al.*, 2007). Sulfides precipitated from these fluids will have corresponding  $\delta^{34}\text{S}$  of between 0-6‰ (given a seawater sulfate value of +21‰). This model implies a larger seawater sulfate contribution to the hydrothermal system compared to the two phase mixing model. However, to clearly distinguish between these two models multiple sulfur isotope analysis is needed ( $\Delta^{33}\text{S}$ , cf. Ono *et al.*, 2007). Ono *et al.* (2007) state that the two models are not mutually exclusive and depend on a range of physical and chemical fluid factors (cf. Chapter 8 and 9). Therefore both models may be applicable to the Troodos VMS systems.

Examples of systems where the two phase mixing model and anhydrite buffer model are applicable include the Galapagos Rift, Snake Pit or Trans Atlantic Geotraverse Field (TAG) (Figure 3.7) (Herzig *et al.*, 1998a; Kase *et al.*, 1990; Skirrow and Coleman, 1982). However, SMS deposits that exhibit  $\delta^{34}\text{S}$  values  $<0\text{‰}$  can also occur e.g. Brothers Cone site (de Ronde *et al.*, 2005, 2001), Hine Hina (Herzig *et al.*, 1998b) or SuSu Knolls (Yeats *et al.*, 2014). No ancient analogues that retain this signature are currently known (Figure 3.7; Chapter 9). The light  $\delta^{34}\text{S}$  signature  $<0\text{‰}$  is probably produced through disproportionation of magmatic  $\text{SO}_2$  forming light  $\text{H}_2\text{S}$  and heavy  $\text{SO}_4$  (de Ronde *et al.*, 2003; Kusakabe *et al.*, 2001; Roxuel *et al.*, 2004; Shanks, 2001).

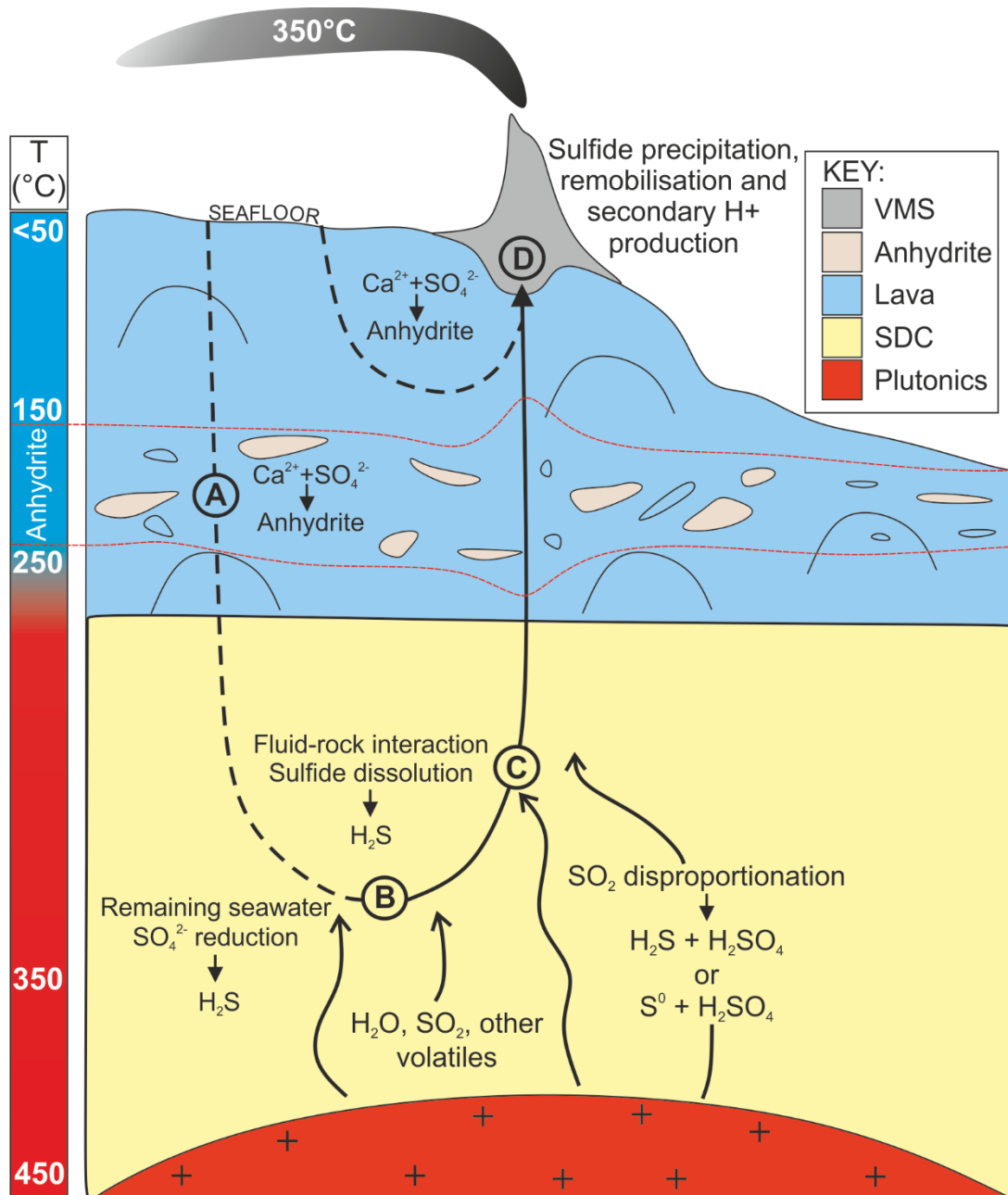


**Figure 3.6:** Sulfur isotope systematics for the VMS hydrothermal system. A) Seawater sulfate reduction at temperatures  $>150^\circ\text{C}$  and anhydrite precipitation. B)  $\text{H}_2\text{S}$  generation through thermochemical seawater reduction or leaching of primary sulfides (Metal Solid Solution). C) Possible magmatic contribution of  $\text{SO}_2$  that disproportionates upon mixing with deep fluids. D) VMS formation and shallow entrainment of seawater (after McDermott *et al.*, 2015).

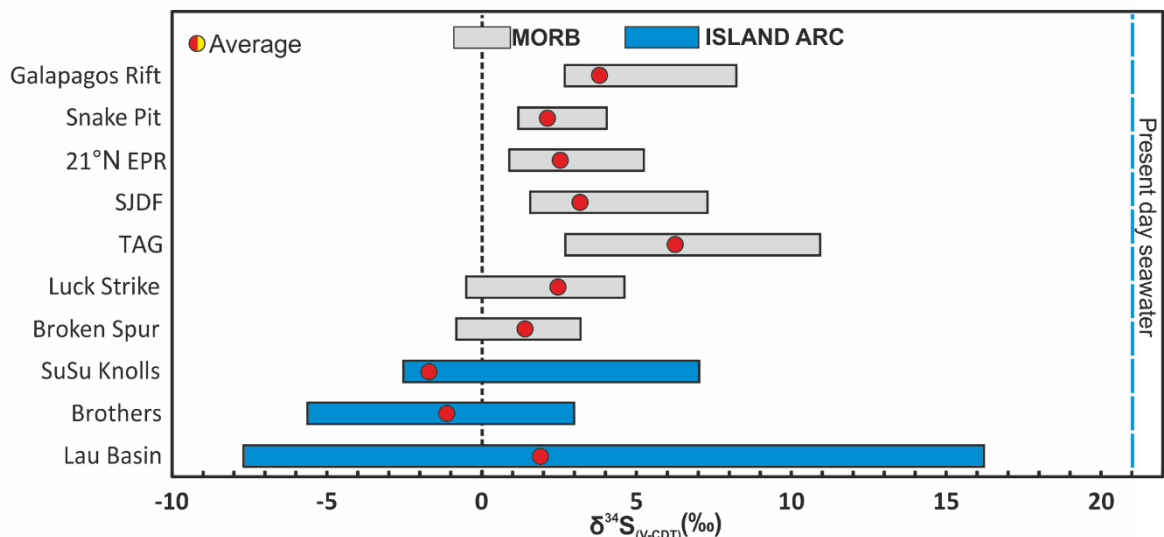


**Figure 3.7:** Summary of sulfur isotope values from sulfides in SMS deposits (BAB/Arc = blue, MOR=grey). Galapagos Rift (Knott *et al.*, 1995), Snake Pit (Kase *et al.*, 1990), 21°N East Pacific Rise (EPR) (Arnold and Sheppard, 1981; Woodruff and Shanks, 1988), Southern Juan de Fuca (SJDF) (Shanks and Seyfried, 1987), Trans-Atlantic Geotraverse Field (TAG) (Friedman, 1998; Herzig *et al.*, 1998b), Lucky Strike (Rouxel *et al.*, 2004), Broken Spur (Butler *et al.*, 1998; Duckworth *et al.*, 1995), SuSu Knolls (Yeats *et al.*, 2014), Brothers (de Ronde *et al.*, 2003; 2005), Lau Basin (Herzig *et al.*, 1998b). Red dots indicate average  $\delta^{34}\text{S}$  value. Black dashed line represents MORB  $\delta^{34}\text{S}$ , blue dashed line is present day seawater (Herzig *et al.*, 1998b).

In addition to sulfur isotopes Selenium/sulfur ratios ( $\text{Se/S} \cdot 10^6$ ) are used to assess magmatic influx in VMS hydrothermal systems (Hannington and Barrie, 1999; Huston *et al.*, 1995; Layton-Matthews *et al.*, 2008). Ratios <500 are inferred to have a predominantly seawater or sedimentary origin whilst those >500 have an increased magmatic component (primitive mantle ~300; Hannington *et al.*, 1999; Layton-Matthews *et al.*, 2008). All values from modern sediment starved SMS fall below 1500 (Chapter 8). However, exceptions such as the Kidd Creek Bornite Zone where Se/S ratios reach 38,700 indicate the addition of a magmatic volatile phase (Hannington and Barrie, 1999; Layton-Matthews *et al.*, 2008). It should be noted that Se/S may be modified by supergene processes and careful mineralogical characterisation of samples is essential for their interpretation (cf. Chapter 6).

The enrichment of magmatic volatile trace elements Se, Te, Cu, Bi and Au are suggested to indicate an increased magmatic volatile component relating to the liberation of magmatic volatiles (and sulfur) through the generation of a magmatic brine or vapour phase from a volatile saturated magmatic source (Berkenbosch *et al.*, 2012; de Ronde *et al.*, 2005; Kelley *et al.*, 1992). This could in turn lead to the enrichment of Se through the degassing of Se as  $\text{SeO}_4^{2-}$  that undergoes disproportionation to  $\text{H}_2\text{Se}$  (similar to  $\text{SO}_2$  to  $\text{H}_2\text{S}$ ) (Layton-Matthews *et al.*, 2008; Marques *et al.*, 2011; Chapter 8).

### 3.3 Modern VMS analogues: Seafloor Massive Sulfides

Seafloor Massive Sulfides (SMS) are widely accepted as analogues for ancient VMS deposits (Barrie and Hannington, 1999; Galley *et al.*, 2007; Mercier-Langevin *et al.*, 2011; Rona, 2005). Since their discovery in the 1970's (e.g. Spiess *et al.*, 1980) seafloor hydrothermal vents have been the subject of intense study. With the discovery of >500 active vent sites (Figure 3.8) in a range of tectonic settings we turn to fossil analogues to better understand 3D relationships, alteration and mineral chemistry and the processes responsible for metal enrichment. Fossil analogues allow us to better understand the depth relationship of mineralisation and trace element distribution, whilst active systems provide direct information on fluid chemistry and mineral precipitation temperatures. Consequently, the combination of modern and fossil analogues provides important information on the distribution of trace metals that may be key in the future feasibility and exploitation of SMS deposits e.g. Solowara-1, Lau back-arc basin (Boschen *et al.*, 2013; Humphris *et al.*, 1995; Humphris and Klein, 2018).

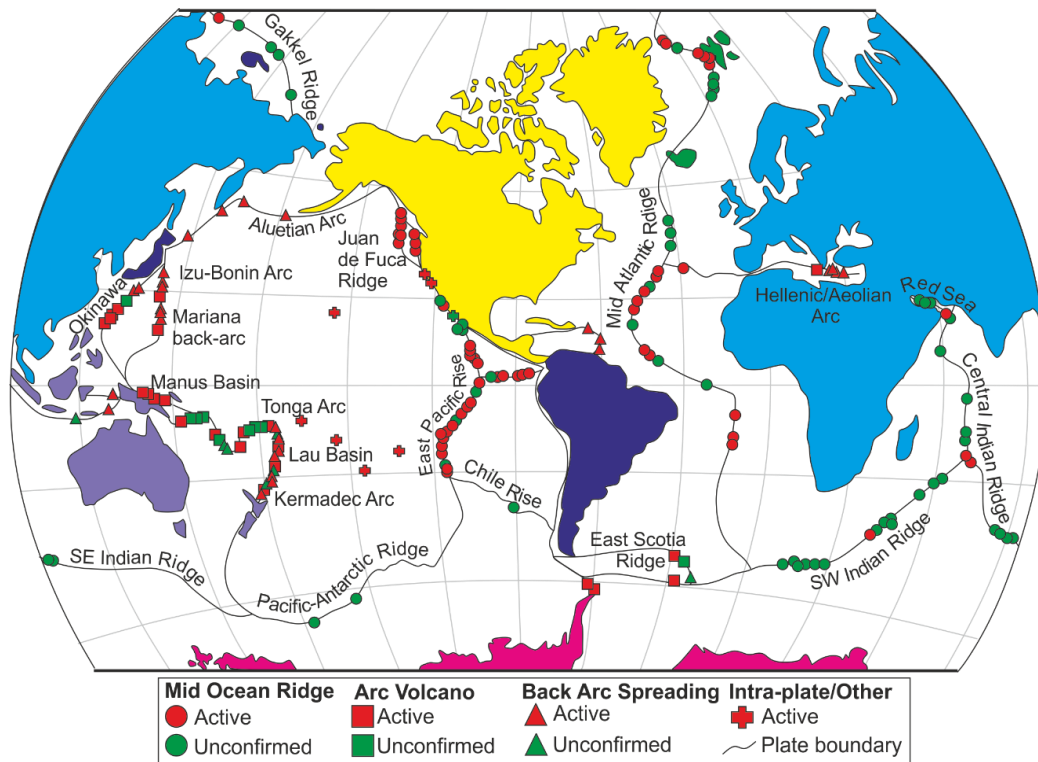


**Figure 3.8:** The distribution of seafloor hydrothermal vent sites (after Hannington *et al.*, 2011).

The spatial distribution of VMS and SMS deposits is intrinsically linked to tectonic environment. Deposits are spatially and temporally associated with the generation of new oceanic crust at both Mid Ocean Ridge (MOR) and subduction related spreading centres (Hannington *et al.*, 2011; Herzig and Hannington, 1995; Figure 3.8). Active 'black smoker' hydrothermal systems on the ocean floor have been recognised as probable analogues for VMS mineralisation preserved in ancient ophiolites (e.g. Trans-Atlantic Geotraverse (TAG) field- Hannington *et al.*, 1998;

Reeves *et al.*, 2013; Allen *et al.*, 2002). The global distribution of active SMS systems is summarised in Figure 3.8. Modern SMS form over a wide range of water depths from 700-4600 m (Monecke *et al.*, 2014); the most Cu-rich deposits form at water depths of >1000 m. Seafloor massive sulfide mounds are characterised by a strataform lens of massive pyrite underlain by a stockwork of brecciated veined material with a pipe-like morphology (Humphris *et al.*, 1995; Petersen *et al.*, 2000). White smokers are common in low temperature <250°C hydrothermal systems and vent Ba-Zn-(Au)-rich fluids (e.g. Humphris *et al.*, 1995; Rona *et al.*, 1986; Von Damm and Lilley, 2004). When a mound reaches thermal maturity physicochemical fluid properties change; seawater ingress decreases and the insulating effect of sulfide and anhydrite precipitation promote high temperature venting (Hannington *et al.*, 1995). Anhydrite (CaSO<sub>4</sub>) is abundant in SMS deposits but rarely preserved in ancient systems due to retrograde solubility leading to its dissolution at temperatures <150°C (Azimi *et al.*, 2007). Anhydrite precipitates from Ca<sup>2+</sup> interaction with ambient seawater SO<sub>4</sub> (e.g. Mills *et al.*, 1996).

The life cycle and initiation of SMS formation is poorly characterised (Ogawa *et al.*, 2007; Tivey *et al.*, 1995). Regardless of spreading rate and tectonic environment the initiation of hydrothermal circulation is indistinguishable between tectonic environments (Knight *et al.*, 2018). Initiation starts with the heating and expulsion of connate pore water that drives the initial hydrothermal convection (Tivey *et al.*, 1995). Thereafter, processes that control SMS development are intrinsically related to spreading structure and magma supply (e.g. Humphris and Cann, 2000; Reeves *et al.*, 2013). Hence a good understanding of spreading environment is key in understanding the distribution of metals in VMS hydrothermal systems.

Dating of active SMS chimneys using <sup>226</sup>Ra in barite from vents sites at the Endeavour Segment of Juan de Fuca ridge suggest deposits, or at least the main site of hydrothermal discharge, may only be active for a few thousand years (Jamieson *et al.*, 2013). Ages obtained from Endeavour show a large spread in sulfide age ranging from 23 (±127) to >6,000 years old. All samples from active sites yield ages <1,300 years (Jamieson *et al.*, 2013). However, in slower spreading ridges e.g. the TAG (MAR), dates from sulfides are up to 15,000 years old (You and Bickle, 1998). This data demonstrates the dynamic, and in many cases short lived nature of hydrothermal venting on the seafloor in an environment that regularly evolves in response to faulting that controls fluid flow. As the preservation of SMS remains poorly characterised, we do not have a clear understanding of supergene processes and the preservation of VMS deposits as migrate away from the spreading axis (e.g. Herzig *et al.*, 1991).

## 3.4 VMS Mineralogy and geochemistry

The physical and chemical composition of fluids in submarine hydrothermal systems dictates the chemistry and therefore mineralogy of associated sulfide mineralisation (e.g. Layton-Matthews *et al.*, 2013; Maslennikov *et al.*, 2017; Metz and Trefry, 2000; Revan *et al.*, 2014; Wohlgemuth-Ueberwasser *et al.*, 2015). Mineralisation forms through a combination of surface detrital and subsurface chemical processes (e.g. Yeats *et al.*, 2017). Metal zonation in VMS occur due to zone refining, a process synonymous with mature deposits; low temperature metastable Zn and Pb (<200°C: Reed and Palandri, 2006) are mobilised and re-precipitated by repeated fluid pulses. Copper occupies only the high temperature >265°C (Safina *et al.*, 2016) central mound and stockwork (Herzig and Hannington, 1995). Pyrite is ubiquitous in SMS and VMS mineralisation, commonly occurring as low-temperature colloform and high temperature euhedral varieties (Keith *et al.*, 2016a). Pyrite often contains appreciable concentrations of economic and/or toxic trace elements such as Au, Te, Se, As and Sb (Genna and Gaboury, 2015; Hannington *et al.*, 1999; Keith *et al.*, 2016a,b; Layton-Matthews *et al.*, 2008).

### 3.4.1. Zone refining

The VMS mound is a dynamic environment that grows through the precipitation, collapse and re-precipitation of sulfide and sulfate minerals (Herzig and Hannington, 1995; Maslennikov *et al.*, 2012). Mound collapse is driven by two main processes: pulsed hydrothermal fluid flow and the occlusion of fluid pathways due to mineral precipitation (Humphris *et al.*, 1995; You and Bickle, 1998). Pulses of hydrothermal fluid related to variation in magma supply lead to fluctuations in temperature and fluid physicochemistry that in turn leads to zone refining within the VMS mound (Figure 3.9). Zone refining forms distinct metal zones reflecting strong physicochemical gradients that govern metal solubility and subsequent precipitation within the VMS mound (Tornos *et al.*, 2015). This zone refining leads to a 'layer cake' distribution of metals that grade from a chalcopyrite-rich inner core to sphalerite and galena-rich marginal facies (Figure 3.9, Galley *et al.*, 2007). During zone refining, low temperature sphalerite and galena are pseudo-stable whilst chalcopyrite is stable at high temperatures >265°C (George *et al.*, 2018; Safina *et al.*, 2016). Increasing mound temperature leads to the dissolution and mobilisation of metastable sphalerite and galena from high temperature zones to the cooler mound margin (Galley *et al.*, 2007; Herzig and Hannington, 1995).

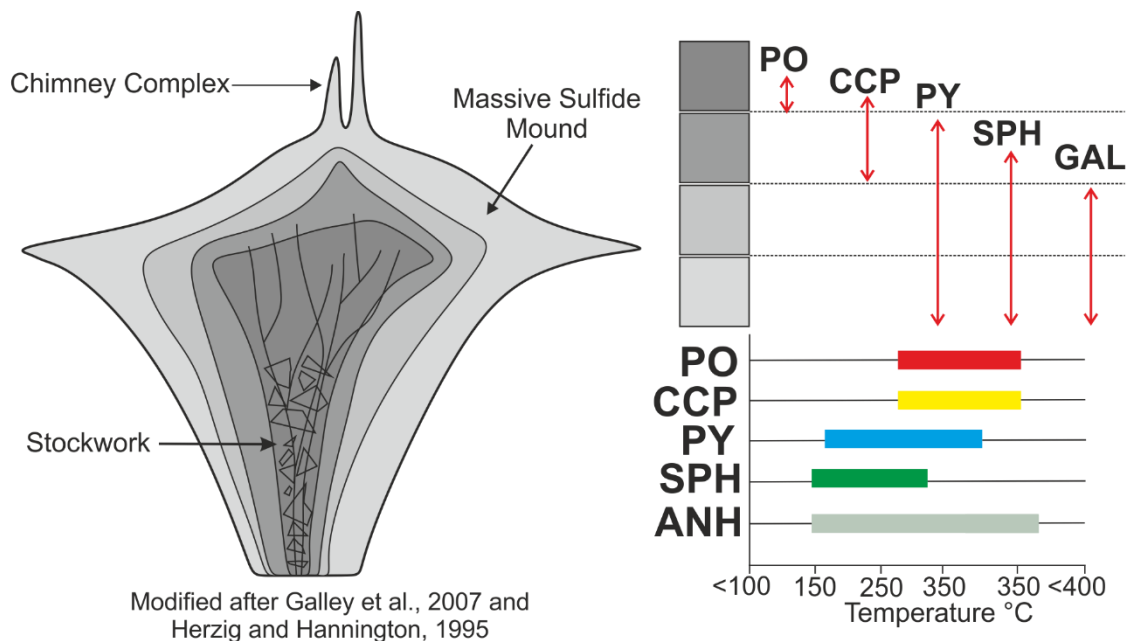


**Figure 3.9:** Schematic cross-section through a VMS mound showing zonation in mineralogy.

### 3.4.2 VMS mineralogy

Four main pyrite morphologies are commonly identified in Cyprus-type VMS deposits (Figure 3.10). Pyrite I is massive, euhedral, and accounts for the majority of the exhalative mound component. Texturally the ore is typically vuggy reflecting collapse and re-precipitation processes. Pyrite II is located in the upper mound region and has a granular to sandy texture, indicating the reworking of initially massive ore (Figure 3.10). Pyrite III has a colloform texture and precipitates at low temperatures in the upper mound at the seawater interface (Keith *et al.*, 2016a). Pyrite IV exhibits a disseminated texture and is restricted to the margins of the VMS mound and alteration halo. Pyrite IV varies from subhedral to anhedral and commonly exhibits frilly resorbed margins (Figure 3.10).

Chalcopyrite ( $\text{CuFeS}_2$ ) is the main Cu bearing mineral in Cyprus-type VMS and occurs interstitially to massive pyrite (Chapter 5). In stockwork, chalcopyrite is often massive, euhedral and vein hosted (Adamides, 2010a, 2010b) (Figure 3.10). Within sub-seafloor replacement VMS, chalcopyrite occurs associated with quartz veins. Sphalerite ( $\text{ZnFeS}$ ) is rare ( $\ll 1$  wt.%) in Cyprus-type VMS but often occurs as micro inclusions in other sulfides (e.g. pyrite) (Hannington *et al.*, 1998; Herzig and Hannington, 1995). Sphalerite with a low Fe content indicates a low temperature fluid source (Keith *et al.*, 2014). Locally high-Fe sphalerite has been analysed from the Mathiatis North and Mousoulos ore bodies (Troodos; Hannington *et al.*, 1998). Sphalerite could potentially be used to reconstruct palaeo mound temperature in Troodos VMS deposits (cf. Chapter 7).

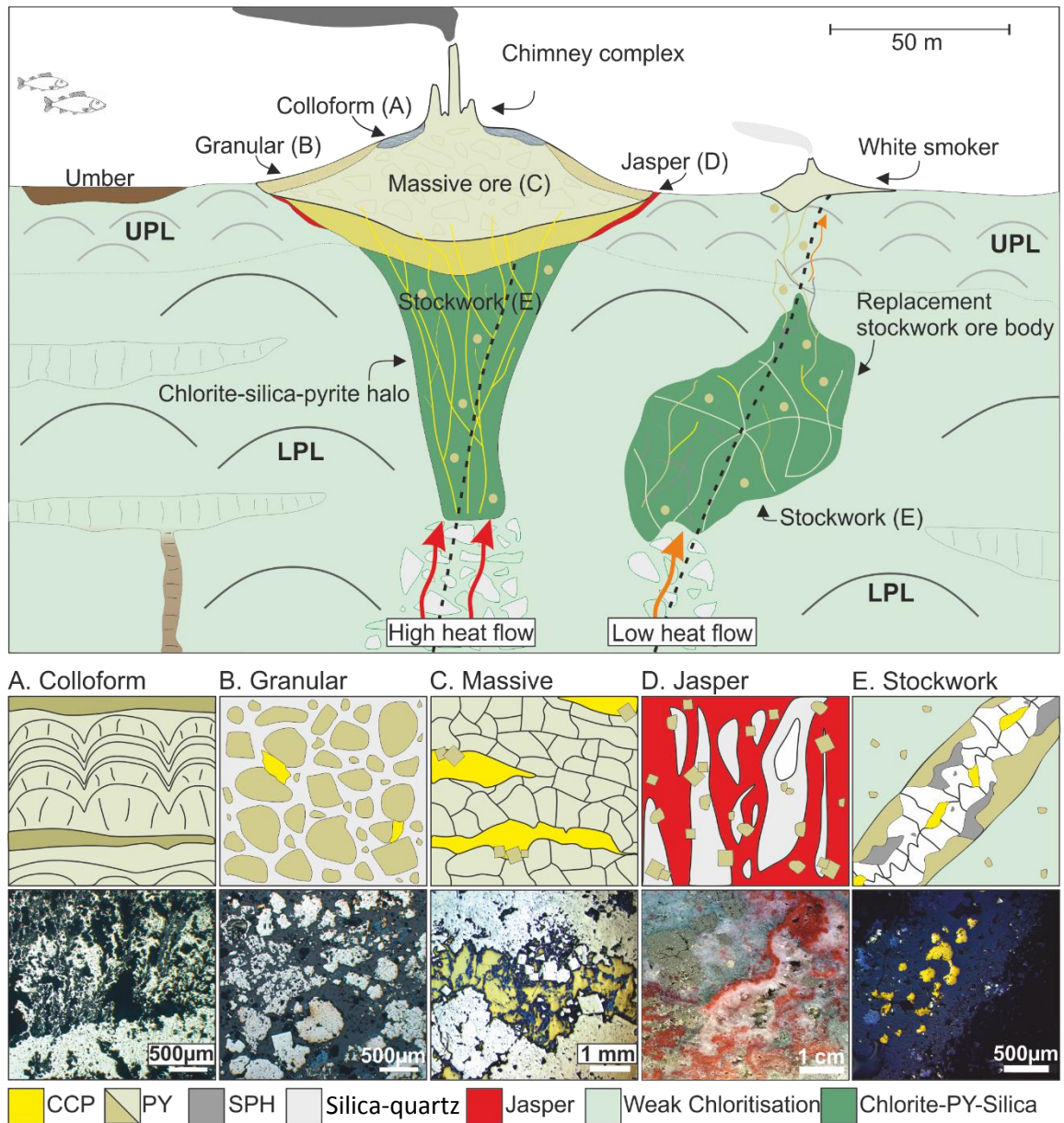


**Figure 3.10:** Summary of common ore mineralogy and textures in Troodos VMS (cf. Chapter 5).

Secondary supergene minerals form in Troodos VMS during both subaerial and seafloor related oxidisation (Parvaz, 2014; Herzig and Hannington 1991). During supergene alteration chalcopyrite alters to covellite ( $\text{CuS}$ ), chalcocite ( $\text{Cu}_2\text{S}$ ), diginite ( $\text{Cu}_9\text{S}_5$ ) and bornite ( $\text{CuFeS}_4$ ). Additionally, subaerial weathering can also lead to the formation of chalcantite ( $\text{CuSO}_4 \cdot 5\text{H}_2\text{O}$ ), malachite ( $\text{Cu}_2\text{CO}_3(\text{OH})_2$ ) and rarely azurite ( $\text{Cu}_3(\text{CO}_3)_2(\text{OH})_2$ ). Sulfates and carbonates commonly occur coating joints, especially in areas of high meteoric water flow. Secondary Fe (oxy)hydroxides and sulfates are common in all deposits and are produced during pyrite oxidation (Hannington *et al.*, 1998; Parvaz, 2014). Gossans, formed through pyrite oxidation, contain goethite, quartz, hematite and natrojarosite (Herzig *et al.*, 1991; Parvaz, 2014).

### 3.4.3 Fluid boiling and phase separation

Depth of mineralisation (i.e. water depth) varies with tectonic environment (Monecke *et al.*, 2014). Water depth equates to hydrostatic pressure in the submarine environment which in turn controls the potential for phase separation of the hydrothermal fluid (Figure 3.11; Humphris and Klein, 2018; Monecke *et al.*, 2014; Sillitoe *et al.*, 1996; Webber *et al.*, 2015). Phase separation and boiling are important physicochemical processes controlling ore deposition in some VMS deposits (Butterfield *et al.*, 1990; Gartman *et al.*, 2018). Fluid venting in active systems ranges in water depth from <50 m (submerged arc volcanos) to depths of >4000 m (back-arc/MOR). The deepest known hydrothermal vent site, the Beebe Vent Field is located in the Cayman Trough at 4960 m below sea level where fluids are discharged at 401°C (Webber *et al.*, 2017, 2015).

Phase separation is directly related to temperature, pressure (i.e. formation depth) and salinity (Monecke *et al.*, 2014; Schmidt *et al.*, 2007). Evidence for supercritical fluids can be inferred from the temperature and salinity of venting fluids in active SMS (Kelley *et al.*, 1993; Lüders *et al.*, 2002; de Ronde *et al.*, 2011; Koschinsky *et al.*, 2008; Monecke *et al.*, 2014; Webber *et al.*, 2015) or fluid inclusions in fossil VMS systems (e.g. Kelley and Robinson, 1990; Kelley *et al.*, 1992). At 5°S on the MAR fluids are intermittently vented at 464°C (average 407°C, 3000 m depth; Koschinsky *et al.*, 2008) well above the critical point of seawater (Figure 3.11). Sub-seafloor phase separation may be an important process in generating metal and Cl<sup>-</sup>-rich brines in SMS systems, this process could be responsible for metal enrichment in fossil analogues if the brine is contributed to the hydrothermal system (de Ronde *et al.*, 2011; Keith *et al.*, 2016b; Koschinsky *et al.*, 2008). Kelley and Robinson (1990) and Kelley *et al.* (1992) pointed out the importance of metal-rich brines in the fossil Troodos hydrothermal system.

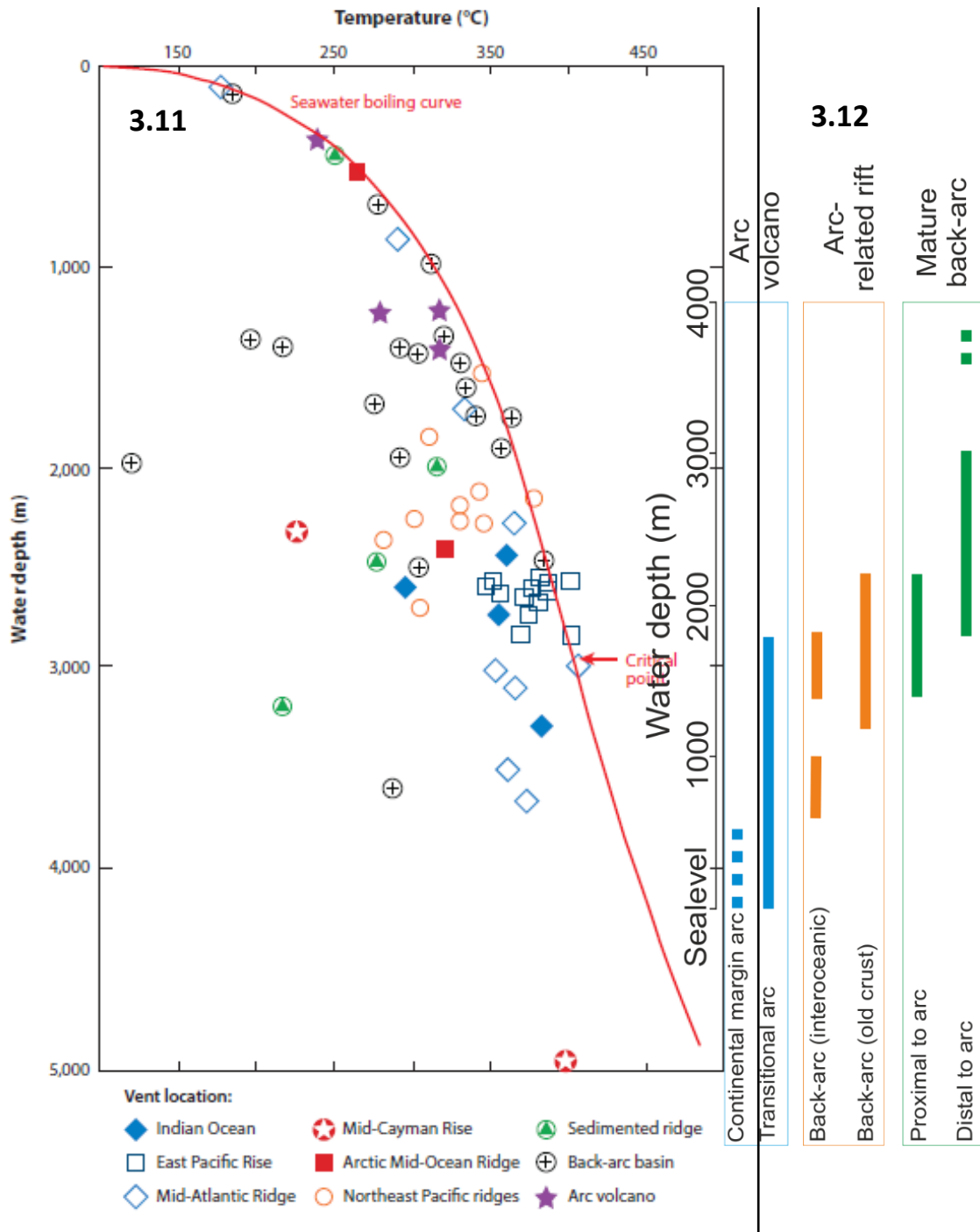


**Figure 3.11 (left):** Seawater boiling curve for select seafloor hydrothermal systems. Note that very few deposits intersect the two-phase boundary (red line) demonstrating that phase separation is a minor process in seafloor hydrothermal systems (Humphris and Klein, 2018).

**Figure 3.12 (right):** Average water depth of mineralisation vs. arc related tectonic setting; mature back-arc environments commonly host the deepest mineralisation (after Monecke *et al.*, 2014).

### 3.4.4 Trace element incorporation in sulfide minerals

Trace elements are incorporated in sulfide minerals primarily in two ways: as discrete mineral inclusions (nano or micro) or as a solid solution within the crystal lattice (Deditius *et al.*, 2011; Huston *et al.*, 1995; Layton-Matthews *et al.*, 2013; Reich *et al.*, 2013; Revan *et al.*, 2014- Chapter 5). Element incorporation varies with crystallographic, chemical and physical fluid factors e.g.  $fO_2$ , pH, temperature, covalent ion radii and the valence state of metal ions (Huston *et al.*, 1995; Keith *et al.*, 2018a; Wohlgemuth-Ueberwasser *et al.*, 2015).

Huston *et al.* (1995) classify elements into three categories based on their incorporation in pyrite: (i) elements that occur as inclusions (Cu, Zn, Pb, Ba, Bi, Ag and Sb), (ii) elements that occur as a non-stoichiometric substitution (As, Tl, Au and Mo) and (iii) elements occurring as a stoichiometric substitution for sulfur (Se and Te) or Fe (Co and Ni). Additionally, Genna and Gaboury (2015) demonstrate that elements hosted in solid solution (e.g. Se) are less extensively mobilised during metamorphism compared to micro or nano-inclusion hosted phases (e.g. Au).

Multiple studies have identified the significance of As bearing pyrite and its associated lattice modifying effects in pyrite. Increased As concentrations in sulfides enhance the substitution potential of large covalent radii elements such as Te or Au (e.g. Deditius *et al.*, 2011; Deditius and Reich, 2016; Keith *et al.*, 2018b; Martin *et al.*, 2019; Reich *et al.*, 2013- See Chapter 5). This suggests that high As pyrite in VMS deposits could contain higher concentrations of Te and associated elements relative to As depleted pyrite (Chapter 5).

Furthermore, the incorporation of elements varies between different co-precipitated sulfide phases. In chalcopyrite two groups of elements are identified based on their incorporation behaviour; group I form inclusions and group II occur as a solid solution. For example Ag, Sn and In are incorporated via substitution with Cu, Fe or S in chalcopyrite (Cook *et al.*, 2009; Huston *et al.*, 1995; George *et al.*, 2018). In contrast, group II elements, Pb, Bi, Zn and Ba commonly form inclusions (Huston *et al.*, 1995).

## 3.5 Te and Se in the VMS hydrothermal system

Because of the historical difficulties in analysing Te and Se at low concentrations, understanding their distribution and mechanisms of enrichment in different geological environments remains poorly characterised (cf. Chapter 1). This includes primary mafic igneous systems and their associated metalliferous VMS deposits (Chapter 1). Their by-product nature of production means that Te and Se are not routinely analysed during mining operations and, due to a lack of interest and high detection limits they are also rarely analysed for in academic research studies, hence very limited data is available characterising the distribution of Te and Se in VMS deposits.

### 3.5.1 Te and Se incorporation in sulfides and discrete mineral phases

Huston *et al.* (1995) state that both Te and Se are incorporated via a stoichiometric substitution with sulfur ions. However for Te this seems unlikely given the larger covalent radii (138 pm) of Te compared to sulfur (105 pm) (e.g. Butler and Nesbitt, 1999; Chouinard *et al.*, 2005). In contrast, Se has a similar covalent radii to sulfur at 120 pm (Butler and Nesbitt, 1999; Maslennikov *et al.*, 2009; Rahm *et al.*, 2016). This leads multiple authors to suggest that Se is incorporated in sulfides in a solid solution via stoichiometric substitution with sulfur (Keith *et al.*, 2018b; Maslennikov *et al.*, 2017). Tellurium, with its much larger covalent radii is suggested to form both a lattice bound substitution and as inclusions (e.g. calavarite) (Keith *et al.*, 2018b; Martin *et al.*, 2019; Maslennikov *et al.*, 2012).

Additionally, both Te and Se in hydrothermal ore deposits can form discrete mineral phases, i.e. tellurides and selenides. Tellurides are generally uncommon in VMS deposits (with the exception of the Urals- Maslennikov *et al.*, 2012, 2009 and references therein). Tellurides in VMS deposits, if present, commonly occur in chimney material (see section 3.5.2). Tellurides could represent a more direct magmatic volatile influx experienced by chimneys or enhanced precipitation efficiency given the extreme physicochemical gradients that occur over a small area or, in the case of the Uralian VMS, the redistribution and coarsening of tellurides during metamorphism (Berkenbosch *et al.*, 2012; Maslennikov *et al.*, 2012). Selenides are exceptionally rare in VMS deposits due to compatible behaviour of Se in sulfides, for example clausthalite (PbSe) that can accommodate up to 27.6 wt.% Se (Layton-Matthews *et al.*, 2008).

### 3.5.2 Physicochemical fluid factors

The process of element substitution in sulfide minerals is influenced by the physicochemical fluid properties. Fluctuations in fluid chemistry in response to variable magmatic influx or changes in fluid flow result in the highly variable distribution of Te and Se in pyrite (Butler and Nesbitt, 1999; Genna and Gaboury, 2015; Huston *et al.*, 1995). Increased Te concentrations in the inner wall of vent chimneys from the Broken Spur vent site (29° MAR) suggest Te is preferentially incorporated in sulfides at high fluid temperatures (Auclair *et al.*, 1987; Butler and Nesbitt, 1999- Figure 3.13). High temperatures also apparently favour the incorporation of Se as Gibbs free energy of mixing becomes increasingly more negative at higher temperatures allowing the lattice structure to tolerate higher concentrations of Se (Maslennikov *et al.*, 2009). Theoretically this should lead to the enrichment of Te and Se in high temperature zones of a VMS deposit (e.g. stockwork) (Maslennikov *et al.*, 2009).

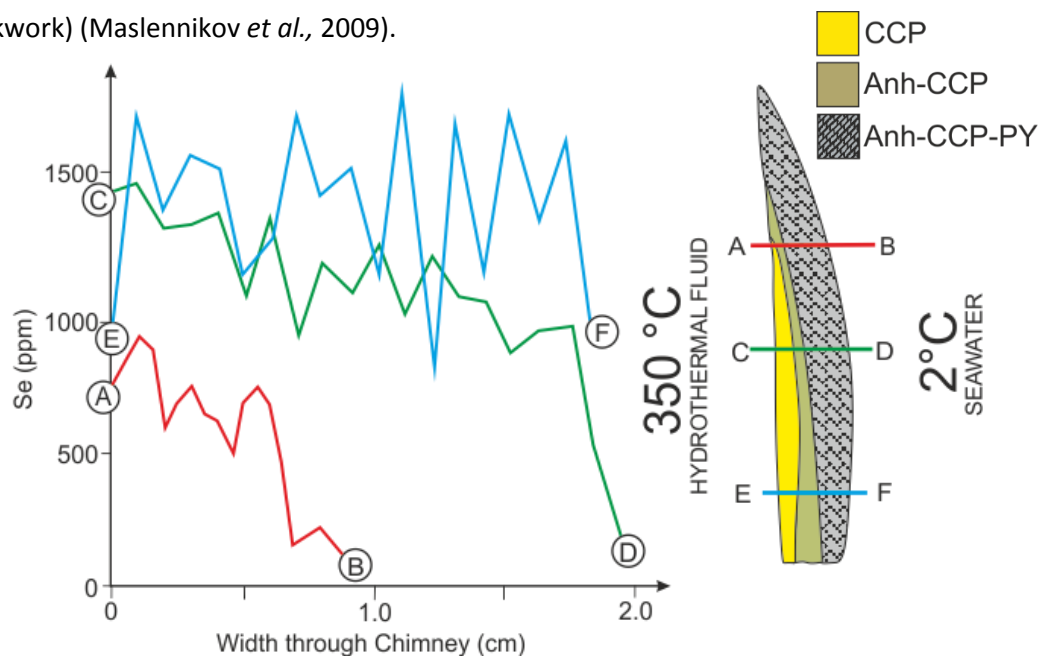


**Figure 3.13:** Selenium concentration through a black smoker chimney. Selenium is concentrated in the high temperature chalcopyrite (yellow-gold) relative to the cooler, pyrite rich outer wall (after Auclair *et al.*, 1987). This could be an artefact of the preferential incorporation of Se in chalcopyrite. Key: CCP= chalcopyrite, Anh= anhydrite, PY= pyrite.

Modelling by Huston *et al.* (1995) argues that Se incorporation is enhanced at low temperatures (Figure 3.14). At temperatures  $<200^{\circ}\text{C}$ , Se incorporation in pyrite is controlled by redox and pH whereas at temperatures  $>200^{\circ}\text{C}$  Se incorporation is controlled by fluid  $\text{H}_2\text{Se}/\text{H}_2\text{S}$  ratios and temperature (Huston *et al.*, 1995). In hydrothermal fluids above  $200^{\circ}\text{C}$   $\text{H}_2\text{Se}/\text{H}_2\text{S}$  are the dominant ligand species and thus approximate Se/S ratios (Huston *et al.*, 1995). At temperatures  $>300^{\circ}\text{C}$  the ratio of  $\text{H}_2\text{Se}/\text{H}_2\text{S}$  in the hydrothermal fluid is constant, equating to uniform Se concentrations in pyrite of 200-250 ppm and Se/S ratios of  $5 \times 10^{-4}$  (Figure 3.14). In contrast at  $150^{\circ}\text{C}$  the concentration of Se in equilibrium with the hydrothermal fluid is more variable leading to Se enrichment in pyrite up to a theoretical value of 100,000 ppm (Huston *et al.*, 1995- Figure

3.14). There remains no clear consensus on the physicochemical fluid factors that lead to the enrichment of Te and Se in VMS deposits (Chapter 5, 6 and 8).

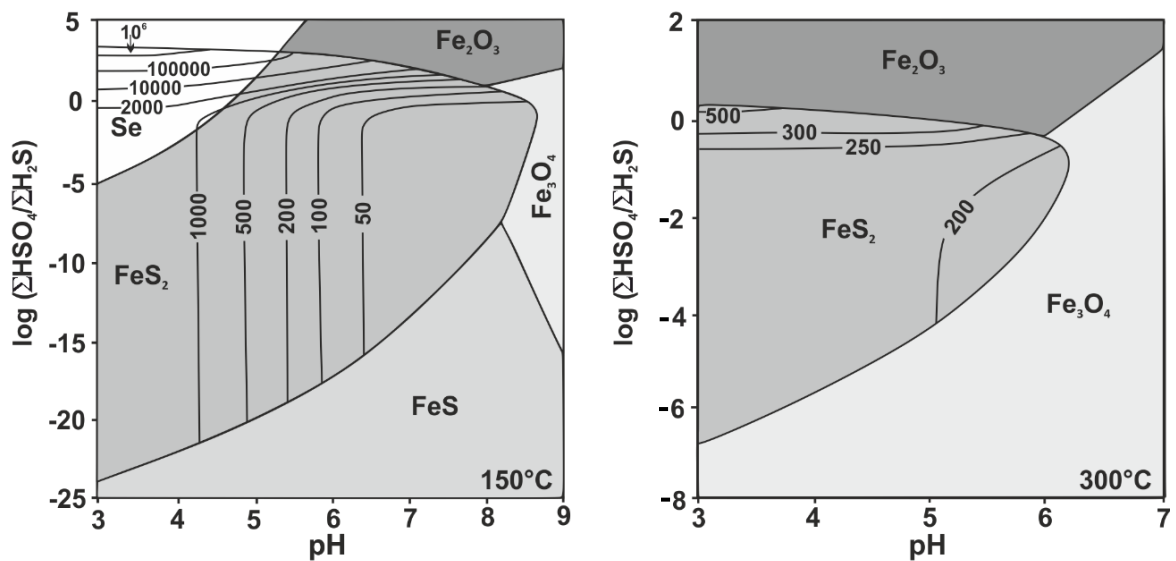


**Figure 3.14:** Theoretical incorporation of Se in pyrite vs.  $fS_2$  and pH at 150°C and 300°C (total S concentration = 0.002 m, NaCl = 1.0 m and total metal =  $2 \times 10^{-3}$  m). Significantly higher concentrations of Se can be accommodated at lower temperature. Contours represent the maximum concentration of Se in pyrite in ppm (after Huston *et al.*, 1995).

When considering telluride formation (as discrete mineral phases) our understanding is more advanced. Analysis of chimney structures from Uralian VMS show zonation in trace elements through the chimney wall from low to high temperature:  $Tl > Ag > Ni > Mn > Co > As > Mo > Pb > Ba > V > Te > Sb > U > Au > Se > Sn > Bi$  (Maslennikov *et al.*, 2009). Telluride formation and mineralogy has been modelled using variable  $fTe_2$  vs.  $fS_2$  (Maslennikov *et al.*, 2012) (Figure 3.15). Data indicates that tellurobismuthite ( $Bi_2Te_3$ ), sylvanite ( $(Ag,Au)Te_2$ ), frobergite ( $FeTe_2$ ) and native tellurium form at high  $fTe_2$ , (Figure 3.15). The absence of high Te bearing phases and appearance of native Au indicates a decrease in  $fTe_2$  probably due to seawater interaction (Maslennikov *et al.*, 2009, 2012).

The thermodynamic properties of Te in an aqueous solution are modelled by Grundler *et al.* (2013) and McPhail (1995). Tellurium species are predicted as a function of pH,  $fO_2$ , and  $fTe$  fluid content. Under reduced, acidic conditions,  $H_2Te$  and  $HTe^-$  form the dominant species (McPhail, 1995). Under oxidised conditions (hematite stability field)  $H_3TeO_3$ ,  $H_2TeO_3$  and  $HTeO_3^-$  species prevail, and above a pH of 10  $Te^{2-}$  and  $TeO_3^{2-}$  are the main species (Grundler *et al.*, 2013; McPhail, 1995). In even more oxidised environments tellurates are stable as  $H_6TeO_6$  and  $H_5TeO_6^-$  (McPhail, 1995). Tellurium oxide ( $TeO_2$ ) solubility goes through a minimum at pH 4 and is most soluble at extreme alkaline pH. Tellurium will partition up to  $>10^5$  in favour of the vapour phase; reduced vapours at 300°C can carry up to 100 ppb Te and possibly up to ppm values demonstrating the significance of vapour phase transport in Te enrichment (Grundler *et al.*, 2013).

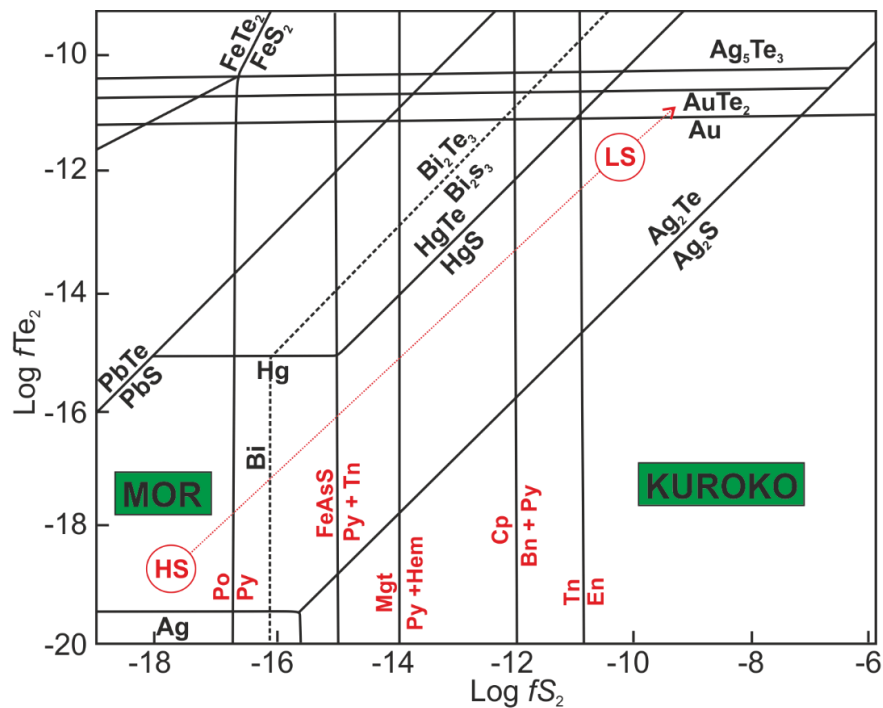


**Figure 3.15:**  $fTe_2$  vs.  $fS_2$  with increasing oxidation Te assemblage become more Te rich and Au/Ag tellurides are stable. Changes in fluid physicochemistry lead to the precipitation of telluride assemblages that can be used as proxy for fluid redox (after Maslennikov *et al.*, 2012).

Thermodynamic data for Se has been modelled at a temperature of 300°C (e.g. Huston *et al.*, 1995; Layton-Matthews *et al.*, 2013; Xiong, 2003). The dominant Se species within the sulfide stability field is  $H_2Se$  that transitions toward  $Se^{2-}$  as the sulfate field is intersected (Figure 3.16). The stability field of  $Se^{2-}$  decreases with increasing temperature and  $Se^{2-}$  is only stable at a pH of >11.8 whilst  $H_2Se$  is stable up to a pH of ~5 suggesting  $H_2Se$  will be the dominant ligand species in the VMS hydrothermal system (Figure 3.16) (Xiong, 2003).

The ratio of  $\Sigma H_2Se : \Sigma H_2S$  is directly relatable to the Se content of pyrite. At a constant  $\Sigma H_2Se : \Sigma H_2S$  ratio, decreasing temperature leads to an increase in  $\Sigma H_2Se$  relative to  $\Sigma H_2S$  and a higher Se content in pyrite; hence the hypothesised enrichment of Se in low temperature environments (Huston *et al.*, 1995- Figure 3.17). The  $\Sigma H_2Se : \Sigma HSe$  ratio is pH sensitive with  $\Sigma H_2Se : \Sigma HSe$  decreasing with increasing pH (Huston *et al.*, 1995; Xiong, 2003). Furthermore, the concentration of Se in pyrite increases drastically when  $SO_4 > H_2S$  (Figure 3.17).

In the supergene environment selenite ( $SeO_3^{2-}$ ) and tellurite ( $TeO_3^{2-}$ ) are the dominant Te and Se species. Tellurium and Se fixation via adsorption can occur through fixation on jarosite, goethite, hematite or organic matter (Bullock *et al.*, 2018). This demonstrates that Se and Te may be enriched not only in hypogene sulfide minerals but also supergene oxides and sulfates (e.g. goethite and jarosite).

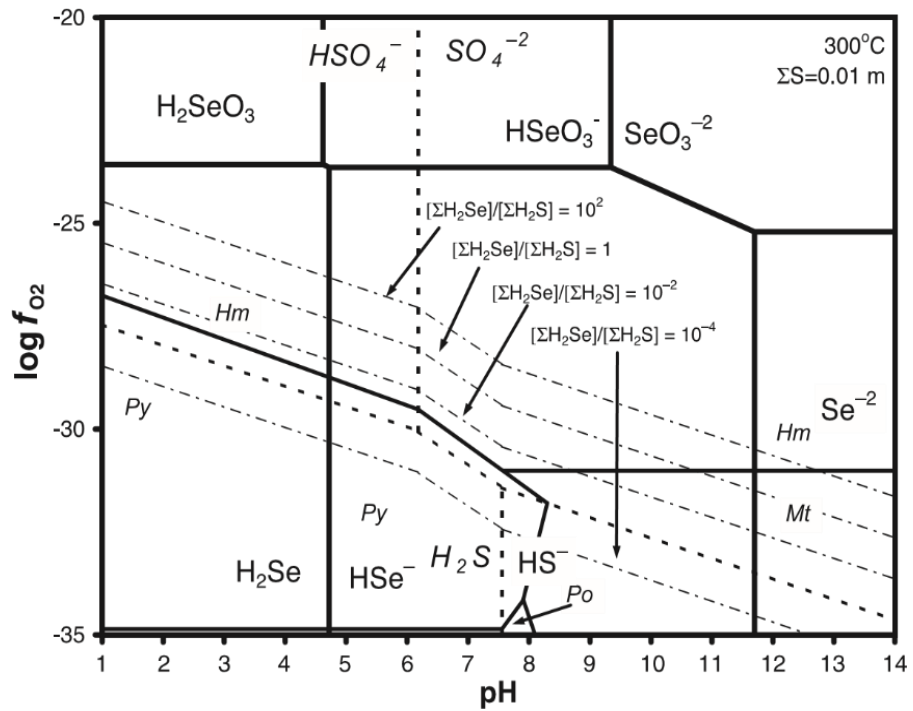


**Figure 3.16:** Selenium species vs. pH and  $f_{O_2}$  of fluid at 300°C.  $H_2Se$  and  $HSe^-$  complexes predominate in the pyrite stability field (bottom left) and  $SeO_3^{-2}$  complexes in more oxidised and alkaline environments (upper right) (Xiong, 2003).

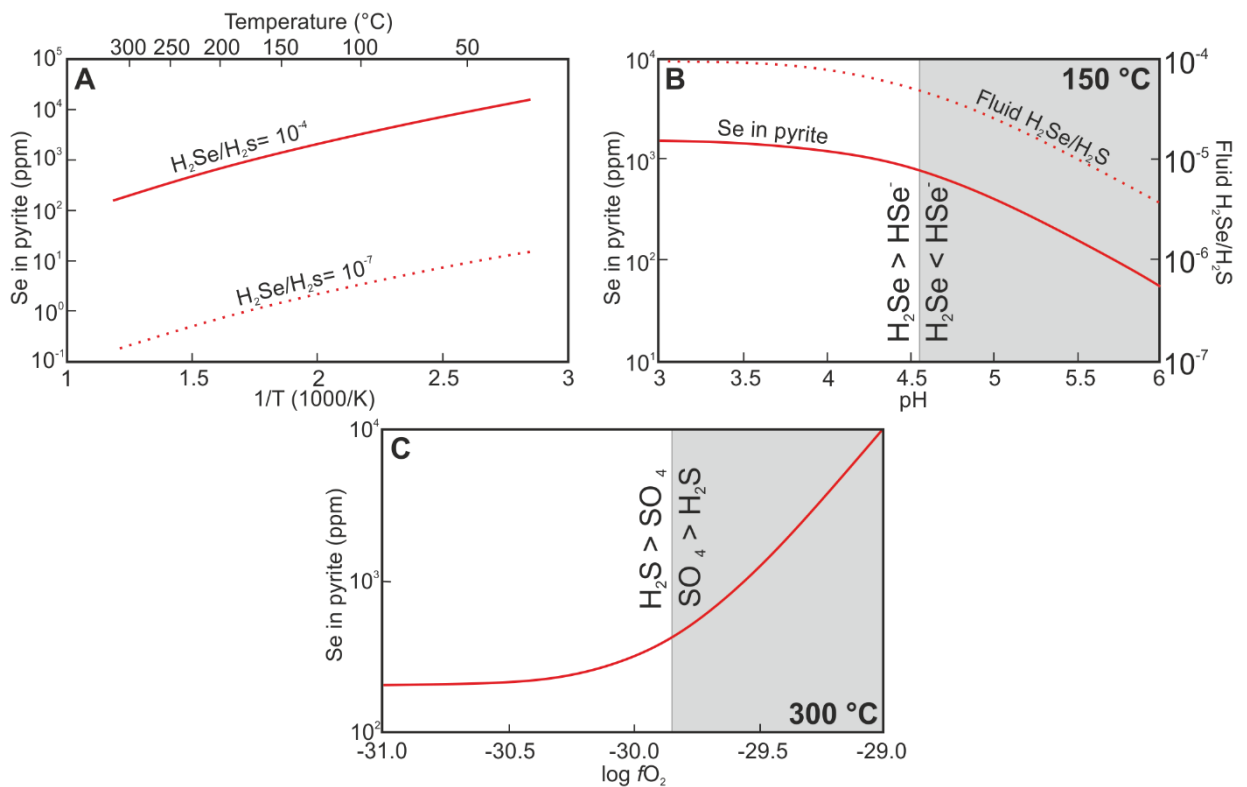


**Figure 3.17:** A) Selenium in pyrite vs. temperature and  $H_2Se:H_2S$  ratio of hydrothermal fluid (dashed line is  $10^{-7}$ , solid line is  $10^{-4}$ ). B) Se in pyrite vs. pH at 150°C assuming a constant  $\Sigma Se/\Sigma S$  ratio and  $f_{O_2} < 10^{-4}$ . C) Se concentration in pyrite vs.  $f_{O_2}$  at 300°C. Selenium enrichment favours reduced pH, low temperature and moderately oxidised fluids (after Huston *et al.*, 1995).

### 3.5.3 Concentrations of Te and Se in VMS

Tellurium and Se concentrations in VMS deposits are poorly characterised. Data presented for many modern SMS deposits has an inherent sampling bias as only chimneys and grab samples that may be enriched due to their location in the VMS stratigraphy are routinely sampled. This notwithstanding, limited geochemical data exists from MOR and arc related hydrothermal systems (Figure 3.18).

Selenium concentrations in pyrite average 481 ppm at the Brothers volcano and 43.4 ppm at TAG. This variation probably reflects a variable magmatic volatile influx related to tectonic environment (Grant *et al.*, 2018; Keith *et al.*, 2016b). Maximum Se concentrations exhibit an order of magnitude variation between SMS deposits, for example at Brothers (Kermadec Arc) maximum concentrations of Se in pyrite are 4102 ppm whilst at Kairei (Indian Ridge) they are just 9.5 ppm in pyrite (Keith *et al.*, 2016b). Tellurium is rarely analysed or is below detection limit in many SMS deposits. The Brothers volcano is enriched in Te with a maximum concentration of 1032 ppm, reflecting the analysis of telluride inclusions (Keith *et al.*, 2016b); typically Te in pyrite is below detection or  $\ll 10$  ppm (Figure 3.18).

With the exception of one study (Keith *et al.*, 2016a), only historic trace element data exists for Troodos VMS (e.g. Hannington *et al.*, 1998). Whole rock Se values range from  $<5$  to 296 ppm and Te is not analysed (Hannington *et al.*, 1998). In situ analysis of pyrite by Keith *et al.* (2016a) from a Troodos VMS (Skouriotissa) yielded average Te concentrations of 0.7-12.4 ppm and 4 to 948 ppm Se in stratigraphically shallow and deep pyrite respectively. Clearly such large variation in Se and Te between VMS and within individual deposits warrants detailed characterisation.

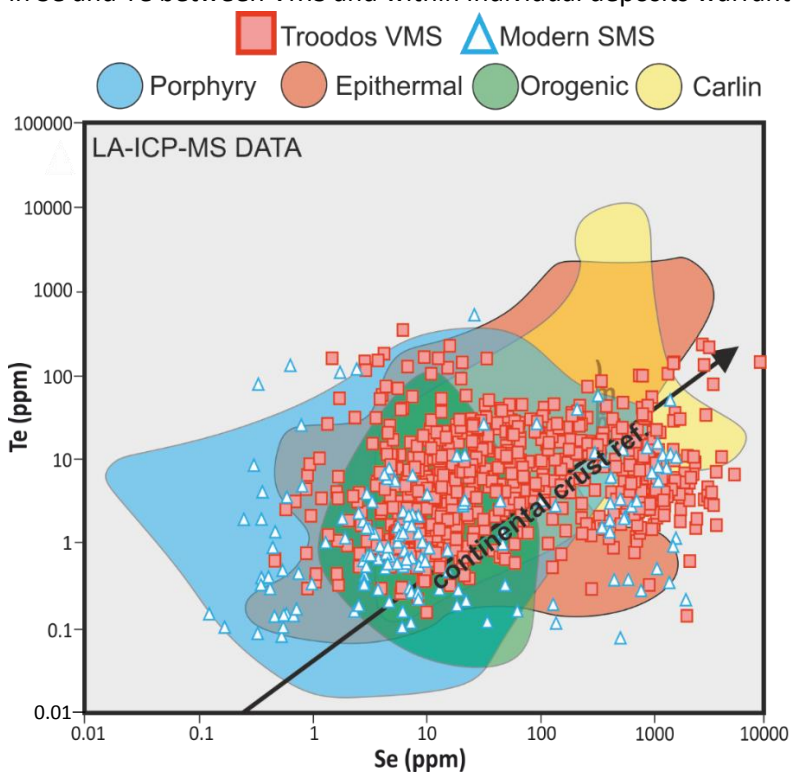


**Figure 3.18:** Se vs. Te (ppm) in all Troodos VMS (This study;  $n = 1514$ ) vs. other common ore forming environments (after Keith *et al.*, 2016b, 2018a; Martin *et al.*, 2018, 2019).

### 3.6 Introducing Troodos VMS

The aim of this section is to briefly introduce the VMS sampled in this study (see Appendix 3.1 for further field characterisation). Specific reference and any further introduction is made on a chapter by chapter basis. Sample localities of VMS considered in each chapter are summarised at the beginning of each section as some chapters specifically focus on a single VMS deposit (e.g. Chapters 6 and 9). A full table detailing individual deposit localities is provided in Appendix 3.1.

#### 3.6.1 VMS distribution

Volcanogenic Massive Sulfide deposits of Troodos occur at the periphery of the ophiolite at major stratigraphic boundaries between or within the UPL, LPL and BG lithologies. Selected sample localities investigated in this study are summarised in Figure 3.19. Localities are categorised into VMS, low-temperature deposits and miscellaneous deposits including stockwork occurrences (e.g. Apliki West- Figure 3.19) and gossanised or disseminated sulfide mineralisation (e.g. Almyras).

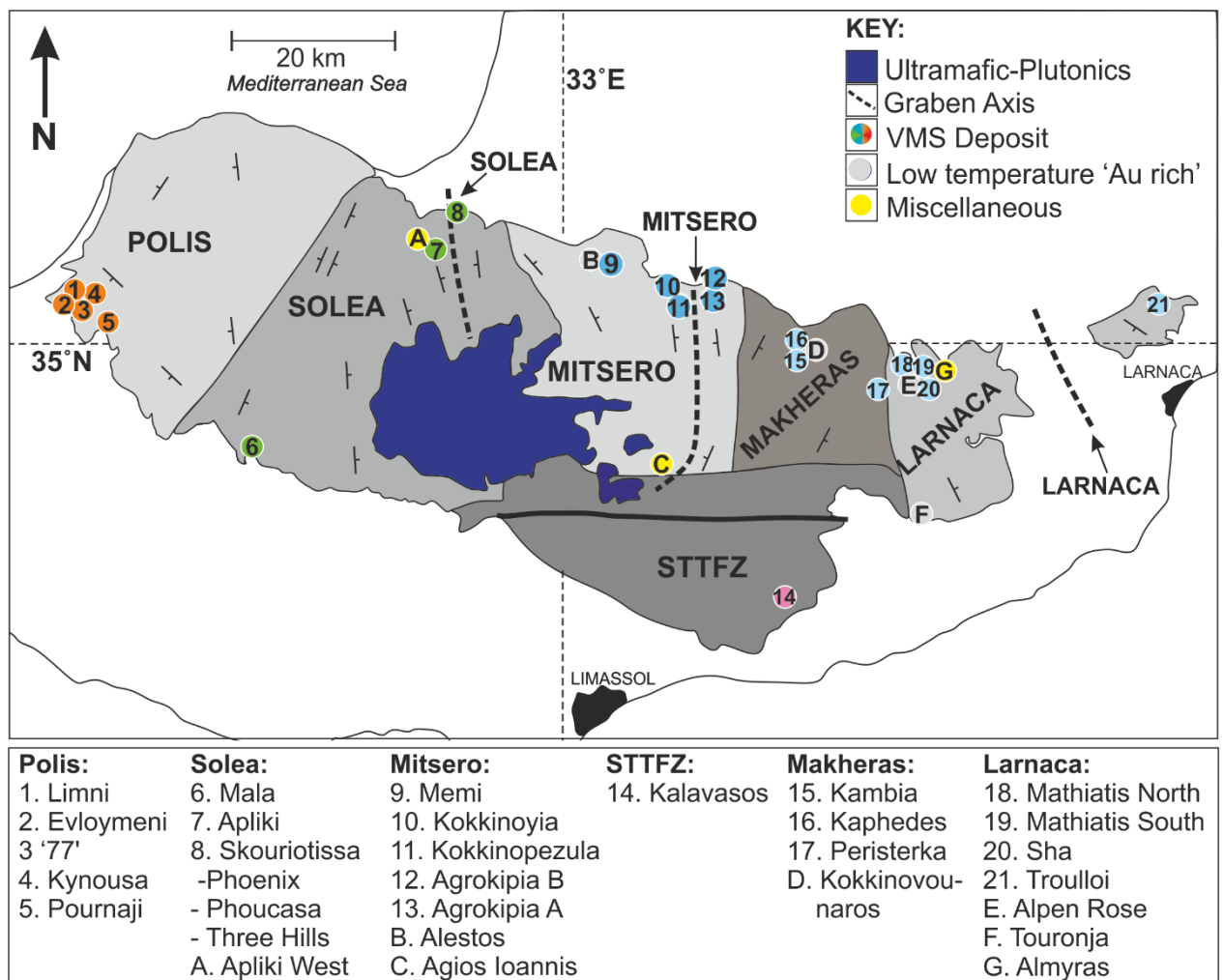


**Figure 3.19:** Summary map of key localities sampled in this study across the Troodos ophiolite (after Martin *et al.*, 2019). See Appendix 3.1 for further detail. Numbers = VMS deposits, letters = other mineralised localities.

### 3.6.2 Troodos VMS in the field

Volcanogenic Massive Sulfide deposits of Troodos vary in tonnage from <0.05 Mt up to >16 Mt, with Cu grades averaging 1.6 wt.%, minor Zn (generally) <0.5 wt.% and trace Pb <<0.1 wt.% (e.g. Adamides, 2010b; Constantinou and Govett, 1973; Hannington *et al.*, 1998). Supergene gossans and associated VMS have been mined for many thousands of years with modern exploration and mining starting c. 1920. Sulfide ore production peaked between 1970 and 1980 with over 10 Mt of sulfide ore produced. Today only the Skouriotissa mine is actively operating in Cyprus producing 99.99% pure Cu cathodes using heap leach extraction followed by a solvent extraction electrowinning (SXEW) process. Gold is also produced in minor quantities via cyanide leaching from gossan material at Skouriotissa.

Many different styles of mineralisation were recorded during sampling in 2016-2018 field seasons. Localities that demonstrate key relationships and different styles of mineralisation are summarised in Figure 3.20. The Agrokipia A VMS (Figure 3.20 A) is located within the Mitsero structural domain and occurs at the contact between UPL and LPL's. Agrokipia is overlain by a thin sequence of unaltered UPL with a cross-cutting dyke that contains a goethite xenolith demonstrating that in some instances VMS formation ceased before magmatism. The two primary ore morphologies in Troodos (stockwork and massive mineralisation) are summarised in Figure 3.20 B and C. Kokkinopezula (Figure 3.20 D) is a typical open-pit exposure with an acid lake (AMD) surrounded by oxidised, silicified, weakly chloritised lavas.

The Apliki VMS (Figure 3.20 E) is one of the best exposed in Cyprus. Two N-S graben parallel (Solea) faults bound the mineralised package. No massive exhalative ore remains but extraction has led to the exposure of deep stockwork horizons termed the South Apliki Breccia Zone (Chapter 6). Apliki also demonstrates the effect of migration away from the spreading axis on the VMS; mineralisation becomes dismembered and the foot wall becomes steeply rotated.

No massive sulfide is recorded in some deposits (e.g. Kokkinovounaros), instead abundant hematite breccias highlight the diversity of mineralisation in Troodos and the effect of fluctuating redox on mineralisation (Figure 3.20 F). Areas such as Kokkinovounaros also highlight the effect of supergene weathering processes. Evidence of low temperature fluid flow is readily observed; for example silicification of umbers (Figure 3.20 G; Chapter 7). In VMS primary sulfide minerals are not always preserved and form Cu secondaries (Figure 3.20 H)

**Figure 3.20:** A) Agrokipia A open pit, B) The massive sulfide mound at Mala VMS, C) Supergene altered stockwork at Apliki West D) Kokkinopezula VMS, E) Apliki VMS, F) Kokkinovounaros low temperature Si-Au mineralisation G) Large silicified umber nodule near Marki, H) Chalcantite and malachite +/- azurite stained semi-massive sulfide ore (Apliki)- See text for explanation.

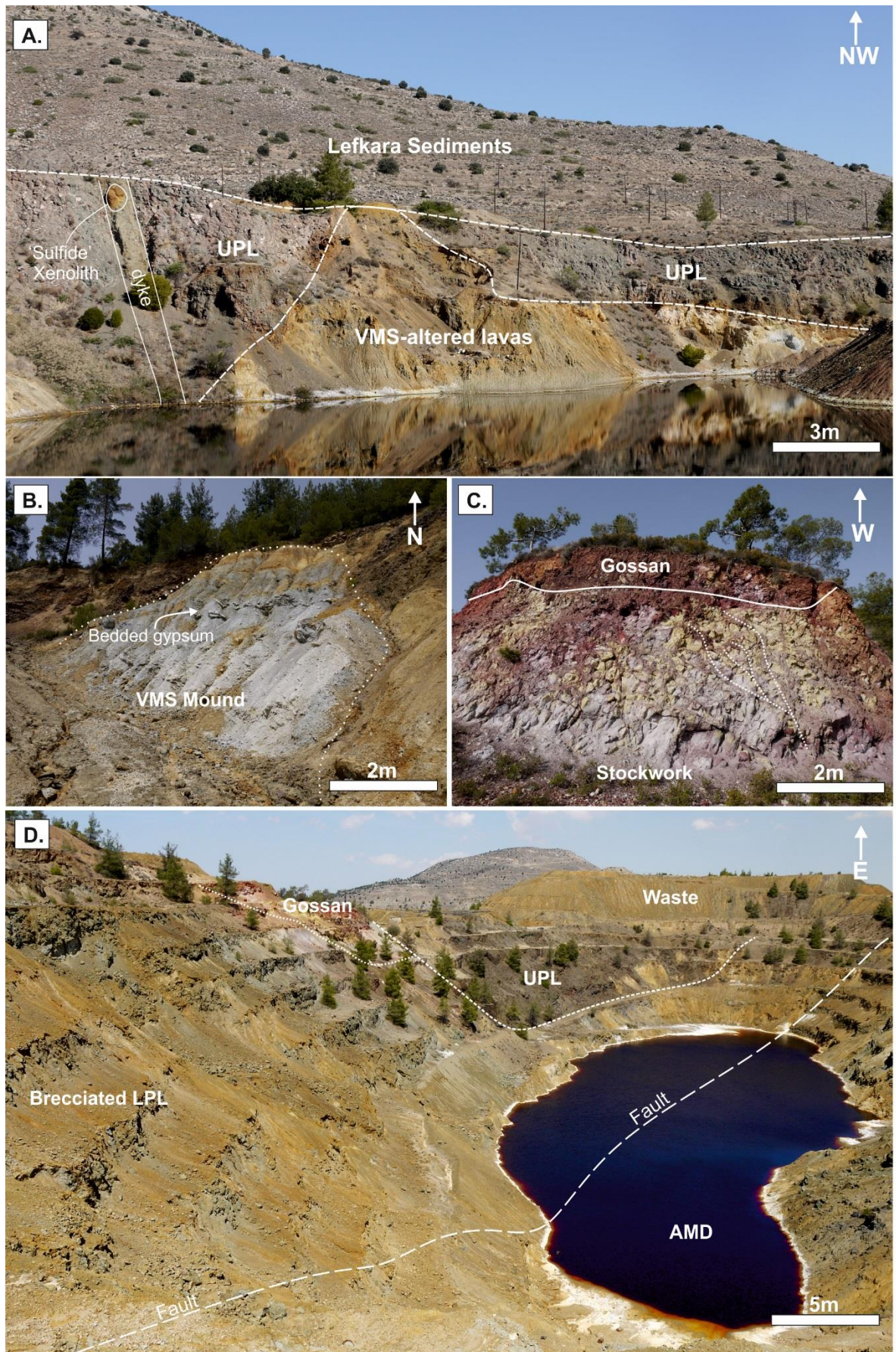


**Figure 3.20:** Examples of mineralisation in Troodos (see page 69 for explanation)  
 \*AMD= Acid Mine Drainage.

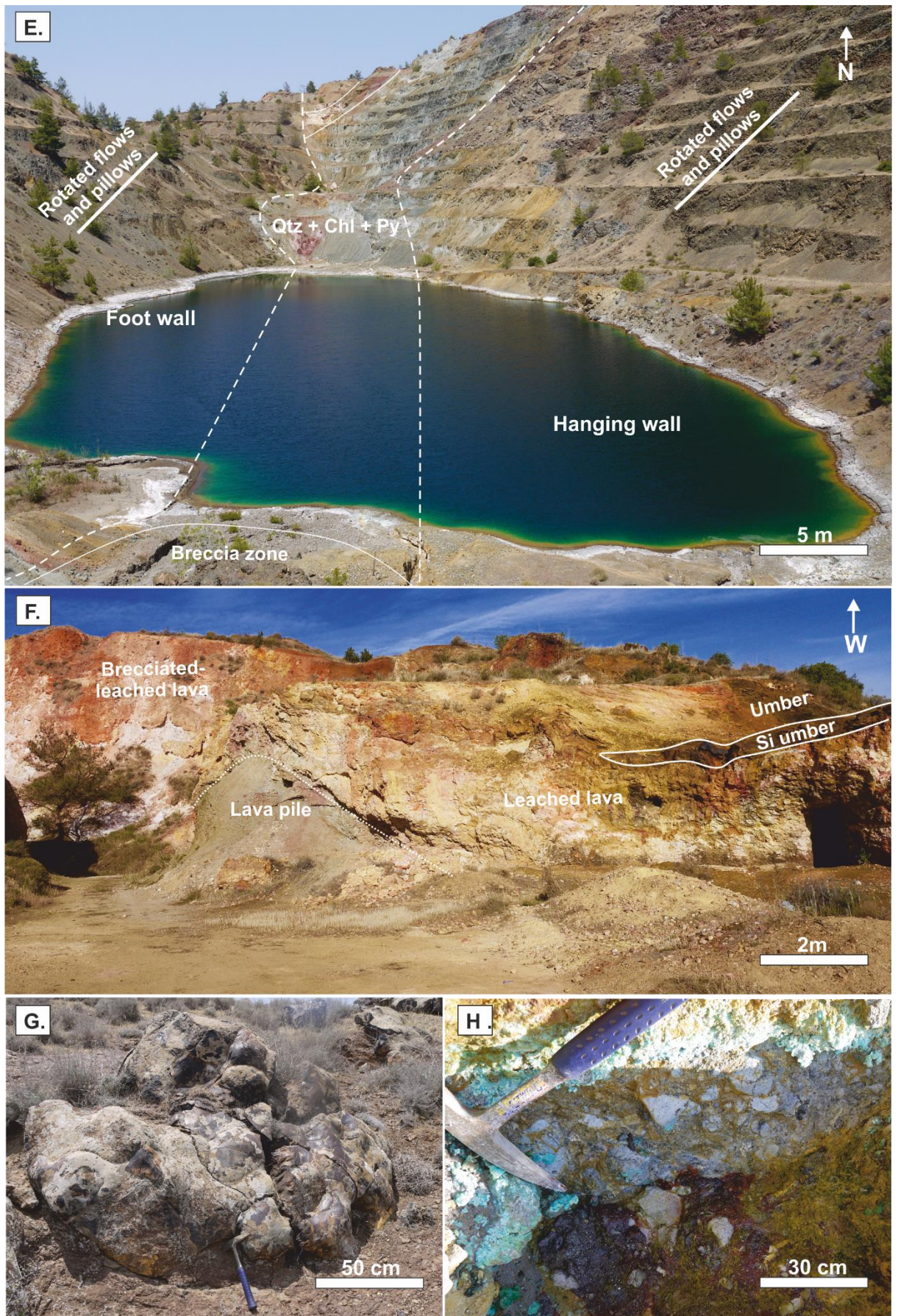


**Figure 3.20:** Examples of mineralisation in Troodos (see page 69 for explanation).

BLANK PAGE

# CHAPTER 4

## Methodology

## 4. Sample preparation

For whole rock geochemistry, field samples were cut and any weathered surface material removed. Samples were dried for 24 hours prior to crushing. Samples were crushed to mm-sized chips using a steel jaw crusher. The chips were pulverised using a W carbide TEMA ring mill until a fine powder was achieved.

Representative polished blocks of selected samples were prepared for in situ mineral analysis including Scanning Electron Microscopy, Laser Ablation ICP-MS and reflected light microscopy. Excess weathered material was first removed and blocks cut. Blocks were then set using Araldite 20/20 resin, highly friable samples were baked in a vacuum oven for 1 hour to ensure good resin impregnation so that the material remained competent during polishing. Initially samples were ground to remove excess resin and ground by hand using a three stage grind (440-1000  $\mu\text{m}$  grit). An ultra-sonic bath was performed prior to polishing to remove excess surface debris. Blocks were then polished using a Logitech PM-5 automated polisher using 0.3 $\mu\text{m}$  aluminium oxide slurry until the desired polish was achieved.

### 4.1 Whole rock geochemistry

#### 4.1.1 Portable X-ray fluorescence analysis

Portable X-ray Fluorescence (P-XRF) analysis was carried out on powdered samples (Section 4.0) at Cardiff University (UK). Portable-XRF was used as a screening tool allowing the rapid determination of whole rock geochemistry prior to SEM and LA-ICP-MS analysis. Twenty grams of sample was pressed into a plastic vessel with a Mylar cover slip (3 $\mu\text{m}$  thickness) ready for analysis (Analytical set-up Appendix 4.1). The use of a Mylar cover slip was preferable to a plastic film as it aided the penetration of X-rays leading to lower uncertainty. Analysis was performed using an Olympus Delta Professional P-XRF analysed in Geochem mode for 60 seconds to determine Mg, Al, Si, P, S, K, Ca, Ti, V, Cr, Mn, Fe, Co, Ni, Cu, Zn, As, Se, Rb, Sr, Y, Zr, Mo, Ag, Cd, Sn, Sb, W, Hg, Pb, Bi, Th and V. Te and Au were not analysable. Data quality was monitored by the repeat analysis of standards KPC1, SU1A and a silica blank every twenty samples. Whilst standards were monitored data is purely qualitative to ascertain the relative variation in elements between different samples.

### 4.1.2 Aqua regia digestion

Aqua regia digest was used preferentially over conventional Li-metaborate/tetraborate flux methods due to the highly volatile nature of Se and the sulfide- and iron or manganese-rich composition of many samples (e.g. Mn-rich umbers) that were not digestible via fusion. Instead a low temperature aqua regia digest was performed, the author does however acknowledge the limitations of this methods for silicates and residual minerals that are not aqua regia soluble. It is assumed that, as shown by in situ mineral analysis, that Se and Te are hosted within the readily soluble sulfide phases or adsorbed onto mineral surfaces, thus they are soluble in aqua regia.

To ascertain whole rock trace element geochemistry 0.5 g of powdered sample (section 4.0) was digested using 5ml of aqua regia (3:1 HCL:HNO<sub>3</sub>). Samples were left for 1 hour at room temperature for the initial reaction to subside then heated at 85 °C for 24 hours and left to cool for a further hour. This ensured the leachate remained well under the boiling point of the aqua regia solution (108°C) therefore limiting the potential for Se volatilisation. Sub-samples of the aqua regia leachate were then diluted using MilliQ 18.2 MΩ de-ionised water (1:5). Samples were stored in sealed 15ml test tubes ready for analysis. Blanks were prepared in the same manner but omitting any sample material.

### 4.1.3 Solution ICP-MS analysis

Quantitative trace element analysis was performed at Cardiff University using a Thermo iCAP RQ ICP-MS and data correction was performed using Thermo Qtegra software. Calibration standards were prepared using mixtures of single element 1000 ppm standard solutions in the same dilute aqua regia matrix as the unknown samples. Detection limits are summarised in Appendix 4.2.

## 4.2 In situ Mineral Analysis

### 4.2.1 LA-ICP-MS spot analysis

Laser Ablation ICP-MS was carried out at Cardiff University (UK) on polished sulfide blocks as described in Section 4.0. Elements analysed include <sup>57</sup>Fe, <sup>65</sup>Cu, <sup>59</sup>Co, <sup>66</sup>Zn, <sup>75</sup>As, <sup>77</sup>Se, <sup>109</sup>Ag, <sup>111</sup>Cd, <sup>121</sup>Sb, <sup>125</sup>Te, <sup>185</sup>Re, <sup>189</sup>Os, <sup>193</sup>Ir, <sup>195</sup>Pt, <sup>197</sup>Au <sup>206</sup>Pb and <sup>209</sup>Bi. In all analysis <sup>77</sup>Se was used for Se due to lower levels of interference from the ablation gas compared to <sup>82</sup>Se. Analyses were performed utilising both a Thermo X Series 2 ICP-MS and a Thermo iCAP RQ ICP-MS, in both cases a New Wave Research UP213 UV laser was used. Samples were analysed in time-resolved mode using a nominal spot diameter of 55 μm and 80 μm (depending on sulfide grain size) with a frequency

of 10 Hz and a fluence of between 6-9 J/cm<sup>2</sup>. Acquisition lasted 45 seconds and a gas blank was measured for 20 seconds prior to the start of analysis followed by a 10 second washout period post ablation. Detection limit for Se varied from 7-15 ppm for the different analytical runs due to mass interference associated with the Ar/Cl gas during ablation (Appendix 4.3). <sup>33</sup>S was used as an internal standard for all analyses. The conversion of counts per second data to concentrations, the subtraction of gas blanks and internal standard corrections were performed using Thermo Plasmalab and Thermo Qtegra software for the X-Series 2 and the iCAP RQ systems respectively.

Data quality was monitored through the repeat analysis of certified sulfide reference standard UQAC-FeS. Analysis of standard reference material, including precision calculations are available in Appendix 4.4. Initial instrument calibration was performed using a series of in house synthetic quenched Ni-Fe-S standards. Standards include S, Ni, Fe and Cu as major elements, and Co, Zn, As, Se, Ru, Rh, Pd, Ag, Cd, Sb, Te, re, Os, Ir, Pt, Au, Bi as trace elements. The repeat analysis of certified reference material yielded RSD values of <10% for Co, As, Se, Ag, Pb and Bi and between 10-18% RSD for Cu, Zn, Sb, Te and Au (see Appendix 4.5). RSD for Cd was 26%. Further compositional information and detailed analytical methods for standards may be found in the supplementary material of Prichard *et al.* (2013) and Smith *et al.* (2014). In all cases a stoichiometric value for S was used during sulfide analysis, this was shown to be within error of measured S values (Martin *et al.*, 2019; Chapter 5).

#### 4.2.2 LA-ICP-MS Line Analysis

Laser Ablation ICP-MS line analysis was performed with a spot size of 55 µm with a frequency of 10Hz in time resolved analysis mode using a New Wave Research UP213 UV laser system coupled to a Thermo X Series 2 ICP-MS. Standards are identical to those outlined for spot analysis (section 4.2.1). For line analysis, acquisition lasted between 80-120 seconds and the beam followed a pre-selected pattern at a scan speed of 6 µm/s aimed to intersect different sulfide phases. Subtraction of gas blanks and internal standard corrections were performed using Thermo Plasmalab software (see Prichard *et al.*, 2013; Smith *et al.*, 2014).

## 4.3 SEM Analysis

### 4.3.1 Automated mineral identification

Automated mineral scanning was used to search for discrete mineral phases, specifically tellurides. A Zeiss Sigma Field Emission Gun Analytical SEM (ASEM) equipped with two Oxford instruments 150 mm<sup>2</sup> X-MaxN silicon drift detector energy dispersive X-ray spectrometers (EDS) at Cardiff University (UK) was used. Scans utilised Oxford Instruments Aztec software's point and ID feature for preselected elements of interest (i.e. ones known to form discrete mineral phases) including S, Fe, Cu, Bi, Au, Ag, Pd, Se, Sb, Pb, Te, As and Pt. Maps were collected using an accelerating voltage of 20 kV, a fixed working distance of 8.9 mm and a 120 µm aperture. A magnification of 300x, image scan size of 512 pixels and a dwell time of 10 µs were used in order to achieve optimum balance between time and analytical resolution allowing the identification of features down to ~2 µm in size. The contrast and brightness of the BSE image was adjusted dependent on the sample analysed, in all cases the aim was to set the threshold so only 1 or 2 phases of the most atomically heavy mineral was identifiable (e.g. galena inclusions in pyrite). Any minerals of interest (i.e. Au, Te or Se phases) were re-analysed using EDS analyses to verify the finding of the automated scans. However, no tellurides were successfully identified using this technique.

### 4.3.2 Mineral/Element mapping

Element maps were constructed to assess zonation of metals in sulfide minerals, maps were constructed using a Sigma HD Field Emission Gun A-SEM equipped with two Oxford Instruments 150 mm<sup>2</sup> X-maxN energy dispersive spectrometers. Operating conditions were set at 20 kV, with a nominal beam current of 4 nA at a fixed working distance of 8.9 mm. Prior to mapping, samples were imaged in BSE mode. Using Aztec software, maps were acquired, and the resolution depended on the aim of the investigation, typically this ranged from a pixel size of 10 µm per pixel with a dwell time of between 1500-5000 µs at a magnification of 300 times. Oxford Instruments Aztec software was used for spectra deconvolution and to construct element maps. Spectral cross matching (i.e. from EDS spot analysis) was used to confirm mineral identification for phase designation (e.g. chalcopyrite- Chapter 6). Despite contrast in brightness of pyrite grains in BSE mode (cf. Chapter 9) EDS element maps were unable to resolve any geochemical differences between zonation in grain brightness. Analysis of samples on the ASEM that were previously identified as containing high Se via LA-ICP-MS (1 wt.%) yielded values below detectable limit on the A-SEM during both point analysis (EDS) and element mapping. This suggests that the ASEM is not capable of resolving Se concentrations even at concentrations of 1 wt.% Se.

## 4.4 X-Ray Diffraction Analysis

X-ray diffraction (XRD) was used for the identification and quantification of modal mineral phases. Analyses were carried out on powdered samples at Cardiff University (Section 4.0). Scans were run using the Philips PW1710 Automated Powder Diffractometer using Cu  $K\alpha$  radiation at 35kV and 40mA. Samples were scanned between 2 and 70  $^{\circ}2\theta$  at a scan speed of 0.04  $^{\circ}2\theta/s$ . From the scans, phases were identified using Philips PC Identify software and from the peak areas, semi-quantitative analysis was performed and a percentage of each phase present estimated.

## 4.5 Sulfur isotope analysis

### 4.5.1 Conventional Sulfur Isotope Analysis

Sulfur isotope ( $\delta^{34}S$ ) analysis was undertaken at the Scottish Universities Environmental research Centre (SUERC) supported by the NERC Isotope Geosciences Facilities Steering Committee grant IP-1766-1117 (Chapter 8 and 9). Samples analysed via conventional S extraction were either micro-drilled sulfide minerals or individual sulfide grains that were optically picked. Each grain was checked for purity using a stereomicroscope. Each analysis used approximately 4-5  $\mu g$  of sample that was subsequently converted to  $SO_2$  by combustion with 0.2 g of cuprous oxide following the methodology of Robinson and Kusakabe (1975). Samples were analysed using a VGA SIRA II gas source mass spectrometer. All values are calculated relative to the Vienna-Canyon-Diablo Troilite (V-CDT) standard, and are reported in standard notation (Chapter 8 and 9; Appendix 8.1). Data quality was monitored through the repeated analysis of standards NBS-123 (+17.1‰), IAEA-S-3 (-31‰), and SUERC's internal standard CP-1 (-4.6‰). The reproducibility of standards for all analyses was better than  $\pm 0.7\text{‰}$  ( $1\sigma$ ) (see Appendix 4.5).

### 4.5.2 In situ Sulfur Isotope Analysis

Laser combustion analysis were performed on polished blocks that were inserted into a sample chamber and air was evacuated and subsequently filled with an excess of oxygen (Fallick *et al.*, 1992). Dependant on sulfide grain size, individual grains with a cumulate area of 100-300  $\mu m$  were analysed. For sulfides  $<100 \mu m$ , a composite of smaller grains were analysed. The sulfide was combusted using a Spectron Lasers 902Q CW Nd:YAG laser (1 W power), operating in TEM<sub>00</sub> mode. Further details on system design, laser characteristics and experimental conditions are described in Kelley and Fallick (1990) and Wagner *et al.* (2002). The released  $SO_2$  gas from each ablation was then purified in a miniature vacuum line utilising an acetone- $CO_2$  slush trap to remove water and a standard n-pentane trap to separate  $SO_2$  from  $CO_2$  (Smith *et al.*, 2016).

Systematic  $\delta^{34}\text{S}$  fractionation of the  $\text{SO}_2$  during laser ablation (Smith *et al.*, 2016) was corrected by fractionation factors established for the SUERC facility: chalcopyrite +0.7‰ and pyrite +0.8‰ (Kelley and Fallick, 1990). Instrumental error for the spectrometer was better than 0.05‰ for all laser ablation analyses. Samples were analysed using a VGA SIRA II gas source mass spectrometer. All values are calculated relative to the Vienna-Canyon Diablo Troilite (V-CDT) standard and are reported in standard notation (Chapter 8 and 9; data Appendix 8.1).



# CHAPTER 5

## **Trace element systematics and ore-forming processes in mafic VMS deposits: Evidence from the Troodos ophiolite, Cyprus**

### **Submitted as:**

Martin, A.J., Keith M., McDonald, I., Hasse, K.M., McFall, K.A., Klemm, MacLeod, C.J., 2019.

**Trace element systematics and ore-forming processes in mafic VMS deposits: Evidence from the Troodos ophiolite, Cyprus.** *Ore Geology Reviews*, 106, 205–225.

### **Co-author contributions:**

M. Keith provided an additional trace element dataset (outlined in Appendix 5.1) that complimented Troodos data collected in this study. I. McDonald supervised laser ablation analysis. All authors were involved in discussion during the writing of this manuscript.

## 5. Abstract

The volcanogenic massive sulfide (VMS) deposits in the Troodos ophiolite (Cyprus) are ancient analogues for modern day seafloor massive sulfide mineralisation formed in a subduction zone environment. This study presents the first detailed in situ study of trace elements in sulfides from twenty VMS deposits hosted in the Troodos ophiolite to better understand factors that influence the distribution, enrichment and incorporation of trace elements in different sulfide minerals.

On a mineral scale, trace elements exhibit systematic variations between pyrite, chalcopyrite and sphalerite. Pyrite preferentially incorporates As, Sb, Au and Te, whilst chalcopyrite is enriched in Co and Se. Sphalerite is trace element poor with the exception of Ag and Cd. Selenium averages 278 ppm (n= 150) in chalcopyrite but only 42 ppm (n=1322) in pyrite. Bismuth and Te in pyrite show a weak positive correlation ( $R^2= 0.35$ ) in some VMS deposits possibly linked with the occurrence of Bi-telluride inclusions. Trace element concentrations also vary between colloform and euhedral pyrite, with an enrichment of Au, As, Sb, Cu and Zn in colloform compared to euhedral pyrite.

Time resolved laser ablation profiles reveal that the trace element distribution on a mineral scale is not uniform and varies with crystallographic effects, fluctuating physicochemical fluid conditions such as temperature, pH,  $fS_2$ ,  $fO_2$  and ligand availability during sulfide precipitation. Incorporation mechanisms in sulfides differ between elements in pyrite, Ag, As, Se and Pb are hosted in solid solution or as nanoscale inclusions, whilst Au, Sb and Te may form micro-scale inclusions.

On a regional scale (20 km) the distribution of trace elements exhibits systematic variations between three major structural domains; namely the Solea, Mitsero and Larnaca grabens. The VMS deposits of the magmatic-tectonic Solea graben are enriched in Se, Co, Te, Au and Cu relative to Mitsero, which is a purely extensional feature. Therefore, this study suggests that a variable magmatic volatile influx related to a) 'magma' volume, b) migration of the magmatic-hydrothermal crack front and associated brine liberation or c) a variation in protolith metal concentration are responsible for regional scale variations in VMS geochemistry. This is suggested to be intrinsically linked to the spreading architecture of Troodos.

## 5.1 Introduction

Subduction zone magmas commonly reach volatile saturation during differentiation in the crust, which results in the release of magmatic volatiles potentially rich in Cu, Au, Pb, As, Tl and other trace metals that can be contributed to the overlying hydrothermal system (de Ronde *et al.*, 2011; Keith *et al.*, 2018b; Herzig *et al.*, 1998a; White and Hedenquist, 1990; Williams-Jones and Heinrich, 2005; Wohlgemuth-Ueberwasser *et al.*, 2015). It is now widely accepted that the Troodos ophiolite hydrothermal systems and associated VMS deposits are fossil analogues to modern systems actively forming on the ocean floor (e.g. Franklin *et al.*, 1981; Hannington *et al.*, 1998; Humphris and Klein, 2018; Monecke *et al.*, 2014, cf. Chapter 3).

Phase separation is directly related to temperature, pressure (i.e. formation depth) and salinity (Monecke *et al.*, 2014; Schmidt *et al.*, 2007). Evidence for supercritical fluids can be inferred from fluid inclusions in fossil VMS systems (e.g. Kelley and Robinson, 1990; Kelley *et al.*, 1992). At 5°S on the Mid Atlantic Ridge (MAR) fluids are intermittently vented at 464°C (average 407°C; 3000 m depth; Koschinsky *et al.*, 2008), well above the critical point of seawater and thus sub-seafloor phase separation may be important in generating metal and chloride-rich brines in SMS systems that may be important for metal enrichment in fossil analogues, if the brine is contributed to the overlying hydrothermal system (de Ronde *et al.*, 2011; Keith *et al.*, 2016b; Koschinsky *et al.*, 2008). Kelley and Robinson (1990) and Kelley *et al.* (1992) pointed out the importance of metal-rich brines in the fossil Troodos hydrothermal systems (cf. Chapter 2).

Back-arc spreading centres and submerged island arc volcanoes account for 34 % of known vent sites (Hannington *et al.*, 2005; Humphris and Klein, 2018). Seafloor sulfide mineralisation in these environments is typically enriched in Zn, Pb, Au, Ag, Te, Se, Sb, Tl, As and Bi compared to MOR hydrothermal systems, which are interpreted to be due to the contribution of a magmatic volatile component derived from subduction zone-related magmas (Dekov *et al.*, 2016; Herzig and Hannington, 1995; Humphris and Klein, 2018; Moss and Scott, 2001).

Fossil analogues of back-arc spreading environments represent ideal natural laboratories to investigate the distribution and incorporation mechanisms of different trace elements in hydrothermal sulfide ores and their host minerals. The Troodos ophiolite (Cyprus) formed in a supra-subduction zone environment possibly associated with back-arc spreading, and therefore may exhibit an enrichment in magmatic volatile elements (Hannington *et al.*, 1998; Regelous *et al.*, 2014; Robertson and Xenophontos, 1993). Hence, the VMS systems hosted in the Troodos ophiolite offer the opportunity to study the processes of ore-formation and trace metal

enrichment with respect to spatial and temporal changes in the tectonic regime of subduction zone-related rift structures.

## 5.2 Sample localities

In total, samples from twenty different VMS deposits were investigated in this study. These have subsequently been classified into districts based on their corresponding structural domain (summarised in Table 5.1, Figure 5.1). For the purpose of this study I simplify the original classification by Moores *et al.* (1990) into five domains, from east to west: Larnaca, Southern Troodos Transform Fault Zone (STTFZ), Mitsero, Solea and Polis (Table 5.1, Figure 5.1). Structural domains are classified based on dip direction of the sheeted dyke complex (after Moores *et al.*, 1990; Figure 5.1).

The wide geographical spread of samples and diverse range of ore types including massive, disseminated, semi-massive and jasper-rich morphologies ensures that a wide range of ore-forming processes are investigated within and between different structural domains (Figure 2.1 and 5.1, Table 5.1). Hence, the data is representative for regional scale ore-forming processes related to spreading centre evolution.

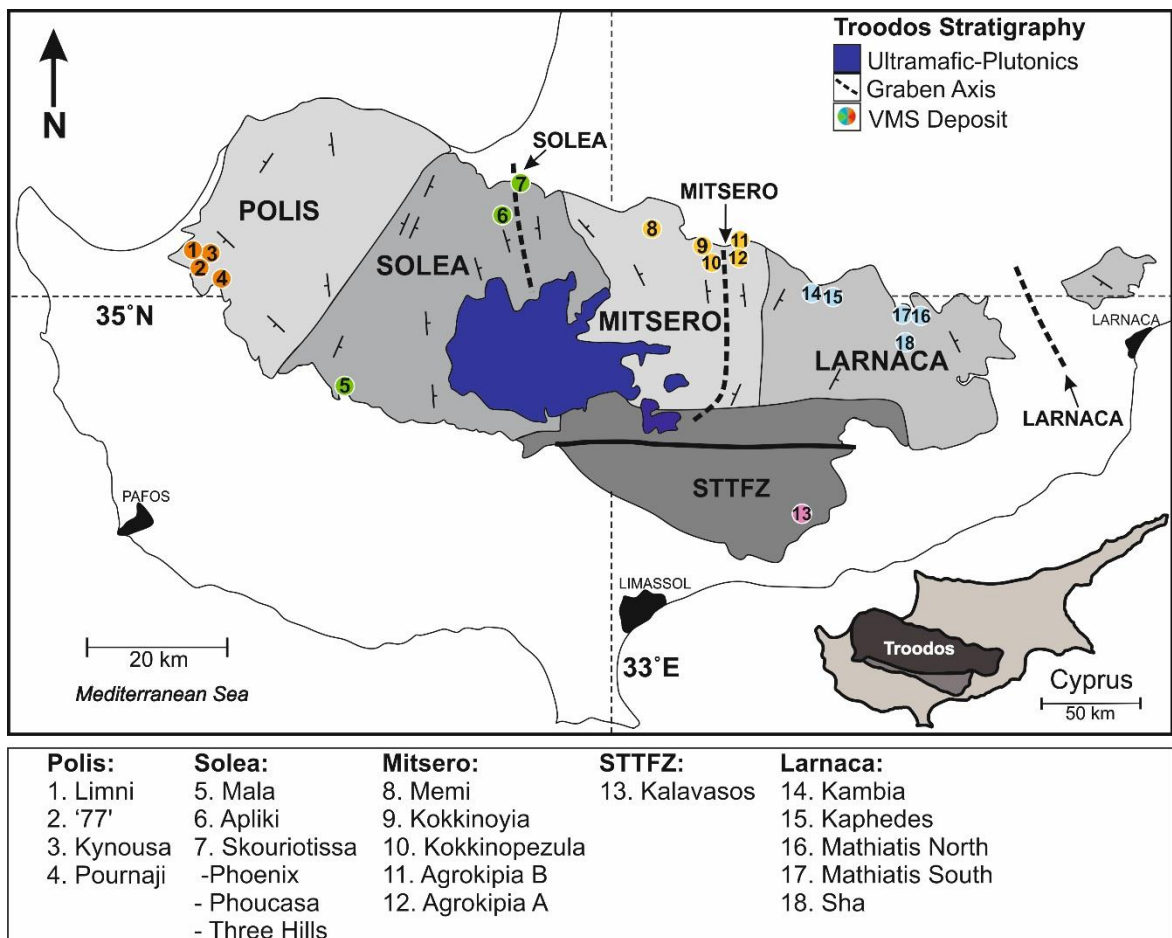


**Figure 5.1 (previous page):** Structural domain map of the Troodos ophiolite showing VMS deposits and structural domains based on dyke dip and strike. Simplified from the nine original districts defined by Moores *et al.* (1990). VMS deposit names analysed in this study are listed from W to E.

**Table 5.1:** Summary, location and mineral occurrences in VMS deposits considered in this study. PY = pyrite, CCP= chalcopyrite, SPH= sphalerite, CV= covellite (see also Appendix 3.1).

Locality	Location (WGS 1984)	Structural domain	Sample type	Mineral
Limni	045294 3877209	Polis	Disseminated, Massive	PY, CCP
Kynousa/Lysos	045555 3876810	Polis	Massive, Stockwork	PY, SPH, CCP
Pournaji	045529 3876352	Polis	Massive	PY
'77'	045404 3877993	Polis	Massive	PY
Mala	047042 3864323	Solea	Massive	PY
Apliki	048575 3881758	Solea	Stockwork	CV, CCP, PY
Phoucasa	048990 3883713	Solea	Stockwork, Massive	CCP, CV, PY
Phoenix	048993 3884050	Solea	Stockwork, Jasper	CCP, PY
Three Hills	049088 3883189	Solea	Stockwork	CCP, PY
Memi	050366 3877476	Mitsero	Massive, Disseminated	PY
Kokkinopezula	051038 3877259	Mitsero	Jasper	PY
Kokkinoyia	050974 3877946	Mitsero	Stockwork, Massive	PY, CCP
Agrokipia A	051327 3878134	Mitsero	Massive, Disseminated	PY
Agrokipia B	N/A	Mitsero	Stockwork	CCP, PY, SPH
Kaphedes	052394 3871610	Larnaca	Massive, Disseminated	PY
Kampia	052501 3872967	Larnaca	Massive, Jasper	PY
Mathiatis N	053185 3870606	Larnaca	Stockwork, Massive	CCP, PY, SPH
Mathiatis S	053170 3867617	Larnaca	Massive	PY
Sha	053414 3867843	Larnaca	Massive	PY
Kalavastos	052371 3850315	STTFZ	Stockwork	PY

### 5.3 Method Summary

Electron microprobe analysis (EMPA) was performed for selected sulfide samples to obtain major element data. Concentrations were obtained using a JEOL JXA-8200 Superprobe at the GeoZentrum Nordbayern (Keith *et al.*, 2016b). The quantitative EMP analyses were performed with a focused beam using an accelerating voltage of 20 kV and a beam current of 20 nA. The electron microprobe was calibrated by the following standards: FeS<sub>2</sub> (Fe,S), CuFeS<sub>2</sub> (Cu) and ZnS (Zn).

Dataset A (M. Keith dataset) was analysed using a New Wave Research UP193 FX laser coupled to an Agilent 7500i ICP-MS. A single spot ablation pattern was utilised at a frequency of 15 Hz with a typical beam size of 25 µm, and on occasion 20 and 15 µm according to pyrite crystal size. Total acquisition time of each spot was 40 seconds including a 20 second gas blank prior to each analysis. Standards used for external calibration (dataset A) include Po724 B2 SRM (Au)

(Memorial University Newfoundland) and MASS-1 (USGS) (V, Cr, Mn, Co, Ni, Cu, Zn, As, Se, Mo, Ag, Cd, Sb, Te, W, Pb, Bi).

Sulfur measurements from EMP analyses ( $n=905$ ) yielded average S concentrations for pyrite of 52.97 wt.%  $\pm$  1.14 ( $2\sigma$ ) ( $n=905$ ), therefore the stoichiometric values of 53.4 to 53.5 wt.% for dataset A are within error of measured values for dataset B (see Appendix 5.1-5.3). Similarly, S concentrations of 34.25 wt.%  $\pm$  0.70 ( $2\sigma$ ) in chalcopyrite are within error of the stoichiometric values for S (35-35.5 wt.%) used in dataset B.

## 5.4 Results

### 5.4.1 Ore petrography

Samples of sulfides have been classified into the following categories based on morphological and textural differences: massive (euhedral and colloform), semi-massive, stockwork, disseminated and jasper (Figure 5.2).

#### 5.4.1.1 Pyrite

Pyrite is present in all samples analysed in this study (Table 5.1). The texture and morphology vary reflecting the fluid conditions under which it formed (e.g. temperature,  $fO_2$ ,  $fS_2$  etc.). Pyrite occurs as massive (>75%) (Figure 5.2 A and B), semi-massive (50-75%) (Figure 5.2 C), colloform (Figure 5.2 D and E), disseminated (10-20%) (Figure 5.2 F and G) and veined varieties (Figure 5.2 H). Within these textures, pyrite grains vary from euhedral to anhedral and rarely framboidal. Many pyrite grains exhibit a degree of dissolution whereby originally euhedral pyrite may be altered to subhedral or 'feathery' textures. Granular pyrite is common in the upper VMS stratigraphy with framboidal grains, associated with jarosite, goethite and covellite (Figure 5.2 L). Resorbed grains commonly exhibit a porous or vuggy core; this is especially common for jasperitic samples where pyrite is intergrown with hematite and silica (Figure 5.2 E, I and L - yellow arrows). Inclusions of galena and sphalerite are present in some pyrite grains and are usually a few microns in size (via SEM- Appendix 5.2).

#### 5.4.1.2 Chalcopyrite

Chalcopyrite in massive pyrite samples (Figure 5.2 A, B, J and K and Table 5.1) forms interstitially as crude layers, surrounded by pyrite (Figure 5.2 A and B). In stockwork samples massive chalcopyrite forms as aggregates of globular grains that are cut by secondary covellite-digenite (Figure 5.2 A, B, K). Disseminated chalcopyrite is rare and overprints early pyrite (Figure 5.2 F). Secondary, seafloor or uplift-exposure related supergene alteration of chalcopyrite is evident in many VMS (e.g. Phoucasa or Apliki- Figure 5.2 K, L and M); in these samples chalcopyrite is variably altered to covellite and chalcocite.

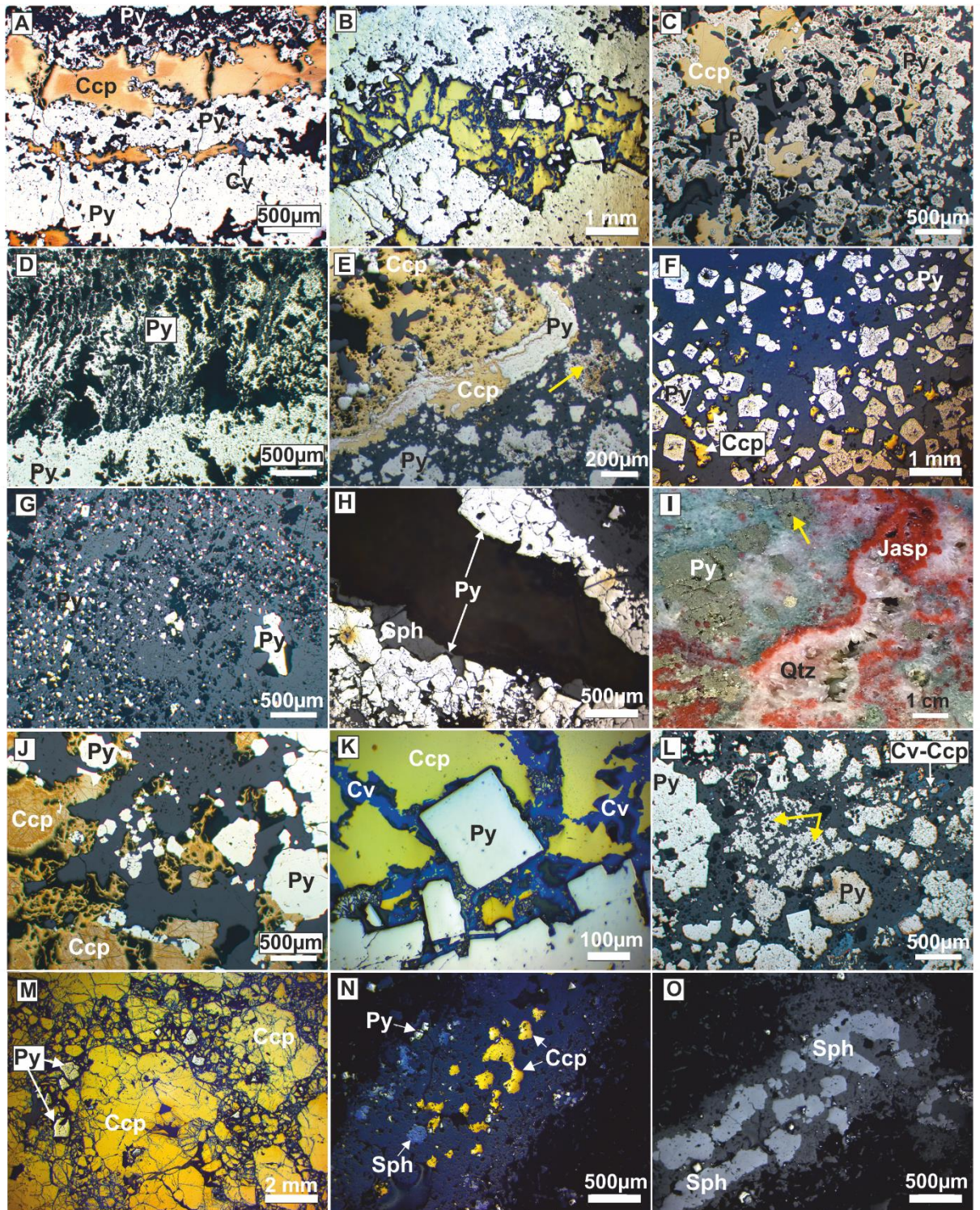


**Figure 5.2:** Reflected light photomicrographs of common sulfide textures in Troodos VMS. A) Banded pyrite-chalcopyrite in massive ore (Kokkinoyia). B) Late euhedral pyrite overprinting chalcopyrite that is altered to covellite (Phoucasa). C) Colliomorphic pyrite with interstitial chalcopyrite and silica. D) Colloform-dendritic, crudely layered pyrite (Mala). E) Pyrite overprinted by chalcopyrite with silica and goethite (Kokkinoyia). F) Disseminated euhedral pyrite in chloritised wall-rock with minor interstitial chalcopyrite (Limni). G) Disseminated pyrite infilling vesicles (Kokkinopezula). H) Anhedral aggregates of pyrite lining vein margins from Agrokippia B. I) Photograph (not reflected light) of jasperer (red) with quartz and feathery pyrite

dissolution texture from Skouriotissa. J) Semi-massive ore from Kokkinoyia, pyrite overprinted by chalcopyrite. K) Close up of euhedral pyrite overprinting chalcopyrite and extensive covellite (Phoucasa). L) Granular upper mound facies, pyrite is subhedral to framboidal (Phoucasa). M) Stockwork with massive chalcopyrite and minor subhedral pyrite (Apliki). N) Chalcopyrite, sphalerite and pyrite in quartz from Agrokipia B. O) Subhedral sphalerite occupying the centre of a quartz vein with minor disseminated pyrite (Agrokipia B). Yellow arrows indicate pyrite cores. PY= pyrite, CCP= chalcopyrite, SPH= sphalerite, CV= covellite.

### 5.4.1.3 Sphalerite

Sphalerite represents a minor constituent of the ores and was only observed at the Agrokipia B and the Mathiatis North VMS deposits (Table 5.1). It occurs as discrete subhedral crystals in veins and usually exhibits variable amounts of chalcopyrite disease (Figure 5.2 N and O). Sphalerite is commonly associated with pyrite and rarely with chalcopyrite (Figure 5.2 H, N and O).

### 5.4.2 Mineral chemistry

The analysed sulfides show a distinct trace element distribution. Variations in trace element concentrations are observed between pyrite ( $n=1322$ ), chalcopyrite ( $n=150$ ) and sphalerite ( $n=86$ ) (Figure 5.3, Table 5.2, 5.3 and 5.4). Pyrite contains elevated As, Te, and Sb relative to chalcopyrite and sphalerite. Chalcopyrite is notably enriched in Se over pyrite averaging 278 ppm ( $n=150$ ) in chalcopyrite but only 42 ppm ( $n=1322$ ) in pyrite (Figure 5.3, Table 5.2 and 5.5). Sphalerite is depleted in most trace elements except Ag and Cd (Figure 5.3). Pyrite that co-precipitated with chalcopyrite is enriched in Cu with concentrations up to 1.1 wt.% (Table 5.2 Apliki, Figure 5.2 M).

In pyrite, systematic variations between colloform and euhedral textures are observed, colloform pyrite is enriched in Ag, Cd and Mo relative to euhedral pyrite and depleted in Te, Co and Sb. Other elements exhibit no variation between different pyrite types. Gold at Skouriotissa, for example, has an average concentration of 0.5 ppm in both the euhedral ( $n=202$ ) and colloform varieties ( $n=53$ ). Most elements in pyrite ( $n=1322$ ) display no notable correlation (linear R values- Table 5.3). Exceptions are Au and As that show a weak to moderate positive correlation ( $R^2=0.46$ ), as well as Pb and Ag ( $R^2=0.31$ ) and Cd and Zn ( $R^2=0.53$ ). On an ophiolite wide scale Te exhibits no correlation with Bi in pyrite ( $R^2=0.05$ ). Pearson correlation coefficients (linear R values) between all elements analysed in pyrite are listed in Table 5.3, those for sphalerite and chalcopyrite can be found in Appendix 5.1.

Locality		Co	Ni	Cu	Zn	As	Se	Mo	Ag	Cd	Sb	Te	Re	Pb	Au	Bi
Pyrite	<i>n</i> = 1322	ppm	ppm	%	ppm	ppm	ppm	ppm	ppm	ppm	ppm	ppm	ppm	ppm	ppm	ppm
<b>Limni</b> <i>n</i> = 19	Max	3333	400	0.4	2040	1047	885.6		0.8		6.2	42.9	2.38	5200	0.02	8.99
	Min	14.1	200	0.01	23.6	20.5	18.8		0.08		0.2	0.7	0.03	226.0	0.02	0.14
	Average	998.9	300	0.14	271.7	278.9	118.0		0.5		1.3	10.2	0.27	1053	0.02	4.0
	Median	551.2	300	0.1	103.5	141.5	44.7		0.5		0.7	5.9	0.07	500		3.3
	$\sigma$	972.3	80.0	0.14	543.4	312.7	201.3		0.3		1.7	11.5	0.70	1325		3.2
<b>Kynousa</b> <i>n</i> = 95	Max	65.6	11.1	0.13	115602	2168	437	0.4	2.5	18.0	9.3	44.3	0.02	232	0.36	93.3
	Min	0.07	0.4	<0.01	5.0	0.4	17	0.04	0.03	0.1	0.06	1.1	0.02	0.1	0.02	0.01
	Average	6.4	2.7	0.03	15321	452.7	234.2	0.1	0.5	1.7	2.1	19.6	0.02	34.9	0.15	9.9
	Median	0.9	1.7	0.02	375.8	274.0	240.0	0.08	0.2	0.3	1.1	20.9	0.01	7.0	0.08	1.0
	$\sigma$	14.7	1.6	0.03	34864	482.3	132.2	0.1	0.7	3.9	2.9	12.9	0.004	60.3	0.12	22.9
<b>Pournaji</b> <i>n</i> = 10	Max	41.2	300	0.02	603.1	341.6	92.0		5.8	6.1	1.1	48.6	0.37	4093		4.4
	Min	2.1	300	0.02	72.2	19.5	45.3		0.5	1.6	0.3	1.2	0.07	1060		0.2
	Average	12.0	300	0.02	369.9	175.1	63.4		2.6	3.6	0.7	15.9	0.20	2500		1.5
	Median	2.5			476.2	247.7	70.1		1.3	3.4	0.7	21.3	0.07	1700		1.4
	$\sigma$	19.5			229.0	148.3	16.4		2.4	1.8	0.4	15.3	0.15	1100		1.4
<b>'77'</b> <i>n</i> = 11	Max				136.8	3962	43.6		3.8		58.3	6.1		15385	0.05	3.5
	Min				21.1	4.3	21.2		0.4		0.3	2.4		1200	0.02	0.2
	Average				66.7	836.7	27.9		2.1		11.4	3.7		7100	0.03	1.1
	Median				42.2	276.2	8.1		2.1		3.7	2.8		5000	0.03	1.0
	$\sigma$				61.6	1265	8.1		2.4		21.0	2.0		6300	0.02	1.5
<b>Mala</b> <i>n</i> = 10	Max	288.3		1.0	912.2	411.0	465.1		6.3	2.8	8.1	14.3	0.12		2.92	1.3
	Min	10.9		0.07	25.4	2.2	17.0		0.9	2.8	0.2	1.9	0.05		0.31	0.2
	Average	82.4		0.3	309.5	72.5	90.0		4.1	2.8	3.0	6.1	0.09		1.74	0.8
	Median	56.0		0.14	201.0	30.2	50.0		4.8		1.9	4.4	0.09		1.92	0.8
	$\sigma$	84.2		0.4	319.8	122.9	133.8		2.2	0	3.3	4.5	0.05		1.12	0.5

**Table 5.2:** Summary of pyrite geochemistry from 20 VMS of Troodos. Maximum (Max), minimum (Min), average, median and standard deviation ( $\sigma$ ) (full data and detection limits are available in supplementary material Appendix 5.1).

Locality	Cont.	Co	Ni	Cu	Zn	As	Se	Mo	Ag	Cd	Sb	Te	Re	Pb	Au	Bi
<b>Pyrite</b>	<b>n= 1322</b>	<b>ppm</b>	<b>ppm</b>	<b>%</b>	<b>ppm</b>											
<b>Apliki</b> <b>n = 98</b>	Max	1892	940.2	1.1	36810	878.1	4942		2.6	4.5	19.6	70.5	5.82	7061	0.95	38.5
	Min	1.5	186.7	0.01	19.3	4.3	28.5		0.3	4.5	0.4	0.7	0.02	184.5	0.01	0.04
	Average	258.3	459.1	0.2	1396	161.0	1229		0.8	4.5	4.1	11.5	0.59	2097	0.23	2.8
	Median	168.0	400	0.1	64.9	122.7	1157		0.5		2.8	6.5	0.6	1100	0.08	1.5
	$\sigma$	303.8	233.7	0.2	5962	158.6	959.7		0.7		4.2	11.8	1.22	2216	0.29	5.4
<b>Phoucasa</b> <b>n = 135</b>	Max	4363	637.8	1.9	2599	399	436.4	37.9	86.4	43.2	6.9	16.4	5.30	8873	4.80	14.8
	Min	0.04	0.2	<0.01	4.2	3.9	1.6	0.3	0.02	0.2	0.2	0.2	0.01	2.9	0.04	0.01
	Average	193.5	15.7	0.05	258.3	84.3	50.2	13.9	3.2	1.4	1.8	4.2	0.27	185.4	0.57	0.8
	Median	12.8	2.0	0.01	68.7	52.4	10.0	103.0	1.1	0.4	1.3	2.0	0.05	40.0	0.42	<0.01
	$\sigma$	564.3	85.6	0.2	487.4	83.5	100.5	10.5	10.4	5.3	1.6	5.1	0.99	1048	0.75	2.3
<b>Phoenix</b> <b>n = 170</b>	Max	5833	7244	12.7	12944	1405	1886	7244	72.5	3.7	51.0	53.0	0.99	6090	0.65	18.2
	Min	8.4	4.0	<0.01	12.5	0.5	4.0	0.1	0.05	0.3	0.1	0.3	0.02	7.0	0.03	0.01
	Average	510.3	529.8	0.3	627.9	111.8	377.4	297.4	3.0	1.0	4.6	8.3	0.13	175.4	0.22	1.3
	Median	223.7	200.0	<0.01	29.6	33.4	155.0	0.9	0.3	0.8	0.5	5.0	0.07	4.0	0.20	0.5
	$\sigma$	847.1	1111	1.5	2525	227.6	487.7	1331	11.6	0.8	14.0	10.2	0.21	872.6	0.17	2.5
<b>Three Hills</b> <b>n=15</b>	Max	1266.9	5426	1.4	12073	564.3	436.4		7.5	27.9	28.2	36.1	0.04	9875	0.48	1.9
	Min	12.4	250.6	0.03	27.0	2.1	17.1		2.9	1.3	15.8	0.5	0.03	204.6	0.02	0.06
	Average	517.0	1522.1	0.5	2384	172.4	114.7		5.2	10.7	21.0	5.8	0.03	3378	0.25	0.8
	Median	401.8	300.0	0.1	35.8	61.7	53.0		5.2	3.0	21.0	1.99	0.03	1700	0.25	0.4
	$\sigma$	473.2	2482.8	0.8	4205	267.1	138.0		3.2	14.9	10.2	10.3	0.01	4420	0.33	0.8
<b>Memi</b> <b>n = 11</b>	Max	18.0		0.05	76359	686.0			1.7	30.1	44.3	152.0	0.03		0.09	506.3
	Min	1.2		<0.01	23.1	2.4			0.05	8.9	0.2	0.9	0.03		0.03	0.5
	Average	6.9		0.02	19985	189.0			0.8	17.1	19.3	27.1	0.03		0.06	66.9
	Median	4.3		0.02	204.6	30.4			0.8	12.2	17.4	12.1			0.06	15.6
	$\sigma$	7.9		0.02	29899	271.4			0.8	11.4	20.1	48.2			0.03	148.9

**Table 5.2:** Summary of pyrite geochemistry from 20 VMS of Troodos. Maximum (Max), minimum (Min), average, median and standard deviation ( $\sigma$ ) (full data and detection limits are available in supplementary material Appendix 5.1).

Locality	Cont.	Co	Ni	Cu	Zn	As	Se	Mo	Ag	Cd	Sb	Te	Re	Pb	Au	Bi
Pyrite	<i>n</i> = 1322	ppm	ppm	%	ppm	ppm	ppm	ppm	ppm	ppm	ppm	ppm	ppm	ppm	ppm	ppm
<b>Kokkino-pezula</b> <i>n</i> = 10	Max	1713		0.02	36.8	139.9	211.5				0.4	118.1				10.1
	Min	5.5		0.01	17.6	5.1	17.2				0.3	1.1				0.1
	Average	318.0		0.01	26.5	67.7	60.8				0.3	26.2				2.7
	Median	136.4		0.01	27.3	49.4	40.1				0.4	15.7		300.0		1.3
	$\sigma$	518.4		<0.01	7.7	58.3	58.6					0.03	36.2			
<b>Kokkinoyia</b> <i>n</i> = 59	Max	223.1		2.1	81011	19082	235.7		84.3	12.5	1123	28.3	0.86	2210	14.11	24.8
	Min	0.8		0.01	11.6	5.6	12.6		0.1	2.3	0.2	0.4	0.02	136.3	0.04	0.1
	Average	31.9		0.1	6270	834.0	77.9		10.6	7.1	56.1	3.3	0.25	709.4	2.08	4.8
	Median	14.4		0.04	173.0	149.0	54.0		3.1	6.2	6.7	3.5	0.03	319.1	0.65	1.7
	$\sigma$	45.4		0.3	19384	2879	73.9		19.1	4.5	179.0	6.3	0.33	769.6	3.38	6.8
<b>Agrokipia A</b> <i>n</i> = 15	Max	2.6		0.05	5931	1316	61.1		14.9	10.1	55.0	20.5	0.09	14503	0.2	24.6
	Min	1.2		0.01	11.6	29.5	14.1		0.1	1.2	0.2	0.6	0.02	14503	0.01	0.2
	Average	1.8		0.03	1825	596.3	32.9		3.5	4.6	21.6	5.6	0.06	14503	0.07	7.3
	Median	1.7		0.02	811.1	569.8	28.9		1.6	3.5	21.6	1.7	0.06		0.04	4.7
	$\sigma$	0.5		0.01	2002	385.5	18.8		4.6	3.3	18.4	6.7	0.04		0.08	8.8
<b>Agrokipia B</b> <i>n</i> = 16	Max	130.9		0.04	251152	5414	82.3		10.3	58.9	195.4	15.4	0.04	10182	0.04	1.8
	Min	1.4		0.01	15.8	3.5	15.2		0.8	1.2	19.4	0.8	0.03	442.9	0.02	0.1
	Average	30.0		0.02	35771	1816	32.1		4.5	18.4	73.0	3.9	0.03	3811	0.03	0.8
	Median	9.1		0.02	2565	14667	20.0		4.0	6.8	63.0	1.3	0.03	3100	0.03	0.6
	$\sigma$	40.6		0.01	81957	1876	28.5		3.1	27.1	55.7	6.4	0.01	3478	0.02	0.6
<b>Kaphedes</b> <i>n</i> = 12	Max	234.4		0.21	23755	302.2	639.7		0.4	9.8	3.8	21.1	0.04	1360		19.7
	Min	1.8		0.01	23.0	1.6	31.3		0.3	9.8	0.4	1.5	0.02	191.3		0.06
	Average	54.9		0.07	2516	100.2	242.9		0.4	9.8	1.4	10.2	0.03	574.2		7.5
	Median	3.8		0.03	495.1	59.3	158.2		0.4		0.6	8.9	0.03	400.0		6.5
	$\sigma$	84.9		0.08	6719	117.2	238.2		0.03		1.5	6.9	0.01	440.5		6.1

**Table 5.2:** Summary of pyrite geochemistry from 20 VMS of Troodos. Maximum (Max), minimum (Min), average, median and standard deviation ( $\sigma$ ) (full data and detection limits are available in supplementary material Appendix 5.1).

Locality	Cont.	Co	Ni	Cu	Zn	As	Se	Mo	Ag	Cd	Sb	Te	Re	Pb	Au	Bi
Pyrite	<i>n</i> = 1322	ppm	ppm	%	ppm	ppm	ppm	ppm	ppm	ppm	ppm	ppm	ppm	ppm	ppm	ppm
<b>Kambia</b> <b>n = 26</b>	Max	561.3		0.04	1974	2840	361.0		7.9		36.5	5.4		18458	0.74	6.0
	Min	0.8		0.04	15.0	3.8	21.8		0.03		0.2	0.5		223.6	0.01	0.1
	Average	74.0		0.04	326.6	632.4	81.1		1.7		7.1	2.1		4115	0.19	2.4
	Median	20.9			42.1	325.9	35.3		1.2		4.1	1.4		1400	0.06	1.8
	$\sigma$	131.8			541.3	840.1	92.8		2.3		9.5	1.4		5655	0.28	2.0
<b>Mathiatis N</b> <b>n = 239</b>	Max	1767	410.0	0.46	23282	1021	342.9	159	9.6	8.7	2873	6.6	0.2	140198	17.10	6.6
	Min	0.06	0.4	<0.01	2.9	5.8	2.9	0.09	0.03	0.2	0.2	0.6	0.02	0.09	0.01	0.01
	Average	94.2	64.0	0.04	59.3	156.4	59.3	21.2	1.3	0.8	72.5	1.6	0.06	2131	1.08	0.6
	Median	4.3	33.0	0.01	17.2	103.0	23.6	5.2	0.8	0.5	4.7	1.1	0.05	330.0	0.31	0.1
	$\sigma$	263.2	83.0	0.08	3902	170.3	92.2	32.6	1.5	1.1	396.7	1.4	0.04	14738	2.74	1.3
<b>Mathiatis S</b> <b>n = 21</b>	Max	403.8		0.05	77306	2077	65.3		25.4	5.1	378.3	14.7	0.06	17601	0.13	2.6
	Min	3.3		0.01	16.1	4.0	15.3		0.4	1.6	1.5	5.8	0.06	202.1	0.03	0.08
	Average	49.5		0.03	10868	569.6	38.3		7.6	2.9	123.5	9.9	0.06	3016	0.06	1.4
	Median	9.5		0.03	33.2	568.7	45.9		5.1	3.4	96.9	9.4		2100	0.06	1.5
	$\sigma$	104.3		0.01	22667	557.0	21.2		7.7	1.5	126.5	3.5		4261	0.06	1.1
<b>Sha</b> <b>n =90</b>	Max	22.7	53.0	0.3	3201	3391	143	26.2	5.1	9.7	25.2	332		93.1	1.6	20.0
	Min	0.16	0.4	<0.01	16.4	0.5	5.8	0.2	0.05	0.3	0.4	1.1		0.1	0.07	0.02
	Average	5.9	2.7	0.03	939.9	512.3	36.8	4.7	0.8	2.4	9.2	70.5		20.6	0.67	4.1
	Median	0.8	2.4	<0.01	407.0	123.0	32.4	1.5	0.4	1.6	6.1	33.0		9.7	0.46	4.1
	$\sigma$	8.7	1.9	0.07	1255	882.4	33.1	7.2	1.2	2.3	8.6	77.5		27.1	0.51	5.8
<b>Kalavasos</b> <b>n = 260</b>	Max	3940	159	0.07	5593	20562	777.0	502.0	11.0	1.1	1082	67.0	0.4	579.0	40.04	14.0
	Min	0.1	0.3	<0.01	2.3	0.3	2.9	0.1	0.02	0.2	0.2	0.1	0.01	0.04	0.02	0.01
	Average	331.6	17.6	0.01	393.3	487.1	60.4	12.5	0.6	0.5	74.2	8.6	0.1	22.9	2.10	1.0
	Median	123.0	7.0	<0.01	32.2	31.4	34.7	1.0	0.1	0.5	5.0	3.8	0.08	1.0	0.12	0.1
	$\sigma$	577.5	29.5	0.01	1342	2160	98.6	57.1	1.6	0.2	226.1	12.2	0.08	73.2	6.65	2.3

**Table 5.2:** Summary of pyrite geochemistry from 20 VMS of Troodos. Maximum (Max), minimum (Min), average, median and standard deviation ( $\sigma$ ) (full data and detection limits are available in supplementary material Appendix 5.1).

Pyrite	Co	Ni	Cu	Zn	As	Se	Mo	Ag	Cd	Sb	Te	Re	Pb	Au	Bi
Co	1														
Ni	0.22	1													
Cu	0.01	0.02	1												
Zn	-0.05	0.14	-0.01	1											
As	-0.05	-0.03	-0.01	0.03	1										
Se	-0.06	0.21	0.05	-0.09	-0.05	1									
Mo	-0.10	-0.05	-0.02	-0.05	0.33	-0.07	1								
Ag	-0.06	0.03	0.04	0.17	0.30	-0.02	0.05	1							
Cd	-0.05	0.00	0.05	0.73	0.03	-0.03	0.00	0.27	1						
Sb	-0.05	-0.02	-0.01	-0.03	0.30	-0.06	0.23	0.12	-0.02	1					
Te	0.07	0.00	-0.04	0.04	0.02	-0.06	-0.09	-0.10	0.01	-0.06	1				
Re	0.11	0.01	0.00	-0.04	0.02	0.27	-0.18	0.00	-0.07	-0.07	0.19	1			
Pb	-0.06	0.28	0.03	0.17	0.41	-0.05	-0.01	0.52	0.27	0.24	-0.09	0.03	1		
Au	-0.05	-0.03	-0.03	-0.04	0.68	-0.16	0.26	0.09	0.03	0.12	-0.02	-0.05	-0.08	1	
Bi	-0.01	0.00	-0.01	0.30	0.01	0.06	-0.02	-0.02	0.25	-0.02	0.23	0.04	0.06	-0.03	1

**Table 5.3:** Correlation matrix (linear R values) of trace elements in pyrite (n=1322). Correlation between trace elements is limited with the notable exception of Zn-Cd, Pb-Ag and Au-As.

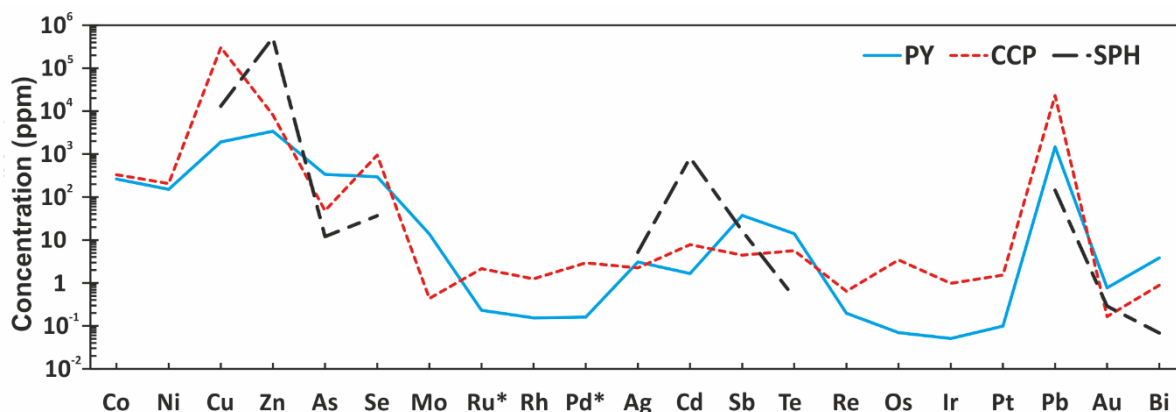


**Figure 5.3:** Average concentration of major and trace elements by mineral in ppm. Ru and Pd are average values of <sup>105,106,108</sup> Pd and <sup>99,101</sup> Ru. Chalcopyrite preferentially incorporates PGE'S, Se, Co and Ni. Pyrite is enriched in Bi, Te, As, Sb and Au. Sphalerite is enriched in Ag and Cd.

### 5.4.3 Time Resolved Analysis

To resolve the distribution of trace elements in different sulfide phases, a series of time-resolved line analyses were carried out by LA-ICP-MS (Figure 5.4). Line analyses are essential to obtain information on trace element distribution and their incorporation mechanism down to a micron-scale in different sulfide phases. Additionally, time resolved analysis provided qualitative information on element concentration with count rate indicating the relative concentration of each given element. Three euhedral pyrites from Apliki (Figure 5.4 E) exhibit variations in element concentrations between and within individual crystals, i.e. trace metal zonation. The variability in each element, i.e. a jagged (Figure 5.4 D- Te) or smooth appearance of the time resolved analysis profile (Figure 5.4 D- Se) may indicate their incorporation mechanism, for example as a lattice bound substitution or as micro inclusions (jagged) (see section 5.4).

Locality		Co	Ni	Cu	Zn	As	Se	Mo	Ag	Cd	Sb	Te	Re	Pb	Au	Bi
Chalcopyrite	<i>n</i> = 150	ppm	ppm	%	ppm	ppm		ppm	ppm	ppm	ppm	ppm	ppm	ppm	ppm	ppm
<b>Apliki</b> <b>n = 55</b>	Max	29.0	493.8	35.8	1831	96.5	3956		3.7	5.9	2.1	30.0	2.9	4800	0.01	12.1
	Min	1.6	493.8	20.8	35.4	17.6	103.7		0.5	1.7	0.4	0.4	0.03	100.0	0.01	0.04
	Average	8.7	493.8	31.4	287.5	47.2	1608		2.3	2.8	1.1	4.9	0.7	1100	0.01	0.6
	Median	4.4		31.7	145.7	27.6	1787		2.4	2.0	0.9	2.9	2.9	700.0		0.1
	$\sigma$	8.1		2.8	354.5	42.9	1065		1.3	1.8	0.7	6.2	1.3	1300	0.13	2.1
<b>Phoucasa</b> <b>n = 20</b>	Max	1335	442.4	40.5	5641	51.8	1040		13.1	12.6	5.8	171.0	4.7	43000	0.52	9.1
	Min	1.8	442.4	25.8	25.2	2.6	248.8		0.2	1.2	0.3	1.0	0.04	200.0	0.03	0.06
	Average	155.4	442.2	30.7	892.7	13.1	593.4		4.7	3.5	2.0	17.8	3.4	14700	0.20	1.5
	Median	15.2		30.0	467.7	4.4	505.1		2.7	2.1	1.1	2.5	0.2	800	0.07	0.4
	$\sigma$	338.8		3.3	1551	18.5	231.6		4.5	3.6	2.1	43.8	5.1	1600	0.06	2.5
<b>Phoenix</b> <b>n = 21</b>	Max	1.8		35.0	40.1	0.5	923.0	0.2	1.6	3.0		1.6		5400	0.03	0.1
	Min	0.3		33.8	32.9	0.5	217.0	0.2	0.05	0.7		0.5		900.0	0.04	0.02
	Average	1.0		34.4	36.1	0.5	666.0	0.2	0.8	1.9		0.9		3100	0.03	0.04
	Median	0.9		35.0	40.1		676.0		0.6	2.1		0.8		3000	0.01	0.02
	$\sigma$	0.5		0.3	2.5		250.3		0.7	0.9		0.4		2300	1.34	0.02
<b>Three Hills</b> <b>n = 15</b>	Max	91.7	958.0	29.4	659271	310.3	87.4		16.3	8.9	9.9	4.2	1.6	16000	0.06	0.6
	Min	26.7	958.0	21.2	260.8	4.0	14.7		0.3	1.6	0.9	0.8	0.2	500.0	0.03	0.1
	Average	60.1	958.0	25.3	45781	86.7	36.2		2.4	4.3	3.9	2.0	0.9	4800	0.04	0.3
	Median	61.8		24.5	780.8	16.2	33.2		1.0	4.0	0.9	1.4	0.9	1300	0.03	0.2
	$\sigma$	32.6		2.7	169731	149.5	21.2		4.4	2.2	5.2	1.3	1.0	6600	0.01	0.2
<b>Mala</b> <b>n = 3</b>	Max	22.8		32.5	222480		14.1		4.5	134.9		0.7				
	Min	18.8		31.5	9044		14.1		2.9	4.3		0.7				
	Average	20.2		31.9	85209		14.1		3.9	50.2		0.7				
	Median	19.0		31.6	23804				4.4	11.5						
	$\sigma$	2.3		0.6	119195				0.9	73.4						

**Table 5.4:** Summary of chalcopyrite geochemistry from 8 VMS of Troodos. Maximum (Max), Minimum (Min), average, median and standard deviation ( $\sigma$ ) (full data is available in Appendix 5.3).

Locality		Co	Ni	Cu	Zn	As	Se	Mo	Ag	Cd	Sb	Te	Re	Pb	Au	Bi
Chalcopyrite	<i>n</i> = 150	ppm	ppm	%	ppm	ppm		ppm	ppm	ppm	ppm	ppm	ppm	ppm	ppm	ppm
<b>Kokkinoyia</b> <b>n = 17</b>	Max	179.4		34.7	3226	3226	387.4	3202	6.9	3.0	3.2	27.7	0.1	8124	0.09	13.4
	Min	179.4		16.9	119.7	119.7	9.5	73.8	0.4	1.1	0.3	0.4	0.04	8124	0.05	0.07
	Average	179.4		29.9	1424	1423	135.5	1437	1.9	2.4	1.3	4.0	0.06	8124	0.07	2.4
	Median			31.4	1375	9.7	1843		0.6	2.6	0.9	1.0	0.05		0.07	0.1
	$\sigma$			4.3	1142	1141	218.1	1306	2.6	0.6	1.3	7.7	0.03		0.03	5.4
<b>Mathiatis N</b> <b>n= 15</b>	Max	4.0		34.9	2457	70.9	79.3	0.7	0.5	3.2	60.7			217000	1.18	0.03
	Min	0.2		33.2	618	1.1	37.4	0.5	0.07	1.0	69.7			2000	0.04	0.02
	Average	1.1		34.6	1754	20.0	54.8	0.6	0.3	2.4	69.7			81900	0.60	0.03
	Median	0.4		34.6	1970	4.0	49.5	0.6	0.4	2.7				54300	0.57	0.03
	$\sigma$	1.7		0.4	869.9	33.9	18.3	0.1	0.2	0.8				90000	0.57	<0.01
<b>Kalavasos</b> <b>n = 4</b>	Max	11.2		34.6	5813		8.1		0.1	16.6						
	Min	5.2		33.7	5145		7.5		0.1	10.9						
	Average	8.2		34.1	5479		7.8		0.1	13.8						
	Median	8.2		34.8	5479		7.8		0.1	13.8						
	$\sigma$	4.3		0.4	472.4		0.4		<0.01	4.0						

**Table 5.4:** Summary of chalcopyrite geochemistry from 8 VMS of Troodos. Maximum (Max), Minimum (Min), average, median and standard deviation ( $\sigma$ ) (full data is available in Appendix 5.3).

Locality		S	Fe	Zn	Cu	As	Se	Ag	Cd	Sb	Te	Re	Pb	Au	Bi	
Sphalerite	n= 86	%	%	%	%	ppm	ppm	ppm	ppm	ppm	ppm	ppm	ppm	ppm	ppm	
EMPA					LA-ICP-MS											
<b>Kynousa</b> n = 2	Max	33.28	1.12	65.46	0.19				3400							
	Min	32.58	0.90	65.22	0.09				3400							
	Average	32.93	1.01	65.34	0.14				3400							
	Median	32.93	1.01	65.34	0.14											
	$\sigma$	0.49	0.16	0.17	0.07											
<b>Phoucasa</b> n = 65	Max	39.35	29.48	55.97	8.97				2060							
	Min	33.51	8.64	30.14	0.07				70.0							
	Average	34.72	14.77	47.52	2.21				910.9							
	Median	34.23	13.91	48.42	1.14				720.0							
	$\sigma$	1.33	3.79	4.56	2.39				461.0							
<b>Agrokipia B</b> n =10	Max			69.0*	0.62*		20.0	1.3	192.8	1.3			382.5		0.07	
	Min	<b>Not Analysed</b>		61.1*	0.46*		20.0	0.7	119.0	0.3			131.2		0.07	
	Average			65.3*	0.53*		20.0	1.1	155.8	0.8			292.7		0.07	
	Median			64.5*	0.52*			1.2	157.7	0.6			364.4			
	$\sigma$			3.0*	0.07*			0.3	26.9	0.4			140.1			
<b>Mathiati N</b> n = 9	Max	33.13	13.98	60.97	0.88	29.7	98.3	26.0	1500	193.0	0.5					
	Min	32.10	5.65	52.11	<0.01	1.1	19.5	1.8	400.0	0.2	0.5					
	Average	32.85	10.59	55.47	0.20	15.4	46.8	8.8	800.0	29.8	0.5					
	Median	32.89	11.45	54.33	0.14	15.4	37.7	6.2	800.0	0.3	0.5					
	$\sigma$	0.31	2.71	2.89	0.07	20.2	31.6	8.1	353.6	72.2	0.01					

**Table 5.5:** Summary of sphalerite geochemistry from 4 VMS of Troodos. Maximum (Max), Minimum (Min), average, median and standard deviation ( $\sigma$ ). \*indicates analysis via LA-ICP-MS (full data is available in Appendix 5.4).

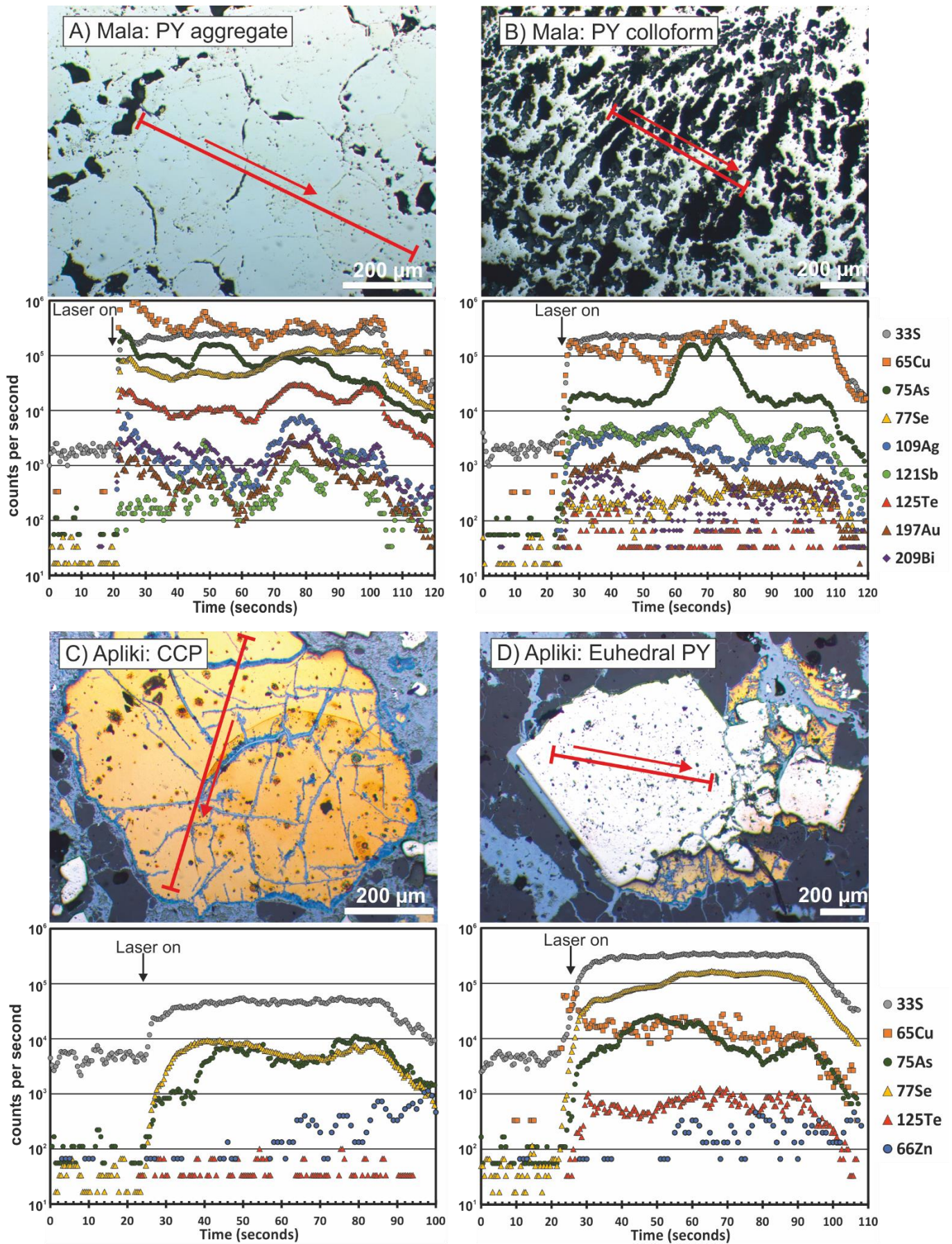
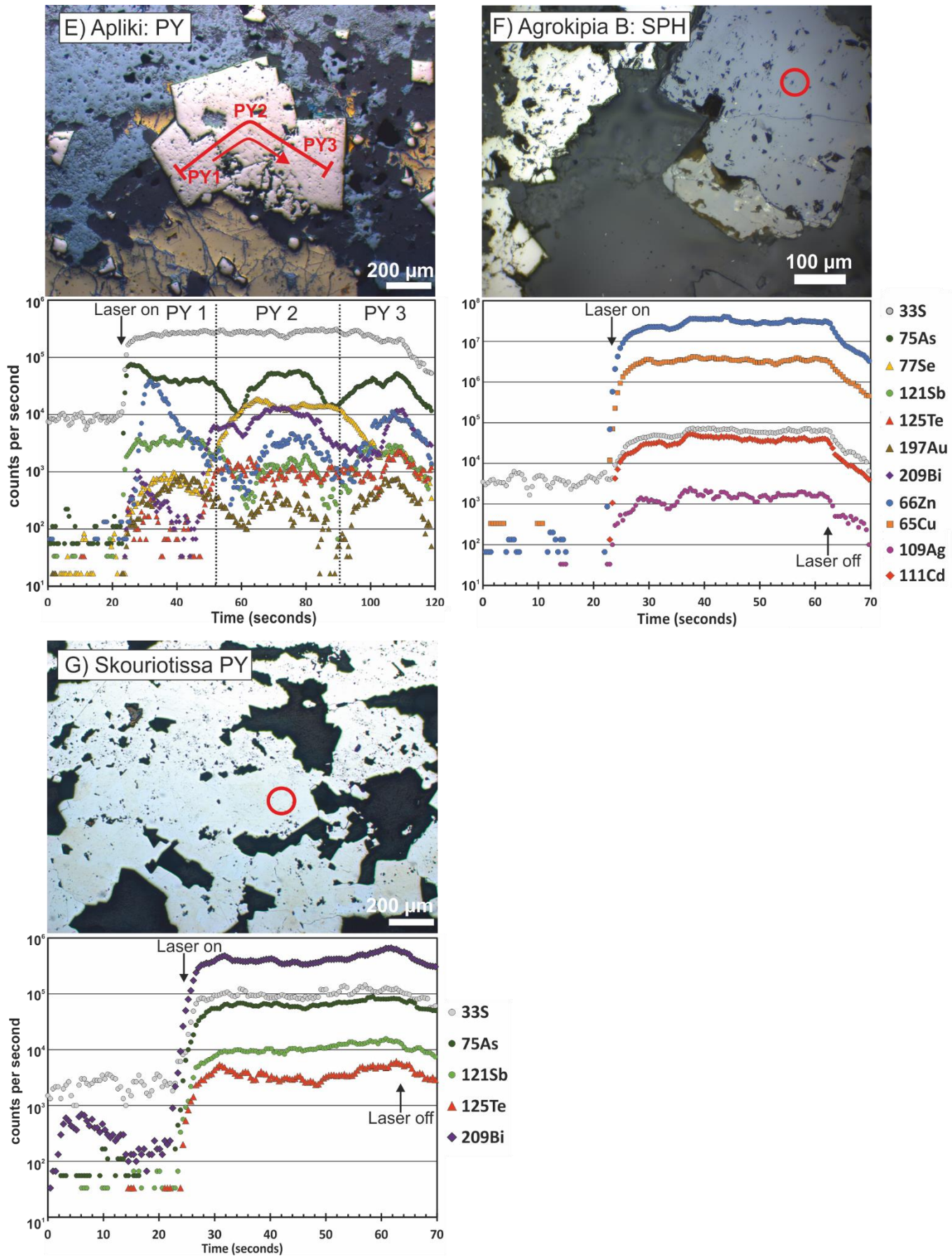


Figure 5.4: Time Resolved Analysis (TRA) of sulfides (explanation overleaf).



**Figure 5.4:** Time Resolved Analysis (TRA) of sulfides (explanation overleaf).

**Figure 5.4:** LA-ICP-MS Time Resolved Analysis (TRA) of selected sulfide minerals (red arrow indicates laser motion). (A) Pyrite aggregate (Mala) multiple pyrite crystals are identifiable due to variation in TRA shape showing variations from core to rim. (B) Colloform pyrite (Mala) is depleted in solid solution hosted elements (e.g. Se) but enriched in inclusion hosted elements (e.g. Sb). (C) Chalcopyrite (Apliki), note the preferential incorporation of Se in chalcopyrite with a smooth ablation profile. (D) Euhedral pyrite (Apliki) exhibiting a smooth TRA profile for Se and a more jagged profile for Te suggesting variable mechanisms of incorporation in pyrite. (E) Multiple generations of euhedral pyrite demonstrating the variable physicochemical conditions during pyrite precipitation (Apliki). (F) Sphalerite spot analysis (Agrokipia B), note correlation of Cd and Ag with Zn. (G) Euhedral to subhedral pyrite (Skouriotissa); Bi and Te profiles mirror each other possibly suggesting a coupled behaviour.

## 5.5 Discussion

### 5.5.1 Mineral scale metal incorporation and distribution

Trace metal incorporation into sulfides is accomplished through either solid solution, i.e. lattice bound substitution, or as micro- to nanoscale mineral inclusions (Abraitis *et al.*, 2004; Cook *et al.*, 2009; Deditius and Reich 2016; Deditius *et al.*, 2011; Genna and Gaboury, 2015; Gregory *et al.*, 2015; Reich *et al.*, 2013; Tardani *et al.*, 2017; Wohlgemuth-Ueberwasser *et al.*, 2015). The incorporation of trace elements depends upon physical and chemical fluid factors (e.g. temperature,  $fO_2$ ,  $fS_2$ : Huston *et al.*, 1995; Wohlgemuth-Ueberwasser *et al.*, 2015, Revan *et al.*, 2014; Keith *et al.*, 2016a, b), as well as crystallographic effects including the valance states and covalent radii of different lattice bound elements (Reich *et al.*, 2005; Keith *et al.*, 2018a).

Laser Ablation-ICP-MS cannot distinguish between nanoscale inclusions and lattice bound elements, as these would both produce a smooth ablation profile (Gregory *et al.*, 2015; Wohlgemuth-Ueberwasser *et al.*, 2015). However, elements that display a jagged saw-tooth pattern most likely occur as mineral inclusions (Figure 5.4 B and D, Te).

Variation of elements in time resolved laser ablation profiles can be explained by different incorporation mechanisms of metals in pyrite. Huston *et al.* (1995) identified three groups of trace elements based on their incorporation mechanisms in VMS pyrite. This includes (1) Cu, Zn, Pb, Ba, Bi, Ag and Sb as micro- or nanoscale inclusions, (2) As, Tl, Au and Mo due to non-stoichiometric substitution and (3) elements with a stoichiometric substitution for S (Se and Te) and Fe (Co and Ni) (Chouinard *et al.*, 2005; Huston *et al.*, 1995).

The incorporation mechanism of Te remains debated with Huston *et al.* (1995) and Butler and Nesbitt (1999) favouring its incorporation in solid solution. Given the larger covalent radii of Te (1.38 Å; Cordero *et al.*, 2008), substitution in solid solution in pyrite is unlikely and Keith *et al.* (2018a) prefer its incorporation as micro- to nanoscale inclusions. Analysis from this study for Te do not favour one single incorporation mechanism; instead Te incorporation appears variable

and depends on the sample analysed. Tellurium in pyrite from Apliki exhibits a saw tooth ablation profile (Figure 5.4 D and E) suggesting incorporation of Te as microscale inclusions compared with Se that has a smooth ablation profile suggesting that Se occurs in solid solution substituting for S in pyrite and chalcopyrite (Huston *et al.*, 1995; Maslennikov *et al.*, 2009, 2017; Keith *et al.*, 2018).

In contrast, pyrite from Skouriotissa exhibits a smoother profile for Te (Figure 5.4 G) indicating nanoscale inclusions or a lattice bound appearance (Deditius *et al.*, 2011). However, variations between pyrite grains suggest different incorporation mechanisms for Te that include nanoscale inclusions or solid solution at Skouriotissa (Figure 5.4 G) to microscale inclusions at Apliki (Figure 5.4 D and E).

It has been shown that As-rich pyrite can incorporate high concentrations of trace elements compared to As poor pyrite either in solid solution or as inclusions (Reich *et al.*, 2005; Deditius *et al.*, 2014, 2011, 2008; Keith *et al.*, 2018). Arsenic can occur in several oxidation states (-I, +II, +III, +V) and therefore may be substituted into the pyrite lattice either as an anion or cation depending on the prevailing redox conditions in the ore-forming fluid (Chouinard *et al.*, 2005; Qian *et al.*, 2013; Reich *et al.*, 2005). Previous studies have identified  $\text{As}(\text{OH})_3$  as the major As species in reduced ore fluids (e.g. Pokrovski *et al.*, 2002). Arsenic as an anion is incorporated in pyrite as a substitution with S and as a cation via a coupled substitution with Fe (Chouinard *et al.*, 2005; Deditius *et al.*, 2008). The author assumes that under reduced conditions As occurs as an anion in Troodos pyrite (e.g. Nesbitt *et al.*, 1995; Simon *et al.*, 1999). This suggests that As rich pyrite from the Troodos VMS deposits may contain appreciable trace element concentrations due to lattice distortion allowing the accommodation of large covalent radii elements (e.g. Te).

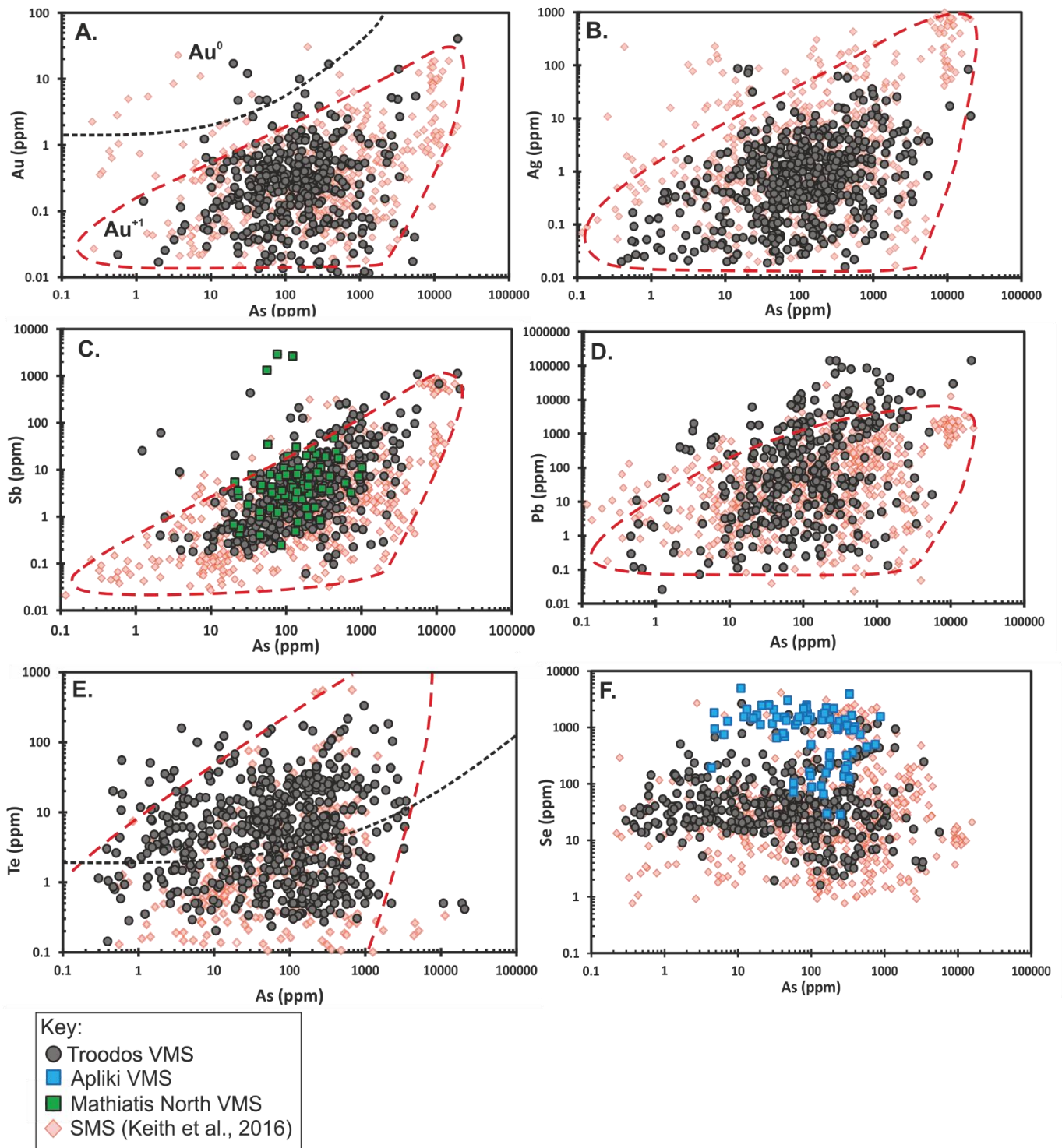


**Figure 5.5:** Concentrations of (A) Au, (B) Ag, (C) Sb, (D) Pb, (E) Te, (F) Se vs. As in pyrite for all Troodos VMS (n=20). Red dashed lines define the wedge-shaped zone that is defined by the solubility of trace elements in pyrite. Points that plot within this zone are considered to be hosted in a solid solution and outside as mineral-nanoscale inclusions (after Deditius *et al.*, 2014; Reich *et al.*, 2005, 2010, 2013 and Keith *et al.*, 2016b; 2018b). Selenium vs. As does not form a wedge shaped zone with high Se concentrations realised at a range of As concentrations- thus supporting Se's incorporation in a solid solution with S. The black dashed line (A and E) represents the solubility limit of Au<sup>0</sup> and Te as discrete mineral phases (i.e. Tellurides) in pyrite as a function of As (Keith *et al.*, 2018b; Reich *et al.*, 2005). Modern SMS data from Keith *et al.* (2016b).

Arsenic is used as a discrimination tool to decipher the incorporation of trace elements in the pyrite structure i.e. their incorporation as a lattice bound substitution or as micro- or nano-particle inclusions (Figure 5.5- after Deditius *et al.*, 2014; Keith *et al.*, 2018a; Reich *et al.*, 2010, 2013). Data points for the trace elements under consideration (Au, Ag, Sb, Pb and Te) plot within the wedge-shaped zone (Figure 5.5) which defines the upper solubility limits between mineral inclusions and lattice substituted elements. Concentrations which plot significantly outside the wedge-shaped or toward the upper solubility limits of the zone suggest inclusions (red dashed line- Figure 5.5), while compositions in the wedge-shaped zone represent lattice bound substitutions or nanoscale-inclusions. When plotted in log-log space the solubility limits of Te and As in pyrite define a wedge shaped zone (after Keith *et al.*, 2018b). This indicates the solubility limits of Te in a lattice bound substitution and as inclusions (Figure 5.5 E). When applied to Troodos VMS pyrite, the vast majority of points fall inside the wedge shaped zone but a fraction fall outside the zone thus representing the occurrence of inclusions. This study applies the Au solubility line (Figure 5.5 A after Reich *et al.*, 2005) defining the solubility limits of Au<sup>0</sup> hosted as sub-micron inclusions to Te-As space (Figure 5.5 E; black dashed line). Keith *et al.* (2018b) suggest on the basis of a positive correlation between Au and Te ( $R^2=0.55$ ) at low As but high Te-(Au) that Au telluride inclusions (e.g. calaverite, AuTe<sub>2</sub>) host appreciable Te. In Troodos VMS the author finds no correlation ( $R^2 = <0.01$ ) between Au and Te. This strongly suggests the incorporation of Te in solid solution for the majority of Troodos pyrite and less commonly as mineral inclusions (Figure 5.5 E). Points that plot to the far right of the wedge-shaped zone (i.e. high As, low Te) could represent As-rich mineral inclusions (e.g. Tennantite).

In this study the author finds that trace element incorporation into pyrite in the ancient Troodos VMS systems is almost identical to the modern analogues considered by Keith *et al.* (2016b; Figure 5.5). Most data for As-Au, As-Ag, As-Sb, As-Pb plot within the wedge-shaped zone and below the solubility limit (for Au). A higher proportion of Sb and Pb points for Troodos plot outside the wedge-shaped zone at 7 and 25 % respectively compared to modern analogues at 3 and 6 % for Sb and Pb (Keith *et al.*, 2016b). This feature relates in particular to Mathiatis North (Figure 5.5 C), where Sb reaches 2873 ppm at a maximum As content of 76 ppm. Additionally, this study finds that a higher proportion of Pb is inclusion-hosted in pyrite from the Troodos ophiolite, this is confirmed microscopically as galena inclusions in pyrite (Appendix 5.2).

Telluride minerals were not observed in this study; however, previous studies highlighted the rare and localised occurrence of tellurobismuthite (Bi<sub>2</sub>Te<sub>3</sub>) at Skouriotissa (Figure 5.6-Taylor, 2015). The systematic variation of Bi and Te in time resolved ablation profiles suggests that concentrations of Bi and Te exhibit a coupled relationship (e.g. Figure 5.4 A). However, Bi and Te exhibit no correlation ( $R^2=0.05$ ) in pyrite across all VMS deposits. The Te-Bi correlation

coefficients in pyrite vary between different deposits (Figure 5.6). This suggests variable incorporation mechanisms for Te, most likely in response to changes in the local physicochemical fluid conditions (e.g. temperature,  $fS_2$ ,  $fO_2$ ,  $fTe_2$ ) and the concentrations of other lattice modifying trace elements, such as As (Figure 5.5; Keith *et al.*, 2018b). The strongest correlation between Bi and Te was observed in pyrite from the Apliki ( $R^2=0.35$ ) and Phoucasa ( $R^2=0.32$ ; Figure 5.6). In contrast, Se exhibits a smooth ablation profile that closely follows that of S (Figure 5.5 A and D) probably indicating a lattice bound substitution of Se for S (Huston *et al.*, 1995).

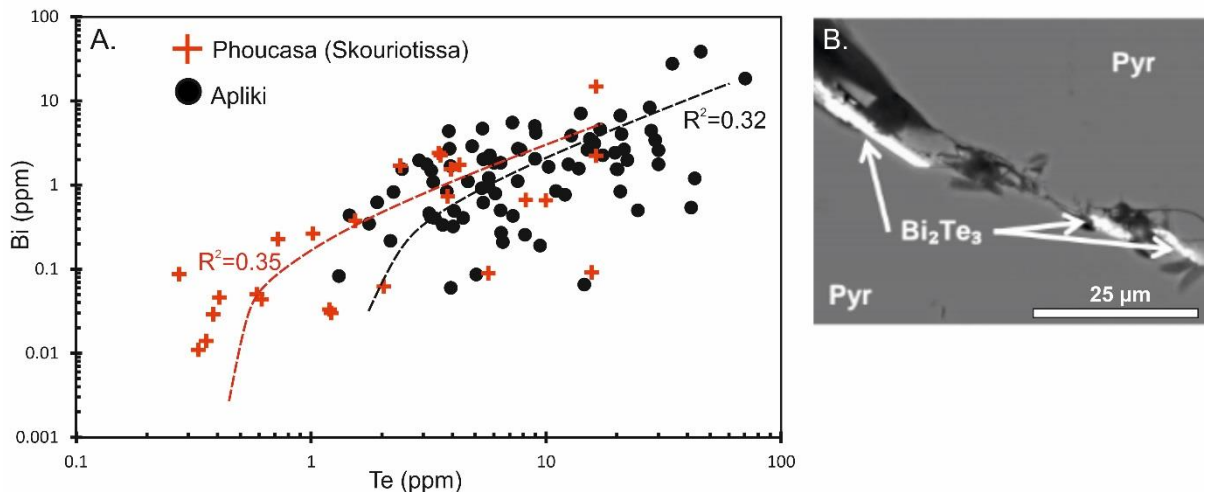


**Figure 5.6:** Concentration of Te vs. Bi for Skouriotissa (Phoucasa) and Apliki VMS. The moderate positive correlation between Bi and Te suggests Te ( $R^2= 0.35$  and  $0.32$ ) may be hosted by Bi-telluride inclusions or discrete mineral phases (B) Tellurobismuthite ( $Bi_2Te_3$ ) from Skouriotissa forming along pyrite grain boundaries (Taylor, 2015).

Trace elements in chalcopyrite are hosted as two distinct groups identified by their incorporation mechanism; namely those incorporated as inclusions (e.g. Pb, Bi, Ba, Zn), or elements in a lattice bound substitution (e.g. Ag, In, Sn, Se, Zn) (Huston *et al.*, 1995). Lattice bound substitution is achieved via either a simple substitution (e.g.  $Zn^{2+} \leftrightarrow Fe^{2+}$  or  $S^{2-} \leftrightarrow Se^{2-}$ ) or a coupled substitution (e.g.  $2 Zn^{2+} \leftrightarrow Cu^+ + In^{3+}$ ) (Ye *et al.*, 2011). The reader is directed to numerous references that address the incorporation of trace elements in chalcopyrite in further detail (e.g. Huston *et al.*, 1995; George *et al.*, 2018; Reich *et al.*, 2013; Revan *et al.*, 2014; Wohlgemuth-Ueberwasser *et al.*, 2015).

Selenium concentrations are consistently elevated in chalcopyrite compared to pyrite (Table 5.4 and 5.2). Selenium exhibits an order of magnitude variation within and between different VMS. At Apliki Se in chalcopyrite ranges from 104 to 3956 ppm; the higher concentrations are comparable to those reported by Butler and Nesbitt (1999) for the active Broken Spur vent field. The smooth time resolved profile (Figure 5.4 C- Apliki) suggests that Se is hosted in a lattice bound substitution with S in chalcopyrite (Huston *et al.*, 1995; Butler and Nesbitt, 1999). Data

suggest that variation in Se concentration is due to local physicochemical factors relating to fluid temperature, magmatic influx or co-precipitating sulfide phases (Layton-Matthews *et al.*, 2008; Huston *et al.*, 1995). Increased magmatic influx favours high Se (e.g. de Ronde *et al.*, 2005; Rouxel *et al.*, 2004) whereas the precipitation of galena (or clausthalite - PbSe) would preferentially incorporate Se leading to a depletion in any co-precipitated chalcopyrite (George *et al.*, 2018; Figure 5.7). Furthermore, Bethke and Barton (1971) state that at 390°C, chalcopyrite can incorporate up to 2150 ppm Se forming a solid solution with eskebornite (CuFeSe<sub>2</sub>). Similar concentrations are observed in this study in chalcopyrite.

Tellurium concentrations in chalcopyrite are notably less variable than in pyrite averaging 6.1 ppm (median 2.2 ppm). From 150 analysis (LA-ICP-MS: Table 5.4) 104 are above detection limit (~0.6 ppm- Appendix 5.1). Several values at Phoucasa (44.1 and 171 ppm Te) are notably higher than the average and median values. Elevated Te correlates with Au (4.30 and 3.58 ppm respectively) and Pt, Ir and Os signifying a possible Au-Pt-Te inclusion (Appendix 5.1). This is consistent with observations from the Urals VMS where elevated Au and Te are attributed to telluride inclusions (e.g. calaverite, AuTe<sub>2</sub>) (Maslennikov *et al.*, 2009).

Zinc in chalcopyrite may be incorporated as both a solid solution element and as inclusions (Huston *et al.*, 1995). Zinc concentrations <2000 ppm are suggested to be incorporated as a solid solution, possibly substituting for Fe and those >2000 ppm tend to be associated with inclusions (Huston *et al.*, 1995). In Troodos VMS, Zn concentrations vary from below detection limit to 22.5 wt.% (Table 4); the latter clearly indicating sphalerite inclusions. For most VMS deposits the available data suggest the incorporation of Zn in a solid solution with median values of 292 ppm, well below the suggested 2000 ppm threshold.

Arsenic values are commonly below detection limit (22 detected out of 150; average ~1.5 ppm) with a maximum of 387.4 ppm at Kokkinoyia. These low but variable concentrations demonstrate the limited incorporation potential of As in chalcopyrite. At concentrations <2000 ppm, As is likely to be incorporated as a solid solution in chalcopyrite (Huston *et al.*, 1995). This is supported by a smooth laser ablation profile for As in chalcopyrite in Troodos VMS (Figure 5.4 E). Additionally, the As profile follows that of other elements hosted in solid solution (e.g. Se – Figure 5.4 E).

Gold and Ag concentrations in chalcopyrite from Troodos VMS are low with 31 and 49 (of 150) analysis above detection limit for Au and Ag respectively (Appendix 5.1). Gold concentrations reach a maximum of 4.3 ppm and in some instances these high Au values correlate with increased Te and Pt suggesting that at high concentrations Au may be hosted as discrete mineral phases (e.g. Maslennikov *et al.*, 2009). Gold is generally below 1 ppm in Troodos VMS (Table

5.4), comparable to concentrations in other VMS (Cook *et al.*, 2011; Maslennikov *et al.*, 2009; Revan *et al.*, 2014).

Silver demonstrates similar variability in chalcopyrite to Au with a maximum value of 16.3 ppm (Three Hills). These low concentrations suggest that Ag is incorporated as  $\text{Ag}^+$  as a lattice bound substitution with  $\text{Cu}^+$  (Huston *et al.*, 1995). Substantially higher Ag values in chalcopyrite are suggested to indicate the presence of argentiferous galena inclusions and in some instances elevated Pb correlates with increased Ag (Huston *et al.*, 1995), however this was not directly observed in Troodos VMS. Concentrations of Ag between different VMS deposits are pronounced; at Apliki with one exception, all analysis are below detection limit, whereas at Three Hills 12 out of 15 analysis are above detection limit. This variation is attributed to the mineral scale partitioning of Ag between different sulfide phases, i.e. galena preferentially incorporates Ag (George *et al.*, 2016, 2018; Large *et al.*, 2009).

Bismuth, Cd and Sb may also form trace constituents in chalcopyrite (Table 5.4). Bismuth occurs consistently in minor amounts <1 ppm throughout most chalcopyrite grains analysed; 82 analyses of 150 yield values above detection limit (>0.05 ppm). High Bi values are reported for Urals VMS (metamorphosed) and active SMS and are associated with inclusions of bismuthinite ( $\text{Bi}_2\text{S}_3$ ) or bismuth tellurides (e.g. tellurobismuthite,  $\text{Bi}_2\text{Te}_3$ ) (Gena *et al.*, 2013; Maslennikov *et al.*, 2012), however comparatively high values were not observed in Troodos. Cadmium concentrations in pyrite vary spatially between different VMS. This reflects variable amounts of co-precipitated sphalerite and its preferential incorporation of Cd over chalcopyrite. High Cd levels correlate with elevated Zn that probably indicate the analysis of Cd rich sphalerite inclusions (Table 5.4 and 5.5) (e.g. Cook *et al.*, 2009; George *et al.*, 2018). Cadmium concentrations range from below detection to 13.4 ppm (average: 0.81 ppm, median: 0.59 ppm). These observations are consistent with data from Huston *et al.* (1995) who state that Cd may occur as a lattice bound substitution in chalcopyrite at levels (<2000 ppm), however mineral inclusions and sulfosalts may also occur. Very little data is available on Sb incorporation and only 22 analysis of 150 in chalcopyrite returned concentrations above detection limit (Table 5.4). Huston *et al.* (1995) suggest that concentrations of Sb >500 ppm are hosted as mineral inclusions of tennantite-tetrahedrite series minerals. In Troodos VMS an  $R^2$  value of >0.01 between As and Sb suggesting tennantite-tetrahedrite inclusions do not host significant Sb.

Sphalerite is a poor host for trace elements in Troodos VMS compared with chalcopyrite and pyrite. The only element notably enriched in sphalerite is Cd with maximum concentrations of 3400 ppm at Kynousa (Table 5.5). Two groups of elements are identified in sphalerite; those forming inclusions (e.g. Ba and Pb) or elements hosted in a lattice bound substitution (e.g. Cd,

Cu, Te, Ag) (Huston *et al.*, 1995; Cook *et al.*, 2009). Cadmium in Troodos VMS was above detection in all but one analyses (n=85) and concentrations exhibit an order of magnitude variation between different deposits (Table 5.4). The smooth ablation profile for Cd in sphalerite (Figure 5.4 F) that closely mimics Zn in shape suggests Cd is hosted as a lattice bound substitution element. Cook *et al.* (2009) state that Cd occurs in concentrations typically >0.2 wt% in sphalerite due to the substitution of Cd<sup>2+</sup> with Zn<sup>2+</sup>; this is likely the case in Troodos VMS.

Copper in sphalerite was detectable in most sphalerite grains and returned concentrations between 0.09 to 8.97 wt.%. Huston *et al.* (1995) suggest that Cu values <1.6 wt.% are likely incorporated in a solid solution and erratically high values (>1.6 wt.%) probably result from chalcopyrite inclusions. This suggests that the majority of Cu in sphalerite at Skouriotissa is hosted as inclusions, and in some cases visible chalcopyrite disease was present to confirm this. This is further supported by the time resolved analysis of sphalerite from Agrokipia (Figure 5.4 F) where Cu at low concentrations >0.62 wt.% has a smooth ablation profile supporting its incorporation as a solid solution. All other elements (Ag, As, Sb, Pb and Se) occur in minor amounts <200 ppm (Table 5.5). Mathiatis North exhibits an enrichment in Se and Ag in sphalerite compared to all other deposits; with limited analyses available, the reason for this enrichment is unclear.

### 5.5.2 Physiochemical conditions of ore formation

Colloform and euhedral pyrite show variable time resolved LA-ICP-MS profiles indicating that pyrite texture influences trace element concentrations (Figure 5.4 A and B). Aggregates of interlocking pyrite (Figure 5.4 A) form crude bands at the base of porous colloform pyrite (Figure 5.4 B). Microscopically multiple pyrite crystals can be distinguished (Figure 5.4 A); laser ablation profiles across three pyrite grains indicate radial zonation in trace elements across different pyrite crystals (Figure 5.4 A). This demonstrates that the physicochemical conditions (e.g. temperature) of the fluid fluctuated temporally during pyrite precipitation probably due to variations in magmatic influx to the hydrothermal systems (e.g. Butterfield *et al.*, 1997; Chapter 9). By comparison, Mo is also enriched in colloform pyrite (18.0 ppm) relative to euhedral varieties (6.1 ppm); this is due to a seawater source of Mo (Kristall *et al.*, 2011; Metz and Trefry, 2000; Keith *et al.*, 2016a,b). A similar trend of trace element enrichment is reported in pyrite from Skouriotissa where deep euhedral pyrite is enriched in Te, Se and Co relative to colloform varieties (Keith *et al.*, 2016b).

Sulfide mound growth is accomplished through the collapse and re-precipitation of sulfides that lead to zone refining in response to changes in fluid composition and the collapse and reworking

of unstable chimney structures (Hannington *et al.*, 1998; Herzig and Hannington, 1995; Revan *et al.*, 2014). Oxygen fugacity,  $fS_2$ , temperature and pH vary spatially and temporally during mound growth and system maturation (e.g., Galley *et al.*, 2007). Such variability is recorded on a micron scale by the laser ablation profiles showing variable trace element intensities from core to rim in euhedral pyrite reflecting changes in physiochemical fluid conditions and metal flux in the VMS systems (Figure 5.4 D and E). Whilst the exact nature of these changes cannot be distinguished, typically reduced conductive cooling, compaction of the sulfide mound and reduced seawater infiltration during maturation increases the precipitation temperatures, whilst fault movement facilitates seawater ingress and cooling leading to fluctuating fluid chemistry that in turn influences trace element incorporation leading to metal zonation in precipitating pyrite (Gillis and Roberts, 1999; Humphris and Cann, 2000; Von Damm, 1990).

Four different types of pyrite mineralisation can be distinguished in the Troodos VMS ores; massive (Figure 5.2 B and K), colloform (Figure 5.2 D), stockwork (Figure 5.2 M) and jasper (Figure 5.2 I). These different pyrite types form in different regions of the VMS stratigraphy (cf. Chapter 3). Jasper (hematite + pyrite + silica) forms at the oxidised margins of the mound as centimetre scale veins, whilst euhedral pyrite forms in the high temperatures regions (Hannington *et al.*, 1998). Colloform pyrite crystallised rapidly indicating disequilibrium conditions associated with the upper mound where seawater interaction is high and the temperatures are relatively low (Berkenbosch *et al.*, 2012; Keith *et al.*, 2016a,b). No clear systematic variation in the trace element distribution in pyrite is noted with depth in the Skouriotissa ore body (i.e. shallow vs. deep stockwork) and the author is unable to convincingly reproduce such systematic variations in other trace elements as reported by Keith *et al.* (2016a) for Te and Se. This strongly suggests that the trace element composition is influenced by complex physicochemical changes on the local scale (cm to m) along fluid pathways that govern trace element incorporation. Thus, explaining the generally poor systematic variation between trace elements in pyrite from Troodos VMS deposits (Table 5.3).

All jasper samples contain pyrite as the only sulfide phase. Chalcopyrite is absent, indicating that jasper precipitated at relatively low temperatures (<265°C: Safina *et al.*, 2016), and due to the inclusion of hematite, under relatively oxidised conditions. Trace element analyses show that pyrite associated with jasper is enriched in Se compared to other samples at, for example, the Phoucasa VMS averaging 193 ppm Se ( $n=17$ ,  $\sigma=132$ ). Huston *et al.* (1995) and Keith *et al.* (2018b) suggested that Se incorporation in pyrite favours lower temperatures and more oxidised conditions, however Hannington *et al.* (1998) and Auclair *et al.* (1987) associate Se enrichment

with high fluid temperatures. In this study the author supports the observation that Se in pyrite is preferentially enriched in low temperature environments.

Chalcopyrite contains higher average Se (278 ppm, n= 150) compared to pyrite (42 ppm, n=1322). Therefore, this study indicates that chalcopyrite-rich VMS ores (i.e. stockwork- Figure 5.7, overleaf) at depth may cause a corresponding Se depletion in pyrite-rich ores, especially in the upper mound regions of the VMS deposit. Selenium in the hydrothermal fluids preferentially partitions into chalcopyrite in the deeper stratigraphic sections of VMS deposits and is therefore depleted in the hydrothermal fluids and associated sulfides at or near the seafloor (Figure 5.7 and Rouxel *et al.*, 2004). At temperatures <260°C associated with the waning stages of the hydrothermal system, chalcopyrite precipitation ceases in response to cooling of the hydrothermal system (Figure 5.7). At these lower temperatures Se is no longer preferentially incorporated into precipitating chalcopyrite but instead migrates through the stockwork to the upper VMS stratigraphy where it is incorporated in pyrite and galena (if present- e.g. George *et al.*, 2018). In this study on a regional scale Se concentrations in pyrite and chalcopyrite are extremely variable ranging from <10 ppm to 4942 ppm and 7.5 to 3955 in pyrite (n=1322) and chalcopyrite (n=150) respectively. This variation can be explained by (a) co-precipitation of different sulfide phases and the preferential uptake of Se by chalcopyrite (Figure 5.7, overleaf), and (b) the effect of zone refining and Se re-mobilisation into late stage pyrite (Martin *et al.*, 2018).

Time resolved LA-ICP-MS analyses across multiple pyrite generations reveal concentric zoning of elements recording the evolution of the hydrothermal fluid and preferential incorporation of trace elements under temporally distinct physicochemical conditions. With no mineralogical (recrystallization or subsequent normal grain growth) or structural evidence of metamorphism (Gass, 1980), it is assumed that the trace element profiles preserved in pyrite from Troodos represent primary features, and thus have not been affected by later metamorphism leading to element mobilisation (e.g. Genna and Gaboury, 2015).

Time resolved profiles across three euhedral pyrite grains (Figure 5.4 E) show that euhedral pyrite 1 is depleted in Se, Te and Bi but enriched in Sb and Zn relative to euhedral pyrites 2 and 3. All pyrite grains contain elevated As but appear to be concentrically zoned with increased As counts measured in the centre of the grain. The author suggests that these zones reflect temporal variations in physicochemical fluid conditions (e.g. pH, temperature) of the ore-forming fluid which are related to pulsed magmatic influx into the VMS system. If As concentrations in the fluid decrease leading to the precipitation of As poor zones, the ability of pyrite to incorporate Te as a solid solution or nanoscale-inclusions would decrease, hence at low

As concentrations (<100 ppm) Te may plot outside the wedge shaped zone indicating the presence of mineral-scale inclusions (cf. section 5.1; Figure 5.5 E).

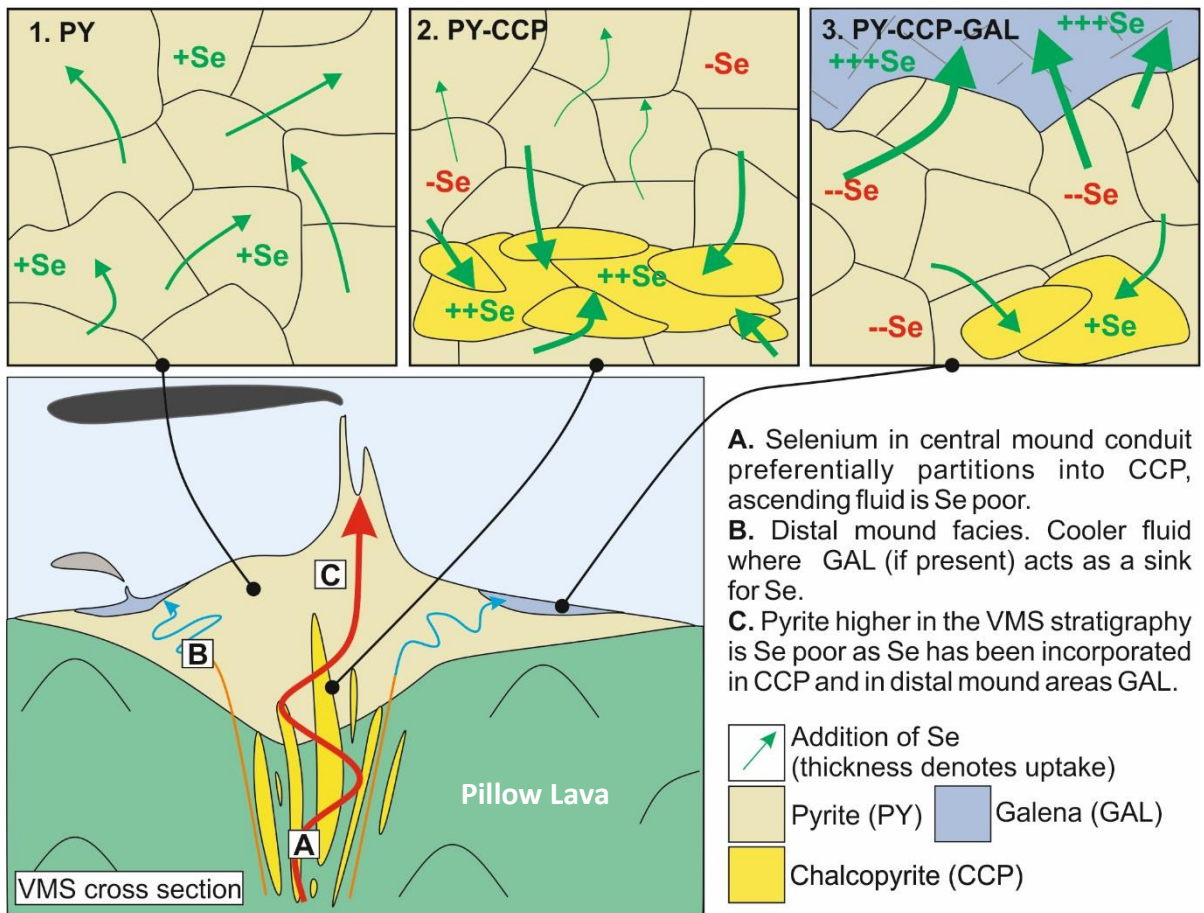


**Figure 5.7:** The partitioning of Se between pyrite, chalcopyrite and galena in VMS. In a monomineralic system (1) Se is partitioned uniformly between pyrite crystals. In a system where both chalcopyrite and pyrite are present (2) chalcopyrite preferentially incorporates Se leading to a Se depletion in pyrite. This is probably a common phenomenon in lower parts of the VMS mound (A) where Se is removed from the fluid in the stockwork zone. The Se depleted fluid that ascends through the mound forms Se poor pyrite (C). If galena is present (3) it will preferentially incorporate Se over both chalcopyrite and pyrite (B). Cooler distal (mound margin) fluids, that do not interact with high temperature stockwork zones will form Se-rich galena, i.e. the source fluid is not previously depleted by chalcopyrite precipitation (path B not A).

In addition to changes in the local physicochemical fluid conditions, systematic variations in magmatophile trace elements in pyrite (Table 5.6: Se, Co, Cu, Te, Bi, Au- de Ronde *et al.*, 2011) on a district or graben scale (~20 km) suggest a variable metal source, namely the host rocks or the potential contribution of magmatic volatiles to the hydrothermal system.

### 5.5.3 Source rock variation and trace element composition

Trace element variation on a district scale may be a function of (a) source rock composition or (b) a variable magmatic volatile influx; all of which ultimately relate to a variable magmatic source (Herzig *et al.*, 1998a; Jowitt *et al.*, 2012; Patten *et al.*, 2017; Yang and Scott, 2002; Keith *et al.*, 2016a,b; 2018; cf. Lüders *et al.*, 2002). The Troodos lithosphere formed in a supra-subduction zone environment and lava geochemistry is considerably different from typical MORB, lavas are enriched in volatile elements, have a higher H<sub>2</sub>O content and may be more evolved in composition (andesites, boninites etc.) (e.g. Kelley and Robinson, 1990; Patten *et al.*, 2017; Pearce and Robinson, 2010; Regelous *et al.*, 2014). Therefore the metal content of VMS deposits is expected to differ compared to MOR hydrothermal systems.

The chemical composition of volcanic glass from the Troodos ophiolite is different from typical MORB due to elevated As (850 ppb), Sb (78 ppb) and Pb (1.93 ppm) contents, which makes it comparable to subduction related hydrothermal systems such as the Manus Basin (Herzig *et al.*, 1998a; Patten *et al.*, 2017; Yeats *et al.*, 2014). In contrast, Se is depleted in the Troodos glass at 119 +/- 53 ppb compared to 243-723 ppb in MORB (Patten *et al.*, 2017). The enrichment of trace metals during magmatic fractionation is not uniform; Cu, Au and Se behave incompatibly during the first stage of crystallisation prior to magnetite saturation (Jenner *et al.*, 2010; Patten *et al.*, 2017). During the second magmatic differentiation stage in Troodos, (i.e. post magnetite) the melt will be depleted in Cu, Se and Au due to sulfide liquid segregation compared to Zn, As, Sb and Pb showing a typical incompatible behaviour (Patten *et al.*, 2017) (further discussion in Chapter 9).

This study highlights the systematic variation of trace metals in VMS ores on a district scale (Figure 5.1). Deposits of the Solea graben are enriched in Cu, Co, Au and Se (e.g. Skouriotissa or Apliki- Table 5.6), whilst deposits of the Mitsero graben (e.g. Kokkinoyia or Agrokippia) are enriched in As and Sb (Table 5.6). This study proposes that variation could be due to chemical differences in the composition of the protolithic material in the epidotised zones or the interaction of hydrothermal fluids with different volumes of fresh plutonic igneous rocks (i.e. sheeted dykes/upper plutonics).

Element	Mitsero	Solea
Au	0.3	0.5
Te	5.4	8.6
Se	47	662
Bi	3.2	1.7
Cu	800	1800
Co	116	299
Sb	52	3.2
As	671	119

**Table 5.6:** Trace element concentrations in pyrite (LA-ICP-MS, in ppm) between the Solea and Mitsero graben structural domains. Solea (n=427) is enriched in magmatophile elements (Te, Se, Cu and Au) relative to Mitsero (n=100).

The extrusive sequence of Troodos is chemically stratified and classified into primitive basaltic upper pillow lavas (UPL) and andesite-dacite lower pillow lavas (LPL) (Gass, 1980; Malpas and Langdon, 1984; Rautenschlein *et al.*, 1985, Chapter 2). Hence, an epidosite zone with a higher proportion of more primitive (UPL affinity) dykes would lead to the relative enrichment in Au, Se and Cu, since these elements are enriched in basaltic relative to an andesitic to dacitic melt (Patten *et al.*, 2017). Given the scale of epidosite zones, estimated at 5-10 km<sup>3</sup> (Jowitt *et al.*, 2012; Patten *et al.*, 2017), local variation (100 m to several km) could account for the formation of a VMS district that contains elevated Cu, Se and Au. This enrichment is observed in the Solea district (Table 5.6) that contains the largest (discovered) VMS deposits in the Troodos ophiolite including Skouriotissa and Phoucasa (5.4 Mt at 2.3 % Cu), Phoenix (15 Mt at 0.5 % Cu) and Three Hills (6.2 Mt at 0.4 % Cu), as well as Mavrovouni (15 Mt at 3.8 % Cu) and the smaller Apliki (1.7 Mt at 1.8 % Cu) and Mala deposits (6 Mt at 0.4 % Cu and 12.3 % Zn- exploration report BMG, 2013; Adamides, 2010a,b; Hannington *et al.*, 1998). The deposits of the Mitsero graben are generally of lower tonnage and contain less Cu, such as Mathiatis North (4.5 Mt at 0.17 % Cu) and Sha (1 Mt at 1.9 % Cu; Hannington *et al.*, 1998). A variation in metal source composition or generation of a magmatic volatile phase would be required to account for the systematic variation in metals between the Solea and Mitsero VMS districts.

The spatial association between source rocks and VMS deposits is clearly demonstrated in the southern Troodos Mountains with the occurrence of auriferous VMS deposits (Au grades >3.5 ppm, Au tonnage  $\geq$  31 t or Au to base metal ratio > 1, Mercier-Langevin *et al.*, 2011). Enrichment of Au at Kalavastos (Table 5.2) on the southern margin of Troodos (Figure 5.1, deposit 13) is attributed to a Au enriched source rock. The lava geochemistry of the southern Troodos Mountains are characterised by increased volumes of mafic-ultramafic basaltic to picritic and boninitic affinity lavas (MacLeod and Murton, 1993; Thy, 1987; Thy and Moores, 1988). Patten *et al.* (2017) show that more primitive basaltic-andesites from Troodos contain higher concentrations of Au (2.1 +/- 0.1 ppb) compared to andesitic glass samples (0.8 ppb). The

increased abundance of primitive lavas in the southern Troodos Mountains may be responsible for the Au enrichment in the Kalavassos mines with reported average Au grades of 1.17 ppm (Mercier-Langevin *et al.*, 2011).

Pyrite from Kalavassos has an average Au concentration of 2.1 ppm ( $n = 260$ ), and is therefore significantly enriched compared to pyrite from the other VMS deposits (average 0.95 ppm,  $n = 1062$ ). Like Kalavassos, Mala is located in the southern Troodos Mountains and is enriched in Au averaging 1.7 ppm in pyrite ( $n=5$ ; Figure 5.8) and therefore could also be classified as auriferous as Au grades are comparable to those observed at Kalavassos.

In Modern SMS that exhibit an enrichment in Au such as the ultramafic-hosted Logatchev vent field on the MAR that contains elevated Au concentrations in pyrite suggest an increased magmatic volatile influx or enriched source rock (Figure 5.8; Keith *et al.*, 2016b). Host rock serpentinization causes a  $H_2S$  increase in the hydrothermal fluids (Klein and Bach, 2009) enhancing Au solubility and transport potential. It has been shown that seafloor serpentinization is a widespread process in the ultramafic domains of the Troodos ophiolite including the southern Troodos Mountains, similar to oceanic core complexes on the modern seafloor (Nuriel *et al.*, 2009). Therefore, it is likely that Kalavassos and Mala are enriched in Au as a function of both source rock Au content and enhanced Au solubility in  $H_2S$  rich fluids caused by the contribution of fluids derived from serpentinisation of the Limassol Forest Complex mantle lithologies (cf. Chapter 2) (William-Jones and Heinrich, 2005).

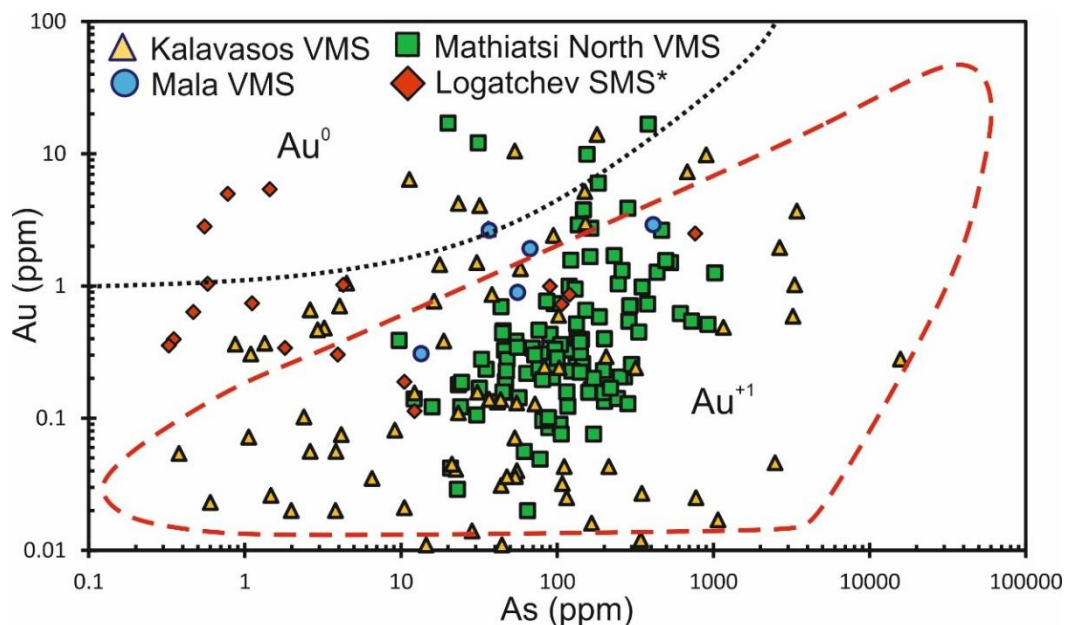


**Figure 5.8:** Concentrations of Au vs. As for auriferous VMS deposits of southern Troodos; Kalavassos ( $n= 39$ ), Mala ( $n= 6$ ), Mathiatis North ( $n=107$ ) and the Logatchev hydrothermal field ( $n=22$ ) (\*Keith *et al.*, 2016b). Data shows that at high Au and low As concentrations  $<1000$  ppm Au may be incorporated as  $Au^0$  in mineral- or nanoscale-inclusions in pyrite. A large proportion of points are hosted as a solid solution located within the  $Au^{+1}$  zone.

At the Semenov 2 hydrothermal field on the MAR (average 65 ppm Au; bulk ore) an additional source is hypothesised to explain Au enrichment (Melekestseva *et al.*, 2017). Whilst the author realises that the Au content of Troodos VMS is significantly less than the 65 ppm average for Semenov 2; Melekestseva *et al.* (2017) also reported elevated concentrations of Se, Te, Cu and Au which they find inconsistent with a purely basaltic-ultramafic source. Elevated Au/Ag ratio, the presence of Ag, Bi and Te minerals and high Au:BMS ratios suggest the addition of a magmatic volatile phase at Semenov 2 (Melekestseva *et al.*, 2017).

### 5.6.3 Magmatic volatile fluid flux to the hydrothermal system

In addition to variation in host rock chemistry a direct magmatic influx through volatiles into the hydrothermal system could explain the enrichment in magmatophile trace elements in the Solea domain (Layton-Matthews *et al.*, 2013; de Ronde *et al.*, 2003, 2005; Yang and Scott, 2002). In principal the Se/S ratio of pyrite (expressed as  $\text{Se/S} \cdot 10^6$ ) can be used as a proxy for the influx of magmatic volatiles into VMS hydrothermal systems (Layton-Matthews *et al.*, 2008, 2013). For example, elevated Se/S ratios in pyrite from the Bornite Zone at Kidd Creek of >20,000 are attributed to and associated with a late magmatic influx compared to other Kidd Creek pyrite with Se/S ratios of 2,000 to 10,000 (Hannington *et al.*, 1999). Selenium/sulfur ratios of >500 in pyrite represent an increased magmatic volatile component in VMS systems and all values for sediment-free ridges (back-arc and MOR), such as Troodos (Robertson and Xenophontos, 1993) are predicted to fall below 1,500 (Figure 5.9) (Layton-Matthews *et al.*, 2008). However, the Se/S ratios in pyrite from this study range from 1.6 to 9240 suggesting a variable magmatic volatile influx into the Troodos hydrothermal systems (Figure 5.9; also Chapter 8).

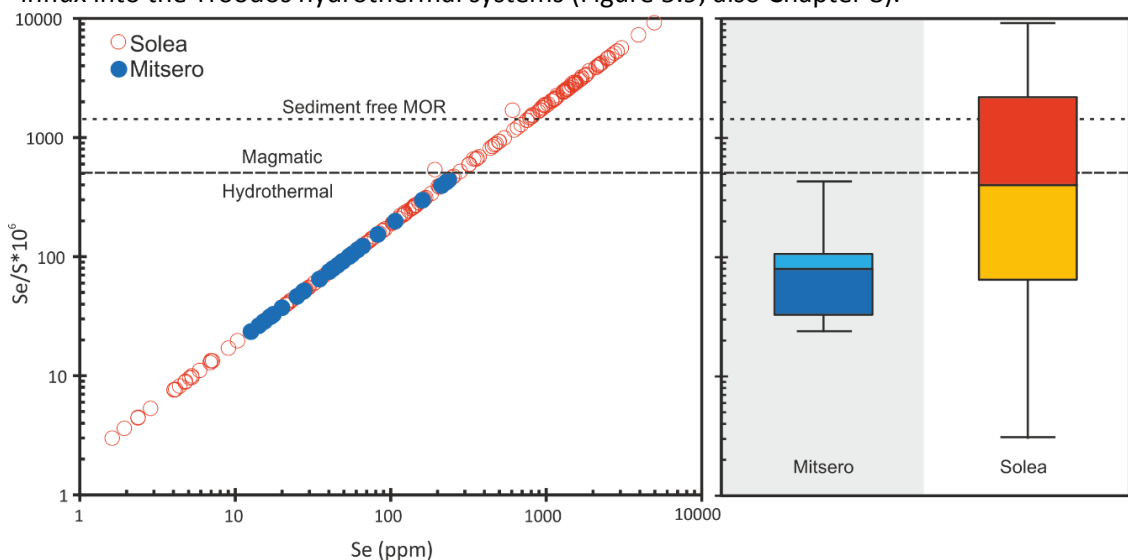


**Figure 5.9:** Selenium/sulfur ratios in pyrite from VMS of the Solea and Mitsero domains. Dashed line indicates the magmatic-hydrothermal threshold (500) identified by Layton-Matthews *et al.*, (2008). Upper dashed line (1500) shows maximum Se/S for modern MOR SMS (Layton-Matthews *et al.*, 2008; Hannington *et al.*, 1999). Selenium/sulfur ratios from Solea are skewed towards magmatic values with a maximum of 9280 whilst Mitsero are lower with a maximum of 640 (Appendix 5.4).

The structural domains of Solea and Mitsero display systematically different pyrite Se/S ratios (Appendix 5.4). The Solea graben shows the highest average Se/S ratio at 581 (max= 9280, n= 427) and the Mitsero graben the lowest at 31 (max= 640, n=100- Figure 5.9). This systematic variation between these two structural domains may be due to a variable magmatic volatile influx with the Solea graben experiencing the highest magmatic contribution (cf. Chapter 2). Keith *et al.* (2016a) reported  $\delta^{34}\text{S}$  isotope values in pyrite (mineral separates) from Skouriotissa that are skewed towards light magmatic (Troodos 0-1‰; Alt, 1994)  $\delta^{34}\text{S}$  values at -1.6 ‰. This is significantly lighter than average  $\delta^{34}\text{S}$  values quoted by Alt (1994) for other Troodos VMS sulfides of +4 to +7 ‰ (Chapter 8). Herzig *et al.* (1998a) demonstrate large variations in  $\delta^{34}\text{S}$  composition in hydrothermal sulfides from the Valu Fa Ridge (Lau Basin). They show that the  $\delta^{34}\text{S}$  composition of SMS pyrite is directly linked to the spreading evolution of the Valu Fa Ridge where vent fields separated by just 30 km are characterised by extreme  $\delta^{34}\text{S}$  variations that range from -7.3‰ at Hine Hina to + 10.9‰ at Vai Lili (Herzig *et al.*, 1998a). Such variations can be attributed to local spreading centre evolution with Hine Hina forming proximal to a magmatic source and thus experiencing an increased ingress of magmatic derived volatiles with a  $\delta^{34}\text{S}$  isotopic signature lighter than typical for a seawater dominated system. Herzig *et al.* (1998a) suggest the disproportionation of magmatic  $\text{SO}_2$  to  $\text{H}_2\text{S}$  in shallow magma conduits and decreased seawater ingress could explain the extremely light  $\delta^{34}\text{S}$  values at Hine Hina (cf. Chapter 9).

Whilst the Se/S ratio in pyrite is only a proxy for the magmatic influx and detailed  $\delta^{34}\text{S}$  analyses are needed to confirm these results, the systematic variation in Se/S between the Solea and Mitsero graben can be preliminary linked to the spreading evolution of the Troodos ophiolite. Cross-cutting relationships at graben boundaries (cf. Chapter 2) suggest that the Solea graben represents a full spreading ridge whilst Mitsero probably formed during migration of spreading between two rift structures, most likely as a propagating ridge tip (Everdingen *et al.*, 1995; Hurst *et al.*, 1994; Varga and Moores, 1985). The lower average Se/S ratio of 31 (n=100) (Figure 5.9) for Mitsero supports the structural observation that Mitsero formed through extension of older oceanic crust in an off-axis position (see Everdingen *et al.*, 1995). In this scenario, the magmatic volatile influx to the VMS system would be expected to be diminished and the pyrite Se/S ratio would be lower relative to Solea envisaged as a 'full' magmatic spreading centre that experienced higher magmatic volatile input (further discussion in Chapter 8).

The Troodos lava geochemistry is different to MORB showing an enrichment in volatile elements and  $\text{H}_2\text{O}$  (2-6 wt.%  $\text{H}_2\text{O}$ - Fonseca *et al.*, 2017; Patten *et al.*, 2017). Highly saline quartz-and epidote hosted fluid inclusions ( $T_{\text{H}}=400\text{-}500^\circ\text{C}$ , 36-61 wt.% NaCl equivalent) provide further evidence for a magmatic volatile contribution to the Troodos hydrothermal systems and

associated VMS deposits (Kelley *et al.*, 1992, 1993; Kelley and Robinson, 1990). The brine-rich inclusions are concentrated in plagiogranites and associated epidotes, the residual products of fractional crystallisation or partial melting of hydrated lower crustal gabbroic rocks (Grimes *et al.*, 2013; Freund *et al.*, 2014). Plagiogranites generally form below the penetration depth of seawater, with only the upper most crack front or contact aureole showing evidence of hydrothermal alteration (epidote veins etc.). Therefore brine and associated volatiles are only partly accessible to the hydrothermal fluid (Gillis and Roberts, 1999; Gillis and Coogan, 2002; Kelley *et al.*, 1992; Vibetti, 1993). Any magma derived brine must breach the boundary conductive layer in order to be accessible to the hydrothermal system otherwise metals may not be transferred upwards from the magmatic to hydrothermal environment (Gillis and Roberts, 1999- Figure 5.10). The repeated non-steady state injection of high level magma conduits would lead to the temporal migration of the boundary conductive layer (Figure 5.10) (Gillis and Roberts, 1999; Kelley and Robinson, 1990). The migration of the boundary and crucially generation of extensive fracturing would allow hydrothermal fluids to penetrate and incorporate magmatic volatile-rich brines (and metals) from the upper plutonics. Thus, we hypothesise that this magmatophile trace element signature is preserved in the Troodos VMS deposits as a systematic variation in Se/S and the distribution of magmatophile elements, such as Te, Se, Bi and Cu between the Solea and Mitsero graben (Figures 5.8, 5.9 and 5.10). At Solea the boundary conductive layer is subject to multiple magma injections, i.e. a full spreading ridge, suggesting a higher fracture density due to repetitive magma injection and penecontemporaneous graben formation leading to an increased probability of brine migration from the magmatic to the hydrothermal system (Figure 5.10). In contrast the boundary would be less mobile at Mitsero and volatile enrichment is less likely to occur leading to a depletion in magmatophile elements and correspondingly lower Se/S ratios in pyrite relative to Solea (Figure 5.10).

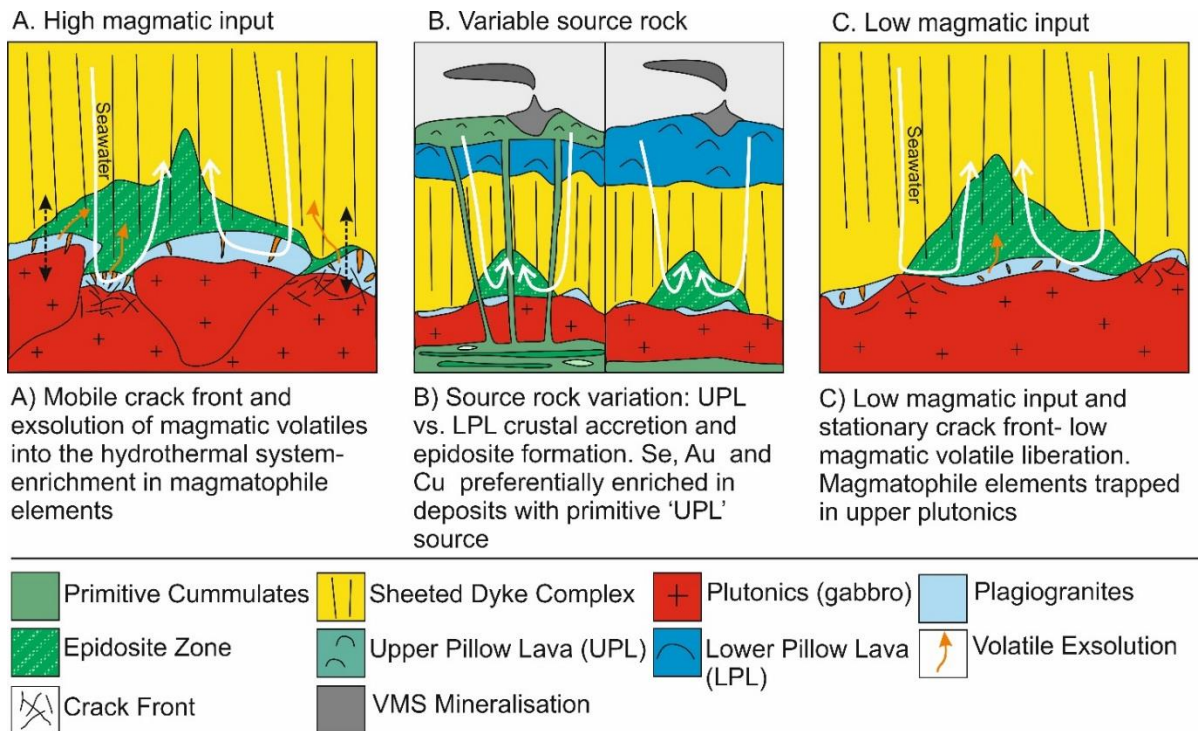


**Figure 5.10:** A preliminary model of magmatic volatile influx in the Troodos VMS system. Figure (A): Increased magmatic influx into the VMS hydrothermal system at Solea due to increased magmatism and a mobile crack front. Figure (B); influence of lava geochemistry and epidosite formation with Solea epidosite zone containing a higher proportion of mafic (basaltic) Se, Au, Cu rich dykes that are subsequently epidotised releasing relatively higher quantities of Se, Au and Cu into the hydrothermal system. The inverse is true at Mitsero that contains less evolved dykes within the epidosite zone. Figure (C); the effect of a low magmatic influx and a static crack front; brine is not liberated into the hydrothermal system and VMS deposits are depleted in magmatophile elements at Mitsero.

## 5.6 Summary

This study provides the first extensive high-resolution in situ data for trace elements in sulfide minerals for the VMS deposits of the Troodos ophiolite allowing the study of regional scale ore-forming processes related to spreading centre evolution. Spot and line analyses by LA-ICP-MS show that the distribution of trace elements in hydrothermal sulfides from various Troodos VMS deposits are extremely variable on both a deposit and a regional scale, i.e. between structural domains (see Chapter 10).

- Selenium is preferentially incorporated in chalcopyrite-rich ore that is more common in the lower VMS stratigraphy. Upon cooling to  $<260^{\circ}\text{C}$  chalcopyrite precipitation ceased leading to a reduction in Se uptake in the lower VMS stratigraphy and the preferential incorporation of Se into pyrite in the upper near seafloor sections of the deposit.
- Time resolved LA-ICP-MS analysis demonstrates that some trace elements are largely incorporated in sulfides via lattice substitution in solid solution (e.g., Se, As, Sb), whilst

others likely occur as both micro- and nanoscale inclusions or in solid solution (e.g. Te). Discrimination diagrams demonstrate the importance of As in incorporating elements with large covalent radii such as Te into the pyrite lattice.

- Colloform pyrite acts as a reservoir for Mo, Sb and Au, while euhedral pyrite exhibits an enrichment in Co, Te, Bi and Se. The variation in trace element composition between the two pyrite types is attributed to the rapid, disequilibrium precipitation of colloform pyrite relative to euhedral pyrite.
- Systematic variations of the Se/S ratio in pyrite on a graben scale coupled with our current understanding of the spreading evolution of Troodos suggest a heterogeneous source of trace metals in the Troodos VMS deposits.
- Compared to typical MOR hydrothermal systems, VMS deposits of the Troodos ophiolite and in particular those of Solea (Mala, Apliki and Skouriotissa) are enriched in magmatophile elements derived from a volatile source.
- This raises the question whether Cyprus-type VMS, especially those of the Solea graben can still be considered representative as true ancient analogues for modern active hydrothermal systems at sediment-free mid-ocean ridge spreading centres.



# CHAPTER 6

## Extreme enrichment of selenium in the Apliki Cyprus-type VMS deposit, Troodos, Cyprus

### **Submitted as:**

Martin, A.J., McDonald, I., MacLeod, C.J., Prichard, H.M., McFall, K., 2018. **Extreme enrichment of selenium in the Apliki Cyprus-type VMS deposit, Troodos, Cyprus.** *Mineralogical Magazine*, **82**, 697–724.

### **Co-author contributions:**

I. McDonald, C.J MacLeod, H.M Prichard and K. McFall were involved in discussion during the writing of this manuscript. I. McDonald supervised laser ablation analysis.

## 6. Abstract

The Troodos ophiolite Cyprus hosts the type locality for Cyprus-type, mafic Volcanogenic Massive Sulfide (VMS) deposits. Regional soil geochemical data for Troodos are highly variable with the Solea graben, one of three regional graben structures on Cyprus, showing enrichment in Te and Se. Of the three VMS deposits sampled within the Solea graben, Apliki exhibits the greatest enrichment in Se above the general background. Samples from the South Apliki Breccia Zone; a zone of hematite-rich breccia containing euhedral pyrite and chalcopyrite, contain up to 4953 and 3956 ppm Se in pyrite and chalcopyrite respectively. Four paragenetic stages are identified at Apliki and different generations of pyrite are distinguishable using trace element chemistry analysed via LA-ICP-MS. Results indicate stage I pyrite formed under reduced conditions at high temperatures >280 °C and contains 182 ppm (n=22  $\sigma$ =253) Se. Later stage III pyrite, which is euhedral and overprints chalcopyrite and hematite, is enriched in Se (averaging 1862 ppm; n=23  $\sigma$ =1394). Sulfide dissolution and hematite formation displaced large amounts of Se as hematite cannot accommodate high concentrations of Se in its crystal structure. The mechanisms proposed to explain the pronounced change in redox are twofold. Fault movement leading to localised seawater ingress coupled with a decreasing hydrothermal flux that generated locally oxidising conditions and promoted sulfide dissolution. Selenium/sulfur (Se/S\*10<sup>6</sup>) ratios of 9280 indicate a probable magmatic component for late stage III pyrite. However,  $\delta^{34}\text{S}$  analysis of chalcopyrite and pyrite suggests a constant magmatic volatile flux into the hydrothermal system but variable amounts of seawater mixing explaining the transition from oxidising to reduced conditions. This study highlights the significance of changes in redox that promote sulfide dissolution, mobilisation and enrichment of Se.

### 6.1 Introduction

The Solea graben is a major tectonic lineament in NW Cyprus and is considered to represent a fossil spreading axis (Varga, 1991) (Figure 6.1A). Three significant VMS deposits are located in close proximity (~4 km) to the Solea axis: Skouriotissa (currently producing), Mavrovouni (exhausted) and Apliki (not currently producing).

The Solea graben is defined by a series of N-S trending normal faults controlling VMS distribution (Figure 6.1B). Skouriotissa is located closest to the inferred graben axis and is thought to be the youngest VMS deposit on the island (e.g. Varga and Moores, 1985); horizontal lava structure at Skouriotissa supports this observation as it has not undergone 'off axis' rotation. Apliki lies 4 km W of Skouriotissa within the LPL's and is inferred to have formed earlier than Skouriotissa as it is located further from the Solea axis and has experienced 'off axis' rotation (see section 5.2).

Apliki is owned by Hellenic Copper Mines and although the deposit is not currently mined potential exists for future extraction of stockwork ore. Based on historic data Apliki has been considered to be a 'typical' Cyprus-type VMS; a cupriferous stockwork overlain by a massive sulfide lens. The exhalative interpretation relies heavily on historic data as no massive sulfide remains. Adamides (2010a) report an average Cu grade of 1.6 wt.% and total tonnage of 1.6 Mt (mainly exhalative ore).

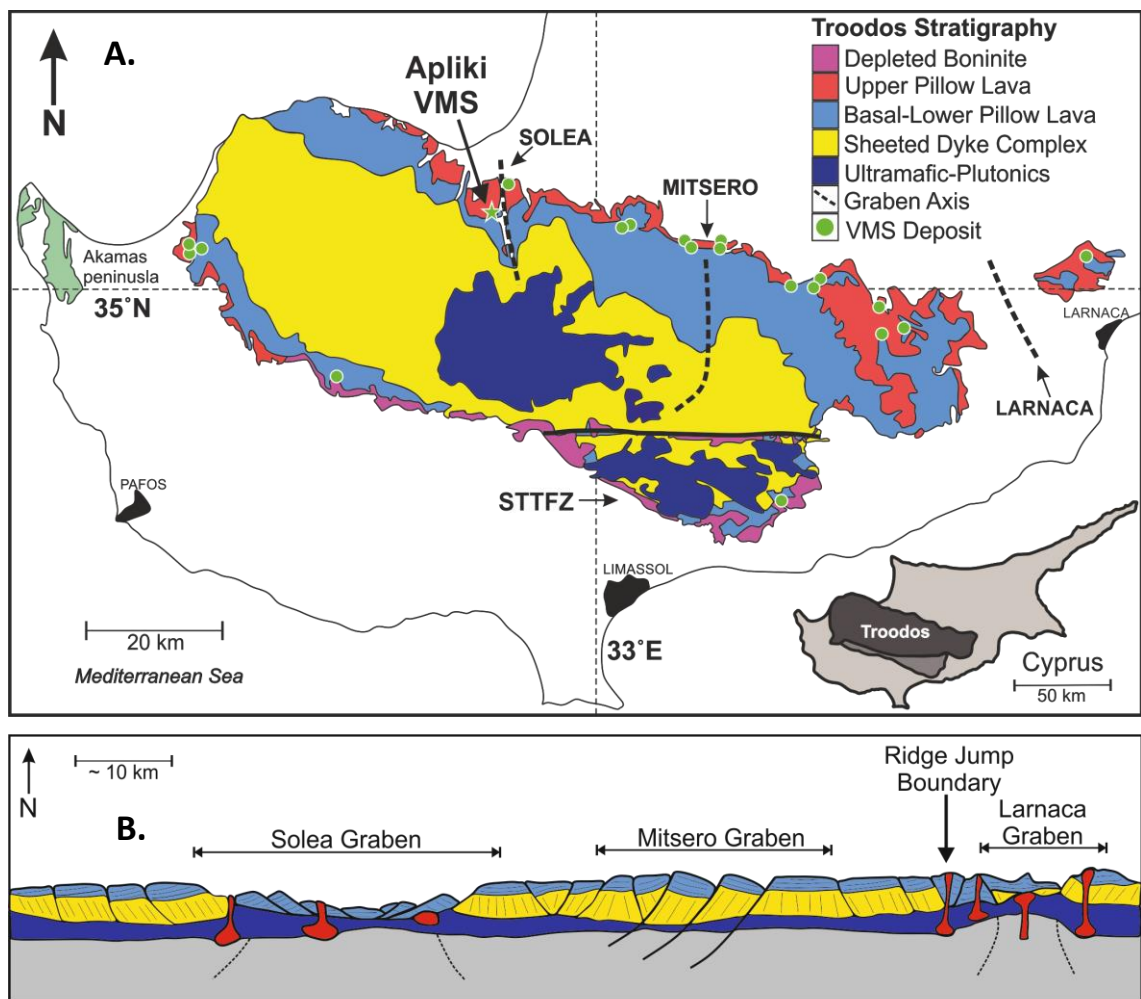


**Figure 6.1:** (A) Simplified geological map of the late Cretaceous (92 Ma) Troodos ophiolite, Cyprus. Apliki VMS is located in NW Troodos, W of the Solea graben axis (adapted from Keith *et al.*, 2016a); (B) Simplified structural cross-section of Troodos. Normal fault rotation leads to inversely dipping dykes and lava stratigraphy. VMS form along faults related to three main grabens: Solea, Mitsero and Larnaca. Location of section corresponds to the north flank of Troodos (adapted from Varga and Moores, 1990).

## 6.2 Sampling and Methodology

To investigate the spatial distribution of Te and Se within southern Cyprus and the Troodos ophiolite in particular, regional soil geochemical data was obtained from the Geological Survey Department of Cyprus (GSD) (see Cohen *et al.*, 2012). Sampling was carried out by the GSD using a nominal grid size of one sample per 2.2 km<sup>2</sup> for Troodos and 1 km<sup>2</sup> for surrounding sedimentary units (Cohen *et al.*, 2012). Two sampling depths were investigated: top soil (Figure 6.2), sampled at a depth of 0-25 cm, and subsoil sampled at 50-75 cm depth. An aqua regia digest followed by ICP-MS analysis for trace elements and XRF for major elements was used (Cohen *et al.*, 2012). Detection limits were 0.01 and 0.1 ppm for Te and Se (via ICP-MS).

Follow up samples for this study were collected during field seasons in 2016 and 2017. All samples obtained from Apliki were in-situ from the surface sampling of pit faces (i.e. not from spoil heaps). Apliki has been historically mined leading to the exposure of different ore horizons within the open pit providing a cross-section through the lower regions of VMS mineralisation.

Following the initial screening of 26 samples from Apliki via P-XRF, seven representative samples containing elevated whole rock Se (>50 ppm) were selected for detailed mineralogical and textural characterisation using reflected light microscopy followed by X-ray diffraction analysis.

X-Ray Diffraction analysis was carried out on powdered sample APL-1 to confirm dominant Fe matrix phase(s). A scan was run using the Philips PW1710 Automated Powder Diffractometer using Cu K $\alpha$  radiation at 35kV and 40mA, between 2 and 70 °2 $\theta$  at a scan speed of 0.04 °2 $\theta$ /s. The Sample was identified using Philips PC-identify software (see Chapter 4).

Variations in trace elements within sulfides were determined by Laser Ablation Inductively Coupled Plasma Mass Spectrometry (LA-ICP-MS). 150 spot analyses were performed on pyrite and chalcopyrite from seven polished blocks (see Chapter 4)

Detection limit for Se varied from 9-15 ppm for the different analytical runs due to mass interference associated with the Ar/Cl gas during ablation. This variation in detection limit does not affect the data significantly as a large proportion of Apliki samples contained >50 ppm Se in sulfides.

## 6.3 Results

### 6.3.1 P-XRF anomaly identification

Regional soil geochemistry (GSD data set) highlights the variable distribution of Te and Se in soils of Cyprus (Figure 6.2). Data displayed in Figure 6.2 are for topsoil transects only (0-25 cm). The interpolated surface uses point data. Classification into 12 categories is arbitrary as source geochemical data has been rounded to one decimal place by the GSD making it difficult to detect natural and more meaningful variation. Nevertheless the data are useful in highlighting areas of enrichment which may otherwise be overlooked. Figure 6.2 (Se transect A) benefits from the addition of P-XRF data for Se. The distribution of Te and Se from soil data is highly variable throughout Troodos with Te and Se data highlighting mine sites, especially the Limni, Kalavassos, Skouriotissa and Mala VMS (red circles- Figure 6.2). All four mines have significant spoil heaps associated with mining activities. Disturbance of sulfide waste leads to the mobilisation of Te and Se into the surrounding soils and the dispersion of Se into the environment creating wider anomalies.

Regional geochemical data and P-XRF anomalies highlight elevated Te and Se within the Solea graben. Two of three deposits in the Solea graben; Mala and Skouriotissa show elevated Te and Se from regional soil chemistry data (Figure 6.2). Apliki is not highlighted by regional soil data, most likely due to its location within the UN buffer zone making it difficult to access, the nearest soil survey point is 0.5 km south of Apliki. Sulfide samples analysed in this study are some of the first new data since the deposit was isolated in the buffer zone along the 1974 'Green Line'.

Out of 640 samples screened via P-XRF from VMS and mineralised localities across Troodos, samples at Apliki were relatively enriched with Se ranging from below detection <12 ppm to 1071 ppm (n=26). By comparison the highest value recorded for Skouriotissa was just 141 ppm Se. Portable-XRF consistently identified samples from the South Apliki Breccia Zone to contain the highest concentrations of Se between 970-1071 ppm representing a significant whole rock enrichment when compared to other VMS in Troodos (full Apliki P-XRF data Appendix D6.1).

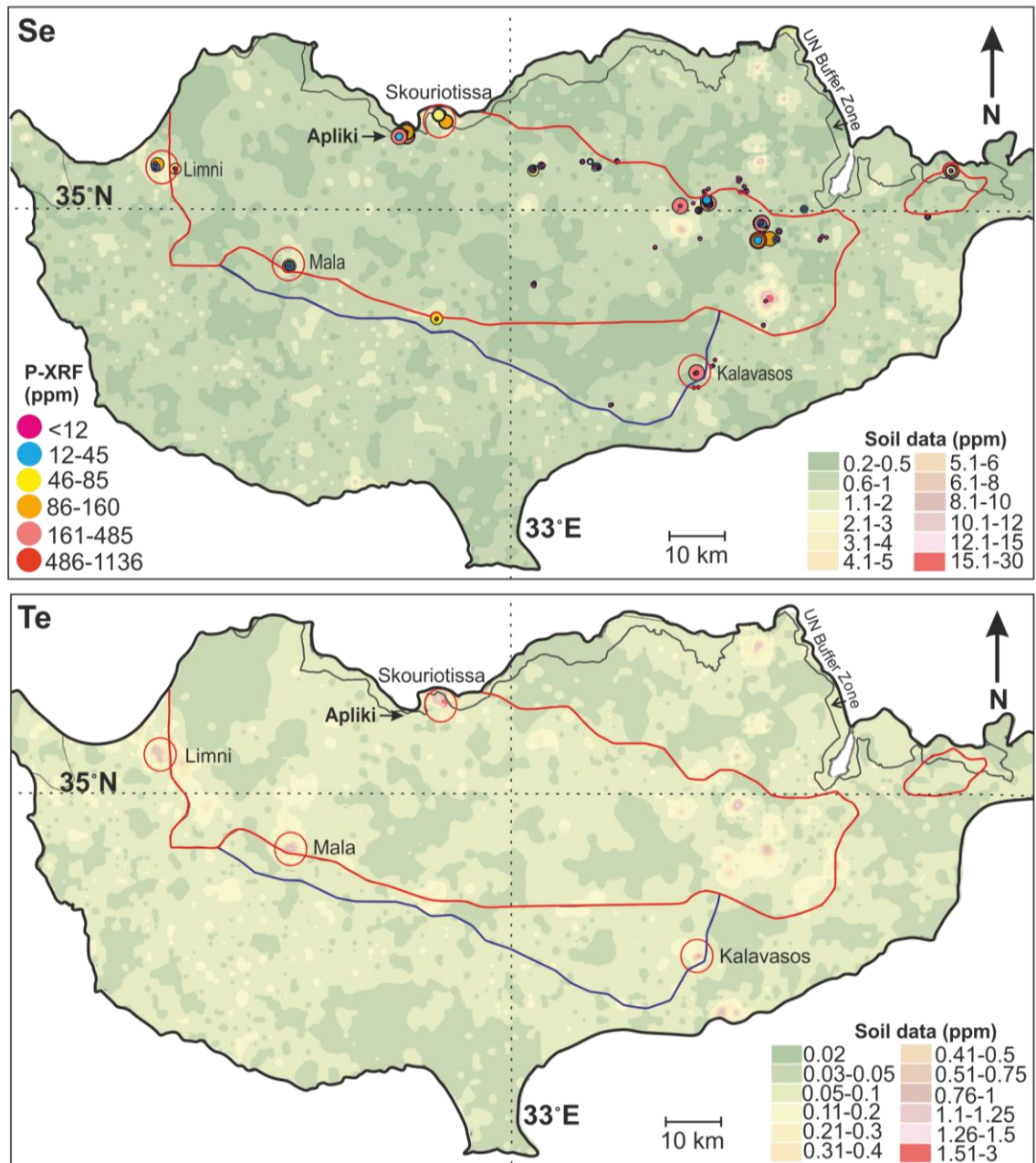


**Figure 6.2:** Distribution of Te and Se within soils in southern Cyprus. Two sets of data are presented for Se. P-XRF (this study) and regional geochemical soil data (Cohen *et al.*, 2012). Tellurium was not analysed by P-XRF. The red line is the outline of the Troodos ophiolite and blue line the STTFZ. Anomalous Te and Se occur at the VMS mines; four of which are highlighted by the red circles. Data provided by the Geological Survey Department of Cyprus (after Cohen *et al.*, 2012).

### 6.3.2 The Apliki VMS

The mineralised VMS package is bound by normal, axis parallel (N-S- 350°) faults dipping 50-55° to the E (towards the Solea axis: 6.3 A and B); the hanging wall contains westward dipping (36-52°) 1-3 m thick flow units (Figure 6.3 A and 6.4). The contact on both parallel bounding faults is sharp; mineralisation does not cross the contact suggesting a degree of post mineralisation fault movement. The footwall unit is highly degraded and the extent of rotation less clear but individual flows have been measured dipping 34° W. The footwall morphology is dominated by pillows and hyaloclastites rather than flows and celadonite abundance increases dramatically indicating a higher temperature of formation and that the footwall formed stratigraphically deeper than the hanging wall (i.e. the fault therefore has a normal geometry). The mineralised fault bound zone is approximately 100m wide and consists of silicified, chloritised brecciated LPL with disseminated pyrite (2-5 modal %) and no massive sulfide mineralisation (Figure 6.3A and 6.4). The lower northern wall region is chalcantinite and azurite-rich.

At the southern end of the pit, fresh sulfide is preserved and material is best accessed via a drainage gully in the centre of the lowermost bench (Figure 6.3B). The area is rich in coarse grained semi-massive pyrite with an unusual hematite-(goethite)-chalcopyrite-pyrite-rich breccia zone (Figure 6.5). In this zone chalcopyrite is more abundant than pyrite accounting for up to 70 wt.% in the samples collected (Figure 6.4 and 6.5). From here onwards this zone will be termed the South Apliki Breccia Zone (SABZ). The breccia zone is continuous for 4-5 m (depth) in cross-section through two bench levels and only well exposed perpendicular to strike for 2-3 m. Within this relatively narrow zone several morphological distinctions can be made based on modal mineralogy and degree of silicification (Figure 6.5 and Table 1). Hematite also occurs in discrete cm wide veins which crosscut pillows in the footwall. Chalcantinite, covellite and azurite are abundant in the southern pit wall (Figure 6.5).

The hematite breccia is to our knowledge unique to the Apliki VMS and although specular hematite is common within pseudo-epithermal 'T' type mineralisation in Troodos defined by Jowitt *et al.* (2005) (e.g. at Alestos or Touronjia: Chapter 7) to the authors knowledge it does not coexist with large quantities of chalcopyrite at any other locality.

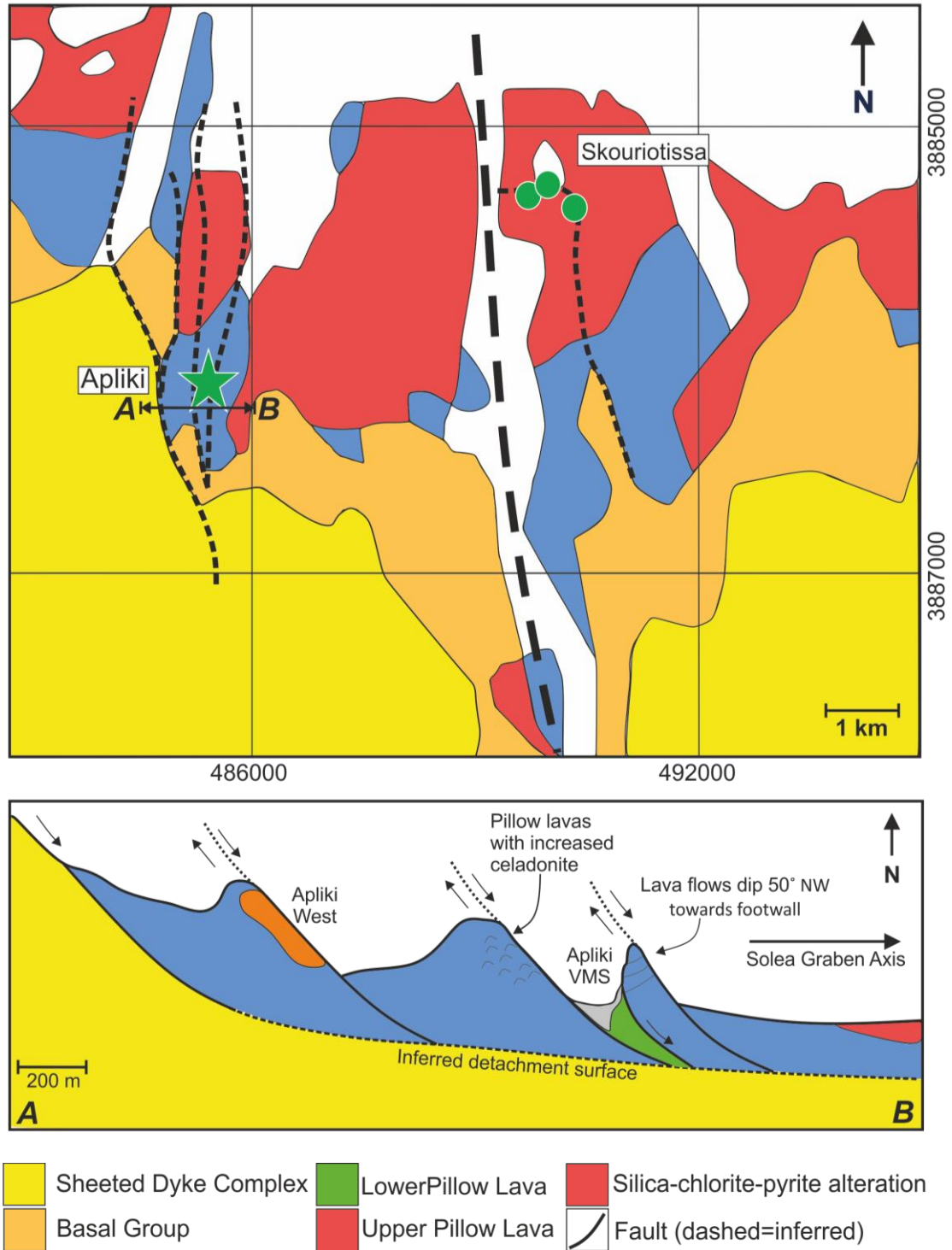


**Figure 6.3A:** Location map of the Apliki VMS and structural schematic cross-section. Apliki is located in NW Troodos within the Solea graben. The deposit is situated within the LPL stratigraphy and bound by two axis parallel (N-S) normal faults. At depth faults are inferred to truncate along a major detachment surface (Data from field mapping and GSD 1:250,000 map).

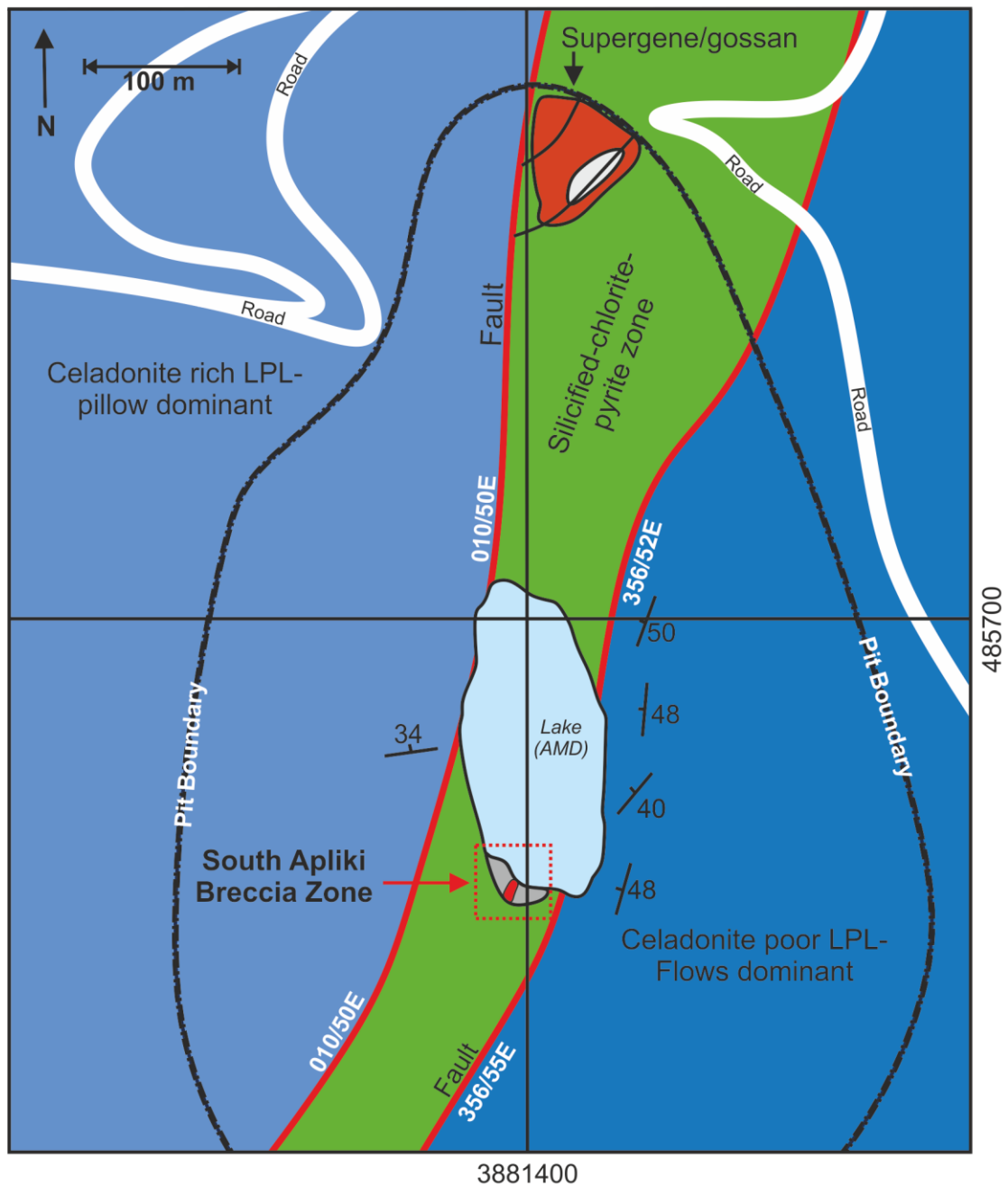


**Figure 6.3B:** Local map of the Apliki open pit mine showing the location of the South Apliki Breccia Zone and major geological features visible within the pit.

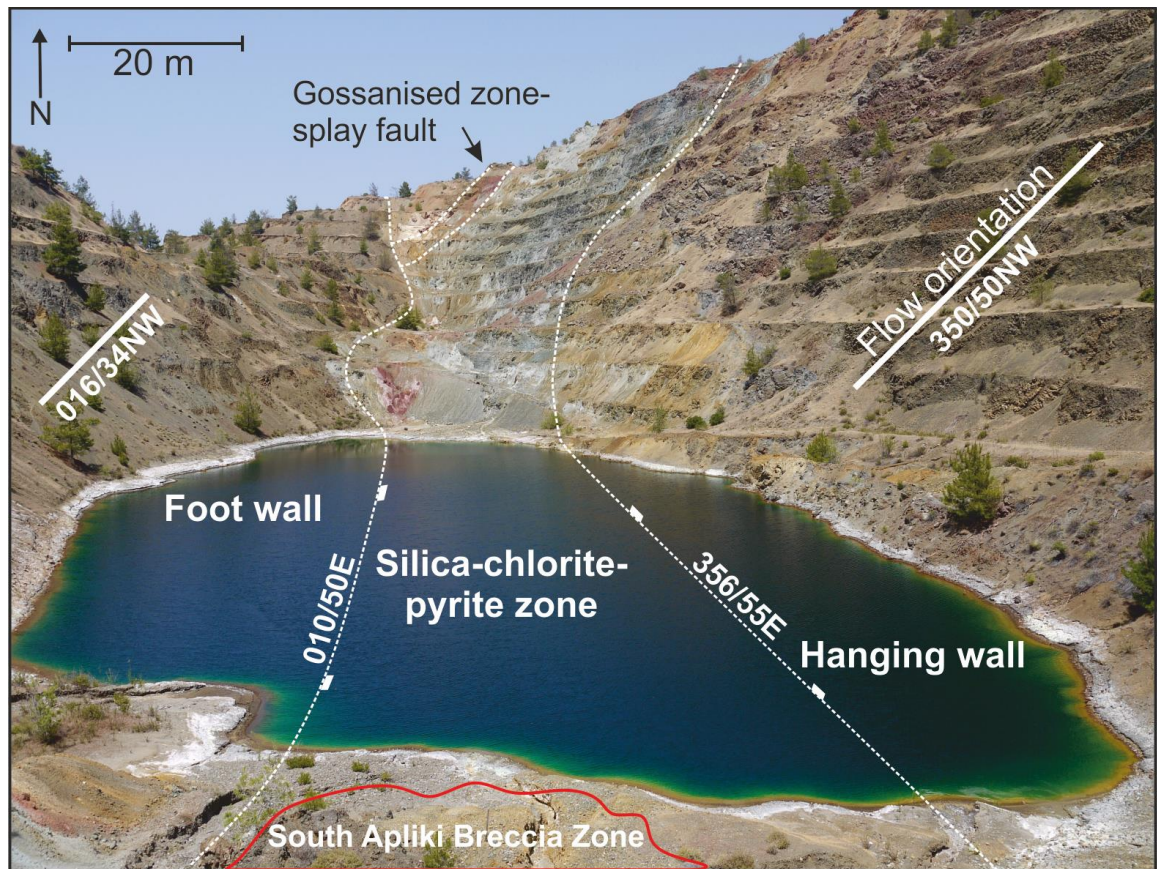


**Figure 6.4:** Annotated field photo of the Apliki VMS open pit. N-S faults bound the mineralised package, both the footwall and hanging wall are steeply rotated.

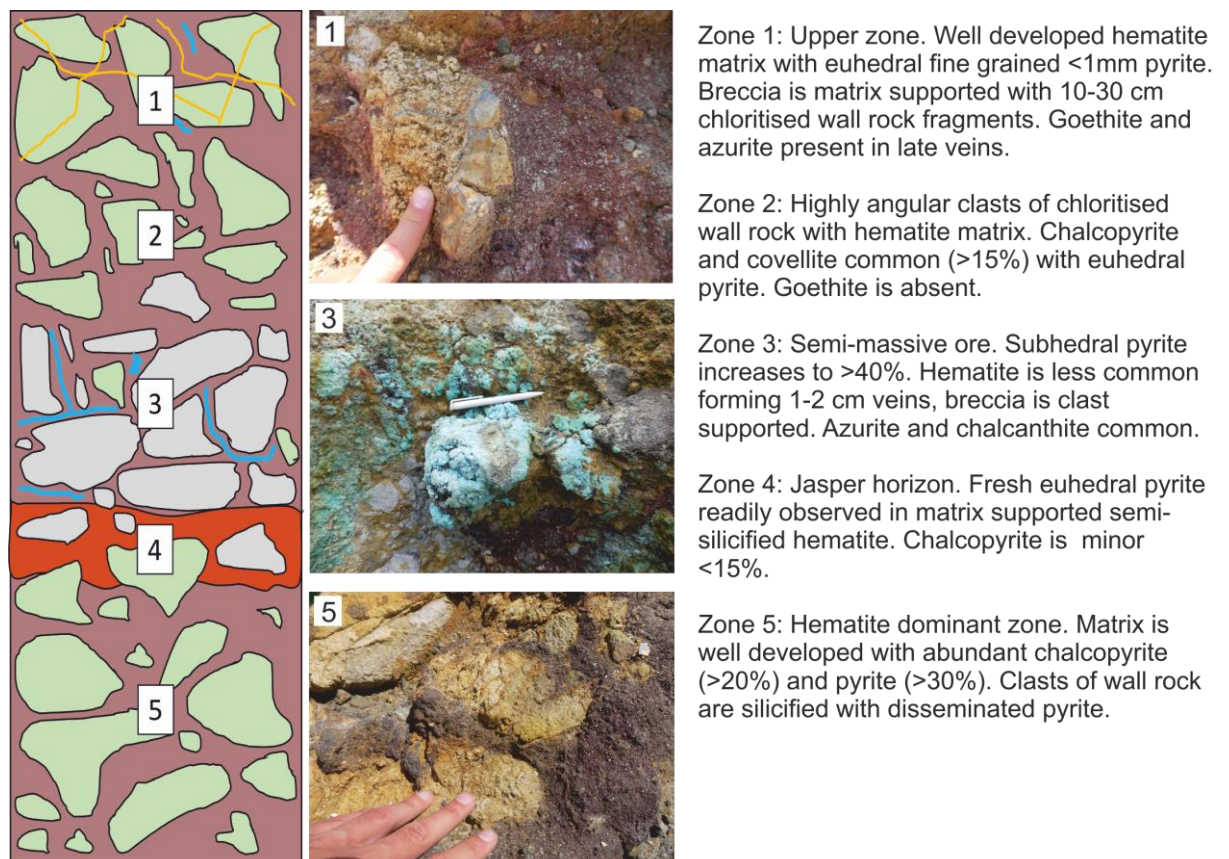


**Figure 6.5:** Stratigraphic cross-section through the South Apliki Breccia Zone (see Table 6.1).

### 6.3.3 Mineralogy of South Apliki Breccia Zone

Reflected light microscopy on seven representative polished blocks from the South Apliki Breccia Zone (Figure 6.6) reveal four stages of paragenesis (summarised in Table 6.1 and Figures 6.6, 6.7 and 6.8). Generally, chalcopyrite is variably altered to covellite and digenite at grain boundaries. Pyrite, when present is euhedral and may be replaced by hematite (Figure 6.6 and 6.7). Semi quantitative XRD (Appendix 6.2) indicates that hematite is the dominant matrix phase occurring in both specular form and mixed with silica as jasper (optically identified). Subsequently samples are grouped into four alteration stages based on pyrite morphology and degree of hematite and covellite alteration (see also Appendix 6.6).

**Table 6.1:** Summary of samples analysed from the South Apliki Breccia Zone. BDL= Below Detectable Limit.  $\sigma$  = one standard deviation (in ppm) PY = pyrite, CCP= chalcopyrite- full dataset available in Appendix 6.3.

Sample	Grid Reference (WGS 1950)	Stage	Mineralogy	Average Se PY (ppm)	Average Te PY (ppm)	Average Se CCP (ppm)	Average Te CCP (ppm)
APL-1	048574 3881375	3	Chalcopyrite (65%), covellite (20%), hematite (10%), pyrite (5%)	2075 (n=5) ( $\sigma$ =1080)	5.3 (n=5) ( $\sigma$ = 3.3)	2648 (n=10) ( $\sigma$ = 745)	3.5 (n=10) ( $\sigma$ = 1.6)
APL-2	048572 3881376	2	Hematite (50%), pyrite (30%), chalcopyrite (15%), covellite (5%)	1223 (n=10) ( $\sigma$ =488)	14.4 (n=10) ( $\sigma$ = 12.6)	906 (n=6) ( $\sigma$ =922)	8.5 (n=6) ( $\sigma$ = 6.8)
APL-3	048574 3881377	2-3	Pyrite (48%), chalcopyrite (30%), hematite (20%), covellite (2%)	1098 (n=12) ( $\sigma$ =837)	11.7 (n=12) ( $\sigma$ = 10.0)	1991 (n=6) ( $\sigma$ = 1246)	5.6 (n=6) ( $\sigma$ =6.9)
APL-4	048574 3881384	4	Jasper (50%), pyrite (20%), hematite (15%), chalcopyrite (10%), covellite (5%)	579 (n=12) ( $\sigma$ = 641)	17.5 (n=12) ( $\sigma$ =15.0)	1012 (n=6) ( $\sigma$ =801)	9 (n=6) ( $\sigma$ = 9.8)
APL-5	048574 3881384	1	Pyrite (60%), Hematite (30%), chalcopyrite (10%)	204 (n=12) ( $\sigma$ = 443)	8.4 (n=12) ( $\sigma$ =10.9)	601 (n=6) ( $\sigma$ =233)	5.0 (n=6) ( $\sigma$ =4.2)
APL-6	048574 3881384	3	Chalcopyrite (40%), hematite (40%), pyrite (20%)	1649 (n=18) ( $\sigma$ = 627)	10.6 (n=18) ( $\sigma$ =7.6)	2014 (n=4) ( $\sigma$ = 1064)	9.0 (n=4) ( $\sigma$ = 11.9)
APL-7	048574 3881385	1	Hematite (55%), chalcopyrite (20%), pyrite (20%), jasper (5%)	177 (n=10) ( $\sigma$ = 123)	11.9 (n=10) ( $\sigma$ = 9.1)	1483 (n=6) ( $\sigma$ =879)	1.5 (n=6) ( $\sigma$ = 0.8)

Stage I samples (APL-5 and APL-7) contain significant amounts of chalcopyrite that exhibits no visible oxidation along grain boundaries. Critically pyrite is subhedral to anhedral and does not overprint chalcopyrite. Pyrite is readily preserved rimming chalcopyrite and is rarely altered to hematite (Figure 6.6 and 6.7). This stage of alteration is characterised by a hematite matrix (55%) with 1-2 mm subhedral pyrite (20%) and chalcopyrite (20%). Pyrite is heavily pitted and commonly observed rimming chalcopyrite. Very few pyrite grains are euhedral; euhedral grains occur overgrowing chalcopyrite whilst subhedral pyrite appears cogenetic and do not overgrow chalcopyrite. Dissolution features are rare occurring only in a small number of pyrite grains (<5%) where pyrite is locally altered to hematite (Figure 6.6 and 6.8).

Stage II samples (APL-2 and APL-3) contain large amounts of hematite forming botryoidal to acicular masses within the matrix. Pyrite is less common than in stage I forming both subhedral grains (<2 mm) and euhedral grains >2 mm. Chalcopyrite is minor compared to stage I and may be altered to covellite and digenite (Figure 6.8 and 6.9).

The third stage of ore formation is well developed in samples APL-1 and APL-6; euhedral coarse pyrite overprints both chalcopyrite and the hematite-goethite matrix. Euhedral pyrite crystals that overprint earlier phases exhibit no hematite alteration suggesting they formed during in the last stage of mineralisation. Stage III comprises roughly equal proportions of hematite (40%) and chalcopyrite (40%) with minor pyrite (20%) which is coarse grained (1-3 mm) and euhedral. Chalcopyrite is interstitial surrounding pyrite and in some areas forms crystals up to 6 mm (Figure 6.6). Chalcopyrite may be oxidised to covellite and digenite (Figures 6.6, 6.8 and 6.9).

Supergene alteration of chalcopyrite (Stage IV) produces dominantly covellite + digenite +/- chalcocite with goethite. Alteration is generally limited to grain boundaries and rarely in stage IV samples grains may be completely dissolved or replaced (Figure 6.6 and 6.7). Stage IV alteration is characterised by a fine matrix of botryoidal to acicular goethite and hematite with variable amounts of jasper. Pyrite is a minor constituent (20%) limited to bands of specular hematite. Pyrite exhibits a subhedral to rounded morphology and may be coarse up to 3 mm. Chalcopyrite is a minor constituent (<10%) forming globular masses 1-5 mm and is rarely overgrown by pyrite. Covellite if present rims chalcopyrite and upon weathering is preserved as a series of sub-rounded voids which indicate relict chalcopyrite-covellite grains. Reaction rims forming Cu secondaries around the margin of chalcopyrite are generally 20-30  $\mu\text{m}$  (Figure 6.6 and 6.7).

Few grains of pyrite show evidence of hematite replacing pyrite, but rarely radial growths of hematite can replace pyrite cores (Figure 6.6). Within the hematite-goethite matrix cubic pyrite pseudomorphs are common (Figure 6.7).

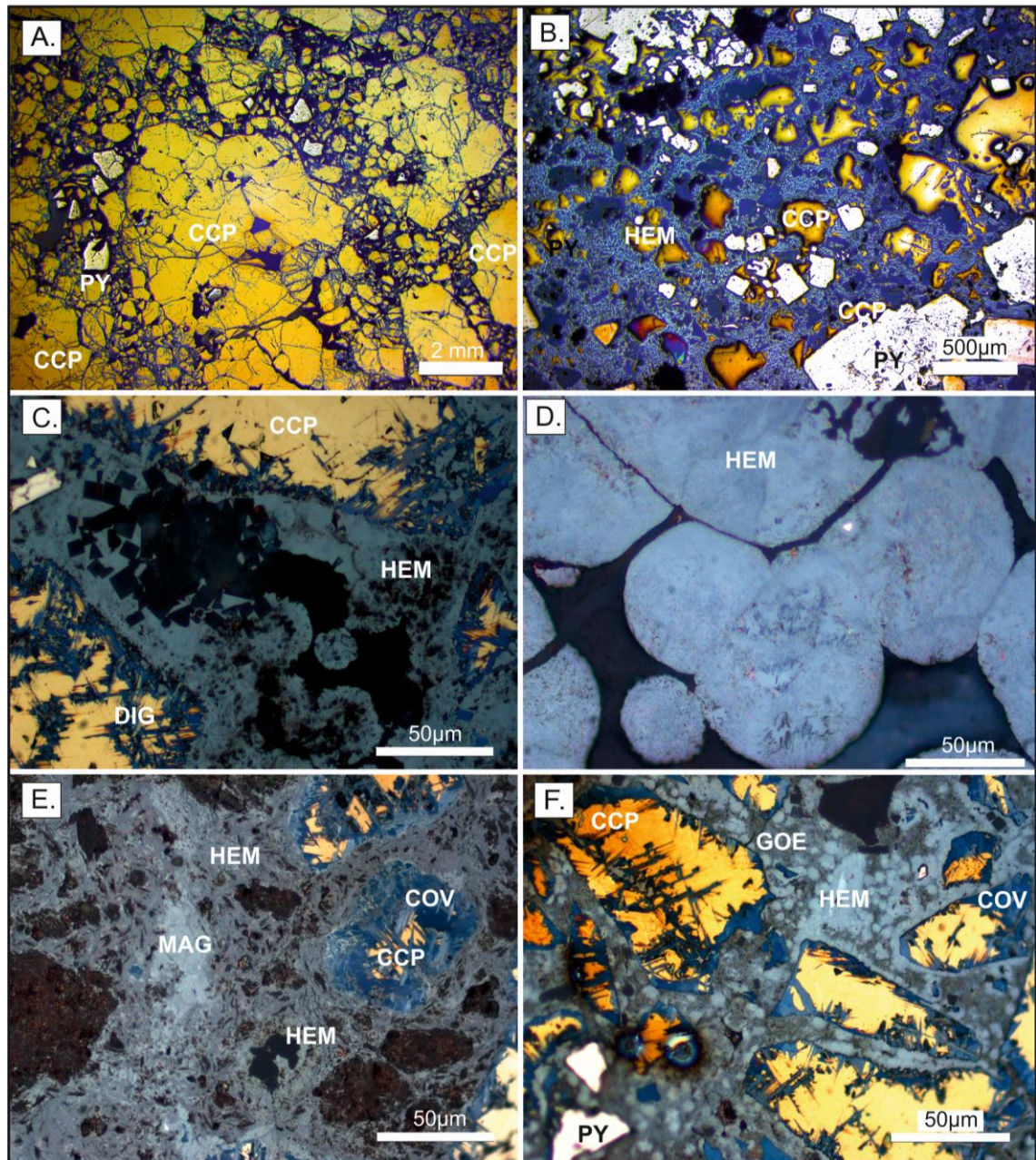


**Figure 6.6:** Photomicrographs in reflected light of South Apliki Breccia Zone samples. A) Massive chalcopyrite with interstitial subhedral pyrite and minor covellite. B) Chalcopyrite with a hematite matrix and euhedral pyrite overgrowths. C) Chalcopyrite rimmed by covellite and digenite with cubic hematite pseudomorphing pyrite. D) Botryoidal hematite with pyrite inclusions (white). E) Extensive alteration of pyrite to hematite with covellite replacing chalcopyrite. F) Botryoidal matrix hematite-goethite with subhedral pyrite and chalcopyrite rimmed by covellite. PY= pyrite CCP= chalcopyrite HEM= hematite COV= covellite DIG= digenite MAG= magnetite GOE= goethite (see also Appendix 6.6).

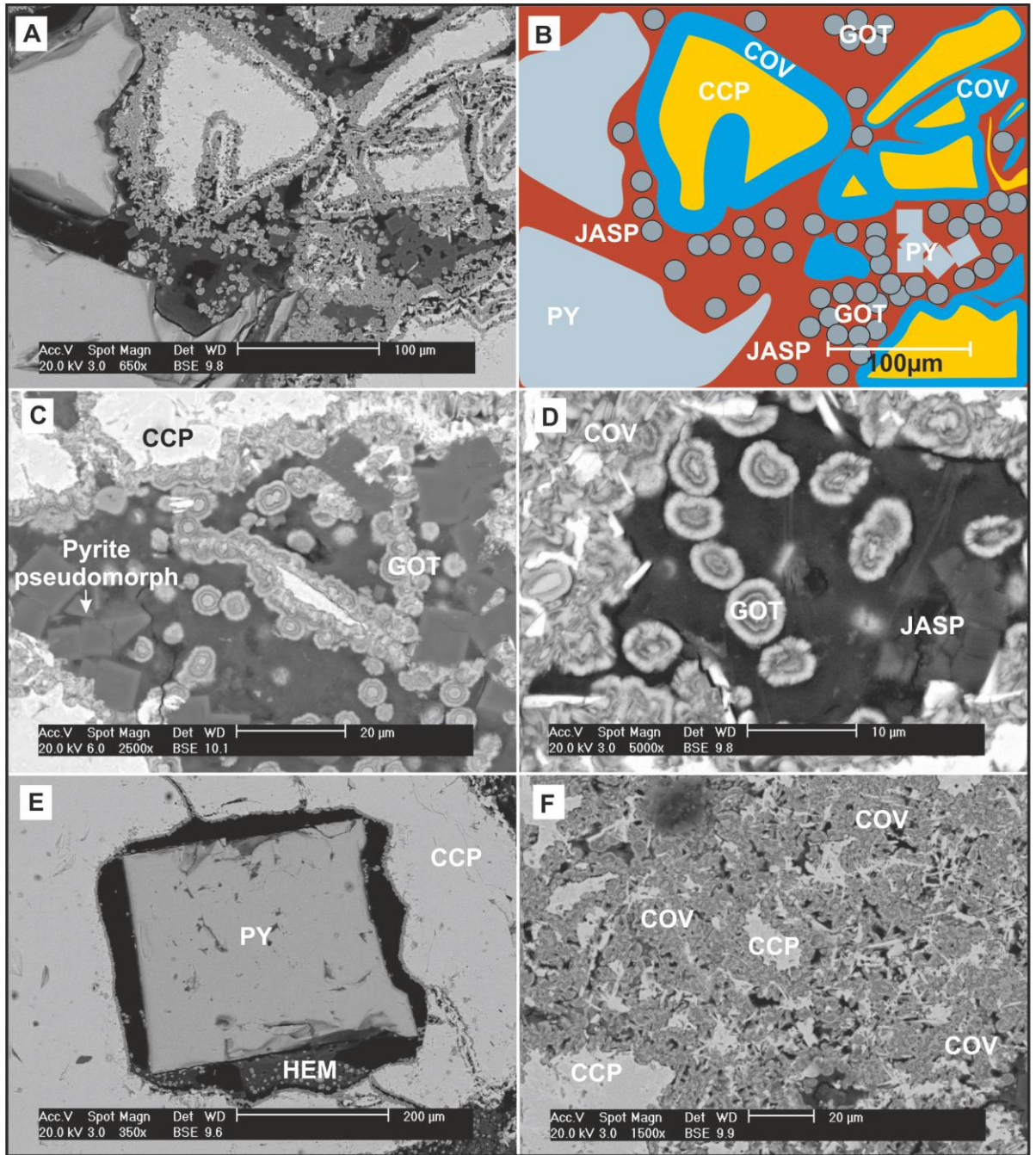


**Figure 6.7:** SEM BSE photomicrographs. A) Chalcopyrite mantled by secondary Cu phases and goethite. B) Sketch showing alteration of CCP. C) Pyrite pseudomorphs and goethite in matrix. D) Botryoidal goethite within jasper matrix. E) Euhedral pyrite in chalcopyrite with minor hematite at margins. F) Extensive alteration of chalcopyrite to covellite. PY= pyrite CCP= chalcopyrite HEM= hematite COV= covellite GOT= goethite JASP= Jasper (hematite + silica) (Appendix 6.6).

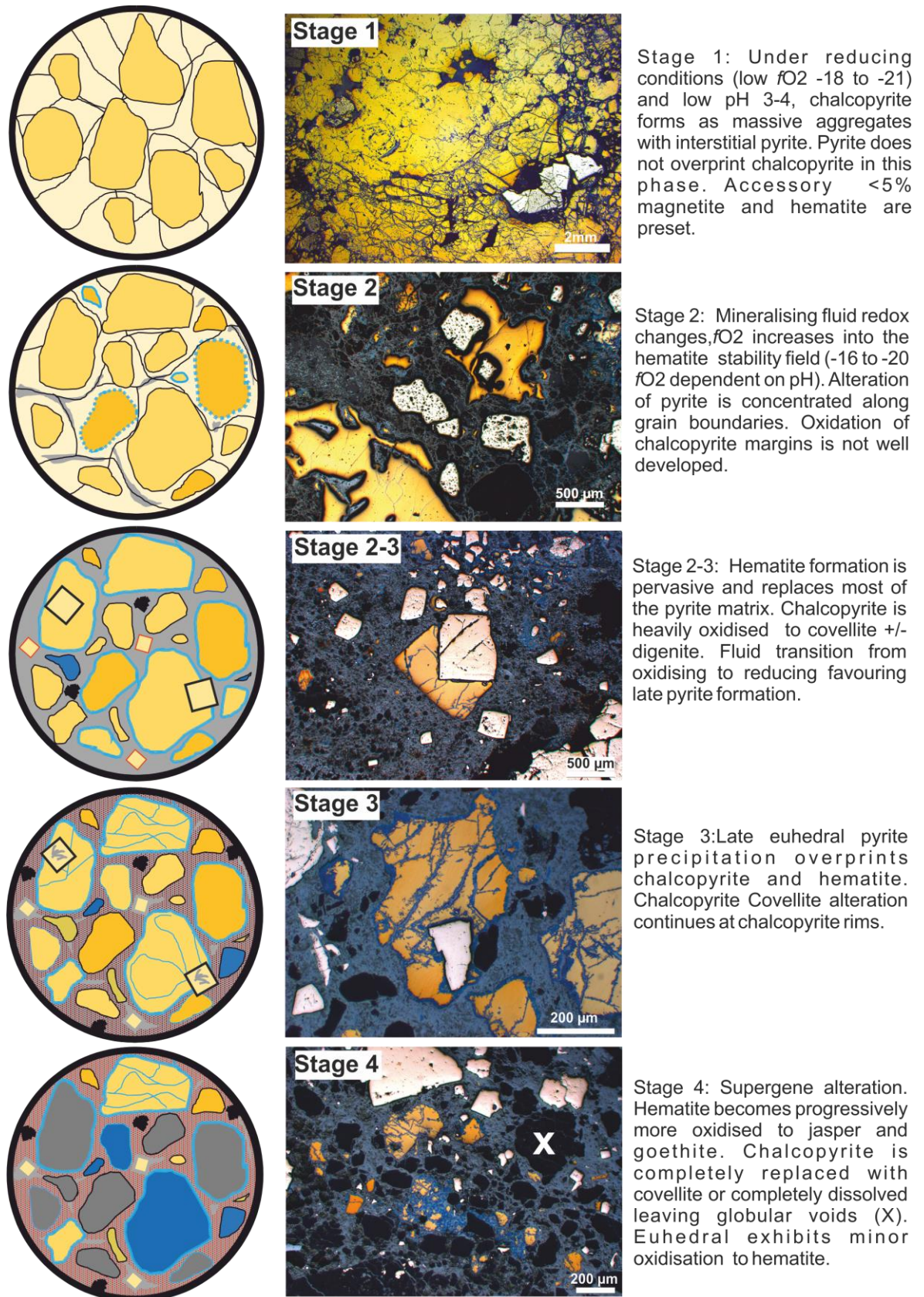


**Figure 6.8:** Paragenesis of the South Apliki Breccia Zone

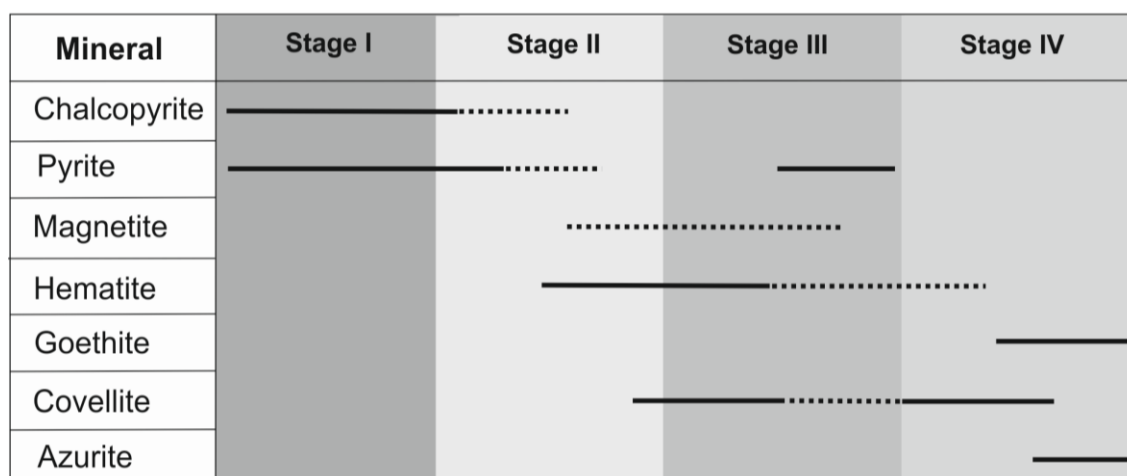


**Figure 6.9:** Summary of sample paragenesis showing multiple phases of pyrite formation and the transition from sulfide to oxide formation. Goethite and chalcocite are related to weathering and supergene alteration.

### 6.3.4 LA-ICP-MS of sulfides

A total of 150 LA-ICP-MS spot analyses from Apliki (96 of pyrite and 54 of chalcopyrite) were carried out using seven representative polished blocks. Tellurium and Se maximum values in pyrite reach 70 and 4953 ppm respectively. LA-ICP-MS of sulfides from Apliki indicate that Te and Se concentration varies systematically with alteration stage. Selenium in pyrite varies enormously from <15 (below detection limit) to 4953 ppm. Similar variation is observed in chalcopyrite with Se concentrations ranging from 104 to 3956 ppm. The average Se concentration in chalcopyrite is consistently greater than pyrite (summarised in Table 6.2: See Appendix 6.3).

**Table 6.2:** Average Se and Te concentration in chalcopyrite and pyrite by alteration stage. Detection limit: 9-15 ppm and 0.4-0.7 ppm for Se and Te respectively (histogram plots available in Appendix 6.4).

(ppm)	Stage I	Stage II	Stage III	Stage IV
<b>Chalcopyrite</b>				
Te	5	8	4	8
Se	601	1210	2215	1012
<b>Pyrite</b>				
Te	16	8	13	10
Se	182	1155	1862	532

Bivariate plots of Te and Se against other trace elements from LA-ICP-MS data are shown in Figure 6.10. Te and Se exhibit no correlation ( $R^2=0.02$ ) suggesting a decoupled behavior during VMS formation. Se exhibits limited correlation with all trace elements whereas Te exhibits a weak positive correlation with Bi ( $R^2=0.3$ ) and Co ( $R^2=0.2$ ) but no correlation with As ( $R^2=0.01$ ).

Arsenic is low in the South Apliki Breccia Zone averageing just 152 ppm in pyrite compared with 496 ppm for all other deposits in Troodos (Table 6.3). Cobalt concentrations in Apliki pyrite average 268 ppm; similar to the mean value for all Troodos deposits at 245 ppm (Table 6.3). Bismuth concentration in pyrite is lower in Apliki at 2.46 ppm compared with all other VMS but marginally higher when compared to Skouriotissa at 1.66 ppm (Table 6.3). A comparison of average trace element concentrations for Apliki and all other VMS of Troodos is summarised in Table 6.3 (full data in Appendix 6.3).

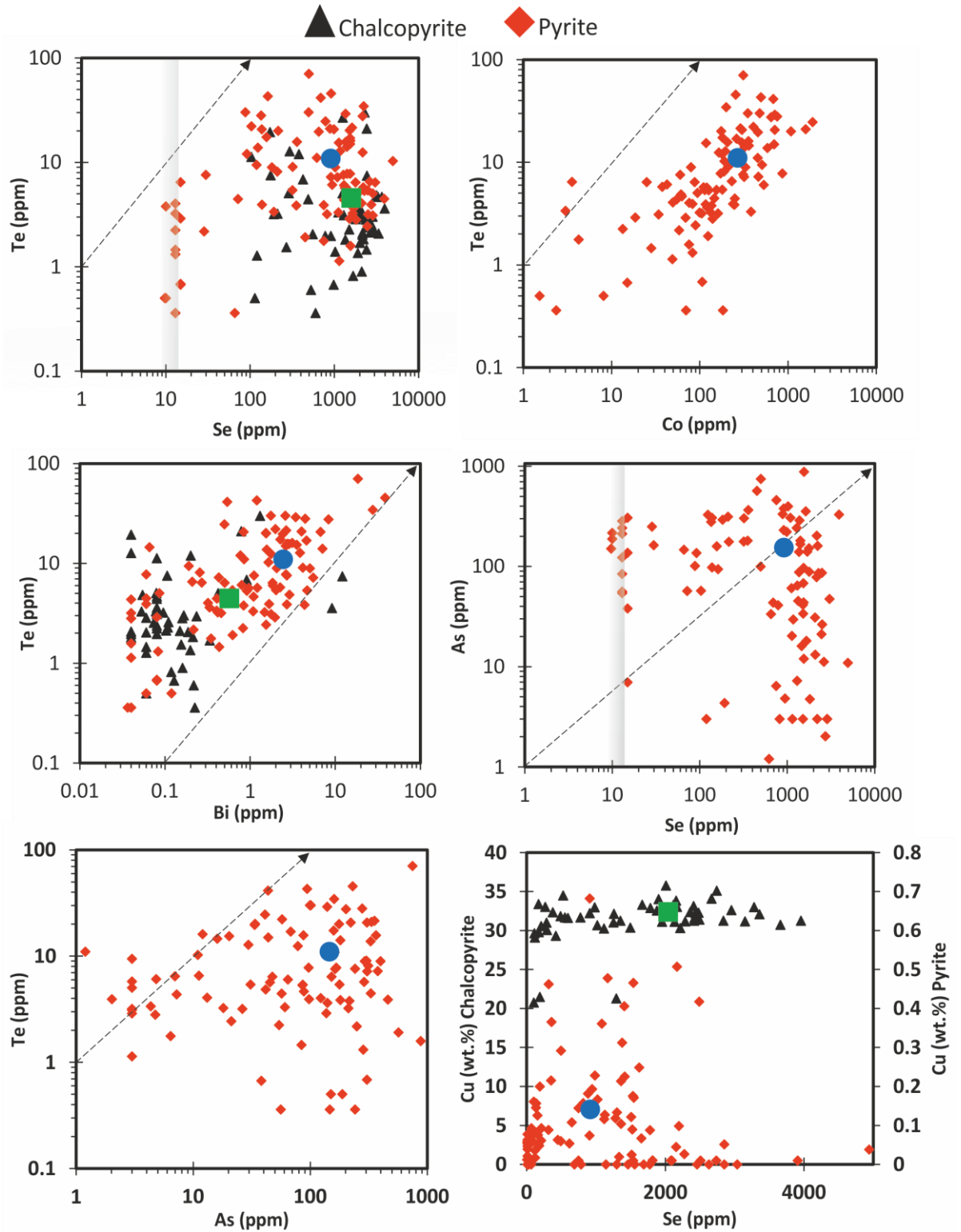
When comparing between chalcopyrite and pyrite clear trends emerge (Table 6.2 and 6.3). Chalcopyrite is enriched in Se relative to pyrite but depleted in Te, As, Co and Bi. Similar trends exist when comparing the relative concentration of elements between pyrite and chalcopyrite for all VMS considered in this study (Table 6.3). Cobalt is elevated at Skouriotissa for both pyrite and chalcopyrite at 406 ppm and 72 ppm respectively compared to 268 and 4.96 ppm for Apliki (Table 6.3). Selenium in chalcopyrite at Apliki is 12 times higher than Skouriotissa and 17 times higher than the average for all Troodos VMS (Table 6.3).

**Table 6.3:** Summary of average LA-ICP-MS spot data. Selenium is enriched in both chalcopyrite and pyrite at the South Apliki Breccia Zone compared to neighbouring Skouriotissa and Troodos VMS (\*subset of 442 LA-ICP-MS spot analyses; cf. Chapter 5). Data shows that Se is preferentially incorporated into chalcopyrite whilst Te partitions into pyrite.

Pyrite (ppm)	Se	Te	Bi	Co	As
<b>Apliki</b>	<b>922</b>	<b>11.2</b>	<b>2.5</b>	<b>268</b>	<b>152</b>
(n= 96)	$\sigma$ 1004	$\sigma$ 12.5	$\sigma$ 5.6	$\sigma$ 325	$\sigma$ 165
<b>Skouriotissa</b>	<b>77</b>	<b>4.5</b>	<b>1.6</b>	<b>406</b>	<b>35</b>
(n= 54)	$\sigma$ 129	$\sigma$ 5.8	$\sigma$ 2.7	$\sigma$ 428	$\sigma$ 93
<b>Troodos VMS*</b>	<b>55</b>	<b>6.7</b>	<b>7.1</b>	<b>245</b>	<b>469</b>
(n= 196)	$\sigma$ 117	$\sigma$ 15	$\sigma$ 36	$\sigma$ 640	$\sigma$ 1585

Chalcopyrite (ppm)	Se	Te	Bi	Co	As
<b>Apliki</b>	<b>1576</b>	<b>4.5</b>	<b>0.6</b>	<b>4.9</b>	<b>5.1</b>
(n= 54)	$\sigma$ 1069	$\sigma$ 5.6	$\sigma$ 2.1	$\sigma$ 7.1	$\sigma$ 13.7
<b>Skouriotissa</b>	<b>315</b>	<b>2.1</b>	<b>1.3</b>	<b>72</b>	<b>16</b>
(n= 27)	$\sigma$ 361	$\sigma$ 2.9	$\sigma$ 1.8	$\sigma$ 263	$\sigma$ 60
<b>Troodos VMS*</b>	<b>77</b>	<b>1.9</b>	<b>0.8</b>	<b>1.3</b>	<b>8.6</b>
(n= 20)	$\sigma$ 130	$\sigma$ 2.6	$\sigma$ 1.5	$\sigma$ 8.1	$\sigma$ 20



**Figure 6.10:** Bivariate plots of LA-ICP-MS spot analyses. Grey box indicates variable detection limit. Blue circle is average concentration for pyrite, green triangle for chalcopyrite (ppm).

### 6.3.5 Sulfur isotope analysis

Laser ablation sulfur isotope ( $\delta^{34}\text{S}$ ) analysis (see Chapter 4) of 19 pyrite and 11 chalcopyrite grains from the South Apliki Breccia Zone were analysed to assess the source of S in the South Apliki Breccia Zone. Analyses of pyrite range from -0.8 to +7.1‰ and for chalcopyrite from +2.4 to +5.2‰ (Figure 6.11). The average for all pyrite is +4.2‰ and +3.6‰ for chalcopyrite respectively.

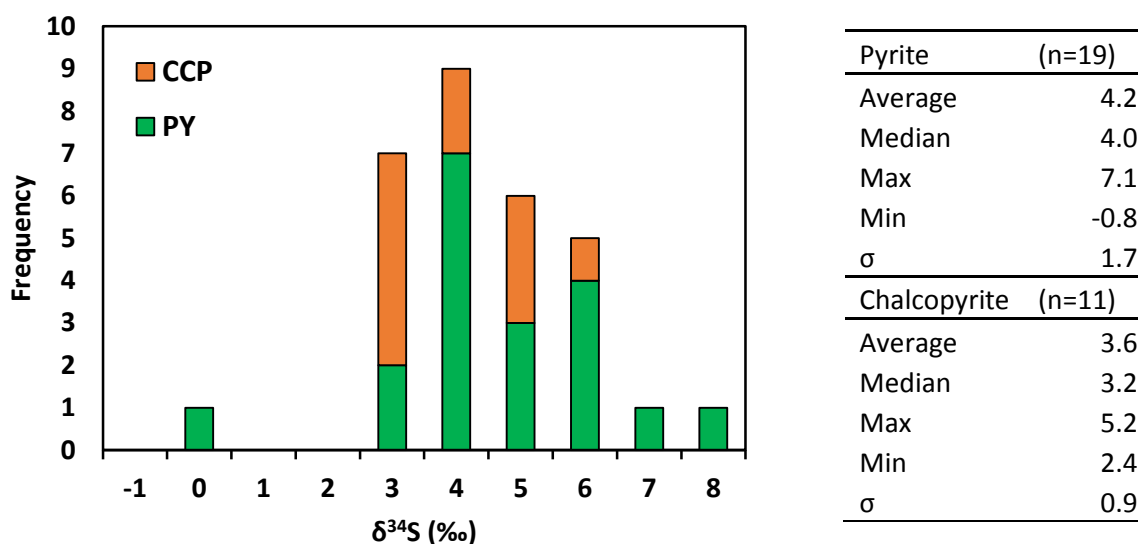


**Figure 6.11:** Sulfur isotope ( $\delta^{34}\text{S}$ ) analysis for pyrite (PY) and chalcopyrite (CCP) from the South Apliki Breccia Zone (cf. Chapter 8).

**Table 6.4:** Summary of sulfur isotope data from South Apliki Breccia Zone sulfides. For full data see appendix 8.1.

### 6.3.6 Time Resolved Analysis (TRA)

This study uses time resolved analysis (TRA) LA-ICP-MS profiles to assess the distribution and mineral scale variation of Se and Te in chalcopyrite, covellite and pyrite from the South Apliki Breccia Zone (Figure 6.12 (overleaf) and Chapter 5). The mineral scale zonation of Te and Se has been assessed by analysing transects across individual sulfide grains i.e. rim-core-rim (Figure 6.12). The zonation of Te and Se is variable dependant on the sulfide grain analysed; for example Figure 6.12 B where Se varies from 1433 around the rim to 4517 ppm in the chalcopyrite core. Tellurium is generally less variable exhibiting variation of only a few ppm between core and rim (Figure 6.12). Time resolved analysis across different mineral phases identified covellite as a significant host for Se (Figure 6.12). Hematite is not capable of incorporating Te or Se with counts at or below detectable limit (Figure 6.12).

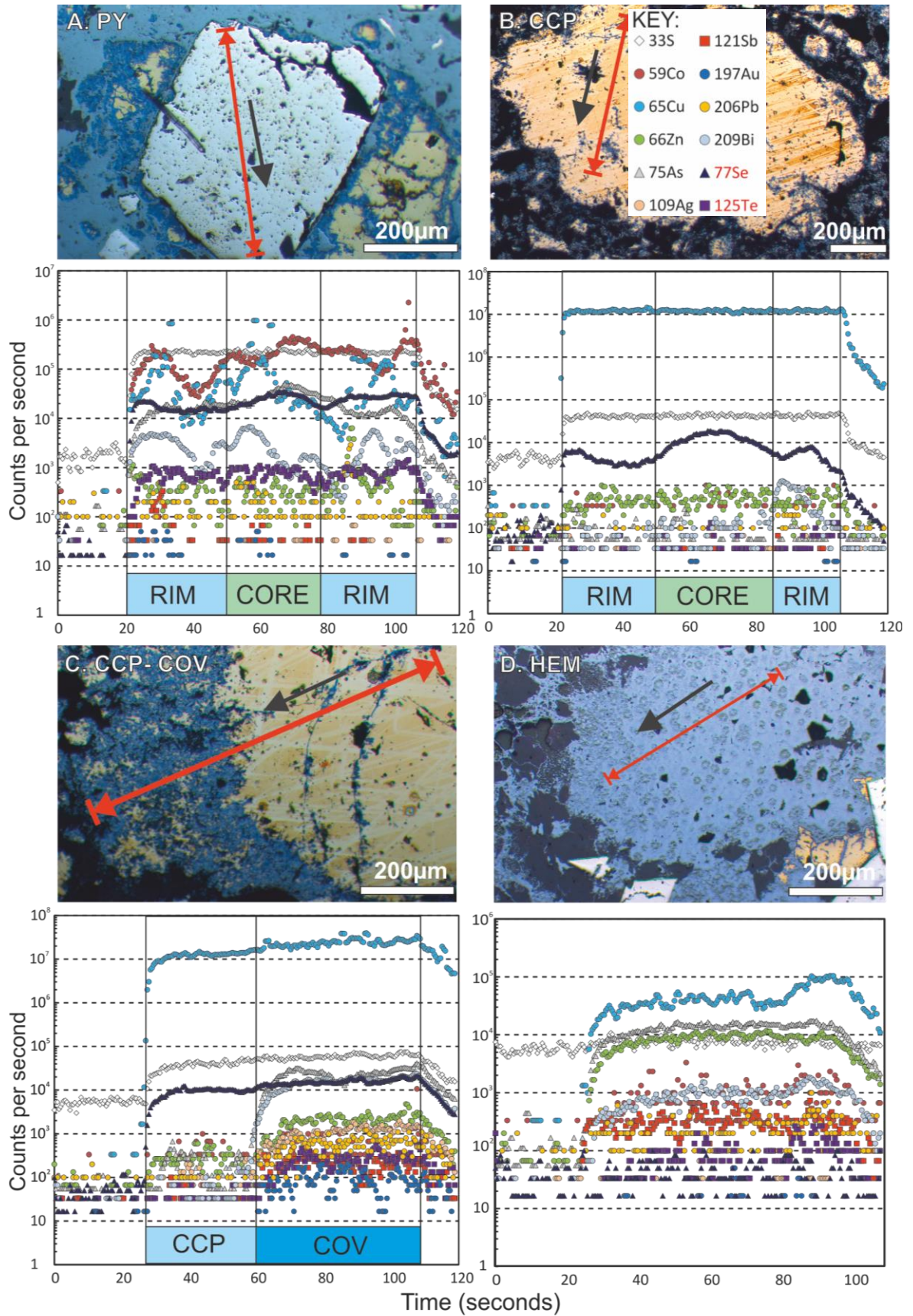


**Figure 6.12:** Time resolved LA-ICP-MS analysis profiles for A) Pyrite, B) Chalcopyrite, C) Chalcopyrite → covellite and D) Hematite. Note variable counts per second (cps) between core and rim for Se in A and B. Selenium cps shows a minor increase between chalcopyrite and covellite. Hematite (D) exhibits low Te and Se signifying below detection limit concentrations.

## 6.4. Discussion

### 6.4.1 Se concentrations in VMS

The South Apliki Breccia Zone appears unique within Troodos in both its mineralogy and unusual enrichment in Se. Very little trace element data (particularly Te and Se) exists for Cyprus-type VMS in general and specifically for Troodos. One study by Keith *et al.* (2016a) on Skouriotissa VMS suggested that Se concentration apparently exhibit systematic variation with depth in the ore body; deeper levels being more enriched (Keith *et al.*, 2016a). Maximum Se and Te values in pyrite from Skouriotissa analysed via LA-ICP-MS are 1886 and 53 ppm respectively (Keith *et al.*, 2016a). The average Se content from euhedral pyrite in Skouriotissa's most enriched deep-stockwork zone is 948 ppm suggesting Se is enriched in deep regions of the VMS mound (Keith *et al.*, 2016a). Tellurium in South Apliki Breccia Zone samples is comparable to concentrations measured in Skouriotissa ranging from 0.7-12 ppm compared to 4-16 ppm with a maximum of 70 ppm at Apliki. By comparison Se exhibits a much greater enrichment in the South Apliki Breccia Zone averaging 182 (n=22) and 1862 (n=23) ppm in stage I and III pyrite respectively. Maximum values for Se are significantly higher at Apliki reaching 4953 ppm in pyrite. Other Cyprus-type deposits exhibit a wide variation in Se content from 20 ppm in the Mathiatis North VMS of eastern Troodos (Economou-Eliopoulos *et al.*, 2008) to 177 and 1 ppm Se in the chalcopyrite and sphalerite-rich zones of the TAG deposit (Mid Atlantic Ridge); a suggested analogue for Troodos VMS deposits (Hannington *et al.*, 1998).

Greater volumes of data exist for VMS deposits formed in bi-modal environments. Three notable Canadian examples which exhibit unusual enrichment in Se are outlined; the Finlayson Lake District (Layton-Matthews *et al.*, 2013), Bracemac-McLeod (Genna and Gaboury, 2015) and Kidd Creek (Hannington *et al.*, 1999).

Selenium from the Bracemac-McLeod deposit occurs in type IV late recrystallized pyrite with a maximum Se content of 1059 ppm. The maximum Se concentration of 4900 ppm in chalcopyrite is comparable to the 3955 ppm recorded at Apliki (Genna and Gaboury, 2015). Layton-Matthews *et al.* (2013) note Se enrichment in 'type-1' pyrite samples from the chalcopyrite-rich zone at Finlayson Lake (Wolverine deposit) with values of up to 3400 ppm. Average Se values for the Wolverine deposit are 1100 ppm. Selenium is also reported to be enriched in the bornite zone of the Kidd Creek deposit (Hannington *et al.*, 1999). Selenium whole rock concentrations from the 'Se-rich halo' average 500 ppm whilst the bornite zone exhibits average concentrations of 2200 ppm. Hannington *et al.* (1999) also report Se enrichment up to 0.8 wt.% in pyrite. However, higher average whole rock Se on a deposit scale, especially within Pb-rich bi-modal VMS is attributed to the presence of galena-clausthalite (Pb-S-Se) that is known to readily incorporate

Se (e.g. Maslennikov *et al.*, 2009). This does not explain high bulk rock Se (1071 ppm) or the higher *in situ* Se content of pyrite at the Apliki VMS.

As Se concentrations at Apliki are more comparable to those recorded in some bi-modal VMS than for other Cyprus-type deposits; a mechanism of Se enrichment is needed to explain such enrichment compared with other Cyprus-type deposits. Bulk ore Se contents in bi-modal VMS deposits is preferentially enriched as a consequence of felsic source rock Se content, an additional magmatic volatile component or high galena-clausthalite contents.

The South Apliki Breccia Zone is significantly enriched in Se with maximum values of 3956 ppm Se in chalcopyrite and 4953 ppm Se in pyrite. These values are substantially higher than any other values reported for Cyprus-type VMS. Concentrations are an order of magnitude higher than those reported for chalcopyrite in the TAG mound (177 ppm; Hannington *et al.*, 1998) and four times higher than maximum values reported by Keith *et al.* (2016a) for the Skouriotissa ore body.

#### 6.4.2 The source of Se in VMS deposits

A magmatic influx into the VMS hydrothermal system via vapour or aqueous phase transfer of volatiles has long been hypothesised to explain enrichment in certain magmatophile elements e.g. Se, Te, Cu, Bi etc. (Chen *et al.*, 2015; Melekestseva *et al.*, 2017; Sillitoe *et al.*, 1996). The  $\delta^{34}\text{S}$  values for most Mid Ocean Ridge and back-arc VMS sulfides fall within a narrow range of generally 0 to 5 ‰  $\delta^{34}\text{S}$  (cf. Chapter 8). The narrow range reflects the mixing of magmatic sourced sulfur (0-1 ‰ for Troodos; Alt, 1994) and sulfur derived from thermochemical/biogenic seawater sulfate reduction (+20.7 ‰, Herzig *et al.*, 1998a; Alt, 1994). Increased magmatic influx leads to a decrease in  $\delta^{34}\text{S}$  values toward 0‰. A modern analogue of an 'end member' magmatic VMS may be found in the Lau Basin, Tonga-Kermadec Arc at the Hine Hina vent site (Herzig *et al.*, 1998a). Sulfides from Hine Hina exhibit the lowest  $\delta^{34}\text{S}$  of any modern hydrothermal field at -5.3 ‰ (Herzig *et al.*, 1998a: Chapter 8 and 9). The variable  $\delta^{34}\text{S}$  of modern seafloor sulfide deposits demonstrates that the source of metals in VMS systems is varied, and when considering elements of magmatic affinity (Se, Te, Cu, Bi) volatile transfer from the magmatic to hydrothermal system may be important in their enrichment (see Chapter 8 and 9).

Limited  $\delta^{34}\text{S}$  data exists for the Skouriotissa VMS and suggests a variable magmatic influx in the Solea graben (Keith *et al.*, 2016a). Deep stockwork ore exhibits a light  $\delta^{34}\text{S}$  signature of -1.4 ‰, a figure unobtainable through the mixing of Cretaceous seawater (+18-19 ‰) and primary magmatic derived S (0 to -1 ‰) (Keith *et al.*, 2016a). The shallow stockwork at Skouriotissa exhibits a positive  $\delta^{34}\text{S}$  signature of +6.1 ‰ suggesting an increased seawater source of S in the

upper VMS stratigraphy (Keith *et al.*, 2016a). The negative  $\delta^{34}\text{S}$  value in deep stockwork may represent a dominant magmatic volatile input (see section 6.4.7).

Sulfur/selenium ratios are used as a proxy for the source of sulfide mineralisation in a range of environments (e.g Graham *et al.* 2017; Layton-Matthews *et al.* 2013; Holwell *et al.*, 2015). More commonly when considering VMS systems Se/S ratios are used (expressed as  $\text{Se/S} \times 10^6$ ) (Layton-Matthews *et al.*, 2008). Chemical similarities between S and Se and the contrasting ratio of Se:S in seawater, mantle sulfides and sediments are used to infer the source of Se in ore deposits (Huston *et al.*, 1995; Layton-Matthews *et al.*, 2008, Hannington *et al.*, 1999). Sulfides with high Se/S (>500) ratios are inferred to have a predominantly magmatic source (primitive mantle  $\sim 300$ ), whereas low Se/S (<500) ratios indicate a predominantly sedimentary or seawater origin (Huston and Large, 1989; Layton-Matthews *et al.*, 2008; Hannington *et al.*, 1999). Selenium/sulfur ratios of pyrite from the South Apliki Breccia Zone are summarised in Figure 6.13.

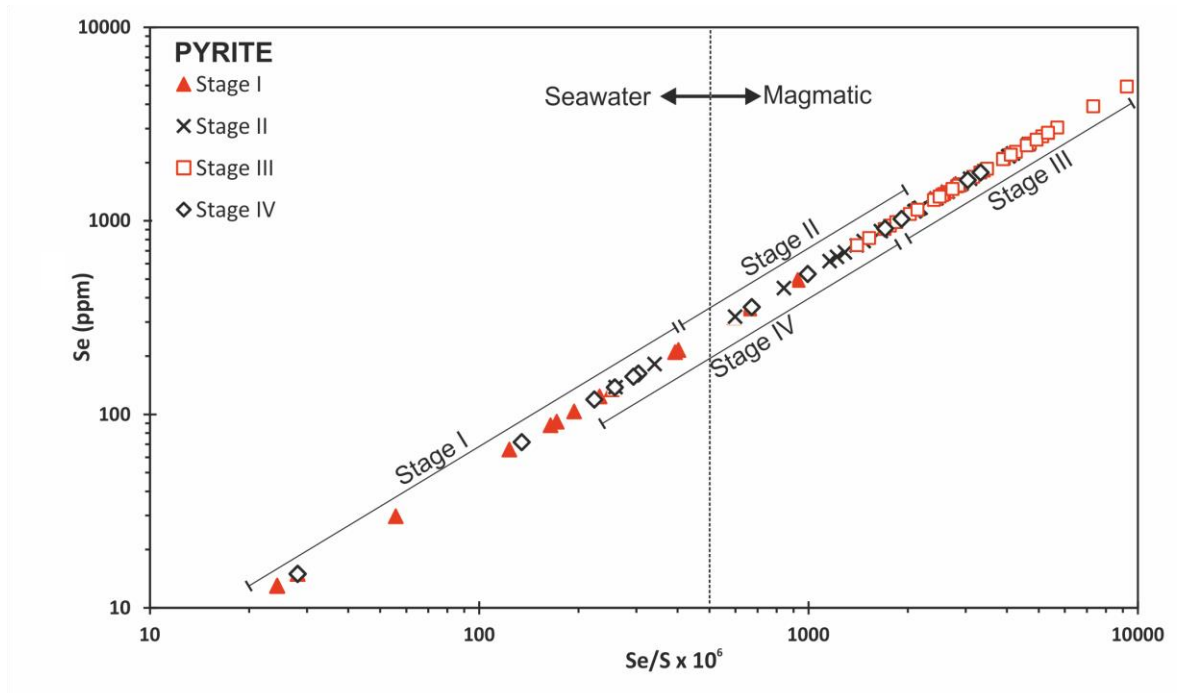


**Figure 6.13:** Selenium/sulfur ratios in pyrite vs. Se (ppm) for the South Apliki Breccia Zone. Selenium/Sulfur ratios in pyrite increase from alteration stages I-III. Stage IV (supergene) is highly variable. Sulfur is estimated at a stoichiometric value of 53.5 % for pyrite.

Selenium/sulfur ratios from the South Apliki Breccia Zone exhibit systematic variation with alteration stage. All stage I samples fall below the proposed seawater-magmatic discrimination line (500 Layton-Matthews *et al.*, 2008) whilst stage II are highly variable and stage III samples plot in the magmatic region ( $\gg 500$ ). Stage IV samples exhibit significant scatter plotting in both the seawater and magmatic domains; this may be a function of supergene processes which leads to the mobilisation of S during oxidisation relative to Se or vice versa. For example Bullock *et al.*

(2018) note the enrichment of Se in secondary weathering products demonstrating Se/S ratios may be biased through supergene, subaerial related processes. The data suggests a change in source from seawater to magmatic with alteration intensity. However, sulfur isotope analysis are presented in section 6.4.7 to validate the increased magmatic influx in stage III pyrite as indicated by the elevated Se/S >500.

Selenium/sulfur ratios vary significantly with alteration stage in the South Apliki Breccia Zone (Figure 6.13). Layton-Matthews *et al.* (2008) state that Se/S ratios for sediment starved ridges such as Troodos are <1500. Forty four of 96 analyses are above the 1500 threshold suggested by Layton-Matthews *et al.* (2008). Three different mechanisms have been proposed to explain elevated Se/S ratios; a sediment source similar to the Wolverine deposit e.g. sulfide-rich shales (Se/S: 38700 Layton-Matthews *et al.*, 2008) or a magmatic volatile input (e.g. Kidd Creek, Hannington *et al.*, 1999) or the seafloor remobilisation and concentration of Se (this study).

No sediment relating to ophiolite formation has been documented in the Troodos stratigraphy (e.g. Robinson and Malpas, 1987), therefore it is unreasonable to assume that Se/S ratios have been significantly modified by sediment-hydrothermal fluid interaction. One plausible explanation that explains the transition in Se/S ratios between stage I and III pyrite is a late magmatic influx into the hydrothermal system at Apliki. In this scenario a late Se-rich magmatic fluid pulse precipitated stage III pyrite (see section 6.4.7). This could effectively explain the elevated Se content and magmatic Se/S ratios of Stage III pyrite. Hannington *et al.* (1999) report high Se/S values (20,000-50,000) for the bornite-rich zone at Kidd Creek that they attributed to a magmatic influx of H<sub>2</sub>Se leading to significantly higher Se/S ratios.

It should be noted that as with previous studies (e.g. Graham *et al.*, 2017) a stoichiometric value for S within pyrite of 53.5 wt.% has been used to calculate Se/S ratios. Actual S concentrations will vary by a few % around this value however the observed trends are expected to prevail (cf. Chapter 5).

In addition to a probable magmatic source of metals in the VMS hydrothermal system, base and trace metals are mobilised from epidosite zones (Jowitt *et al.*, 2012; Patten *et al.*, 2017; Schiffman *et al.*, 1990). Mass balance calculations suggest epidosite zones of the Solea graben are capable of mobilising enough metal to form a medium sized VMS deposit (Jowitt *et al.*, 2012; Patten *et al.*, 2017).

Studies by Jowitt *et al.* (2012) demonstrate the significance of epidosite zone formation in fulfilling metal budgets for VMS in a supra-subduction setting. Similarly, the findings of Patten *et al.* (2017) demonstrate the importance of epidosite zones in Se budget with a 90% depletion

in Se when compared to cogenetic volcanic glass (Patten *et al.*, 2017). Using an average Se concentration of 41 ppm for Cyprus-type VMS and a theoretical hydrothermal reaction zone of 10.9 km<sup>2</sup> (5 km<sup>2</sup> epidosite and 5.9 km<sup>2</sup> diabase), an estimated 3100 ± 700 t Se was mobilised in the Solea graben (Patten *et al.*, 2017). If this was the case higher average Se would be expected in VMS of Troodos. Trapping efficiencies are suggested to account for the low Se content of Cyprus-type VMS with only 27% of all mobilised Se being trapped in VMS (Patten *et al.*, 2017).

The bulk Se content of VMS in Troodos is poorly constrained with Patten *et al.* (2017) reporting average compiled data values of 41 ppm (bulk ore), whilst in this study we find an average of 55 ppm in pyrite (n=345) and 77 ppm (n=20) in chalcopyrite excluding the extreme values recorded at Apliki. It is unclear from Patten *et al.*'s (2017) study if the mineral scale distribution of Se is considered in mass balance calculations (see Chapter 5 and 8). As demonstrated in this study (Chapter 5; Martin *et al.*, 2019) the mineral scale distribution of Se favours chalcopyrite with average Se contents of 77 and 315 ppm for all Troodos deposits and Skouriotissa respectively. Taking the mineral scale distribution of Se into account, the trapping efficiency of Se is likely to be higher than the 27% reported by Patten *et al.* (2017). While it is likely that Se is mobilised largely from epidosite zones as suggested by Patten *et al.* (2017), VMS which are unusually rich in Se may have an additional source of enrichment.

#### 6.4.3 Mineral scale distribution of Te and Se in the South Apliki Breccia Zone

The mineral scale distribution of Te and Se in South Apliki Breccia Zone sulfides is complex (Figure 6.14). To assess mineral scale variation in trace element concentrations lines across sulfide grains have been analysed (Figure 6.14). Data from this study highlights the variable concentrations of Te and Se across individual sulfide grains; there is no unified sense of enrichment explaining the distribution and concentration of Te and Se. The variation in Te-Se concentration across an individual sulfide grain shows no systematic relationship with grain margins (Figure 6.14); Te and Se are elevated in both the core and rim of the grain dependant on the individual sulfide grain analysed (Figure 6.14). The concentration of Se is elevated in chalcopyrite relative to pyrite in agreement with thermodynamic data that indicate increasing affinity for Se decreasing in concentration from galena-clausthalite >> chalcopyrite (covellite) > sphalerite > pyrite > pyrrhotite (Layton-Matthews *et al.*, 2008). Despite high Se concentrations within sulfides at Apliki no selenide phases have been identified suggesting Se is incorporated solely in sulfide minerals.

In agreement with previous studies, Se exhibits a smooth ablation profile in both pyrite and chalcopyrite at Apliki. Incorporation of Se is likely accomplished through stoichiometric substitution of Se for S (Maslennikov *et al.*, 2009: Chapter 5). When analysing across a single

sulfide grain no systematic variation in Se and Te concentration was observed (Figure 6.14). This is best illustrated by comparing Figure 6.14 C and D. Chalcopyrite C exhibits minimal variation in Se concentration between core and rim averaging 1634 and 2009 ppm. In contrast chalcopyrite D has a Se depleted rim (1598 ppm) but enriched core at 4517 ppm. Data suggests that in chalcopyrite D Se may have been preferentially mobilised from the chalcopyrite rim during seafloor oxidisation, however this relationship is not consistent across all grains suggesting it was a localised process (see Section 6.4.5).

Analysis of covellite and chalcopyrite demonstrate the potential for copper secondaries to act as a sink for substantial concentrations of trace elements. Profile E (Figure 6.14) intersects both chalcopyrite and covellite; Se concentration is uniform between the two phases at 2436 and 2197 ppm Se respectively. Additionally, TRA profiles suggest that covellite can incorporate higher concentrations of other trace elements relative to chalcopyrite (e.g. Bi and Te: Chapter 5). The inverse is true for hematite that contains semi-quantitatively less Te and Se than pyrite and chalcopyrite (Figure 6.14 F).

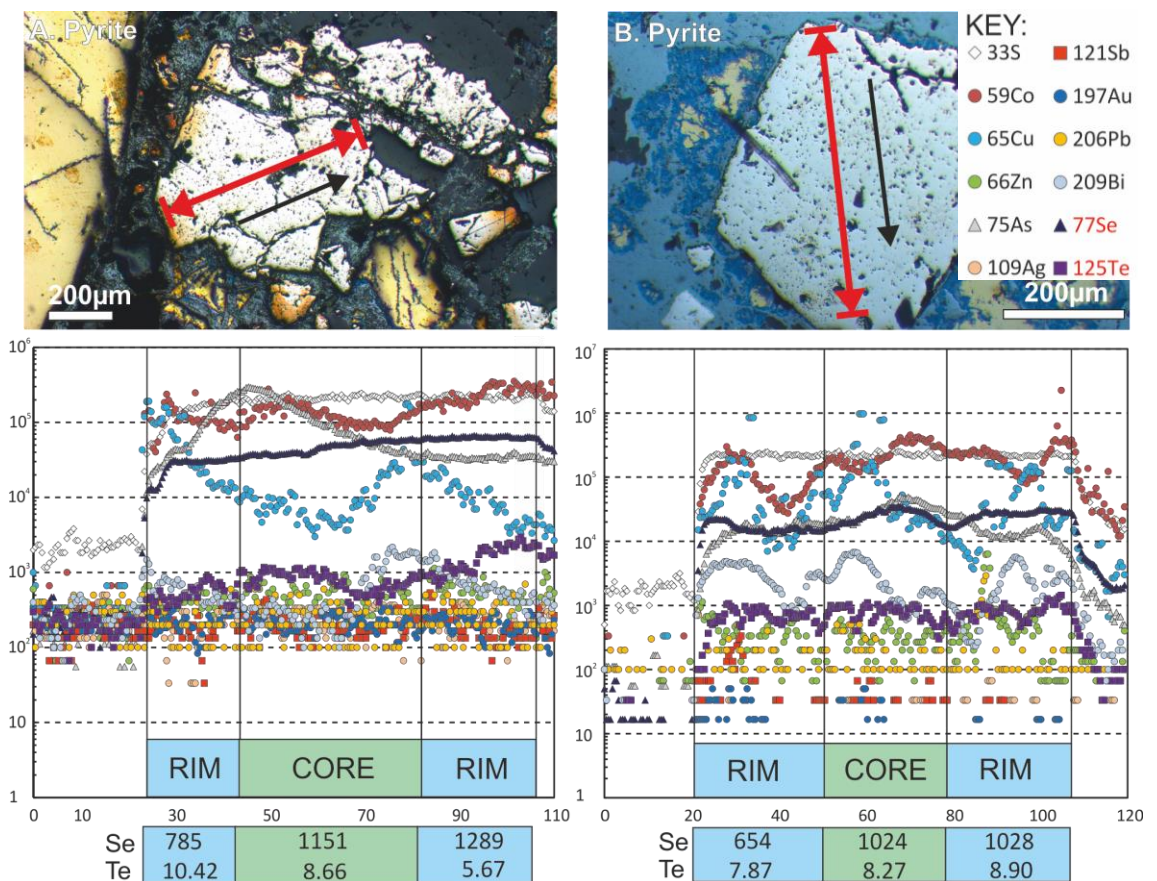
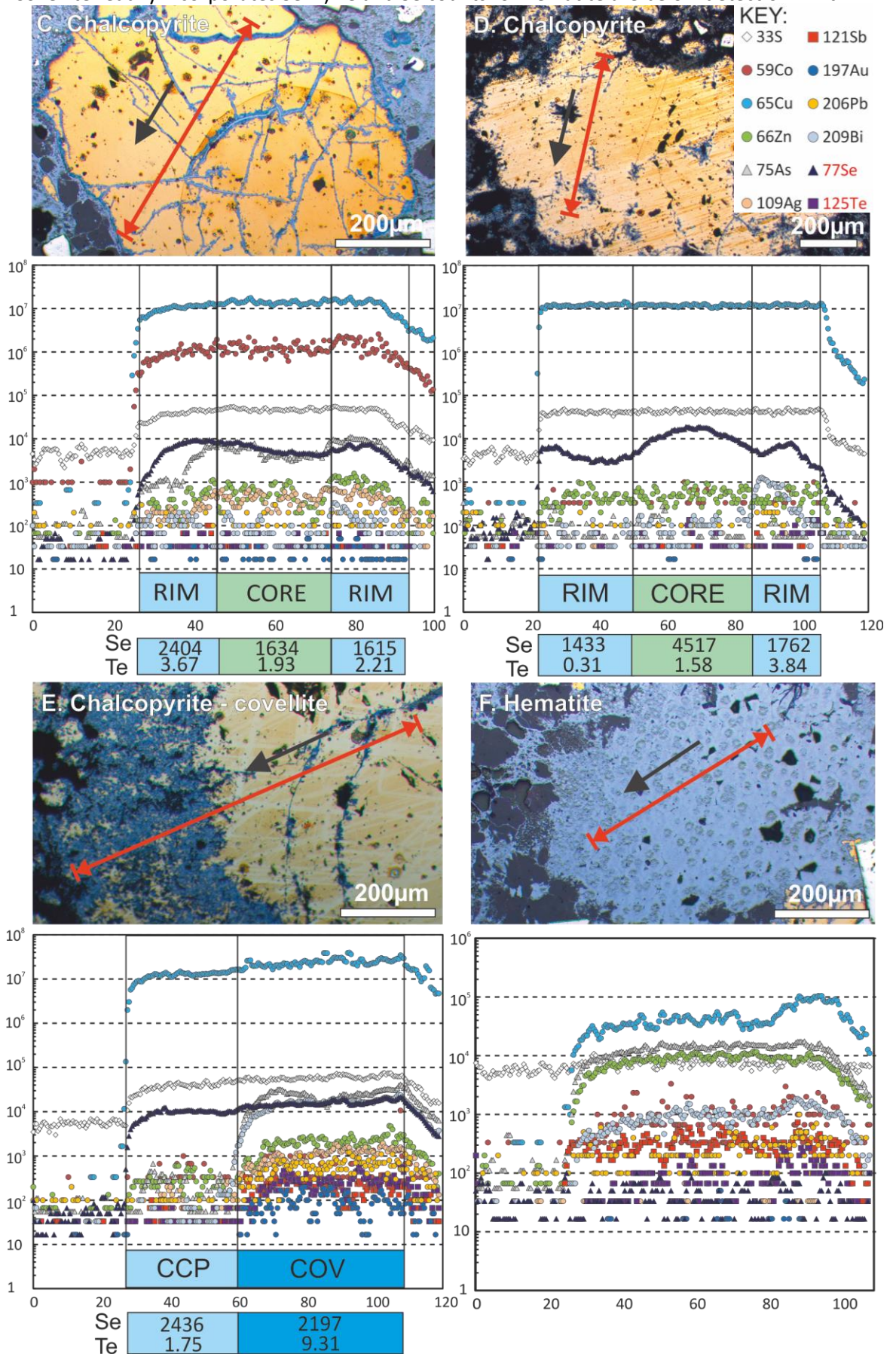


**Figure 6.14 (continued overleaf):** Laser ablation ICP-MS TRA of pyrite (A and B), chalcopyrite (C and D), chalcopyrite - covellite (E) and hematite (D) from the South Apliki Breccia Zone. Concentrations for Te and Se are summarised below each figure. A and B) TRA profiles for Py exhibit no systematic variation in Te and Se concentrations between core and rim. C and D) Chalcopyrite grains exhibit the opposite relationship; grain D is depleted in Se in its core whilst

D is enriched (Full element concentrations and further TRA are available in Appendix 6.5). E) Covellite readily incorporates Se. F) Te and Se counts for hematite are below detection limit.



#### 6.4.4 Physicochemical factors effecting the incorporation of Te and Se

The Apliki mineralogy (Stage I-III) is dominated by chalcopyrite indicating mineralisation temperatures of 280-350°C (Gill *et al.*, 2016; Safina *et al.*, 2016) (Figure 6.15, stage I). The increased incorporation potential of Se at high temperatures is not supported by low average Se in chalcopyrite (601 ppm, n=12) and pyrite (182 ppm, n=22) from early stage I sulfides at the South Apliki Breccia Zone. In contrast, stage III pyrite contain an average of 1862 ppm (n=23) Se and formed at lower temperatures (<280°C). Temperature alone does not explain the significant enrichment of Se in stage III sulfides over stage I sulfides at Apliki. Samples analysed from the South Apliki Breccia Zone represent the highest Se values not only at Apliki, but the whole of Troodos (excluding Mala; Chapter 9) and to the authors knowledge Cyprus-type VMS in general. They occur in a distinct zone not recorded in any other Cyprus-type VMS system on Troodos. The zone exhibits textural and mineralogical similarities to the Alestos deposit of north-central Troodos; a deposit thought to have formed from late, low temperature oxidised fluids (Eddy *et al.*, 1998; Jowitt *et al.*, 2005). Brecciation, silicification and chloritisation with abundant hematite are common features between the two deposits however Se analyses from Alestos were below detection limit (LA-ICP-MS pyrite, n=5; Chapter 7). The similarity in mineralogy suggests late, low temperature, oxidising fluid may be responsible for hematite formation in the South Apliki Breccia Zone however a more complex paragenesis is needed to explain the enrichment in Se.

The Ortaklar VMS Turkey is a more comparable analogue to the South Apliki Breccia Zone as it has a late oxidised overprint (Yildirim *et al.*, 2016). No Te or Se data were presented in the latter study however similarities in ore texture and mineralogy suggest the two deposits share a similar paragenesis. At Ortaklar magnetite cross-cuts high temperature hypogene chalcopyrite ore. Yildirim *et al.* (2016) envisage two stages of ore formation; an early high temperature pyrite and chalcopyrite dominated phase involving, reduced, hot, low pH fluids (e.g. Tornos, 2006) and a second stage of magnetite formation. Increasing  $fO_2$  promoted the dissolution and replacement of sulfides with magnetite, hematite and specularite and the oxidisation of chalcopyrite (Yildirim *et al.*, 2016).

The South Apliki Breccia Zone and Ortaklar exhibit paragenetic sequences indicative of multiple mineralising phases under varied but different redox conditions (Figure 6.15). At Ortaklar magnetite is the main secondary mineral whereas at Apliki hematite is dominant. Fluids at Apliki are inferred to be of lower pH with a log  $fO_2$  less than -30 to -40 at >300 °C promoting the precipitation of hematite over magnetite (Figure 6.15: stage II/III) (Galley *et al.*, 2007). Hematite could also have formed during supergene oxidation of magnetite ( $4 Fe_3O_4 + O_2 = 6 Fe_2O_3$ )

however a purely supergene origin for hematite is not likely as fresh euhedral pyrite is also preserved in an entirely hematized matrix. This suggests ore formation remained active after the formation of hematite. If hematite were solely a supergene phase, pyrite and chalcopyrite would be extensively oxidised, dissolved or completely absent, and this is not observed.

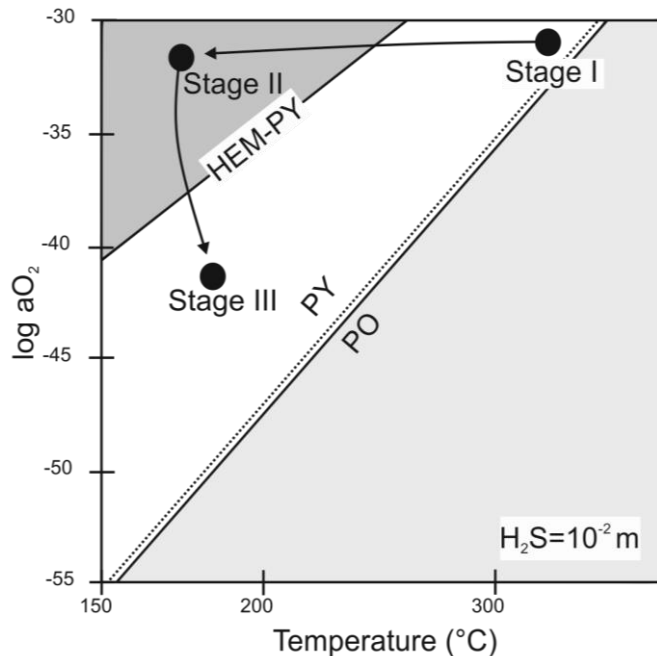


**Figure 6.15:** Stability field for pyrrhotite (PO), pyrite (PY) and hematite (HEM) in  $\log a_{O_2}$  and temperature space. Stage I, II and III refer to sample paragenesis from reducing to oxidising and then returning to reducing, low temperature conditions at the South Apliki Breccia Zone (adapted from Layton-Matthews *et al.*, 2008)

A similar paragenesis of replacement over precipitation of new mineral phases is proposed for the Ortaklar VMS (Yildirim *et al.*, 2016). Exsolution and zoned textures are common at Ortaklar indicating replacement of early stage mineralisation under varied temperature and redox conditions (Yildirim *et al.*, 2016). At Ortaklar magnetite represents the last stage in VMS mineralisation (Yildirim *et al.*, 2016) whilst at Apliki both hematite and chalcopyrite are overprinted by euhedral pyrite. The formation of stage III pyrite suggests a temporary influx of oxidised fluids that reverted back toward more reducing conditions and sulfide precipitation (Figure 6.15: stage III). The final stage of sulfide precipitation is inferred to be cooler than initial stage I mineralisation ( $<280^{\circ}\text{C}$ ) as chalcopyrite overgrowths are absent (Gill *et al.*, 2016; Safina *et al.*, 2016).

#### 6.4.5 Paragenesis and mechanisms of Se enrichment

A mechanism for such a pronounced and temporary shift in hydrothermal fluid conditions needs to explain the observed paragenesis. Magmatism is considered to be the ultimate driving force in VMS hydrothermal circulation (Choi and Lowell, 2015; Patten *et al.*, 2016). But the magmatic heat input into the hydrothermal system varies temporally as a function of magmatic flux. This was especially true in Troodos where spreading is considered to have been accomplished by graben development and crustal thinning during periods of low magmatism (Varga and Moores,

1990). During periods of magmatic quiescence increased fault movement along graben bounding faults is predicted. Near surface fault movement could potentially increase permeability leading to seawater ingress into the upper VMS stratigraphy promoting a locally oxidising environment at Apliki. The South Apliki Breccia Zone is located between two faults with extensive rotation evident in both foot wall and hanging wall lithologies, thus frequent fault movement seems likely. The mineralised contact is sharp with no clear indication of mineralisation outside the fault bounded block. This study infers that late slip on these bounding faults during the waning stages of VMS formation coupled with a reduced hydrothermal influx led to increased seawater ingress into the shallow hydrothermal system and locally oxidising neutral pH fluids temporarily promoted sulfide dissolution. The brecciated morphology of the South Apliki Breccia Zone supports this observation. Renewed magmatism and the sealing of permeability pathways due to mineral precipitation, renewed hydrothermal influx and re-established reducing conditions that led to the formation of late stage III pyrite; a similar model is hypothesised for Ortaklar (see Yildirim *et al.*, 2016).

From textural analyses three stages of hypogene overprinting have been identified followed by a fourth stage of supergene alteration. Alteration stages based on geochemistry and mineralogy may be summarised as follows (see Figures 6.16 and 6.17- overleaf)

Stage I: Chalcopyrite-pyrite mineralisation under reducing low pH <4, hypogene (>350°C) fluids and the development of main stage VMS mineralisation under a steady state magmatic-hydrothermal flux (Figure 6.8). Seawater dominated Se/S ratios (averaging 330; n=22) prevail in pyrite; Se is sourced from epidosite zones +/- a minor magmatic component (Figure 6.13).

Stage II: Hematite mineralisation involving restricted hydrothermal input and ingress of seawater into the shallow hydrothermal system. Fluid with near neutral pH and increased  $fO_2$  promotes sulfide dissolution and hematite formation. This phase is relatively short-lived given the modest alteration of chalcopyrite rims (Figure 6.6 and 6.7). Selenium/sulfur values rapidly transition between seawater and magmatic dominant conditions averaging 2158 in pyrite (n=23) (Figure 6.13).

Stage III: Renewed magmatism and decreased fault movement limit further ingress of seawater and reducing conditions are re-established leading to the precipitation of Se-rich euhedral pyrite overgrowths. Late chalcopyrite overgrowths are absent suggesting lower temperatures of formation (<280°C) than stage I mineralisation. Selenium/sulfur ratios within Stage III pyrite is elevated averaging 3480 (n=22) indicating a possible magmatic influx **or** the preferential mobilisation of Se relative to S (Figure 6.13).

Stage IV represents supergene enrichment of chalcopyrite and pyrite. Samples span a wide range of Se/S ratios (28-3200) and contain significant amounts of covellite, chalcocite and digenite. Selenium/sulfur ratios have not been determined for Cu secondaries but are likely to show a large amount of scatter due to the mobilisation of Se in low temperature fluids (Huston *et al.*, 1995).

#### 6.4.6 The Extreme Enrichment of Se at the South Apliki Breccia Zone

This study suggests that during its mature stages VMS mineralisation at the South Apliki Breccia Zone would have formed a high-temperature (>280°C) stockwork overlain by massive sulfide. Stage I pyrite and chalcopyrite were formed under high temperature reduced conditions synonymous with VMS formation. In this period Se fractionated 'normally' and is preferentially enriched in chalcopyrite over pyrite. The transition to oxidising conditions and replacement of pyrite with hematite expelled Se from the dissolving pyrite (Figures 6.16 and 6.17). Laser ablation-ICP-MS studies by Genna and Gaboury (2015) and qualitative TRA from this study (Figure 6.14 F) show that Se cannot be accommodated in the crystal lattice of hematite in any significant concentrations. The dissolution of early stage I pyrite consequently led to an excess of Se in solution. Minor goethite is present in some South Apliki Breccia Zone samples, goethite can adsorb significant concentrations of Se (e.g. Bullock *et al.*, 2018). The formation of goethite as an intermediate phase between pyrite and hematite could have trapped Se which was expelled from the dissolution of stage I pyrite in the South Apliki Breccia Zone. Upon dehydration of goethite to hematite the adsorbed Se was released back into solution and incorporated in later stage III pyrite that precipitated under reducing conditions and due to the elevated concentration of Se in solution readily incorporated elements expelled from the dissolution of stage I pyrite (Figure 6.16). Tellurium concentration remains constant in late pyrite as higher temperatures which favour Te incorporation (>280°C) were absent during stage III mineralisation.

Theoretical data from Huston *et al.* (1995) shows that Se concentrations in pyrite decrease with increasing temperature from 700 ppm to <250 ppm as temperature increases from 150-300°C (Huston *et al.*, 1995). Modelling also demonstrates that Se concentrations in pyrite increase rapidly under oxidising conditions ( $\log(\Sigma\text{SO}_4/\Sigma\text{H}_2\text{S}) > 0$ ) (refer back to Chapter 3). Based on this, stage III pyrite may have precipitated at temperatures as low as 150°C at near neutral pH promoting the incorporation of Se into the crystal lattice. Higher temperatures of >300°C are less favourable for Se incorporation in pyrite with a theoretical maximum of 500 ppm Se; much less than the measured 1862 ppm average (n=23) (Figure 6.16 and 6.17). On this basis pyrite should be distinguishable on Se content which relates to temperature. At Apliki two generations

of pyrite are clearly distinguishable based on Se content; stage I low Se high temperature pyrite (<250 ppm) and stage III pyrite that formed under cool <300°C oxidised conditions containing >>250 ppm Se (Huston *et al.*, 1995) (see Chapter 3, Figure 3.14).

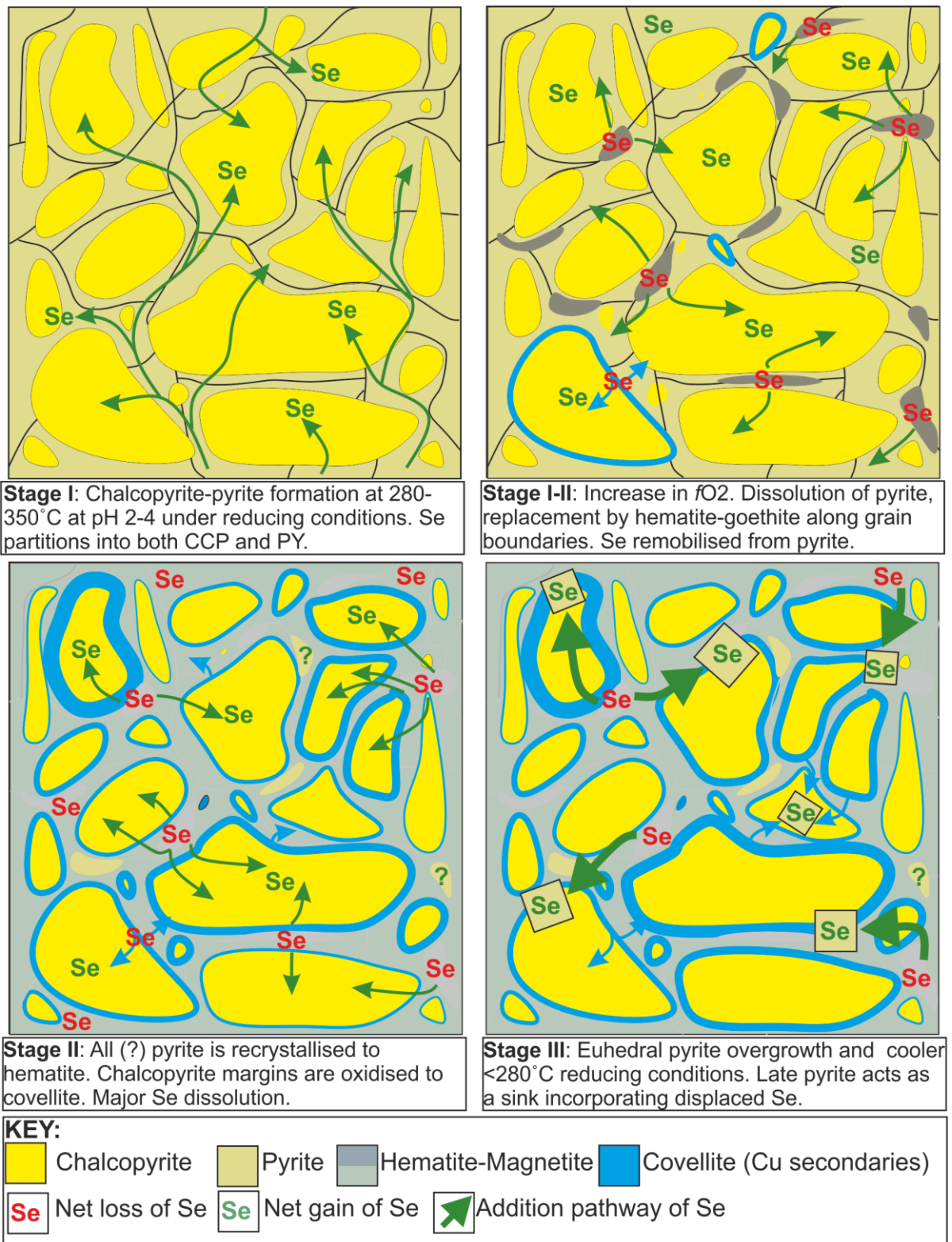


**Figure 6.16:** Summary for the extreme enrichment of Se at the South Apliki Breccia Zone.

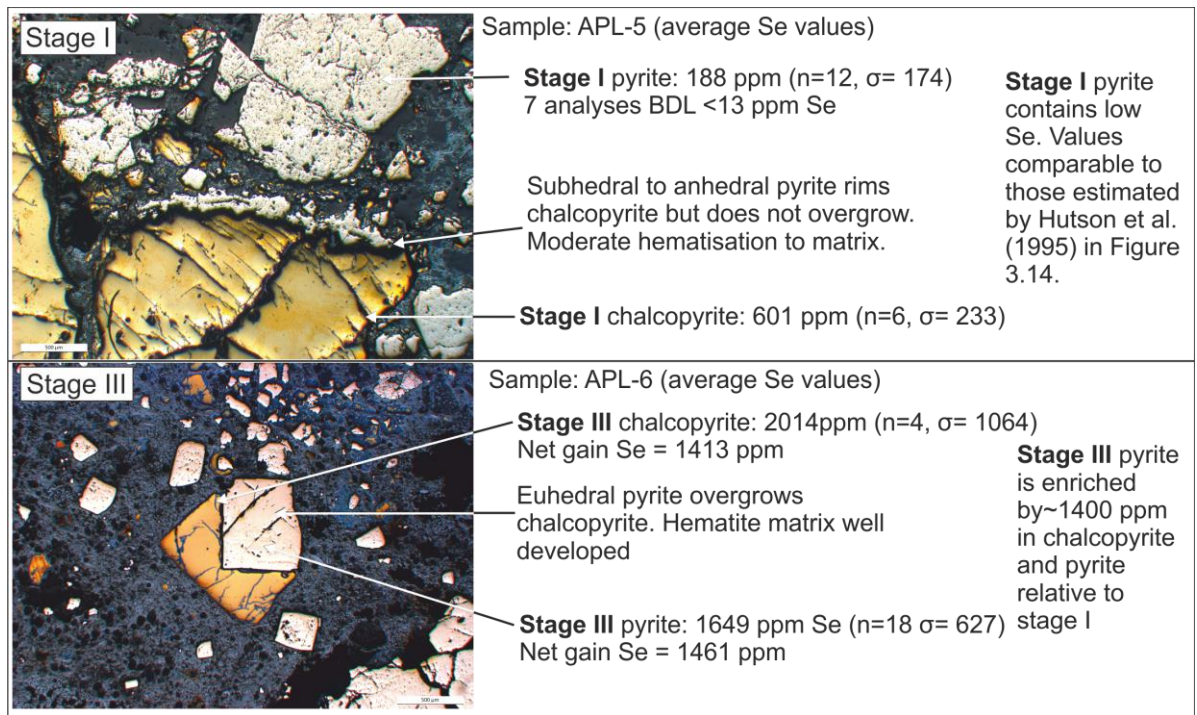


**Figure 6.17:** Geochemical comparison of stage I and III pyrite and chalcopyrite. Data is highly variable but demonstrates a net gain in Se of ~1400 ppm between stage I and III pyrite.

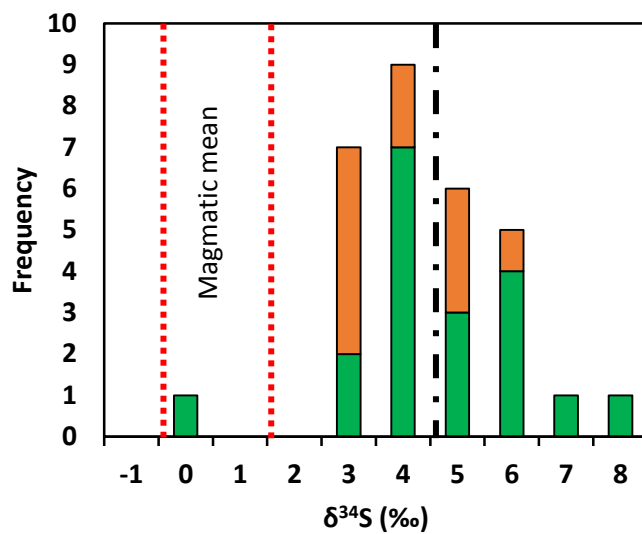
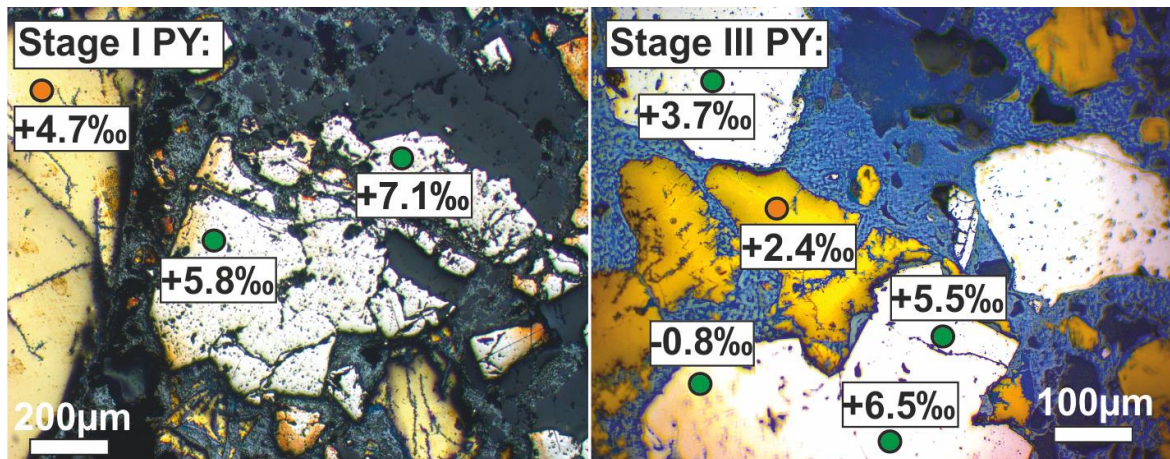
The ability of Cu secondary minerals such as covellite to incorporate Se is poorly characterised (cf. Chapter 8). Auclair *et al.* (1987) show that the Se content in chalcopyrite remains homogenous with increasing proportions of covellite and digenite. High concentrations of Se for digenite average 0.44 wt.% with a maximum of 2.13 wt.% (Hannington *et al.*, 1999). In agreement with previous studies we find that covellite can incorporate significant concentrations of Se (Section cf. 6.4.3 and Chapter 5) with values up to 4310 ppm (average=2436, n=5).

The clear distinction in geochemistry between stage I and III pyrite suggests the timing of mineralisation is important in controlling localised Se enrichment in the South Apliki Breccia Zone. Selenium incorporation was not simply a function of fluctuating redox; in deposits such as Alestos (Troodos; Chapter 7, Appendix 3.1) a late pyrite overprint is absent and no enrichment in Se is recorded, however hematite is present, which indicates oxidised conditions. Oxidising conditions present during the waning stage of VMS formation would have been short-lived and alone do not account for the observed enrichment in Se. Instead the author favours the mobilisation of Se from early stage I sulfides during the precipitation of hematite (Figure 6.16). The dissolution of Se from pyrite during hematite formation provides a mechanism explaining a) the distribution of Se and b) the extreme enrichment in late stage III pyrite.

### 6.4.7 An additional magmatic volatile source of Se in the Apliki VMS?

To confirm an oxidation a remobilisation related paragenesis for the enrichment of Se in the South Apliki Breccia Zone detailed  $\delta^{34}\text{S}$  analysis were undertaken. Analysis of 30 hydrothermal sulfides suggests a paragenesis of oxidation and seafloor secondary enrichment of Se and not an additional Se enriched source of increased magmatic volatile affinity as suggested by elevated Se/S ratios in stage III pyrite (Figure 6.13 and 6.18). With the exception of one value measured at the South Apliki Breccia zone all  $\delta^{34}\text{S}$  measurements are above the Troodos magmatic mean (0-1‰- Alt, 1994). This suggest the fluid responsible for the formation of the South Apliki Breccia Zone were sourced from the thermochemical reduction of seawater sulfate and the leaching of primary magmatic sulfur from igneous rocks (i.e. epidiosites/sheeted dykes- cf. Chapter 8). If the South Apliki Breccia Zone, specifically stage III pyrite, had formed from a magmatic volatile (Se) rich fluid then hydrothermal sulfides would be skewed towards light  $\delta^{34}\text{S}$  values of <0-1‰ (Figure 6.18, overleaf; Herzig *et al.*, 1998a; McDermott *et al.*, 2015). Instead, at Apliki both pyrite (n=19) and chalcopyrite (n=11) exhibit average  $\delta^{34}\text{S}$  values well above the Troodos magmatic mean at +4.2 and +3.6‰ respectively (Figure 6.18). This is comparable to analyses presented for other Troodos VMS that average +4.7‰ (Martin *et al.*, 2019; Chapter 8). Additionally, there is no systematic variation between  $\delta^{34}\text{S}$  values in stage I and III pyrite suggesting they formed from a fluid with a similar isotopic composition, source and crucially Se content (Figure 6.18).

Selenium/sulfur ratios from different stage pyrite at the South Apliki Breccia zone suggest a late magmatic pulse could be responsible for Se enrichment in late stage III pyrite (section 6.2.4). If a late magmatic influx was present in the South Apliki Breccia Zone then late stage III pyrite is expected to exhibit lighter  $\delta^{34}\text{S}$  ratios closer to the Troodos magmatic mean (0-1‰). However, uniform  $\delta^{34}\text{S}$  values across stage I and III pyrite and comparable average  $\delta^{34}\text{S}$  values with the Troodos VMS average +4.7‰ suggests a predominantly seawater source of fluids in both early stage I and late stage III pyrite (Figure 6.18; Martin *et al.*, submitted; Chapter 8). This strongly suggests that Se at the South Apliki Breccia Zone is enriched through secondary seafloor oxidation and remobilisation of Se and not a late discrete Se-rich magmatic fluid pulse. Sulfur isotope analysis indicate that magmatic influx into the Apliki VMS hydrothermal system remained constant during the precipitation of all pyrite generations and the absence of values  $\leq 0\text{‰}$  as observed in modern seafloor hydrothermal systems that experienced an increased magmatic influx (e.g. Hine Hina; Herzig *et al.*, 1998a) suggests no additional magmatic volatile source of S-(Se) at Apliki, therefore validating the current model of mobilisation and concentration of Se in stage III pyrite in response to fluctuating redox.



(‰, $\delta^{34}\text{S}$ )	Chalcopyrite (n=11)	Pyrite (n=19)
Average	3.6	4.2
Range	2.8	7.9
$\sigma$	0.9	2.7

**Figure 6.18:** Sulfur isotope ( $\delta^{34}\text{S}$ ) analysis of pyrite and chalcopyrite from the South Apliki Breccia Zone. Whole rock and laser ablation analysis were undertaken (see Chapter 8; Martin *et al.*, submitted). Stage I pyrite analysis yield similar  $\delta^{34}\text{S}$  values to stage III pyrite indicating a constant magmatic volatile influx at Apliki (Full dataset see Chapter 8, Appendix 8.2). Sulfur is sourced from both the thermochemical/biogenic reduction of seawater sulfate and leaching of primary magmatic sulfur in variable quantities. Red dashed lines indicated magmatic mean for Troodos (Alt, 1994), black dashed line is Troodos average (Chapter 8; Martin *et al.*, submitted).

## 6.5 Summary

The South Apliki Breccia Zone is both mineralogically and geochemically distinct within the Solea graben and the Troodos ophiolite. It is significantly enriched in Se with maximum values of 4953 ppm in pyrite and 3956 ppm in chalcopyrite, which are greater than any previously known values for sulfides in Cyprus-type VMS (except Mala; Chapter 9).

- Dissolution of sulfides and precipitation of oxides caused by an influx of seawater due to fault movement and decreased magmatic-hydrothermal input led to fluctuations in  $f\text{O}_2$  from reduced to oxidising conditions.

- Selenium/sulfur ratios suggest an initially seawater dominated system transitioning to magmatic in stage III pyrite, however  $\delta^{34}\text{S}$  of hydrothermal sulfides suggest a uniform magmatic influx during mineralisation.
- Hematite does not have the same ability as pyrite to accommodate large volumes of Se within its crystal lattice and so the dissolution of early sulfide minerals (chalcopyrite and pyrite) and precipitation of oxides left an excess of Se in solution.
- Late stage III pyrite acted as a sink for excess Se and is enriched up to 4953 ppm (averaging 1862 ppm, n=23). By comparison stage I pyrite, which was not affected by Se displaced during earlier hematite formation averages 182 ppm Se (n =22).

# CHAPTER 7

## Low temperature silica-rich Au mineralisation in the Troodos ophiolite, Cyprus

## 7. Abstract

The Troodos ophiolite Cyprus hosts the on-land analogue for mafic, Cu-rich or Cyprus-type VMS deposits. In addition to high temperature (>350°C) sulfide mound type mineralisation, other mineralising systems are known to operate. This chapter describes the occurrence of mineralisation characterised by a) an enrichment in Au and, b) abundant silicification. The mineralogy and geochemistry of four Au and silica-rich mineralised localities in Troodos are considered, these include: Kokkinovounaros, Mathiatis South, Touronjia and Alpen Rose. This study presents whole rock geochemical and mineralogical data characterising Au-rich deposits of the Troodos ophiolite highlighting the diversity of hydrothermal fluid venting in fossil seafloor mafic hosted hydrothermal systems.

Aqua regia digest followed by ICP-MS analysis (n= 235) of whole rock samples from the localities listed above demonstrates an enrichment in Au relative to Troodos VMS mineralisation. Troodos VMS mineralisation averages 0.18 ppm Au (n=66). By comparison samples of Au silica-rich mineralisation may be enriched to concentrations >1 ppm Au (n=25). The enrichment of Au in these deposits is attributed to the enhanced capacity of HS<sup>-</sup> ligands to transport Au in low temperature fluids (<300°C) as an enrichment in Pb, Zn and silica suggests these deposits form at low temperatures. Additionally, the significance of supergene Au-(Te-Se) enrichment is realised at Mathiatis South where high Au samples are associated with jarosite, goethite and natroalunite. Iron-rich lithologies may also contain appreciable Te and Se (>100 ppm). In most deposits Au exhibits a strong mineralogical and geochemical association with silica.

Troodos silica-rich mineralisation is comparable to sites of low temperature fluid discharge (i.e. white smokers) in modern seafloor hydrothermal systems. The deposits are structurally controlled and form distally to known VMS mineralisation. Deposits may have formed during the migration of newly formed oceanic crust off axis, or coeval with VMS mineralisation due to local scale permeability variation. The complex structural controls on these deposits are considered to reflect local variation in stress regimes related to the migration of spreading between different seafloor graben structures. Mineralisation commonly exhibits two prominent fault orientations reflecting the reactivation of older faults under new stress regimes that subsequently acted as conduits for late stage hydrothermal fluids. These deposits represent potential Au resources and highlight the significance and diversity of low temperature vent sites within ancient seafloor hydrothermal systems.

## 7.1 Introduction

Gold is widely associated with seafloor sulfide mineralisation in a range of tectonic settings from island arcs to Mid Ocean Ridges (Hannington *et al.*, 1991; Knight *et al.*, 2018; Melekestseva *et al.*, 2017; Mercier-Langevin *et al.*, 2011; Moss and Scott, 2001). Volcanogenic Massive Sulfide (VMS) deposits associated with the Troodos ophiolite are no exception; although generally depleted in Au (cf. Chapter 5), some Troodos VMS may be enriched to ppm levels including the auriferous Kalavassos and Limni deposits (Mercier-Langevin *et al.*, 2011). Gold is also concentrated in low temperature silicified mineralisation usually associated with metalliferous sediments (Prichard and Maliotis, 1998). Our current understanding of gold mineralisation suggest it postdates VMS formation and formed within close proximity to, but not at, the ridge axis. Instead, off axis mineralisation formed distally to the spreading ridge as the crust cooled and migrated away from the spreading axis (e.g. Prichard and Maliotis, 1998). Gold is also concentrated in supergene gossans, for example, ochres of the Skouriotissa VMS that contain up to 28.4 ppm Au (Cyprus, Herzig *et al.*, 1991). In modern spreading environments black-smoker systems characterise only the active, high temperature portion of the hydrothermal system (Tivey *et al.*, 2005) with extinct sulfide accumulations observed distally but within a few km of the spreading axis. For example, at the Lost City hydrothermal vent field on the Mid Atlantic Ridge (30°N) alkaline low temperature fluids (40-75°C) are vented 15 km from the ridge axis in ~1.5 Myr old crust (Kelley *et al.*, 2001).

In this study new field evidence, geochemical and mineralogical data are presented highlighting the distribution of Au and other pathfinder elements (Te, As, Se, Bi etc.) in mineralised localities across Troodos. For comparison, whole rock and *in situ* mineral analyses are reported for Troodos VMS. In many instances low temperature silica-rich systems contain appreciable Au. Deposits outlined in this study include Alpen Rose, Touronjia, Kokkinovounaros and Mathiatis South. Geochemical and mineralogical data indicate that these deposits may have formed low temperature, distal, silica-rich vent sites equivalent to modern day white smoker or effusive discharge complexes.

### 7.1.1 Gold geochemistry in hydrothermal systems

The abundance of Au in the earth's crust is low, averaging just 1 ppb however ore deposits may be enriched to over 10,000 times this (Pokrovski *et al.*, 2014). The transport of Au in a wide range of ore forming systems (e.g. Epithermal and VMS) is well characterised. Gold is mobilised and transported via hydroxide, hydrogen bisulfide or chloride complexation dependant on the prevailing physicochemical fluid conditions (e.g.  $fS_2$ , pH etc., Pokrovski *et al.*, 2014). The most important complexes in ore forming fluids are AuOH, AuCl<sup>2</sup>, AuHS and Au(HS)<sup>2</sup> with different

ligand complexes exhibiting distinct stability fields (e.g. with pH - Figure 7.1) (Pokrovski *et al.*, 2014). Complexes  $\text{AuHS}$  and  $\text{Au}(\text{HS})_2^-$  are stable at near neutral pH and temperatures  $<350^\circ\text{C}$ , by contrast  $\text{AuCl}_2^-$  is important at high temperatures  $>350^\circ\text{C}$  (Seward, 1973; William-Jones *et al.*, 2009; Figure 7.1). Thus, the solubility and transport of Au in VMS hydrothermal systems is controlled by the availability of two main ligands species:  $\text{Cl}^-$  and  $\text{HS}^-$ . Both  $\text{Cl}^-$  and  $\text{HS}^-$  ligands are extremely sensitive to fluid temperature and the dominant ligand in solution changes in response to temperature and/or pH (Figure 7.1 and 7.2). At temperatures  $<200^\circ\text{C}$ ,  $\text{AuHS}^0$  is dominant transitioning to  $\text{AuHS}^0 + \text{Au}(\text{HS})_2^-$  between 250-450 $^\circ\text{C}$  and  $\text{AuCl}_2^-$  at temperatures  $>500^\circ\text{C}$  (Pokrovski *et al.*, 2014).

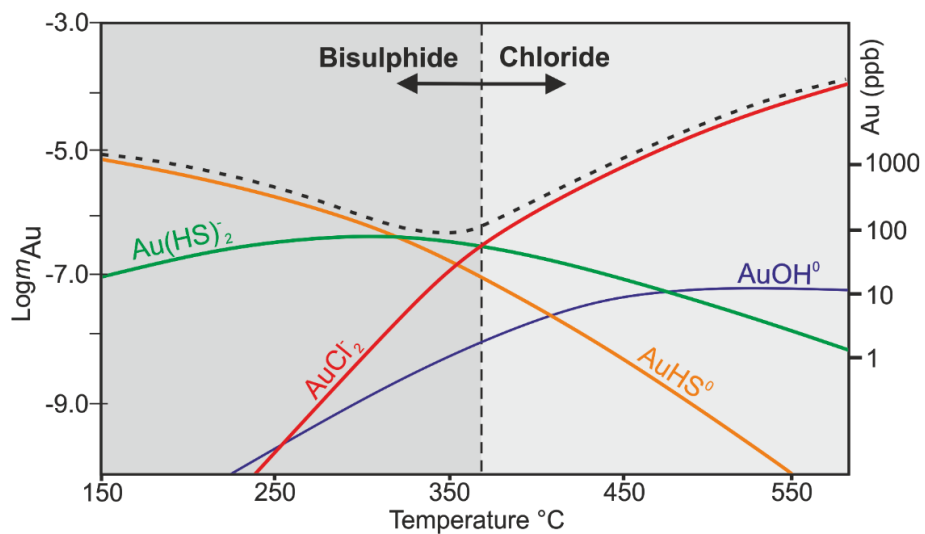


**Figure 7.1:** Solubility of major ligand species with temperature at 1Kbar in an aqueous solution containing 1.5 m (molar) NaCl, 0.5 m KCl, with pH buffered by the assemblage feldspar-muscovite-quartz. Total S is 0.01 m and  $f\text{O}_2$  is buffered by hematite-magnetite.  $\text{AuCl}_2^-$  ligands are important at high temperatures  $\gg 350^\circ\text{C}$ . Sulfide and bi-sulfide complexes dominate at low temperatures  $<350^\circ\text{C}$  (after William-Jones *et al.*, 2009).

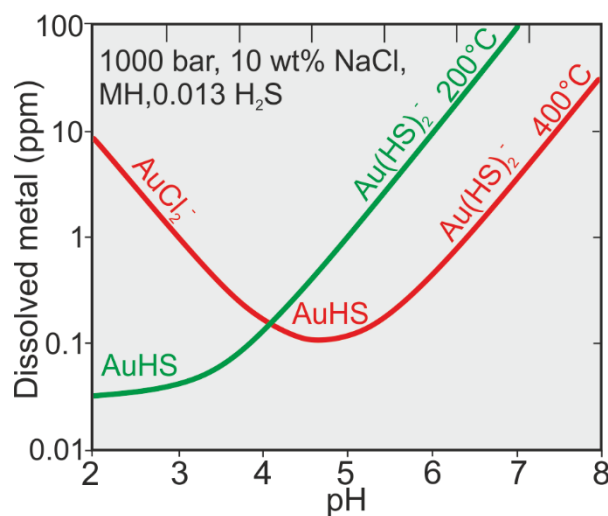


**Figure 7.2:** The effect of pH on chloride and sulfide Au complexes. Note that Au complexes have a minimum solubility at  $\text{pH} \sim 4$  and  $\text{AuHS}$  complexes favour near neutral pH (after Pokrovski *et al.*, 2014).

In addition to the processes outlined above, Au may also be transported in the vapour phase or in super saturated systems as colloidal particles (Heinrich *et al.*, 2004; Herrington and Wilkinson, 1993; Saunders and Schoenly, 1995; Williams-Jones and Heinrich, 2005). The 'soft' aqueous geochemistry of Au allows bonds to easily form between individual Au atoms leading to the formation of colloidal aggregates forming nano-particles (Herrington and Wilkinson, 1993; Pokrovski *et al.*, 2014; Saunders and Schoenly, 1995). For example, at the active Niua hydrothermal field, colloidal particles were found in venting fluids at 250-325°C (Gartman *et al.*, 2018). Recently the importance of vapour phase transport of Au has been demonstrated at high temperatures >400°C (Gartman *et al.*, 2018; Heinrich *et al.*, 2004; Williams-Jones and Heinrich, 2005). Gold concentrations in a HCl-H<sub>2</sub>O vapour may reach ppb concentrations (0.5 ppb) at temperatures similar to those found in high sulfidation epithermal environments and; over the duration of ore formation this can equate to the transport of several tonnes of Au (Zezin *et al.*, 2011).

The precipitation and concentration of Au occurs in response to a range of processes: boiling, cooling, change in pH, oxidisation, sulfidation or a combination of these factors (Pokrovski *et al.*, 2014; William-Jones *et al.*, 2009; William-Jones and Heinrich, 2005). Reducing fluid temperature has a profound effect on Au solubility. The AuCl<sub>2</sub><sup>-</sup> ligand at 300-500°C (500 bar) exhibits extreme sensitivity to decreasing temperature, a decrease in temperature of 50°C in the region of 500-300°C will lead to the deposition of >95% of the Au from solution (William-Jones *et al.*, 2009). In contrast, Au transported as a bisulfide complex is less affected by cooling and is stable at lower temperatures (Pokrovski *et al.*, 2014). The effect of redox on Au solubility is two-fold, under reduced conditions where H<sub>2</sub>S is dominant Au solubility is proportional to  $fO_2$  (Pokrovski *et al.*, 2014). This trend continues at temperatures <500°C until the magnetite-hematite buffer is intersected, at this point H<sub>2</sub>S is oxidised to SO<sub>4</sub> or SO<sub>2</sub> (Pokrovski *et al.*, 2014). The hematite buffer marks a minimum in Au solubility due to the decreased ability of oxidised sulfur species to transport Au (Pokrovski *et al.*, 2014). The precipitation of pyrite may be important in facilitating Au precipitation as the reaction of Fe bearing wall-rock with the hydrothermal solution leads to a decrease in HS<sup>-</sup> concentrations thus decreasing Au solubility (William-Jones *et al.*, 2009).

### 7.1.2 Off axis silicification in Troodos

Studies have identified areas distal to high temperature VMS that contain elevated Au concentrations (Jowitt *et al.*, 2005; Naden *et al.*, 2006; Prichard and Maliotis, 1998). These deposits fall into two categories; those described as 'pseudo epithermal' (Jowitt *et al.*, 2005) and

---

silicified umbers (Prichard and Maliotis, 1998). The addition of silica, usually in an amorphous form in umbers is fault controlled and faults provide a permeability pathway controlling the distribution of silicification (e.g. Theotokos- see Appendix 3.1). Silicification is pervasive but localised over a few metres. Gold concentrations in non-silicified umbers were 5 ppb whilst silicified umbers are enriched up to 5.3 ppm (Prichard and Maliotis, 1998), demonstrating the significance of low temperature silica-rich fluids in Au enrichment (e.g. Pyrga, Appendix 3.1)

The timing of silicification postdates umber formation that is associated with high temperature venting and VMS formation in Troodos (Robertson, 1975). Silicification occurs late, most likely at lower temperatures as the newly formed oceanic crust migrated away from the spreading axis. It remains unclear how far off axis hydrothermal activity remained active in Troodos although hydrothermal activity is reported for 20-30 km off axis in seafloor environments (Honorez *et al.*, 1981).

## 7.2 Sample Localities

This study presents four detailed examples of mineralisation that display variable mineralisation styles all distinctly different from VMS that exhibit a variable enrichment in Au. For comparison whole rock Au concentrations for 10 VMS across Troodos are also presented (Table 7.1). Samples presented in this study are divided into high temperature VMS deposits and low temperature silica-rich mineralisation. The 10 VMS considered span the entire Troodos ophiolite and contain a full suite of ore morphologies including massive, disseminated, jasperitic and stockwork type mineralisation, thus they are representative of a broad range of physicochemical processes (Martin *et al.*, 2019). Localities are summarised in Table 7.1.

Deposits investigated include: Alpen Rose, Kokkinovounaros, Mathiatis South and Touronjia (Figure 7.3 and Table 7.1). These localities were selected as they exhibit a diverse range of textures, mineralogical associations and varied geochemistry that are different from VMS suggesting variable mechanisms of Au enrichment, different physiochemical fluid parameters and the supergene vs. hypogene enrichment of Au. In contrast to a typical Troodos VMS (cf. Chapter 3 and 5), Alpen Rose, Kokkinovounaros, Touronjia and Mathiatis South are silica-rich with minor or absent massive sulfide. The four deposits highlight the diversity of mineral deposits in the Troodos crust. Hence, these deposits are representative of the wider Troodos 'off axis' hydrothermal system.

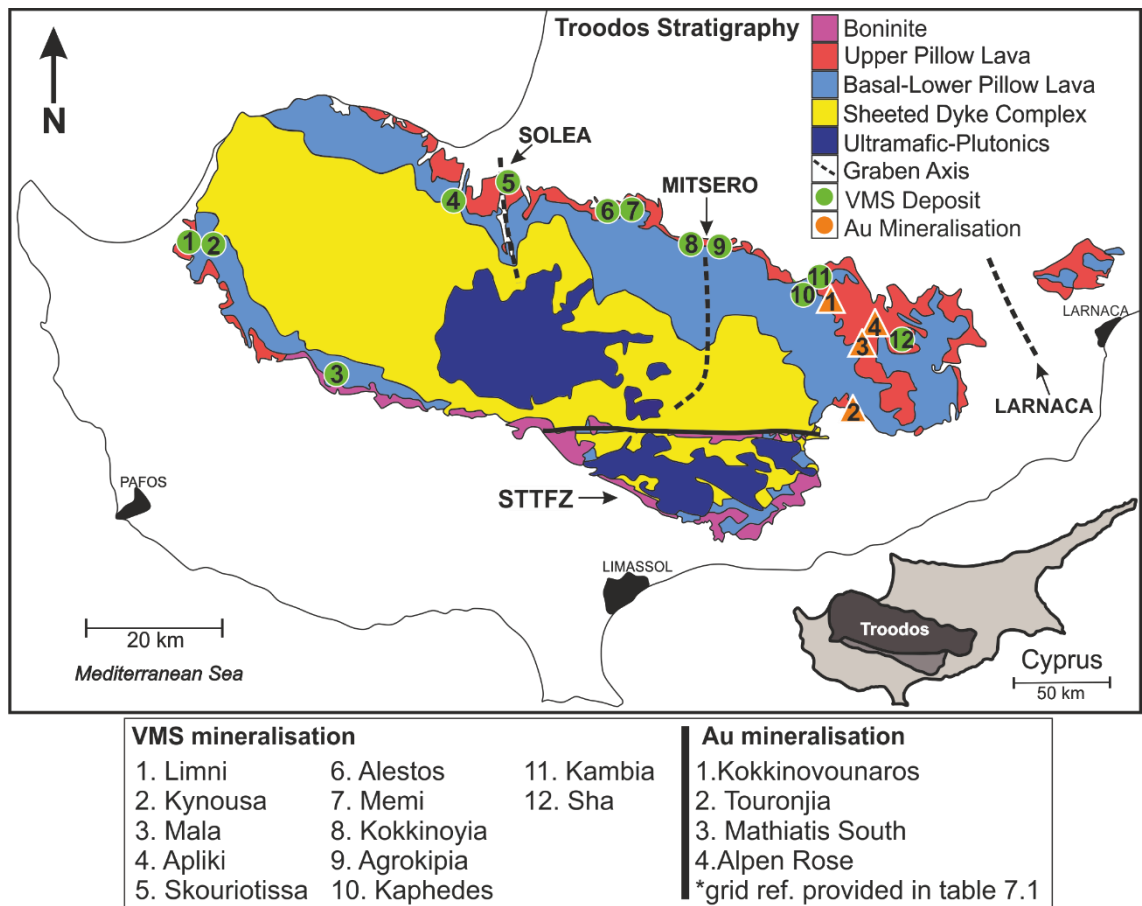


**Figure 7.3:** Sample location map of 10 VMS (1-10, green) and low temperature silica-rich deposits considered in this study (1-4 orange) (after Martin *et al.*, 2018; Chapter 5).

Deposit	Location (WGS 1984)	Sample type analysed
<b>Low temperature Au</b>		
Touronjia	053242 3856597	N/A
Kokkinovounaros	052523 3872643	N/A
Alpen Rose	053229 3869042	N/A
Mathiatis South	053168 3867704	N/A
<b>VMS</b>		
Limni	045294 3877209	SEMI, STOCK, DIS
Kynousa	045555 3876810	MAS, STOCK
Mala	047042 3864323	JASP, MAS
Apliki	048575 3881758	JASP, MAS, SABZ, SEMI, DIS
Skouriotissa	048990 3883713	GOS, MAS, OCH, STOCK, DIS
Alestos	050232 3876999	JASP
Memi	050352 3877516	JASP, MAS
Agrokipia (A)	051327 3878134	JASP, MAS, SEMI, DIS
Kambia	052501 3872967	JASP, MAS
Kaphedes	052394 3871610	MAS, DIS
Sha	053414 3867843	MAS, SEMI, DIS

**Table 7.1:** Summary of sample localities and sample type (VMS). JASP= jasper, GOS= gossan, MAS= massive, SEMI= Semi-massive, OCH= ochre, DIS=disseminated, SABZ= South Apliki Breccia Zone, STOCK= stockwork.

---

## 7.3 Description of localities

### 7.3.1 Alpen Rose

Alpen Rose forms a prominent NW-SE striking ridge (Figure 7.4) in eastern Troodos approximately 300 m E of the Mathiatis North VMS deposit and 1.2 km W of the Sha VMS deposit (Table 7.1, Figure 7.3). Locally the geology consists of basal group outcrops forming topographic highs, LPL flows and a relatively thick sequence of UPL. Disseminated sulfide mineralisation and VMS occur in the surrounding area (e.g. Almyras and Mathiatis North- Appendix 3.1).

Alpen Rose rises >100 m above surrounding lavas, the ridge is quartz-rich comprising a breccia unit cross-cut by quartz veins (Figure 7.5). The surrounding lavas are highly weathered but appear to be of LPL affinity. The southern side of the ridge forms a prominent near vertical scarp that increases in height to the E (Figure 7.5). The northern ridge is shallower dipping with minimal brecciation. Surrounding the ridge are 3-10 m wide, near vertical dyke swarms that cross-cut horizontal pillow lavas. To the NW, a small faulted outlier of younger Lefkara group limestone (~75 Ma) was recorded (Figure 7.4).

Structurally Alpen Rose is complex; the scarp on the southern side of Alpen Rose is clearly fault bound with a thick unit (1-3 m) of breccia striking parallel to the ridge (Figure 7.4 and 7.5). Rarely kinematic indicators are preserved and indicate an oblique strike-slip sense of movement (Figure 7.4 and 7.5). Local scale strike-slip faulting subsequently cross-cut and offset the ridge striking N-S. Small faults are traceable not only transecting Alpen Rose but also across vertical adjacent dyke intrusions (Figure 7.4 and 7.5). Cross-cutting faults are minor with a displacement of only a few metres leading the offset of the main NW-SE ridge by 1-5 m. There is no unified sense of movement on cross-cutting faults and both sinistral and dextral kinematic indicators are preserved, most likely representing fault reactivation under a different stress regime. The author infers that Alpen Rose is bound to the SE by a further N-S fault as the ridge and mineralisation end abruptly (Figure 7.4).

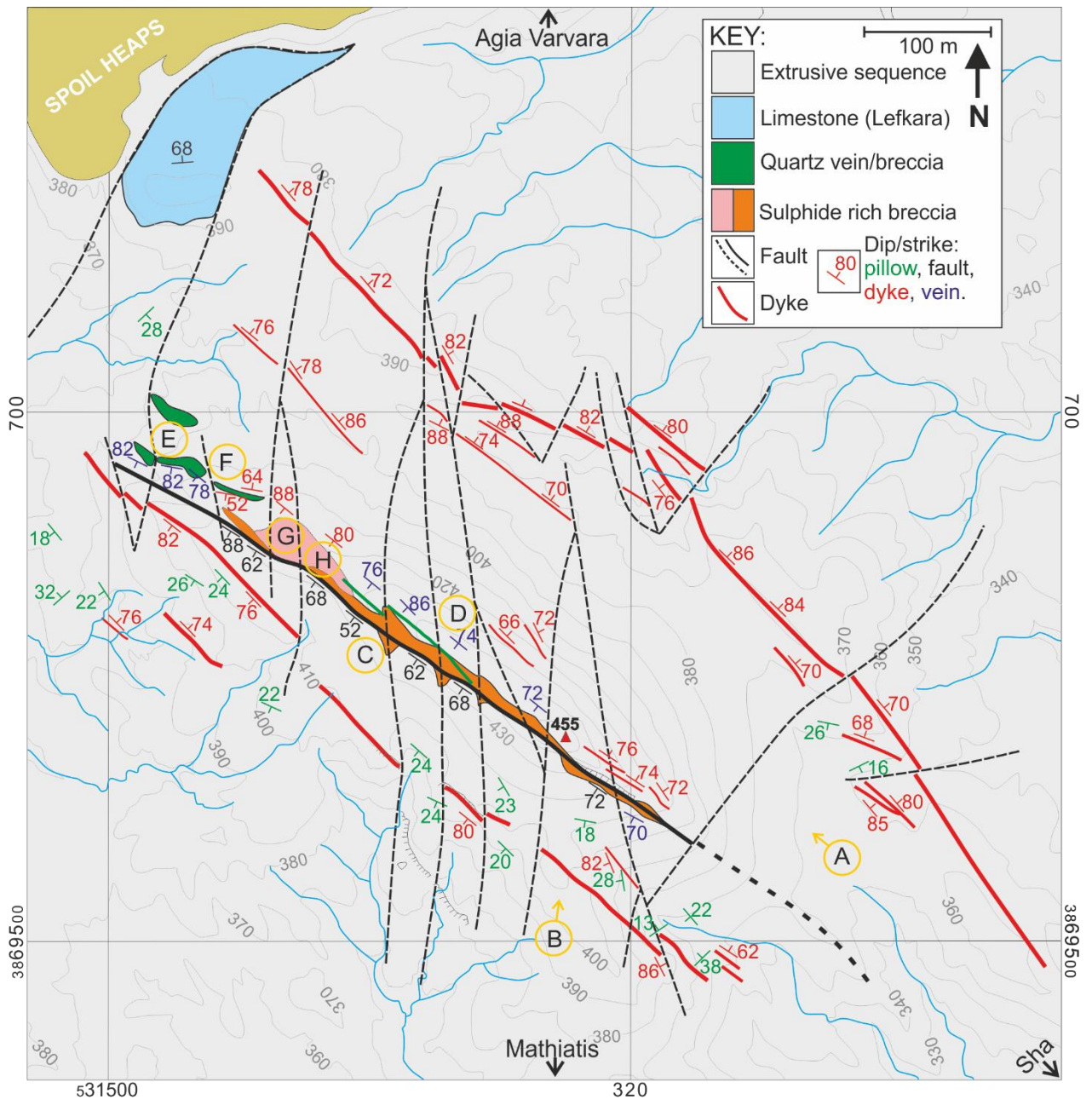


**Figure 7.4:** Field map (1:5000) of Alpen Rose mineralisation. The main ridge strikes NW-SE forming a prominent scarp to the S (Figure 7.5) - likely a fault with an oblique strike-slip movement. Small strike-slip faults cross-cut the length of the ridge causing the quartz-sulfide breccia unit to boudinage. Where faults are intersected, quartz and sulfide abundance increases. The surrounding extrusive sequence is cross-cut by a series of dyke swarms (parallel to Alpen Rose) that are also truncated by strike-slip faults suggesting that N-S faulting postdates the formation of the main NW-SE fault and early Alpen Rose mineralisation. Yellow rings indicate photo locations in Figure 7.5.

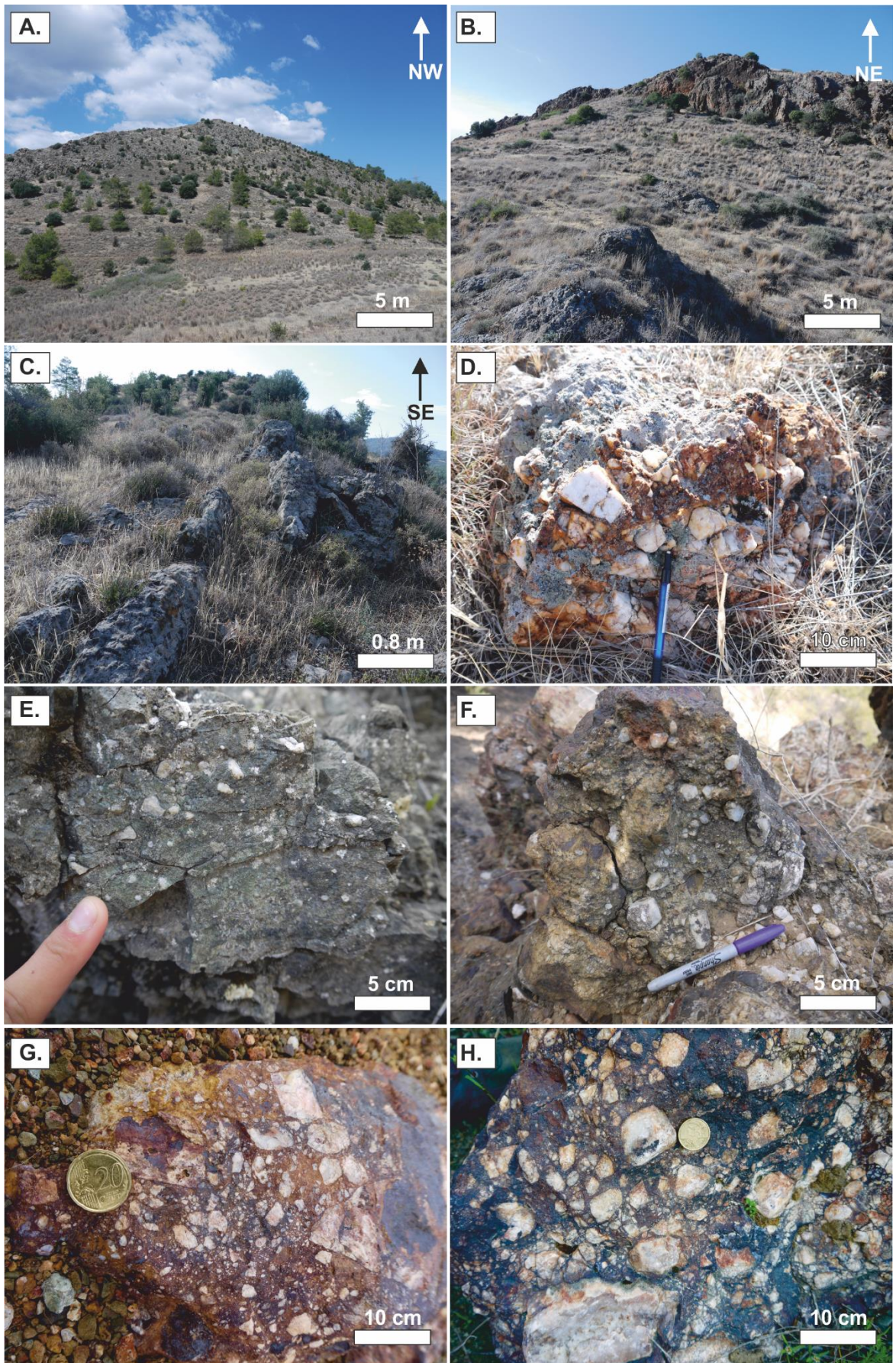


**Figure 7.5 (previous page):** Key field observations from Alpen Rose. A) View looking NW from the base of Alpen Rose. Alpen Rose forms a prominent topographic high. B) View looking NE, note the prominent steep sided fault scarp delineating the main breccia zone at Alpen Rose. C) On top of the main ridge, massive quartz vein offset by minor dextral strike-slip faulting. D) Quartz breccia vein with silica cement. E and F) Angular quartz fragments in a hydrothermally altered weakly silicified matrix. G and H) Typical hydrothermal 'sulfide-rich' breccias. White clasts are sub-angular quartz fragments in a goethite-hematite matrix, probably produced through pyrite oxidation.

Mineralisation is dominantly breccia or vein hosted and quartz-rich. Textures are consistent with multiple phases of sulfide and silica dominant mineralisation. No fresh sulfides were observed at Alpen Rose however hematite, goethite and minor jarosite (see section 7.5.1) are abundant in matrix phases (Figure 7.5 G and H). Clast angularity varies from angular to sub-angular (Figure 7.5 D and H). The second style of mineralisation is massive vein hosted quartz; veins are less common than breccia and exhibit a laminated morphology and are 30-70 cm wide (Figure 7.5 C and D). Veins exclusively occur in the NW portion of the ridge and are only continuous for intervals of several metres.

Quartz occurrence at Alpen Rose is structurally controlled. Vein hosted mineralisation strikes approximately parallel to the ridge bounding fault to the south of Alpen Rose (F1- thick black line Figure 7.4). Toward the NW, the breccia zone and vein is approximately 3 m from the main fault scarp and progressively pinches out towards the SE where, at the end of the ridge it is located on the edge of the fault scarp itself. Brecciation, associated Fe-oxyhydroxides and quartz increase in abundance where minor N-S faults intersect the ridge (Figure 7.4). In these areas the breccia zone boudinages and thickness increases by 2-3 m. The quartz vein is discontinuous and offset by 1-3 m (Figure 7.4 and 7.5).

### 7.3.2 Mathiatis South

The Mathiatis South deposit has been previously exploited for Au and Cu. It is located 1.7 km SE of the village of Mathiatis in E Troodos approximately 2.5 km S of the Mathiatis North VMS (Table 7.1, Figure 7.3). The northern margin of the deposit contains a Cu-rich massive pyrite lens (Figure 7.6 A). The centre of the historic open pit is dominated by inter-fingered goethite, hematite, jarosite and limonite-rich zones with distinct areas of silica-rich bleached material (Figure 7.6 C and H). Brecciation is prolific throughout the entire deposit occurring at a range of scales (Figure 7.6 B, C and D). In the upper mineralisation to the S, brecciation becomes less pronounced instead grading to crudely banded layers (Figure 7.6 B).

### 7.3.3 Kokkinovounaros

Kokkinovounaros (Red Hill) forms a prominent hill 2 km SW of Analiontas and 1 km S of the Kambia VMS deposit (Table 7.1, Figure 7.3). Mineralisation is bound to the E and W by two parallel N-S striking and eastward dipping (358/64E) normal faults (F1- Figure 7.7 and 7.8). Mineralisation is traceable along strike for ~500 m and is truncated and offset to the E by a NE trending fault where mineralisation reappears to the S of the main road (Figure 7.7). Mineralisation is spatially associated with N-S trending faults with a clear decrease in alteration intensity with distance from the fault plane (~5 m) (Figure 7.8 A and B). The deposit is situated within the upper LPL stratigraphy.

The main pit (Figure 7.8 A) is characterised by highly bleached and brecciated lithologies that are now unrecognisable as lava. Silica is prolific and characterises the most leached zone (Figure 7.8 B, Section 7.4.1). Alteration intensity reduces rapidly with distance from the fault plane to a red-pink zone of jarosite and hematite, transitioning to goethite-rich facies at the margins (Figure 7.8 B, Section 7.4.1). To the E, an unaltered pillow lava pile is preserved with discernible pillow structures. Gypsum and malachite staining are developed localised to its margin.

Brecciation is common throughout Kokkinovounaros. Within the small exploration adit, brecciation appears fault controlled. Hematite-silica (jasper)-rich lithologies are brecciated into highly angular fragments approximately 15-20 cm in diameter, the surface is coated in a white sulfate mineral with no clear matrix between fragments (Figure 7.8 F, G and H). In the wider area, fault breccias contain angular to sub-angular clasts up to 10 cm in diameter and comprise bleached white-yellow lava fragments usually with a hematite-goethite matrix and with relict cubic pyrite voids (hematite residue - Figure 7.8 D). Minor faults with an oblique geometry to the main F1 and F2 planes cross-cut the open pit, and are best exposed in exploration trenches and strike 060 dipping 52 towards the NW.

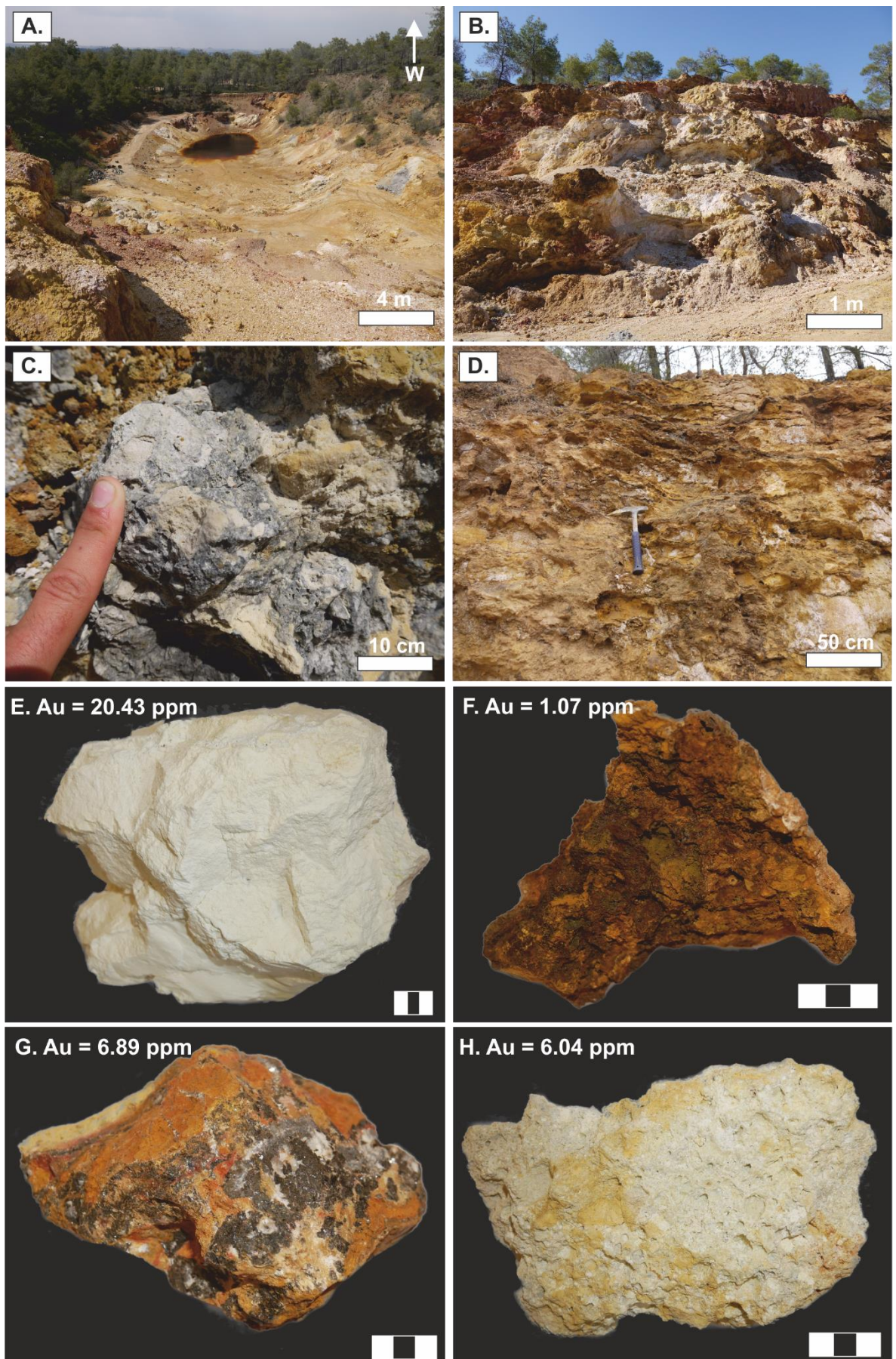
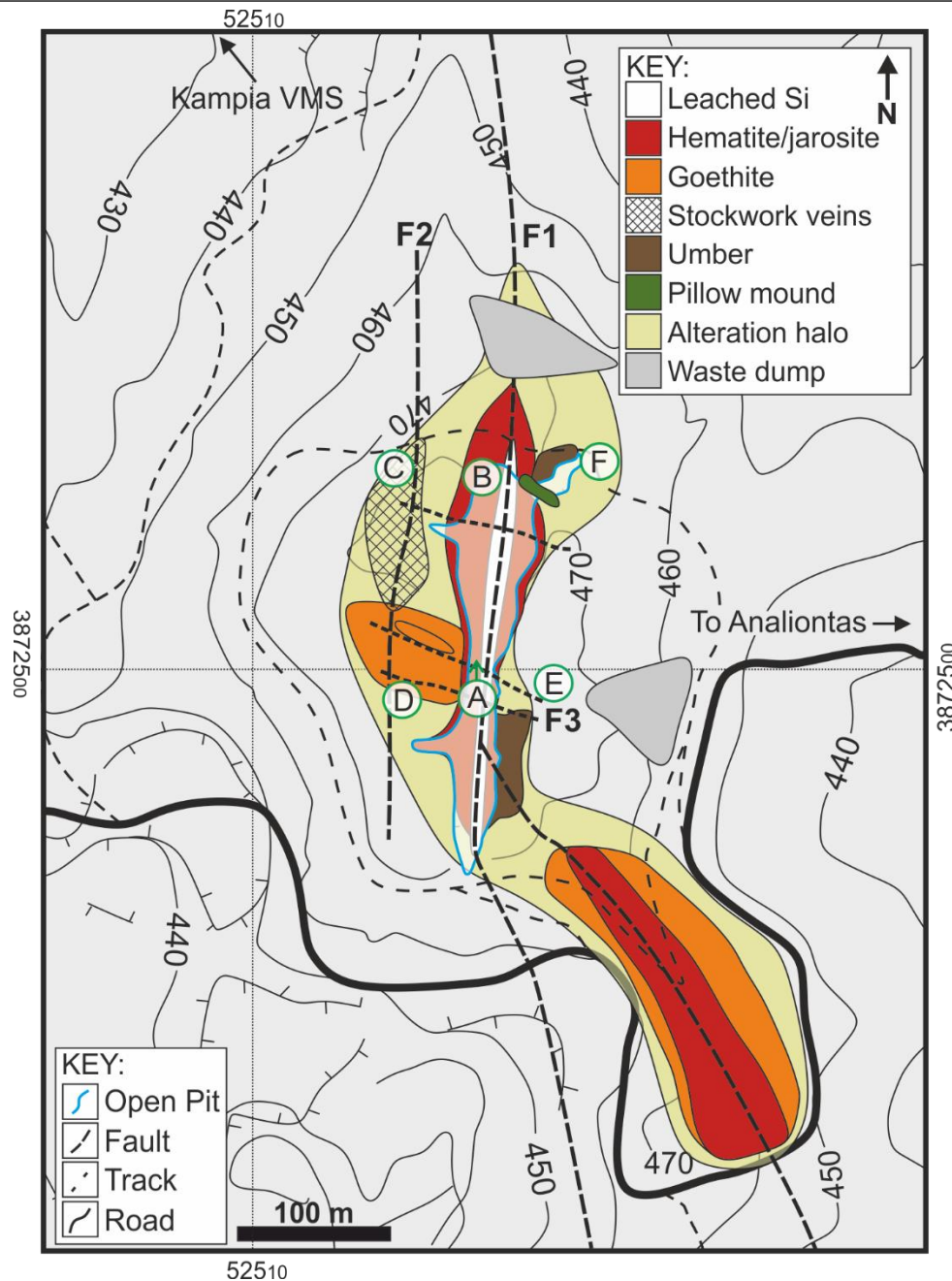


Figure 7.6: Field photographs and high Au samples from Mathiatis South (explanation overleaf).

**Figure 7.6:** Key field observations from the Mathiatis South deposit. A) View over the historic open pit, previously extracted for Au, note extensive Fe staining. B) Typical gossan exposure, interlayered goethite, silica, jarosite and hematite. C) Silica breccia from the main pit exposure. D) Layered gossan exposure highlighting the complex nature of supergene alteration at Mathiatis South. E) Silicified bleached basalt containing high Au. F) Typical gossan sample consisting of goethite with minor quartz. G) Calcite-goethite-rich sample, black mineral is Mn carbonate. H) Silica breccia exhibiting a vuggy silica texture.

The bounding fault to the W (F2) exhibits a different alteration style to the main pit (F1) fault (Figure 7.7). The alteration halo is less pronounced and generally limited to 5 cm wide veins coalescing to form a stockwork texture (Figure 7.8 C). Goethite-jarosite veins are 5-10 cm wide with a narrow alteration halo (typically 10 cm) that grades into moderately hematized but not brecciated lavas. Localised to the W of the fault, veins become increasingly silica-rich with localised jasper. The silicified matrix contains fresh, disseminated subhedral pyrite (Figure 7.8 C). Distally from the two bounding faults, alteration becomes more chaotic with interfingering reds, yellows, whites and purples indicating variable amounts of hematite, goethite, silica and jarosite respectively (section 7.4.1). The distribution and relative proportion of minerals varies on a metre scale from massive pervasive alteration to brecciated and vein hosted types; it is difficult to distinguish a single dominant alteration type (Figure 7.7 and 7.8).

Silicified umber is present at the northern and southern margin of Kokkinovounaros. To the N it forms a relatively thin 50-80 cm crust (Figure 7.8 E) on the hanging wall of the main pit fault. UMBER is interbedded with more ochreous horizons that become pervasively silicified towards the base whilst in the upper horizons umber is finely bedded and un-silicified. To the S, umber thickens significantly outcropping to the E of the main pit fault (hanging wall). The silicified umber reaches a maximum thickness of 4 m (Figure 7.8 E) and Fe-rich breccias are common. This, like the northern area is closely associated with minor patches of un-silicified umber. Additionally, 200 m to the E of the main Kokkinovounaros pit is a third N-S fault associated with silicified ochre and umber (see Appendix 3.1). Looking E from the main deposit a line of silicified umber forms a prominent ridge. This demonstrates a strong spatial relationship between faulting and silica-rich fluids at Kokkinovounaros, potentially this suggests further mineralisation could be present at depth to the E of Kokkinovounaros.



**Figure 7.7:** Simplified map of Kokkinovounaros highlighting the main alteration zones. A bleached silica core is surrounded by hematite and goethite rich lithologies. Main faults (F1 and F2) strike N-S and F3 is NW-SE. Blue line = pit outline. See Appendix 3.1 for further detail. Green circles locate photos in Figure 7.8.

**Figure 7.8 (overleaf):** Key field photos from Kokkinovounaros. A) View of the historic open pit (along fault strike). Note highly bleached lavas. B) Cross-section of alteration surrounding the main pit fault. The fault plane is marked by intense leaching (white) grading through goethite to hematite (orange to red) and finally into 'fresh' green-grey pillow lavas. C) Stockwork veins in close proximity to the western fault, inset image shows subhedral pyrite occurrence. D) Supergene altered lava: euhedral voids indicate the leaching of pyrite now replaced by hematite. E) Extensive silicified umber to the S of the main pit exposure. Brecciated texture and un-silicified horizons are common. F) Exposure in small adit to the N of Kokkinovounaros preserving hypogene breccia mineralisation. Mineralisation is hematite and quartz-rich. White staining is a sulfate-rich powder. G and H) Examples of high Au jasper mineralisation from location F (Adit).

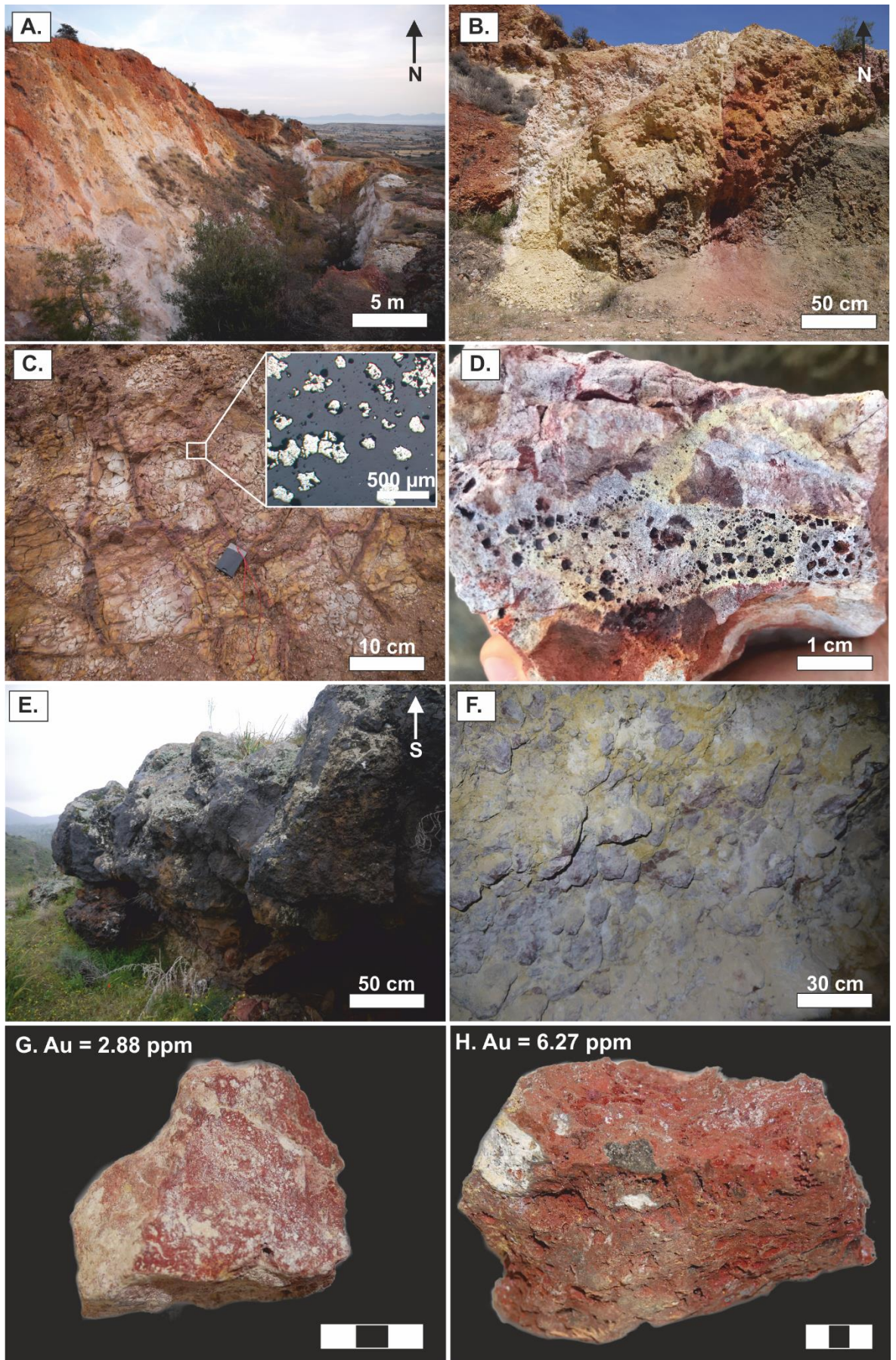


**Figure 7.8:** Field photographs from Kokkinovounaros (explanation on previous page).

### 7.3.4 Touronjia

Touronjia is located in southeast Troodos, W of the Dipotamos Reservoir, 3.5 km ESE of Kato Lefkara (Table 7.1, Figure 7.3). Silica-sulfide mineralisation occurs in basal group lithologies and grades upwards into LPL flows and brecciated pillows which are directly overlain by bedded limestones/chalks (Figure 7.9). In the lower regions, sinuous crudely sheeted dykes are highly oxidised grading upwards into a bleached gossanous, silica-rich zone in the upper horizons. In the upper zones of the deposit silicification and kaolinisation are common (Figure 7.10).

Mineralisation at Touronjia is characterised by pervasive silicification with disseminated pyrite, minor chalcopyrite and sphalerite with a brecciated texture (Figure 7.11 C). Sulfides are mostly altered and were only observed on fresh unweathered surfaces (Figure 7.11 C, G and H). Clasts of basal group lithologies are brecciated exhibiting variable degrees of silicification. Supergene alteration ranges from kaolinite to goethite dominated. Sulfides are associated with silicification in the matrix of breccia units (Figure 7.9); pyrite is subhedral to framboidal occurring as sub mm scale aggregates and disseminations (Figure 7.9). Breccia clasts range in size from 8-10 cm to mm scale and are sub-angular to angular. In the uppermost mineralised horizon, silicification is less pervasive and breccia fragments are hosted in a fine rock-flour matrix (most likely kaolinite) with variable amounts of goethite (Figure 7.11 A, E and F). In the upper horizons of the deposit crude banding is observed, possibly representing an intact lava horizon. In the lower regions, mineralisation is less pervasively silicified and lavas are identifiable (Figure 7.11 E and F). Veins of goethite, hematite and silica occur cross-cutting oxidised, but not pervasively altered lava material and no fresh sulfides were observed. Crucially, no massive sulfide mineralisation is identified at Touronjia.

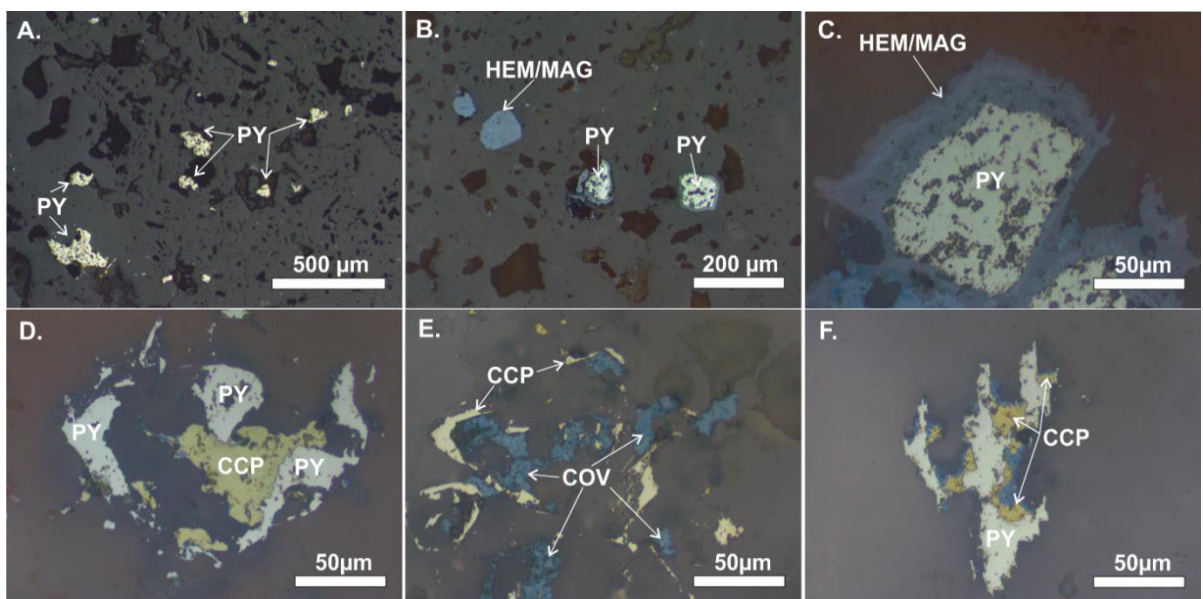


**Figure 7.9:** Reflected light photomicrographs of sulfides from Touronjia (see overleaf).

**Figure 7.9 (previous page):** Reflected light photomicrographs of sulfides from Touronjia. A) Disseminated PY, B) PY rimmed by MAG/HEM, C) Close up of PY rim, D) CCP associated with PY, E) COV rimming CCP, F) PY mantled by CCP and COV. PY=pyrite, CCP=chalcopyrite, COV=covellite, MAG/HEM=Fe oxide.

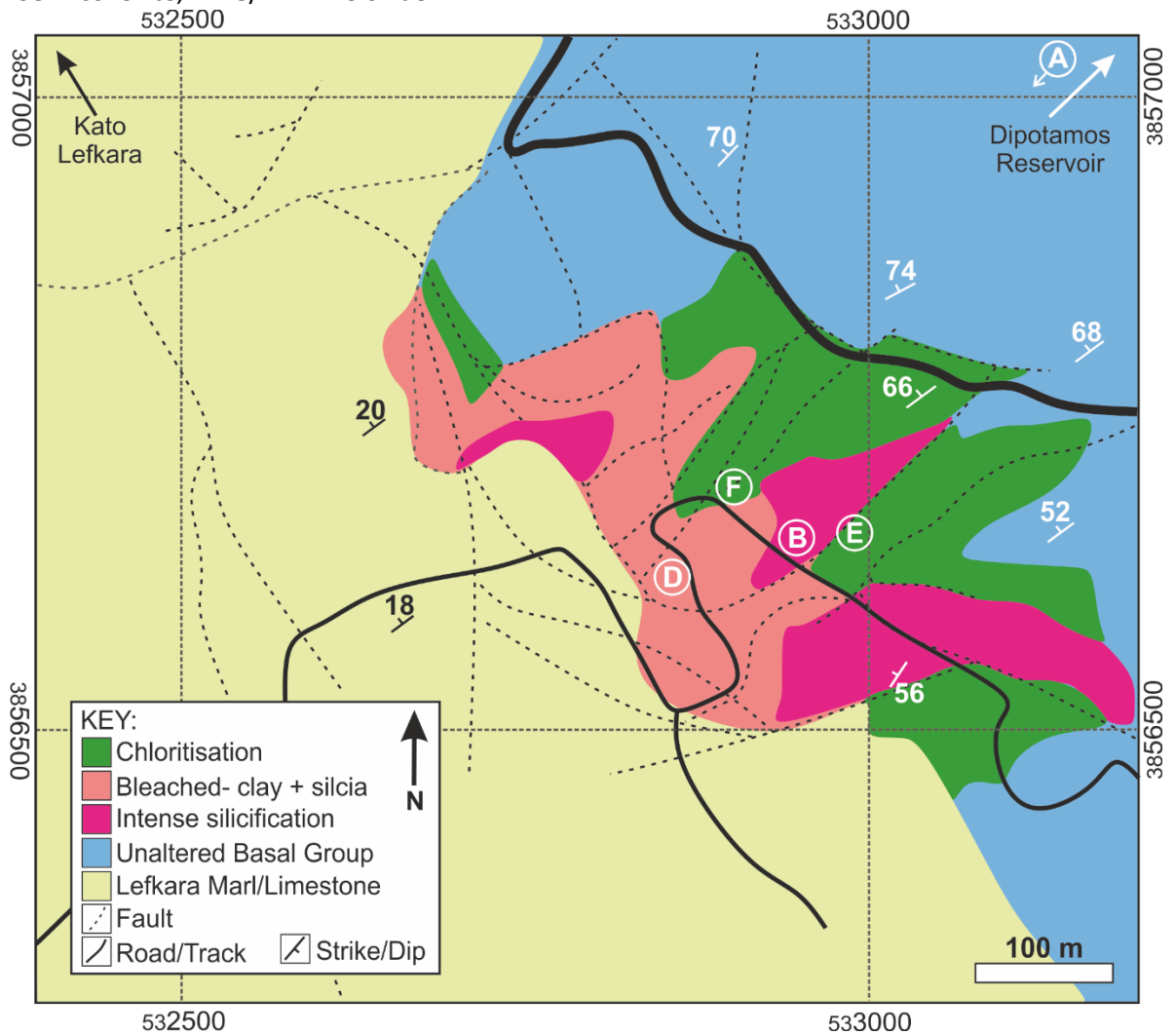


**Figure 7.10:** Simplified field map of Touronjia. Mineralisation is highlighted in green and pink. Bleached clay-silica alteration corresponds to Figure 7.11 B, E and F and intense silicification to Figure 7.11 C. Mineralisation occurs within the lower pillow lava-basal group transition. Mineralisation is directly overlain by marly limestone of the Lefkara Group. Numerous NE-SW and N-S faults were observed, alteration is spatially associated with these fault sets. White letters indicate photo location in Figure 7.11 (adapted from Naden *et al.*, 2006- structural measurements and field interpretation added).

**Figure 7.11 (overleaf):** Key field photographs of mineralisation at Touronjia. A) View over the mineralised area, the far hill tops are Lefkara group limestones. The mineralisation extends along strike for several 100 m. B) Upper Touronjia exposure, brecciated highly silicified unit with variable amounts of Fe staining. C) Fresh surface of Touronjia breccia, the unit is pervasively silicified with trace base metal sulfides (Figure 7.9). D) Close-up of clast supported Fe stained breccia. E and F) Vein hosted 'sulfide' mineralisation, now altered to goethite-jarosite cross-cutting a bleached-altered lava. G and H) examples of high Au samples. Samples exhibit a distinct brecciated morphology with a highly silicified matrix that commonly hosts disseminated sulfides (Figure 7.9).

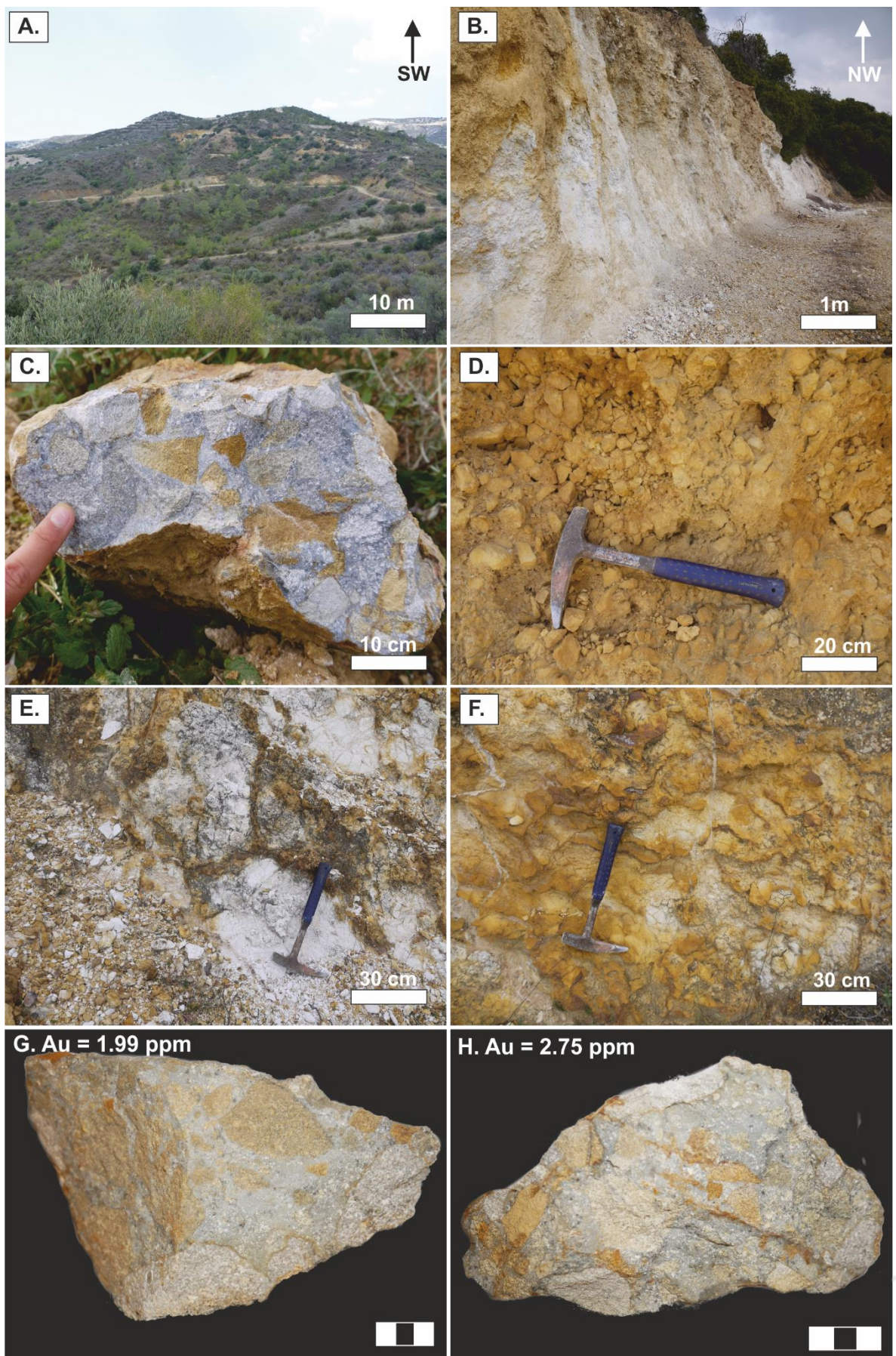


**Figure 7.11:** Field photographs of mineralisation at Touronjia (explanation on previous page).

### 7.3.5 VMS: The on axis hydrothermal system

In this study whole rock geochemical data for 10 VMS are presented. Samples were classified based on their sulfide abundance and morphology into: Massive (n=9), semi-massive (n=9), disseminated (n=9), jasper (n=11), stockwork (n=8), South Apliki Breccia Zone type (n=5), ochre (n=7) and gossan samples (n=4) (Figure 7.12; Chapter 5). Massive sulfide comprises >90% sulfide, mainly pyrite with minor chalcopyrite and trace sphalerite. Semi-massive samples contain >50% sulfides but contain a higher proportion of silica (Figure 7.12). Disseminated samples contain fine-grained pyrite (10-20%) but predominantly consist of altered wall-rock. Jasperitic samples contain only pyrite (10-20%), hematite and silica (amorphous or quartz- Figure 7.12). Stockwork samples are characterised by discrete veins of pyrite and chalcopyrite (Figure 7.12). South Apliki Breccia Zone (SABZ) samples contain high concentrations of chalcopyrite (up to 50%) and variable amounts of covellite, hematite, pyrite and silica (Martin *et al.*, 2018; Chapter 6). Ochre samples are finely bedded and contain goethite, jarosite and minor hematite (Figure 12). The wide range of ore morphologies sampled ensure data represents a diverse range of hypogene and supergene enrichment processes. See Chapter 5 for further sample characterisation.

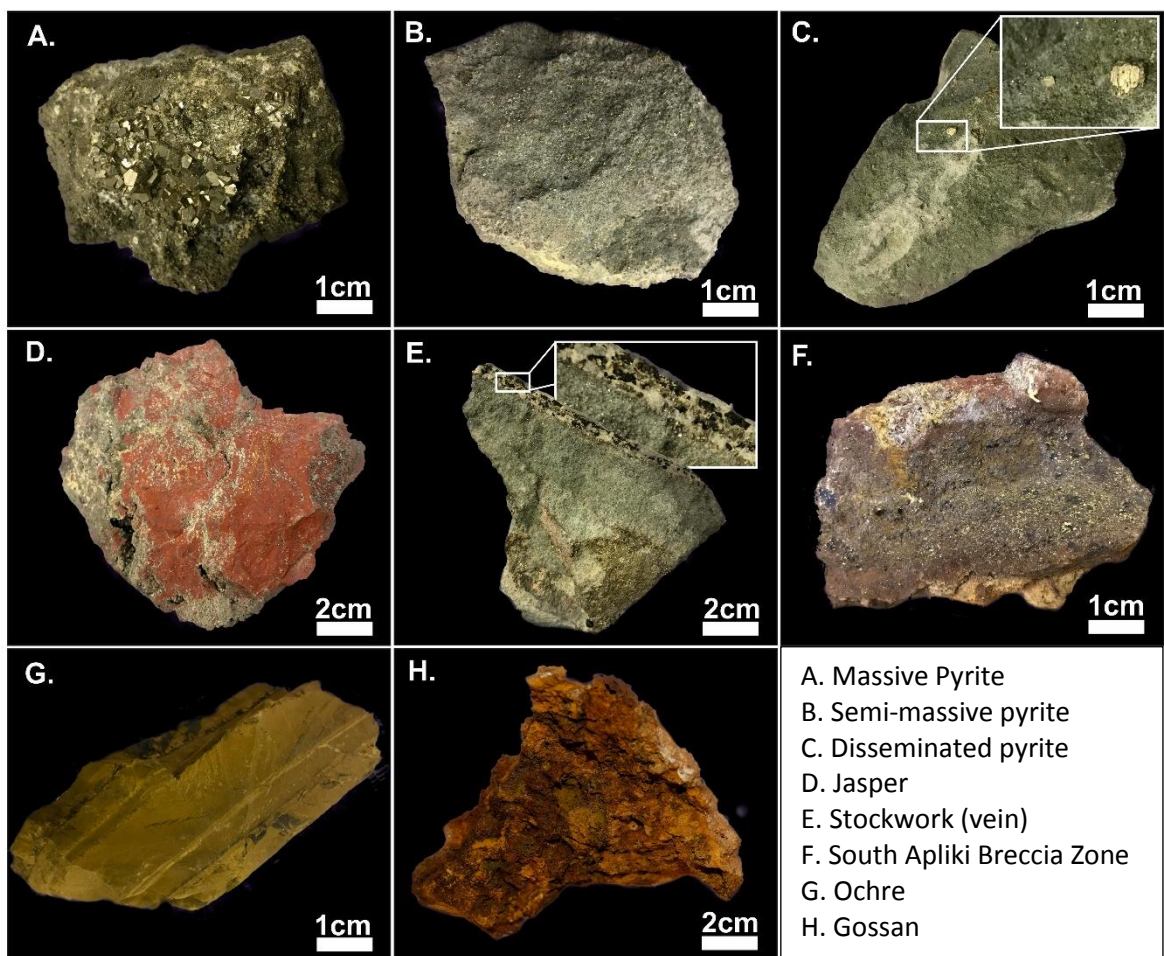


**Figure 7.12:** Examples of VMS hand specimens analysed in this study.

## 7.4 Method summary

Whole rock geochemistry was prepared using an aqua regia digest followed by Inductively Coupled Plasma Mass Spectrometry (ICP-MS) analyses at Cardiff University. A 1:5 dilution was then performed using MilliQ 18.2 M $\Omega$  de-ionised water ready for analyses. Trace elements were analysed using a Thermo iCAP RQ ICP-MS at Cardiff University, data correction was performed using Thermo Qtegra software (see Chapter 4).

Laser Ablation ICP-MS (LA ICP-MS) was used to determine in situ trace element concentrations in pyrite (n=28). Laser ablation ICP-MS spot analysis utilised a New Wave Research UP213 UV laser coupled to an iCAP RQ ICP-MS at Cardiff University, data correction was performed using Thermo Qtegra software (see Chapter 4).

For the identification and quantification of modal mineralogy, X-ray Diffraction (XRD) analyses were carried out on powdered samples at Cardiff University. Scans were run using the Philips PW1710 Automated Powder Diffractometer using Cu K $\alpha$  radiation at 35kV and 40mA. From the scans, phases were identified using Philips PC Identify software and from the peak areas, semi-quantitative analysis was performed and a percentage of each phase present estimated (see Chapter 4).

---

## 7.5 Sample characterisation

### 7.5.1 Mineralogy

Modal mineralogy analysed by XRD is summarised in Figure 7.13. Minerals identified include quartz, critsobalite and amorphous silica, multiple Fe phases including goethite ( $\text{FeO}(\text{OH})$ ), jarosite ( $\text{KFe}^{3+}_3(\text{OH})_6(\text{SO}_4)_2$ ), hematite ( $\text{Fe}_2\text{O}_3$ ), carphosiderite ( $\text{H}_2\text{O}\cdot\text{Fe}_3(\text{SO}_4)_2(\text{OH})_5\text{H}_2\text{O}$ ) and other sulfate, oxide, clay and hydrous minerals including: natroalunite ( $\text{NaAl}_3(\text{SO}_4)_2(\text{OH})_6$ ), anatase ( $\text{TiO}_2$ ), sergeevite ( $\text{Ca}_2\text{Mg}_{11}(\text{CO}_3)_9(\text{HCO}_3)_4(\text{OH}_4\cdot 6\text{H}_2\text{O})$ ), calcite ( $\text{CaCO}_3$ ) and kaolinite  $\text{Al}_2\text{SiO}_5(\text{OH})_4$  (see Figure 7.13; Appendix 7.1). Quartz is the most common mineral occurring in 19 out of 24 samples; quartz abundance varies significantly from ~5 vol.% to 99.7 vol.%. Samples from Mathiatis South are the most mineralogically diverse whilst all other deposits analysed contain predominantly quartz with minor goethite, hematite (Alpen Rose) and kaolinite (Touronjia). Full data available in Appendix 7.1.

### 7.5.2 Geochemistry

In total 169 whole rock samples were analysed, 55 from Alpen Rose, 49 from Mathiatis South, 59 at Kokkinovounaros and 6 from Touronjia (Table 7.2). Additionally, 70 whole rock analyses from 10 VMS across 7 ore types including disseminated (n=9), jasper (n=11), massive (n=17), ochre (n=7), SABZ (n=5), semi-massive (n=9) and stockwork (n=8, Table 7.3) types are included for comparison. In situ LA-ICP-MS analysis of pyrite was undertaken from Kokkinovounaros (n=18) and Touronjia (n=10) to assess Au enrichment in hypogene sulfides (see section 7.5.3, Table 7.4).

Of the 169 samples analysed, 25 samples returned Au concentrations >1 ppm. These include 1 from Alpen Rose, 15 from Mathiatis South, 6 at Kokkinovounaros and 3 from Touronjia (Table 7.2, full data available in Appendix 7.2). Gold concentrations at Mathiatis South are the highest averaging 1.56 ppm (n=49) with a maximum Au concentration of 20.43 ppm (Table 7.2). Alpen Rose exhibits the lowest average Au concentration at 0.10 ppm (n=55, Table 7.2) with a maximum Au concentration of 1.02 ppm (Table 7.2, Figure 7.14). In all cases Au concentrations are highly positively skewed. Silver concentrations are variable with a maximum concentration of 32.74 ppm with an average of 3.82 ppm recorded at Kokkinovounaros (Figure 7.14). The Au-Ag ratio varies from 0.14 at Alpen Rose to 0.52 at Touronjia.

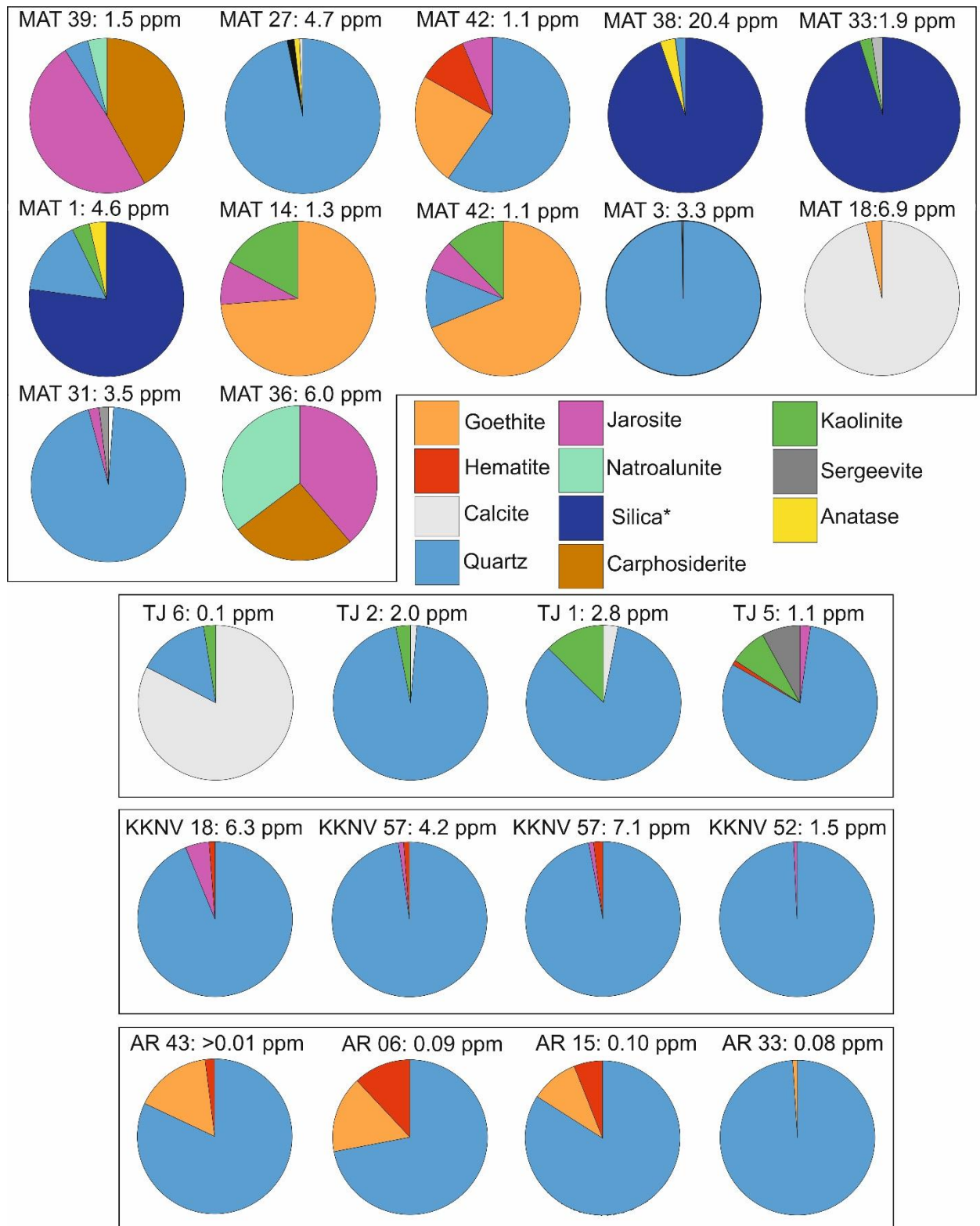


**Figure 7.13:** Modal mineralogy analysed by XRD of samples from Mathiatis South (MAT S), Touronjia (TJ), Kokkinovounaros (KKNV) and Alpen Rose (AR). Data from semi-quantitative XRD analysis (see Chapter 4). Samples from Touronjia, Kokkinovounaros and Alpen Rose are quartz dominated with minor Fe phases whilst Mathiatis South are generally jarosite, goethite and silica-rich. (Silica\* = cristobalite and amorphous phase). Gold grades of corresponding sample shown above in ppm.

	<b>Mn</b> ppm	<b>Fe</b> %	<b>Co</b> ppm	<b>Ni</b> ppm	<b>Cu</b> ppm	<b>Zn</b> ppm	<b>As</b> ppm	<b>Se</b> ppm	<b>Mo</b> ppm	<b>Ag</b> ppm	<b>Cd</b> ppm	<b>Sb</b> ppm	<b>Te</b> ppm	<b>Au</b> ppm	<b>Pb</b> ppm	<b>Bi</b> ppm
<b>Alpen Rose</b>	<b>n=55</b>															
Average	489.1	6.7	85.8	8.5	951.8	294.9	24.8	19.6	9.1	0.70	0.26	1.1	1.4	0.10	9.0	0.47
Median	206.5	3.9	67.1	4.5	161.8	74.3	1.8	5.5	0.72	0.23	0.15	0.16	0.1	0.02	2.2	0.02
Max	2451	43.7	563.7	38.9	5877	5322	376.0	235.7	297.6	6.5	3.3	7.3	27.7	1.0	189.8	14.2
$\sigma$	603.9	8.2	87.3	8.8	1442	737.3	69.2	44.1	40.5	1.1	0.51	1.9	4.3	0.19	26.0	1.96
<b>Mathiatis South</b>	<b>n=49</b>															
Average	3313	14.5	38.2	11.2	1079	258.2	214.4	53.6	123.2	6.6	1.4	11.3	14.0	1.6	216.4	6.8
Median	52.0	8.8	22.8	3.4	275.1	76.3	129.7	17.3	37.2	2.3	0.3	3.0	4.7	0.4	31.8	1.0
Max	64011	37.7	421.5	85.6	23852	2029	1237	1261	1309	31.7	19.9	110.2	109.9	20.4	1508	57.1
$\sigma$	11939	12.8	64.8	19.9	3376	465.2	280.2	177.4	223.4	8.2	3.3	22.9	23.6	3.2	389.0	13.3
<b>Kokkinovounaros</b>	<b>n=59</b>															
Average	2193	10.9	33.6	14.2	1906	470.5	144.1	20.5	30.7	3.8	0.9	6.2	2.6	0.6	130.0	2.4
Median	137.2	6.3	23.1	3.1	142.5	40.3	30.3	7.6	4.3	0.66	0.05	2.0	0.17	0.08	22.5	0.13
Max	24489	48.9	144.2	198.4	57596	7621	2057	423.8	586.2	32.7	19.6	34.4	64.3	7.1	1908	69.2
$\sigma$	5281	10.9	35.2	32.2	7944	1217	373.9	54.8	81.9	7.3	2.8	8.5	11.6	1.3	318.9	9.5
<b>Touronjia</b>	<b>n=6</b>															
Average	17.3	0.90	48.6	2.6	66.9	54.8	94.9	1.5	0.70	2.0	0.13	13.1	0.35	1.0	48.1	0.05
Median	13.4	0.76	39.6	2.2	68.3	38.5	86.0	1.3	0.59	2.0	0.09	9.9	0.11	0.61	31.6	0.02
Max	36.8	1.8	98.4	5.7	146.8	132.9	181.5	3.4	1.2	3.3	0.3	34.8	1.1	2.8	153.7	0.17
$\sigma$	9.8	0.55	26.6	1.6	46.9	51.9	53.3	0.9	0.31	0.81	0.12	10.4	0.40	1.1	51.4	0.06

**Table 7.2:** Whole rock geochemistry (ICP-MS) via aqua-regia digest of low temperature Au-silica deposits. Full data available in Appendix 7.2.

	Mn ppm	Fe %	Co ppm	Ni ppm	Cu ppm	Zn ppm	As ppm	Se ppm	Mo ppm	Ag ppm	Cd ppm	Sb ppm	Te ppm	Au ppm	Pb ppm	Bi ppm
<b>Disseminated</b>	<b>n=9</b>															
Average	1123.6	11.1	69.9	47.5	1106.0	262.9	30.8	33.0	9.3	0.39	0.43	0.80	1.9	0.06	9.3	0.41
Median	1000.9	11.0	47.4	40.1	933.5	158.9	12.2	3.2	0.87	0.22	0.13	0.29	1.5	0.02	2.7	0.56
Max	3299.7	16.9	145.4	141.4	3481.1	845.8	112.0	245.6	72.5	0.94	1.2	4.3	5.4	0.16	58.3	0.87
$\sigma$	1009.2	3.7	38.9	40.3	1105.4	269.3	38.1	75.7	22.4	0.32	0.47	1.3	1.6	0.05	17.5	0.33
<b>Gossan</b>	<b>n=4</b>															
Average	139.8	22.3	36.6	17.1	432.0	279.9	30.5	57.0	14.3	3.0	0.75	0.64	1.2	0.09	84.3	0.57
Median	89.7	23.0	13.9	6.1	201.6	29.3	22.7	47.5	8.9	1.0	0.12	0.37	1.2	0.08	1.5	0.03
Max	363.2	31.7	114.5	56.0	1283.7	1057.8	75.6	130.3	38.3	9.4	2.7	1.8	2.4	0.18	333.9	2.2
$\sigma$	140.7	7.3	45.6	22.9	505.9	449.6	31.4	51.1	15.3	3.8	1.1	0.70	1.1	0.06	144.1	1.0
<b>Jasper</b>	<b>n=11</b>															
Average	250.0	15.7	54.7	9.8	660.7	181.2	84.0	22.9	10.1	1.1	0.5	4.7	3.1	0.07	29.1	1.2
Median	106.7	12.9	36.5	5.1	195.2	80.7	74.9	7.1	2.8	0.61	0.2	2.4	0.5	0.02	18.1	0.09
Max	1607.0	37.8	160.5	28.1	3257.4	1046.9	224.2	176.0	51.0	3.1	2.5	16.6	14.6	0.19	81.2	7.2
$\sigma$	439.3	10.9	45.0	8.9	919.9	290.1	72.3	48.7	14.6	1.0	0.86	5.2	5.2	0.07	27.8	2.3
<b>Massive</b>	<b>n=17</b>															
Average	68.3	27.7	75.7	7.9	1632.1	446.8	176.4	74.3	22.9	2.1	1.0	5.5	15.5	0.14	27.2	5.8
Median	36.7	32.3	67.0	6.5	724.4	161.2	145.1	16.3	13.4	1.4	0.24	3.6	5.3	0.07	27.2	0.38
Max	318.8	39.5	207.5	30.8	6557.1	2529.2	498.3	317.3	134.0	8.2	6.9	19.5	102.3	0.60	62.3	46.0
$\sigma$	81.1	10.6	56.5	7.0	2005.5	617.0	155.7	98.3	32.2	2.3	1.7	5.6	23.7	0.17	19.1	12.1

**Table 7.3:** Whole rock geochemistry (ICP-MS) via aqua-regia digest of VMS samples classified by sample morphology. Full data available in Appendix 7.3.

<i>7.3 continued</i>	<b>Mn</b>	<b>Fe</b>	<b>Co</b>	<b>Ni</b>	<b>Cu</b>	<b>Zn</b>	<b>As</b>	<b>Se</b>	<b>Mo</b>	<b>Ag</b>	<b>Cd</b>	<b>Sb</b>	<b>Te</b>	<b>Au</b>	<b>Pb</b>	<b>Bi</b>
	ppm	%	ppm													
<b>Ochre</b>	<b>n=7</b>															
Average	26601.1	23.2	164.8	81.0	20051.3	233.4	107.1	100.9	30.8	3.1	0.12	3.1	12.4	0.52	48.5	0.75
Median	1095.7	25.8	96.2	30.6	2475.8	225.2	70.9	105.5	23.9	1.7	0.08	2.9	6.6	0.24	41.9	0.55
Max	161332.3	36.4	512.2	199.4	79598.5	526.2	287.3	230.8	66.3	11.8	0.39	5.0	36.3	2.06	86.4	1.5
$\sigma$	55385.3	9.9	146.7	77.5	29329.5	138.8	76.8	72.1	21.7	3.7	0.12	1.3	11.8	0.70	29.5	0.51
<b>SABZ</b>	<b>n=5</b>															
Average	349.2	17.3	148.2	9.4	4303.7	174.8	216.9	269.3	71.0	0.52	0.31	3.3	5.4	0.13	10.0	0.31
Median	302.8	12.1	31.1	2.5	2652.1	164.5	225.8	47.4	74.8	0.56	0.30	2.1	4.7	0.06	6.1	0.03
Max	920.6	30.6	396.6	27.8	13690.2	322.5	371.7	1002.5	113.0	0.72	0.52	6.7	10.9	0.30	26.7	0.89
$\sigma$	345.1	7.8	156.2	10.4	4948.3	81.3	102.0	377.7	37.7	0.17	0.14	2.4	3.6	0.10	8.9	0.36
<b>Semi-massive</b>	<b>n=9</b>															
Average	61.6	20.2	177.1	15.3	4313.3	60.2	130.8	105.3	23.4	1.7	0.13	2.8	11.0	0.30	11.7	0.86
Median	25.3	25.6	45.4	14.6	932.7	54.2	135.0	66.0	6.7	1.3	0.12	1.5	10.1	0.26	10.2	0.84
Max	327.5	33.5	763.0	35.1	21856.4	130.3	529.3	271.6	89.7	4.9	0.30	10.6	26.2	0.78	27.8	1.8
$\sigma$	96.3	11.4	233.7	10.6	7194.3	38.4	153.9	99.6	32.6	1.3	0.08	3.1	8.0	0.22	7.1	0.58
<b>Stockwork</b>	<b>n=8</b>															
Average	647.4	17.6	83.0	35.4	5656.2	119.2	66.5	37.5	5.5	1.2	0.25	0.24	5.4	0.07	10.2	0.19
Median	427.8	13.8	81.7	39.3	2435.2	44.8	4.4	16.3	1.9	1.5	0.10	0.18	3.3	0.02	0.55	0.11
Max	2829.3	39.6	145.2	53.6	22379.3	584.9	485.9	131.6	27.7	2.2	1.12	0.49	18.2	0.28	62.8	0.57
$\sigma$	849.9	9.5	43.0	15.1	7168.6	179.3	158.6	40.5	8.5	0.68	0.34	0.18	5.4	0.09	20.4	0.19

**Table 7.3 (cont.):** Whole rock geochemistry (ICP-MS) via aqua-regia digest of VMS samples classified by sample morphology. Full data available in Appendix 7.3.

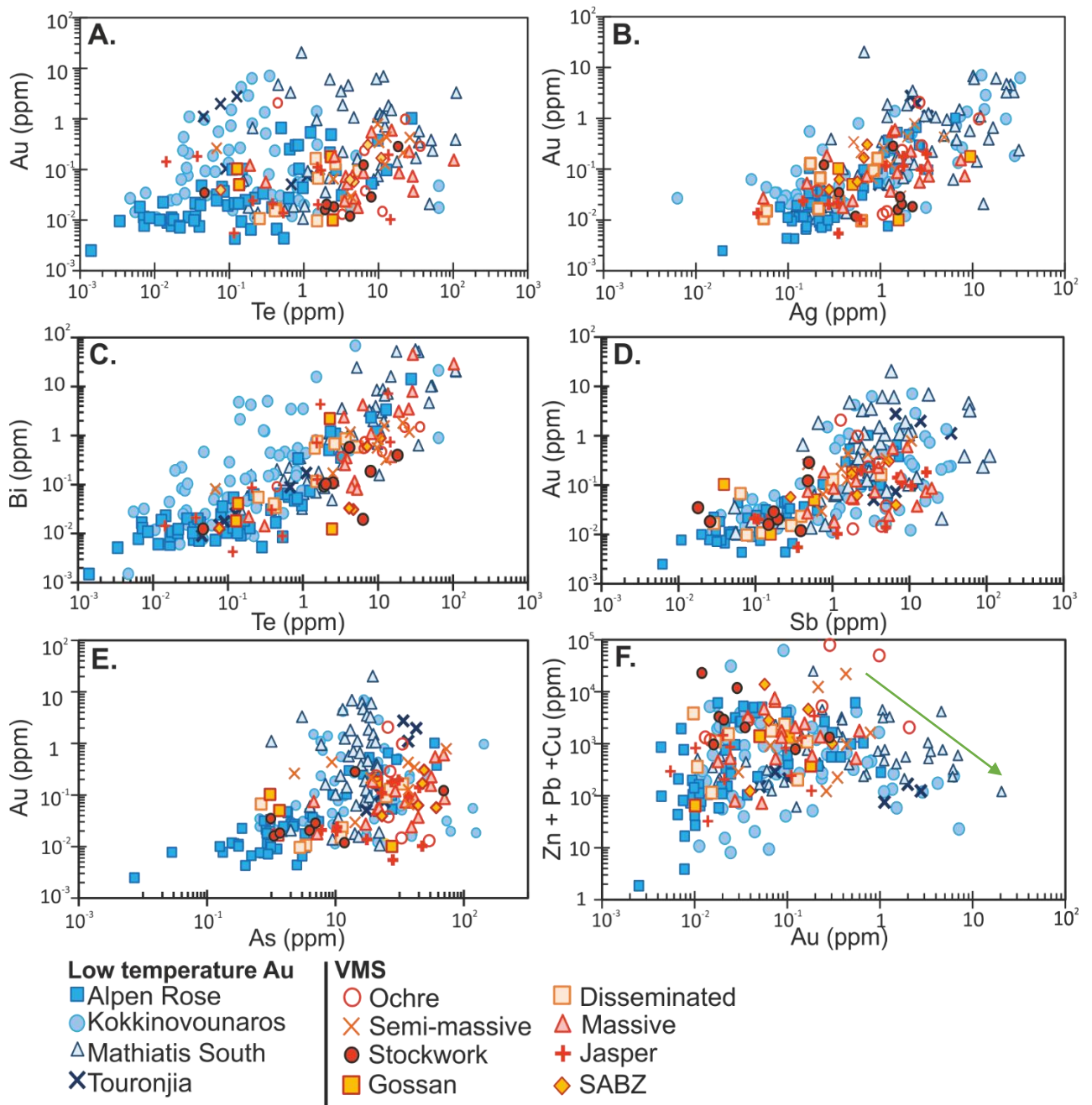


**Figure 7.14:** Whole rock geochemistry (aqua regia) for low temperature silica-rich mineralisation (n=169) and VMS (n=69) classified by location and sample morphology (in ppm). A) Au vs. Te, B) Au vs. Ag, C) Bi vs. Te, D) Au vs. Sb, E) Au vs. As and F) BMS vs. Au; note increasing Au at decreasing BMS (green arrow). Element correlation is summarised in Figure 7.15 and 7.16. Broad positive correlations are noted between Au and Ag, Sb and between Bi and Te. Note Te enrichment in massive samples at Mathiatis South to >1000 ppm. Detection limits available in Appendix 4.

Correlations between elements are summarised in Figure 7.15. Uniformly across all low temperature silica-rich deposits Cu, Ni and Zn exhibit a negative correlation with Au. Conversely, only Ag exhibits a positive correlation with Au across all deposits. At Alpen Rose a positive correlation is noted between Au and Fe, As, Mo, Sb, Te, Pb and Bi. For all other deposits Au exhibits a negative correlation with Fe (Figure 7.15): Full correlation matrices are available in Appendix 7.5.

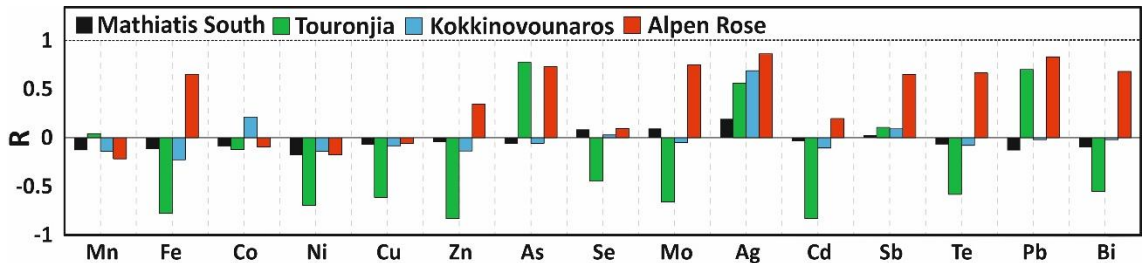


**Figure 7.15:** Linear R values of selected elements vs. Au (full correlation matrices in Appendix 7.5). Note the moderate correlation between Zn, Pb and Fe with Au at Alpen Rose. In all other deposits, most notably Touronjia, Au exhibits a negative correlation with Fe and Cu. Minimal correlation between Au and all elements considered is recorded at Mathiatis South.

Gold concentrations in VMS samples are low averaging 0.18 ppm across all ore types (n=70), they are highly positively skewed towards low concentrations (n=70; Table 7.3, Figure 7.14 and 7.17). Ochres, Fe-rich sediments produced from the weathering of hypogene sulfide contain the highest average Au at 0.56 ppm (max= 2.1 ppm- n=7) (Table 3). Semi-massive sulfide samples contain twice as much Au as massive samples at 0.30 compared to 0.17 ppm in massive samples (Table 7.3). Semi metals Bi and Sb are enriched in massive samples and Ag is concentrated in ochres (Table 7.3 and Figure 7.14). Element correlation with Au in VMS is highly variable (Figure 7.16). With the exception of massive sulfide and stockwork samples, Au exhibits a positive correlation with Ag (Figure 7.16). Correlation between Au and Te is variable ranging from 0.90 in stockwork ore to -0.17 in ochre (Figure 7.16).

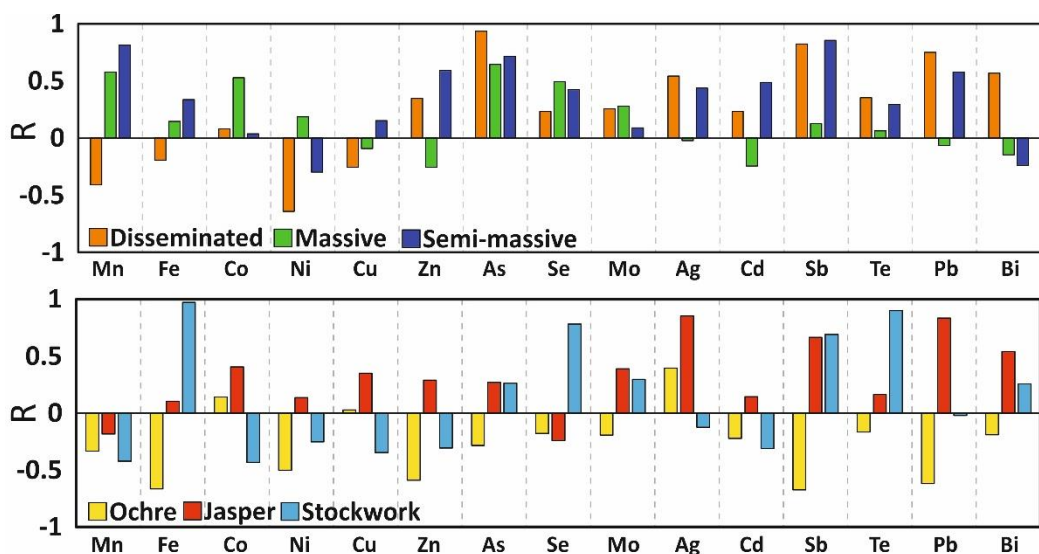


**Figure 7.16 (previous page):** Linear R values of selected elements vs. Au for VMS samples (full correlation matrix in Appendix 7.5). Correlation between different ore morphologies is extremely variable. A strong correlation with Fe suggests Au is hosted in sulfide material (e.g. in massive and semi-massive samples).

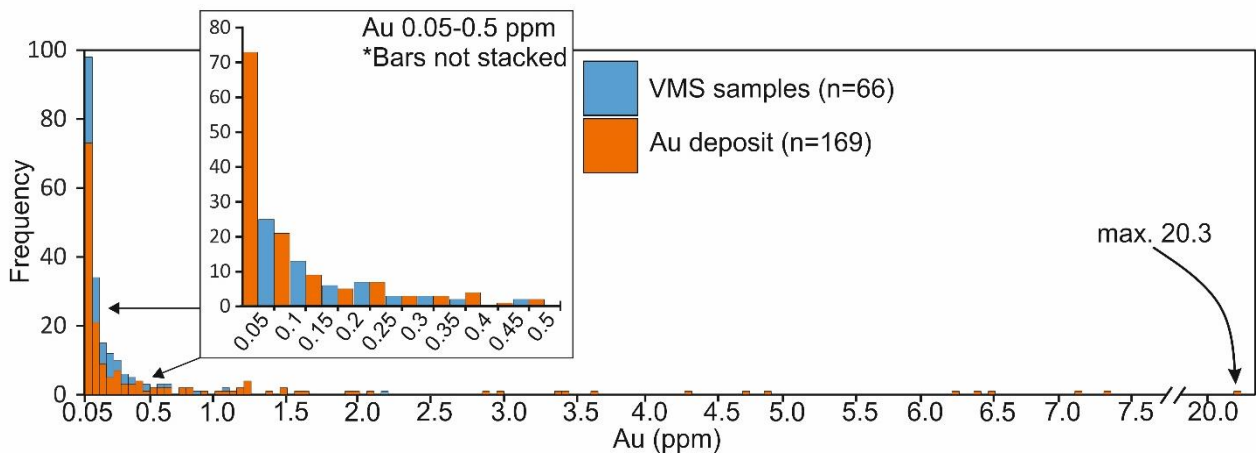


**Figure 7.17:** Histogram of Au concentrations in VMS and Au deposits (Touronjia, Mathiatis South, Alpen Rose and Kokkinovounaros). Gold concentrations are highly skewed towards concentration >0.5 ppm.

## 7.6 Discussion

### 7.6.1 Gold in VMS deposits

High temperature >350°C black smoker VMS mineralisation in the Troodos ophiolite generally contains low Au concentrations (Adamides, 2010a,b; Martin *et al.*, 2019 (Chapter 5); Hannington *et al.*, 1998). Deposits of the Kalavasos mining district of southern Troodos are enriched in Au to ppm levels in pyrite (Chapter 5) reflecting the increased proportion of ultramafic Au-rich footwall lithologies and the enhanced stability of AuHS<sup>-</sup> complexes (Patten *et al.*, 2016; Chapter 5). Gold from 10 VMS analysed in this study average 0.18 ppm (n=66) in whole rock compared with 0.95 ppm in pyrite (Martin *et al.*, 2019- Chapter 5 and 8). This demonstrates that Au is probably hosted in pyrite and not as discrete native grains, if this was the case whole rock Au concentrations would be higher relative to those analysed in pyrite. Gold is enriched in semi-massive ore relative to all other ore types at 0.3 ppm (n=9). Semi-massive mineralisation is silica-rich and forms on the margin of the VMS mound, the enrichment in Au relative to massive (0.14 ppm, n=17) and stockwork (0.07, n=8) samples reflects the formation of semi-massive ore at lower-temperatures under more oxidising conditions (cf. section 7.6.7).

The low Au content in stockwork ore samples (0.07 ppm, n=8) is attributed to the increased abundance of chalcopyrite relative to pyrite and the diminished ability of chalcopyrite to incorporate Au relative to pyrite (George *et al.*, 2018; Huston *et al.*, 1995; Martin *et al.*, 2019, Chapter 5). Chalcopyrite-rich zones in modern SMS systems such as TAG are generally Au-poor

relative to massive pyrite or sphalerite bearing samples (Hannington *et al.*, 1998). High temperature (>300°C) massive pyrite samples from TAG contain 0.48 ppm Au compared with low temperature white smoker massive pyrite samples that average 2.8 ppm (Hannington *et al.*, 1995). Ultimately the low Au grades in Troodos VMS are attributed to the low potential of  $\text{AuCl}_2^-$  and  $\text{AuHS}_2^-$  complexes to transport Au at temperatures in excess of 350°C at low pH (2-4) and moderately reduced conditions synonymous with mature VMS hydrothermal systems (e.g. Tivey *et al.*, 1995) (Figure 7.1 and 7.2; section 7.5.6). Furthermore, lower temperature fluids associated with off axis hydrothermal fluid flow may become enriched in Au relative to Troodos VMS due to enhanced stability of  $\text{AuHS}^-$  complexes at low temperatures that lead to the preferential mobilisation of Au from source regions (cf. Figure 7.1).

### 7.6.2 Low temperature venting

Temperature data for two deposits in Troodos suggest that sites of low temperature venting occurred distally to high temperature discharge zones associated with VMS deposits. Application of the sphalerite geothermometer to previously published Zn/Fe data from sphalerite after Adamides (2013) highlights sites of lower temperature mineralisation in the Troodos hydrothermal system. A low Fe content in sphalerite indicates formation at lower temperatures (Hannington and Scott, 1989; Keith *et al.*, 2014; Tivey *et al.*, 1995) and using the equation  $\text{Fe}/\text{Zn}_{\text{sphalerite}} = 0.0013 (T) - 0.2953$  (Keith *et al.*, 2014) a minimum precipitation temperature has been calculated (Figure 7.18, overleaf). Adamides (2013) describe a Zn-rich prospect S of Mitsero (Adamides, 2013) where sphalerite Zn/Fe ratios yield average precipitation temperatures of 246°C (max= 273°C, min=230°C, n=14; Figure 7.18). This temperature is significantly lower than those typical in black smoker vents (Keith *et al.*, 2016a; Tivey *et al.*, 1995).

When compared to sphalerite data for modern vents (Keith *et al.*, 2016b; Koski *et al.*, 1984; Tivey *et al.*, 1995) and the Skouriotissa VMS in Troodos (Keith *et al.*, 2016a) a bimodal distribution in temperature is observed (Figure 7.18). White smoker hosted sphalerite from TAG (Tivey *et al.*, 1995) and the Cleft segment of the southern Juan de Fuca Ridge (Koski *et al.*, 1984) yield identical temperatures to those analysed at Touronjia (fluid inclusions) and those reported for the mineral prospect S of Mitsero (Adamides, 2013; Figure 7.18). In contrast, sphalerite from Skouriotissa VMS yields average temperatures consistent with a high temperature fluid source averaging 495°C (Keith *et al.*, 2016a), comparable to other active high-temperature vents (Figure 7.18).

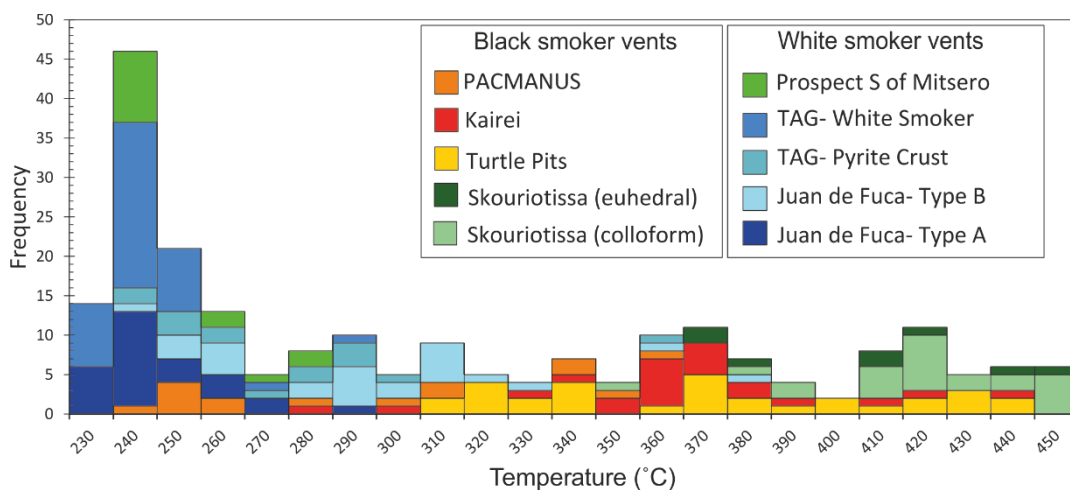


**Figure 7.18:** Temperature derived from sphalerite geothermometry for sediment free hydrothermal fields (after Keith *et al.*, 2014). Data highlights a bimodal distribution in vent temperature. Sphalerite from white smoker vents yields a temperature averaging 240°C while sphalerite from black smoker vents yield a higher temperature of >350°C. Troodos data is highlighted in green, two populations exist between a 'typical VMS' and low temperature deposits (prospect S of Mitsero) (Data from Adamides, 2013; Keith *et al.*, 2014; 2016a,b; Koski *et al.*, 1986; Tivey *et al.*, 1995).

The temperature derived from sphalerite Zn/Fe ratios in Troodos at the mineral prospect S of Mitsero calculated in this study using data from Adamides *et al.* (2013) are identical to those calculated using published data for TAG and the South Juan de Fuca ridge in low temperature white smoker vent sites. Low temperature discharge sites in active hydrothermal fields are reported as localised features for example, the Kremlin area of the TAG mound is approximately 20-50 m in diameter and situated <100 m away from high temperature black smoker vents (Tivey *et al.*; 1995). Increased silica abundance is also described for white smoker vents with amorphous silica and barite commonly intergrown with sulfides (Tivey *et al.*, 1995; Koski *et al.*, 1984).

### 7.6.3 Touronjia

At Touronjia high Au concentrations are associated with a silicified breccia unit (Figure 7.11). Clasts of angular, oxidised lava and basal group material occur in a pervasively silicified quartz-rich matrix. Clasts are variably silicified, presumably reflecting variation in their primary mineralogy and permeability. Within the matrix pyrite forms subhedral to anhedral grains (generally < 100 µm) with sphalerite and chalcopyrite as accessory phases (<1 wt.%: Figure 7.9). The inclusion of magnetite/hematite rimming sulfide grains and oxidisation of chalcopyrite to covellite suggests the presence of oxidising late stage fluids (Figure 7.9). Touronjia has previously been described as a pseudo-epithermal type deposit; a deposit that formed from an increased magmatic volatile influx characterised by advanced argillic alteration assemblages indicating the presence of acidic fluids, similar to subaerial epithermal type systems (Naden *et al.*, 2006; Jowitt *et al.*, 2005).

In this study the author prefers an explanation for the oxidised mineralisation from a low temperature, moderately oxidised (hematite stability field) seawater derived fluid. It is acknowledged that sub-seafloor epithermal style 'high sulfidation' mineralisation (e.g. Sillitoe *et al.*, 1996) does exist in back-arc (e.g. Hine Hina, Lau Basin; Herzig *et al.*, 1998a) and arc volcanos (e.g. Cone site, Brothers, Kermadec Arc; de Ronde *et al.*, 2005) however there is limited evidence for this style of mineralisation in Troodos (Jowitt *et al.*, 2005). The tectonic setting between active 'high sulfidation' environments and Troodos is distinctly different from for example, the Brothers vents site, that is influenced by the occurrence of more felsic volatile-rich magma compositions and a shallow water depth of ~1.6 km (de Ronde *et al.*, 2005); both of which promote the generation of high sulfidation mineral assemblages.

Sulfur isotope ( $\delta^{34}\text{S}$ ) values in pyrite from Touronjia indicate fluids of seawater origin with a minor magmatic component. Sulfur isotope values at Touronjia ( $\delta^{34}\text{S}_{\text{V-CDT}}\text{‰}$ ) range between +1.3-2.9 ‰ and average +2.3 ‰ (n=5) (Parvaz 2014; Chapter 8). These values reflect a sulfur source derived from the thermochemical reduction of Cretaceous seawater sulfate (18-19‰-Kampschulte and Strauss, 2004; cf. Chapter 8) and the leaching of sulfur from igneous rocks (Troodos magmatic mean 0-1‰ -Alt, 1994) (McDermott *et al.*, 2015). In contrast,  $\delta^{34}\text{S}$  values for seafloor epithermal style magmatic dominated mineralisation are consistently light (i.e. <0‰) reflecting an increased magmatic influx and associated  $\text{SO}_2$  disproportionation. For example at the Brothers Cone site  $\delta^{34}\text{S}$  values in pyrite average -4.2 ‰ (n=4; de Ronde *et al.*, 2005) and those at Hine Hina average -5.3 ‰ (n=9; Herzig *et al.*, 1998a), significantly lighter than those in pyrite at Touronjia. Thus the average  $\delta^{34}\text{S}$  at Touronjia is analogous of a seawater dominated hydrothermal system (+4.4 to +8.2; Hannington *et al.*, 1998) with sulfur derived principally from thermochemical seawater sulfate reduction.

Fluid boiling and phase separation have been proposed by some authors as a mechanism explaining the enrichment of Au at Touronjia and the generation of acid-sulfate low pH fluids responsible for the 'high sulfidation' mineral assemblage observed (e.g. dickite and kaolinite; Naden *et al.*, 2006). However, fluid inclusion analyses by Naden *et al.* (2006) suggest a single phase, seawater derived fluid at Touronjia. Salinities of 11 quartz hosted fluid inclusions ranged from 2.8 to 6.1 wt.% NaCl equivalent (average 3.8 wt.%). If boiling was an ore forming process at Touronjia, fluid inclusions would yield NaCl contents significantly lower or higher than seawater salinity (3.5 wt.% NaCl) reflecting the formation of a vapour and brine, and a 'boiling assemblage' consisting of associated vapour and brine inclusions would be expected, which was not observed (e.g. de Ronde *et al.*, 2011; Koschinsky *et al.*, 2008). Furthermore, homogenisation

temperatures of fluid inclusions yielded temperatures ranging from 111 to 249°C (average=209°C, n=12: Naden *et al.*, 2006). At these temperatures the critical point of seawater would not be expected to be intersected (Chapter 3). Either a significant increase in temperature (>400°C) or a large decrease in hydrostatic pressure (i.e. water depths >1000 m) would be required to exceed the critical point of seawater (Humphris and Klein, 2018; Keith *et al.*, 2016a; Mercier-Langevin *et al.*, 2011). The inferred water depth of the Troodos ophiolite, as constrained by carbonate free radiolarite-rich sediments directly overlying the ophiolite (Robertson, 1975) is inferred to be below the carbon compensation depth (CCD) at approximately 3500 m water depth (Tyrrell and Zeebe, 2004). At 3500 m water depth (~350 bars) and temperatures <250°C the critical point of seawater would not be intersected, thus phase separation would not occur.

At Touronjia the alteration mineral assemblage identified in this study does not support the occurrence of a high sulfidation type fluid. Samples contain predominantly quartz (average 73 vol.%, n=5), minor kaolinite (average 7 vol.%, n=4), variable calcite (1 to 83 vol.%) and minor jarosite, hematite and sergeevite (<<10 vol.%- Figure 7.13). The elevated calcite in sample TJ 6 (83 vol.%) is attributed to country rock contamination and the analysis of Lower Lefkara group limestone that overlies the formation, this sample also contains low Au. Previous studies (Jowitt *et al.*, 2005; Naden *et al.*, 2006) identify kaolinite, dickite and nacrite at Touronjia. These minerals have been previously identified in 'epithermal type' seafloor mineralisation (Ishibashi *et al.*, 2015; Jade, Okinawa; Sillitoe *et al.*, 1996, Kamikita-Honko) but the lack of any other characteristic high sulfidation mineral assemblage e.g. diaspore, natroalunite or pyrophyllite suggests a secondary origin for kaolinite. The author suggests a supergene, low temperature (~50°C) origin for kaolinite-(dickite) through the alteration of plagioclase bearing lithologies at Touronjia (Curtis and Spears, 1971; Papoulis *et al.*, 2004). Other high temperature  $\text{Al}_2\text{Si}_2\text{O}_5(\text{OH})_4$  polymorphs are difficult to explain through a supergene processes, however as no dickite was identified in this study (below XRD detection <5 vol.%) the author is unable to comment on its significance.

#### 7.6.4 Kokkinovounaros

Gold at Kokkinovounaros averages 0.56 ppm (n=59) with 7 samples containing > 1 ppm Au (max 7.08 ppm). Gold is enriched in samples containing quartz and hematite collected from within an exploratory adit to the N of Kokkinovounaros (Figure 7.8 G and H). Mineralisation is fault controlled, sulfide poor and with a prominent brecciated morphology. The absence of sulfide minerals and abundant hematite suggests a higher  $f\text{O}_2$  relative to the VMS hydrothermal system where pyrite is the major iron bearing phase. As shown by Herzig *et al.* (1991) Au may also be

concentrated in both supergene seafloor and subaerial environments. In addition to the hypogene enrichment of Au in silicified breccias at Kokkinovounaros, Au may be concentrated via the supergene oxidation of pyrite. Cubic shaped voids and an alteration assemblage characterised by Fe oxy-hydroxides and jarosite suggest extensive pyrite dissolution generating H<sub>2</sub>SO<sub>4</sub> (Parvaz 2014; Vear and Curtis, 1981). The effect of supergene leaching is extreme in some areas (Figure 7.19 overleaf), especially where a bleached halo associated with the main pit fault contains 100% amorphous silica (+/- cristobalite) (Figure 7.13, KKNV 52) reflecting the, oxidation, replacement and leaching of Fe phases leaving only residual silica. This likely reflects increased permeability and fluid flow along the fault plane during supergene weathering. A high pyrite volume in adjacent units and increased permeability would lead to the formation and channelling of large quantities of H<sub>2</sub>SO<sub>4</sub> rich fluids facilitating extensive leaching and alteration of wall-rock.

Laser ablation ICP-MS of disseminated pyrite at Kokkinovounaros (n=18) show low Au concentrations with 12 analysis above detection limit (<0.01 ppm), however, pyrite is enriched in As, Ag, Pb and Sb (Table 7.4). Therefore, pyrite dissolution during supergene alteration does not effectively explain the enrichment of Au in hematite-rich samples to ppm concentrations. Pyrite oxidation does however explain high As levels in goethite-Jarosite-rich samples (max 3058 ppm) as pyrite originally contained high As (average 771 ppm, n=18, Table 7.4 and Figure 7.20) that was liberated and concentrated during oxidation and the formation of residual Fe phases (Figure 7.18 and 7.19; Lu *et al.*, 2005). Gold enrichment in hematite-silica samples at Kokkinovounaros is interpreted to be hypogene in origin i.e. a primary seafloor feature (Figure 7.20) as jasper mineralisation exhibits no evidence of acid leaching.

**Table 7.4:** Laser Ablation ICP-MS analysis of pyrite from Kokkinovounaros. Gold concentrations are low (6 of 18 BDL). Pyrite is notably enriched in Ag, As, Pb and Sb.

(ppm)	Co	Cu	Zn	As	Se	Ag	Cd	Sb	Te	Au	Pb	Bi
Average	52.9	0.02	194.8	851	163.3	24.4	2.4	55.3	1.4	<b>0.15</b>	457	0.15
Median	40.6	0.01	28.6	771	163.3	25.1	2.4	65.9	1.3	<b>0.15</b>	433	0.15
Max	172	0.03	1613.6	1675	193.5	48.5	4.5	139	3.0	<b>0.35</b>	917	0.35
$\sigma$ (n=18)	46.6	0.01	473.7	498	30.3	11.4	2.1	38.7	0.65	<b>0.08</b>	258	0.08

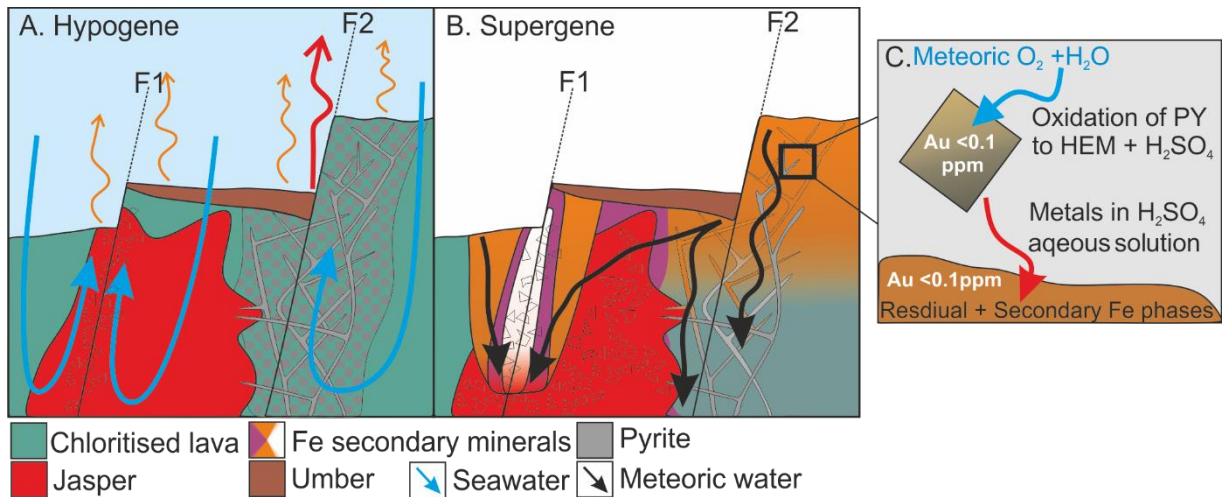


**Figure 7.19:** Schematic cross-section through Kokkinovounaros mineralisation. A) Kokkinovounaros forming on the seafloor. Hypogene mineralisation is focused around two N-S faults. The main pit fault (F1- mined for Au) is characterised by extensive seawater interaction and the precipitation of jasper (hematite + silica). In contrast the second fault (F2) was characterised by higher temperature more reduced fluids forming a pyrite stockwork. B) Upon exposure and weathering, supergene oxidisation of pyrite (C) is centred along zones of increased permeability (F1 and F2) and leads to the formation of secondary Fe phases (jarosite, goethite, hematite and residual silica). See text for further discussion.

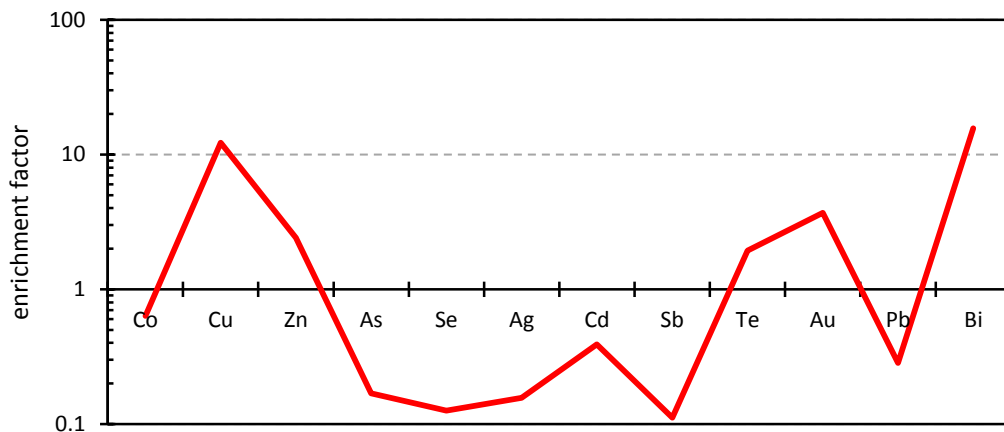


**Figure 7.20:** Enrichment factor for average Kokkinovounaros whole rock trace element composition (n=59) against average Kokkinovounaros pyrite trace element composition (n=18). Elements that plot above 1 are enriched in whole rock samples relative to pyrite. In conjunction with the mineralogy of Au-rich samples, this suggests a hypogene seafloor origin for Au at Kokkinovounaros.

This study demonstrates that a wide variety of elements including Te and Se may potentially become enriched in goethite-jarosite (Fe(oxy)hydroxide)) supergene material with maximum concentrations of 64.3 and 423 ppm respectively (Table 7.2). Tellurium and Se in these samples are probably adsorbed onto Fe oxides (e.g. Bullock *et al.*, 2018; Rovira *et al.*, 2008). Previous studies have demonstrated that Fe phases such as goethite and hematite can effectively adsorb large quantities of Se (e.g. 1590 ppm, Kisgruva VMS; Bullock *et al.*, 2018). This is due to the

fixation of Se and Te as  $\text{SeO}_3^{2-}$  and  $\text{TeO}_3^{2-}$  ion species (selenite and tellurite) and their direct adsorption onto secondary Fe phases. In this study Te and Se concentrations in supergene Fe oxide phases at Kokkinovounaros (and Mathiatis South) are comparable to those described by Bullock *et al.* (2018) and suggest Te and Se are enriched via similar mechanisms. This highlights the potential to concentrate Te and Se to in VMS weathering products (i.e. ochres) in both a seafloor and subaerial related supergene processes.

Hydrothermal fluid flow at Kokkinovounaros may have been short lived and ceased before lava eruption (magmatism) had ended as 'unaltered' lava is directly overlain by highly altered lava (Figure 7.21). To the N of Kokkinovounaros lavas are moderately brecciated but pillow outlines are discernible and the contact with overlying bleached unit is sharp containing gypsum and malachite indicating fluid channelling (Figure 7.21). The unaltered nature of this lava pile suggest at least in part, oxidisation and supergene processes at Kokkinovounaros must have occurred on the seafloor. Seafloor alteration was most likely overprinted by later supergene subaerial weathering during the emergence of Troodos. If oxidation was solely due to uplift and exposure then the lava pile, that now appears unaltered, would be extensively leached to a similar degree as surrounding lavas. The close proximity of the lava pile to the F1 pit fault (Figure 7.21) and relatively thin crust of material that overlies the lava would preferentially channel fluids away from the lava pile due to increased permeability along the fault and could explain its apparent unaltered appearance.

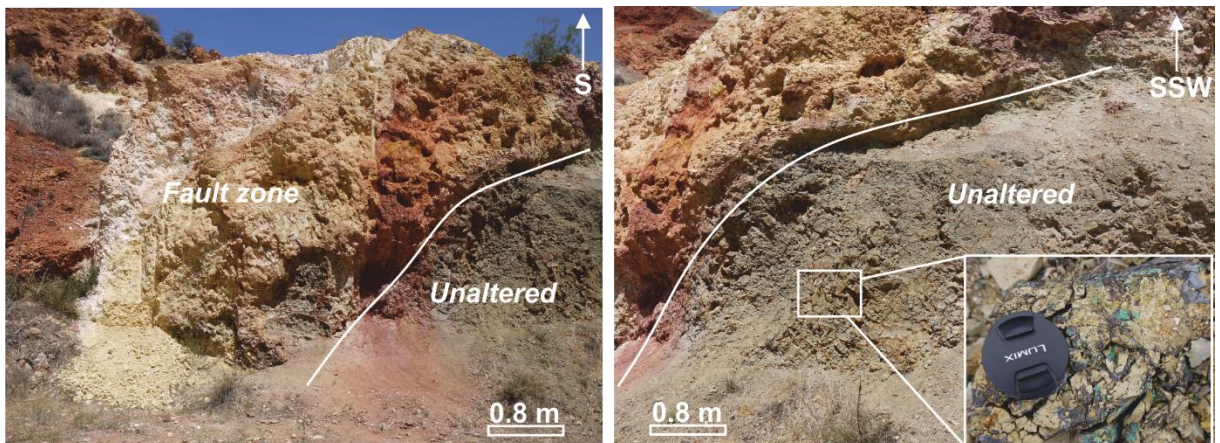


**Figure 7.21:** Unaltered lava pile in close proximity to fault zone at Kokkinovounaros.

### 7.6.5 Mathiatis South

The Mathiatis South deposit contains the highest Au concentrations analysed in this study. Several small massive sulfide lenses are limited to the N of the open pit and the exposed lenses are 3-4 m wide, pyritic with abundant chalcantite. Laser Ablation ICP-MS of pyrite from

Mathiatis South yields low Au concentrations averaging 0.06 ppm but high average Zn at 10,868 ppm (n=21) (Martin *et al.*, 2019; Chapter 5). These low Au concentrations in massive pyrite samples are confirmed in this study with the analyses of bulk-rock massive sulfide samples that contain 0.09 and 0.19 ppm Au respectively (Appendix 7.2).

Mechanisms for Au enrichment at Mathiatis South are two-fold: namely supergene gossan formation and hypogene silicification related. The mineralogy of Au bearing samples at Mathiatis South is diverse suggesting that a combination of hypogene and supergene processes are responsible for Au enrichment. High Au concentrations are associated predominantly with either goethite-jarosite samples (Figure 7.13: Mat 42/14) or quartz dominant samples (Figure 7.13: MAT 3/38).

Gossan formation is most extensive to the S of the Mathiatis South open pit. Supergene weathering is well-developed with a thick profile of goethite-jarosite-hematite-rich earthy gossan (5-6 m) representing the oxidation of hypogene disseminated pyrite mineralisation (as for Kokkinovounaros, section 7.5.3). Gold is dissolved from primary pyrite (or other sulfides), transported in solution and deposited in response to changes in groundwater pH, interaction with carbonate material or in a subaqueous environment due to seawater interaction. The progressive weathering of sulfide ore (submarine or subaerial) leads to an enrichment in Au as described for ochres by Herzig *et al.* (1991). Furthermore, Au is also enriched in zones containing quartz with only minor jarosite and goethite; these zones occur as discrete pods 2-3 m wide in the centre of the pit. Within these zones no sulfides were discovered and samples typically exhibit a brecciated vuggy texture (Figure 7.6 E and H). These areas could represent localised conduits of cooler, oxidised fluids that formed low temperature 'white smoker type' vent sites (Berkenbosch *et al.*, 2012; Maslennikov *et al.*, 2017; Urabe and Kusakabe, 1990).

X-ray diffraction of samples from Mathiatis South identify the occurrence of natroalunite (MAT36/39/27- Figure 7.13). Natroalunite is associated with acidic hydrothermal fluids, generally within acid sulfate or advanced argillic alteration assemblages documented in active seafloor hydrothermal systems such as the Brothers Cone site (de Ronde *et al.*, 2005; Reyes *et al.*, 2006). At Mathiatis South natroalunite generally occurs in trace amounts <5 vol.% with the exception of sample MAT36 where it constitutes 35 vol.% (Figure 7.13). To the authors knowledge, outside Tournonjia (Naden *et al.*, 2006) this is the only documented occurrence of natroalunite in Troodos. Whilst natroalunite does form a hypogene alteration phase in seafloor hydrothermal systems, at Mathiatis South a supergene origin is preferred. Alunite - natroalunite are widely documented in supergene environments (e.g. Arehart *et al.*, 1992; Bladh, 1982;

Cunningham *et al.*, 2005; Long *et al.*, 1992). At Mathiatis South this is supported by the occurrence of jarosite in natroalunite bearing samples; the formation of jarosite vs. natroalunite being controlled by the relative molarity of  $\text{Al}^{3+}$  and  $\text{Fe}^{3+}$  (Bladh, 1982). It is therefore likely that natroalunite formed under low pH conditions during weathering of sulfide and generation of  $\text{H}_2\text{SO}_4$ . Whilst this study prefers a supergene origin for natroalunite, a seafloor origin is unlikely but cannot be excluded.

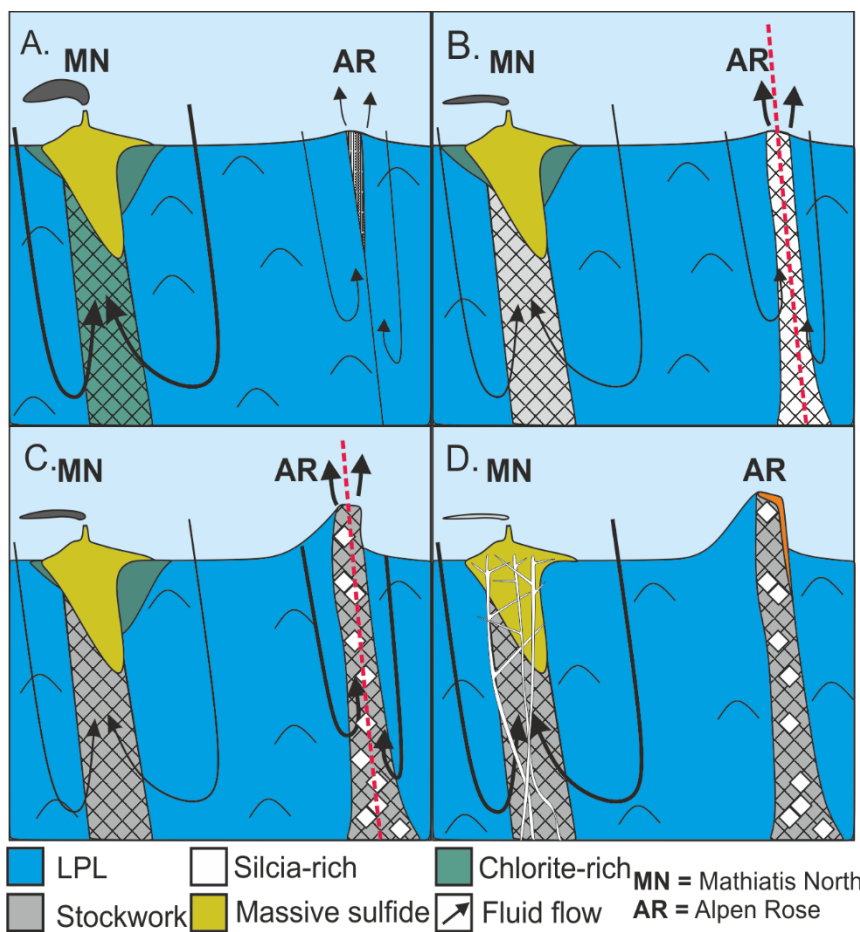
In addition to jarosite, natroalunite and goethite-rich samples, Au exhibits a close correlation with quartz and silica (cristobalite + amorphous phase) (Figure 7.13, MAT 38). As observed in Kokkinovounaros, this probably represents the occurrence of low temperature, and in samples with abundant amorphous silica (+/- cristobalite), silica saturated fluids. Samples with high silica contents exhibit low jarosite-goethite concentrations suggesting the silica-Au association is hypogene in origin further supporting that discrete pods formed low temperature fluid discharge sites and were not produced through leaching during supergene alteration (cf. section 7.6.7).

### 7.6.6 Alpen Rose

This study is the first to describe the Alpen Rose area. Initially Alpen Rose was investigated as a potential Au prospect, though average Au concentrations analysed in this study were low at only 0.10 ppm (n=55). However, the complex relationship between structure and silicification at Alpen Rose helps to constrain the timing and factors leading to the enrichment of Au in other areas. Mineralisation at Alpen Rose exhibits remarkable similarities to other deposits considered: it is quartz-rich with no visible massive sulfide but in contrast to many other deposits it contains low Au. This study suggests that Au at Alpen Rose is associated with sulfide mineralisation and not silicified facies. Alpen Rose is the only locality where Au exhibits a moderate positive correlation with Fe ( $R=0.65$ - Figure 7.15). Furthermore, Au concentrations are similar to massive sulfide samples at 0.18 ppm (n=66) suggesting now secondary Fe phases were probably once sulfide dominated.

The geochemistry of Alpen Rose samples is distinctly different from other low temperature silica-rich deposits considered in this study. Unlike Kokkinovounaros, Mathiatis South and Touronjia where mineralisation is enriched in Cd, Pb, Ag, Sb and As (Table 7.2 and 7.3) relative to massive VMS samples. Alpen Rose is depleted in Au, Te and Zn but enriched in Mn and Co, this could suggest it formed a site of distal but relatively high temperature venting as Mn

commonly remains in solution longer than other trace elements during seawater mixing and Co is preferentially enriched in high temperature fluids (e.g. Cu- Seewald and Seyfried Jr., 1990). Field observations suggest that the majority of quartz at Alpen Rose formed early in deposit paragenesis (Figure 7.22 A). Brecciation at Alpen Rose shows that quartz formation predates sulfide mineralisation (Figure 7.22 A and B). Initial quartz brecciation occurred during a period of increased fault movement that led to a localised increase in permeability at Alpen Rose facilitating a high temperature phase of sulfide precipitation (Figure 7.22 C and D). The precipitation of sulfide minerals occluded initial permeability pathways effectively sealing the Alpen Rose hydrothermal system from later, low temperature silica and Au-rich fluids (Figure 7.22 D). Low Au concentrations at Alpen Rose can be explained by a) the timing of silicification and quartz formation relating to fault movement, b) the high temperature origin and reduced solubility of Au in associated fluids, and C) sulfide precipitation leading to the occlusion of late stage fluid pathways (Figure 7.22).



**A.** Alpen Rose forms as fault bound mineralisation S of the Mathiatis North VMS. Low temp. Si-rich fluids precipitate quartz.

**B.** Fault movement increases fluid flow at Alpen Rose, large quartz veins and quartz breccias form

**C.** Occlusion of fluid pathways at Mathiatis North and ongoing fault movement at Alpen Rose leads to high-T fluid phase and sulfide precipitation at Alpen Rose

**D.** Occlusion of flow pathways at Alpen Rose- fault movement ceases- and Low-T fluids channelled through Mathiatis N.

**Figure 7.22:** Schematic summary of Alpen Rose formation.

---

### 7.6.7 Models for gold enrichment

The distribution of Au between VMS and silica-rich deposits of the Troodos ophiolite is bimodal with silica-rich deposits enriched in Au relative to a typical Troodos VMS. This study suggests that silica-rich deposits of Troodos are comparable to modern day sites of effusive low temperature venting (i.e. white smoker type; Hannington *et al.*, 1991; Hannington and Scott, 1989; Maslennikov *et al.*, 2017; Tivey *et al.*, 1995). Deposits share many similar attributes to modern low temperature seafloor vents; a) abundant silica and silicification, b) vents occur distally to high temperature VMS deposits, c) contain elevated Au and d) contain indirect mineralogical and geochemical evidence of low temperature fluids <300 °C.

Whole rock trace element geochemistry is systematically different at sites of low temperature venting with an enrichment of Cd, Pb, Ag, Sb, As and Au due to I) their preferential incorporation in sphalerite (e.g. Cd; Cook *et al.*, 2009) and II) their increased affinity or enhanced ligand stability in low temperature fluids (e.g. Auclair *et al.*, 1987; Huston and Large, 1989; Keith *et al.*, 2016a; Metz and Trefry, 2000; Williams-Jones *et al.*, 2009). At Mathiatis South an enrichment in Cd, Pb, Ag, Sb, As and Au relative to average concentrations from massive Troodos VMS ore is observed. For example, As averages 214 ppm (n=49) at Mathiatis South and only 176 (n=17) ppm in massive ore (Table 7.2 and 7.3). Furthermore, high temperature elements such as Co are depleted in silica-rich deposits relative to massive ore except at Alpen Rose at 75.7 and 85.8 ppm for massive ore and Alpen Rose samples respectively (Table 7.2 and 7.3). As no temperature data exists for Mathiatis South the enrichment of Cd, Pb, Ag, Sb, As and Au accompanied by discrete pods of silica-rich material is suggested as supporting evidence for the classification of areas within Mathiatis South as a sites of low temperature fluid venting.

Mineralogical and geochemical similarities between silica-rich deposits suggest a low temperature origin for Kokkinovounaros and Touronjia. The approximate formation temperature at Touronjia is constrained by existing fluid inclusion data with temperatures ranging from 111 to 249°C (Naden *et al.*, 2006). These temperatures are comparable to those recorded using the sphalerite geothermometer in modern and ancient low temperature vent sites (Figure 7.18; Hannington and Scott, 1989; Keith *et al.*, 2014; Tivey *et al.*, 1995). The association of silica with Au is widely demonstrated at Touronjia with silicified breccias containing high Au (average=1.01 ppm, n=6). Furthermore, trace element geochemistry at Touronjia exhibits an enrichment in Pb and Sb that are commonly enriched in low temperature mineralisation and Au relative to massive VMS samples (Table 7.2 and 7.3).

Geochemical similarities between Touronjia, Mathiatis South and Kokkinovounaros suggest a similar fluid physicochemistry during mineralisation. No sphalerite or fluid inclusion data exist for Kokkinovounaros allowing the temperature of mineralisation to be estimated. Sample geochemistry shows an enrichment in Pb, Ag, Sb and Au (n=59, Table 7.2) relative to Troodos massive sulfide samples (Table 7.3). The most compelling evidence for a low temperature origin at Kokkinovounaros is sample mineralogy. Gold is enriched in silicified, hematite-rich breccias that are similar to jasperitic samples commonly associated with the margin of VMS deposits (Hannington *et al.*, 1998a; Martin *et al.*, 2018; Chapter 3 and 5). These samples may characterise the low temperature oxidised margins of the mound (Oudin and Constantinou, 1984) but are rarely reported in Troodos in such massive quantities, instead forming veins and caps (Adamides, 2010a; Hannington *et al.*, 1998; Parvaz, 2014). Given the absence of high temperature elements e.g. Co, Se, Cu etc. in primary sulfides (Table 7.4), and occurrence of massive jasper horizons, data suggest that fluids responsible for the formation of Kokkinovounaros were <300°C and more oxidising than the VMS hydrothermal system leading to the widespread development of jasper (hematite stability field- Figure 7.23 A).

Relative to other silica-rich deposits considered in this study Alpen Rose is Au-poor yet it displays mineralogical similarities to other deposits that are associated with an enrichment in Au (e.g. abundant silicification). In this study the nearby Mathiatis North VMS was also sampled and contains appreciable Au, averaging 1.08 ppm Au (LA-ICP-MS, pyrite, n=239) associated with a late silica overprint (Figure 7.22). The depletion of Au at Alpen Rose probably reflects the timing of silicification relative to high temperature sulfide precipitation with sulfide (now Fe oxides) forming the dominant matrix minerals at Alpen Rose. Early, high temperature sulfide mineralisation led to the occlusion of fluid pathways at Alpen Rose decreasing permeability and sealing the system from late stage fluid flow. Consequently, late stage silica and Au-rich fluids were channelled through the nearby Mathiatis North VMS deposit, an area of increased permeability. When comparing VMS in close proximity to other silica-rich deposits, e.g. Kokkinovounaros and Kambia VMS, located just 400 m from each other, the inverse relationship is true. Kambia VMS is Au poor (0.19 ppm, n=26; Chapter 5) with no apparent silica overprint suggesting that late stage Au-rich fluids were channelled through Kokkinovounaros, hence its relative enrichment in Au compared to Kambia. This highlights the importance of local scale permeability variation and the timing of silicification that explains the depletion in Au at Alpen Rose.

Both Mathiatis South and Touronjia are located distally from any known high temperature VMS mineralisation (approximately 10 km for Touronjia and 2.5 km at Mathiatis South). Given this association, three scenarios can explain their formation: a) Increased permeability 'off axis' related to faulting and fluid channelling, b) location distal to the underlying heat source i.e. away from the ridge axis or, c) failed maturation of a high temperature VMS systems.

At Touronjia and Mathiatis South, low temperature (<300°C) fluids are channelled into areas of increased permeability in the upper crust, these areas formed secondary permeability pathways and sites of less focused, effusive venting. The source of fluid may have been cooler, this could relate to the distance from the axial ridge (i.e. moving off axis) or the timing of fluid flow in the hydrothermal system, both scenarios having the same outcome. At the prospect S of Mitsero, Adamides (2013) suggest that the Cu-rich Kokkinoyia VMS deposit (see Chapter 5) formed close to the ridge axis whilst the prospect S of Mitsero formed distally and is therefore Zn-rich and formed at a lower temperature (based on sphalerite temperatures; Figure 7.18).

Alternatively, low temperature fluids could be generated when the crust migrated away from the axial ridge. In this scenario the timing of silicification and low temperature circulation is critical. As demonstrated at Mathiatis North and the silicification of umbers at Kokkinovounaros (after Prichard and Maliotis, 1998), silicification in some instances clearly postdates VMS and umber formation suggesting it is temporally late in the hydrothermal evolution of Troodos. Relationships at Mathiatis South and Touronjia are not conducive to establishing the timing of silicification relative to sulfide mineralisation and whilst evidence for multiple fluid pulses are recognised at Touronjia (e.g. oxidation of pyrite to hematite/magnetite- Figure 7.9) how this relates to silicification remains unclear. Mathiatis South could represent a failed VMS systems that formed during the initiation of hydrothermal circulation due to the occurrence of minor massive sulfide. Fluid flow would have been short lived and did not mature to black smoker temperatures >350°C due to the occlusion of permeability pathways or the opening up of more permeable regions in the surrounding area that led to the preferential channelling of fluid away from Mathiatis South.

### 7.6.8 Gold transport in the Troodos hydrothermal system

Temperature has a major effect on the solubility and transportation of Au in hydrothermal fluids (Hannington *et al.*, 1991; Hannington and Scott, 1989; Moss and Scott, 2001; Pokrovski *et al.*, 2014; White and Hedenquist, 1990). The distribution of Au in VMS, sites of low temperature discharge (white smokers) and off axis silicified areas (Prichard and Maliotis, 1998) reflects the

increased affinity of Au in cooler  $\text{HS}^-$  dominated fluids (Pokrovski *et al.*, 2014; Williams-Jones *et al.*, 2009). The low Au concentration in Troodos VMS sulfides reflects the reduced solubility of Au as  $\text{AuCl}_2^-$  complexes at temperatures of  $\sim 350^\circ\text{C}$  under moderately reduced conditions in the source region of metals for the VMS hydrothermal system (i.e. the Sheeted Dykes) (Figure 7.23-VMS)(Hannington and Scott, 1989; Keith *et al.*, 2016a; Webber *et al.*, 2017).

This study indicates that the enrichment of Au in off axis deposits, regardless of their exact paragenesis or mode of formation (i.e. Touronjia, Mathiati South and Kokkinovounaros) is a function of fluid temperature and the preferential affinity of Au as  $\text{Au}(\text{HS})_2^-$  in lower temperature ( $<300^\circ\text{C}$ ) fluids (A and B, Figure 7.23). This accounts for the enrichment of Au at Touronjia with evidence suggesting fluid temperatures of  $<250^\circ\text{C}$ . Hannington and Scott (1995) state that in modern low temperature ( $<250^\circ\text{C}$ ) vent fluids close to seawater salinity (i.e. similar to Troodos), the solubility of  $\text{AuHS}^-$  is orders of magnitude higher than  $\text{AuCl}_2^-$ . As the fluid temperature decreases from  $350^\circ\text{C}$  the ability of  $\text{AuHS}_2^-$  to transport Au increases (Figure 7.23). The low Au concentrations at Alpen Rose are explained by the decreased solubility of Au at high temperatures ( $\sim 350^\circ\text{C}$ ) where neither  $\text{Cl}^-$  or  $\text{HS}^-$  complexes effectively transport Au (cf. Section 7.1.1; Hannington and Scott, 1989; Pokrovski *et al.*, 2014; Williams-Jones and Heinrich, 2005).

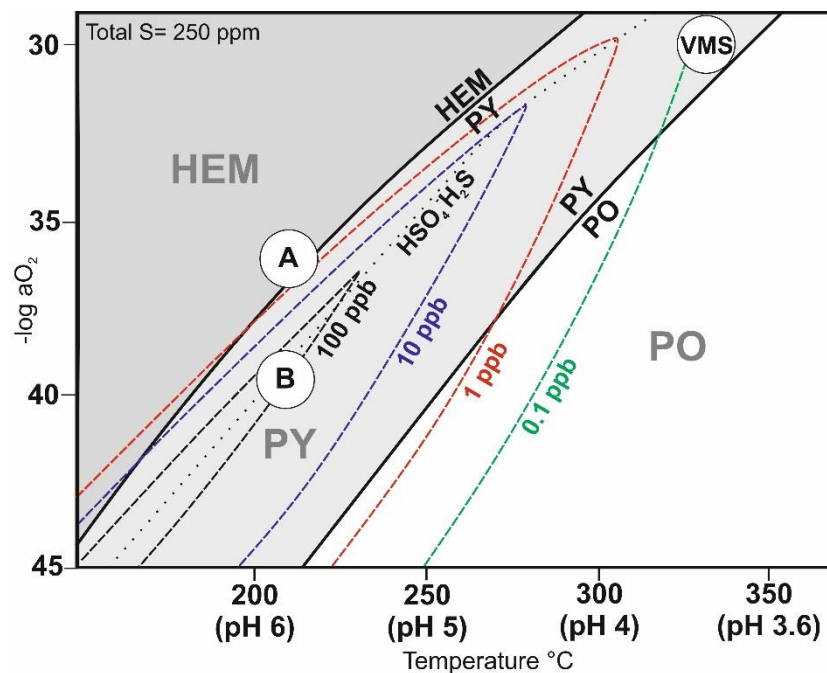


**Figure 7.23:** Solubility of Au as  $\text{Au}(\text{HS})_2^-$  in hydrothermal seawater derived fluids as a function of  $\log f_{\text{O}_2}$  vs. temperature and pH (after Hannington and Scott, 1995). Coloured dashed lines indicate gold solubility (0.1-100 ppb).  $\text{HSO}_4\text{-H}_2\text{S}$  spotted line indicates major ligand species in solution. HEM= hematite, PY= pyrite, PO= pyrrhotite. Point A represents an estimation of cooler fluids with a higher  $f_{\text{O}_2}$  (hematite) for Kokkinovounaros and B for Touronjia where sulfides are the dominant phase. Both are representative of cooler relatively more oxidised fluids of the off axis and low temperature Au mineralisation relative to the VMS hydrothermal system (VMS). The VMS point is estimated based on fluid temperature and Au content. At the PY/PO boundary

Hannington and Scott (1995) analysed Au contents in pyrite of 0.2 ppm. This concentration is similar to the average of 0.18 ppm found in this study.

### 7.6.9 Structural implications

All low temperature silica-rich deposits and mineralisation at Alpen Rose are structurally controlled and occur within the eastern portion of the Troodos ophiolite in a structurally complex region known as the Makheras domain (see Chapter 2; Varga and Moores, 1990). The Makheras domain is situated between the Larnaca graben to the E and the Mitsero graben to the W. Throughout the area two distinct structural trends were observed; NW-SE and N-S. This suggests that the intersection of these two fault directions was important in controlling the distribution of Au and silicification.

Low temperature silica-rich mineralisation is spatially associated with either normal or strike-slip faulting. The domain between Mitsero and Larnaca exhibits cross-cutting relationships consistent with multiple, temporally distinct faulting and hydrothermal events. For example at Alpen Rose NW-SE trending faults and dykes are cross-cut by strike slip N-S trending faults. This suggests axial parallel (Larnaca) NW-SE faults (Varga, 1991) were later cross-cut by re-activated faults associated with the N-S Mitsero graben. The interplay between these two structural regimes relates to the migration of spreading between ridges (Chapter 2) that led to local dilation, reactivation and propagation of new faults aligned to the developing stress regime. Renewed faulting in older, cooler, more permeable crust by late cross-cutting faults acted as a conduit for late silicifying fluids (Prichard and Maliotis, 1998). Similar cross-cutting fault regimes were observed at Touronjia and Kokkinovounaros. The effect of renewed magmatism in old crust is clearly demonstrated in the inter graben zone between Solea and Mitsero grabens by Eddy *et al.* (2008). They demonstrate that local pluton injection in old, off axis crust provided a localised heat source driving ore formation at the Alestos 'low temperature deposit' (see Appendix 3.1) and the Memi VMS (Chapter 5). A similar but large-scale system probably operated at the margin between the Mitsero and Larnaca graben boundary.

## 7.7 Summary

This study provides some of the first fundamental description, mineralogical characterisation and whole rock geochemical data from low temperature Au-rich deposits of the Troodos ophiolite. Geochemical data identify an enrichment in Au at Kokkinovounaros, Mathiatis South and Touronjia relative to VMS deposits of Troodos with Au concentrations of up to 20 ppm. Deposits share common attributes including their enrichment in Cd, Pb, Ag, Sb, As and Au,

---

abundant quartz and amorphous silica and their location distal to sites of high temperature venting.

- Zn/Fe ratios in sphalerite from silica-rich deposits averages 247°C (n=14, min=230°C, max=273°C). This is in good agreement with fluid inclusion data that averages  $T_H = 209^\circ\text{C}$  (n=12, min 111°C, max= 249°C). These temperatures are comparable to those reported for white smoker and low temperature vent sites.
- Low temperature mineralisation is enriched in silica, Au, As, Sb, Pb and Zn relative to massive sulfide samples (VMS).
- Lower temperature vent sites favour the preferential mobilisation of Au as  $\text{AuHS}_2^-$  ligands leading to its enrichment in low temperature mineralisation.
- In the VMS system at approximately 350°C, Au solubility, as  $\text{AuCl}_2^-$  complexes, is minimal leading to the formation of Au poor VMS averaging 0.18 ppm (n=66).
- Tellurium and Se (and other elements) can be significantly enriched in supergene weathering products, especially goethite and jarosite-rich lithologies.
- The distribution of low temperature Au deposits suggests a complex interplay between tectonics and hydrothermal fluid flow, specifically renewed faulting in older off axis crust.



# CHAPTER 8

## **Assessing variable magmatic volatile influx in mafic VMS hydrothermal systems: Evidence from the Troodos ophiolite, Cyprus**

### **Submitted as:**

Martin, A.J, Keith, M., Parvaz D.B., McDonald I., Boyce A.J., McFall K.A., Jenkin G.R.T., MacLeod C.J. and Strauss H. **Effects of magmatic volatile influx in mafic VMS hydrothermal systems: evidence from the Troodos ophiolite, Cyprus** (submitted, Chem. Geol).

### **Co-author contributions:**

M. Keith and D.B. Parvaz provided an additional sulfur isotope dataset that complimented the Troodos data collected in this study (outlined in Appendix 8.2). I. McDonald supervised laser ablation analysis. A.J. Boyce (and A. MacDonald) supervised sulfur isotope analysis (SUERC). All authors were involved in discussion during the writing of the manuscript.

## 8. Abstract

The Troodos ophiolite, Cyprus is the principal on-land analogue for mafic-hosted Volcanogenic Massive Sulfide (VMS) deposits. This study, for the first time, presents sulfur isotope ( $\delta^{34}\text{S}$ ) data on a regional scale from VMS deposits and other mineralised zones across the Troodos ophiolite. In combination  $\delta^{34}\text{S}$ , Se/S ratios and trace element chemistry of different hydrothermal sulfides are used to assess variations in magmatic volatile influx in the ancient hydrothermal system.

Sulfur isotope analyses (n=180) across 19 mineral deposits indicate variable sources of sulfur in the Troodos VMS hydrothermal system, this in turn allows a variable source of metals to be inferred. Pyrite  $\delta^{34}\text{S}$  range from -5.5‰ to +13.2‰ with an average of +4.6‰ (n=160) for all deposits investigated. These  $\delta^{34}\text{S}$  variations cannot only be explained solely by variable proportions of thermochemical seawater sulfate reduction ( $\delta^{34}\text{S}$  +18 to +19‰) and leaching of primary magmatic sulfur from igneous rocks ( $\delta^{34}\text{S}$  0-1‰). The author suggests that the unusually light (<0‰)  $\delta^{34}\text{S}$  values recorded in some VMS deposits may be related to the direct contribution of magmatically derived  $\text{SO}_2$ , to the hydrothermal systems from an underlying magma chamber by volatile exsolution from a volatile saturated magmatic source. This  $\text{SO}_2$  subsequently disproportionated to isotopically light  $\text{H}_2\text{S}$ , that formed low  $\delta^{34}\text{S}$  in sulfides, and heavier  $\text{SO}_4^{2-}$ . However, Se/S ratios and magmatophile trace element signatures of sulfides (e.g. Se, Cu, Au) vary between VMS deposits independent of their  $\delta^{34}\text{S}$  composition.

Consequently, two processes are proposed explaining the trace metal and  $\delta^{34}\text{S}$  variation across the Troodos ore-forming system. These are; i) a variable source of metals in the sheeted dyke complex and, ii) the addition of a magmatic volatile-rich phase to the VMS hydrothermal system. Two distinct lava units exist in the Troodos stratigraphy, namely the upper and lower pillow lavas (UPL and LPL). Volcanogenic Massive Sulfide deposits in Troodos occur at major lithological contacts between the LPL-UPL or overlying the UPL. The more primitive UPL are enriched in Au, Se and Cu relative to As, Sb and Zn that are concentrated in the LPL. Deposits that postdate the accretion of the UPL are expected to show an enrichment in UPL affinity elements Cu, Se and Au relative to those that occur within the LPL and therefore pre-date UPL formation. Hence, the stratigraphic position of VMS deposits and the ratio of UPL:LPL affinity elements (e.g. As +Zn +Sb vs. Cu + Se + Au) imply a systematic relationship between the source of trace elements in VMS deposits and stratigraphic depth. This relates to the relative proportion of UPL and LPL affinity lavas within the metal source region that in turn relates to the location of the VMS in the Troodos stratigraphy.

## 8.1 Introduction

Sulfur isotopes and trace element analyses in seafloor hydrothermal systems in a range of tectonic settings have been used to provide constraints on the links between magmatic influx, hydrothermal system maturity and its effect on trace element geochemistry (de Ronde *et al.*, 2005; Herzig *et al.*, 1998a; Sun *et al.*, 2004; Wohlgemuth-Ueberwasser *et al.*, 2015; Yang and Scott, 2002). In MOR hosted hydrothermal systems sulfur isotope systematics show that sulfur is sourced primarily through the leaching of igneous rocks and reduction of seawater sulfate (Herzig *et al.*, 1998a,b; Humphris *et al.*, 1995). In these systems metals are principally sourced through fluid-rock interaction (cf. Humphris and Cann 2000). In contrast, variation in protolith geochemistry and the ability of melts in back-arc/island arc environments to exsolve a magmatic volatile phase can lead to the enrichment of magmatophile trace elements in subduction related environments (de Ronde *et al.*, 2003, 2005; Hedenquist and Lowenstern, 1994; Herzig *et al.*, 1998a; Yeats *et al.*, 2014). Additionally, variations in regional scale SMS chemistry are attributed to variable proportions of magmatic volatile influx (Herzig *et al.*, 1998a; Rouxel *et al.*, 2004). For example, modern SMS deposits in the Lau back-arc basin exhibit distinctly different sulfur isotope profiles suggesting regional variations in the magmatic volatile influx over a relatively localised scale (~40 km; Herzig *et al.*, 1998a).

Previous studies on Troodos have largely focused on local mound scale variation in sulfur isotopes within a single deposit. For example Keith *et al.* (2016b) found a systematic relationship between sulfur isotope values in pyrite and stratigraphic depth in the Skouriotissa VMS deposit varying from -1.4‰ to +6.1‰ in deep and shallow stockwork, respectively. Pederson *et al.* (2017) identified a biogenic sulfur isotope signature in pyrite from the Akaki River section (Troodos) characterised by extremely light  $\delta^{34}\text{S}$  in pyrite of -22‰ and Hannington *et al.* (1998) report limited analysis from Troodos VMS deposits that range from +1.9‰ to +8.2‰ in sulfides. Sulfur isotope data also exists for the bulk Troodos crust with Alt (1994) recording primary magmatic sulfur values of 0-1‰ that become progressively enriched towards heavier values with increasing degree of hydrothermal alteration (e.g. epidiosites at +6.2‰). New data presented in this study aims to address regional and local mound scale variation in sulfur isotopes, linking sulfur isotope variations to the enrichment of trace metals in Troodos VMS.

Multiple sources of sulfur may be incorporated into hydrothermal sulfides in modern SMS and ancient VMS systems. These include the biogenic/bacterial (<140°C) or thermochemical reduction of seawater sulfate, leaching from igneous rocks and the disproportionation of  $\text{SO}_2$  derived from magmatic volatiles (Berkenbosch *et al.*, 2012; Herzig *et al.*, 1998a; Pedersen *et al.*, 2017). Primary Troodos magmatic sulfides have a  $\delta^{34}\text{S}$  composition of 0-1‰ (Alt, 1994) whilst Cretaceous seawater is 18-19‰ (Kampschulte and Strauss, 2004). In modern SMS systems the

majority of sulfur isotope values lie between 0‰ and seawater (+21-22‰) indicating the variable sourcing of sulfur from these two isotopically distinct reservoirs. During hydrothermal alteration of the Troodos crust, seawater derived fluids become heated and reduced in the subsurface leading to the thermochemical reduction of seawater sulfate at temperatures >180°C (e.g. Machel, 2001). Additionally, at low temperatures <140°C bacterial seawater sulfate reduction can occur (e.g. Pedersen *et al.*, 2017; Rouxel *et al.*, 2008; Seal, 2006). Bacterial sulfate reduction of seawater at lower temperatures (<140°C) in an open system can lead to sulfide precipitates with extremely light  $\delta^{34}\text{S}$  signatures reaching -43.5‰ (Pedersen *et al.*, 2017; Rouxel *et al.*, 2008; Seal, 2006). Light sulfur isotope values <0‰ may also form from magmatic  $\text{SO}_2$  that is subsequently disproportionated to  $\text{H}_2\text{S}$  and isotopically heavier  $\text{SO}_4^{2-}$  (e.g. de Ronde *et al.*, 2005; Herzig *et al.*, 1998a; Kusakabe *et al.*, 2000). Therefore, the sulfur isotope signature preserved in ancient Troodos VMS deposits is related to the relative contribution of sulfur from different reservoirs or processes that occurred in the ancient Troodos VMS hydrothermal systems.

This study presents the first extensive  $\delta^{34}\text{S}$  dataset for 19 VMS deposits and associated mineralised occurrences across the Troodos ophiolite, Cyprus. Data indicates a systematic variation in Se/S ratios and magmatophile trace element concentrations on a regional scale. The  $\delta^{34}\text{S}$  composition of sulfides varies between VMS deposits due to either a variable magmatic volatile influx or different proportions of sulfur derived from thermochemical seawater reduction or leaching from igneous rocks.

## 8.2 Sample localities

Volcanogenic Massive Sulfide deposits investigated in this study are distributed across the entire Troodos ophiolite spanning six different structural domains (Figure 8.1), and are therefore representative of a range of regional scale ore-forming processes (Table 8.1). Deposits range in size from 0.1 Mt to >15 Mt (Hannington *et al.*, 1998) with grades of <0.1 wt.% to 3.8 wt.% Cu (Adamides, 2010a; Constantinou and Govett, 1973; Hannington *et al.*, 2011). In some deposits a clear exhalative mound or vent fauna are present providing unambiguous evidence for deposit formation at the seafloor (Figure 8.2 A- Skouriotissa) (Little *et al.*, 1999; Oudin and Constantinou, 1984). However, due to a long legacy of mining, the exhalative mound may have been removed and is not always preserved. Deposits also form at different stratigraphic levels within the extrusive sequence occurring, for example, above the Upper Pillow Lavas (UPL) overlain by sediments (Figure 8.2 A- Skouriotissa) or at the contact between the upper and Lower Pillow Lava horizons (LPL) (Figure 8.2 B- Agrokipia) or the lower pillow-basal group (LPL-BG)(Figure 8.2 C and D- West Apliki/Kaphedes).

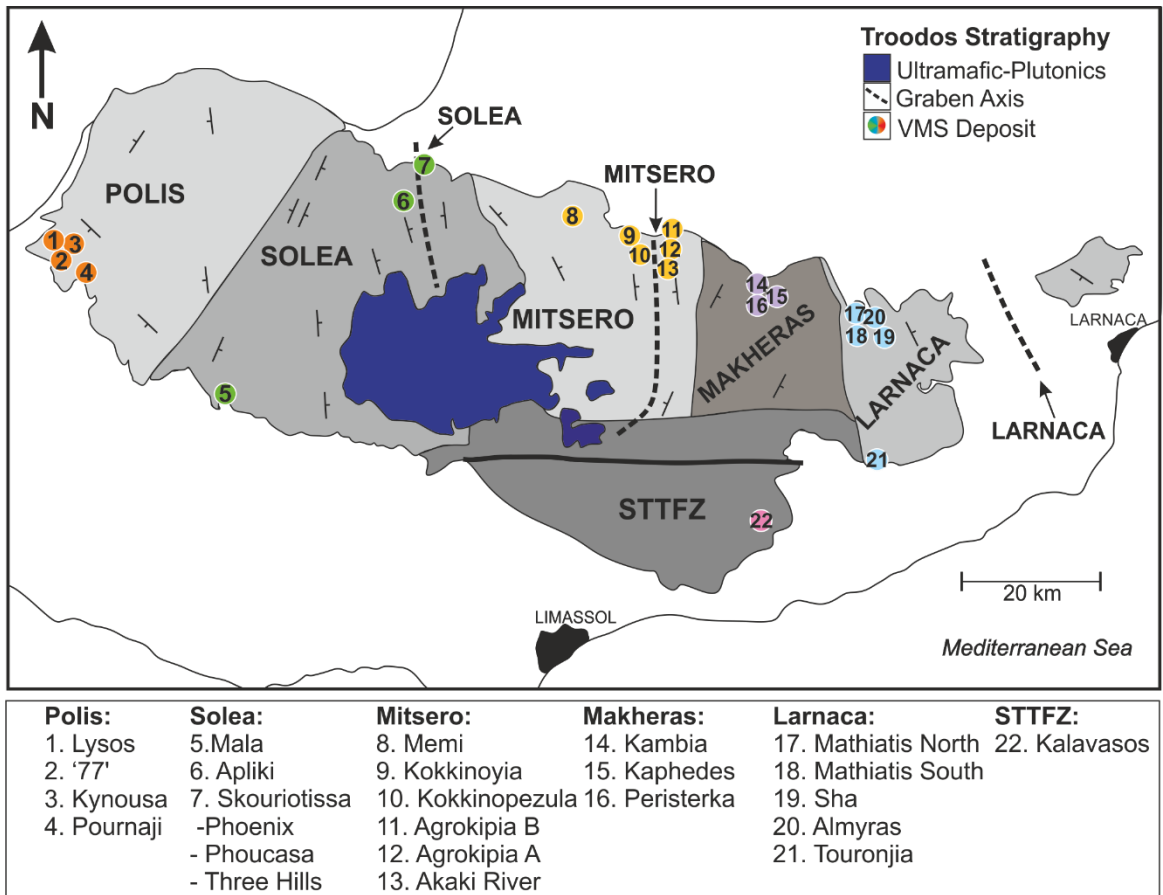


**Figure 8.1:** Structural domains of the Troodos ophiolite as classified by Varga and Moores (1985). VMS deposits in this study span all structural domains.

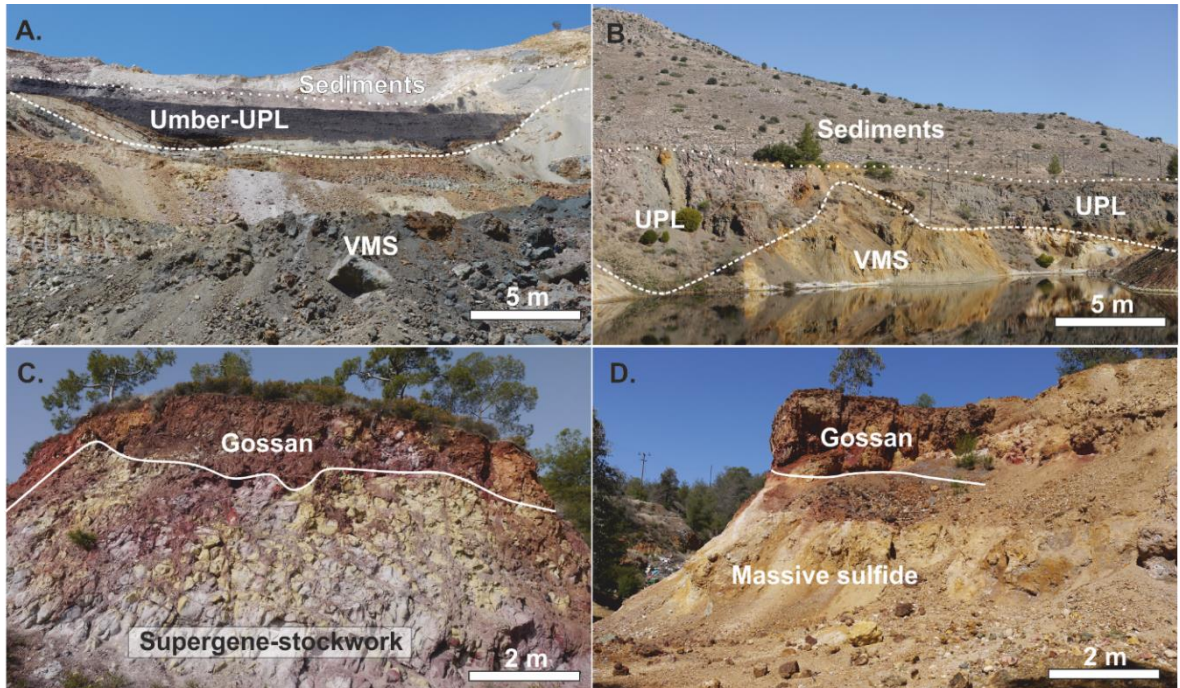


**Figure 8.2:** Field photographs showing key relationships between mineralisation, lavas and sediment: (A) Phoucasa, Skouriotissa VMS, massive sulfide overlain directly by umber and calcareous sediment, (B) the Agrokipia A VMS located at the contact between LPL and unaltered UPL that are overlain by calcareous sediments, (C) stockwork zone in LPL at Apliki West, veins of supergene altered pyrite to goethite, jarosite and hematite overlain by an earthy coloured gossan, (D) gossan overlying massive sulfide at Kaphedes mine (BG-LPL contact).

Deposit	(WGS 1984)		Description
	N	E	
<b>Polis Domain</b>			
Lysos	45536	3877125	VMS
'77'	45404	3877993	VMS
Kynousa	45555	3876810	VMS
Pournaji	45536	3876197	VMS
<b>Solea Domain</b>			
Mala	47046	3864224	VMS
Apliki	48573	3881812	VMS
Skouriotissa	49018	3884032	VMS
<b>Mitsero Domain</b>			
Memi	50366	3877476	VMS
Kokkinoyia	50974	3877992	VMS
Kokkinpozeula	51038	3877259	VMS
Agrokipia A	51336	3878056	VMS
Agrokipia B	51164	3880110	VMS
Akaki River	51643	3878559	Disseminated/veins
<b>Makheras Domain</b>			
Kambia	52473	3873019	VMS
Kaphedes	52394	3871610	VMS
Peristerka	52151	3872174	VMS
<b>Larnaca Domain</b>			
Mathiatis North	53185	3870606	VMS
Mathiatis South	53170	3867617	VMS
Sha	53421	3867790	VMS
Almyras	55390	3870761	Disseminated/veins
Touronja	53242	3856597	Low T silica rich
<b>STTFZ</b>			
Kalavasos	52356	3850308	VMS

**Table 8.1:** Location summary of samples analysed from this study for  $\delta^{34}\text{S}$  in sulfide minerals. All coordinates in WGS 1984 (36S)- See Appendix 3.1 for further details.

## 8.3 Methods summary

### 8.3.1 Trace element geochemistry

Laser Ablation ICP-MS (LA-ICP-MS) was used to determine the *in situ* trace element composition of hydrothermal sulfides (Table 8.2-4: n= 250 this study). A combination of spot and line analyses were performed. Measurements were carried out at Cardiff University utilising a New Wave Research UP213 UV laser coupled to an iCAP RQ ICP-MS (spot analysis) and a Thermo X-series 2 ICP-MS (line analysis- see Chapter 4). Data reduction and subtraction of gas blanks was performed using Thermo Qtegra and Thermo Plasmalab software (cf. Chapter 4).

### 8.3.2 Sulfur isotope analyses

Sulfur isotope ( $\delta^{34}\text{S}$ ) analysis was performed at the Natural Environmental Research Council (NERC) stable isotope laboratory at the Scottish Universities Environmental Research Centre (SUERC) and at the Westfälische Wilhelms-Universität, Münster. Subsequently these datasets are divided into dataset A (n=112; Martin and Parvaz), analysed at SUERC and dataset B (n=68; Keith) analysed at Münster (see Appendix 8.1 and Chapter 4). For dataset A pyrite, chalcopyrite and covellite samples were analysed. *In situ* measurements were performed by laser combustion and these were combined with conventional sulfur extraction of mineral separates. The methodology for dataset B is outlined by Keith *et al.* (2016b) and for dataset A in Chapter 4. Results are reported in per mil values relative to Vienna-Canyon Diablo Troilite (V-CDT).

## 8.4 Results

### 8.4.1 Ore mineralogy and petrography

Samples have been classified based on their mineralogy and morphology into massive, semi-massive, stockwork and South Apliki Breccia Zone sample types. Representative photomicrographs of each sample type are shown in Figure 8.3 (overleaf). Massive samples are characterised by >90% sulfide, mainly pyrite, with interstitial to crudely banded chalcopyrite (Figure 8.3 A). At Mala, dendritic pyrite forms crude bands with coarse interlocking grains towards the base (Figure 8.3 B). Semi-massive samples contain <90% sulfide with interstitial Fe-oxides, covellite and silica (Figure 8.3 C and D). Stockwork samples consist of discrete veins of silica, pyrite, chalcopyrite and sphalerite (Figure 8.3 E). South Apliki Breccia Zone samples (see Martin *et al.*, 2018) contain coexisting hematite, chalcopyrite and pyrite (Figure 8.3 F). In combination, these samples represent a wide range of ore-forming processes from the shallow near-seafloor VMS stratigraphy (Figure 8.3 C) to the lower stockwork zone (Figure 8.3 E) (Martin *et al.*, 2019).

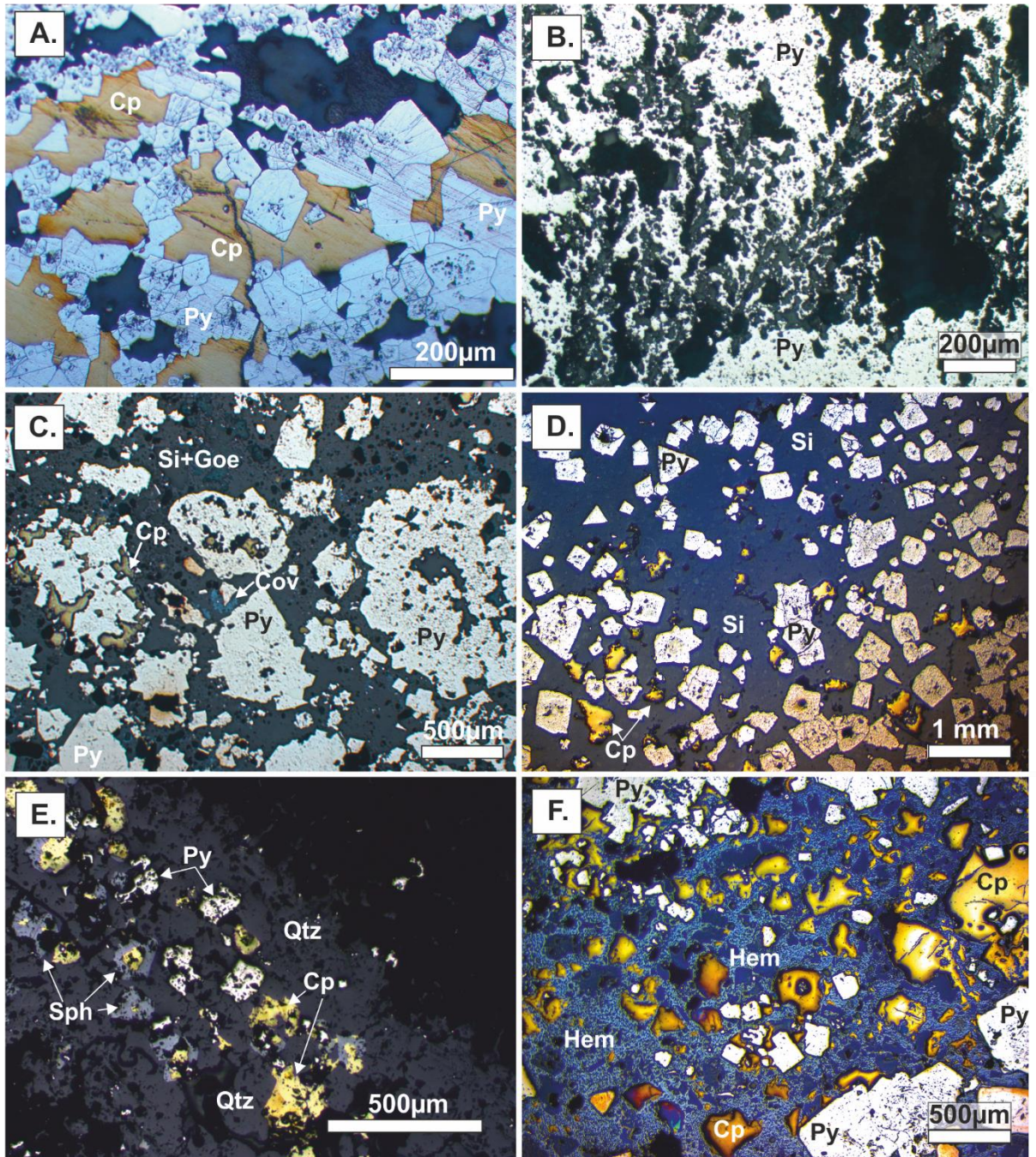


**Figure 8.3:** Representative reflected light photomicrographs: (A) Massive pyrite and chalcopyrite (Kokkinoyia), (B) crudely banded pyrite (Mala), (C) granular anhedral semi-massive pyrite (Skouriotissa), (D) semi-massive sulfide with goethite and silica (Kokkinoyia), (E) stockwork ore with pyrite, chalcopyrite and sphalerite (Agrokippia B), (F) South Apliki Breccia Zone mineralisation, hematite-pyrite-chalcopyrite (Apliki). Cp=chalcopyrite, Py=pyrite, Sph=sphalerite, Cov= covellite, Hem=hematite, Qtz=quartz, Goe=goethite, Si= silica.

### 8.4.2 Trace element geochemistry

In this study *in situ* trace element geochemistry of pyrite (n=191; Table 8.2, Figure 8.4), chalcopyrite (n=28; Table 8.3) and covellite (n=4; Table 8.4) are presented. Trace element concentrations in sulfides from the Troodos VMS deposits are highly variable (cf. Chapter 5; Martin *et al.*, 2019). For example, Se in pyrite varies over more than two orders of magnitude between different VMS deposits from 10.1 to 4513 ppm (Table 8.2). Concentrations of Te, Co, Bi, Sb and Zn in chalcopyrite are the same or lower than in pyrite, whilst Se is generally enriched in chalcopyrite (Table 8.2 and 8.3). Covellite contains appreciable Se averaging 1970 ppm (n=4, Table 8.4). Covellite also contains high concentrations of Ag, As, Zn and Bi with minor Au (Table 8.4). Systematic variation in sulfide trace element geochemistry is noted on a regional scale between different structural districts (Figure 8.4). Correlation (Linear R values) between elements in pyrite are limited with the exception of a minor correlation between Bi-Te (R=0.56), Au-Ag (R=0.57) and Cd-Zn (R=0.64). In chalcopyrite, a moderate positive correlation is observed between Au-Te (R=0.68) and Cd-Ag (R=0.88) (See Appendix 8.2).

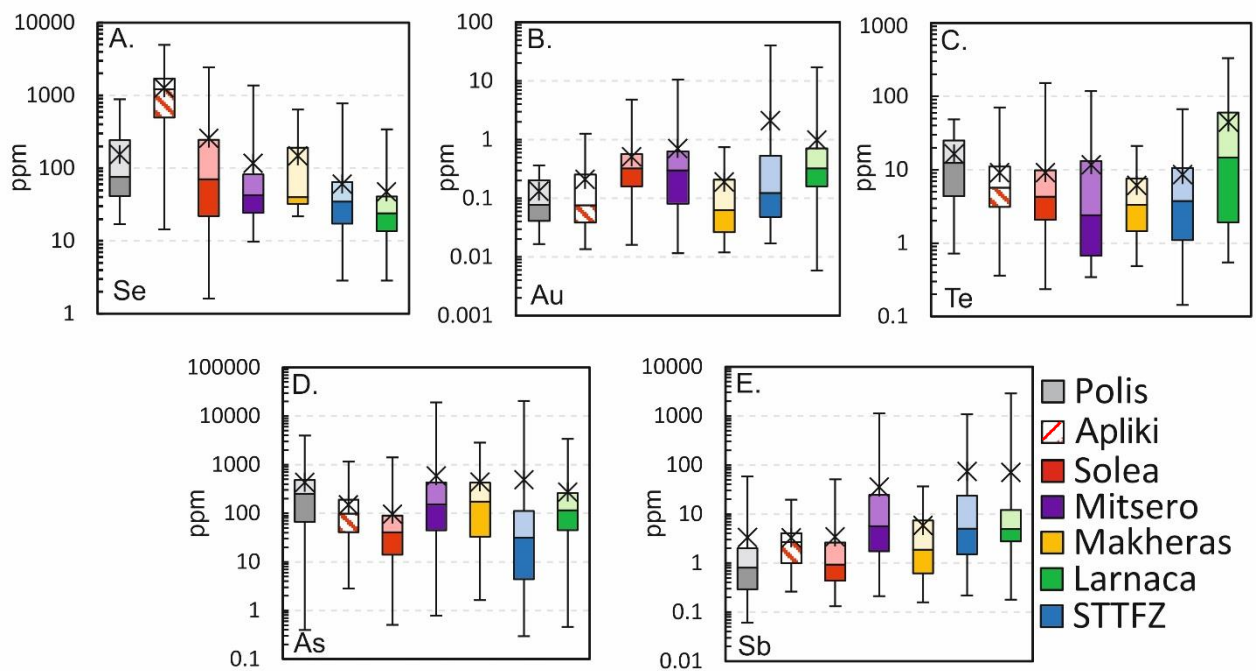


**Figure 8.4:** Box plots of trace element concentrations in pyrite analysed via LA-ICP-MS (n=1514) classified by structural domain (refer to Figure 8.1): (A) Se, (B) Au, (C) Te, (D) As and (E) Sb. Apliki VMS is present separately due to its unusual oxidation related enrichment in Se (See Martin *et al.*, 2018) (Data compiled from: this study, Keith *et al.*, 2016a; Martin *et al.*, 2018, 2019). Dark colours= lower quartile, black line=median, light colours=upper quartile and whiskers = min/max, X = average.

Ratios of Se/S in pyrite (n=1514; Se/S \*10<sup>6</sup> - compiled data, Figure 8.5) from Troodos VMS deposits exhibit variation between different structural domains (Figure 8.1 and 8.5). Pyrite from deposits of the Solea graben shows the highest average Se/S ratio at 480 (n=362), whilst the

Larnaca domain averages 89 (n=350). Analyses also indicate a large variation in Se/S ratios in pyrite from individual structural domains; at Solea Se/S ratios range from 3 to 3650 (Figure 8.5).

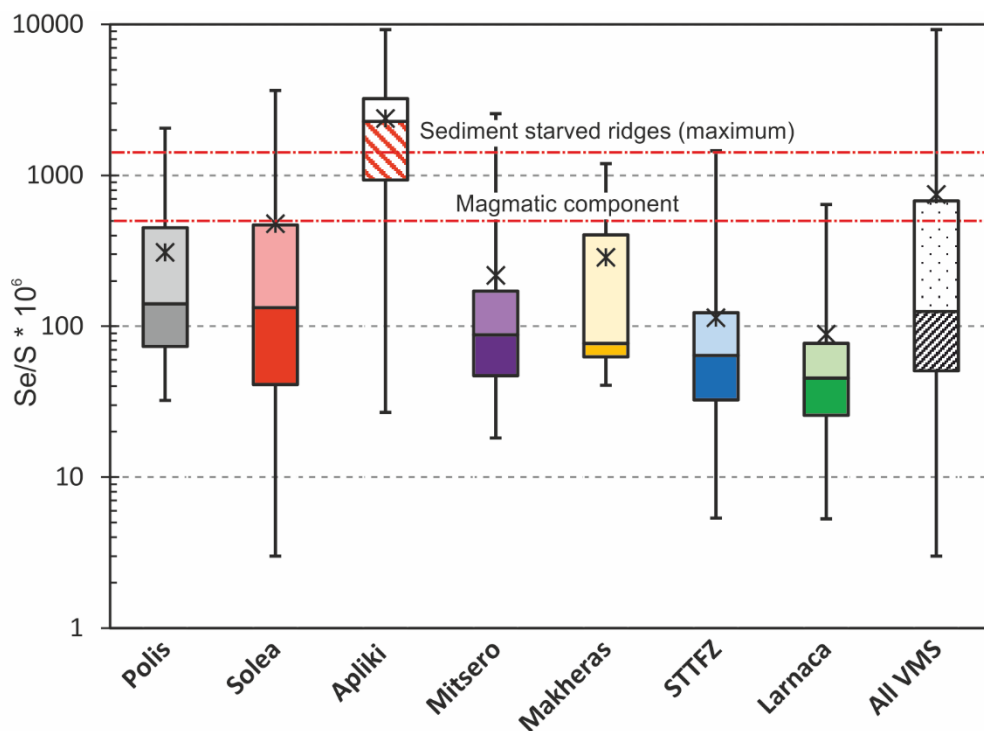


**Figure 8.5:** Selenium/sulfur ( $\text{Se/S} \times 10^6$  vs. Se) ratio in pyrite (n=1514) analysed using LA-ICP-MS and classified by structural domain (Figure 8.1). All VMS = All Troodos VMS. Lower red dashed line indicates an increased magmatic influx into the VMS hydrothermal system (>500). Upper dashed line marks the maximum Se/S ratio for modern sediment starved hydrothermal systems (1500; Layton-Matthews *et al.*, 2008; 2013). Light coloured box = lower quartile, dark coloured box = upper quartile, black line = median, X = average, error bars represent minimum and maximum values. Data compiled from: This study, Keith *et al.*, 2016a; Martin *et al.*, 2018, 2019) (KEY = as for Figure 8.4).

### 8.4.3 Sulfur isotope analysis

Sulfur isotope analysis was performed on pyrite (n=160), chalcopyrite (n=15) and covellite (n=5) across 19 VMS deposits and mineralised zones across all structural domains (Figure 8.1, Table 8.5). The average  $\delta^{34}\text{S}$  value for all samples regardless of the analysed mineral was +4.6‰. Values in pyrite range from -5.5‰ to +13.2‰ (Figure 8.6). Pyrite from deposits of the Larnaca domain exhibit the lowest average  $\delta^{34}\text{S}$  value at +3.4‰ (n=55) and the STTFZ the highest at +8.0‰ (n=18) (Figure 8.7, Table 8.5). Analyses of chalcopyrite and covellite yield values indistinguishable from pyrite with  $\delta^{34}\text{S}$  ranging from +0.6 to +5.6‰ and +3.7 to +5.3‰, respectively (Table 8.5). Results obtained in this study are broadly comparable to previous studies however, this study identifies variation in sulfur isotope composition in sulfides that have not previously been reported in Troodos VMS (Figure 8.6 and 8.7), for example extremely heavy and light values at Kalavassos and Sha VMS. In some instances clear populations are identified, for example in the STTFZ (Figure 8.7 E) where  $\delta^{34}\text{S}$  values cluster around +2-3‰ and +11-13‰.

Deposit	Pyrite	Co ppm	Cu %	Zn ppm	As ppm	Se ppm	Ag ppm	Cd ppm	Sb ppm	Te ppm	Au ppm	Pb ppm	Bi ppm
Agrokipia A n=12	<b>Average</b>	<b>58.7</b>	<b>0.03</b>	<b>1070</b>	<b>1013</b>	<b>351</b>	<b>1.3</b>	<b>3.1</b>	<b>2.7</b>		<b>0.62</b>	<b>14.5</b>	
	Max	182	0.04	5194	6251	449	5.1	5.9	4.9		1.6	25.2	
	Min	3.03	0.01	>0.01	12.7	279	0.39	0.72	1.1		0.21	4.9	
	Median	47.8	0.03	560	307	324	0.92	3.1	2.4		0.52	12.6	
	σ	53.5	0.01	1541	1806	71.8	1.4	1.9	1.2		0.35	6.5	
Agrokipia B n=10	<b>Average</b>	<b>387</b>	<b>0.03</b>	<b>408</b>	<b>81.7</b>	<b>30.5</b>	<b>2</b>	<b>2.3</b>	<b>2.4</b>	<b>6.0</b>	<b>0.18</b>	<b>145</b>	<b>6.8</b>
	Max	1151	0.06	1492	608	65.9	3.8	3.9	4.5	27.1	0.18	411	28.2
	Min	3.3	>0.01	25.9	1.1	10.1	0.26	0.30	0.2	0.38	0.18	3.6	0.08
	Median	232	0.03	65.2	4.2	28.1	2.0	2.8	2.4	2.5	0.18	19.2	1.3
	σ	420	0.02	569	188	17	1.8	1.5	2.2	8.1		189	10.9
Kokkinopezula n=18	<b>Average</b>	<b>59.7</b>	<b>0.05</b>	<b>2749</b>	<b>487</b>	<b>486</b>	<b>4.7</b>	<b>4.6</b>	<b>38.9</b>	<b>6.4</b>	<b>1.3</b>	<b>56.2</b>	<b>1.5</b>
	Max	215.6	0.36	9390	1103	1371	11.0	11.3	98.9	11.4	10.6	103	4.2
	Min	4.1	>0.01	44.1	40.0	25.3	0.30	0.30	2.3	1.2	0.07	11.3	0.06
	Median	98.3	0.01	92.3	5.3	20.2	0.65	0.50	0.35	17.6	0.07	5.0	5.3
	σ	82.8	0.1	3864	375	626	3.0	4.8	34.5	4.2	2.6	32.4	1.6
Kokkinoyia n=43	<b>Average</b>	<b>111</b>	<b>0.13</b>	<b>6708</b>	<b>278</b>	<b>297</b>	<b>3.3</b>	<b>5.7</b>	<b>22.5</b>	<b>14.6</b>	<b>1.3</b>	<b>64.1</b>	<b>9.5</b>
	Max	797	1.7	62591	1103	1371	11	15.8	117	88.4	10.6	232.4	96.1
	Min	4.1	>0.01	15.5	2.3	18.2	0.27	0.26	0.47	1.2	0.01	2.9	0.06
	Median	56.0	0.03	659.4	185.1	93.9	1.9	4.6	7.5	4.2	0.26	55.0	2.1
	σ	167	0.3	14003	287	387	3	4.9	32.4	19	1.9	51.8	18.8
Apliki n=84	<b>Average</b>	<b>127</b>	<b>0.31</b>	<b>337</b>	<b>134</b>	<b>1297</b>	<b>0.36</b>	<b>1.1</b>	<b>2.4</b>	<b>6.8</b>	<b>0.19</b>		<b>1.0</b>
	Max	447	2.2	4307	1151	4513	0.69	1.2	6	32.5	1.3		6.1
	Min	2.3	>0.01	15.6	2.8	14.4	0.21	1.1	0.31	0.71	0.02		0.03
	Median	98.4	0.09	32.8	85.2	1217	0.31	1.1	2.5	5.1	0.07		0.8
	σ	108	0.5	948	183	954	0.15	0.08	1.7	5.9	0.27		1.2

**Table 8.2:** Pyrite geochemistry analysed via LA-ICP-MS. Blank cells indicate all analyses are below detection limit. All data in Appendix 8.2.

Deposit	Pyrite cont.	Co ppm	Cu %	Zn ppm	As ppm	Se ppm	Ag ppm	Cd ppm	Sb ppm	Te ppm	Au ppm	Pb %	Bi ppm
Skouriotissa n=22	<b>Average</b>	<b>393</b>	<b>0.4</b>	<b>2917</b>	<b>48.7</b>	<b>397</b>	<b>1.4</b>		<b>1.3</b>	<b>17.3</b>	<b>0.37</b>		<b>1.5</b>
	Max	2289	1.9	23954	130.1	2430	7.1		3.1	82	0.86		4.5
	Min	2.9	0.02	43	3.1	17.8	0.23		0.3	2.6	0.02		0.05
	Median	184.0	0.21	474.6	44.4	226.7	0.56		0.78	12.4	0.32		1.1
	σ	557	0.56	6312	40.2	600	1.9		1	18.2	0.29		1.3
Kambia n=2	Average	4.7		17	7.2	23.4						260	0.3
	Max	4.7		17	7.2	23.4						260	0.4
	Min	4.7		17	7.2	23.4						260	0.2
	Median	4.7		17	7.2	23.4						260	0.3
	σ												0.1

**Table 8.2 (continued):** Pyrite geochemistry analysed via LA-ICP-MS. Blank cells indicate all analyses are below detection limit. The repeated analysis of sulfide standards during the Laser Ablation ICP-MS yielded <10% RSD for Co, As, Se, Ag, Pb and Bi and between 10-18% RSD for Cu, Zn, Sb, Te and Au. RSD for Cd was 26%. See Appendix 8.2.

Deposit	Chalcopyrite	Co ppm	Cu %	Zn ppm	As ppm	Se ppm	Ag ppm	Cd ppm	Sb ppm	Te ppm	Au ppm	Pb ppm	Bi ppm
Apliki n=19	<b>Average</b>	<b>14.0</b>	<b>26.8</b>	<b>261</b>	<b>261</b>	<b>2415</b>	<b>1.5</b>	<b>1.5</b>	<b>5.6</b>	<b>8.2</b>	<b>0.29</b>		<b>0.58</b>
	Max	34.1	32.7	1193	1270	4517	3.8	2.1	16.8	43.4	1.5		3.4
	Min	3.3	20.2	56.0	5.8	281	0.23	0.92	0.53	0.13	0.02		>0.01
	Median	6.5	27.3	154	110	2436	0.89	1.8	4.0	2.9	0.06		0.23
	$\sigma$	11.3	2.8	258	364	1162	1.3	0.53	5.2	13.7	0.47		0.80
Skouriotissa n=9	<b>Average</b>	<b>117</b>	<b>22.7</b>	<b>5789</b>	<b>3.3</b>	<b>342</b>	<b>2.6</b>	<b>17.3</b>	<b>0.90</b>	<b>7.1</b>	<b>0.25</b>		<b>0.55</b>
	Max	378	28.5	18864	88.5	1549	11.6	109	1.0	39.7	0.26		3.6
	Min	2.2	16.7	392	2.7	19.9	0.24	1.1	0.75	0.54	0.22		0.05
	Median	43.7	24.3	5990	3.3	37.3	2.2	2.3	0.90	1.2	0.24		0.12
	$\sigma$	152	4.3	5252	0.6	574	4.6	37.6	0.15	12.6	0.02		1.1

**Table 8.3:** Summary of LA-ICP-MS chalcopyrite geochemistry by VMS deposit. Blank cells represent analyses below detectable limit. Full data available in Appendix 8.1. The repeated analysis of sulfide standards during the Laser Ablation ICP-MS yielded <10% RSD for Co, As, Se, Ag, Pb and Bi and between 10-18% RSD for Cu, Zn, Sb, Te and Au. RSD for Cd was 26%. See Appendix 8.2.

Deposit	Covellite	Co ppm	Cu %	Zn ppm	As ppm	Se ppm	Ag ppm	Cd ppm	Sb ppm	Te ppm	Au ppm	Pb ppm	Bi ppm
Apliki n=2	<b>Average</b>		<b>52.1</b>	<b>257</b>	<b>365</b>	<b>3254</b>	<b>16.7</b>	<b>1.8</b>	<b>15.0</b>	<b>6.0</b>	<b>0.17</b>		<b>8.3</b>
	Max		52.8	275	439	4310	29.4	1.8	29.2	9.3	0.26		16.3
	Min		51.4	237	290	2197	4.0	1.8	0.78	2.7	0.09		0.30
	Median		52.1	257	365	3254	16.7	1.8	15.0	6.0	0.17		8.3
	$\sigma$		0.68	18.7	74.3	1502	12.7		14.2	3.3	0.08		8.0
Skouriotissa n=2	<b>Average</b>	<b>135</b>	<b>46.2</b>	<b>2649</b>	<b>83.9</b>	<b>1073</b>	<b>8.4</b>		<b>3.3</b>	<b>24.6</b>	<b>0.38</b>	<b>201</b>	<b>2.6</b>
	Max	191	50.9	4369	108	1320	12.8		5	29.5	0.46	201	2.8
	Min	79	41.4	930	59.1	825	4.1		1.6	19.7	0.3	201	2.4
	Median	135	46.2	2650	83.9	1073	8.4		3.3	24.6	0.38	201	2.6
	$\sigma$	56.3	4.7	1720	24.8	278	4.3		1.7	4.9	0.1		0.18

**Table 8.4:** Summary of covellite geochemistry analysed using LA-ICP-MS. Blank cells are below detectable limit. Full data available in Appendix 8.1. The repeated analysis of sulfide standards during the Laser Ablation ICP-MS yielded <10% RSD for Co, As, Se, Ag, Pb and Bi and between 10-18% RSD for Cu, Zn, Sb, Te and Au. RSD for Cd was 26%. See Appendix 8.2.

<b>PYRITE</b>					
<b>Deposit</b>		$\sigma$	<b>Average</b>	<b>Min.</b>	<b>Max.</b>
<b>Larnaca domain</b>		<b>n=55</b>			
Mathiatis North	40	1.3	5.1	2.5	7.2
Sha	9	2.4	1.5	-5.5	4.5
Touronja	2	0.6	1.9	1.3	2.4
Almyras	4	0.8	5.0	3.9	6.2
<b>STTFZ</b>		<b>n=18</b>			
Kalavastos	18	4.3	8.0	2.0	13.2
<b>Makheras</b>		<b>n=5</b>			
Kambia	2	0.4	7.0	6.5	7.4
Kaphedes	2	1.7	5.0	3.3	6.6
Peristerka	1			5.4	5.4
<b>Mitsero</b>		<b>n=20</b>			
Agrokipia A	3	0.6	4.8	4.1	5.6
Kokkinopezula	5	1.7	4.4	2.8	7.3
Kokkinoyia	8	3.5	3.2	-0.6	8.4
Akaki River	4	0.7	3.9	3.0	4.5
<b>Solea</b>		<b>n=51</b>			
Apliki	19	1.7	4.2	-0.8	7.1
Memi	1			4.4	4.4
Skouriotissa	31	1.4	4.4	0.9	6.4
<b>Polis</b>		<b>n=11</b>			
'77'	1			5.1	5.1
Kynousa	8	2.2	4.7	2.2	7.0
Lysos	1			7.1	7.1
Pournaji	1			9.5	9.5
<b>CHALCOPYRITE</b>					
<b>Deposit</b>	<b>n=</b>	$\sigma$	<b>Average</b>	<b>Min.</b>	<b>Max.</b>
Kokkinoyia	1			0.6	0.6
Kokkinopezula	1			1.3	1.3
Apliki	11	0.9	3.6	2.4	5.2
Skouriotissa	2	0.7	4.9	4.2	5.6
<b>COVELLITE</b>					
<b>Deposit</b>	<b>n=</b>	$\sigma$	<b>Average</b>	<b>Min.</b>	<b>Max.</b>
Skouriotissa	5	0.7	4.5	3.7	5.3

**Table 8.5:** Summary of sulfur isotope values in pyrite, chalcopyrite and covellite presented in per mil  $\delta^{34}\text{S}_{(\text{V-CDT})}$ . All data within  $\pm 0.7\text{‰}$  ( $1\sigma$ ). Full data is available in Appendix 8.1.

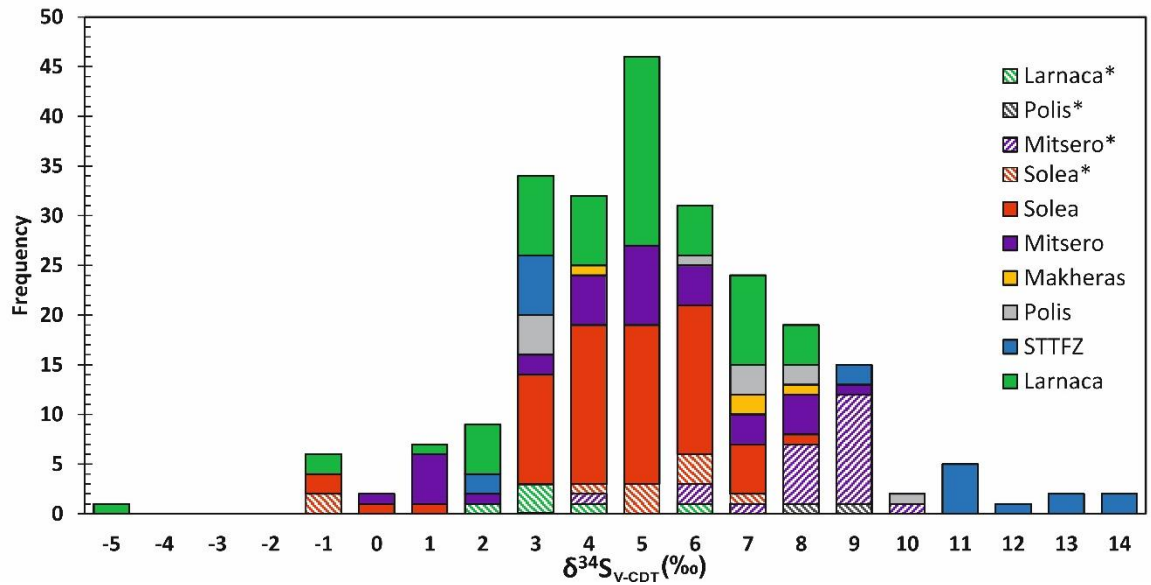


Figure 8.6: Sulfur isotope data for Troodos VMS for all sulfides. Caption overleaf.

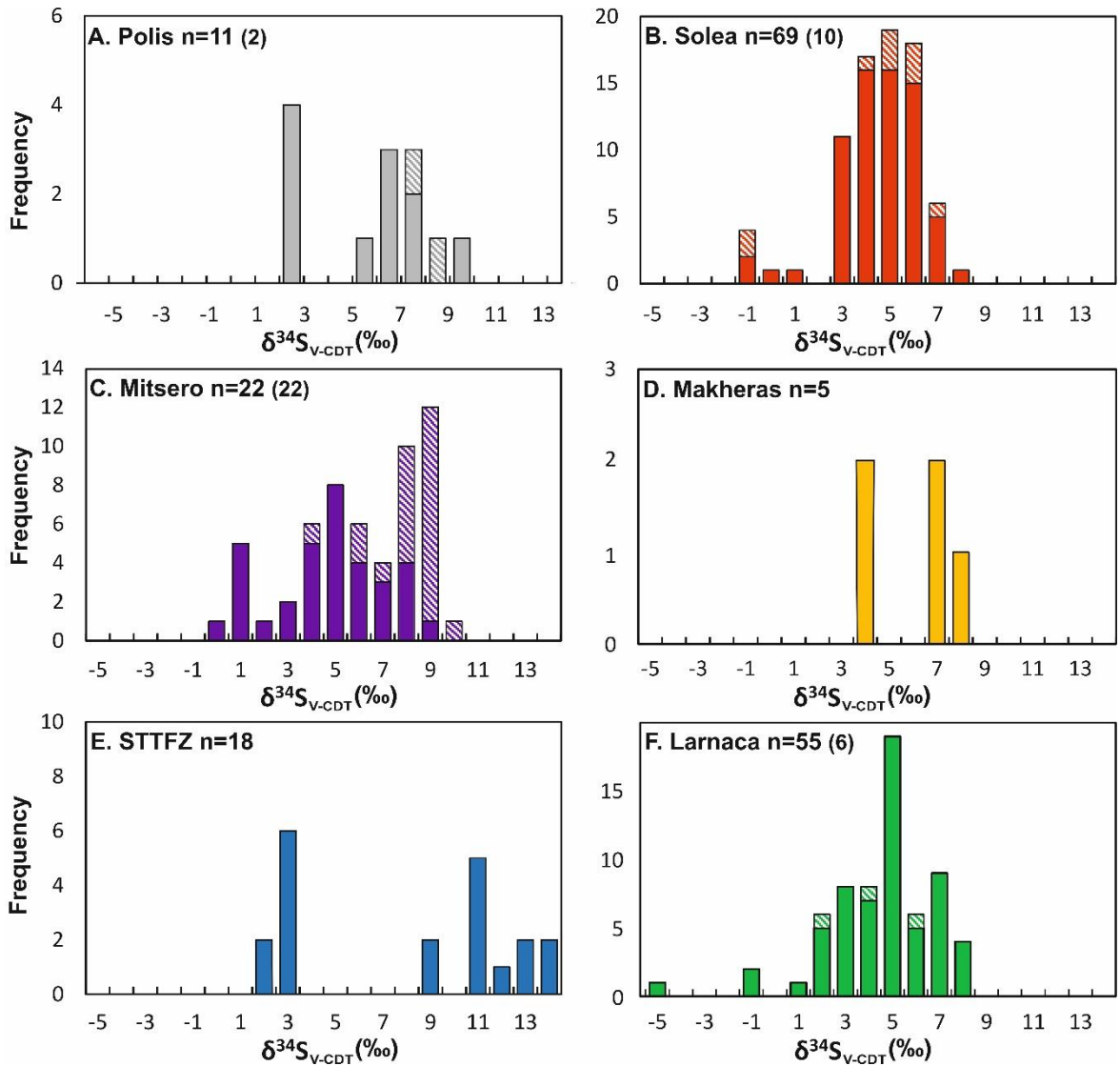


Figure 8.7: Sulfur isotope  $\delta^{34}\text{S}$  (‰ V-CDT) data (all sulfides) classified by structural domain Full description overleaf.

**Figure 8.6:** Histogram of sulfur isotope ( $\delta^{34}\text{S}_{\text{V-CDT}}$ ) composition for all sulfides ( $n=220$ : pyrite, chalcopyrite and covellite (Table 8.5) from Troodos VMS/mineralised localities classified by structural domain (Figure 8.1). Average  $\delta^{34}\text{S}$  for all data is +4.7‰. \*and crosshatching indicates compiled data (after Hannington *et al.*, 1998; Keith *et al.*, 2016a; Pederson *et al.*, 2017:  $n=40$ ). Full data is available in Appendix 8.1.

**Figure 8.7:** Sulfur isotope ( $\delta^{34}\text{S}$  (‰  $\text{V-CDT}$ )) data (all sulfides) classified by structural domain (Figure 2). Dashed boxes refer to compiled data after Hannington *et al.* (1998); Keith *et al.* (2016a) and Pederson *et al.* (2017). Number of analyses for each domain denoted by  $n$ , compiled values denoted by ( $n$ - in brackets). Note variable Y axis between different structural domains.

## 8.5 Discussion

### 8.5.1 Trace element variation

The incorporation of trace elements in VMS sulfide minerals is controlled by the fluid composition and physicochemical fluid parameters including temperature,  $f\text{O}_2$  and pH (Berkenbosch *et al.*, 2012; Huston *et al.*, 1995; Keith *et al.*, 2016a,b; Maslennikov *et al.*, 2009; Wohlgemuth-Ueberwasser *et al.*, 2015). Since the exact fluid composition responsible for the formation of the Troodos VMS deposits is unknown, mineralogy and mineral chemistry are assumed to be an indirect proxy (Keith *et al.*, 2016a,b; Wohlgemuth-Ueberwasser *et al.*, 2015). The trace element composition of pyrite varies between different structural domains (Figure 8.4), some domains are enriched in elements of magmatic affinity, such as Se, Cu, Au and Te (e.g. Solea), whilst others are depleted (e.g. Makheras). Results from the Apliki VMS deposit are excluded from the Solea domain as previous studies have identified Apliki as being extremely enriched in Se due to unusual oxidisation related processes (Martin *et al.*, 2018; Chapter 6). Subsequently trace element geochemistry from Apliki is excluded when considering the Solea domain and instead Apliki geochemistry is presented as a sub-classification (Figure 8.4 and 8.5; Martin *et al.*, 2018). The highest average Se concentration in pyrite (excluding Apliki) was from the Solea domain at 257 ppm ( $n=366$ ,) compared to 47 ppm ( $n= 89$ ) at Larnaca (Figure 8.4). In contrast, As and Sb are enriched in pyrite from the Mitsero and Makheras domains relative to Solea (Figure 8.4). These trace element variations between structural domains suggest different physicochemical conditions during ore formation or a heterogeneous source of metals between VMS on a regional scale.

Volcanogenic Massive Sulfide deposits form throughout the extrusive sequence of the Troodos ophiolite at the contact between basal group-LPL, LPL-UPL or overlying the UPL (Adamides, 2010b; Constantinou and Govett, 1973) (Figure 8.8). The stratigraphic position of VMS formation may have important implications for the source characteristics of different trace metals as it determines both the timing of and the available source(s) of metal to support VMS formation relative to the eruption of the UPL and LPL's (cf. Chapter 2). Patten *et al.* (2017) state that the LPL are enriched in As, Zn and Sb relative to the UPL and that the UPL are enriched in Se, Cu and

Au relative to the LPL. They report that basaltic-andesite (i.e. UPL) samples from Troodos contain  $96 \pm 36$  ppm Cu,  $120 \pm 61$  ppb Se and  $2.1 \pm 1$  ppb Au compared to andesitic (i.e. LPL) samples at 29 ppm Cu, 69 ppb Se and 0.77 ppb Au. For example the Agropkipia A deposit (Mitsero domain, Figure 8.2 B, Figure 8.8) is overlain by unaltered UPL therefore demonstrating at Agropkipia A that metals must have been derived from the BG or LPL lithologies without any input from the UPL. In other areas, VMS occur above the UPL sequence and are directly overlain by unaltered and calcareous sediments (Skouriotissa, Figure 8.2 A, Figure 8.8).

Making the assumption that the metals in pyrite are only sourced from leaching of underlying sheeted dykes, the ratio of Au + Se + Cu (UPL affinity) to As + Zn + Sb (LPL affinity) elements in pyrite from VMS is used to estimate the relative contribution of UPL and LPL lithologies within epidosite zones (or the wider sheeted dyke complex) at the time of VMS formation. Deposits situated in the lower stratigraphy, predating UPL accretion (BG and LPL) are expected to contain lower Au, Se and Cu relative to those that post-date UPL accretion. For all VMS (Table 8.6 A) UPL to LPL ratios range from 0.01 (Agropkipia A and Memi) to 7.63 at Mala. There is however significant variation in deposits formed at the same stratigraphic level, for example Mala and Kaphedes both occur at the BG-LPL contact but exhibit UPL:LPL ratios of 7.63 and 0.35 respectively (Table 8.6 A, overleaf).

When all deposits are grouped based on stratigraphic depth a broad correlation exists between the UPL:LPL ratio and depth of VMS mineralisation in the Troodos stratigraphy (Table 8.6 B, Figure 8.8). Deposits that post-date UPL accretion exhibit the highest average ratio of 0.53 (Table 8.6 B) and those that pre date UPL accretion average 0.25 and 0.35 respectively (excluding Mala - see Chapter 9). The high value for BG hosted VMS that should be depleted in Cu + Se + Au, specifically Mala with a UPL:LPL ratio of 7.63 probably suggests an additional source of magmatophile elements in the VMS hydrothermal system (cf. Chapter 9). The broad correlation between UPL:LPL ratio and stratigraphic depth suggest that on a regional scale source rock composition may influence VMS geochemistry (discussed further in section 8.5.4)

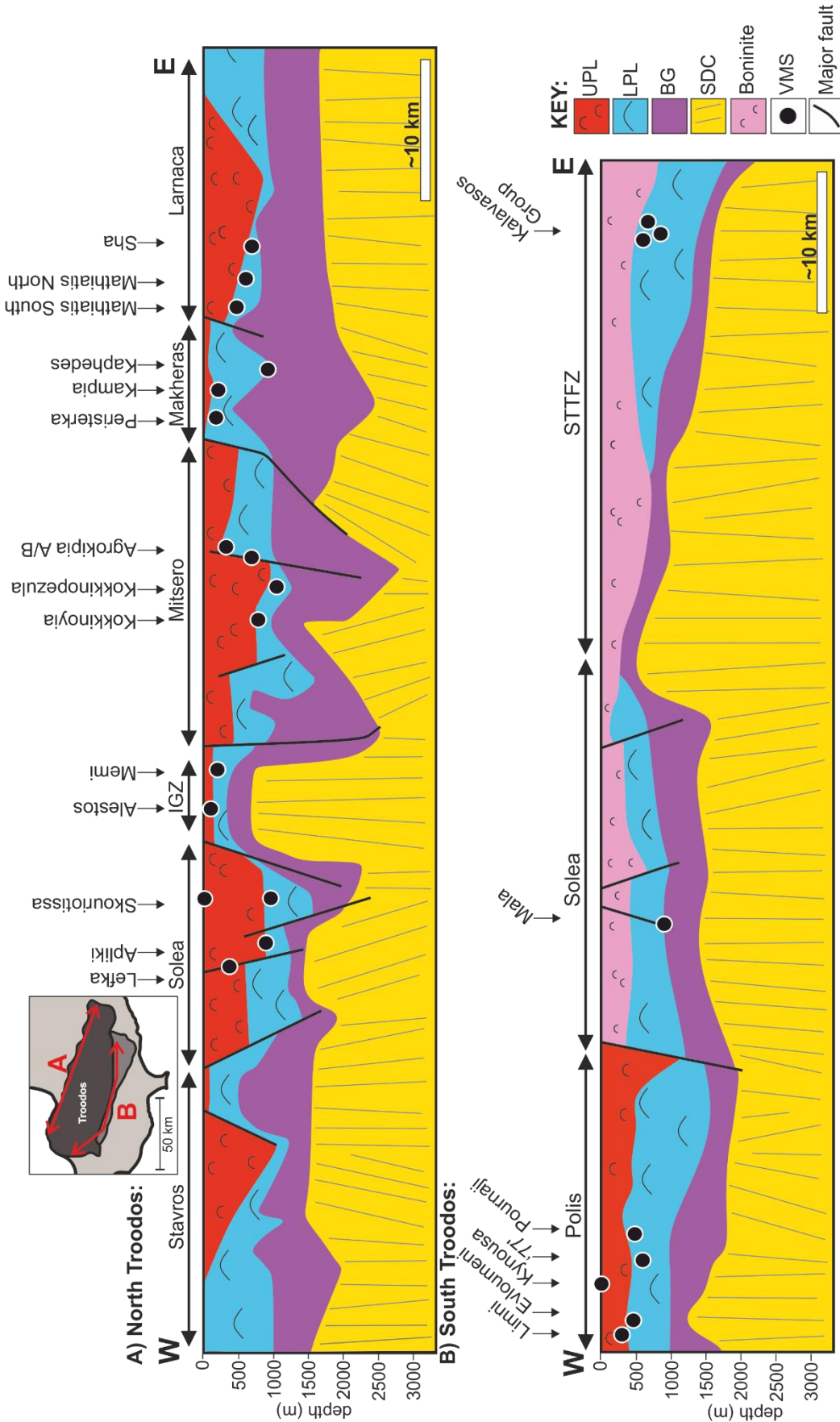


**Figure 8.8:** Schematic summary showing the location of VMS deposits in the Troodos stratigraphy. Inset map displays the approximate location of transect A (N Troodos) and B (S Troodos). Transect A is adapted from Young (2014); high Ti lavas are interpreted as broadly representing the LPL whilst low Ti lavas represent the UPL. VMS occur across four main structural domains: Solea, Mitsero, Makheras and Larnaca. The zone between the Solea and Mitsero grabens is termed the Inter Graben Zone (IGZ-Eddy et al., 1998). Some deposits occur overlying the UPL (e.g. Skouriotissa, Phoucasa) whilst others occur deep in the extrusive stratigraphy (e.g. Kaphedes) at the BG-LPL transition. VMS deposits that formed at the UPL-LPL boundary, the BG-LPL transition or within the LPL pre-date the eruption of the more primitive Se, Cu and Au-rich UPL. VMS in transect B correspond to three main structural domains: Polis, Solea and the Southern Troodos Transform Fault Zone (STTFZ). Deposits occur throughout the extrusive sequence from Mala at the BG-LPL transition to Kynousa that overlies the UPL. Note that faulting in S Troodos is parallel to the section, hence, for example, at Kalavassos no faults are visible in the section. The author emphasises the schematic nature of this figure, the scale and lithological contacts provided are approximate.

<b>Deposit</b>	<b>Cu+Se+Au</b>	<b>Zn+Sb+As</b>	<b>UPL:LPL</b>	<b>Strat. level</b>
<b>Larnaca domain</b>	(ppm)	(ppm)		
Mathiatis South	304	11561	0.03	UPL-LPL
Mathiatis North	482	1079	0.45	UPL-LPL
Sha	302	1158	0.26	UPL-LPL
<b>STTFZ domain</b>				
Kalavasos	121	955	0.13	UPL-LPL
<b>Makheras domain</b>				
Kampia	449	910	0.49	LPL
Kaphedes	920	2618	0.35	BG-LPL
<b>Mitsero domain</b>				
Agrokipia A	383	2352	0.16	UPL-LPL
Agrokipia B	307	21431	0.01	LPL
Kokkinopezula	199	185	1.08	LPL
Kokkinoyia	1599	7073	0.23	UPL-LPL
<b>Solea domain</b>				
Apliki	3200	932	3.43	LPL
Mala	2937	385	7.63	BG-LPL
Memi	207	20193	0.01	LPL
Skouriotissa	1381	1401	0.99	TOP OF UPL
<b>Polis domain</b>				
'77'	28	915	0.03	LPL
Kynousa	1209	15718	0.08	TOP OF UPL
Limni	1423	7289	0.20	UPL
Pournaji	279	579	0.48	LPL

**Table 8.6 A:** Total 'UPL' Cu+Se+Au affinity elements vs. 'LPL' affinity elements Zn+Sb+As vs. the stratigraphic position of different VMS in the Troodos ophiolite classified by corresponding structural domain (Figure 8.1). Au+Se+Cu and Zn+Sb+As are in ppm from LA-ICP-MS analysis of pyrite. The UPL:LPL ratio is derived from total Cu+Se+Au/Zn+Sb+As in a given VMS deposit or district. BG= Basal Group, LPL= Lower Pillow Lava, UPL= Upper Pillow Lava.

<b>Stratigraphic depth</b>	<b>n</b>	<b>Au +Se +Cu</b>	<b>As + Zn + Sb</b>	<b>UPL:LPL</b>
Basal Group-LPL	2	920	2618	0.35
LPL/LPL-UPL contact	14	717	6284	0.25
Overlying UPL	2	1295	8559	0.53

**Table 8.6B:** Summary of all Troodos VMS deposits group by corresponding stratigraphic position. A higher UPL:LPL ratio suggest VMS that overly the UPL formed from a source enriched in Au+Se+Cu, i.e. metals may have been leached form a higher proportion of primitive UPL affinity dykes during epidosite formation. Deposits that pre-date the eruption of the UPL have a lower ratio. Note the high UPL:LPL ratio for BG-LPL deposits. See text for discussion.

### 8.5.2 Selenium/Sulfur ratios in Troodos VMS

The Se/S ratio is commonly used in hydrothermal ore deposits as a tracer of magmatic volatile influx (Hannington *et al.*, 1999; Huston *et al.*, 1995; Layton-Matthews *et al.*, 2008, 2013). In previous studies the author used Se/S ratios to propose that the magmatic volatile influx between the Mitsero and Solea structural domains is distinct (Martin *et al.*, 2019; Chapter 5).

Layton-Matthews *et al.* (2008, 2013) state that Se/S ratios >500 represent an increased magmatic volatile component in VMS hydrothermal systems. In this study new Se/S data in pyrite representing the six structural domains in the Troodos ophiolite is presented (Figure 8.5).

Pyrite from the Skouriotissa deposit in the Solea domain shows Se/S ratios reaching 3650 with an average of 481 (n=362) which could be interpreted as an increased magmatic influx relative other structural domains (values >500; Layton-Matthews *et al.*, 2008). Selenium/sulfur ratios clearly demonstrate variation across different VMS deposits and their corresponding structural domain (Figure 8.5). According to the Se/S ratios in pyrite, the VMS deposits of the Larnaca domain experienced the lowest magmatic influx, if any, as indicated by the lowest average Se/S ratio of 89 and an average Se content of 47.2 ppm (n=350). If Se/S ratios in pyrite are diagnostic for a magmatic volatile influx to an overlying hydrothermal system then this should correlate with a systematic decrease in the  $\delta^{34}\text{S}$  signature towards lighter, magmatic sulfur values and this is not clearly demonstrated in Troodos VMS deposits with an  $R^2$  values of 0.1 between  $\delta^{34}\text{S}$  and Se concentration on a domain scale (see Table 8.7), probably indicating the modification of Se/S during zone refining or an additional source for Se (cf. Chapter 5 and 9).

### 8.5.3 Variation in sulfur isotopes

Sulfur isotope data from sulfides in VMS of the Troodos ophiolite in this study range from -5.5‰ to +13.2‰ in pyrite (n=160, av.= +4.7‰), +0.6‰ to +5.6‰ in chalcopyrite (n=15, av.= +3.4‰) and +3.7‰ to +5.3‰ in covellite (n=5, av.= +4.5‰) (Table 8.5). This range is similar to that observed in modern seafloor sulfides from sediment starved back-arc basins, however the spread of data is much greater than typically observed in sediment starved MOR settings (Figure 8.9). Values for modern seafloor sulfides in the Lau back-arc basin range from -7.7‰ at Hine Hina to +16.2‰ at Vai Lili (Herzig *et al.*, 1998a; Figure 8.8). In contrast,  $\delta^{34}\text{S}$  in pyrite from the TAG hydrothermal field at the Mid-Atlantic ridge (MAR) average +6.4‰ (Herzig *et al.*, 1998b) (Figure 8.9). These variations highlight the variable sources of sulfur in active hydrothermal systems and their fossil VMS counterparts, such as those preserved in the Troodos stratigraphy.

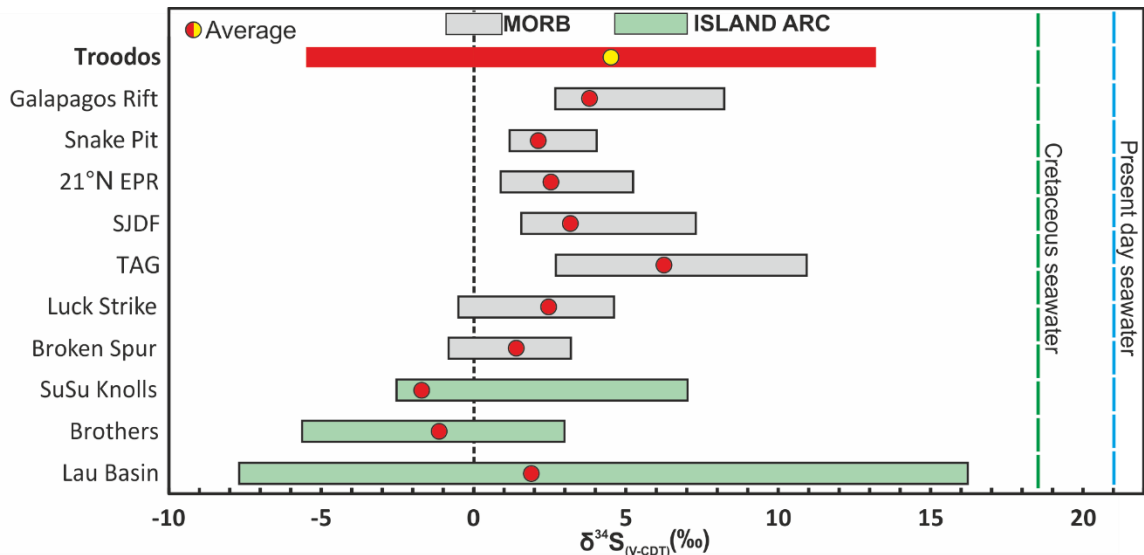


**Figure 8.9:** Comparison plot of range of  $\delta^{34}\text{S}$  from sulfide minerals of Troodos (red bar) with active seafloor hydrothermal systems in arc related (green bar) and MOR sediment starved (grey bar) hydrothermal systems (pyrite, marcasite, sphalerite and chalcopyrite). Troodos (This study, Hannington *et al.*, 1998; Keith *et al.*, 2016; Pederson *et al.*, 2017), Galapagos Rift (Knott *et al.*, 1995), Snake Pit (Kase *et al.*, 1990), 21°N East Pacific Rise (EPR) (Arnold and Sheppard, 1981; Woodruff and Shanks, 1988), Southern Juan de Fuca (SJDF) (Shanks and Seyfried, 1987), Trans-Atlantic Geotraverse Field (TAG) (Friedman, 1994; Herzig *et al.*, 1998b), Lucky Strike (Rouxel *et al.*, 2004), Broken Spur (Butler *et al.*, 1998; Duckworth *et al.*, 1995), SuSu Knolls (Yeats *et al.*, 2014), Brothers (de Ronde *et al.*, 2003; 2005), Lau Basin (Herzig *et al.*, 1998a). Red/yellow dots indicate average  $\delta^{34}\text{S}$  value. Black dashed line represents MORB  $\delta^{34}\text{S}$ , blue dashed line is present day seawater, green box is Island arc lava  $\delta^{34}\text{S}$  (Herzig *et al.*, 1998a). Green dashed line is Cretaceous seawater (Kampschulte and Strauss, 2004).

A significant proportion of  $\delta^{34}\text{S}$  from modern vent sites occur between the magmatic mean (MOR and Island Arc 0-7‰- Figure 8.9) and seawater sulfate (+21-22‰). This indicates that sulfur in active sediment starved, MOR hydrothermal systems is principally sourced from two reservoirs; seawater and the leaching of primary igneous lithologies during hydrothermal alteration. This is supported by the low  $\Delta^{33}\text{S}$  of pyrite that are commonly used to distinguish between microbial and inorganic processes as microbial activity leads to  $\Delta^{33}\text{S} > 0.04\text{‰}$  compared to the starting sulfate  $\Delta^{33}\text{S}$  composition (Brunner and Bernasconi, 2005). A  $\Delta^{33}\text{S}$  value of  $< 0.00\text{‰}$  in many sediment starved ridge vent sulfides suggests an absent or minimal contribution of sulfide through biologically mediated processes (e.g. 13°N on the EPR, Ono *et al.*, 2007). Additionally, light  $\delta^{34}\text{S}$  values  $< 0\text{-}1\text{‰}$  in the Lau Basin, Brothers volcano and SuSu Knolls vent sites are attributed to a fluid source that has undergone  $\text{SO}_2$  disproportionation (e.g. de Ronde *et al.*, 2005; Herzig *et al.*, 1998a; Yeats *et al.*, 2014; Figure 8.9).

The Troodos ophiolite formed in a sediment starved supra-subduction zone spreading environment, therefore a sedimentary source of sulfur is unlikely (Gass, 1980; Robertson, 2002, 1975). The bacterial reduction of seawater sulfate can also produce extremely negative  $\delta^{34}\text{S}$

values (Pedersen *et al.*, 2017; Peters *et al.*, 2011; Rouxel *et al.*, 2008; Seal, 2006). For example pyrite in Troodos analysed from the Akaki River section exhibit a bacterial  $\delta^{34}\text{S}$  signature of -15 to -22‰ and  $\Delta^{33}\text{S}$  of between 0.00 and 0.30‰. This is attributed to low temperature (<140°C) recharge related fluid flow where bacterial sulfate reduction is possible (Pedersen *et al.*, 2017). Biogenic seawater sulfate reduction (BSR) is limited to low temperature and generally organic rich environments, typically at temperatures <140°C (Alt and Shanks, 2011; Machel, 2001; Rouxel *et al.*, 2008). Given the high temperature nature of the VMS hydrothermal system (>200°C), typically up to >350°C in the lower sheeted dykes and the sediment and organic poor environment of Troodos, BSR is likely to be a minor component in typical high temperature discharge zones. This is confirmed by Pederson *et al.* (2017) for the Agrokipia VMS where  $\Delta^{33}\text{S}$  values up to 0.22‰ signifies a minor biogenic component in pyrite. Instead, the majority of sulfur isotope data in this study can be explained by the mixing of sulfur sourced from the leaching of igneous rocks (0-1‰; Alt, 1994) and the thermochemical reduction of Cretaceous seawater sulfate (18-19‰; Kampschulte and Strauss, 2004) in variable amounts at temperatures of >160°C.

Two models have been proposed for the thermochemical reduction of seawater sulfate and the sulfur isotope values preserved in hydrothermal sulfides; the two component mixing of seawater derived sulfate and igneous derived sulfide (Ono *et al.*, 2007) and the anhydrite buffer model (Ohmoto *et al.*, 1983). During hydrothermal circulation anhydrite ( $\text{CaSO}_4$ ) precipitates at temperatures >150°C depleting downward circulating fluid in sulfate (Ono *et al.*, 2007). Within the sheeted dykes the hydrothermal fluids circulate at temperatures >250°C gain  $\text{H}_2\text{S}$  through i) the reduction of seawater sulfate by  $\text{Fe}^{2+}$  bearing minerals or, ii) the leaching of primary magmatic sulfides (Ono *et al.*, 2007). The two component mixing of seawater sulfate ( $\delta^{34}\text{S} \approx 21\text{‰}$ ) and igneous derived sulfide ( $\delta^{34}\text{S} \approx 0\text{‰}$ ) in active hydrothermal systems indicate that >75% of  $\text{H}_2\text{S}$  is derived from the leaching of igneous sulfides with a minor seawater-derived sulfate component (<25%). Seawater is quantitatively reduced to  $\text{H}_2\text{S}$  under low water:rock ratios in systems where fluid redox is buffered by the quartz-fayalite-magnetite buffer. Sulfides precipitated from this process follow the two phase mixing curve and are predicted to contain  $\delta^{34}\text{S}$  of between 0-5‰ (Ono *et al.*, 2007; Pedersen *et al.*, 2017; Appendix 8.3).

An alternate model proposed by Ohmoto *et al.* (1983) is the anhydrite buffer model. This model is based on the buffering of hydrothermal  $\text{H}_2\text{S}$  (and sulfide) by previously precipitated anhydrite. Therefore, the  $\delta^{34}\text{S}$  of precipitated sulfide reflects fractionation between sulfate ( $\text{SO}_4$ ) and sulfide ( $\text{H}_2\text{S}$ ). Equilibrium fractionation factors between sulfate and sulfide are temperature dependent, and fractionation factors range from 21.5‰ to 15.8‰ at 300 and 400°C respectively (Ono *et al.*, 2007; Ohmoto *et al.*, 1983; Ohmoto and Lasaga, 1982). In contrast to the two phase

mixing model the anhydrite buffer model predicts that a greater proportion of VMS sulfide is sourced from seawater sulfate (>75%).

Both the two phase mixing model (cf. Figure 8.10, see also Chapter 3, Figure 3.6) and the anhydrite buffer model are applicable to Troodos VMS deposits as the average  $\delta^{34}\text{S}$  of sulfides, +4.7‰ falls within the expected range that these models predict for precipitated sulfides (0-6‰: vent sulfides). Furthermore, in active systems both processes are important in controlling sulfur isotope composition of sulfide minerals in SMS. The models are not mutually exclusive, for example at TAG, deep  $\text{H}_2\text{S}$  rich and  $\text{SO}_4$  depleted (<1 mmol/kg) fluids in equilibrium with surrounding rock undergo mixing within the up flow zone with anhydrite and  $\text{SO}_4$  rich fluids (Humphris and Tivey, 2000). Anhydrite precipitation in the mixing zone is maintained by complex dissolution and re-precipitation processes and isotopic exchange with deep  $\text{H}_2\text{S}$ -rich fluid during mixing and entrainment of seawater (Ono *et al.*, 2007). If isotope equilibrium occurs during mixing then the composition of  $\text{H}_2\text{S}$  would plot along the anhydrite buffer line at the corresponding temperature (Appendix 8.3; Ono *et al.*, 2007). If equilibrium is not reached during mixing due to short fluid residence time in the system, leading to the incomplete exchange between  $\text{SO}_4$  and  $\text{H}_2\text{S}$  then fluids would lie on the two phase mixing line (Ono *et al.*, 2007). Further multiple sulfur isotope studies ( $\Delta^{33}\text{S}$ ) would need to be undertaken to elucidate a single model.

The negative  $\delta^{34}\text{S}$  (<0‰) values recorded in pyrite in Troodos VMS deposits from some localities (e.g. Sha) require either an additional light source of sulfur or in the anhydrite buffer model, equilibrium between  $\text{SO}_4$  and  $\text{H}_2\text{S}$  at low temperatures <300°C. Assuming a Cretaceous seawater sulfate value of 18-19‰ (Kampschulte and Strauss, 2004) with a fluid that was progressively heated to temperatures of 300°C or less, the corresponding isotopic fractionation assuming equilibrium was achieved would be 21.5‰ between sulfate and sulfide at 300°C. Thus the thermochemical reduction of Cretaceous seawater sulfate could lead to  $\delta^{34}\text{S}$  in sulfides of between -2.5 and -3.5‰ (Ono *et al.*, 2007). Furthermore, low temperature TSR (200°C) is capable of producing even lighter  $\delta^{34}\text{S}$  in sulfides due to even greater fractionation factors between sulfate and sulfide that could theoretically precipitate sulfides with corresponding  $\delta^{34}\text{S}$  of -11.7 to -12.7‰ at 200°C (fractionation factor of 30.7‰; Ohmoto and Lasaga, 1982, Appendix 8.3).

Sulfur isotope values in pyrite from the Sha VMS deposit range from -5.5 to +4.5‰ and contain the lowest values reported in this study. These  $\delta^{34}\text{S}$  values are similar to those reported for sulfides in the Lau back-arc basin (Herzig *et al.*, 1998a), at SuSu Knolls in the Manus back-arc basin (Yeats *et al.*, 2014) and at the Brothers arc volcanic system, Kermadec Arc (de Ronde *et*

*al.*, 2005) (Figure 8.9). The negative  $\delta^{34}\text{S}$  values reported at modern vent sites are generated by disproportionation of  $\text{SO}_2$  in a volatile phase. Exsolved  $\text{SO}_2$  mixes with deep hydrothermal fluids causing disproportionation that generates both  $\text{H}_2\text{S}$  and  $\text{SO}_4^{2-}$ ; sulfides formed from this solution can contain  $\delta^{34}\text{S} < 0\text{‰}$  (Berkenbosch *et al.*, 2012; de Ronde *et al.*, 2005; Kusakabe *et al.*, 2000). This is proposed as an alternative mechanism to the anhydrite buffer model explaining  $\delta^{34}\text{S}$  values in sulfides that are lower than the mean  $\delta^{34}\text{S}$  composition of the Troodos igneous host rocks (0-1‰: Alt, 1994).

Significant internal  $\delta^{34}\text{S}$  variation of up to 11.2‰ are recorded from pyrite within a single VMS deposit (Table 8.5). Previous studies (Keith *et al.*, 2016b) have proposed that mound scale variation is related to the local channelling or reduced ingress of seawater with increasing depth in the VMS stratigraphy (i.e. stockwork vs. mound mineralisation) leading to a decrease of the high  $\delta^{34}\text{S}$  seawater component and progressively lower  $\delta^{34}\text{S}$  signatures in pyrite. For example, at Skouriotissa  $\delta^{34}\text{S}$  values in pyrite become lighter with stratigraphic depth; ranging from +6.4‰ in the upper mound to +0.9‰ in the stockwork. This is consistent with decreased seawater ingress and suggests that sulfide precipitation is influenced by complex physicochemical changes relating to permeability and temperature fluctuations on the local scale (cm to m) along fluid flow pathways rather than homogenous fluid flow throughout the mound (Humphris and Cann, 2000; Martin *et al.*, 2019). Additionally, the dissolution and re-precipitation of sulfide and sulfate within the mound is an important process (Gemmell and Sharpe, 1998; Pedersen *et al.*, 2017).

When classified into regional structural domains (after Varga and Moores, 1985; Figure 8.1), distinct  $\delta^{34}\text{S}$  populations may also be identified (Figure 8.7, Table 8.7). This is best illustrated within the STTFZ domain where two distinct  $\delta^{34}\text{S}$  populations in pyrite are identified around +3‰ and +11‰ at Kalavassos (Figure 8.7 E). Firstly, the average  $\delta^{34}\text{S}$  in pyrite for the STTFZ (+8.0‰, n=18) is significantly higher than for all other domains (+4.7‰, pyrite, n=160) suggesting a larger volume of seawater ingress. The heavier  $\delta^{34}\text{S}$  population (up to 13.2‰  $\delta^{34}\text{S}$ ) probably formed through increased seawater mixing leading to the preferential sourcing of sulfur through thermochemical seawater reduction. This is supported by the location of Kalavassos within the active transform terrain. In this zone, frequent fault movement facilitates brecciation allowing more extensive seawater ingress near active fault margins. If seawater percolated deep in the crust and reached temperatures  $>150^\circ\text{C}$  (anhydrite window) then it would become progressively depleted in  $\text{SO}_4$  during anhydrite precipitation. Hence a shallow entrainment depth of seawater prior to the complete reduction of seawater  $\text{SO}_4$  is favoured as this would explain heavier  $\delta^{34}\text{S}$  values in precipitated pyrite. More distal VMS deposits located away from faults experienced relatively less seawater ingress, hence they have lower  $\delta^{34}\text{S}$  values in pyrite. All Troodos structural domains (Figure 8.1) contain  $\delta^{34}\text{S}$  populations around 0-1‰

(Figure 8.6) and the relative contribution of sulfur sourced from seawater and leaching of igneous rocks assuming a two phase mixing model has been calculated using Equation 1 below.

$$\text{Equation 1: } \delta^{34} S_{\text{mix}} = X \delta^{34} S_{\text{SW}} + (1-X) \delta^{34} S_0 \quad (\text{Keith et al., 2016b})$$

The sulfur isotope ratio of fluid at each VMS are represented by pyrite before mixing ( $\delta^{34} S_0=0.5\text{‰}$ : Alt, 1994) and after mixing ( $\delta^{34} S_{\text{mix}} = \text{maximum measured } \delta^{34} S$ ) with an unknown quantity of sulfur from thermochemical reduction of Cretaceous seawater ( $X$ ) ( $\delta^{34} S_{\text{SW}}=18\text{-}19\text{‰}$ : Kampschulte and Strauss, 2004). The relative amount of sulfur sourced from seawater and leaching of igneous rock is summarised in Figure 8.10 (Keith et al., 2016b; Ono et al., 2007).

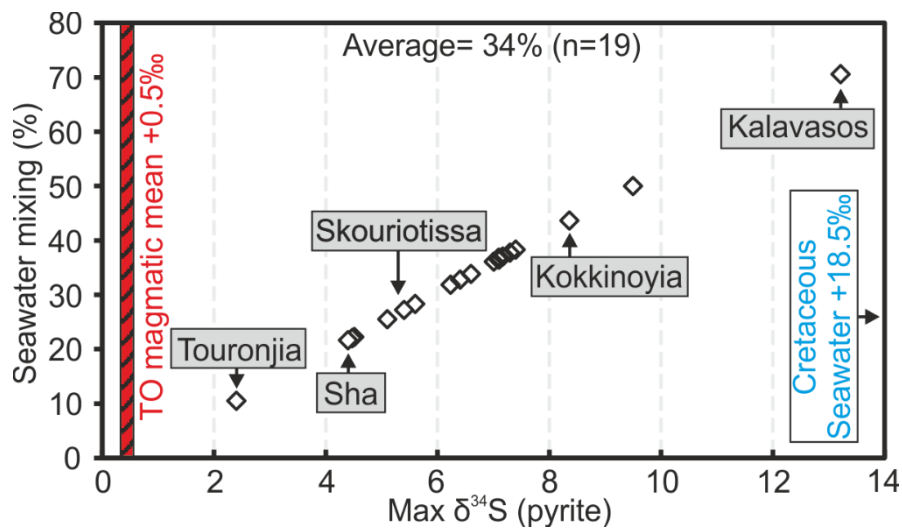


**Figure 8.10:** Two stage mixing model: proportion of sulfur derived from seawater sulfate reduction vs. maximum  $\delta^{34}S$  in pyrite (equation 1). The author assumes a Troodos magmatic mean  $\delta^{34}S$  value of  $+0.5\text{‰}$  and a value for Cretaceous seawater of  $+18.5\text{‰}$ . Results demonstrate variable amounts of sulfur sourced from seawater with an average for all deposits ( $n=19$ ) of 34% of sulfur derived from seawater.

The relative contribution of sulfur sourced from seawater was calculated for 19 Troodos VMS deposits (Table 8.5 and Figure 8.10). Values for VMS range from 22% seawater derived sulfur at Sha to 71% at Kalavassos with an average for all deposits of 34% (Figure 8.10). This is comparable to previous estimates by Keith et al. (2016b) for the Skouriotissa VMS where 38% of sulfur is estimated to have been derived from seawater.

These data provide an estimate of the relative proportion of seawater sourced sulfate reduction and how this might vary between different Troodos VMS deposits. The two phase mixing model of Ono et al. (2007) estimates that approximately 25% of sulfur is derived from seawater; this is comparable to the average of 34% in this study assuming the Troodos hydrothermal system is similar to those analysed in sediment starved MOR environments. In further support of the two phase mixing model for Troodos sulfides is data from Pederson et al. (2017); multiple sulfur isotope ratios ( $\Delta^{33}S$ ) of pyrite from Agrokipia B VMS plot below the  $H_2S/SO_4^{2-}$  equilibrium line

indicating two phase mixing (cf. Ono *et al.*, 2007- Appendix 8.3). Therefore observed  $\delta^{34}\text{S}$  in VMS sulfides probably represent the mixing of two isotopically distinct reservoirs with the addition of a shallow seawater derived fluid which formed the heavy values in some VMS near active fault margins (e.g. Kalavassos). The two phase mixing model is incapable of producing  $\delta^{34}\text{S}$  values less than the mean  $\delta^{34}\text{S}$  composition of Troodos igneous rocks ( $\sim 0\text{-}1\text{‰}$ ). Therefore, a value of  $-5.5\text{‰}$  at Sha is not explainable by the two phase mixing model and possibly suggests the contribution of an additional light source of sulfur to some Troodos VMS deposits (cf. section 8.5.5.).

#### 8.5.4 Linking source rock and VMS composition

In order to explain variation in magmatophile trace element (e.g., Te, Se, Au, Cu), Se/S ratios and  $\delta^{34}\text{S}$  variations in hydrothermal sulfides between structural domains and individual VMS deposits two processes are proposed: i) a heterogeneous source of metals within the lower sheeted dyke complex (Figure 8.11) and, ii) the addition of a magmatic volatile phase (Figure 8.12).

Previously, models have attributed variations in trace element geochemistry to local physicochemical fluid factors, such as temperature (Hannington *et al.*, 1998). Whilst the author agrees that local factors will influence metal distribution on a deposit scale it does not explain the variation observed on a regional scale. A variable magmatic influx or variation in protolith metal concentration into the VMS hydrothermal systems would explain variation between structural domains.

The Troodos extrusive sequence contains two distinct lava suites; the upper and lower pillow lavas (UPL and LPL; Malpas and Langdon, 1984; Schouten and Kelemen, 2002). The UPL are largely basaltic to picritic in composition with low  $\text{TiO}_2$  ( $<0.4$  wt.%) whilst the LPL are basaltic-andesites with high  $\text{TiO}_2$  ( $>0.8$  wt.%) (Robinson and Malpas, 1990; cf. Chapter 2). The LPL represent the main 'on axis' accretionary phase and were erupted by frequent, high viscosity eruptions (Schouten and Kelemen, 2002). In contrast the UPL were erupted in temporally distinct, high volume eruptions (Schouten and Kelemen, 2002). The VMS deposits presented in this study either overly the UPL (e.g. Phoucasa, Skouriotissa), occur at the UPL-LPL contact (e.g. Agrokipia A) or within LPL (e.g. Kokkinopezula, Table 8.6 A, Figure 8.8).

Patten *et al.* (2017) report a systematic increase in As, Zn and Sb with increasing fractionation from basalt to andesite and primitive samples contain the highest Cu, Au and Se (Patten *et al.*, 2017). Upper pillow lavas contain  $120 \pm 61$  ppb Se compared to the LPL which contain 69 ppb (Patten *et al.*, 2017). Concentrations of sulfide compatible chalcophile elements, such as Se, Au

and Cu are highest prior to magnetite saturation at 3.5 wt.% MgO (Jenner *et al.*, 2010; Patten *et al.*, 2017). In contrast, poorly chalcophile Zn, As and Sb are incompatible and become preferentially enriched with increasing fractionation at low MgO contents (<3.5 wt.%), thus explaining trace element fractionation between UPL and LPL lithologies.

Epidosite zones within the lower sheeted dyke complex (SDC) are widely accepted as a source of metals for associated VMS hydrothermal systems in the Troodos ophiolite (Jowitt *et al.*, 2012; Patten *et al.*, 2017; Richardson *et al.*, 1987). Mass balance calculations indicate that  $-88 \pm 16\%$  Au,  $-91 \pm 20\%$  Se and  $-84 \pm 18\%$  Cu is mobilised from epidosite zones relative to protolith metal concentrations (Jowitt *et al.*, 2012; Patten *et al.*, 2017). The amount of metal mobilised from 5 km<sup>3</sup> of epidosites and 5.9 km<sup>3</sup> of 'altered' sheeted dykes is enough to supply a VMS district (e.g., Solea- Apliki, Mavrovouni, Skouriotissa; Patten *et al.*, 2017).

Trace element variations in VMS deposits are partly a function of source heterogeneity within the sheeted dyke complex and epidosite zones that form the source of metals in any given VMS deposit or district (Figure 8.11). If the alteration zone responsible for the formation of a given VMS deposit has relatively different proportions of the two lava units, i.e. UPL and LPL (as dykes), then the trace element signature of the VMS would be different but the sources of sulfur, and therefore the  $\delta^{34}\text{S}$  values would remain constant (Figure 8.11).

This has important implications for the distribution of trace metals in the Troodos VMS deposits. The sheeted dyke complex represents the link between the plutonics and seafloor, therefore UPL and LPL lava affinity dykes are geochemically discernible within the sheeted dykes (Baragar *et al.*, 1990; Staudigel *et al.*, 2000). The author proposes that an epidosite zone with a relatively high volume of UPL affinity dykes would be expected to produce a VMS deposit with elevated concentrations of Se, Au and Cu (Figure 8.11). In contrast a zone comprised solely of andesitic LPL affinity dykes would form a VMS deposit relatively enriched in As, Zn and Pb (Figure 8.11) (Patten *et al.*, 2017; Staudigel *et al.*, 2000). Ultimately the relative enrichment in UPL affinity elements relates to the timing of VMS formation relative to lava eruption; VMS that postdate the eruption of the UPL are enriched in Se, Au and Cu (e.g. Skouriotissa, Phoucasa) relative to those situated within the LPL's (e.g. Mathiatis North).

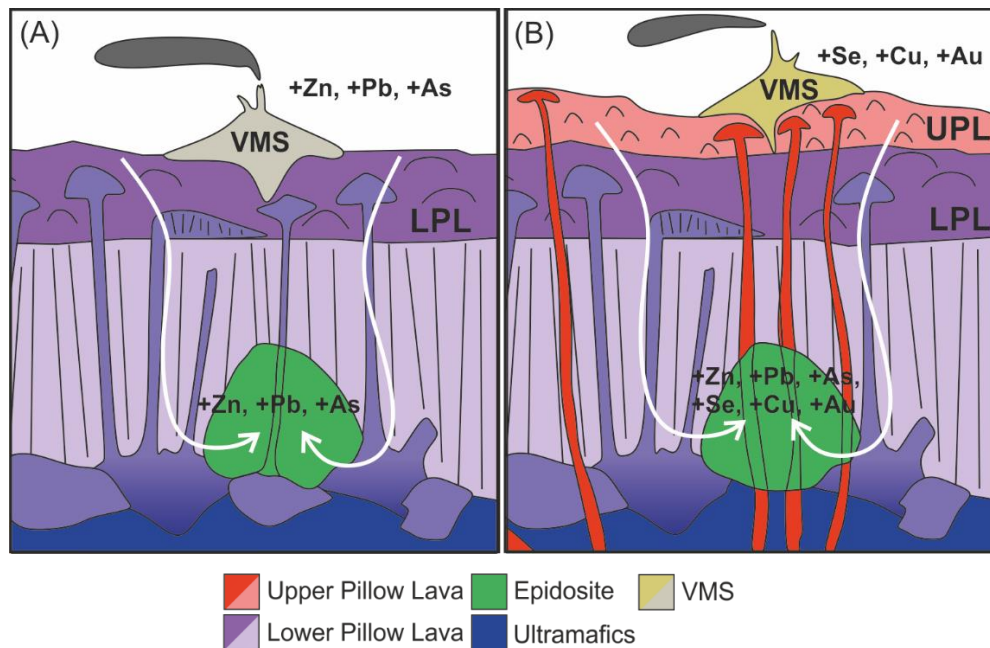


**Figure 8.11:** Schematic view of the Troodos hydrothermal system (not to scale) indicating the effect of source rock variation on VMS trace metal composition. (A) LPL source with VMS formation predating UPL accretion (e.g. Mathiatis North) and, (B) VMS forming simultaneously or postdating UPL formation (e.g. Skouriotissa, Phoucasa). VMS that formed through the alteration of Se, Cu and Au-rich UPL affinity dykes are relatively enriched compared to those that predate UPL formation, forming exclusively from the leaching of LPL affinity dykes. The source of sulfur remains constant in both scenarios with  $\delta^{34}\text{S}$  at or above the Troodos magmatic mean (0-1‰).

This model predicts that the ratio of UPL affinity elements (Cu + Se + Au) to LPL affinity elements (Zn+Sb+As) will vary independent of  $\delta^{34}\text{S}$  values in VMS sulfides as the source of sulfur remains the same irrespective of source lithology. If this is true then comparing VMS that postdate (e.g. Skouriotissa) and predate the eruption of the UPL (e.g. Mathiatis North) should exhibit different trace element signatures; Skouriotissa should be enriched in Cu, Se and Au relative to Mathiatis North. Skouriotissa contains a total of 1381 ppm UPL affinity elements in pyrite compared with 482 ppm at Mathiatis North (Table 8.6A). Sulfur isotope values between the two deposits are comparable at +5.1‰ and +4.4‰ for Skouriotissa and Mathiatis North, respectively. This demonstrates that stratigraphic depth of VMS mineralisation and its relationship to the UPL's controls trace element enrichment in some deposits (Figure 8.11). However, some VMS deposits exhibit an enrichment in Cu + Se + Au despite forming prior to the eruption of the UPL e.g. Mala (UPL:LPL ratio of 7.63); an alternate process is needed to explain their relative enrichment in UPL affinity elements.

### 8.5.5 Magmatic volatile influx

The exsolution and liberation of a magmatic volatile phase into the hydrothermal system during VMS formation can affect both  $\delta^{34}\text{S}$  values and trace element concentrations of a deposit (de Ronde *et al.*, 2005; Herzig *et al.*, 1998a; Keith *et al.*, 2018b; Naden *et al.*, 2005; Sillitoe *et al.*,

1996; Yang and Scott, 2002). The Troodos lava chemistry is distinct compared to typical mid-ocean ridge basalts (MORB) and more comparable to melts generated in a subduction zone related setting (e.g. Lau back-arc; Table 8.7) (Fonseca *et al.*, 2017; Jenner *et al.*, 2010; Miyashiro, 1973). This is in line with the elevated H<sub>2</sub>O (2-8 wt.%; Fonseca *et al.*, 2017), Au, As and Sb contents in the Troodos lavas relative to MORB (Table 8.7), also the suggestion that magmas were more oxidising (FMQ +1.5) (Jenner *et al.*, 2010; Patten *et al.*, 2017). As residual melts reached water saturation the exsolution of a magmatic volatile phase could have occurred (Keith *et al.*, 2018b; Kelley and Robinson, 1990; Sun *et al.*, 2004; Yang and Scott, 2002, 1996).

		SiO <sub>2</sub>	MgO	Au	As	Sb	Se	Cu	Zn	Pb
		(%)	(%)	(ppb)	(ppb)	(ppb)	(ppb)	(ppm)	(ppm)	(ppm)
Troodos	Average	55.5	4.70	1.9	850	78	120	62	101	1.93
	σ	3.5	2.35	0.97	370	34	54	51	90	0.56
Manus	Average	62.8	2.84	3.1	2500	87	230	72	83	5.10
	σ	6.9	2.82	2.2	890	35	65	88	16	5.98
Lau	Average	50.2	7.53	4.3	290	20	390	134	95	0.64
	σ	2.4	1.56	3.5	140	10	69	43	34	0.43
MORB	Average	50.5	7.52	1.5	230	16	360	88	104	0.55
	σ	0.9	0.97	1.2	170	13	67	26	20	0.45

**Table 8.7:** Comparison between Troodos, MORB and BAB lava geochemistry from fresh glass (data from Patten *et al.*, 2017). Note the enrichment in As and Sb in BAB/Troodos lava relative to MORB. The Lau basin (Lau) and Manus basin (Manus) lavas are comparable to the composition of Troodos lavas.

Fluid inclusions from fresh and epidotised plagiogranites contain fluids of 46-56 wt.% NaCl equivalent with homogenisation temperatures between 400-500°C (Cowan and Cann, 1988; Freund *et al.*, 2014; Kelley *et al.*, 2002, 1992; Kelley and Robinson, 1990). The pervasive occurrence of brines in the upper plutonics are explained by two hypotheses; i) phase separation of seawater derived fluids and, ii) the direct exsolution of brine from a silicate melt (Kelley *et al.*, 1992). Kelley *et al.* (1992) show that at a crustal depth of 3.5 km (550 bars pressure) that fluids of seawater salinity would intersect the two-phase boundary at 500°C, however fluids generated from this processes would yield salinities of 20-30 wt.% NaCl, significantly less than the up to 56 wt.% NaCl observed.

Alternatively, brines could be directly exsolved from a silica saturated late stage melt in a low-pressure system (Kelley *et al.*, 1992; Kelley and Robinson, 2010). Initially magmatic fluids have a salinity of 1-7 wt.% NaCl that, as the first fluid evolved, and at high degrees of silicate crystallisation reached salinities up to 80-90 wt.% NaCl. At higher pressures the salinity trend is reversed with maximum salinities reaching ~60 wt.% NaCl, comparable to those observed in fluid inclusions from Troodos plutonics (Kelley *et al.*, 1992). Similar processes have been

identified in active spreading ridges e.g. MAR (Kelley *et al.*, 1993) suggesting processes at active spreading ridges may be analogous to Troodos.

The analysis of primary fluid inclusions in plutonic rocks show that with progressive melt fractionation, magmatic volatile phases evolve from CO<sub>2</sub> – SO<sub>2</sub> rich vapours to immiscible CO<sub>2</sub> – H<sub>2</sub>O-rich vapours and finally metal – CO<sub>2</sub> – H<sub>2</sub>O – NaCl brines (Kelley and Früh-Green, 2000; Kelley *et al.*, 2002); the latter are preserved in the Troodos plutonics. Pulsed volatile influx would cause the release of magmatic derived SO<sub>2</sub> that undergoes disproportionation, forming H<sub>2</sub>S and SO<sub>4</sub><sup>2-</sup> (de Ronde *et al.*, 2005; Herzig *et al.*, 1998a). Disproportionation causes kinetic isotope effects that lead to the sulfide becoming enriched in <sup>32</sup>S and sulfate <sup>34</sup>S (de Ronde *et al.*, 2005). Sulfides formed from this fluid will have a δ<sup>34</sup>S signature of <0‰. Evidence for a vapour phase is not readily preserved in Troodos but the preservation of ‘end member’ magmatic brines that form post-degassing suggest that SO<sub>2</sub> and other volatiles with an affinity for the vapour phase were likely contributed to the hydrothermal system early in magmatic evolution and prior to brine segregation.

The generation of magmatic volatile-rich phases in the Troodos hydrothermal systems is preserved sporadically in associated VMS deposits. Keith *et al.* (2016b) attribute light δ<sup>34</sup>S (-1.4‰) in deep stockwork ores at Skouriotissa VMS to a magmatic volatile phase and this study also presents δ<sup>34</sup>S values in pyrite significantly below the δ<sup>34</sup>S composition of primary lava units (<0-1‰; Table 8.5 A).

Negative δ<sup>34</sup>S values in pyrite are caused by the liberation of a magmatic volatile-rich phase from the upper plutonics that is contributed in pulses to the overlying hydrothermal ore-forming systems (cf. Butterfield *et al.*, 1997). The limited preservation of sulfides with negative δ<sup>34</sup>S signatures could reflect the episodic nature of volatile release from the upper plutonics and the progressive overprinting and dilution of this volatile signature by seawater (cf. Chapter 9; Gillis and Roberts, 1999; Kelley *et al.*, 2002; Kelley and Robinson, 1990).

Isotopic evidence (<sup>87</sup>Sr/<sup>86</sup>Sr, δ<sup>18</sup>O etc.) suggests that the boundary conductive layer between the sheeted dykes and plagiogranites defines the lower limit of major hydrothermal convection (Bickle and Teagle, 1992; Gillis and Roberts, 1999; Richardson *et al.*, 1987). The boundary conductive layer is mobile, fluctuating with the migrating crystallisation front, with changes in volatile exsolution and the transition from ductile to brittle stress regimes (Kelley *et al.*, 2002, 1992; Kelley and Robinson, 1990).

At Troodos, epidote veins occur within the uppermost plagiogranites indicating that interactions with hydrothermal fluids have penetrated this far (Gillis and Roberts, 1999; Richardson *et al.*, 1987) (Figure 8.12). The liberation of volatiles and associated brines would have been temporally

distinct events but potentially important for the enrichment of trace elements and the contribution of  $\text{SO}_2$  rich vapours and  $\text{Cl}^-$  rich brines to the hydrothermal systems and the associated VMS deposits. The  $\text{Cl}^-$  rich and high temperature nature ( $400\text{--}500^\circ\text{C}$ ) of brines could transport significant amounts of metals, leading to the enrichment of certain magmatophile elements in VMS deposits or districts (Brugger *et al.*, 2007). The partitioning of metals between brine and vapour phase is variable and generally poorly constrained (e.g. William-Jones and Heinrich, 2005). Copper and Au have been suggested to preferentially partition into the vapour phase due to their enhanced complexation with sulfur species (Audétat, 2000; Audétat *et al.*, 1998; William-Jones and Heinrich, 2005). In contrast, Audétat and Pettke (2003) stated that the partitioning of Cu between vapour and brine is more complex and may vary between different magmatic-hydrothermal systems. Therefore, it remains enigmatic how metals in the Troodos and other hydrothermal systems would partition between a vapour and brine phase liberated from an underlying magma body and contributed to an overlying hydrothermal system. However, it is clear that the liberation of either a volatile-rich brine or vapour phase into the overlying VMS hydrothermal systems would have a significant impact on the metal budget of the VMS deposits (e.g. Hedenquist and Lowenstern, 1994; Figure 8.12).

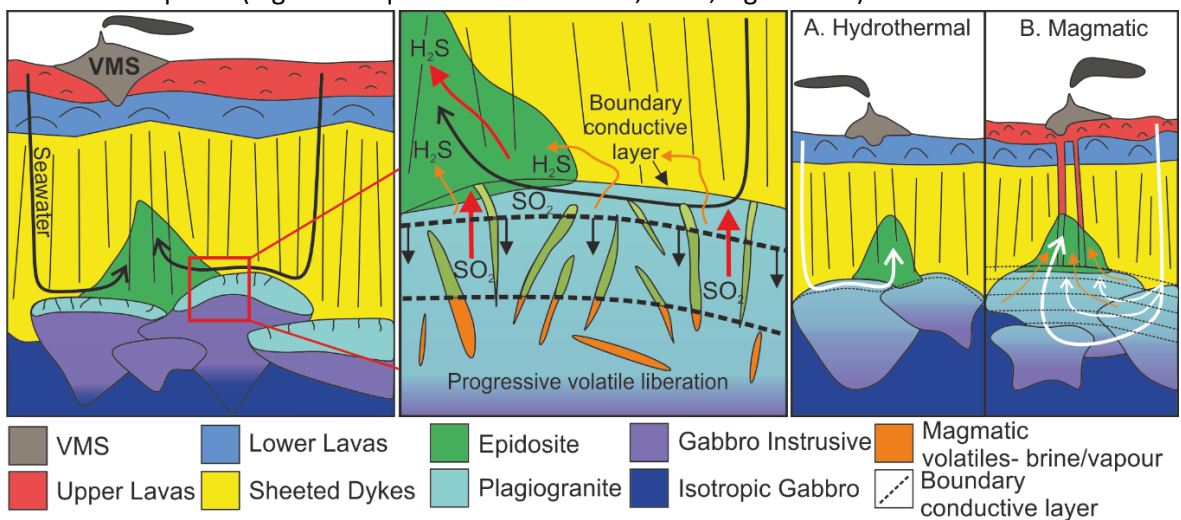


**Figure 8.12:** Volatile liberation in the Troodos VMS system. Volatiles are exsolved directly from a magma. The progressive migration and fracturing of the boundary conductive layer due to crystallisation, repeat magma intrusion or overpressure caused by volatile saturation leads to the periodic migration of the boundary to deeper levels (black dashed lines) and the release of pulses of magmatic volatiles (orange and red arrows) into the overlying hydrothermal system in temporally distinct events. A periodically during volatile release or during renewed magma injection, magma derived  $\text{SO}_2$  will disproportionate upon mixing with hydrothermal fluid forming  $\text{H}_2\text{S}$  leading to the sporadic preservation of  $\delta^{34}\text{S} < 0\text{‰}$  in some Troodos VMS. The two scenarios demonstrating an active (A) an immobile boundary conductive layer (B) are summarised by magmatic and hydrothermal schematic models.

If this scenario was true then some VMS deposits that are located within the LPL units could exhibit an enrichment in magmatic volatile elements (Cu, Se and Au). The Mala VMS deposit (cf. Chapter 9) is located within the LPL lavas but is enriched in Se and Au relative to all other Troodos

VMS (Martin *et al.*, 2019). Analysis of pyrite from Mala also yields consistently light  $\delta^{34}\text{S}$  values (average =  $-3.4\text{‰}$ ; Chapter 9). This strongly suggests that Mala formed from the addition of a magmatic volatile phase that probably underwent  $\text{SO}_2$  disproportionation. In other Troodos VMS (e.g. Mathiatis North and Skouriotissa), deposits that exhibit  $\delta^{34}\text{S}$  values  $>0\text{‰}$ , metals are principally sourced from varying volumes of UPL and LPL lavas respectively dependent on their stratigraphic depth.

### 8.5.6 Implications for trace element distribution

Trace element geochemistry, Se/S ratio and sulfur isotope analysis highlight heterogeneities in the magmatic influx preserved in Troodos VMS (Figure 8.13). The data presented in this study suggests a combination of variable protolith compositions and the addition of a magmatic volatile phase controlling the metal budget in the VMS systems. The relatively uniform distribution of sulfur isotope values between VMS (Figure 8.7 and 8.13) suggests the majority of sulfur is sourced from leaching of volcanic rocks (av.= 66%; Figure 8.10) and TSR in varying quantities (22-75%; Figure 8.10), favouring the two phase mixing model over the anhydrite buffer model. Regardless of the sheeted dyke trace element chemistry (i.e. basaltic vs. andesitic) the source of sulfur does not vary, since the UPL and LPL both contain primary magmatic  $\delta^{34}\text{S}$  values between 0-1‰ (Alt, 1994). Therefore, the limited variation in  $\delta^{34}\text{S}$  values in sulfides but variable Se/S ratios and variations in trace element geochemistry (Cu, Se, Au vs. Zn, Sb, As) between structural domains can be explained by variable source rock geochemistry relating to the relative proportion of leached UPL and LPL affinity dykes (Table 8.8, overleaf).

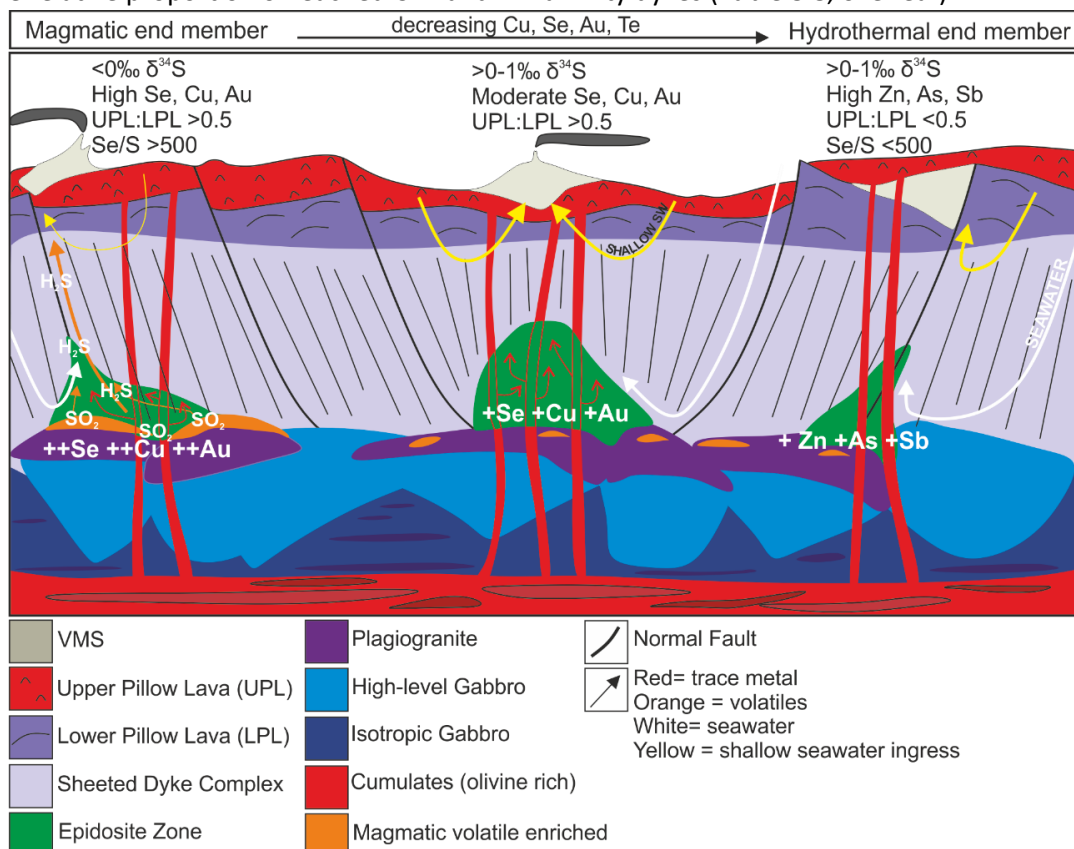


**Figure 8.13 (previous page):** Summary of VMS formation in the Troodos hydrothermal system. Three scenarios explaining the transition from magmatic to hydrothermal ‘end member’ VMS. (A) Both an UPL (Se, Cu, Au) source and magmatic volatile influx. VMS formed are enriched in Se, Cu, Au (and other magmatophile elements), exhibit a high UPL-LPL ratio and elevated Se/S ratio >500 (Table 8.6 A) and may exhibit negative  $\delta^{34}\text{S}$  values. (B) Same as scenario A but with no evidence of volatile influx, or volatile influx has been subsequently overprinted by a seawater signature (e.g. Skouriotissa). Selenium, Cu and Au are enriched and UPL-LPL ratio remains elevated but  $\delta^{34}\text{S}$  values <0‰ are absent. (C) Metals are sourced from a LPL source with minimal/no volatile influx (e.g. Mathiatis North or Agrokipia A). VMS are relatively enriched in Zn, As and Sb and exhibit a low UPL-LPL ratio and Se/S <500.  $\delta^{34}\text{S}$  values are as for scenario B: >0-1‰.

Domain	Geochemistry (pyrite)			Isotopes (all sulfides)			Total
	Se/S	Se	n	$\delta^{34}\text{S}$	n	$\delta^{34}\text{S}^*$	
Polis	309	161	137	5.4	11	5.4	13
Apliki <sup>+</sup>	2381	1273	182	4.0	30	N/A	30
Solea	481	251	362	4.4	39	4.2	49
Mitsero	217	116	183	3.7	22	5.6	44
Makheras	286	153	40	6.0	5	6.0	5
STTFZ	114	60	260	8.0	18	N/A	18
Larnaca	89	47	350	4.1	55	4.0	61
<b>All VMS</b>	<b>326</b>	<b>397</b>	<b>1514</b>	<b>4.6</b>	<b>180</b>	<b>4.8</b>	<b>220</b>

**Table 8.8:** Summary of Se/S ratios, Se concentration (ppm) in pyrite and  $\delta^{34}\text{S}$  values from this study (pyrite, chalcopyrite and covellite) and all compiled data for Troodos VMS (\*Hannington *et al.*, 1998; Keith *et al.*, 2016; Pederson *et al.*, 2017). Data is classified based on structural domain. \* denotes data inclusive of compiled values. + denotes Apliki VMS that is not a structural domain.

The extremely low  $\delta^{34}\text{S}$  values in pyrite at Sha (-5.5‰), Skouriotissa (-1.6‰) (Keith *et al.*, 2016a), Apliki (-0.8‰) and Kokkinoyia (-0.6‰) (Table 8.8, Figure 8.13) less than the Troodos magmatic mean cannot be explained through the leaching of primary igneous lithologies. Additionally, the enrichment of Cu + Au + Se at Mala (UPL:LPL ratio of 7.63) cannot be explained through a purely LPL source (cf. Chapter 9). An additional metal and sulfur source is proposed for these VMS deposits, most likely from the addition of a magmatic volatile phase (Figure 8.13). The sporadic distribution of negative  $\delta^{34}\text{S}$  values in pyrite suggests that these events were temporally and geographically discrete and in many cases are not preserved due to overprinting by later seawater dominated fluid pulses, a phenomenon observed in modern immature SMS deposits (e.g., Hine Hina; Herzig *et al.*, 1998a, Lucky Strike; Rouxel *et al.*, 2004). Extensive evidence exists in modern SMS deposits for pulsed magmatic activity (Butterfield *et al.*, 1997; de Ronde *et al.*, 2005; Von Damm *et al.*, 1997, 1985; see Chapter 9).

## 8.6 Summary

The regional application of trace element geochemistry, Se/S ratios and sulfur isotopes reveals a variable source of metals in the hydrothermal system and associated VMS deposits of the Troodos ophiolite. This relates to i) variable geochemistry of dykes in the source region and, ii) the addition of a magmatic volatile phase to the hydrothermal systems. This study applies a new regional scale ore forming model to the Troodos ophiolite that explains the distribution and enrichment of magmatophile trace elements and  $\delta^{34}\text{S}$  values in hydrothermal sulfides across Troodos.

- The majority of sulfur in the Troodos VMS hydrothermal systems is sourced from the thermochemical reduction of seawater and the leaching of primary igneous lithologies during epidotisation of the sheeted dyke complex with a variable source of shallow seawater derived fluid: the 'three stage mixing model'.
- The timing of VMS formation relative to crustal accretion influences the enrichment of Se, Cu and Au as these are enriched in UPL affinity dykes. VMS that postdate the formation of the UPL are enriched in these elements but exhibit a uniform sulfur isotope signature ( $>0\text{‰}$ ).
- The extremely light  $\delta^{34}\text{S}$  values ( $-5.5\text{‰}$ ) preserved in some VMS are not explainable by the leaching of magmatic sulfur and thermochemical reduction of seawater sulfate suggesting an additional but localised source of light sulfur.
- The liberation of volatiles, and thus the occurrence of light sulfur isotope values ( $<0\text{‰}$ ) in VMS deposits were temporally and geographically discrete events facilitated by crack-front migration (see Chapter 9).

These results highlight the complexity of ore-forming systems probably similar in scale to those observed in the Lau back-arc basin. On a regional scale, the SMS systems of the Valu Fa Ridge exhibit variations in  $\delta^{34}\text{S}$  values from  $-5.3\text{‰}$  ( $n=9$ ) to  $+11.7\text{‰}$  ( $n=4$ ) in the Hine Hina and Vai Lili deposits respectively; deposits located just  $\sim 40$  km apart (Herzig *et al.*, 1998a). Arguably, similar  $\delta^{34}\text{S}$  variation is detected in pyrite from the Troodos hydrothermal systems. For example, pyrite  $\delta^{34}\text{S}$  from the Sha deposit reaches values as low as  $-5.5\text{‰}$ , while pyrite from Kalavassos reach  $\delta^{34}\text{S}$  values of up to  $+13.2\text{‰}$ , these deposits are located only 20 km apart.



# CHAPTER 9

**Pulsed magmatic volatile influx: A true magmatic end member deposit, the Mala VMS, Troodos**

## 9. Abstract

A continuum between epithermal-type, magmatic dominated and volcanogenic massive sulfide, seawater dominated mineralisation actively forming on the seafloor and in ancient on land analogues has long been hypothesised. This study presents the first *in situ* trace element and sulfur isotope data bridging the continuum between these two environments in a fossil analogue, the Troodos ophiolite, Cyprus.

The Mala VMS deposit is located in SW Troodos and exhibits an enrichment in magmatophile trace elements (Se, Te, Au) in pyrite coupled with an unusual  $\delta^{34}\text{S}$  isotopic signature in pyrite that is 8.1‰ lighter than the Troodos average. A negative  $\delta^{34}\text{S}$  signature, averaging -3.4‰ is significantly lower than the Troodos ophiolite magmatic mean of 0-1‰ and consistent with an increased magmatic volatile influx in the VMS hydrothermal system at Mala. Additionally, Se is enriched to the highest concentrations reported for any Troodos VMS at 9,565 ppm in pyrite with a deposit average of 923 ppm (n=58). Gold is also enriched averaging 1.33 ppm (n=58), nearly twice the Troodos VMS average (Chapter 5).

In addition to deposit scale processes, LA-ICP-MS time resolved analyses in pyrite demonstrate the extreme variation in trace element concentration at a mineral scale. The correlation between Te, Se and Co could represent the influx of a new high temperature volatile-rich fluid pulse into the Mala hydrothermal system, furthermore As and Au show the inverse relationship to Te, Se and Co favouring lower temperature  $\text{Cl}^-$  rich fluid.

Light magmatic  $\delta^{34}\text{S}$  signatures have only been recorded previously in modern seafloor massive sulfide systems associated with arc environments where an additional magma derived volatile phase (fluid or vapour) may be contributed to the overlying hydrothermal system (e.g. Hine Hina or SuSu Knolls). This study highlights the complexity and diversity of ore forming processes that are apparently rarely preserved in ancient VMS hydrothermal systems that could relate to the rapid burial of the VMS mound whilst still active that leads to the sealing of the VMS system from 'off axis' fluid overprinting. This study also highlights the link between increased magmatic volatile influx and the enrichment of Se, Te and Au in mafic VMS deposits. Fundamentally, the Mala VMS provides important evidence furthering our understanding of the evolution and preservation of ancient VMS deposits that provide an important insight into the immature stage of sulfide accumulation on the seafloor.

## 9.1 Introduction

It is now widely accepted that a continuum exists between epithermal style mineralisation in deep and shallow submarine environments in back-arc and arc related hydrothermal systems, e.g. Hine Hina (Herzig *et al.*, 1998a), Brothers volcano (de Ronde *et al.*, 2005) or the Aegean Arc (Naden *et al.*, 2005). In epithermal environments evidence for increased magmatic volatile influx may be preserved as high-sulfidation alteration assemblages (e.g. natroalunite or native sulfur), light  $\delta^{34}\text{S}$  values in hydrothermal sulfides, the generation of supercritical brines and processes involving disproportionation of  $\text{SO}_2$  and the enrichment of magmatic volatile elements (e.g. Se, Te, Au, Bi; de Ronde *et al.*, 2003; Sun *et al.*, 2004; Yeats *et al.*, 2014; Chapter 8).

Previous studies in Troodos (Chapter 8) have identified that the distribution of  $\delta^{34}\text{S}$  in pyrite and therefore indirectly that magmatic volatile influx varies spatially across the Troodos ophiolite. Negative  $\delta^{34}\text{S}$  signatures below the Troodos magmatic mean (0-1‰: Alt, 1994) are sporadically preserved in pyrite in only two VMS (Sha and Skouriotissa); all other  $\delta^{34}\text{S}$  analysis of sulfides indicate a sulfur source consistent with the leaching of igneous rocks and the thermochemical reduction of seawater sulfate in varying amounts with an average  $\delta^{34}\text{S}$  of +4.7‰ in all sulfides (Chapter 8; Martin *et al.*, submitted). The Mala VMS is distinctly different from a traditional Troodos VMS as it exhibits consistently light  $\delta^{34}\text{S}$  values in pyrite and an enrichment in magamtophile elements Te, Se and Au relative to other Troodos VMS deposits.

## 9.2 Sample location

The Mala VMS is located in the SW Troodos ophiolite approximately 4.5 km E of Pano Panagia in the Pafos Forest region (047042/3864323, WGS 1984- Figure 9.1). Mala is located deep in the lava stratigraphy at the basal-lower pillow lava (BG-LPL) contact (Figure 9.1 and 8.8). The deposit contains a massive pyrite lens that has been exposed by historic mining that exhibits a crudely layered appearance with abundant colloform and dendritic textured pyrite (Figure 9.2). Within the VMS mound are crude laminations of fine-grained gypsum (10-60 cm thick) that occur parallel to the mound margins (Figure 9.2). The gypsum is commonly intergrown with un-oxidised disseminated pyrite (Figure 9.2 E – G). The Mala VMS has recently been investigated by the Brazilian Metals Group as a potential base metal sulfide prospect with drilling intersections of 5 metres of massive sulfide at 2.15 g/t and 15 m at 1.23 g/t Au (BMG, 2013).

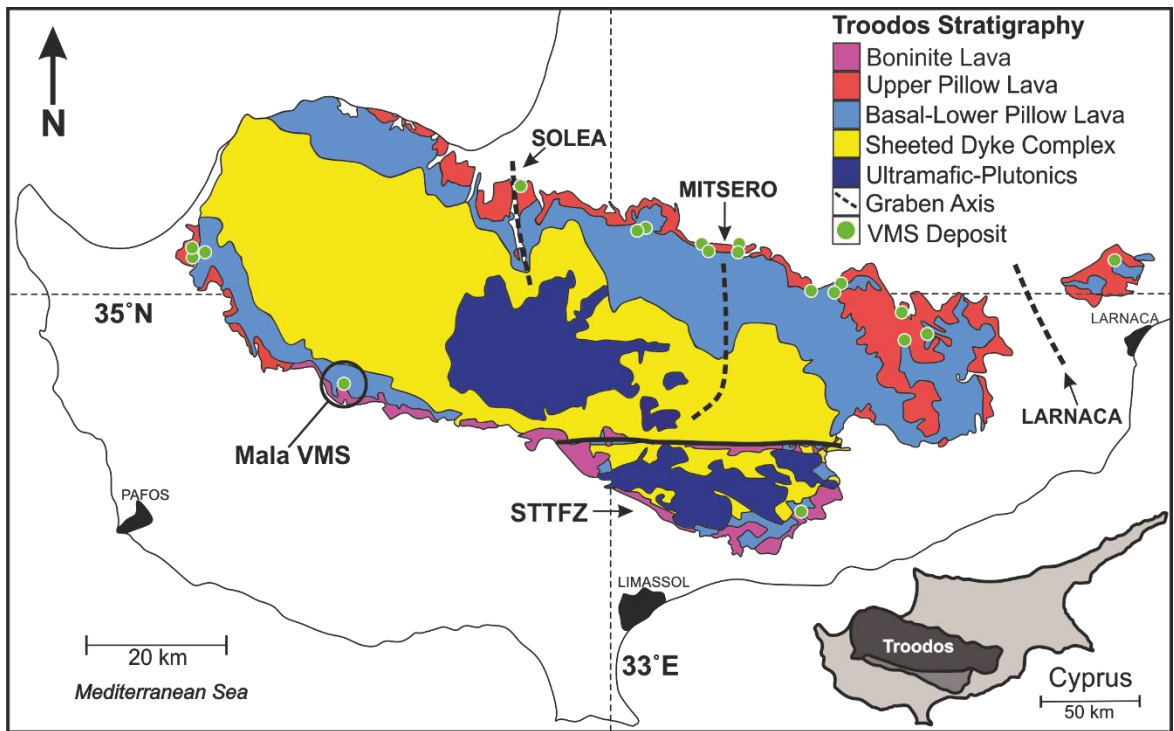


**Figure 9.1:** Location map of the Mala VMS deposit in the SW of the Troodos ophiolite. The Mala VMS forms part of the Solea graben structural domain (after Martin *et al.*, 2018).

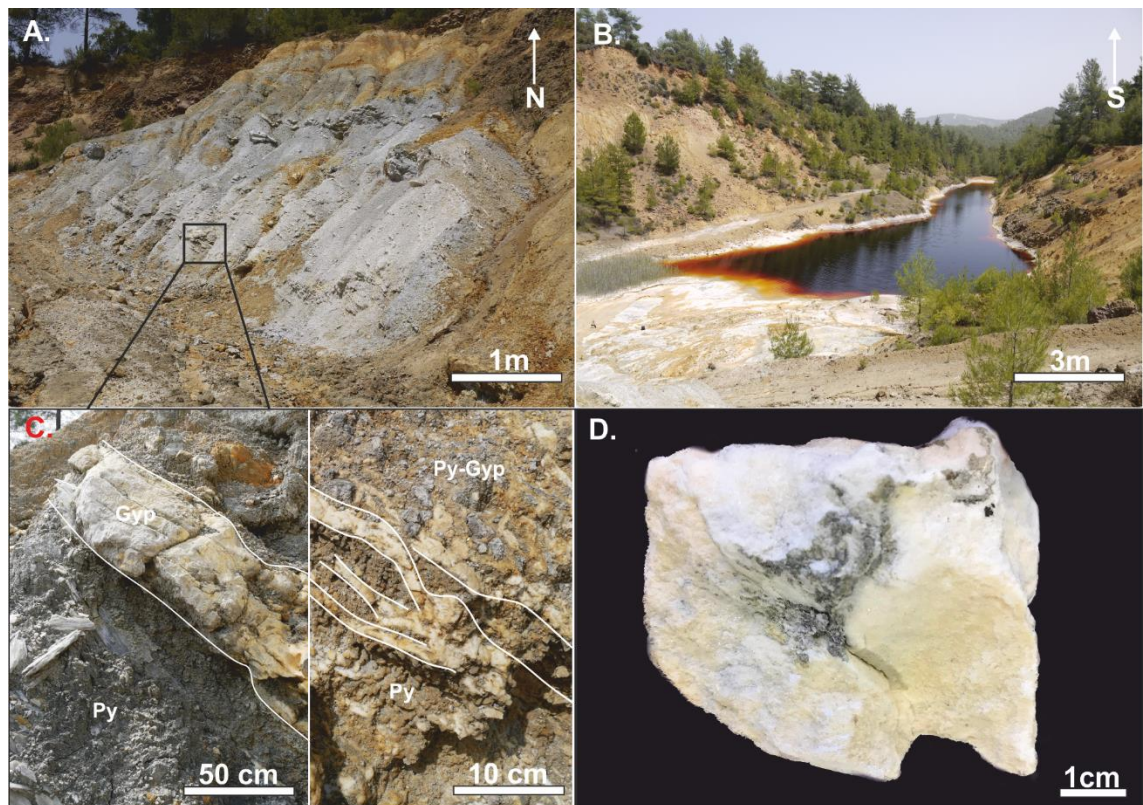


**Figure 9.2A:** Key field and hand specimen photographs from the Mala VMS. A) The exposed mound mineralisation sampled in this study: massive pyrite with bedded gypsum. Wall rock is oxidised to secondary Fe phases. B) View south over the historic open pit with a prominent AMD lake. C) Close-up images of bedded gypsum (Gyp- white lines) in massive pyrite (Py) mound (A). D) Gypsum with minor pyrite (grey) from the Mala mound (*continued overleaf*).

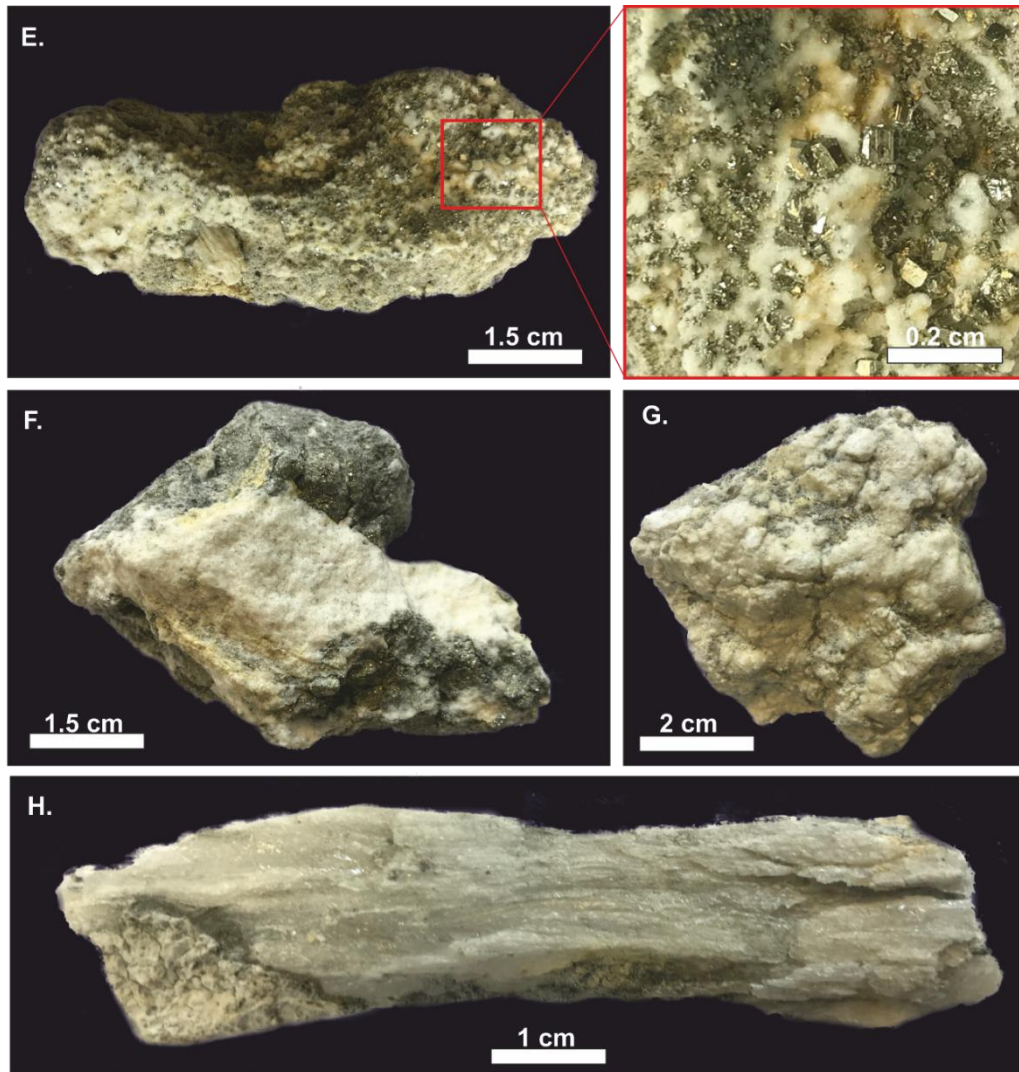


**Figure 9.2B:** Photographs demonstrating key relationships between pyrite and gypsum from the Mala VMS mound. E) Euhedral pyrite disseminated in fine grained gypsum. F) Clast of pyrite (grey) cemented by gypsum with disseminated pyrite intergrowth. G) Fine veins of pyrite (grey) in massive gypsum. H) Bladed supergene (?) gypsum.

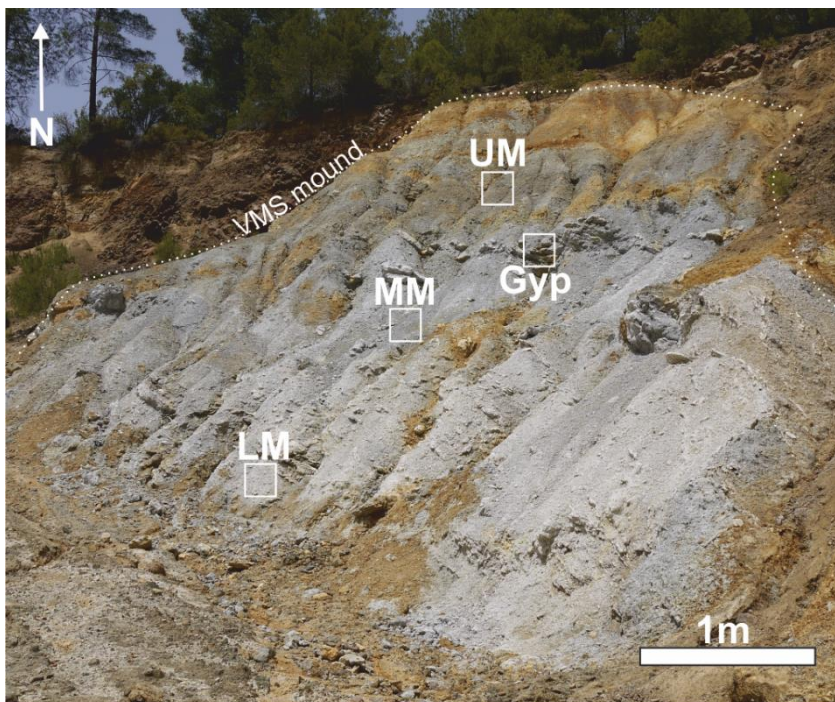


**Figure 9.2C:** Location of samples analysed in this study from the Mala VMS mound. LM= lower mound, MM= mid-mound, UM= upper mound, Gyp= gypsum. Samples analysed transect the entire VMS mound.

## 9.3 Results

### 9.3.1 Mineralogy

Altered wall-rock samples were collected from outcrops proximal to the Mala VMS (Figure 9.2) for XRD analysis to quantify modal mineralogy (Figure 9.3). Specifically, XRD analysis aimed at establishing the occurrence of any acid stable, high sulfidation mineral phases (i.e. an advanced argillic assemblage). The six analysed samples from this study exhibit a diverse alteration mineral assemblage. Quartz is the most abundant phase occurring in most samples ranging from 14 to 92 vol.%. Jarosite and hematite are the major iron bearing phases (Figure 9.3). Mordenite ((Ca, Na<sub>2</sub>, K<sub>2</sub>)Al<sub>2</sub>Si<sub>10</sub>O<sub>24</sub> · 7H<sub>2</sub>O), a zeolite mineral commonly forming during the alteration and hydration of volcanic glass (Mumpton, 2018) was also present in one sample. Primary mafic minerals including albite and their clay alteration products (illite, montmorillonite and kaolinite) were also identified (Figure 9.3). Full XRD results available in Appendix 9.1.

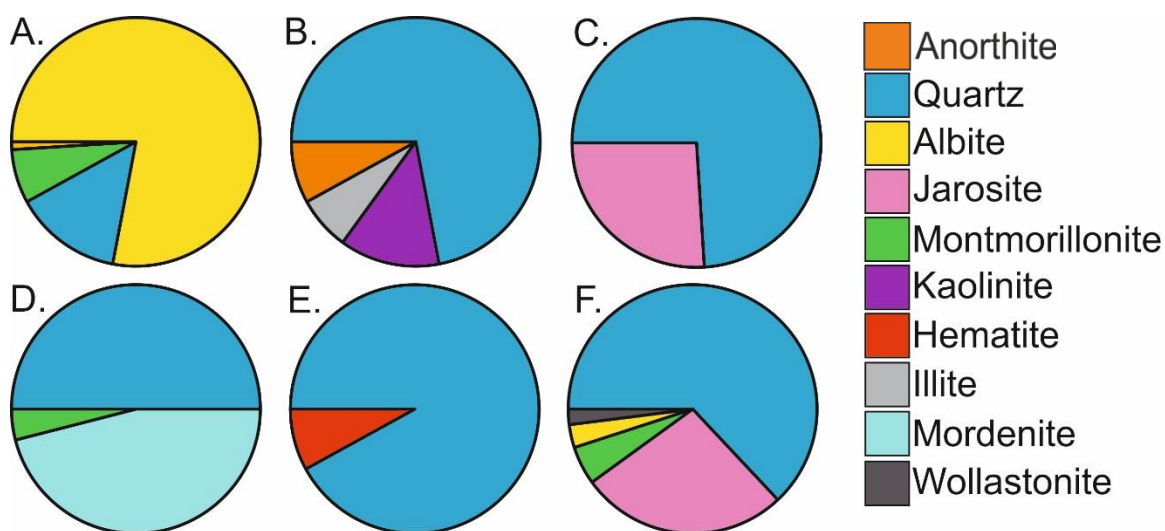


**Figure 9.3:** Modal mineralogy of wall-rock samples from the Mala VMS. No high sulfidation minerals (e.g. natroalunite or pyrophyllite) have been identified by XRD analysis at Mala suggesting fluid was near neutral pH or low pH fluids were discretely channelled and did not alter large volumes of surrounding wall-rock.

Mineral relationships in Mala samples were assessed through a combination of SEM-BSE imaging and reflected light microscopy (Figure 9.4). Two distinct pyrite morphologies are identified: interlocking coarse euhedral pyrite and dendritic pyrite (Figure 9.4). Interlocking pyrite often contain small vugs and in BSE 'bright' crystals were identifiable (Figure 9.4 C and D). Euhedral pyrite forms crude bands beneath well-developed extremely porous dendritic pyrite (Figure 9.4 A and B). Minor chalcopyrite and sphalerite occur as inclusions.

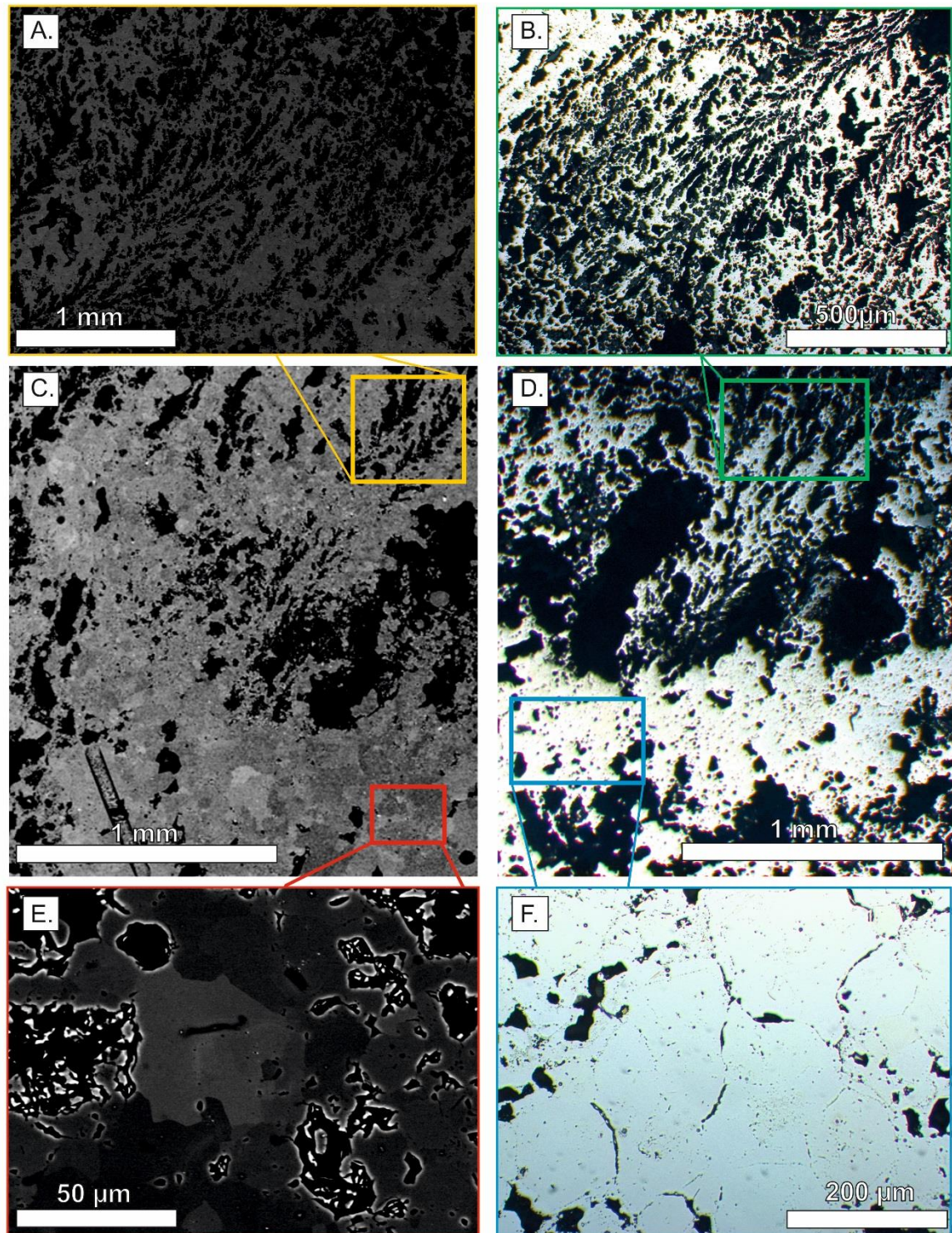


**Figure 9.4:** Mineralogy of Mala pyrite samples (A, C, E- BSE images) and reflected light photomicrographs (D, B, F). Two distinct pyrite morphologies are identified, dendritic textured (A and B) and euhedral interlocking grains (E and F). Typically, massive euhedral grains form crude laminations at the base of colloform pyrite. Euhedral pyrite is often inclusion-rich (F) and shows zoning in BSE indicated by variable brightness in images C and E.

### 9.3.2 Geochemistry

Laser ablation ICP-MS analysis ( $n=61$ ) of polished blocks ( $n=5$ ) reveals an enrichment in magmatophile trace elements Te, Se and Au at Mala. Mala is enriched in Se averaging 923 ppm and also Te (average 42.2 ppm) and Au (average 1.3 ppm,  $n=61$ ) (Figure 9.5). Despite the strong positive correlation between Au and Ag no electrom was identified. Mala is relatively depleted in Bi, Sb, Pb, Ag, As and Zn compared to other Troodos VMS (Figure 9.5: Chapter 5 and 8; Martin *et al.*, 2019). A moderate to strong positive correlation is noted between Au-Ag ( $R^2=0.77$ ), Te-Se ( $R^2=0.67$ ) and Co-Se ( $R^2=0.84$ ) (Figure 9.6). At Mala there is no correlation ( $R^2 > 0.05$ ) between Bi and Te (Figure 9.6 F). Additionally, the solubility limits of Te and Au in pyrite from Mala are included in Figure 9.6. Full data is available in Appendix 9.2.

The mineral scale distribution of Co, As, Se, Te and Au was assessed using LA-ICP-MS line analysis ( $n=13$ ) and is summarised in Figure 9.7. Laser ablation time resolved analysis (TRA) profiles demonstrate the extremely variable distribution of elements on a mineral scale. For example in Figure 9.7 A, a profile across three interlocking euhedral pyrite grains, Se varies over a distance of 600  $\mu\text{m}$  from 9565 ppm in pyrite 1 to just 1363 ppm in pyrite 2. The shape of the time resolved profile for Co, Te and Se exhibit a good correlation i.e. they mirror each other. Gold and As exhibit the inverse trend and decrease with increasing Se (Figure 9.7 A). When comparing profile A and B (Figure 9.7) of euhedral pyrite with C and D analysed in dendritic pyrite an enrichment in Te and Se is observed in euhedral pyrite relative to colloform–dendritic varieties (Figure 9.7).

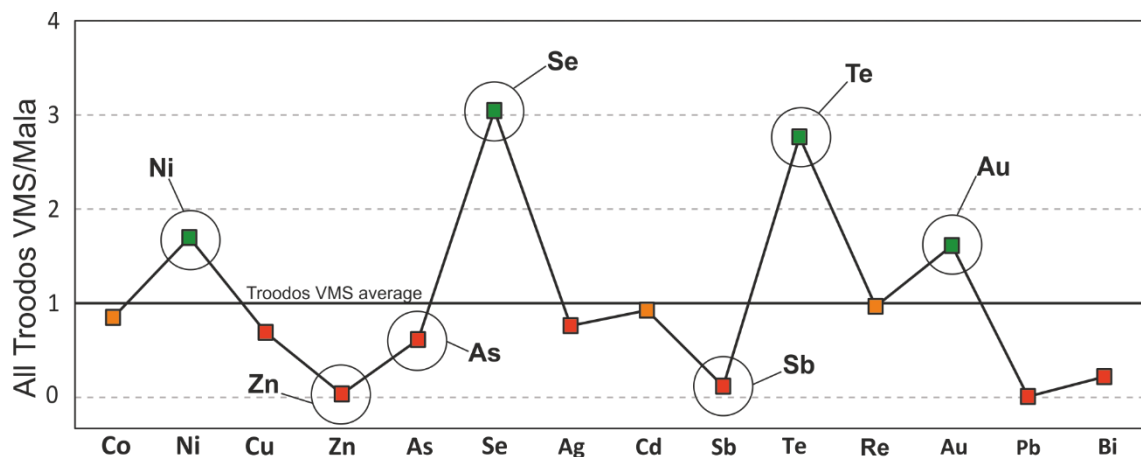


**Figure 9.5:** Ratio of average trace element concentrations in all Troodos VMS ( $n=1489$ ; Chapter 5,6 and 9) vs. Mala ( $n=61$ ) in pyrite (LA-ICP-MS data). All elements that plot above one (green points) are enriched in Mala. Orange points plot near the Troodos VMS average. Mala is enriched in Ni, Se, Te and Au relative to all other Troodos VMS but depleted in 'LPL lava affinity elements' Zn, Sb and As (red points).

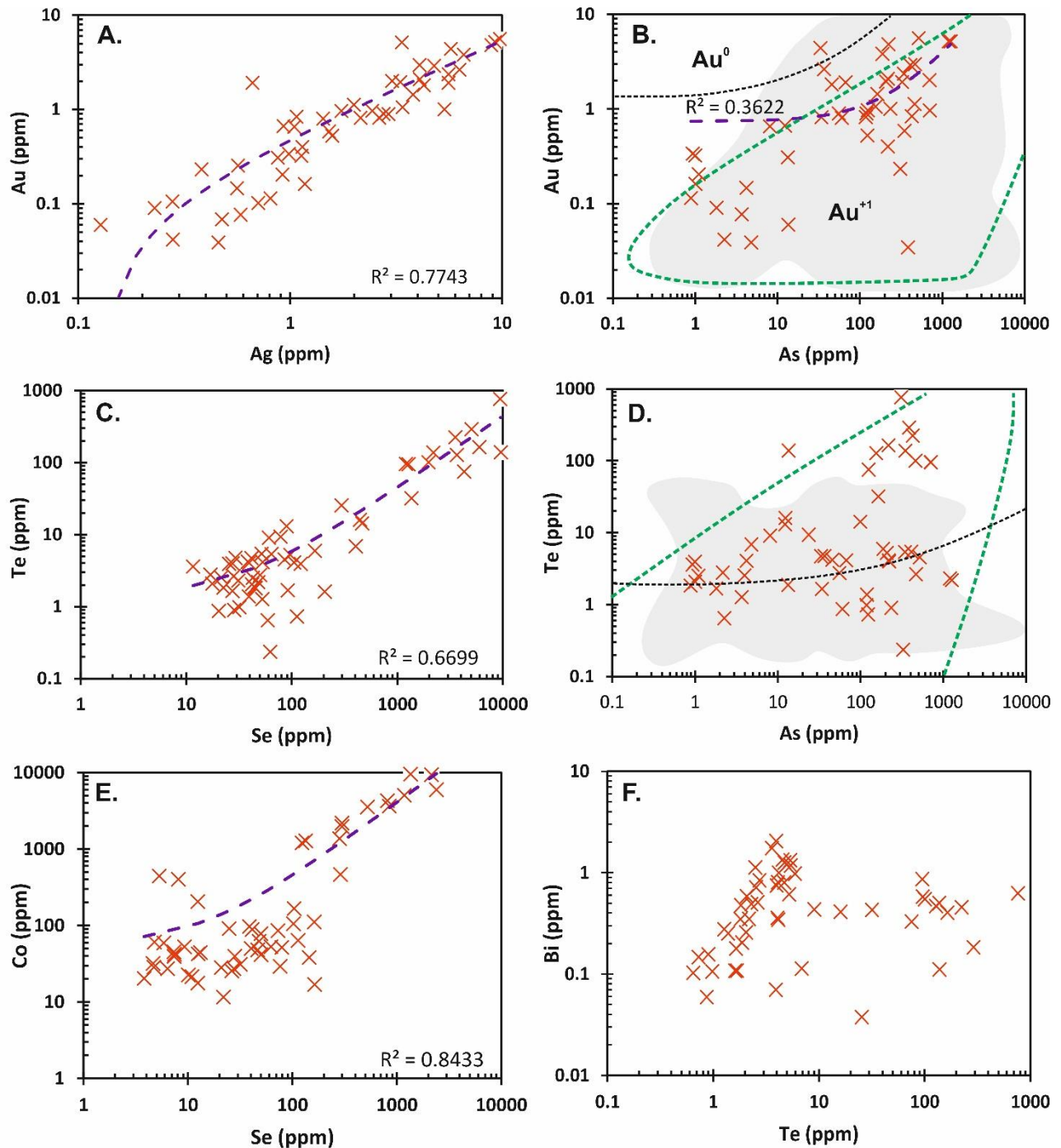


**Figure 9.6:** Bi-variate plots of selected elements in pyrite (LA-ICP-MS) for the Mala VMS. A) Au-Ag, B) Au-As, green dashed line indicates the solubility of Au in pyrite. Points that plot within the green line are hosted in a solid solution (as  $\text{Au}^{+1}$ ) whilst those that plot outside are likely hosted as inclusions. The grey field indicates data spread for 'other Troodos VMS' (after Deditius *et al.*, 2014; Martin *et al.*, 2019). C) Te-Se, note moderate positive correlation ( $R^2=0.67$ ) suggesting a coupled relationship. D) Te-As, green dashed line indicates the solubility limit of Te in pyrite (as for B, after Keith *et al.*, 2018b; Martin *et al.*, 2019). Grey shaded area represents 'other Troodos VMS' (cf. Chapter 5 and 8). E) Se-Co exhibiting a strong positive correlation. F) Bi-Te that exhibit no correlation ( $R^2 < 0.05$ ). The repeated analysis of sulfide standards during the Laser Ablation ICP-MS yielded  $<10\%$  RSD for Co, As, Se, Ag, Pb and Bi and between 10-18% RSD for Cu, Zn, Sb, Te and Au. RSD for Cd was 26% (Full data available in Appendix 9.2).

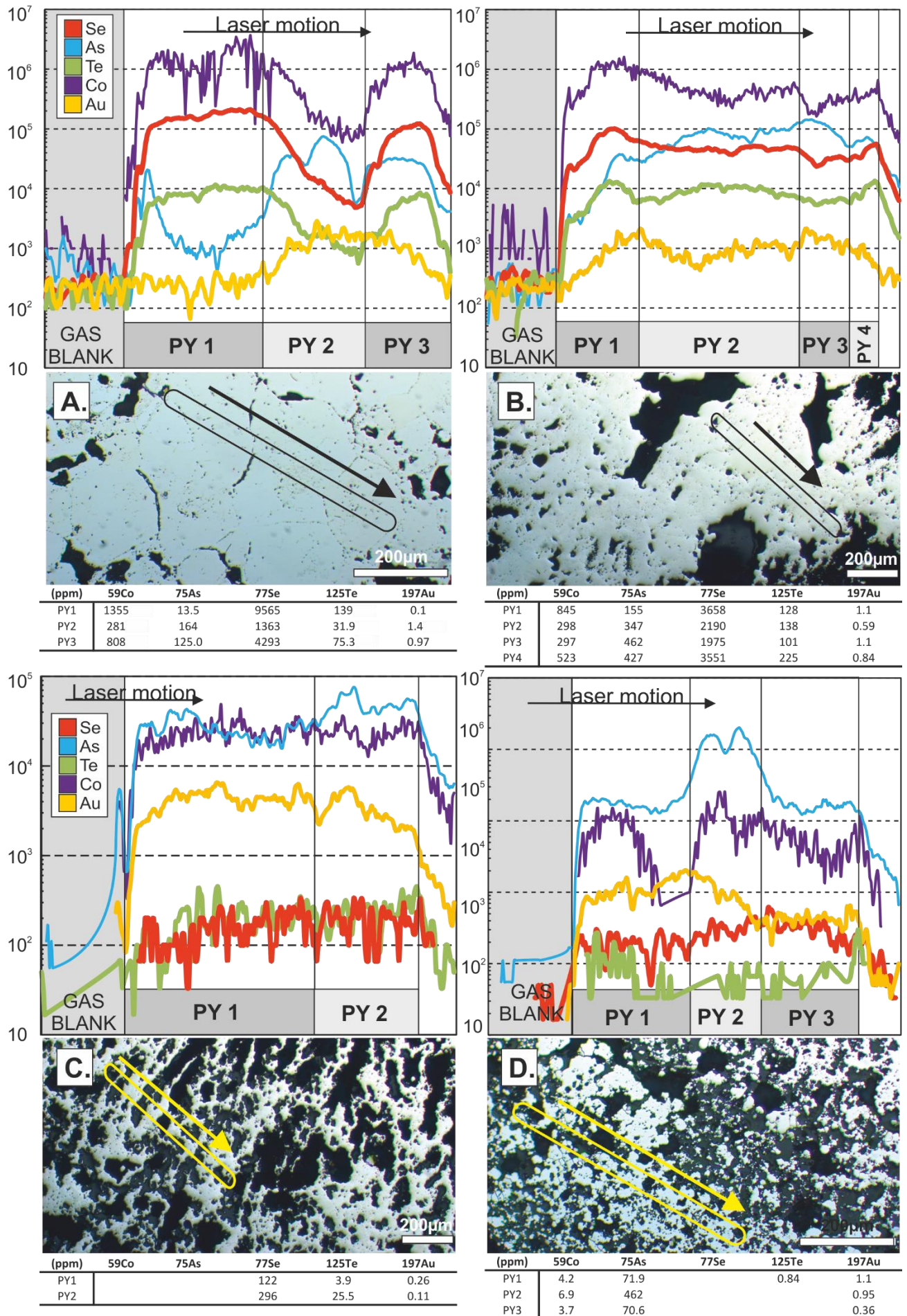


**Figure 9.7 (previous page):** Time resolved analysis (LA-ICP-MS) (counts per second vs. time/distance) of selected pyrite samples from the Mala VMS. Image below displays laser track and arrow indicates laser movement. Corresponding element concentrations of each pyrite are summarised in the table below each laser profile. A and B) Examples of massive, euhedral pyrite. Tellurium and Se are enriched relative to colloform-dendritic textured pyrite (C and D). C and D) Dendritic pyrite, note enrichment in As and Au relative to Te and Se.

### 9.3.3 Sulfur isotope analysis

Sulfur isotope analyses were performed on three pyrite samples (n=7) and one gypsum sample (n=3) from the Mala VMS (section 9.3.1). Analyses were performed on pyrite mineral separates and are presented in standard notation (‰) relative to the Vienna-Canyon Diablo Troilite ( $\delta^{34}\text{S}_{\text{V-CDT}}$ ). See Chapter 4 for further method information. The pyrite samples analysed were collected in situ i.e. from the massive pyrite mound and not from waste and span the lower, mid and upper levels of the VMS mound (Table 9.1). Results yield  $\delta^{34}\text{S}$  values averaging -3.4‰ (Table 9.1). Gypsum that occurs in massive beds within the pyrite mound produced values averaging +18.0‰ (Table 9.1, Figure 9.2C).

Sample	$\delta^{34}\text{S}_{\text{‰(V-CDT)}}$
UM-PY-1	-2.8
UM-PY-2	-3.0
MM-PY-1	-3.7
MM-PY-2	-3.2
LM-PY-1	-3.7
LM-PY-2	-3.5
LM-PY-3	-3.9
<b>Pyrite (Av.)</b>	<b>-3.4</b>
Gyp-1	18.1
Gyp-2	17.9
Gyp-3	17.9
<b>Gypsum (Av.)</b>	<b>18.0</b>
All VMS*	4.7

**Table 9.1:** Sulfur isotope analyses for the Mala VMS. UM= Upper mound, MM= Mid mound, LM= Lower mound. Av.= average. Gyp= gypsum. All VMS from Chapter 8; Martin *et al.*, submitted. For sample location see Figure 9.2 C.

## 9.4 Discussion

### 9.4.1 Enrichment of magmatophile elements

The trace element composition of Mala is distinctly different from all other Troodos VMS (Martin *et al.*, 2019, submitted; Chapter 5 and 8). Relative to other Troodos VMS (n=19, Figure 9.8) Mala is strongly depleted in Bi, Pb, Sb and Zn, moderately depleted in Co, As and Ag but enriched in Au, Te and Se (Figure 9.5 and 9.8). Previous studies suggest that increased Te, Se and Au concentrations indicate an increased magmatic volatile influx to the VMS hydrothermal system (Berkenbosch *et al.*, 2012; de Ronde *et al.*, 2003; Yeats *et al.*, 2014). Selenium at Mala is enriched

by a factor of three times in pyrite relative to other Troodos VMS that average 303 ppm (n=1514), comparatively Mala averages 923 ppm (n=61; Figure 9.8). Furthermore, Mala pyrite contains the highest Se content of any known mafic VMS at 9,565 ppm, a result reproducible in several pyrite grains (Appendix 9.2). Pyrite also exhibits an enrichment in Au with average concentrations of 1.3 ppm and Te at 42 ppm (max 763 ppm, n=61). The systematic enrichment in Te, Se and Au relative to all other Troodos VMS strongly suggest an increased magmatic influx at Mala through the addition of a magmatic volatile phase (vapour or aqueous) as observed in other magmatic dominated submarine environments that exhibit a similar enrichment in magmatophile elements (e.g. Brothers or SuSu Knolls- de Ronde *et al.*, 2005; Yeats *et al.*, 2014).

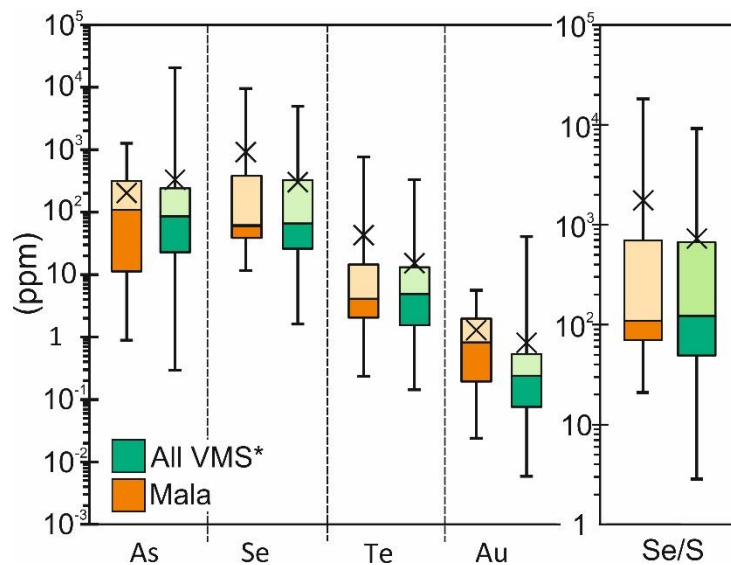


**Figure 9.8:** Comparison of the Mala VMS with 'All Troodos VMS' (LA-ICP-MS, pyrite). Mala is relatively depleted in As but enriched in Se, Te and Au compared to all VMS. Selenium/sulfur ( $\text{Se/S} \cdot 10^6$ ) ratios are also elevated at Mala providing additional evidence of an increased magmatic volatile influx (see also Figure 9.5) (\*Martin *et al.*, 2019)

Increased magmatic volatile influx is further supported by a depletion in As, Sb and Zn that are generally sourced from epidosite formation (cf. Chapter 8). The Mala VMS is located stratigraphically deep; it formed at the BG-LPL contact, therefore the metal source for the Mala VMS should be predominantly one of LPL affinity elements, lavas that are enriched in As, Sb and Zn relative to the more primitive (basaltic) UPL (cf. Chapter 8) (Patten *et al.*, 2017). If the Mala VMS formed solely through the leaching of metal from LPL affinity igneous rocks within the sheeted dyke complex then subsequent sulfides will be expected to show an enrichment in As, Sb and Zn relative to UPL hosted VMS (e.g. Skouriotissa) and this is not observed (Chapter 8; UPL:LPL ratio of 7.6 vs. 0.5 for Skouriotissa). This suggests that leaching of LPL affinity lithologies in the sheeted dyke complex did not provide the sole source of metal in the Mala VMS deposit. Instead additional magmatophile elements may have been contributed from an underlying magma chamber. This is suggested to be an important phenomenon in subduction related

magmas relative to anhydrous MOR hosted hydrothermal systems that are relatively poor in volatiles (e.g. Saal *et al.*, 2002), hence magmas rarely reach volatile saturation in MOR systems (e.g. Cu at the Brothers volcano; Keith *et al.*, 2018a). Selenium/sulfur ratios (Huston *et al.*, 1995; Layton-Matthews *et al.*, 2013) in pyrite at Mala also indicate an increased but variable magmatic component with Se/S averaging 1725 (median= 112) compared to 747 (median=125) for all other VMS (including the Se-rich Apliki- Martin *et al.*, 2018; Chapter 6). In combination the increased concentration of magmatophile elements and elevated but variable Se/S ratios (Figure 9.8) suggest ore forming processes at Mala that are different from other Troodos VMS analysed in this study.

Elevated Te and Au suggest the occurrence of mineral inclusions; the incorporation of Te and Au is assessed in Figure 9.6 as a function of As (after Deditius *et al.*, 2008; Keith *et al.*, 2018b). Data shows that the majority of Te plots within the wedge shaped zone (Figure 9.6 D) indicating its incorporation in pyrite as a lattice bound solid solution (Keith *et al.*, 2018b; Chapter 5). Additionally, the Au-Te solubility line indicates Te may be incorporated as Au-Te inclusions (e.g. calavarite) however an  $R^2$  value of  $>0.01$  does not support this observation. In some Troodos VMS there is a moderate positive correlation between Bi and Te (e.g. Apliki  $R^2=0.32$ ; Chapter 5). At Mala there is no correlation between Bi and Te ( $R^2=0.02$ ; Figure 9.6 F) suggesting a decoupled relationship between Bi and Te and the absence of discrete bi-telluride phases (e.g. bismuthotelluride).

#### 9.4.2 Sulfur isotope signature

Sulfur in VMS hydrothermal systems is derived from multiple sources (Chapter 8). Previous studies have identified that the thermochemical reduction of Cretaceous seawater sulfate ( $\delta^{34}\text{S}$  18-19‰; Kampschulte and Strauss, 2004) and the leaching of Troodos igneous host rock ( $\delta^{34}\text{S}$  0-1‰; Alt, 1994) are the principal sources of sulfur in the Troodos hydrothermal system (Chapter 8; Alt, 1994; Hannington *et al.*, 1998; Keith *et al.*, 2016b). This leads to an average  $\delta^{34}\text{S}$  in sulfides from Troodos VMS of +4.7‰ (Figure 9.9 A) that reflects the variable mixing of end member seawater and magmatic derived sulfur from the leaching of igneous rocks with 22-71% of sulfur derived from TSR (Figure 8.10). Additionally, values less than the Troodos magmatic mean of 0-1‰ (e.g. Sha -5.5‰; Chapter 8) probably indicate the variable and sporadic preservation of pyrite precipitated from fluid affected by  $\text{SO}_2$  disproportionation during the mixing and cooling of magmatic volatiles by deep circulating hydrothermal fluid (de Ronde *et al.*, 2003; 2011; Herzig *et al.*, 1998a; Kim *et al.*, 2004).

Sulfur isotope ( $\delta^{34}\text{S}$ ) values in pyrite from Mala (n=7; Table 9.1) are distinctly different from any analyses previously reported for VMS of the Troodos ophiolite. Pyrite was obtained from three localities that transect the entire VMS mound (refer to Figure 9.2C) ensuring a range of mound scale physicochemical conditions were sampled. Pyrite  $\delta^{34}\text{S}$  values from Mala consistently yield values <0-1‰, the Troodos magmatic mean (Figure 9.9 A). These low  $\delta^{34}\text{S}$  values in pyrite at Mala are inconsistent with a simple seawater mixing model whereby sulfur is sourced through thermochemical seawater reduction and the leaching of igneous rocks (see discussion in Chapter 8; McDermott *et al.*, 2015; Ono *et al.*, 2007; Tivey *et al.*, 1995). The  $\delta^{34}\text{S}$  of Mala pyrite average -3.4‰, some 8‰ less than the Troodos VMS average and exhibit a tight range of between -2.8 to -3.9‰ irrespective of their location within the VMS mound (Table 9.1; Figure 9.9 A). To the authors knowledge Mala exhibits a unique insight into the evolution of a Cyprus-type VMS that until now has only rarely been identified in actively forming arc related SMS (e.g. Hine Hina; Herzig *et al.*, 1998a).

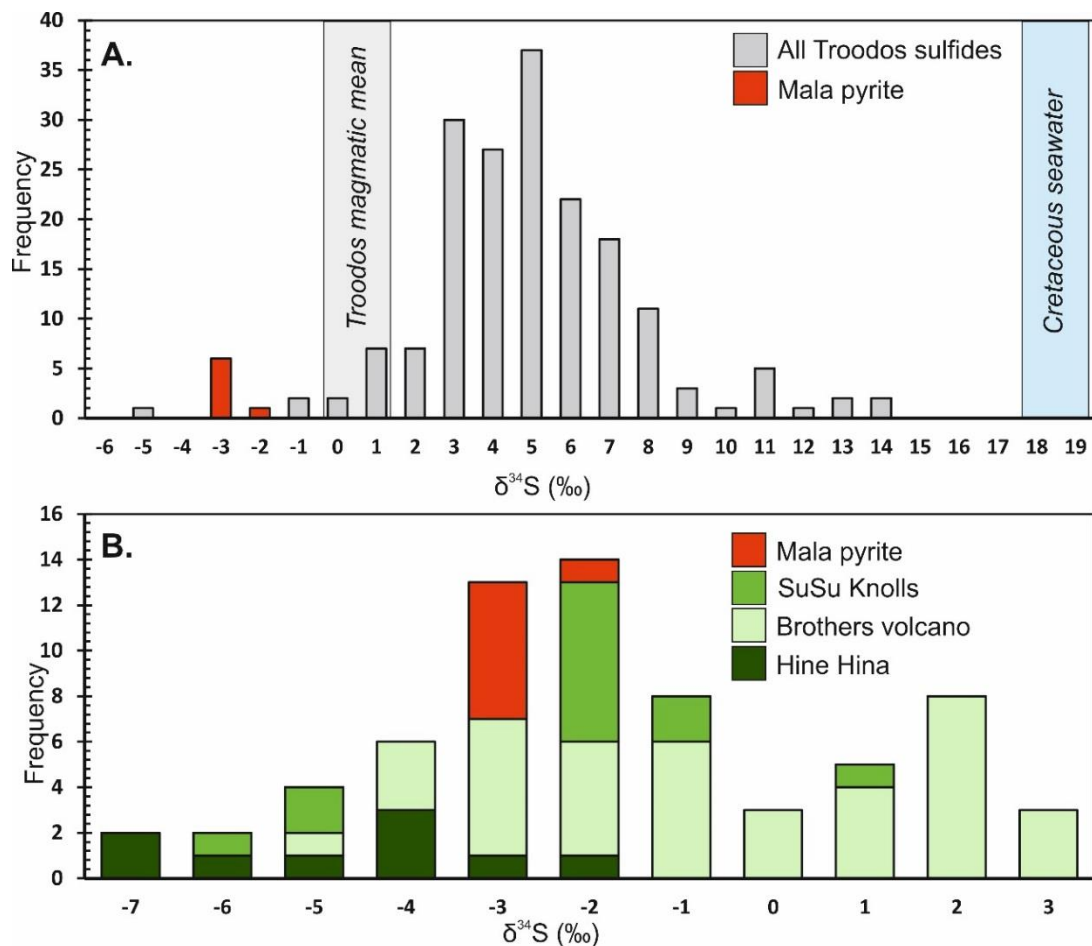


**Figure 9.9:** Histogram summary plot of sulfur isotope values. A) Troodos sulfides (cf. Chapter 8). The average  $\delta^{34}\text{S}$  in pyrite for all VMS (n=206) is +4.7‰ and at Mala the average in pyrite is -3.4‰ and B) A comparison of Mala pyrite data with sulfides (sphalerite, chalcopyrite and pyrite) from comparable SMS analogues. Note similar light values are found in back-arc/arc environments in some modern vent sites (Hine Hina (n=9); Herzig *et al.*, 1998a; Brothers (n=39); de Ronde *et al.*, 2005; SuSu Knolls (n=13), Kim *et al.*, 2004, Yeats *et al.*, 2014)

The closest modern analogue to the Mala VMS may be SMS deposits forming in back-arc environments such as Hine Hina (Herzig *et al.*, 1998a) or SuSu Knolls (Kim *et al.*, 2004; Yeats *et al.*, 2014). In these actively forming deposits the  $\delta^{34}\text{S}$  values of sulfides is consistently less than the magmatic mean (Figure 9.9 B). For example at Hine Hina, pyrite  $\delta^{34}\text{S}$  values average  $-5.3\text{‰}$  (Herzig *et al.*, 1998a) and at SuSu Knolls  $-3.8\text{‰}$  (Figure 9.9 B) (Kim *et al.*, 2004; Yeats *et al.*, 2014). With the exception of sediment hosted sites e.g. Guaymas Basin or the Red Sea, light  $\delta^{34}\text{S}$  values in sulfides ( $<-1\text{‰}$ ) are exclusively associated with back-arc/arc vent sites (Herzig *et al.*, 1998a; Kim *et al.*, 2004; Moss and Scott, 2001; Yang and Scott, 2002). It is widely accepted that in active systems and by inference their fossil analogues that a sulfur isotope signature of  $<0\text{‰}$  in sulfides are associated with the direct addition of a volatile phase from an underlying magma conduit where  $\text{SO}_2$  is released and experiences disproportion via the following reaction:  $4\text{SO}_2 + 4\text{H}_2\text{O} = 3\text{H}_2\text{SO}_4 + \text{H}_2\text{S}$  (Ohmoto and Lasaga, 1982). Through this reaction  $\text{SO}_2$  that initially has the isotopic composition of magmatic sulfur ( $\sim 0\text{‰}$ ) is partitioned into  $\text{H}_2\text{S}$  and  $\text{SO}_4^{2-}$  that due to kinematic fractionation effects are respectively lighter and heavier than the original magmatic  $\text{SO}_2$  (Kim *et al.*, 2004; Ohmoto and Lasaga, 1982).

Other possibilities explaining the light  $\delta^{34}\text{S}$  signature of pyrite at Mala include: a) a sediment source, b) the biogenic reduction of sulfate to sulfide, c) low temperature TSR under the anhydrite buffer model (cf. Chapter 8) or, d) fluid boiling (de Ronde *et al.*, 2005; Herzig *et al.*, 1998a; Kim *et al.*, 2004; Ohmoto *et al.*, 1983; Yang and Scott, 2002). As previously discussed in Chapter 8 a possible sediment source in Troodos is discounted as the earliest sediments that overly the Troodos ophiolite are some 8 Myrs younger than the formation of Troodos crust (Robertson, 1975). Biogenic reduction of sulfate to sulfide is an important process in sediment or organic-rich hydrothermal systems (e.g. Escabana Trough: Morton *et al.*, 1994). Biogenic sulfate reduction can produce light  $\delta^{34}\text{S}$  values, however the remaining sulfate is generally heavier in  $\delta^{34}\text{S}$  (see section 9.4.2; Peters *et al.*, 2010). Furthermore, at temperatures  $>160^\circ\text{C}$ , biogenic sulfate reduction is considered ineffective (Machel, 2001; Trudinger *et al.*, 1985). It therefore seems reasonable to assume that under VMS forming temperatures of at least  $200^\circ\text{C}$  (i.e. low temperature white smokers; Chapter 7) that biogenic sulfate reduction would be minor. Boiling that produces large shifts in the fluid oxidation state can also produce light values in sulfides. However, as previously discussed (Chapter 7), the deep water origin of Troodos makes boiling unlikely. Given the enrichment in magmatophile elements at Mala relative to all other Troodos VMS deposits that exist alongside the light sulfur isotope signature the author favours an additional magmatic volatile phase over low temperature ( $<300^\circ\text{C}$ ) TSR that could also produce a light signature in pyrite  $\delta^{34}\text{S} <0\text{‰}$  through temperature dependent equilibrium fractionation between sulfide and sulfate (Chapter 8- the anhydrite buffer).

### 9.4.3 The origin of gypsum

Anhydrite ( $\text{CaSO}_4$ ) is described in many SMS deposits independent of water depth and tectonic setting i.e. back-arc vs. MOR or sediment vs. sediment free ridges (Kuhn *et al.*, 2003; Nozaki *et al.*, 2016; Ogawa *et al.*, 2007; Tivey *et al.*, 1995). Anhydrite forms through the interaction of ambient seawater with hydrothermal fluid (Mills *et al.*, 1998). Anhydrite predominantly occurs cementing massive pyrite breccias, as veins or chimney structures and infilling cavities (Mills *et al.*, 1998). Humphris *et al.* (1995) estimate that the active TAG field contains approximately  $3 \times 10^8$  kg of anhydrite demonstrating the widespread distribution of anhydrite in active systems (Appendix 9.3). In ancient VMS systems anhydrite is rarely preserved due to its retrograde solubility. In seawater anhydrite is only stable between temperature of 150-250°C and thus will dissolve in response to changing fluid regimes on the seafloor or when hydrothermal activity ceases (Haymon and Kastner, 1981; Kuhn *et al.*, 2003).

In Troodos VMS and the wider Troodos stratigraphy anhydrite is not commonly preserved, however vuggy textures that probably indicate anhydrite infill and cementation are ubiquitous (Chapter 7; Figure 7.12). Unusually at the Mala VMS, massive (up to 60 cm thick) beds of gypsum ( $\text{CaSO}_4 \cdot \text{H}_2\text{O}$ ) are preserved within the pyrite mound (Figure 9.2 A-C). Gypsum occurs as fine grained <1mm needles intergrown with crudely banded to disseminated pyrite (Figure 9.2 B). Supergene gypsum is a common phase preserved in many Troodos VMS where it occurs as late, discordant, coarsely crystalline veins. Parvaz (2014) report sulfur isotope values for gypsum from the Sha and Skouriotissa VMS that support their supergene origin (Figure 9.10). Veins analysed by Parvaz (2014) yield  $\delta^{34}\text{S}$  values indistinguishable from primary Troodos sulfides averaging +6.8‰ (Figure 9.10). This suggest unequivocally that the source of sulfur in supergene gypsum veins in some VMS is sourced through the oxidation and release of  $\text{SO}_4$  from weathering of primary sulfides (Brunner *et al.*, 2008; Parvaz, 2014). However, distinct morphological differences are observed between typical supergene gypsum and the massive, fine-grained bedded gypsum at Mala. Furthermore, at Mala, gypsum exhibits a distinctly different  $\delta^{34}\text{S}$  signature of +18‰ (n=3) compared to supergene veined gypsum (Figure 9.10). In modern seafloor analogues gypsum is comparatively rare and reported only as minor phases in most MOR hosted SMS deposits (e.g. Haymon and Kastner, 1981; Mills *et al.*, 1998; Nozaki *et al.*, 2016; Peters *et al.*, 2010; Tivey *et al.*, 1995).

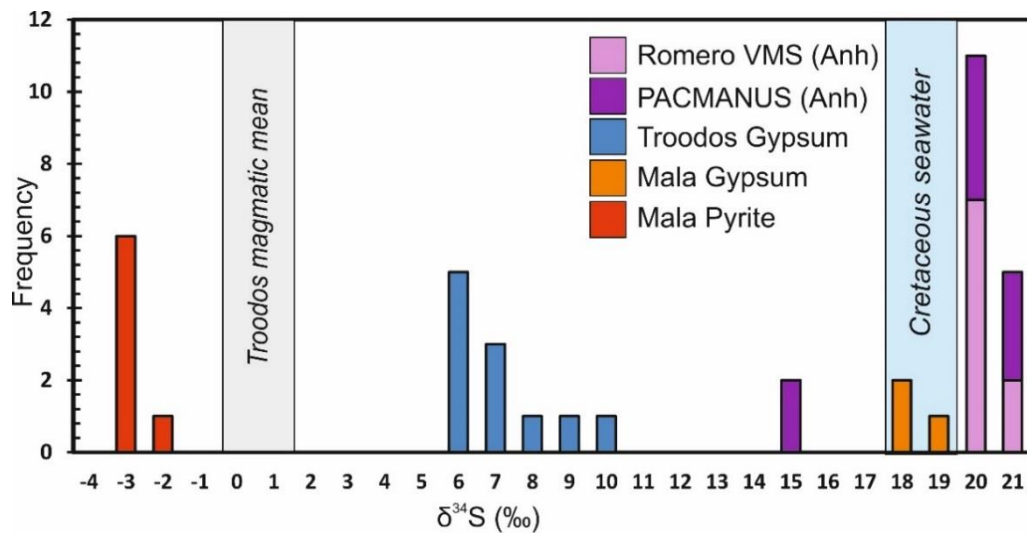


**Figure 9.10:** Sulfur isotope analysis of gypsum and pyrite from Troodos and anhydrite (Anh) from the PACMANUS vent site (Manus basin) and the sulfate-rich Romero VMS (Dominican Republic). Secondary gypsum in Troodos yields  $\delta^{34}\text{S}$  values comparable to primary sulfides (0-13‰; Chapter 8). However, gypsum at Mala records heavier values identical to Cretaceous seawater. Analysis of SMS and VMS yield  $\delta^{34}\text{S}$  values indicating a seawater origin for anhydrite (>18-21‰) (data from Kim *et al.*, 2004; Parvaz, 2014; Torró *et al.*, 2018).

Sulfur isotope analysis of gypsum from Mala yield  $\delta^{34}\text{S}$  values indistinguishable from Cretaceous seawater (18-19‰: Kampschulte and Strauss, 2004). This suggests that the bedded gypsum preserved at Mala formed from the circulation of ambient Cretaceous seawater and is not the product of either pyrite oxidation or interaction with meteoric fluid as these processes would bias analysis toward lighter  $\delta^{34}\text{S}$  values (Herzig *et al.*, 1998a; Kim *et al.*, 2004; Parvaz, 2014).

In actively forming vent sites seawater  $\delta^{34}\text{S}$  signatures are recorded in sulfate minerals (barite and anhydrite) (e.g. Herzig *et al.*, 1998a; Kim *et al.*, 2004; Teagle *et al.*, 1998). Circulating hydrothermal fluids become depleted in sulfate during wall-rock interactions and the reduction of sulfate to sulfide at temperatures >250°C (Shanks and Seyfried, 1987). This leads to the enrichment of Ca relative to  $\text{SO}_4^{2-}$  in the hydrothermal fluid. Buoyant hydrothermal fluid migrates toward the seafloor where it mixes with ambient seawater. Anhydrite precipitated from the hydrothermal fluid incorporates  $\text{Ca}^{2+}$  from both seawater and the hydrothermal fluid, and  $\text{SO}_4^{2-}$  from seawater (Kim *et al.*, 2004; Teagle *et al.*, 1998). As a result, sulfate precipitated from this solution preserves the  $\delta^{34}\text{S}$  value of contemporaneous seawater i.e. 18-19‰ in the Cretaceous, thus explaining the heavy isotopic signature of gypsum at Mala. This does not explain why such large quantities of gypsum and not anhydrite are preserved at Mala.

It is assumed that bands that are now >95% gypsum (Appendix 9.4) were probably anhydrite on the seafloor; gypsum is comparatively minor in actively forming seafloor vents systems relative to anhydrite (e.g. Humphris *et al.*, 1995). Additionally, the morphology of gypsum preserved at Mala is inconstant with, for example TAG where anhydrite is usually brecciated or vein hosted

and to our knowledge not coherently bedded (Humphris *et al.*, 1995; Tivey *et al.*, 1995; Appendix 9.3). The closest analogue to gypsum at Mala is that described for anhydrite in actively forming Kuroko type deposits where anhydrite and gypsum form crude pods and banded facies (Ogawa *et al.*, 2007; Yeats *et al.*, 2017). Within these discrete horizons coarse hypogene anhydrite undergoes later hydration and recrystallisation forming minor gypsum aggregates (e.g. Hanaoka Kuroko VMS deposit; Ogawa *et al.*, 2007).

None of the outlined scenarios adequately explain the finely crystalline nature of gypsum, the quantity, bedded morphology and preserved  $\delta^{34}\text{S}$  signature. The lack of a modern analogue elucidating all attributes observed at Mala is paralleled by a poor understanding of the preservation of SMS deposits on the seafloor and our limited understanding of complex sub-surface processes in seafloor hydrothermal systems i.e. we lack the third dimension.

The preservation of gypsum at the Mala VMS is enigmatic given that it is not observed to our knowledge in such large quantities in any other Troodos VMS. This study favours the presence of gypsum at Mala related to the generation of primary anhydrite on the seafloor. The bedded, coherent nature of gypsum is consistent with a seafloor origin that most likely represented frequent pulsed magmatic influx into the Mala VMS mound (section 9.4.4). Each pulse of 'magmatic' fluid into the VMS mound facilitated pyrite precipitation with pyrite crusts forming above previously precipitated anhydrite layers near the seawater-sulfide interface (Figure 9.11). Abundant colloform and dendritic textures preserved throughout the Mala VMS mound suggest pyrite precipitation in a crustiform manner, a texture recognised elsewhere and associated with disequilibrium pyrite precipitation due to high volumes of seawater circulation in the upper VMS stratigraphy (Keith *et al.*, 2016b; Martin *et al.*, 2019). Each subsequent fluid pulse would effectively seal or cap underlying anhydrite with a pyrite veneer (Figure 9.11). Temperatures must have remained within the anhydrite stability field as collapse or vuggy textures indicating dissolution are minor (150-250°C- Haymon and Kastner, 1981). Observations made in this study strongly suggest that the Mala mound and its associated gypsum (anhydrite) are hypogene features that formed during fluid discharge and not a replacement feature that formed during fluid recharge (Figure 9.11). A recharge model for gypsum (anhydrite) formation is discounted due to the bedded morphology of the gypsum and the absence of obvious textures that indicate dissolution at temperatures below 150°C. If gypsum formed during recharge related fluid draw down at the mound margin then it would be expected to infill and cement breccias and not form massive bands. Additionally, it seems unreasonable to assume that ambient seawater would have become heated to temperatures >150°C in the upper VMS stratigraphy in close proximity to ambient seawater (a few m), instead, fluid would have been cooler at temperatures below the anhydrite stability field <<150°C. Anhydrite precipitation would have been limited to lower

regions of the VMS mound or active discharge sites at physicochemical fronts where temperatures were within the anhydrite stability field (150-250°C).

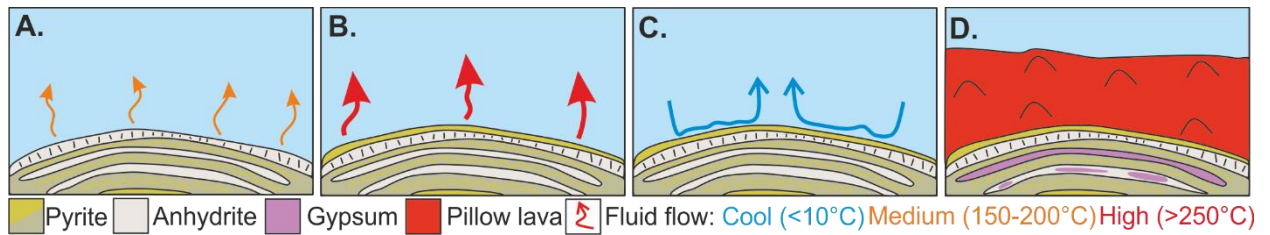


**Figure 9.11:** Schematic summary of mound growth and sulfate precipitation at Mala. A) Anhydrite grows as a crust capping pyrite in times of reduced and more diffusive hydrothermal influx at temperatures of  $\sim 150^{\circ}\text{C}$ . B) Renewed magmatic-hydrothermal influx leads to the precipitation of coarse euhedral pyrite that grades to colloform textures at the seawater interface. C) When fluid flow ceased (or migrates) within the mound the pyrite acts as a cap sealing anhydrite from further seawater ingress. D) Hydrothermal circulation ceased rapidly and Mala is blanketed by LPL limiting further seawater ingress and preserving gypsum.

Studies of the active TAG hydrothermal field, a deposit considered analogous for Troodos VMS, suggest an alternative paragenesis for the initial accumulation of sulfide. You and Bickle (1998) used  $^{234}\text{U}$ - $^{230}\text{Th}$  dating of sulfides to constrain the paragenesis of early sulfide accumulation and mound growth at TAG. They suggest that during initial stages of sulfide accumulation (i.e. the oldest samples), that the TAG mound was composed of a pyrite-silica breccia that transitions towards sulfide-silica-anhydrite breccias with maturity (You and Bickle, 1998). This model differs from observations at Mala and the model proposed in Figure 9.11. In Mala there is no evidence of pervasive silicification as suggested by You and Bickle (1998) neither is there any evidence for extensive brecciation as recorded in the juvenile stages of sulfide accumulation at TAG. They do however note a very complex growth history spanning approximately  $\sim 50,000$  years with the well-established (Hannington *et al.*, 1998), zone refined 'TAG model' only forming at an age of 6,000-4,000 years i.e. 40,000 years after initial sulfide formation. There is no way to reconcile the two opposing models presented in this study and by You and Bickle (1998); continued drilling and exploration of immature active vent sites is needed. It is however likely that extensive brecciation would be linked to i) fault movement and ii) water depth. Areas of high fault movement would facilitate high degrees of brecciation and high temperature or shallow vent fields could lead to fluid boiling and 'hydrothermal' or hydraulic breccia formation.

This does not however explain why such large quantities of gypsum are preserved at Mala as in most VMS that experience seafloor weathering anhydrite dissolves. At Mala pyrite bands acted as a cap sealing in any retained pore fluid and preventing the percolation of meteoric/seawater and subsequent dissolution of anhydrite during uplift/seafloor exposure. During this period anhydrite underwent hydration to form finely crystalline gypsum; a reaction that has been experimentally modelled (e.g. Klimchouk, 1996; Sievert *et al.*, 2005).

The stratigraphic depth of Mala at the LPL-BG contact suggests it may have been rapidly buried whilst hydrothermal discharge was still active. A thin crust of altered LPL overlies the Mala VMS mound (Figure 9.2A) indicating that the mound was active during the initial stages of burial. This would have reduced exposure of the mound on the seafloor and reduced later off axis fluid interaction. Lava flows that overly the mound remain unaltered indicating the further burial of the Mala mound occurred shortly after VMS formation had ceased. Field observations suggest that depth of burial in the Troodos stratigraphy led to the exceptional preservation of Mala. However, this does not explain the unique geochemical and isotopic signature preserved in Mala sulfides, for example at Kaphedes (Makheras domain), a deposit that also forms at the BG-LPL contact,  $\delta^{34}\text{S}$  in pyrite average 5‰ and pyrite is not enriched in magmatophile elements (UPL:LPL ratio: 0.35, Chapter 8) or neither is any visible gypsum preserved. It therefore seems likely that a combination of different hydrothermal processes and not only the rapid burial or stratigraphic depth of Mala are responsible for the preservation of its unique morphology and geochemistry.

However, it is hard to envisage a completely closed hydrothermal system at Mala needed for the preservation of anhydrite/gypsum, especially given the nature of low temperature fluid flow and 'off axis' modification of primary VMS (e.g. Silicification at Mathiatis North, Chapter 7). Further investigation to elucidate different scenarios could include a) a more extensive sampling campaign through the mound to ascertain any variation with depth and b) Sr or multiple sulfur isotopes ( $\Delta^{33}\text{S}$ ) to determine the relative degree of seawater and magmatic-hydrothermal fluid mixing to ascertain if disproportionation occurred as inferred here (e.g. Roberts *et al.*, 2003; Shanks and Seyfried, 1987).

#### 9.4.4 Pulsed magmatic influx

Magmatic influx in VMS hydrothermal systems may fluctuate temporally in response to the injection of magma at depth and liberation of magmatic volatile-rich phases in newly formed oceanic crust. Both the physical and chemical properties of the fluid change in response to these discrete magmatic events (Butterfield *et al.*, 1997; de Ronde *et al.*, 2011; Von Damm *et al.*, 1997). The injection of new magma or sheeted dyke intrusion potentially increases heat flux, sulfur, key ligands ( $\text{H}_2\text{S}$  and  $\text{Cl}^-$ ) and metals in the hydrothermal system (Figure 9.12). Volcanic events may also facilitate temporally distinct events such as phase separation or addition of a vapour phase in deep hydrothermal fluids (e.g. Gillis and Roberts, 1999; Yang and Scott, 2002). These subsurface processes in actively forming vents are manifested in changes in vent fluid chemistry (i.e. pH, temperature, salinity or major ion species) that transition from a vapour to brine dominated system with time (Butterfield 1997; Von Damm *et al.*, 1997; Figure 9.12). It is noteworthy that the modification of the system depends on the environment of formation e.g. arc vs. MOR and ultimately the characteristics of the parental magma, specifically volatile

content; bi-modal environments are more likely to exsolve a volatile phase (e.g. de Ronde *et al.*, 2011; Von Damm *et al.*, 1997).

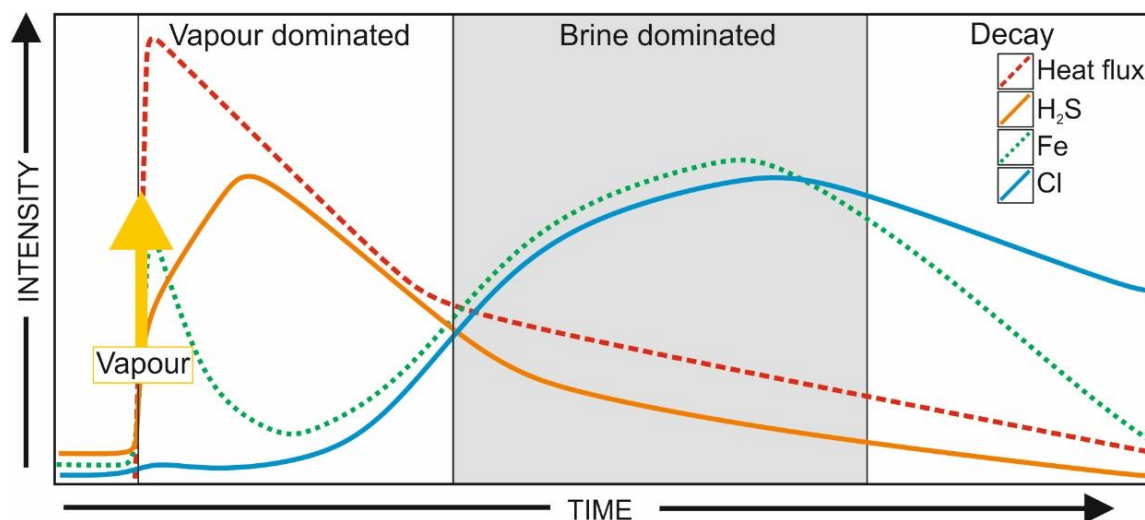


**Figure 9.12:** Response of a hydrothermal system to a magmatic/volcanic event. Relative intensity of heat flux, H<sub>2</sub>S, Fe and Cl content vs. time. Initially fluids evolve from vapour (and H<sub>2</sub>S-SO<sub>2</sub>) rich toward a cooler brine-dominated composition. This cyclic processes is repeated in response to subsequent intrusive events, the timescale of intrusion events varies dependant on the magmatic-tectonic environment and rate of magma injection (after Butterfield *et al.*, 1997).

In ancient systems primary hydrothermal fluids are scarcely preserved, and instead mineral and isotope chemistry provide evidence of past physicochemical processes (Keith *et al.*, 2016b; Martin *et al.*, 2019). At Mala, LA-ICP-MS time resolved analysis profiles of pyrite reveal variation that may indicate a pulsed magmatic influx (Figure 9.13). Time resolved analysis show a systematic increase in Co, Se and Te with distance across three pyrite grains. Results indicate that PY 1 and PY 3 formed from an increased magmatic volatile influx as they are enriched in volatile elements Te and Se (Figure 9.13). Furthermore, Co is enriched in high temperature fluids, leading to the formation of high Co pyrite from high temperature fluid (e.g. Skouriotissa, Cyprus; Keith *et al.*, 2016b). Increased Co in PY1 and PY3 could represent the influx of a high temperature fluid associated with renewed heat flux.

The modifying effect of As on Te solubility (cf. Chapter 5) is insignificant in the pyrite considered here. At high As concentrations the substitution potential of Te is enhanced (Keith *et al.*, 2018a; Martin *et al.*, 2019). If this was true at Mala, pyrite As content is expected to correlate with Te in TRA profiles however this is not the case (Figure 9.13). Furthermore, this does not explain the correlation between Se and Co with Te as these elements are unaffected by pyrite As content due to their smaller covalent radii (cf. Chapter 5). In combination TRA data suggest that the correlation between Te, Se and Co could indicate the addition of a temporally distinct magmatic volatile phase to the Mala VMS system. Element distribution supports this; as Te, Se and Co increase, As, Au and Cu decrease (Figure 9.13). For Au this most likely reflects the increased

affinity of Au as  $\text{Au}(\text{HS}^-)$  species in low temperature fluids (Pokrovski *et al.*, 2014). Copper concentration closely correlates with Au reflecting the increased solubility of Cu as  $\text{CuCl}^-$  species in a Cl-rich fluid (Audétat *et al.*, 2000; Seyfried and Bischoff, 1977). Pyrite 1 and PY3 formed under vapour dominated conditions in response to renewed heat influx and the addition of a magmatic volatile phase in the Mala VMS system (Figure 9.13). With increasing time from the event, magmatic volatile influx i.e. degassing of volatile species (and  $\text{SO}_2$ ) (cf. Pokrovski *et al.*, 2008) decreases and low temperature, and in the case of Cu, metals with an increase affinity for  $\text{Cl}^-$  complexes increase. This leads to the enrichment of Au and Cu in PY2 that formed under brine dominated conditions (Figure 9.13). The transition between vapour and brine dominated fluid is rapid and is reported as being as short as several weeks in active SMS (Butterfield *et al.*, 1997).

In addition to the pronounced correlation between magmatophile elements on a mineral scale discernible trends are also identified at the deposit scale. In all other Troodos VMS (Martin *et al.*, 2019; Chapter 5) no correlation is observed between Te and Se or Se and Co in pyrite ( $R^2 > 0.05$ ), in contrast at Mala  $R^2$  values for Te-Se and Se-Co are 0.67 and 0.84 respectively (Figure 9.6;  $n=61$ ). This suggests that ore forming physicochemical processes that control element distribution at Mala are different compared to a 'typical' Cyprus-type VMS where for example Te and Se do not exhibit a coupled behaviour.

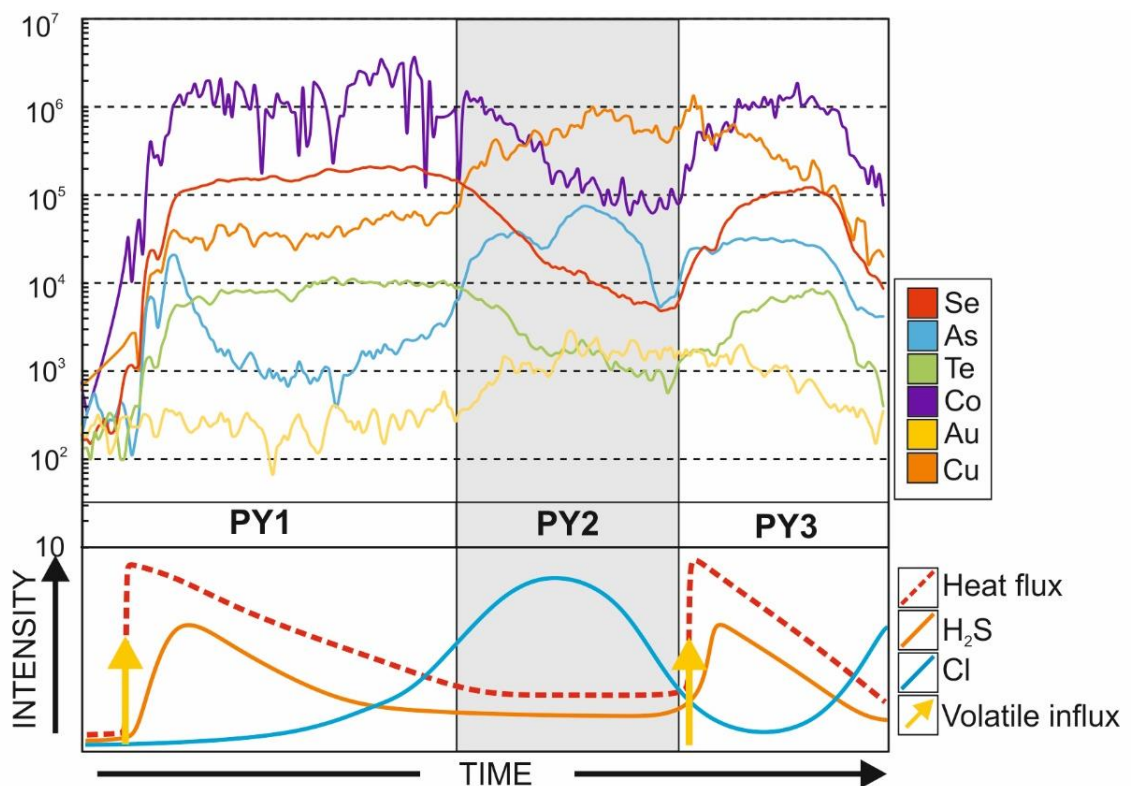


**Figure 9.13:** Time resolved LA-ICP-MS profile (cps vs. time/distance- see also Figure 9.7) vs. magmatic volatile influx in the VMS hydrothermal system. Pulsed volatile influx leads to an increase in Te and Se. The associated increase in temperature leads to an increase in Co. The inverse is true for elements that demonstrate an increased affinity to a) lower temperature fluids (Au) or b)  $\text{Cl}^-$  complexes (Cu) (after Butterfield *et al.*, 1997).

### 9.4.5 A true magmatic end member VMS

In Chapter 8 (section 8.5.6) the author predicts that 'true magmatic end member' deposits occur within the Troodos ophiolite but the juvenile, immature trace element and sulfur isotope signature of sulfides is commonly overprinted during VMS maturation and zone refining (Hannington *et al.*, 1998; Humphris *et al.*, 1995; Tivey *et al.*, 1995). Mala represents a rare magmatic end member deposit, it is enriched in magmatophile elements and with light  $\delta^{34}\text{S}$  isotope values less than the Troodos magmatic mean (0-1‰: Alt, 1994) that provides the missing link between actively forming seafloor analogues and the ancient Troodos hydrothermal system.

The most comparable actively forming analogue of the Mala VMS is the Hine Hina deposit of the Lau back-arc basin (Fouquet *et al.*, 1993; Herzig *et al.*, 1998a) or the SuSu Knolls vent site of the Manus basin (Kim *et al.*, 2004; Yeats *et al.*, 2014). At these sites immature sulfide accumulations are characterised by a light sulfur isotope signature derived from an increased magmatic volatile influx and fluids where disproportionation of magmatic  $\text{SO}_2$  occurred (Herzig *et al.*, 1998a; Kim *et al.*, 2004; Schmidt *et al.*, 2017; Shanks and Seyfried, 1987). Herzig *et al.* (1998a) envisage three stages in VMS maturation that manifest in distinct physicochemical fluid conditions during sulfide precipitation: (i) the immature volcanic stage, (ii) volcanic-tectonic and (iii) tectonic stage of ore formation. From the volcanic to tectonic stage Herzig *et al.* (1998a) demonstrate a reduction in magmatic volatile influx and increased seawater influx through a) a bias towards heavier  $\delta^{34}\text{S}$  values in sulfides and b) a reduction in magmatophile trace element concentrations. This model is by no means unique to back-arc environments or the Lau basin, with Rouxel *et al.* (2004) predicting a similar trend for the MOR hosted Lucky Strike hydrothermal field.

In the Lau back-arc basin three deposits at different stages of magmatic-tectonic development highlight the progression in  $\delta^{34}\text{S}$  values and sulfide geochemistry with decreasing magmatic influx and increased seawater mixing with distance from the actively propagating ridge tip (i.e. from young to old) (Herzig *et al.*, 1998a). Hine Hina represents the most immature deposit and exhibits consistently light  $\delta^{34}\text{S}$  values in sulfides from -2.8 to -7.7‰. In contrast the Vai Lili and White Church deposits in the magmatic-tectonic and tectonic stages respectively exhibit  $\delta^{34}\text{S}$  values indicating increased seawater influx with  $\delta^{34}\text{S}$  ranging from +2.2‰ to +16.2‰, broadly comparable to the range observed in all other Troodos VMS (Chapter 8; -3.9‰ to +13.2‰).

This study suggests that Mala represents the only known preservation of an immature VMS deposit within the Troodos ophiolite. The geochemical signature of the deposit suggest a more direct magmatic volatile source that leads to the enrichment of Te, Se and Au that would otherwise be dispersed or overprinted during extensive zone refining synonymous with VMS maturation (Hannington *et al.*, 1998; Schmidt *et al.*, 2017; Tivey *et al.*, 1995). Given the evolution

in geochemistry and isotopic signature of modern analogues in the Lau Basin (Hine Hina vs. White Church) it seems likely that many other VMS deposits sampled in this study (Chapter 8 and 5; Martin *et al.*, 2018, 2019) once exhibited a similar geochemical signature to Mala that has since been overprinted by 'seawater dominated' processes in the tectonic stage of mineralisation (cf. Herzig *et al.*, 1998a; Figure 9.14). This demonstrates a much greater diversity in ore forming processes in the Troodos hydrothermal system than previously recognised.

The observations at Mala and indeed the heterogeneity between many other Troodos VMS (Chapter 5 and 8) suggest that a significant portion of metals (e.g. Au, Te, Se and Cu) may be derived from the addition of a magmatic volatile phase and not exclusively from the leaching of metals from igneous rocks and the formation of epidiosites (Jowitt *et al.*, 2012; cf. Chapter 8). New evidence from the Troodos ophiolite presented in this study highlights complexities and processes in ore formation akin to well-studied deposits forming in modern hydrothermal vent sites. Therefore, this study redefines the current Troodos ore forming model to include an immature (or volcanic) VMS category that accounts for the variable contribution of a magmatic volatiles to the VMS hydrothermal systems (Figure 9.14- overleaf).

#### 9.4.6 The significance of epidiosites in immature VMS

The leaching of primary igneous lithologies and epidiosite formation have been hypothesised as a source of metal in some VMS deposits with early conceptual models of wall-rock - fluid interaction (e.g. Cann and Strens 1982; Scott *et al.*, 1974) validated by the discovery of epidiosites in ophiolites (e.g. Gass and Smith, 1963; Richardson *et al.*, 1987; Schiffman *et al.*, 1987) and more recently in active fore-arc spreading centres (e.g. Banerjee and Gillis, 2000). However,  $\delta^{34}\text{S}$  of pyrite and magmatophile trace element signatures from Mala suggest that the leaching of metals linked to epidiosite formation may only play a minor role in immature, newly forming mafic hosted VMS deposits. Sulfur isotope values presented in this study record a transition from  $<0\text{‰}$  to  $>0\text{‰}$  and are accompanied by a systematic decrease in magmatic volatile elements such as Te and Se that could indicate a transition from a magmatic volatile dominated source to metals sourced from epidiosite formation under seawater dominated conditions (water:rock ratios  $>125$ , cf. Chapter 3). In the immature stage of sulfide accumulation metals are sourced primarily through volatile exsolution and magmatic degassing and only under high water:rock ratios ( $>125$ ) when a steady-state hydrothermal convection is established do significant volumes of epidiosites form. As these phases overprint one another the early immature magmatic signature is overprinted, therefore only the mature metal source of VMS formation is commonly preserved i.e. epidiosites (Figure 9.14).

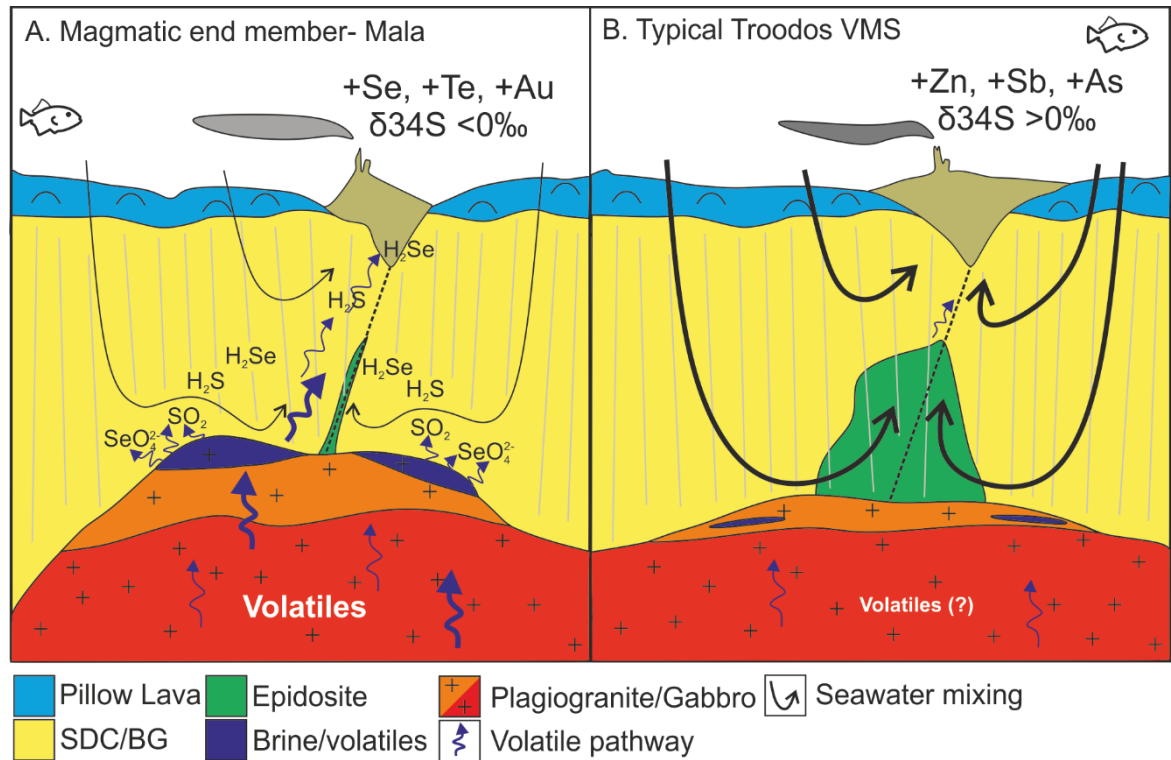


**Figure 9.14:** A new model for the Troodos hydrothermal system. A) Magmatic end member VMS. Deposits are immature and have a more direct magmatic volatile-rich source. Metals (and sulfur) are sourced from the leaching of igneous rocks and an additional volatile component, seawater mixing is minimal. Deposits exhibit a distinct enrichment in magmatophile elements and  $\delta^{34}\text{S} < 0\text{‰}$ . B) A typical Troodos VMS. Sulfur isotopes suggest variable mixing between hydrothermal and seawater derived fluids (20-70%; Chapter 8). Zone refining overprints the magmatophile trace element signature of immature-volcanic stage VMS.

## 9.5 Summary

Based on its unusual sulfur isotopes and enrichment in magmatophile trace elements coupled with evidence from modern analogues, the Mala VMS was fossilised during the immature volcanic stage of mineralisation. During the initial stages of hydrothermal circulation venting at Mala was dominated by magmatic volatile-rich fluids enriched in Au, Te and Se. Pulsed magmatic influx driven by renewed magma injection (or volcanic events) led to the perseveration of a distinct magmatophile trace element signature that varies on a mineral scale probably representing short time periods (weeks to months) of transitional fluid geochemistry toward lower temperature Cl<sup>-</sup> dominated fluids that preferentially transported Au, As and Cu.

- Mala VMS is proposed to represent a magmatic end member with a  $\delta^{34}\text{S}$  signature in pyrite averaging  $-3.4\text{‰}$ . Bedded gypsum preserves a  $\delta^{34}\text{S}$  signature of  $+18.0\text{‰}$  consistent with contemporaneous Cretaceous seawater, it is therefore primary in origin.
- Alteration mineralogy at Mala is dominated by quartz with jarosite, hematite, mordenite and albite. No high sulfidation minerals were identified.

- The occurrence of gypsum is enigmatic but is interpreted to represent the pulsed influx of fluid within the Mala VMS mound and subsequent in situ hydration of anhydrite in a closed system.
- Mineral scale variability in trace elements and element correlation on a wider deposit scale suggest pulsed magmatic influx in the Mala hydrothermal system.
- The most comparable modern analogue to Mala that is actively forming today is the Hine Hina deposit of the Lau back-arc basin.
- Evidence from Mala suggest complexities in the Troodos ore forming system akin to the Lau back-arc basin with trace element and  $\delta^{34}\text{S}$  signature of sulfides transitions with VMS maturity.

# CHAPTER 10

## Synthesis and Conclusion

## 10.1 Introduction

Chapters 5 to 9 investigate aspects of Te and Se enrichment in different Troodos VMS hydrothermal systems. This study provides one of the first and most geographically widespread geochemical and sulfur isotope datasets for mafic VMS deposits of the Troodos ophiolite. The data generated in this study allows the comparison of a range of ore forming environments and processes as well as temporal aspects of mafic VMS maturation to be established. Key questions addressed in this thesis are: (1) What is the mineral scale incorporation and partitioning of Te and Se between hydrothermal sulfide minerals?; (2) What seafloor processes enrich Te and Se in mafic VMS; and (3) How do ancient Troodos VMS compare to actively forming SMS deposits?

This study demonstrates a robust link between magmatic volatile influx and the enrichment of Te, Se and associated magmatic volatile elements in mafic VMS deposits (section 10.3). Tellurium and Se are enriched in immature VMS that experienced an increased magmatic volatile influx from the degassing of shallow magma bodies. This signature may be subsequently overprinted by a seawater dominated signature leading to the dilution and dispersion of Te and Se by local physicochemical fluid factors. Specifically, this study highlights the impact of co-precipitating sulfide phases on the mineral scale distribution of Te and Se (Figure 10.1 and 10.2; Martin *et al.*, 2019).

## 10.2 Mineral and deposit scale variation

Tellurium and Se are enriched in different sulfide phases in mafic VMS; on a broad scale Se is preferentially incorporated in covellite and chalcopyrite whilst Te is enriched in pyrite (Figure 10.1 and 10.2). Based on these data, the uptake of Te and Se by different hydrothermal sulfides has been established (Figure 10.2). The incorporation of Te and Se in sulfides, for example as nano or micro-scale inclusions or in a lattice bound substitution (Figure 10.1) has been investigated for mafic VMS deposits of Troodos. In agreement with previous studies (e.g. George *et al.*, 2018; Huston *et al.*, 1995) this study suggests that Se on a micron-scale at least is hosted in a solid solution in both pyrite and chalcopyrite (Figure 10.1). Selenium consistently produced smooth time resolved analysis profiles that exhibit co-variation with sulfur (cf. Chapter 5). Tellurium demonstrates significantly more variation between individual deposits and sulfide grains (Figure 10.1 and 10.2); time resolved analysis profiles exhibit examples of both a jagged or smooth profile suggesting variable incorporation mechanisms for Te. Using log As-Te plots (after Keith *et al.*, 2018a) this study suggests that the majority of Te is hosted as a solid solution in pyrite, however a moderate correlation ( $R^2 \approx 0.4$ ) between Bi and Te in some deposits and in bulk-rock samples demonstrates that Bi-Te inclusions present on a micron to sub-micron scale could host significant Te (Chapter 5; Martin *et al.*, 2019). Given the large covalent radii of Te

relative to sulfur, this is an important observation, therefore demonstrating variable incorporation mechanisms for Te in sulfides in mafic VMS.

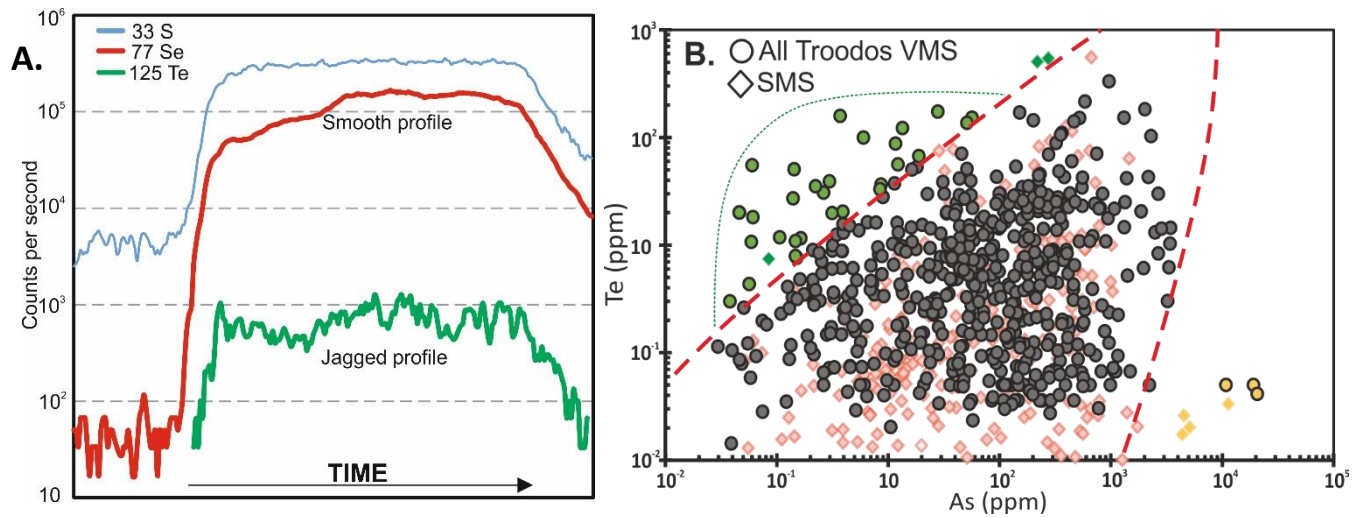


**Figure 10.1:** Incorporation of Te and Se in VMS sulfides. A) Time resolved analysis profile in pyrite highlighting smooth (Se) and jagged (Te) profile (Apliki VMS). B) Te vs. As in log-log space. Red dash line indicates solubility limit of Te in solid solution. Green dots occur as inclusions. Yellow dots are possible tennantite inclusions (after Martin *et al.*, 2019).

Previous studies suggest the enrichment of Se in high temperature environments, most likely due to its preferential enrichment in high temperature mineral phases such as chalcopyrite (e.g. Butler and Nesbitt, 1999). Data from this study favours the enrichment of Se in pyrite in both lower temperature environments and in chalcopyrite-rich zones, for example the South Apliki Breccia Zone and jasper-rich samples (Figure 10.3 and 10.4; Martin *et al.*, 2018). There appears to be no robust temperature control on Se distribution, for example Se is enriched in sulfides from both low temperature jasper-rich samples and high temperature stockwork. It is therefore likely that in chalcopyrite-rich regions of the VMS e.g. stockwork or the central mound area that co-precipitating pyrite will be depleted in Se (Figure 10.2 and 10.3). This is due to the sequestration of Se during chalcopyrite precipitation in the stockwork zone (Figure 10.3). Conversely, during the waning stages of hydrothermal activity or at the mound margins where fluids are not depleted in Se (i.e. chalcopyrite is not precipitated- Figure 10.2 and 10.3) and pyrite may contain elevated Se. Galena is generally an accessory phase in mafic VMS (<<0.5 wt.%) and was not directly analysed in this study but if present it has been shown to incorporate Se into its structure forming a solid solution with clausthalite (PbSe). Therefore, sulfides that were co-precipitated with galena are expected to be depleted in Se.

The link between the formation of SMS deposits and their preservation as on-land VMS is poorly characterised but will be a fundamental element in any future exploration for SMS away from active vent sites. This study identifies fluctuating redox seafloor processes that lead to the

extreme enrichment of Se (Martin *et al.*, 2018; Chapter 6, Figure 10.4). At Apliki VMS, seafloor oxidisation and hematite formation followed by renewed hydrothermal activity and pyrite precipitation led to the mobilisation and concentration of Se to extremely high levels (>4000 ppm). Therefore, seafloor oxidisation of sulfide is one key process leading to the enrichment of Se to potentially economic or, for monetary and remediation, toxic levels (Figure 10.4). Additionally, both Te and Se may become enriched during supergene alteration (either subaerial or seafloor) during the formation of ochre and gossans. Both elements readily adsorb onto Fe(oxy)hydroxide surfaces, to >500 ppm concentration levels (e.g. Kokkinovounaros), demonstrating the significance of gossan formation in the supergene concentration of Te and Se in mafic VMS systems (Figure 10.4; Chapter 7).

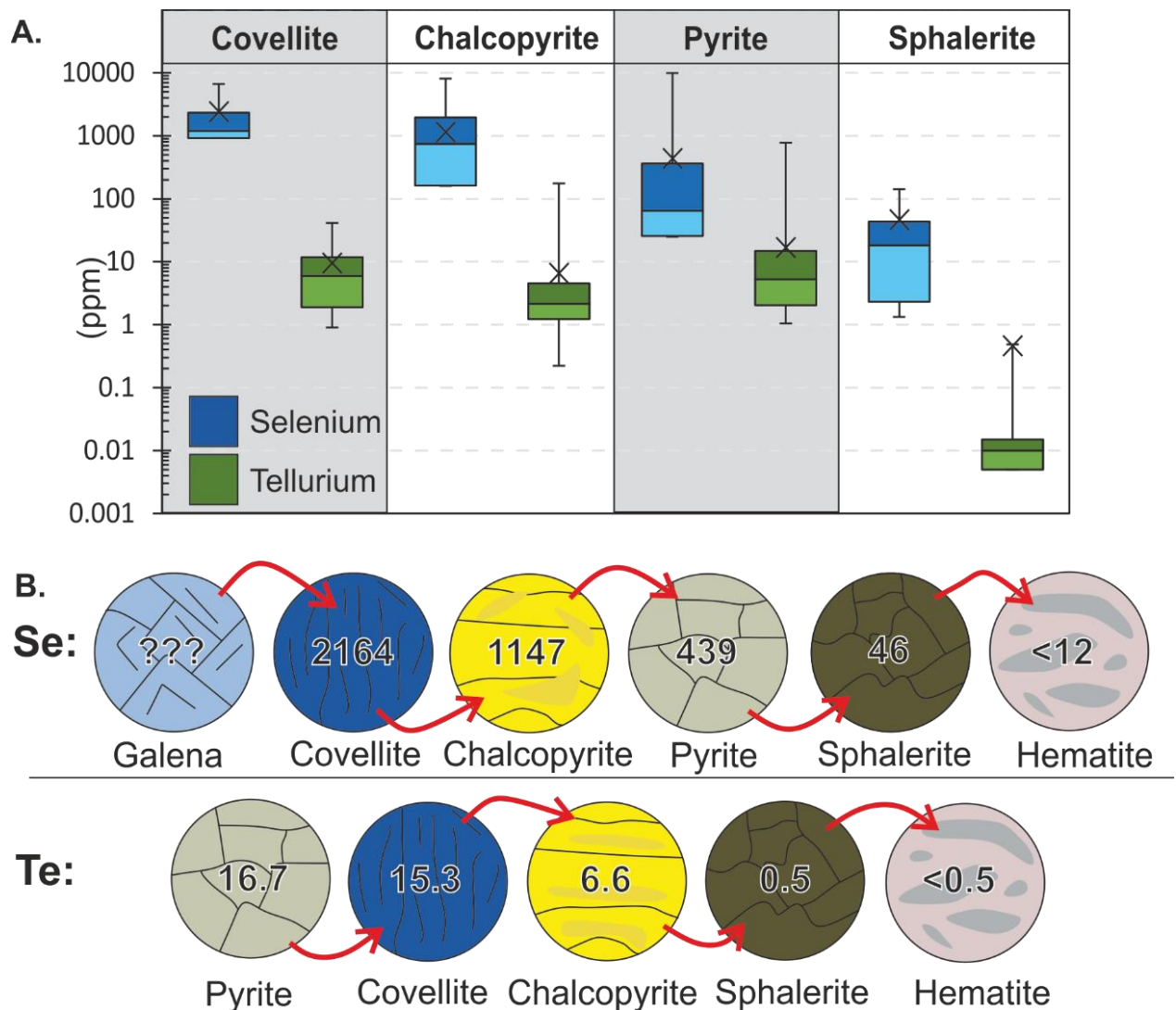
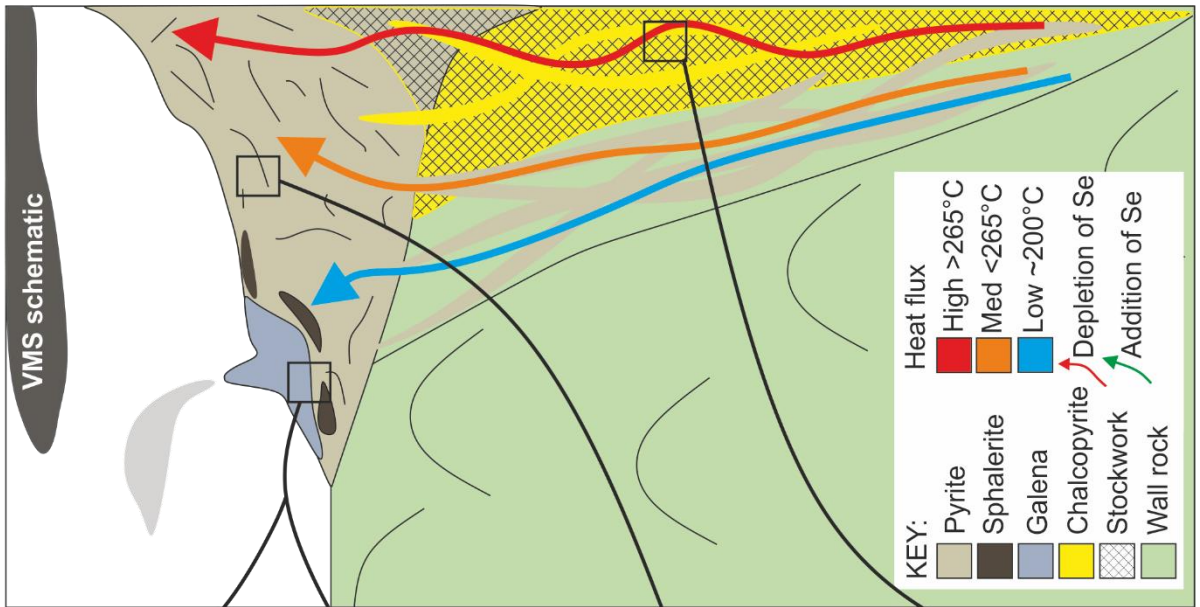


**Figure 10.2:** Mineral scale distribution of Te and Se in mafic VMS. A) Average concentration in different sulfide minerals (n=1514) for Troodos VMS. B) Average concentrations (in ppm) of Te and Se for different sulfide phases. Tellurium is preferentially hosted in pyrite whilst Se in covellite and chalcopyrite.

This study highlights important mineral and deposit scale processes that lead to the enrichment of Te and Se. Most notably on a deposit scale Te and Se are influenced by i) co-precipitating sulfide phases and ii) seafloor oxidation (Chapter 5 and 6). On a mineral scale Te and Se exhibit different partitioning behaviour with Se favouring chalcopyrite and Te favouring pyrite. The incorporation of Se in pyrite is likely achieved in a lattice bound substitution (probably with sulfur) whilst Te occurs as both micro to nano-scale inclusions and as a solid solution. Furthermore, our data is identical to actively forming SMS deposits, illustrating that many of the physicochemical processes that formed Troodos VMS are closely analogous to SMS deposits that are actively forming, or recently formed on the seafloor (section 10.4).

### 10.3 Co-precipitated sulfides



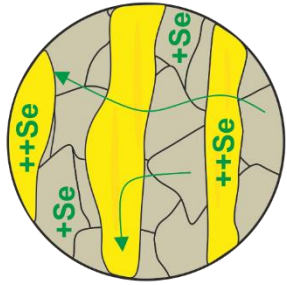
**A.** Sphalerite co-precipitating with pyrite does not effect Se partitioning behaviour as sphalerite is a poor host for Se.

**B.** Selenium preferentially partitions into galena leading to a depletion in all other co-precipitated sulfide phases.

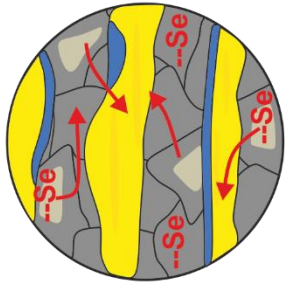
**C.** In monomineralic pyrite systems Se is incorporated uniformly between euhedral pyrite grains.

**D.** High temperature chalcopyrite rich zones preferentially incorporate Se: Ascending fluid is depleted in Se.

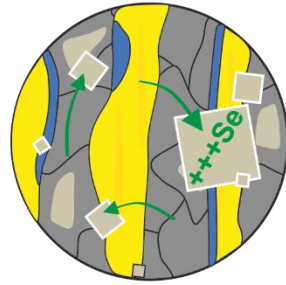
### 10.4 Fluctuating redox



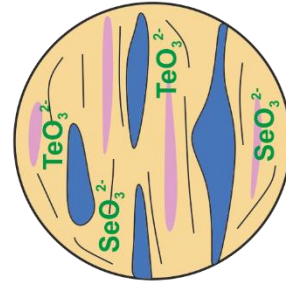
**A.** High temperature (>260°C) reduced fluid. Selenium partitions into chalcopyrite preferentially over pyrite (number of +/- symbols indicates relative amount of Se added/lost).



**B.** Reduced hydrothermal influx and increased  $fO_2$ . Pyrite and chalcopyrite undergo dissolution forming hematite. Hematite cannot incorporate Se. Selenium excess in solution.



**C.** Renewed hydrothermal influx leads to pyrite precipitation. Pyrite acts as a sink for late stage Se displaced during hematite formation. Selenium is not mobilised from chalcopyrite as covellite can incorporate large quantities of Se.



**D.** Supergene alteration leads to the formation of Fe(oxy)hydroxides, sulfates and Cu secondary phases. Tellurium and Se are adsorbed as  $SeO_3^{2-}$  and  $TeO_3^{2-}$ .

**KEY:**

- Hematite
- Jarosite/goethite
- Covellite

### 10.3 Metal source(s)

Sulfur isotope and trace element geochemistry from Troodos VMS redefine our current understanding of the Troodos hydrothermal system, with implications for the metal source(s) in mafic hosted VMS systems (Chapters 5, 8 and 9). Geochemical and sulfur isotope data suggest the variable sourcing of metals both from the SDC (e.g. Skouriotissa) and, in some VMS deposits, an additional magmatic volatile source (e.g. Mala).

It is widely accepted that in Troodos and mafic VMS systems more widely that metals are principally sourced through the leaching of igneous lithologies under greenschist facies metamorphic conditions i.e. epidosite formation (Figure 10.5; Banerjee and Gillis, 2001). In the Troodos ophiolite two distinct lava suites exist; the UPL that are enriched in Au+Se+Cu and the LPL that are enriched in Zn+As+Sb (cf. Patten et al., 2017). Assuming the SDC and epidosite formation are the only source of metal in the VMS hydrothermal system, then deposits that formed in the lower lava stratigraphy, predating the eruption of the 'off axis' UPL suite are expected to be relatively depleted in Cu, Se and Au (e.g. Kaphedes or Agrokipia). A broad correlation is observed between stratigraphic depth and the ratio of total Cu+Se+Au (UPL elements) to Zn+As+Sb (LPL elements) in VMS sulfides that range from between 0.25 for deposits that predate the formation of the UPL (e.g. Agrokipia) to 0.53 for deposits that postdate UPL formation (e.g. Phoucasa, Skouriotissa). Therefore, variation in metal content between different VMS relates to the timing of VMS formation relative to the accretion of the UPL in Troodos. A source region within the sheeted dykes with a higher proportion of UPL affinity dykes is expected to form a VMS that is relatively enriched in Cu, Se and Au (e.g. Skouriotissa, Phoucasa). However, the Mala VMS that is located in the BG-LPL stratigraphy and is expected to show a depletion in Cu+Au+Se instead exhibits a UPL:LPL ratio of 7.63 and is significantly enriched in Cu+Au+Se (Chapter 8). This paradox suggests an additional source of Cu, Se and Au at the Mala VMS that is not explainable by a variable source rock geochemistry.

### 10.4 Magmatic volatile influx

In arc environments the sourcing of metals solely from the leaching of igneous host rocks has been challenged (e.g. de Ronde *et al.*, 2011; Keith *et al.*, 2018b; Sun *et al.*, 2004; Yang and Scott, 2002). In these environments' metals can be sourced from a volatile phase and not exclusively through the leaching of igneous lithologies. This is proposed as a mechanism that explains the unusual trace metal content and isotopic signature of the Mala VMS deposit (Chapter 9).

With the continued exploration of active and recently inactive SMS deposits, repeated analysis of vent fluid over prolonged timescales (years) and the dating of sulfide material, the academic community has begun to develop models explaining the maturation and paragenesis of SMS

deposits. Sulfide mineralisation that formed during the mature stage of sulfide accumulation exhibits a sulfur isotope signature largely consistent with a mixture of seawater and igneous derived sulfur ( $>0\text{‰}$ ; e.g. White Church, Lau back-arc basin; Chapter 8).

Evidence from the Troodos ophiolite in this study suggests that this seawater dominated sulfur isotope signature and a relative depletion in magmatophile elements only reflects the mature stage of VMS formation and, that immature VMS exhibit a different and distinct sulfur isotope and geochemical signature. In the mature stage of VMS mineralisation, hydrothermal convection is relatively stable (a pseudo steady state) and metals are principally sourced through epidosite formation (cf. section 10.3) with a minor magmatic component (Figure 10.5). However, data from the Mala VMS are inconsistent with our current understanding of how a 'typical' mafic VMS might be expected to form. This study suggests a temporal variation in mafic VMS geochemistry and sulfur isotope composition of sulfides that evolves over time in response to a variable magmatic volatile influx (see summary Figure 10.10).

Initially the mafic VMS hydrothermal system is influenced by the release of magmatic volatile elements (e.g. Te, Se, Au) and the disproportionation of  $\text{SO}_2$  sourced from magmatic degassing coupled with the mixing of deep-seated seawater derived hydrothermal fluids (Figure 10.5). Over time the volatile influx diminishes, and seawater ingress increases, effectively overprinting and diluting the initial magmatic signature with a seawater one through processes such as zone refining. Modern day analogues of this early venting processes have, so far, only been identified in back-arc environments (e.g. Lau back-arc basin). Evidence from the Troodos ophiolite suggest this process may be a widespread phenomenon and not only occur in arc/back-arc environments but the wider mafic VMS environment (Figure 10.5 and 10.6). Crucially, these immature vent sites whether bimodal or mafic are enriched in critical and economic elements Se, Te and Au (Figure 10.6).

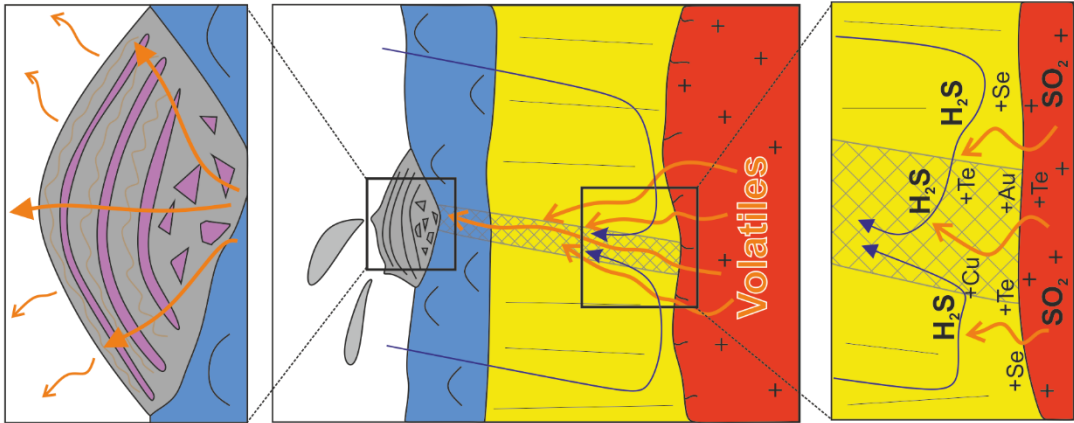
Consequently, this study identifies distinct end member Troodos VMS deposits (Figure 10.6; Chapter 8 and 9). Magmatic and hydrothermal 'end member' VMS (Mala and Skouriotissa respectively) have been identified in the Troodos ophiolite based on i) magmatophile element concentrations, ii) sulfur isotope composition of pyrite and, iii) variable physical attributes outlined in Figure 10.6.

Mala, with its immature geochemical and extremely light sulfur isotopic signature, is to our knowledge unique within the Troodos ophiolite and the Cyprus-type (mafic hosted) tectonic environment as a whole. Such immature signatures have not been identified previously in Troodos VMS and only occur in active arc related SMS deposits (e.g. Hine Hina, Lau back-arc basin; section 10.5).

10.5 Variable magmatic volatile influx

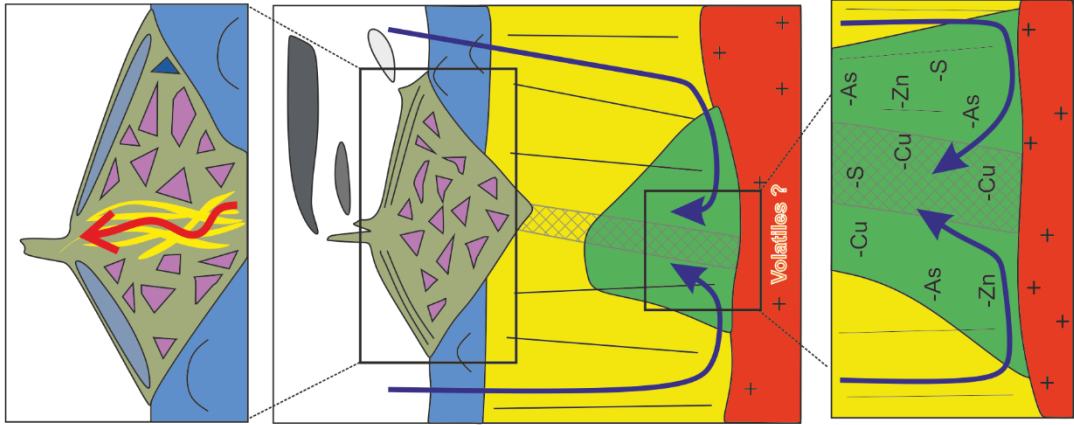
**Magmatic end member**

- The VMS mound**
- Low tonnage sulfide accumulation
  - Abundant **colloform textures** with a banded mound morphology
  - Zone refining in poorly developed
  - Fluid flow is effusive and stockwork zone is immature
  - Sulfides exhibit  $\delta^{34}\text{S}$  values  $<0\text{‰}$
  - Enrichment of Te, Se and Au



**Hydrothermal end member**

- The VMS mound**
- Large sulfide accumulation with mature stockwork
  - Mound exhibits **zone refinement** with high temperature black smoker conduit-fluid flow is highly focused
  - Anhydrite **breccia and vuggy textures** common



**The hydrothermal system**

- Immature magmatic source i.e. a recent intrusion or initiation of spreading
- Seawater ingress is minimal
- Metals and sulfur sourced from a **magmatic volatile phase** through degassing or volatile exsolution
- Fluid influx is pulsed reflecting distinct volcanic events

**The hydrothermal system**

- Seawater ingress is high and convection well established in a pseudo steady state system
- Metals sourced from **epidosite formation** in the SDC
- Minor residual volatile component

**Metal signature and source**

- Sulfur isotope values of  $<0\text{‰}$  suggests the **disproportionation** of magmatic  $\text{SO}_2$  to  $\text{H}_2\text{S}$
- Volatile elements such as Te and Se will be rapidly degassed from a magma and contributed to the overlying hydrothermal system
- Leaching of igneous rocks provides only a minor source of the total metal budget

**Metal signature and source**

- Initial magmatic signature becomes overprinted and diluted by subsequent seawater dominated fluid pulses
- Sulfur isotope values of  $>0\text{‰}$  indicate **thermochemical reduction of seawater sulfate and leaching of primary igneous lithologies** as the source of S in the hydrothermal system

**KEY:**

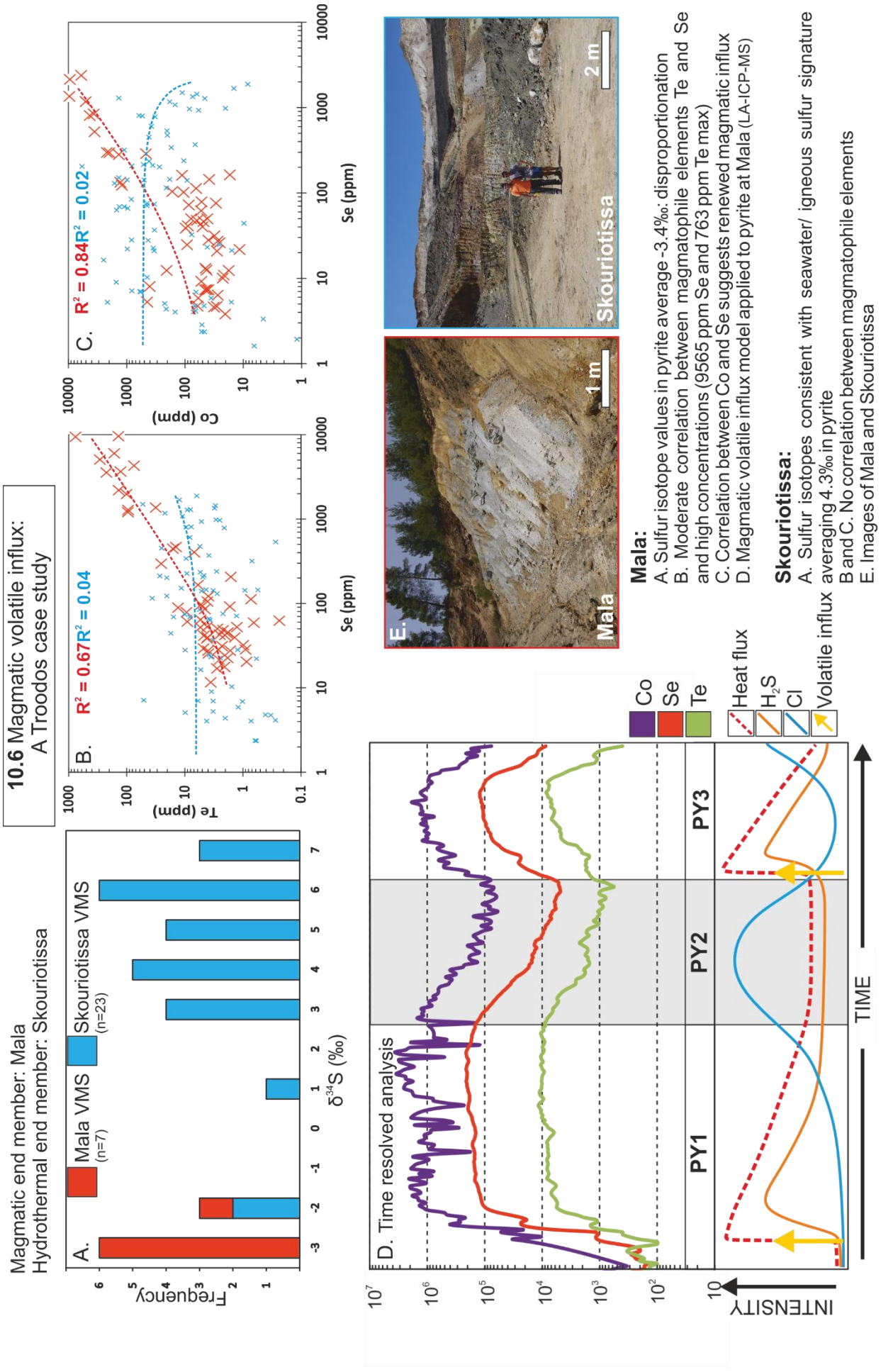
Extrusives	Massive sulfide
Sheeted dykes	Anhydrite
Epidosite	Fault zone
Plutonics	Volatiles
	Seawater

TIME

The links between magmatism and hydrothermal processes at Mala at both a deposit and mineral scale are clear. Mala is enriched in Te and Se to levels previously unrecorded in a mafic VMS deposit (Figure 10.6). In addition, Mala contains the lightest average  $\delta^{34}\text{S}$  values ( $-3.4\text{‰}$ ,  $n=7$ ) of any Troodos VMS. This is inconsistent with the leaching of primary igneous lithologies and suggests metal may be sourced through the direct addition of a magmatic volatile phase that underwent disproportionation as widely reported in active subduction influenced magmatic-hydrothermal systems (e.g. Brothers volcano; de Ronde et al., 2005; 2011).

In contrast, Skouriotissa is a 'typical' Cyprus-type VMS that exhibits a  $\delta^{34}\text{S}$  signature consistent with the sourcing of sulfur (and by inference metals) from the leaching of igneous rocks during seawater circulation (Figure 10.5 and 10.6). This likely incorporates the overprinting of a primary magmatic sulfur isotope signature (i.e.  $<0\text{‰}$ ; Mala) by a seawater signature (Troodos average  $+4.7\text{‰}$ ; Chapter 8). During sustained hydrothermal fluid flow magmatophile elements are lost or remobilised through zone refining (Figure 10.5 and 10.6). Thus, it seems likely that at some point during the initial stage of VMS formation that all Troodos VMS exhibit a magmatic signature and are enriched in magmatophile elements Te, Se and Au (Chapter 8 and 9).

In modern, actively forming seafloor analogues, physical changes in vent chemistry vary temporally in response to discrete magmatic events tracking pulses of renewed magmatic-hydrothermal influx. In fossil analogues this information is absent, however, evidence of pulsed magmatic volatile influx is expected to be traceable using mineral chemistry. Distinct pulses of magmatic volatile influx are identified at Mala. On a mineral scale, increases in Co, Te and Se exhibit pronounced fluctuations with Au and As that exhibit the inverse trend (Figure 10.6 D). Each magmatic fluid pulse is preserved as increased volatile concentrations representing the initial intrusion and degassing of a volatile saturated magmatic source. This is followed by cooler Cl<sup>-</sup> dominant fluids that preferentially mobilise Au, As  $\pm$  Cu (Chapter 9). This signature is only preserved at the immature Mala VMS, probably due to the extensive overprinting and remobilisation of metals in the VMS mound during zone refining in mature systems, hence this correlation between magmatophile, immature trace elements in pyrite is rarely preserved (cf. Chapter 8). These pronounced trends are also observable on a deposit scale at Mala where, in contrast to Skouriotissa, magmatophile elements Te and Se and Co and Se both exhibit moderate positive correlations (Figure 10.6 B and C). This clearly identifies a link between magmatic volatile influx and the enrichment of Te and Se in mafic VMS deposits of Troodos.



## 10.5 Comparison with modern analogues

### 10.5.1 An updated comparison with TAG

Previous studies by Hannington *et al.* (1998) have drawn comparisons between the Troodos ophiolite and the Trans-Atlantic Geotraverse Field (TAG) at the MAR. However, the current study demonstrates that on a mineral scale and at a trace element level that Troodos VMS deposit **cannot** be regarded as a directly comparable analogue to TAG (Figure 10.7). New trace element data from this study (Martin *et al.*, 2019) and Grant *et al.* (2018) for TAG demonstrate an enrichment in magmatic volatile elements in Troodos VMS relative to TAG (Figure 10.7). Whilst TAG and Troodos appear similar on a morphological level, they exhibit distinctly different but variable geochemical signatures (Figure 10.7).

The inclusion of highly saline plagiogranite hosted brine and the presence of wehrlite indicating a hydrous melt source (>2wt.% H<sub>2</sub>O) for Troodos magmas and a magmatic system that is distinctly different to the anhydrous basalt-dominated MAR. The author therefore questions the use of Troodos as an appropriate on land analogue for ‘mafic’ or MOR hosted VMS hydrothermal systems. This study suggests that i) Troodos is comparable to a marginal basin (back-arc system) and not a MOR system and/or ii) that magmatic volatile influx in MOR hosted hydrothermal systems transition from volatile to seawater dominated with time. Perhaps Troodos VMS are best thought of as a hybrid between a true marginal basin (back-arc) spreading centre and an MOR environment? This adequately explains their apparent enrichment in magmatic volatile elements and evolved but not truly bimodal host rock assemblage.

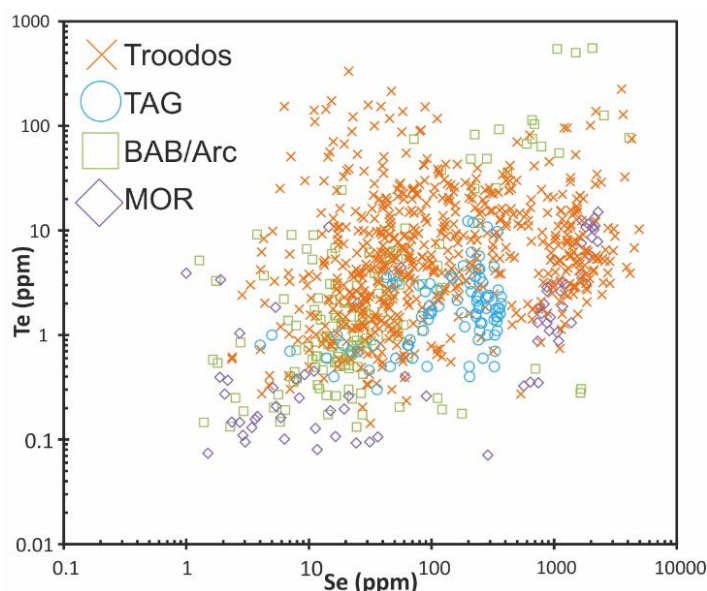


**Figure 10.7:** Geochemical comparison between all VMS deposits. Troodos spans nearly the entire range for back-arc (BAB) and MOR hosted systems. Troodos VMS are enriched in Te and Se relative to most TAG samples (Grant *et al.*, 2018; Keith *et al.*, 2016b; Martin *et al.*, 2018, 2019).

### 10.5.2 An analogue for the Troodos VMS hydrothermal system

Considering new trace element and sulfur isotope data for Troodos VMS the author suggests a more comparable analogue to Troodos VMS formation, and the wider hydrothermal system

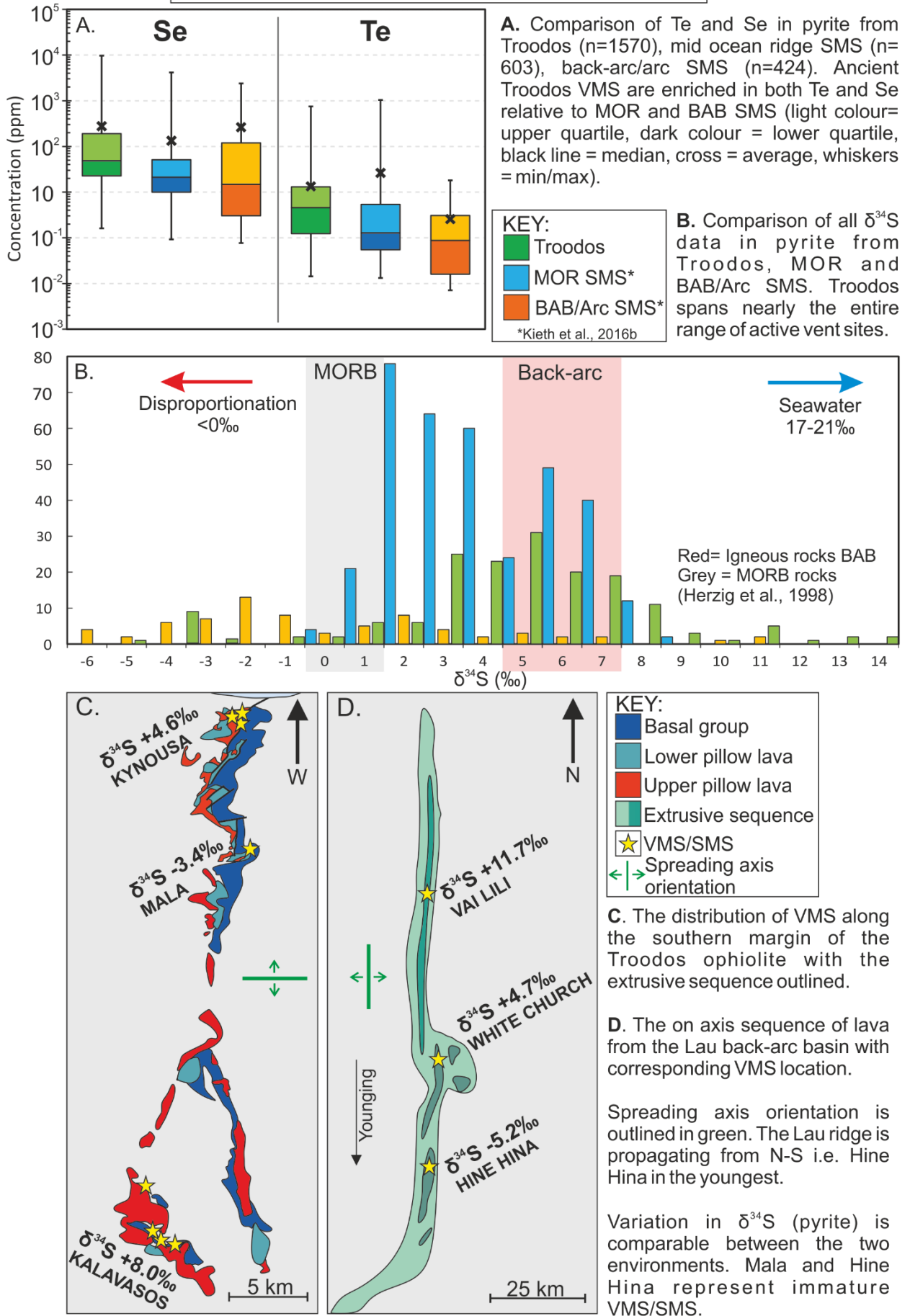
could be considered an arc related spreading environment (e.g. Valu Fa ridge, Lau back-arc basin). This is in line with our current understanding of the geodynamic environment of Troodos, which as demonstrated by multiple studies formed in a supra-subduction zone, most likely a nascent-arc environment (e.g. Pearce et al., 1984). Whilst parallels may be drawn between the VMS systems of the Lau back-arc basin and Troodos, the author acknowledges that the geodynamic regime between the two environments is different (e.g. lava geochemistry) and that direct comparisons between these VMS hydrothermal systems is challenging. This issue notwithstanding, data from this study suggests that the Valu Fa ridge of the Lau back-arc basin could represent a comparable modern-day analogue to VMS deposits of the Troodos ophiolite.

Troodos VMS are apparently enriched in Te and Se relative to both MOR and back-arc/arc hosted SMS (Figure 10.8 A). This finding is surprising given the generally volatile poor nature of mafic (basaltic-andesitic) hosted VMS systems compared to arc and back-arc, bimodal hosted environments (basaltic-rhyolitic) where parental magmas formed in subduction zone settings contain a higher volatile content (e.g. Wallace, 2005). It has long been established that the Troodos ophiolite is not a typical open ocean MOR environment and instead formed in a supra-subduction zone environment (e.g. Pearce and Robinson, 2010). It is therefore perhaps not surprising that this volatile, subduction related signature appears to influence the geochemistry of the VMS hydrothermal system and associated mineral deposits i.e. VMS demonstrate an enrichment in magmatophile subduction associated volatile elements.

When compared to MOR hosted hydrothermal systems (Chapter 8; Martin *et al.*, submitted)  $\delta^{34}\text{S}$  of pyrite in some deposits exhibit a light signature ( $<0\text{‰}$ ) (Figure 10.8 B). The scale of variation of  $\delta^{34}\text{S}$  in sulfides is comparable to modern back-arc ridges (Figure 10.8 C and D), for example, the southward propagating Valu Fa ridge, where average  $\delta^{34}\text{S}$  in pyrite ranges from  $-5.4\text{‰}$  at Hine Hina to  $+11.7\text{‰}$  at White Church (Chapter 8 and 9; Figure 10.8 C and D). In Troodos VMS pyrite range from  $-3.4\text{‰}$  at Mala to  $+8.0\text{‰}$  at Kalavassos and such variation has not yet been discovered in MOR hydrothermal systems. Considering all empirical evidence, this study suggests that a modern analogue of the Troodos VMS hydrothermal system are the SMS deposits of the Valu Fa ridge (Lau back-arc) and perhaps not the Mid Atlantic Ridge TAG hydrothermal field as previously suggested.

Conversely, understanding the paragenesis of mafic hosted SMS deposits is incomplete and we lack adequate data to sufficiently draw comparisons between fossil and modern mafic hosted SMS systems. For example, we are yet to explore for immature sulfide mounds in MOR settings and, whilst studies have documented the evolution of SMS systems using vent fluid chemistry (Chapter 5 and 8), it remains unclear what effect this has on sub-seafloor mound physicochemical processes and magmatophile trace element systematics.

**Figure 10.8** Comparing Troodos to modern analogues



## 10.6 The off axis hydrothermal system

This study provides some of the first comprehensive mineralogical and geochemical data for sites of effusive low temperature fluid discharge in Troodos (e.g. Kokkinovounaros). These sites form either during the initial stages of spreading during ridge propagation (cf. Figure 10.10) or during the waning stages of hydrothermal activity on the ridge flanks, or ridge flank faults, as newly-formed crust cooled and migrated away from the spreading axis.

Previously these deposits have been compared to pseudo-epithermal type Au deposits (Jowitt *et al.*, 2005; Naden *et al.*, 2006). Although similar textures exist, in this study the author favours a low temperature seawater-dominated origin for mineralisation that provides a link between the on axis VMS hydrothermal system and the ultra-low temperature (<100°C?) silicification observed in umbers (Prichard and Maliotis, 1998). The findings detailed in Chapter 7 highlight the diverse nature of low temperature effusive venting in mafic VMS systems and highlight that in mafic VMS that are traditionally Au-poor, significant Au may still be concentrated away from known VMS occurrences. This suggests that in seafloor hydrothermal systems and their ancient analogues that potentially economic concentrations of Au may be located distally (100's of m to km) to VMS deposits in sites of low temperature venting (Figure 10.9).

The Au poor nature of mafic VMS reflects the low solubility of Au at VMS forming temperatures of ~350°C (Figure 10.9). In addition to off axis silica-rich Au mineralisation this study finds extensive evidence for the concentration of Au in supergene weathering products e.g. ochre and gossans. The strong association of Au with silica/silicification suggest that Au enrichment in Troodos is related to both hypogene seafloor processes and supergene subaerial processes.

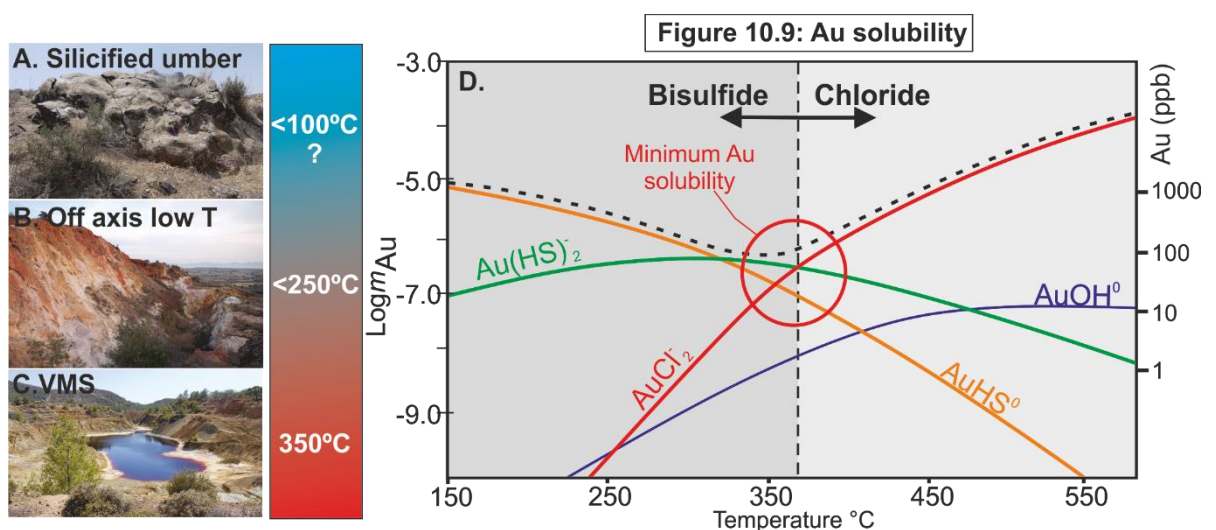


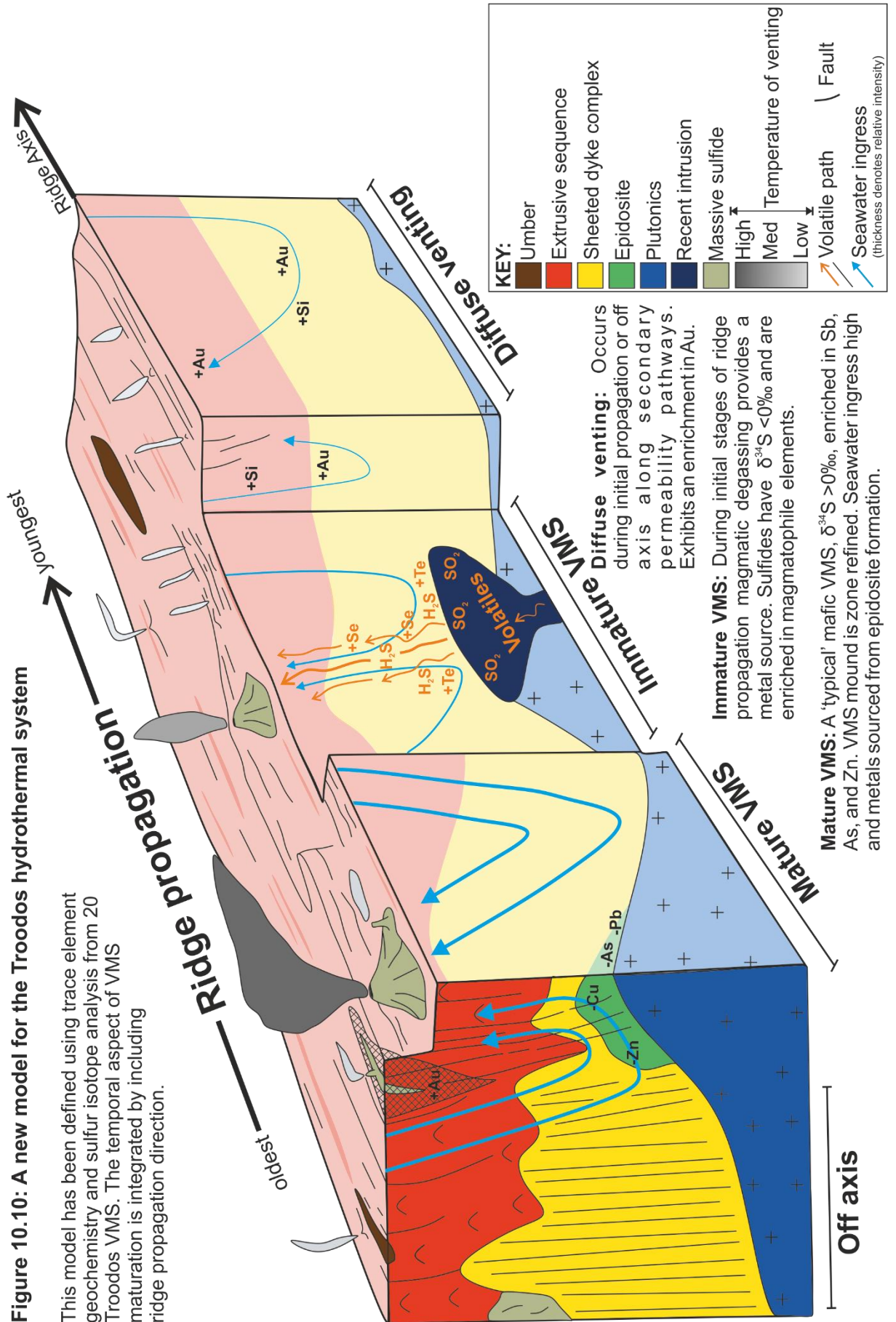
**Figure 10.9:** A, B and C) Approximate temperature of mineralisation in the Troodos hydrothermal systems. D) Major Au ligand species with temperature. Gold transport favours lower temperatures as sulfide-bisulfide complexes. Gold exhibits a minimum solubility at temperatures of ~350°C (cf. Chapter 7).

## 10.7 Concluding statement

This study demonstrates that our previous assumptions and understanding of the mafic VMS hydrothermal systems was too simplistic. New data and new models presented here redefine our understanding of the initial stages of ore formation in mafic VMS hydrothermal systems. Unlike previously thought, during the initial stage of VMS formation metals may be sourced directly from a magmatic volatile source leading to the enrichment of immature VMS in Te, Se and Au (Figure 10.10). This signature is subsequently refined and overprinted during VMS maturation by a seawater dominated signature (Figure 10.10). This has two implications, it either suggests the Troodos hydrothermal system is more comparable to a back-arc setting or, that all mafic VMS initially possess a very different geochemical signature to the one readily preserved in many MOR hosted SMS deposits (e.g. TAG). Ultimately more seafloor exploration of immature SMS in MOR or basalt hosted settings is needed to validate this observation.

Further investigation is required to integrate our new model with the spreading dynamics of the Troodos ophiolite, for example, if Mala is an immature VMS why was it preserved and not affected by off axis processes (including anhydrite dissolution), and does this relate in any way to the development of the Solea graben? Reliable dating to constrain crustal accretion processes across the Troodos ophiolite would greatly aid the temporal aspect of VMS maturation, currently we do not categorically know the direction of ridge migration in Troodos. Additionally, understanding these relationships would advance our understanding of the timing of low temperature Au-rich mineralisation relative to crustal accretion and VMS formation; did these processes occur at the same time related to local permeability changes or subsequently during the migration of crust off axis (Figure 10.10)?

Finally, Te and Se distribution and enrichment in mafic VMS is complex and influenced by mineral, mound and regional scale processes. This study demonstrates that exploration potential of mafic VMS deposits for Te and Se has been under appreciated and some VMS may be enriched to 1000's of ppm Se and 100's of ppm Te. These are significantly higher concentrations than the few ppm extracted from porphyry deposits that are currently our primary source of Te and Se, thus mafic VMS could represent a future resource for Te and Se if they are considered sensibly as valuable co-products of Cu extraction. A robust link between magmatic volatile influx and Te and Se predict that arc/back-arc, subduction influenced environments should contain higher Te and Se relative to MOR systems. However, mafic VMS maturity clearly influences their enrichment with immature deposits containing higher Te and Se than mature deposits (Figure 10.10).



BLANK PAGE

## References

- Abelson, M., Baer, G., Agnon, A., 2001. Evidence from gabbro of the Troodos ophiolite for lateral magma transport along a slow-spreading mid-ocean ridge. *Nature* 409, 72. <https://doi.org/10.1038/35051058>
- Abratis, P.K., Patrick, R.A.D., Vaughan, D.J., 2004. Variations in the compositional, textural and electrical properties of natural pyrite: a review. *International Journal of Mineral Processing* 74, 41–59. <https://doi.org/10.1016/j.minpro.2003.09.002>
- Adamides, N.G., 2010a. Mafic-dominated volcanogenic sulphide deposits in the Troodos ophiolite, Cyprus Part 2- A review of genetic models and guides for exploration. *Appl. Earth Sci.* 119, 193–204.
- Adamides, N.G., 2010b. Mafic-dominated volcanogenic sulphide deposits in the Troodos ophiolite, Cyprus Part 1- The deposits of the Solea graben. *Appl. Earth Sci.* 119, 65–77.
- Adamides, N.G., 2013. South Mathiatis: An unusual volcanogenic sulphide deposit in the Troodos ophiolite of Cyprus. *Appl. Earth Sci.* 122, 194–206. <https://doi.org/10.1179/1743275814Y.0000000037>
- Agar, S.M., Klitgord, K.D., 1995. A mechanism for decoupling within the oceanic lithosphere revealed in the Troodos ophiolite. *Nature* 374, 232. <https://doi.org/10.1038/374232a0>
- Allen, R., Weihed, P., Blundell, D., Crawford, T., Davidson, G., Galley, A., Gibson, H., Hannington, M., Herrington, R., Herzig, P., Large, R., Lentz, D., Maslennikov, V., McCutcheon, S., Peter, J., Tornos, F., 2002. Global comparisons of volcanic-associated massive sulphide districts; The timing and location of major ore deposits in an evolving orogen.
- Allerton, S., Vine, F., 1991. Spreading evolution of the Troodos ophiolite, Cyprus. *Geology* 19, 637–640.
- Allerton, S., Vine, F.J., 1987. Spreading structure of the Troodos ophiolite, Cyprus: Some paleomagnetic constraints. *Geology* 15, 593–597. [https://doi.org/10.1130/0091-7613\(1987\)15<593:SSOTTO>2.0.CO;2](https://doi.org/10.1130/0091-7613(1987)15<593:SSOTTO>2.0.CO;2)
- Alt, J.C., 1994. A sulfur isotopic profile through the Troodos ophiolite, Cyprus: Primary composition and the effects of seawater hydrothermal alteration. *Geochimica et Cosmochimica Acta* 58, 1825–1840. [https://doi.org/10.1016/0016-7037\(94\)90539-8](https://doi.org/10.1016/0016-7037(94)90539-8)
- Alt, J.C., 1995. Subseafloor processes in mid-ocean ridge hydrothermal systems. *GEOPHYSICAL MONOGRAPH-AMERICAN GEOPHYSICAL UNION*, 91, pp.85-85.
- Alt, J.C., Shanks, W.C., 2003. Serpentinization of abyssal peridotites from the MARK area, Mid-Atlantic Ridge: sulfur geochemistry and reaction modeling. *Geochim. Cosmochim. Acta* 67, 641–653. [https://doi.org/10.1016/S0016-7037\(02\)01142-0](https://doi.org/10.1016/S0016-7037(02)01142-0)
- Alt, J.C. and Shanks, W.C., 2011. Microbial sulfate reduction and the sulfur budget for a complete section of altered oceanic basalts, IODP Hole 1256D (eastern Pacific). *Earth and Planetary Science Letters*, 310(1-2), pp.73-83.

- Arehart, G.B., Kesler, S.E., O'Neil, J.R., Foland, K.A., 1992. Evidence for the supergene origin of alunite in sediment-hosted micron gold deposits, Nevada. *Econ. Geol.* 87, 263–270. <https://doi.org/10.2113/gsecongeo.87.2.263>
- Arnold, M., Sheppard, S.M.F., 1981. East Pacific Rise at latitude 21°N: isotopic composition and origin of the hydrothermal sulphur. *Earth Planet. Sci. Lett.* 56, 148–156. [https://doi.org/10.1016/0012-821X\(81\)90122-9](https://doi.org/10.1016/0012-821X(81)90122-9)
- Auclair, G., Fouquet, Y. and Bohn, M., 1987. Distribution of selenium in high-temperature hydrothermal sulfide deposits at 13 degrees North, East Pacific Rise. *The Canadian Mineralogist*, 25(4), pp.577-587.
- Audétat, A., Günther, D., Heinrich, C.A., 2000. Causes for Large-Scale Metal Zonation around Mineralized Plutons: Fluid Inclusion LA-ICP-MS Evidence from the Mole Granite, Australia. *Econ. Geol.* 95, 1563–1581. <https://doi.org/10.2113/gsecongeo.95.8.1563>
- Audétat, A., Günther, D., Heinrich, C.A., 1998. Formation of a Magmatic-Hydrothermal Ore Deposit: Insights with LA-ICP-MS Analysis of Fluid Inclusions. *Science* 279, 2091–2094. <https://doi.org/10.1126/science.279.5359.2091>
- Audétat, A., Pettke, T., 2003. The magmatic-hydrothermal evolution of two barren granites: A melt and fluid inclusion study of the Rito del Medio and Canada Pinabete plutons in northern New Mexico (USA). *Geochim. Cosmochim. Acta* 67, 97–121. [https://doi.org/10.1016/S0016-7037\(02\)01049-9](https://doi.org/10.1016/S0016-7037(02)01049-9)
- Azimi, G., Papangelakis, V.G., Dutrizac, J.E., 2007. Modelling of calcium sulphate solubility in concentrated multi-component sulphate solutions. *Fluid Phase Equilibria, 3rd Fluid Properties Challenge* 260, 300–315. <https://doi.org/10.1016/j.fluid.2007.07.069>
- Ballhaus, C., Fonseca, R.O.C., Münker, C., Kirchenbaur, M., Zirner, A., 2015. Spheroidal textures in igneous rocks – Textural consequences of H<sub>2</sub>O saturation in basaltic melts. *Geochim. Cosmochim. Acta* 167, 241–252. <https://doi.org/10.1016/j.gca.2015.07.029>
- Banerjee, N.R., Gillis, K.M., 2001. Hydrothermal alteration in a modern suprasubduction zone: The Tonga forearc crust. *J. Geophys. Res. Solid Earth* 106, 21737–21750. <https://doi.org/10.1029/2001JB000335>
- Banks, G.J., 2004. Accretion of the lower oceanic crust in the Troodos ophiolite: textural and geochemical constraints from drill core CY-4, Cyprus (Doctoral dissertation, The University of Wales College of Cardiff (United Kingdom)).
- Baragar, W.R., Lambert, N., Baglow, N., Gibson, I., 1990. The sheeted dyke zone in the Troodos ophiolite, in: OPHIOLITES Oceanic Crustal Analogues, Proceedings of the Symposium “Troodos 1987.” The Geological Survey Department, Ministry of Agriculture and Natural Resources, Nicosia, Cyprus, pp. 37–51.
- Barrie, C.T., D Hannington, M., 1999. Classification of Volcanic-Associated Massive Sulfide Deposits Based on Host-Rock Composition, in: *Rev. Econ. Geo.* pp. 1–11.
- Bendnarz, U., Schmincke, H.-U., 1990. Chemical patterns of seawater and hydrothermal alteration in the north-eastern Troodos extrusive series and the sheeted dyke complex (Cyprus), in: OPHIOLITES Oceanic Crustal Analogues, Proceedings of the Symposium “Troodos 1987.” The Geological Survey Department, Ministry of Agriculture and Natural Resources, Nicosia, Cyprus, pp. 639–653.

- Benn, K. and Laurent, R., 1987. Intrusive suite documented in the Troodos ophiolite plutonic complex, Cyprus. *Geology*, 15(9), pp.821-824.
- Berkenbosch, H.A., Ronde, C.E.J. de, Gemmell, J.B., McNeill, A.W., Goemann, K., 2012. Mineralogy and Formation of Black Smoker Chimneys from Brothers Submarine Volcano, Kermadec Arc. *Economic Geology* 107, 1613–1633. <https://doi.org/10.2113/econgeo.107.8.1613>
- Bethke, P.M., Barton, P.B., 1971. Distribution of some minor elements between coexisting sulfide minerals. *Econ. Geol.* 66, 140–163. <https://doi.org/10.2113/gsecongeo.66.1.140>
- Bickle, M.J., Teagle, D. a. H., Beynon, J., Chapman, H.J., 1998. The structure and controls on fluid-rock interactions in ocean ridge hydrothermal systems: constraints from the Troodos ophiolite. *Geol. Soc. Lond. Spec. Publ.* 148, 127–152. <https://doi.org/10.1144/GSL.SP.1998.148.01.08>
- Bickle, M.J., Teagle, D.A.H., 1992. Strontium alteration in the Troodos ophiolite: implications for fluid fluxes and geochemical transport in mid-ocean ridge hydrothermal systems. *Earth Planet. Sci. Lett.* 113, 219–237. [https://doi.org/10.1016/0012-821X\(92\)90221-G](https://doi.org/10.1016/0012-821X(92)90221-G)
- Bladh, K.W., 1982. The formation of goethite, jarosite, and alunite during the weathering of sulfide-bearing felsic rocks. *Econ. Geol.* 176–184.
- Boschen, R.E., Rowden, A.A., Clark, M.R., Gardner, J.P.A., 2013. Mining of deep-sea seafloor massive sulfides: A review of the deposits, their benthic communities, impacts from mining, regulatory frameworks and management strategies. *Ocean & Coastal Management* 84, 54–67. <https://doi.org/10.1016/j.ocecoaman.2013.07.005>
- Brazilian Minerals Group, 2013; Appendix 5B: "HIGH-GRADE COPPER-ZINC SULPHIDE MINERALISATION IDENTIFIED AT MALA PROSPECT – VRECHIA"- accessed 30/07/2018
- Brugger, J., Etschmann, B., Liu, W., Testemale, D., Hazemann, J.L., Emerich, H., van Beek, W., Proux, O., 2007. An XAS study of the structure and thermodynamics of Cu(I) chloride complexes in brines up to high temperature (400 °C, 600 bar). *Geochim. Cosmochim. Acta* 71, 4920–4941. <https://doi.org/10.1016/j.gca.2007.08.003>
- Brunner, B., Yu, J.-Y., Mielke, R.E., MacAskill, J.A., Madzunkov, S., McGenity, T.J., Coleman, M., 2008. Different isotope and chemical patterns of pyrite oxidation related to lag and exponential growth phases of *Acidithiobacillus ferrooxidans* reveal a microbial growth strategy. *Earth Planet. Sci. Lett.* 1–2, 63–72. <https://doi.org/10.1016/j.epsl.2008.03.019>
- Brunner, B., Bernasconi, S.M., 2005. A revised isotope fractionation model for dissimilatory sulfate reduction in sulfate reducing bacteria. *Geochim. Cosmochim. Acta* 69, 4759–4771. <https://doi.org/10.1016/j.gca.2005.04.015>
- Bullock, L.A., Perez, M., Armstrong, J.G., Parnell, J., Still, J., Feldmann, J., 2018. Selenium and tellurium resources in Kisgruva Proterozoic volcanogenic massive sulphide deposit (Norway). *Ore Geol. Rev.* 99, 411–424. <https://doi.org/10.1016/j.oregeorev.2018.06.023>
- Butler, I.B., Fallick, A.E., Nesbitt, R.W., 1998. Mineralogy, sulphur isotope geochemistry and the development of sulphide structures at the Broken Spur hydrothermal vent site, 29°10'N, Mid-Atlantic Ridge. *J. Geol. Soc.* 155, 773–785. <https://doi.org/10.1144/gsjgs.155.5.0773>

- Butler, I.B., Nesbitt, R.W., 1999. Trace element distributions in the chalcopyrite wall of a black smoker chimney: insights from laser ablation inductively coupled plasma mass spectrometry (LA-ICP-MS). *Earth Planet. Sci. Lett.* 167, 335–345.
- Butterfield, D.A., Jonasson, I.R., Massoth, G.J., Feely, R.A., Roe, K.K., Embley, R.E., Holden, J.F., McDuff, R.E., Lilley, M.D. and Delaney, J.R., 1997. Seafloor eruptions and evolution of hydrothermal fluid chemistry. *Philosophical Transactions of the Royal Society of London. Series A: Mathematical, Physical and Engineering Sciences*, 355(1723), pp.369-386.
- Butterfield, D.A., Massoth, G.J., McDuff, R.E., Lupton, J.E., Lilley, M.D., 1990. Geochemistry of hydrothermal fluids from Axial Seamount hydrothermal emissions study vent field, Juan de Fuca Ridge: Subseafloor boiling and subsequent fluid-rock interaction. *J. Geophys. Res. Solid Earth* 95, 12895–12921. <https://doi.org/10.1029/JB095iB08p12895>
- Cameron, W., Nisbet, E., Dietrich, V.J., 1979. Boninites, komatiites and ophiolitic basalts. *Nature* 280, 550–553.
- Cann, J.R., Strens, M.R., 1982. Black smokers fuelled by freezing magma. *Nature* 298, 147. <https://doi.org/10.1038/298147a0>
- Cann J. R., Elderfield H., Laughton A., Butterfield D. A., Jonasson I. R., Massoth G. J., Feely R. A., Roe K. K., Embley R. E., Holden J. F., McDuff R. E., Lilley M. D., Delaney J. R., 1997. Seafloor eruptions and evolution of hydrothermal fluid chemistry. *Philos. Trans. R. Soc. Lond. Ser. Math. Phys. Eng. Sci.* 355, 369–386. <https://doi.org/10.1098/rsta.1997.0013>
- Cann, J.R., Blackman, D.K., Smith, D.K., McAllister, E., Janssen, B., Mello, S., Avgerinos, E., Pascoe, A.R., Escartin, J., 1997. Corrugated slip surfaces formed at ridge–transform intersections on the Mid-Atlantic Ridge. *Nature* 385, 329. <https://doi.org/10.1038/385329a0>
- Cann, J.R., Prichard, H.M., Malpas, J.G., Xenophontos, C., 2001. Oceanic inside corner detachments of the Limassol Forest area, Troodos ophiolite, Cyprus. *J. Geol. Soc.* 158, 757–767. <https://doi.org/10.1144/0016-764900-143>
- Cann, J.R., Smith, D.K., Escartin, J. and Schouten, H., 2015. Tectonic evolution of 200 km of Mid-Atlantic Ridge over 10 million years: Interplay of volcanism and faulting. *Geochemistry, Geophysics, Geosystems*, 16(7), pp.2303-2321.
- Carr, J.M. and Bear, L.M., 1960. The geology and mineral resources of the Peristerona-Lagouthera area (Vol. 2). authority of the Government of Cyprus.
- Chen, M., Campbell, I.H., Xue, Y., Tian, W., Ireland, T.R., Holden, P., Cas, R.A.F., Hayman, P.C., Das, R., 2015. Multiple Sulfur Isotope Analyses Support a Magmatic Model for the Volcanogenic Massive Sulfide Deposits of the Teutonic Bore Volcanic Complex, Yilgarn Craton, Western Australia. *Econ. Geol.* 110, 1411–1423. <https://doi.org/10.2113/econgeo.110.6.1411>
- Choi, J., Lowell, R.P., 2015. The response of two-phase hydrothermal systems to changing magmatic heat input at mid-ocean ridges. *Deep Sea Res. Part II Top. Stud. Oceanogr., Exploring New Frontiers in Deep-Sea Research: In Honor and Memory of Peter A. Rona* 121, 17–30. <https://doi.org/10.1016/j.dsr2.2015.05.005>
- Chouinard, A., Paquette, J., Williams-Jones, A.E., 2005. Crystallographic Controls on Trace-Element Incorporation in Auriferous Pyrite from the Pascua Epithermal High-Sulfidation

- Deposit, Chile–Argentina. *Can Mineral* 43, 951–963.  
<https://doi.org/10.2113/gscanmin.43.3.951>
- Clube, T.M.M. and Robertson, A.H.F., 1986. The palaeorotation of the Troodos Microplate, Cyprus, in the late Mesozoic–early Cenozoic plate tectonic framework of the eastern Mediterranean. *Surveys in Geophysics*, 8(4), pp.375–437.
- Clube, T.M.M., Creer, K.M. and Robertson, A.H.F., 1985. Palaeorotation of the Troodos microplate, Cyprus. *Nature*, 317(6037), p.522.
- Cohen, D.R., Rutherford, N.F., Morisseau, E., Zissimos, A.M., 2012. Geochemical patterns in the soils of Cyprus. *Sci. Total Environ.* 420, 250–262.
- Constantinou, G., 1972. The geology and genesis of the sulphide ores of Cyprus (Doctoral dissertation, Imperial College London (University of London)).
- Constantinou, G., 1980. Metalogenesis associated with Troodos ophiolite, in: *Ophiolites, Proceedings: International Ophiolite Symposium, Cyprus 1979*. The Geological Survey Department, Ministry of Agriculture and Natural Resources, Nicosia, Cyprus, pp. 663–674.
- Constantinou, G., Govett, G.J.S., 1973. Geology, geochemistry, and genesis of Cyprus sulfide deposits. *Econ. Geol.* 68, 843–858. <https://doi.org/10.2113/gsecongeo.68.6.843>
- Coogan, L.A., Banks, G.J., Gillis, K.M., MacLeod, C.J., Pearce, J.A., 2003. Hidden melting signatures recorded in the Troodos ophiolite plutonic suite: evidence for widespread generation of depleted melts and intra-crustal melt aggregation. *Contrib. Mineral. Petrol.* 144, 484–506.
- Cook, N.J., Ciobanu, C.L., Danyushevsky, L.V., Gilbert, S., 2011. Minor and trace elements in bornite and associated Cu–(Fe)-sulfides: A LA-ICP-MS study Bornite mineral chemistry. *Geochimica et Cosmochimica Acta* 75, 6473–6496.  
<https://doi.org/10.1016/j.gca.2011.08.021>
- Cook, N.J., Ciobanu, C.L., Pring, A., Skinner, W., Shimizu, M., Danyushevsky, L., Saini-Eidukat, B., Melcher, F., 2009. Trace and minor elements in sphalerite: A LA-ICPMS study. *Geochimica et Cosmochimica Acta* 73, 4761–4791. <https://doi.org/10.1016/j.gca.2009.05.045>
- Cooke, A.J., Masson, L.P., Robertson, A.H.F., 2014. Construction of a sheeted dyke complex: evidence from the northern margin of the troodos ophiolite and its southern margin adjacent to the arakapas fault zone. *Ophioliti* 39, 1–30.  
<https://doi.org/10.4454/ofioliti.v39i1.426>
- Cordero, B., Gómez, V., Platero-Prats, A.E., Revés, M., Echeverría, J., Cremades, E., Barragán, F., Alvarez, S., 2008. Covalent radii revisited. *Dalton Trans.* 0, 2832–2838.
- Cowan, J., Cann, J., 1988. Supercritical two-phase separation of hydrothermal fluids in the Troodos ophiolite. *Nature* 333, 259–261. <https://doi.org/10.1038/333259a0>
- Cox, D., Singer, D.A., 1986. Mineral Deposit Models- US Geological Survey Bulletin 1693, 1st ed, US Geological Survey Bulletin. U.S Geological Survey.
- Cunningham, C.G., Rye, R.O., Rockwell, B.W., Kunk, M.J., Councill, T.B., 2005. Supergene destruction of a hydrothermal replacement alunite deposit at Big Rock Candy Mountain, Utah: Mineralogy, spectroscopic remote sensing, stable-isotope, and argon-age evidences. *Chem. Geol.* 215, 317337. <https://doi.org/10.1016/j.chemgeo.2004.06.055>

- Curtis, C.D., 1971. Diagenetic Development of Kaolinite. *Clays Clay Miner.* 19, 219–227. <https://doi.org/10.1346/CCMN.1971.0190403>
- de Ronde, C.E., Faure, K., Bray, C.J., Chappell, D.A., Wright, I.C., 2003. Hydrothermal fluids associated with seafloor mineralization at two southern Kermadec arc volcanoes, offshore New Zealand. *Miner. Deposita* 38, 217–233. <https://doi.org/10.1007/s00126-002-0305-4>
- de Ronde, C.E.J., Hannington, M.D., Stoffers, P., Wright, I.C., Ditchburn, R.G., Reyes, A.G., Baker, E.T., Massoth, G.J., Lupton, J.E., Walker, S.L., Greene, R.R., Soong, C.W.R., Ishibashi, J., Lebon, G.T., Bray, C.J., Resing, J.A., 2005. Evolution of a Submarine Magmatic-Hydrothermal System: Brothers Volcano, Southern Kermadec Arc, New Zealand. *Econ. Geol.* 100, 1097–1133.
- de Ronde, C.E.J., Massoth, G.J., Butterfield, D.A., Christenson, B.W., Ishibashi, J., Ditchburn, R.G., Hannington, M.D., Brathwaite, R.L., Lupton, J.E., Kamenetsky, V.S., Graham, I.J., Zellmer, G.F., Dziak, R.P., Embley, R.W., Dekov, V.M., Munnik, F., Lahr, J., Evans, L.J., Takai, K., 2011. Submarine hydrothermal activity and gold-rich mineralization at Brothers Volcano, Kermadec Arc, New Zealand. *Miner. Deposita* 46, 541–584. <https://doi.org/10.1007/s00126-011-0345-8>
- Deditius, A.P., Reich, M., 2016. Constraints on the solid solubility of Hg, Tl, and Cd in arsenian pyrite. *Am. Mineral.* 101, 1451–1459. <https://doi.org/10.2138/am-2016-5603>
- Deditius, A.P., Reich, M., Kesler, S.E., Utsunomiya, S., Chryssoulis, S.L., Walshe, J., Ewing, R.C., 2014. The coupled geochemistry of Au and As in pyrite from hydrothermal ore deposits. *Geochimica et Cosmochimica Acta* 140, 644–670. <https://doi.org/10.1016/j.gca.2014.05.045>
- Deditius, A.P., Utsunomiya, S., Reich, M., Kesler, S.E., Ewing, R.C., Hough, R., Walshe, J., 2011. Trace metal nanoparticles in pyrite. *Ore Geology Reviews, Nanogeoscience in ore systems research: principles, methods, and applications* 42, 32–46. <https://doi.org/10.1016/j.oregeorev.2011.03.003>
- Deditius, A.P., Utsunomiya, S., Renock, D., Ewing, R.C., Ramana, C.V., Becker, U., Kesler, S.E., 2008. A proposed new type of arsenian pyrite: Composition, nanostructure and geological significance. *Geochimica et Cosmochimica Acta* 72, 2919–2933. <https://doi.org/10.1016/j.gca.2008.03.014>
- Dietrich, D., Spencer, S., 1993. Spreading-induced faulting and fracturing of oceanic crust: examples from the Sheeted Dyke Complex of the Troodos ophiolite, Cyprus. *Geol. Soc. Lond. Spec. Publ.* 76, 121–139. <https://doi.org/10.1144/GSL.SP.1993.076.01.06>
- Dilek, Y., Thy, P., Moores, E.M., Ramsden, T.W., 1990. Tectonic evolution of the Troodos Ophiolite within the Tethyan Framework. *Tectonics* 9, 811–823. <https://doi.org/10.1029/TC009i004p00811>
- Doyle, M.G., Allen, R.L., 2003. Subsea-floor replacement in volcanic-hosted massive sulfide deposits. *Ore Geol. Rev.* 23, 183–222. [https://doi.org/10.1016/S0169-1368\(03\)00035-0](https://doi.org/10.1016/S0169-1368(03)00035-0)
- Duckworth, R.C., Knott, R., Fallick, A.E., Rickard, D., Murton, B.J., Dover, C.V., 1995. Mineralogy and sulphur isotope geochemistry of the Broken Spur sulphides, 29°N, Mid-Atlantic Ridge. *Geol. Soc. Lond. Spec. Publ.* 87, 175–189. <https://doi.org/10.1144/GSL.SP.1995.087.01.15>

- Economou-Eliopoulos, M., Eliopoulos, D.G., Chryssoulis, S., 2008. A comparison of high-Au massive sulfide ores hosted in ophiolite complexes of the Balkan Peninsula with modern analogues: Genetic significance. *Ore Geol. Rev.*, Special Issue on Ore-forming Processes associated with Mafic and Ultramafic Rocks 33, 81–100.  
<https://doi.org/10.1016/j.oregeorev.2006.10.009>
- Eddy, C.A., Dilek, Y., Hurst, S., Moores, E.M., 1998. Seamount formation and associated caldera complex and hydrothermal mineralization in ancient oceanic crust, Troodos ophiolite (Cyprus). *Tectonophysics* 292, 189–210. [https://doi.org/10.1016/S0040-1951\(98\)00064-X](https://doi.org/10.1016/S0040-1951(98)00064-X)
- Escartín, J. and Canales, J.P., 2011. Detachments in oceanic lithosphere: Deformation, magmatism, fluid flow, and ecosystems. *Eos, Transactions American Geophysical Union*, 92(4), pp.31-31.
- Escartín, J., Smith, D.K., Cann, J., Schouten, H., Langmuir, C.H., Escrig, S., 2008. Central role of detachment faults in accretion of slow-spreading oceanic lithosphere. *Nature* 455, 790.  
<https://doi.org/10.1038/nature07333>
- Everdingen, D.A. van, Cawood, P.A., Everdingen, D.A. van, Cawood, P.A., 1995. Dyke domains in the Mitsero graben, Troodos ophiolite, Cyprus: an off-axis model for graben formation at a spreading centre. *J. Geol. Soc.* 152, 923–932.  
<https://doi.org/10.1144/GSL.JGS.1995.152.01.07>
- Fonseca, R.O.C., Kirchenbaur, M., Ballhaus, C., Münker, C., Zirner, A., Gerdes, A., Heuser, A., Botcharnikov, R., Lenting, C., 2017. Fingerprinting fluid sources in Troodos ophiolite complex orbicular glasses using high spatial resolution isotope and trace element geochemistry. *Geochimica et Cosmochimica Acta* 200, 145–166.  
<https://doi.org/10.1016/j.gca.2016.12.012>
- Fouquet, Y., Charlou, J.L. (Centre de B., Stackelberg, U. von, Wiedicke, M. (Bundesanstalt fuer G. und R., Erzinger, J. (Justus-L.-U., Herzig, P.M. (r W.T.H., Muehe, R. (Univ K. (Germany) G.I.), 1993. Metallogenesis in back-arc environments: The Lau basin example. *Econ. Geol. Plus Bull. Soc. Econ. Geol. U. S.* 88:8. <https://doi.org/10.2113/gsecongeo.88.8.2154>
- Fouquet, Y., Stackelberg, U. von, Charlou, J.L., Erzinger, J., Herzig, P.M., Muehe, R., Wiedicke, M., 1993. Metallogenesis in back-arc environments; the Lau Basin example. *Econ. Geol.* 88, 2154–2181. <https://doi.org/10.2113/gsecongeo.88.8.2154>
- Franklin J.M., Sangster D.M., and Lydon, J.W., 1981, Volcanic-associated massive sulfide deposits: *Economic Geology 75th Anniversary Volume*, p. 485-627.
- Franklin, J.M., H.L. Gibson, I.R. Jonasson, and A.G. Galley, 2005, Volcanogenic Massive Sulphide Deposits: in Hedenquist, J.W., Thompson, J.F.H., Goldfarb, R.J., and Richards, J.P., eds., *Economic Geology, 100th Anniversary Volume*, The Economic Geology Publishing Company, 523-560.
- Freund, S., Haase, K.M., Keith, M., Beier, C., Garbe-Schönberg, D., 2014. Constraints on the formation of geochemically variable plagiogranite intrusions in the Troodos Ophiolite, Cyprus. *Contrib. Mineral. Petrol.* 167, 978. <https://doi.org/10.1007/s00410-014-0978-6>
- Friedman, C.T., 1998. Analysis of stable sulfur isotopes and trace cobalt on sulfides from the TAG hydrothermal mound (Doctoral dissertation, Massachusetts Institute of Technology).

- Galley, A.G., Hannington, M.D. and Jonasson, I.R., 2007. Volcanogenic massive sulphide deposits. Mineral deposits of Canada: A synthesis of major deposit-types, district metallogeny, the evolution of geological provinces, and exploration methods: Geological Association of Canada, Mineral Deposits Division, Special Publication, 5, pp.141-161.
- Gartman, A., Hannington, M.D., Jamieson, J.W., Peterkin, B., Garbe-Schönberg, D., Findlay, A.J., Fuchs, S., Kwasnitschka, T., 2018. Boiling-induced formation of colloidal gold in black smoker hydrothermal fluids. *Geology* 46, 39–42. [https://doi.org/Gartman, Amy, Hannington, Mark D., Jamieson, John William, Peterkin, Ben, Garbe-Schönberg, Dieter, Findlay, Alyssa J., Fuchs, Sebastian and Kwasnitschka, Tom \(2018\) Boiling-induced formation of colloidal gold in black smoker hydrothermal fluids. \*Geology\*, 46 \(1\). pp. 39-42. DOI 10.1130/G39492.1 <http://dx.doi.org/10.1130/G39492.1>](https://doi.org/Gartman, Amy, Hannington, Mark D., Jamieson, John William, Peterkin, Ben, Garbe-Schönberg, Dieter, Findlay, Alyssa J., Fuchs, Sebastian and Kwasnitschka, Tom (2018) Boiling-induced formation of colloidal gold in black smoker hydrothermal fluids. Geology, 46 (1). pp. 39-42. DOI 10.1130/G39492.1 <http://dx.doi.org/10.1130/G39492.1>).
- Gass, I. G., 1960. The geology and mineral resources of the Dhali area. Cyprus Geol. Survey Dept. Mere. 4, 116 pp.
- Gass I.G., Masson-Smith D., Bullard C.E, 1963. The geology and gravity anomalies of the Troodos massif, Cyprus. *Philos. Trans. R. Soc. Lond. Ser. Math. Phys. Sci.* 255, 417–467. <https://doi.org/10.1098/rsta.1963.0009>
- Gass, I.G., 1968. Is the Troodos massif of Cyprus a fragment of Mesozoic ocean floor? *Nature*, 220(5162), p.39.
- Gass, I.G., 1980. The Troodos massif: Its role in the unravelling of the ophiolite problem and its significance in the understanding of constructive plate margin processes, in: *Ophiolites, Proceedings: International Ophiolite Symposium, Cyprus 1979*. The Geological Survey Department, Ministry of Agriculture and Natural Resources, Nicosia, Cyprus, pp. 23–35.
- Gass, I.G., MacLeod, C.J., Murton, B.J., Panayiotou, A., Simonian, K.O. and Xenophontos, C., 1994. The geological evolution of the Southern Troodos transform fault zone (No. 9). Geological Survey Department.
- Gass, I.G., Neary, C.R., Plant, J., Robertson, A.H.F., Simonian, K.O., Smewing, J.D., Spooner, E.T.C. and Wilson, R.A.M., 1975. Comments on “The Troodos ophiolitic complex was probably formed in an island arc”, by A. Miyashiro and subsequent correspondence by A. Hynes and A. Miyashiro. *Earth and Planetary Science Letters*, 25(2), pp.236-238.
- Gass, I.G., Smewing, J.D., 1973. Intrusion, Extrusion and Metamorphism at Constructive Margins: Evidence from the Troodos Massif, Cyprus. *Nature* 242, 26–29. <https://doi.org/10.1038/242026a0>
- Gemmell, J.B., Sharpe, R., 1998. Detailed sulfur-isotope investigation of the TAG hydrothermal mound and stockwork zone, 26 N, Mid-Atlantic Ridge. In: *Proceedings-Ocean Drilling Program Scientific Results*. National Science Foundation, pp. 71–84.
- Gibson, I.L. (Ed.), 1991. Cyprus Crustal Study Project: Initial Report, Holes CY-1 and 1a.
- Gena, K., Chiba, H., Kase, K., Nakashima, K., Ishiyama, D., 2013. The Tiger Sulfide Chimney, Yonaguni Knoll IV Hydrothermal Field, Southern Okinawa Trough, Japan: The First Reported Occurrence of Pt-Cu-Fe-Bearing Bismuthinite and Sn-Bearing Chalcopyrite in an Active Seafloor Hydrothermal System. *Resour. Geol.* 63, 360–370. <https://doi.org/10.1111/rge.12015>
- Genna, D., Gaboury, D., 2015. Deciphering the Hydrothermal Evolution of a VMS System by LA-ICP-MS Using Trace Elements in Pyrite: An Example from the Bracemac-McLeod Deposits,

- Abitibi, Canada, and Implications for Exploration. *Economic Geology* 110, 2087–2108.  
<https://doi.org/10.2113/econgeo.110.8.2087>
- George Jr, R.P., 1978. Structural petrology of the Olympus ultramafic complex in the Troodos ophiolite, Cyprus. *Geological Society of America Bulletin*, 89(6), pp.845-865
- George, L.L., Cook, N.J., Ciobanu, C.L., 2016. Partitioning of trace elements in co-crystallized sphalerite–galena–chalcopyrite hydrothermal ores. *Ore Geol. Rev. C*, 97–116.  
<https://doi.org/10.1016/j.oregeorev.2016.02.009>
- George, L.L., Cook, N.J., Crowe, B.B.P., Ciobanu, C.L., 2018. Trace elements in hydrothermal chalcopyrite. *Mineral. Mag.* 1–61. <https://doi.org/10.1180/minmag.2017.081.021>
- Gillis M., K., 2002. The Rootzone of an Ancient Hydrothermal System Exposed in the Troodos Ophiolite, Cyprus. *J. Geol.* 110, 57–74. <https://doi.org/10.1086/324205>
- Gillis, K.M., Coogan, L.A., 2002. Anatectic Migmatites from the Roof of an Ocean Ridge Magma Chamber. *J. Petrol.* 43, 2075–2095
- Gillis, K.M., Roberts, M.D., 1999. Cracking at the magma–hydrothermal transition: evidence from the Troodos Ophiolite, Cyprus. *Earth Planet. Sci. Lett.* 169, 227–244.  
[https://doi.org/10.1016/S0012-821X\(99\)00087-4](https://doi.org/10.1016/S0012-821X(99)00087-4)
- Gillis, K.M., Robinson, P.T., 1980. Multistage alteration in the extrusive sequence of the Troodos ophiolite, Cyprus, in: OPHIOLITES Oceanic Crustal Analogues, Proceedings of the Symposium “Troodos 1987.” The Geological Survey Department, Ministry of Agriculture and Natural Resources, Nicosia, Cyprus, pp. 655–664.
- Gillis, K.M., Robinson, P.T., 1990. Patterns and processes of alteration in the lavas and dykes of the Troodos Ophiolite, Cyprus. *J. Geophys. Res. Solid Earth* 95, 21523–21548.  
<https://doi.org/10.1029/JB095iB13p21523>
- Graham, S.D., Holwell, D.A., McDonald, I., Jenkin, G.R.T., Hill, N.J., Boyce, A.J., Smith, J., Sangster, C., 2017. Magmatic Cu-Ni-PGE-Au sulfide mineralisation in alkaline igneous systems: An example from the Sron Garbh intrusion, Tyndrum, Scotland. *Ore Geol. Rev.* 80, 961–984. <https://doi.org/10.1016/j.oregeorev.2016.08.031>
- Grant, H.L.J., Hannington, M.D., Petersen, S., Frische, M., Fuchs, S.H., 2018. Constraints on the behavior of trace elements in the actively-forming TAG deposit, Mid-Atlantic Ridge, based on LA-ICP-MS analyses of pyrite. *Chem. Geol.* 498, 45–71.  
<https://doi.org/10.1016/j.chemgeo.2018.08.019>
- Greenbaum, D., 1972. Magmatic Processes at Ocean Ridges: Evidence from the Troodos Massif, Cyprus. *Nat. Phys. Sci.* 238, 18–21.
- Greenbaum, D., 1977. The chromitiferous rocks of the Troodos ophiolite complex, Cyprus. *Economic Geology*, 72(7), pp.1175-1194.
- Gregory, D. D., Large, R. R., Halpin, J. A., Baturina, E. L., Lyons, T. W., Wu, S., Danyushevsky, L., Sack, P. J., Chappaz, A., and Maslennikov, V. V. (2015a) Trace Element Content of Sedimentary Pyrite in Black Shales. *Econ. Geol.* 110, 1389-1410.
- Grimes, C.B., Ushikubo, T., Kozdon, R., Valley, J.W., 2013. Perspectives on the origin of plagiogranite in ophiolites from oxygen isotopes in zircon. *Lithos* 179, 48–66.

- Grundler, P.V., Brugger, J., Etschmann, B.E., Helm, L., Liu, W., Spry, P.G., Tian, Y., Testemale, D., Pring, A., 2013. Speciation of aqueous tellurium (IV) in hydrothermal solutions and vapors, and the role of oxidized tellurium species in Te transport and gold deposition. *Geochim. Cosmochim. Acta* 120, 298–325. <https://doi.org/10.1016/j.gca.2013.06.009>
- Hannington, M., Herzig, P., Scott, S., Thompson, G., Rona, P., 1991. Comparative mineralogy and geochemistry of gold-bearing sulfide deposits on the mid-ocean ridges. *Mar. Geol., Cenozoic Geology of the Northwest European Continental Margin and Adjacent Deep-Sea Areas* 101, 217–248. [https://doi.org/10.1016/0025-3227\(91\)90073-D](https://doi.org/10.1016/0025-3227(91)90073-D)
- Hannington, M., Jamieson, J., Monecke, T., Petersen, S., Beaulieu, S., 2011. The abundance of seafloor massive sulfide deposits. *Geology*. 39, 1155-1158
- Hannington, M., Jonasson, I., Herzig, P., Petersen, S., 1995. Physical and Chemical Processes of Seafloor Mineralization at Mid Ocean Ridges. Wash. DC Am. Geophys. Union Geophys. Monogr. Ser. 91, 115–157. <https://doi.org/10.1029/GM091p0115>
- Hannington, M.D., Barrie, C.T., 1999. The giant Kidd Creek volcanogenic massive sulfide deposit: Western Abitibi Subprovince, Canada. *Economic Geology Pub.*, Littleton, CO.
- Hannington, M.D., Barrie, C.T., Bleeker, W., 1999. The Giant Kidd Creek Volcanogenic Massive Sulfide Deposit, Western Abitibi Subprovince, Canada: Summary and Synthesis, in: Hannington, M.D., Barrie, C.T. (Eds.), *The Giant Kidd Creek Volcanogenic Massive Sulfide Deposit, Western Abitibi Subprovince, Canada*. Soc. of Econ Geol.
- Hannington, M.D., de Ronde, C.D.J., Petersen, S., 2005. Sea-floor tectonics and submarine hydrothermal systems, in: Hedenquist, J.W., Thompson, J.F.H., Goldfarb, R.J., Richards, J.P. (Eds.), *Economic Geology 100th Anniversary Volume*. Soc. of Econ. Geol., Littleton, Colorado, USA, pp. 111–141.
- Hannington, M.D., Galley, A., Gerzig, P., Petersen, S., 1998. Comparison of the TAG mound and stockwork complex with Cyprus-type massive sulfide deposits. *Proc. Ocean Drill. Program Sci. Results* 158, 389–415. <https://doi.org/10.2973/odp.proc.sr.158.217.1998>
- Hannington, M.D., Herzig, P.M., Alt, J.C., 1990. The distribution of gold in sub-seafloor stockwork mineralization from DSDP hole 504B and the Agrokipia B deposit, Cyprus. *Can. J. Earth Sci.* 27, 1409–1417.
- Hannington, M.D., Jonasson, I.R., Herzig, P.M. and Petersen, S., 1995. Physical and chemical processes of seafloor mineralization at mid-ocean ridges. *Seafloor hydrothermal systems: Physical, chemical, biological, and geological interactions*, 91, pp.115-157. *Program Sci. Results* 158, 389–415. <https://doi.org/10.2973/odp.proc.sr.158.217.1998>
- Hannington, M.D., Scott, S.D., 1989. Sulfidation equilibria as guides to gold mineralization in volcanogenic massive sulfides; evidence from sulfide mineralogy and the composition of sphalerite. *Econ. Geol.* 84, 1978–1995. <https://doi.org/10.2113/gsecongeo.84.7.1978>
- Haymon, R.M., Kastner, M., 1981. Hot spring deposits on the East Pacific Rise at 21°N: preliminary description of mineralogy and genesis. *Earth Planet. Sci. Lett.* 53, 363–381. [https://doi.org/10.1016/0012-821X\(81\)90041-8](https://doi.org/10.1016/0012-821X(81)90041-8)
- Hedenquist, J.W. and Lowenstern, J.B., 1994. The role of magmas in the formation of hydrothermal ore deposits. *Nature*, 370(6490), p.519.

- Heinrich, C.A., Driesner, T., Stefánsson, A., Seward, T.M., 2004. Magmatic vapor contraction and the transport of gold from the porphyry environment to epithermal ore deposits. *Geology* 32, 761–764. <https://doi.org/10.1130/G20629.1>
- Herrington, R.J., Wilkinson, J.J., 1993. Colloidal gold and silica in mesothermal vein systems. *Geology* 21, 539. [https://doi.org/10.1130/0091-7613\(1993\)021<0539:CGASIM>2.3.CO;2](https://doi.org/10.1130/0091-7613(1993)021<0539:CGASIM>2.3.CO;2)
- Herrington, R.J., Maslennikov, V., Zaykov, V., Seravkin, I., Kosarev, A., Buschmann, B., Orgeval, J.-J., Holland, N., Tesalina, S., Nimis, P., Armstrong, R., 2005. 6: Classification of VMS deposits: Lessons from the South Uralides. *Ore Geol. Rev., Special Issue on Geodynamics and Ore Deposit Evolution in Europe* 27, 203–237.
- Herrington, R., Piercey, S., Franklin, J., Crawford, T. and Weihed, P., 2008. Tectonic settings of VMS deposits. In *International Geological Congress: 06/08/2008-14/08/2008*. <https://doi.org/10.1016/j.oregeorev.2005.07.014>
- Herzig, P.M., Hannington, M.D., 1995. Polymetallic massive sulfides at the modern seafloor a review. *Ore Geology Reviews* 10, 95–115. [https://doi.org/10.1016/0169-1368\(95\)00009-7](https://doi.org/10.1016/0169-1368(95)00009-7)
- Herzig, P.M., Hannington, M.D., Jr, A.A., 1998a. Sulfur isotopic composition of hydrothermal precipitates from the Lau back-arc: implications for magmatic contributions to seafloor hydrothermal systems. *Miner. Deposita* 33, 226–237. <https://doi.org/10.1007/s001260050143>
- Herzig, P.M., Petersen, S. and Hannington, M.D., 1998b. Geochemistry and sulfur-isotopic composition of the TAG hydrothermal mound, Mid-Atlantic Ridge, 26 N. In *PROCEEDINGS-OCEAN DRILLING PROGRAM SCIENTIFIC RESULTS* (pp. 47-70). National Science Foundation.
- Herzig, P.M., Hannington, M.D., Scott, S.D., Maliotis, G., Rona, P.A., Thompson, G., 1991. Gold-rich sea-floor gossans in the Troodos Ophiolite and on the Mid-Atlantic Ridge. *Econ. Geol.* 86, 1747–1755. <https://doi.org/10.2113/gsecongeo.86.8.1747>
- Honnorez, J., Von Herzen, R.P., Barrett, T.J., Becker, K., Bender, M.L., Borella, P.E., Hubberten, H.W., Jones, S.C., Karato, S.I., Laverne, C. and Levi, S., 1981. Hydrothermal mounds and young ocean crust of the Galapagos: Preliminary Deep Sea Drilling results, Leg 70. *Geological Society of America Bulletin*, 92(7), pp.457-472.
- Humphris, S.E., Cann, J.R., 2000. Constraints on the energy and chemical balances of the modern TAG and ancient Cyprus seafloor sulfide deposits. *J. Geophys. Res.* 105, 28477–28488. <https://doi.org/10.1029/2000JB900289>
- Humphris, S.E. and Tivey, M.K., 2000. A synthesis of geological and geochemical investigations of the TAG hydrothermal field: Insights into fluid-flow and mixing processes in a hydrothermal system. *SPECIAL PAPERS-GEOLOGICAL SOCIETY OF AMERICA*, pp.213-236.
- Humphris, S.E., Herzig, P.M., Miller, D.J., Alt, J.C., Becker, K., Brown, D., Brüggmann, G., Chiba, H., Fouquet, Y., Gemmell, J.B., Guerin, G., Hannington, M.D., Holm, N.G., Honnorez, J.J., Iturrino, G.J., Knott, R., Ludwig, R., Nakamura, K., Petersen, S., Reysenbach, A.-L., Rona, P.A., Smith, S., A. A, S., Tivey, M.K., Zhao, X., 1995. The internal structure of an active sea-floor massive sulphide deposit. *Nature* 377, 713–716. <https://doi.org/10.1038/377713a0>

- Humphris, S.E., Klein, F., 2018. Progress in Deciphering the Controls on the Geochemistry of Fluids in Seafloor Hydrothermal Systems. *Annual Review of Marine Science* 10, 315–343. <https://doi.org/10.1146/annurev-marine-121916-063233>
- Humphris, S.E., Klein, F., 2018. Progress in Deciphering the Controls on the Geochemistry of Fluids in Seafloor Hydrothermal Systems. *Annu. Rev. Mar. Sci.* 10, 315–343. <https://doi.org/10.1146/annurev-marine-121916-063233>
- Humphris, S.E., Klein, F., 2018. Progress in Deciphering the Controls on the Geochemistry of Fluids in Seafloor Hydrothermal Systems. *Annu. Rev. Mar. Sci.* 10, 315–343. <https://doi.org/10.1146/annurev-marine-121916-063233>
- Hurst, S.D., Moores, E.M., Varga, R.J., 1994. Structural and geophysical expression of the Solea graben, Troodos Ophiolite, Cyprus. *Tectonics* 13, 139–156. <https://doi.org/10.1029/93TC02066>
- Huston, D.L., Large, R.R., 1989. A chemical model for the concentration of gold in volcanogenic massive sulphide deposits. *Ore Geol. Rev.* 4, 171–200. [https://doi.org/10.1016/0169-1368\(89\)90017-6](https://doi.org/10.1016/0169-1368(89)90017-6)
- Huston, D.L., Sie, S.H., Suter, G.F., 1995. Selenium and its importance to the study of ore genesis: the theoretical basis and its application to volcanic-hosted massive sulfide deposits using PIXE analysis. *Nucl. Instrum. Methods Phys. Res. Sect. B Beam Interact. Mater. At., Nuclear Microprobe Technology and Applications* 104, 476–480. [https://doi.org/10.1016/0168-583X\(95\)00462-9](https://doi.org/10.1016/0168-583X(95)00462-9)
- Huston, D.L., Sie, S.H., Suter, G.F., Cooke, D.R., Both, R.A., 1995. Trace elements in sulfide minerals from eastern Australian volcanic-hosted massive sulfide deposits; Part I, Proton microprobe analyses of pyrite, chalcopyrite, and sphalerite, and Part II, Selenium levels in pyrite; comparison with delta 34 S values and implications for the source of sulfur in volcanogenic hydrothermal systems. *Econ. Geol.* 90, 1167–1196. <https://doi.org/10.2113/gsecongeo.90.5.1167>
- Hynes, A., 1975. Comment on “The Troodos ophiolitic complex was probably formed in an island arc”, by A. Miyashiro. *Earth and Planetary Science Letters*, 25(2), pp.213-216.
- Ishibashi, J., Ikegami, F., Tsuji, T., Urabe, T., 2015. Hydrothermal Activity in the Okinawa Trough Back-Arc Basin: Geological Background and Hydrothermal Mineralization, in: Ishibashi, J., Okino, K., Sunamura, M. (Eds.), *Subseafloor Biosphere Linked to Hydrothermal Systems: TAIGA Concept*. Springer Japan, Tokyo, pp. 337–359.
- Jackson, J., McKenzie, D., 1984. Active tectonics of the Alpine–Himalayan Belt between western Turkey and Pakistan. *Geophys. J. R. Astron. Soc.* 77, 185–264. <https://doi.org/10.1111/j.1365-246X.1984.tb01931.x>
- Jamieson, J.W., Hannington, M.D., Clague, D.A., Kelley, D.S., Delaney, J.R., Holden, J.F., Tivey, M.K., Kimpe, L.E., 2013. Sulfide geochronology along the Endeavour Segment of the Juan de Fuca Ridge. *Geochem. Geophys. Geosystems* 14, 2084–2099. <https://doi.org/10.1002/ggge.20133>
- Jenner, F.E., O’Neill, H.S.C., Arculus, R.J., Mavrogenes, J.A., 2010. The Magnetite Crisis in the Evolution of Arc-related Magmas and the Initial Concentration of Au, Ag and Cu. *J. Petrol.* 51, 2445–2464. <https://doi.org/10.1093/petrology/egq063>

- Josso, P., Roberts, S., Teagle, D.A.H., Pourret, O., Herrington, R., Ponce de Leon Albarrañ, C., 2018. Extraction and separation of rare earth elements from hydrothermal metalliferous sediments. *Miner. Eng.* 118, 106–121. <https://doi.org/10.1016/j.mineng.2017.12.014>
- Jowitt, S.M., Jenkin, G.R.T., Coogan, L.A., Naden, J., 2012. Quantifying the release of base metals from source rocks for volcanogenic massive sulfide deposits: Effects of protolith composition and alteration mineralogy. *Journal of Geochemical Exploration* 118, 47–59. <https://doi.org/10.1016/j.gexplo.2012.04.005>
- Jowitt, S.M., Osborn, R.G.M., Thomas, R.D.H., Naden, J., Gunn, A.G., Herrington, R.J., Nicolaidis, S., 2005. 'T'-type mineralisation — a pseudo-epithermal style of VHMS associated gold mineralisation, Cyprus, in: *Mineral Deposit Research: Meeting the Global Challenge*. Springer, Berlin, Heidelberg, pp. 635–637.
- Kampschulte, A., Strauss, H., 2004. The sulfur isotopic evolution of Phanerozoic seawater based on the analysis of structurally substituted sulfate in carbonates. *Chem. Geol., Applications of Stable Isotope Techniques to Geological and Environmental Problems* 204, 255–286. <https://doi.org/10.1016/j.chemgeo.2003.11.013>
- Kase, K., Yamamoto, M. & Shmata, T. 1990. Copper-rich sulfide deposits near 23° MidAtlantic Ridge: chemical composition, mineral chemistry, and sulfur isotopes. *Proceedings, Ocean Drilling Program, 106/109, Scientific Results*, 163-177.
- Kusakabe, M., Komoda, Y., Takano, B. and Abiko, T., 2000. Sulfur isotopic effects in the disproportionation reaction of sulfur dioxide in hydrothermal fluids: implications for the  $\delta^{34}\text{S}$  variations of dissolved bisulfate and elemental sulfur from active crater lakes. *Journal of Volcanology and Geothermal Research*, 97(1-4), pp.287-307.
- Keith, M., Haase, K.M., Klemd, R., Krumm, S., Strauss, H., 2016a. Systematic variations of trace element and sulfur isotope compositions in pyrite with stratigraphic depth in the Skouriotissa volcanic-hosted massive sulfide deposit, Troodos ophiolite, Cyprus. *Chemical Geology*. <https://doi.org/10.1016/j.chemgeo.2015.12.012>
- Keith, M., Haase, K.M., Klemd, R., Smith, D.J., Schwarz-Schampera, U., Bach, W., 2018a. Constraints on the source of Cu in a submarine magmatic-hydrothermal system, Brothers volcano, Kermadec island arc. *Contrib. Mineral. Petrol.* 173, 40. <https://doi.org/10.1007/s00410-018-1470-5>
- Keith, M., Haase, K.M., Schwarz-Schampera, U., Klemd, R., Petersen, S., Bach, W., 2014. Effects of temperature, sulfur, and oxygen fugacity on the composition of sphalerite from submarine hydrothermal vents. *Geology* 42, 699–702. <https://doi.org/10.1130/G35655.1>
- Keith, M., Häckel, F., Haase, K.M., Schwarz-Schampera, U., Klemd, R., 2016b. Trace element systematics of pyrite from submarine hydrothermal vents. *Ore Geol. Rev.* 72, 728–745.
- Keith, M., Smith, D.J., Jenkin, G.R.T., Holwell, D.A., Dye, M.D., 2018b. A review of Te and Se systematics in hydrothermal pyrite from precious metal deposits: Insights into ore-forming processes. *Ore Geol. Rev.* <https://doi.org/10.1016/j.oregeorev.2017.07.023>
- Kelley, D.S., Baross, J.A., Delaney, J.R., 2002. Volcanoes, Fluids, and Life at Mid-Ocean Ridge Spreading Centers. *Annu. Rev. Earth Planet. Sci.* 30, 385–491. <https://doi.org/10.1146/annurev.earth.30.091201.141331>

- Kelley, D.S. and Fruh-Green, G.L., 2000. Volatiles in mid-ocean ridge environments. *Special Papers-Geological Society of America*, pp.237-260.
- Kelley, D.S., Gillis, K.M., Thompson, G., 1993. Fluid evolution in submarine magma-hydrothermal systems at the Mid-Atlantic Ridge. *J. Geophys. Res. Solid Earth* 98, 19579–19596.
- Kelley, D.S., Karson, J.A., Blackman, D.K., Früh-Green, G.L., Butterfield, D.A., Lilley, M.D., Olson, E.J., Schrenk, M.O., Roe, K.K., Lebon, G.T., Rivizzigno, P., AT3-60 Shipboard Party, 2001. An off-axis hydrothermal vent field near the Mid-Atlantic Ridge at 30 degrees N. *Nature* 412, 145–149. <https://doi.org/10.1038/35084000>
- Kelley, D.S., Robinson, P.T., 1990. Development of a brine-dominated hydrothermal system at temperatures of 400–500°C in the upper level plutonic sequence, Troodos ophiolite, Cyprus. *Geochim. Cosmochim. Acta* 54, 653–661.
- Kelley, D.S., Robinson, P.T., Malpas, J.G., 1992. Processes of brine generation and circulation in the oceanic crust: Fluid inclusion evidence from the Troodos Ophiolite, Cyprus. *J. Geophys. Res. Solid Earth* 97, 9307–9322.
- Kidd, R.G.W., Cann, J.R., 1974. Chilling statistics indicate an ocean-floor spreading origin for the Troodos complex, Cyprus. *Earth Planet. Sci. Lett.* 24, 151–155. [https://doi.org/10.1016/0012-821X\(74\)90020-X](https://doi.org/10.1016/0012-821X(74)90020-X)
- Kim, J., Lee, I., Lee, K.-Y., 2004. S, Sr, and Pb isotopic systematics of hydrothermal chimney precipitates from the Eastern Manus Basin, western Pacific: Evaluation of magmatic contribution to hydrothermal system. *J. Geophys. Res. Solid Earth* 109. <https://doi.org/10.1029/2003JB002912>
- Kinnaird, T.C., Robertson, A.H.F., Morris, A., 2011. Timing of uplift of the Troodos Massif (Cyprus) constrained by sedimentary and magnetic polarity evidence. *J. Geol. Soc.* 168, 457–470. <https://doi.org/10.1144/0016-76492009-150>
- Klein, F., Bach, W., 2009. Fe–Ni–Co–O–S Phase Relations in Peridotite–Seawater Interactions. *J. Petrol.* 50, 37–59.
- Klimchouk, A., 1996. The dissolution and conversion of gypsum and anhydrite. *Int. J. Speleol.* 25, 2.
- Knight, R., Roberts, S., P. Webber, A., 2018. The influence of spreading rate, basement composition, fluid chemistry and chimney morphology on the formation of gold-rich SMS deposits at slow and ultraslow mid-ocean ridges. *Miner. Deposita* 53, 143–152. <https://doi.org/10.1007/s00126-017-0762-4>
- Knott, R., Fallick, A.E., Rickard, D., Bäcker, H., 1995. Mineralogy and sulphur isotope characteristics of a massive sulphide boulder, Galapagos Rift, 85°55'W. *Geol. Soc. Lond. Spec. Publ.* 87, 207–222. <https://doi.org/10.1144/GSL.SP.1995.087.01.17>
- Koschinsky, A., Garbe-Schönberg, D., Sander, S., Schmidt, K., Gennerich, H.-H., Strauss, H., 2008. Hydrothermal venting at pressure-temperature conditions above the critical point of seawater, 5°S on the Mid-Atlantic Ridge. *Geology* 36, 615–618. <https://doi.org/10.1130/G24726A.1>

- Koski, R.A., Clague, D.A., Oudin, E., 1984. Mineralogy and chemistry of massive sulfide deposits from the Juan de Fuca Ridge. *GSA Bull.* 95, 930–945. [https://doi.org/10.1130/0016-7606\(1984\)95<930:MACOMS>2.0.CO;2](https://doi.org/10.1130/0016-7606(1984)95<930:MACOMS>2.0.CO;2)
- Kristall, B., Nielsen, D., Hannington, M.D., Kelley, D.S., Delaney, J.R., 2011. Chemical microenvironments within sulfide structures from the Mothra Hydrothermal Field: Evidence from high-resolution zoning of trace elements. *Chem. Geol.* 290, 12–30.
- Kuhn, T., Herzig, P.M., Hannington, M.D., Garbe-Schönberg, D., Stoffers, P., 2003. Origin of fluids and anhydrite precipitation in the sediment-hosted Grimsey hydrothermal field north of Iceland. *Chem. Geol.* 202, 5–21. [https://doi.org/10.1016/S0009-2541\(03\)00207-9](https://doi.org/10.1016/S0009-2541(03)00207-9)
- Lapierre, H., 1975, Les formations sédimentaires et éruptives des nappes de Mamonia et leurs relations avec le Massif du Troodos (Chypre occidentale): *Soc. Géol. France Mém.*, v. 123, 132 p.
- Lapierre, H., Bosch, D., Narros, A., Mascle, G.H., Tardy, M. and Demant, A., 2007. The Mamonia Complex (SW Cyprus) revisited: remnant of Late Triassic intra-oceanic volcanism along the Tethyan southwestern passive margin. *Geological Magazine*, 144(1), pp.1-19.
- Large, R.R., Danyushevsky, L., Hollit, C., Maslennikov, V., Meffre, S., Gilbert, S., Bull, S., Scott, R., Emsbo, P., Thomas, H., Singh, B., Foster, J., 2009. Gold and Trace Element Zonation in Pyrite Using a Laser Imaging Technique: Implications for the Timing of Gold in Orogenic and Carlin-Style Sediment-Hosted Deposits. *Econ. Geol.* 104, 635–668. <https://doi.org/10.2113/gsecongeo.104.5.635>
- Layton-Matthews, D., Leybourne, M.I., Peter, J.M., Scott, S.D., Cousens, B., Eglinton, B.M., 2013. Multiple sources of selenium in ancient seafloor hydrothermal systems: Compositional and Se, S, and Pb isotopic evidence from volcanic-hosted and volcanic-sediment-hosted massive sulfide deposits of the Finlayson Lake District, Yukon, Canada. *Geochimica et Cosmochimica Acta* 117, 313–331. <https://doi.org/10.1016/j.gca.2013.05.002>
- Layton-Matthews, D., Peter, J.M., Scott, S.D., Leybourne, M.I., 2008. Distribution, Mineralogy, and Geochemistry of Selenium in Felsic Volcanic-Hosted Massive Sulfide Deposits of the Finlayson Lake District, Yukon Territory, Canada. *Economic Geology* 103, 61–88. <https://doi.org/10.2113/gsecongeo.103.1.61>
- Little, C.T.S., Cann, J.R., Herrington, R.J., Morisseau, M., 1999. Late Cretaceous hydrothermal vent communities from the Troodos ophiolite, Cyprus. *Geology* 27, 1027–1030. [https://doi.org/10.1130/0091-7613\(1999\)027<1027:LCHVCF>2.3.CO;2](https://doi.org/10.1130/0091-7613(1999)027<1027:LCHVCF>2.3.CO;2)
- Long, D.T., Fegan, N.E., McKee, J.D., Lyons, W.B., Hines, M.E., Macumber, P.G., 1992. Formation of alunite, jarosite and hydrous iron oxides in a hypersaline system: Lake Tyrrell, Victoria, Australia. *Chem. Geol., The Geochemistry of Acid Groundwater Systems* 96, 183–202. [https://doi.org/10.1016/0009-2541\(92\)90128-R](https://doi.org/10.1016/0009-2541(92)90128-R)
- Lu, D., Chang, Y., Yang, H., Xie, F., 2015. Sequential removal of selenium and tellurium from copper anode slime with high nickel content. *Trans. Nonferrous Met. Soc. China* 25, 1307–1314. [https://doi.org/10.1016/S1003-6326\(15\)63729-3](https://doi.org/10.1016/S1003-6326(15)63729-3)
- Lu, L., Wang, R., Chen, F., Xue, J., Zhang, P., Lu, J., 2005. Element mobility during pyrite weathering: implications for acid and heavy metal pollution at mining-impacted sites. *Environ. Geol.* 49, 82–89. <https://doi.org/10.1007/s00254-005-0061-8>

- Lüders, V., Banks, D.A., Halbach, P., 2002. Extreme Cl/Br and  $\delta^{37}\text{Cl}$  isotope fractionation in fluids of modern submarine hydrothermal systems. *Miner. Deposita* 37, 765–771.
- Machel, H.G., 2001. Bacterial and thermochemical sulfate reduction in diagenetic settings—old and new insights. *Sedimentary Geology*, 140(1-2), pp.143-175.
- MacLeod, C.J., Allerton, S., Gass, I.G., Xenophontos, C., 1990. Structure of a fossil ridge–transform intersection in the Troodos ophiolite. *Nature* 348, 717–720.  
<https://doi.org/10.1038/348717a0>
- MacLeod, C.J., Murton, B.J., 1993. Structure and tectonic evolution of the Southern Troodos Transform Fault Zone, Cyprus. Geological Society, London, Special Publications 76, 141–176. <https://doi.org/10.1144/GSL.SP.1993.076.01.07>
- MacLeod, C.J., Murton, B.J., 1995. On the sense of slip of the Southern Troodos transform fault zone, Cyprus. *Geology* 23, 257–260. [https://doi.org/10.1130/0091-7613\(1995\)023<0257:OTSOSO>2.3.CO;2](https://doi.org/10.1130/0091-7613(1995)023<0257:OTSOSO>2.3.CO;2)
- MacLeod, C.J., Robertson, A.H.F., Allerton, S., Browning, P., Gass, I.G., Taylor, R.N., Vine, F.J., Xenophontos, C., 1992. Comment [on “Tectonic evolution of the Troodos ophiolite within the Tethyan framework” by Y. Dilek, P. Thy, E. M. Moores, and T. W. Ramsden]. *Tectonics* 11, 910–915. <https://doi.org/10.1029/92TC00458>
- Maffione, M., van Hinsbergen, D.J., de Gelder, G.I., van der Goes, F.C. and Morris, A., 2017. Kinematics of Late Cretaceous subduction initiation in the Neo-Tethys Ocean reconstructed from ophiolites of Turkey, Cyprus, and Syria. *Journal of Geophysical Research: Solid Earth*, 122(5), pp.3953-3976.
- Magaritz, Taylor, 1974. Oxygen and hydrogen isotope studies of serpentinization in the Troodos ophiolite complex, Cyprus. *Earth Planet. Sci. Lett.* 23, 8–14.  
[https://doi.org/10.1016/0012-821X\(74\)90023-5](https://doi.org/10.1016/0012-821X(74)90023-5)
- Malpas, J., 1990. Crustal accretionary processes in the Troodos ophiolite, Cyprus: evidence from field mapping and deep crustal drilling, in: *OPHIOLITES Oceanic Crustal Analogues, Proceedings of the Symposium “Troodos 1987.”* The Geological Survey Department, Ministry of Agriculture and Natural Resources, Nicosia, Cyprus, pp. 65–74.
- Malpas, J., Langdon, G., 1984. Petrology of the Upper Pillow Lava suite, Troodos ophiolite, Cyprus. *Geol. Soc. Lond. Spec. Publ.* 13, 155–167.
- Mandl, G., 1987. Tectonic deformation by rotating parallel faults: the “bookshelf” mechanism. *Tectonophysics* 141, 277–316. [https://doi.org/10.1016/0040-1951\(87\)90205-8](https://doi.org/10.1016/0040-1951(87)90205-8)
- Marques, A.F.A., Scott, S.D., Guillong, M., 2011. Magmatic degassing of ore-metals at the Menez Gwen: Input from the Azores plume into an active Mid-Atlantic Ridge seafloor hydrothermal system. *Earth Planet. Sci. Lett.* 310, 145–160.  
<https://doi.org/10.1016/j.epsl.2011.07.021>
- Martin, A.J., Keith, M., McDonald, I., Haase, K.M., McFall, K.A., Klemd, R., MacLeod, C.J., 2019. Trace element systematics and ore-forming processes in mafic VMS deposits: Evidence from the Troodos ophiolite, Cyprus. *Ore Geol. Rev.* 106, 205–225.  
<https://doi.org/10.1016/j.oregeorev.2019.01.024>
- Martin, A.J., McDonald, I., MacLeod, C.J., Prichard, H.M., McFall, K., 2018. Extreme enrichment of selenium in the Apliki Cyprus-type VMS deposit, Troodos, Cyprus. *Mineral. Mag.*

- Extreme enrichment of selenium in the Apliki Cyprus-type VMS deposit, Troodos, Cyprus. *Mineralogical Magazine* 10.1180/mgm.2018.81
- Maslennikov, V.V., Maslennikova, S.P., Large, R.R., Danyushevsky, L.V., 2009. Study of Trace Element Zonation in Vent Chimneys from the Silurian Yaman-Kasy Volcanic-Hosted Massive Sulfide Deposit (Southern Urals, Russia) Using Laser Ablation-Inductively Coupled Plasma Mass Spectrometry (LA-ICPMS). *Economic Geology* 104, 1111–1141. <https://doi.org/10.2113/gsecongeo.104.8.1111>
- Maslennikov, V.V., Maslennikova, S.P., Large, R.R., Danyushevsky, L.V., Herrington, R.J., Stanley, C.J., 2012. Tellurium-bearing minerals in zoned sulfide chimneys from Cu-Zn massive sulfide deposits of the Urals, Russia. *Mineral. Petrol.* 107, 67–99. <https://doi.org/10.1007/s00710-012-0230-x>
- Maslennikov, V.V., Maslennikova, S.P., Large, R.R., Danyushevsky, L.V., Herrington, R.J., Ayupova, N.R., Zaykov, V.V., Lein, A.Y., Tseluyko, A.S., Melekestseva, I.Y., Tessalina, S.G., 2017. Chimneys in Paleozoic massive sulfide mounds of the Urals VMS deposits: Mineral and trace element comparison with modern black, grey, white and clear smokers. *Ore Geology Reviews, Overview of mineral deposits in the Urals* 85, 64–106. <https://doi.org/10.1016/j.oregeorev.2016.09.012>
- McDermott, J.M., Ono, S., Tivey, M.K., Seewald, J.S., Shanks, W.C., Solow, A.R., 2015. Identification of sulfur sources and isotopic equilibria in submarine hot-springs using multiple sulfur isotopes. *Geochim. Cosmochim. Acta* 160, 169–187. <https://doi.org/10.1016/j.gca.2015.02.016>
- McElduff, B., Stumpf, E.F., 1991. The chromite deposits of the Troodos complex, cyprus — Evidence for the role of a fluid phase accompanying chromite formation. *Miner. Deposita* 26, 307–318. <https://doi.org/10.1007/BF00191079>
- McPhail, D.C., 1995. Thermodynamic properties of aqueous tellurium species between 25 and 350°. *Geochim. Cosmochim. Acta* 59, 851–866. [https://doi.org/10.1016/0016-7037\(94\)00353-X](https://doi.org/10.1016/0016-7037(94)00353-X)
- Melekestseva, I.Y., Maslennikov, V.V., Tret'yakov, G.A., Nimis, P., Beltenev, V.E., Rozhdestvenskaya, I.I., Maslennikova, S.P., Belogub, E.V., Danyushevsky, L., Large, R., Yuminov, A.M., Sadykov, S.A., 2017. Gold- and Silver-Rich Massive Sulfides from the Semenov-2 Hydrothermal Field, 13°31.13'N, Mid-Atlantic Ridge: A Case of Magmatic Contribution?
- Mercier-Langevin, P., Hannington, M.D., Dubé, B., Bécu, V., 2011. The gold content of volcanogenic massive sulfide deposits. *Miner Deposita* 46, 509–539. <https://doi.org/10.1007/s00126-010-0300-0>
- Metz, S., Trefry, J.H., 2000. Chemical and mineralogical influences on concentrations of trace metals in hydrothermal fluids. *Geochim. Cosmochim. Acta* 64, 2267–2279. [https://doi.org/10.1016/S0016-7037\(00\)00354-9](https://doi.org/10.1016/S0016-7037(00)00354-9)
- Mills, R.A., Teagle, D. a. H., Tivey, M.K., 1998. Fluid mixing and anhydrite precipitation within the TAG mound. *Oceanogr. Lit. Rev.* 8, 1350.
- Miyashiro, A., 1973. The Troodos ophiolitic complex was probably formed in an island arc. *Earth Planet. Sci. Lett.* 19, 218–224. [https://doi.org/10.1016/0012-821X\(73\)90118-0](https://doi.org/10.1016/0012-821X(73)90118-0)

- Monecke, T., Petersen, S., Hannington, M.D., 2014. Constraints on Water Depth of Massive Sulfide Formation: Evidence from Modern Seafloor Hydrothermal Systems in Arc-Related Settings. *Economic Geology* 109, 2079–2101. <https://doi.org/10.2113/econgeo.109.8.2079>
- Moores, E. M., 1975, Discussion of Origin of Troodos and other ophiolites: A reply to Hynes,<sup>1</sup> by Akiho Miyashiro: *Earth and Planetary Science Letters*, v. 25, p. 223-226.
- Moores, E.M., Kellogg, L.H. and Dilek, Y., 2000. Tethyan ophiolites, mantle convection, and tectonic" historical contingency": A resolution of the" ophiolite conundrum". *SPECIAL PAPERS-GEOLOGICAL SOCIETY OF AMERICA*, pp.3-12.
- Moores, E.M., Robinson, P.T., Malpas, J., Xenophonotos, C., 1984. Model for the origin of the Troodos massif, Cyprus, and other mideast ophiolites. *Geology* 12, 500–503. [https://doi.org/10.1130/0091-7613\(1984\)12<500:MFTOOT>2.0.CO;2](https://doi.org/10.1130/0091-7613(1984)12<500:MFTOOT>2.0.CO;2)
- Moores, E.M., Varga, R.J., Verosub, K.L., Ramsden, T.W., 1990. Regional structure of the Troodos dyke complex. In: Malpas, J., Moores, E.M., Panayiotou, A., Xenophonotos, C. (Eds.), *Troodos 1987: Ophiolites, Oceanic Crustal Analogues*. Geol. Surv. Dept. Cyprus, Nicosia, pp. 27–35.
- Moores, E.M., Vine, F., 1971. The Troodos Massif, Cyprus and other ophiolites as oceanic crust: evaluation and implication. *Phil. Trans. Roy. Soc. of Lon.* 268, 443–466.
- Morag, N., Haviv, I., Katzir, Y., 2016. From ocean depths to mountain tops: Uplift of the Troodos ophiolite (Cyprus) constrained by low-temperature thermochronology and geomorphic analysis. *Tectonics* 35, 2015TC004069. <https://doi.org/10.1002/2015TC004069>
- Morris, A., Creer, K.M. and Robertson, A.H.F., 1990. Palaeomagnetic evidence for clockwiserotations related to dextral shear along the southern Troodos transform fault, Cyprus. *Earth and Planetary Science Letters*, 99(3), pp.250-262.
- Morris, A., Maffione, M., 2016. Is the Troodos ophiolite (Cyprus) a complete, transform fault–bounded Neotethyan ridge segment?
- Morton, J.L., Zierenberg, R.A., Reiss, C.A., 1994. *Geologic, Hydrothermal, and Biologic Studies at Escanaba Trough, Gorda Ridge, Offshore Northern California*. U.S. Department of the Interior, U.S. Geological Survey.
- Moss, R.L., Tzimas, E., Kara, H., Willis, P., Kooroshy, J., 2013. The potential risks from metals bottlenecks to the deployment of Strategic Energy Technologies. *Energy Policy* 55, 556–564. <https://doi.org/10.1016/j.enpol.2012.12.053>
- Moss, R., Scott, S.D., 2001. Geochemistry and Mineralogy of Gold-Rich Hydrothermal Precipitates from the Eastern Manus Basin, Papua New Guinea. *Can. Mineral.* 39, 957–978. <https://doi.org/10.2113/gscanmin.39.4.957>
- Mottl, M.J., Holland, H.D., 1978. Chemical exchange during hydrothermal alteration of basalt by seawater—I. Experimental results for major and minor components of seawater. *Geochimica et Cosmochimica Acta* 42, 1103–1115. [https://doi.org/10.1016/0016-7037\(78\)90107-2](https://doi.org/10.1016/0016-7037(78)90107-2)

- Muenow, D.W., Garciat, M.O., Aggrey, K.E., Bednarz, U., Schmincke, H.U., 1990. Volatiles in submarine glasses as a discriminant of tectonic origin: application to the Troodos ophiolite. *Nature* 343, 159–161. <https://doi.org/10.1038/343159a0>
- Mukasa, S.B., Ludden, J.N., 1987. Uranium-lead isotopic ages of plagiogranites from the Troodos ophiolite, Cyprus, and their tectonic significance. *Geology* 15, 825–828. [https://doi.org/10.1130/0091-7613\(1987\)15<825:U1AOPF>2.0.CO;2](https://doi.org/10.1130/0091-7613(1987)15<825:U1AOPF>2.0.CO;2)
- Mumpton, F.A., 2018. *Mineralogy and Geology of Natural Zeolites*. Walter de Gruyter GmbH & Co KG.
- Murton, B.J. and Cass, I.G., 1986. Western Limassol Forest complex, Cyprus: part of an Upper Cretaceous leaky transform fault. *Geology*, 14(3), pp.255-258.
- Murton, B.J., 1986, Anomalous oceanic lithosphere formed at a leaky transform fault: Evidence from the Western Limassol Forest Complex, Cyprus: *Geological Society of London Journal*, v. 143, p. 845-854.
- Murton, B.J., 1990. Was the Southern Troodos Transform Fault a victim of microplate rotation. *Ophiolites. Oceanic Crustal Analogues*, pp.87-98. Pearce, J.A., Lippard, S.J., Roberts, S., 1984. Characteristics and tectonic significance of supra-subduction zone ophiolites. *Geol. Soc. Lond. Spec. Publ.* 16, 77–94. <https://doi.org/10.1144/GSL.SP.1984.016.01.06>
- Naden, J., Herrington, R.J., Jowitt, S.M., McEvoy, F.M., Williamson, J.P. and Monhemius, A.J., 2006. New methodologies for volcanic-hosted copper sulphide mineralization on Cyprus: a GIS–prospectivity analysis-based approach.
- Naden, J., Kiliyas, S.P., Darbyshire, D.P.F., 2005. Active geothermal systems with entrained seawater as modern analogs for transitional volcanic-hosted massive sulfide and continental magmato-hydrothermal mineralization: The example of Milos Island, Greece. *Geology* 33, 541–544. <https://doi.org/10.1130/G21307.1>
- Nesbitt, H.W., Muir, I.J., Prarr, A.R., 1995. Oxidation of arsenopyrite by air and air-saturated, distilled water, and implications for mechanism of oxidation. *Geochimica et Cosmochimica Acta* 59, 1773–1786. [https://doi.org/10.1016/0016-7037\(95\)00081-A](https://doi.org/10.1016/0016-7037(95)00081-A)
- Nozaki, T., Ishibashi, J.-I., Shimada, K., Nagase, T., Takaya, Y., Kato, Y., Kawagucci, S., Watsuji, T., Shibuya, T., Yamada, R., Saruhashi, T., Kyo, M., Takai, K., 2016. Rapid growth of mineral deposits at artificial seafloor hydrothermal vents. *Sci. Rep.* 6, 22163. <https://doi.org/10.1038/srep22163>
- Nuriel, P., Katzir, Y., Abelson, M., Valley, J.W., Matthews, A., Spicuzza, M.J., Ayalon, A., 2009. Fault-related oceanic serpentinization in the Troodos ophiolite, Cyprus: Implications for a fossil oceanic core complex. *Earth and Planetary Science Letters* 282, 34–46. <https://doi.org/10.1016/j.epsl.2009.02.029>
- Ogawa, Y., Shikazono, N., Ishiyama, D., Sato, H., Mizuta, T., Nakano, T., 2007. Mechanisms for anhydrite and gypsum formation in the Kuroko massive sulfide-sulfate deposits, north Japan. *Miner. Deposita* 42, 219–233. <https://doi.org/10.1007/s00126-006-0101-7>
- Ohmoto, H., Lasaga, A.C., 1982. Kinetics of reactions between aqueous sulfates and sulfides in hydrothermal systems. *Geochim. Cosmochim. Acta* 46, 1727–1745. [https://doi.org/10.1016/0016-7037\(82\)90113-2](https://doi.org/10.1016/0016-7037(82)90113-2)

- Ohmoto, H., Mizukami, M., Drummond, S.E., Eldridge, C.S., Pisutha-Arnond, V. and Lenagh, T.C., 1983. Chemical processes of Kuroko formation: ECONOMIC GEOLOGY MONOGRAPH 5.
- Ono, S., Shanks, W.C., Rouxel, O.J., Rumble, D., 2007. S-33 constraints on the seawater sulfate contribution in modern seafloor hydrothermal vent sulfides. *Geochim. Cosmochim. Acta* 71, 1170–1182. <https://doi.org/10.1016/j.gca.2006.11.017>
- Oudin, E., Constantinou, G., 1984. Black smoker chimney fragments in Cyprus sulphide deposits. *Nature* 308, 349–353. <https://doi.org/10.1038/308349a0>
- Papoulis, D., Tsohis-katagas, P., Katagas, C., 2004. Progressive stages in the formation of kaolin minerals of different morphologies in the weathering of plagioclase. *Clays Clay Miner.* 275–286.
- Parvaz, D.B., 2014. Oxidation Zones of Volcanogenic Massive Sulphide Deposits in the Troodos Ophiolite, Cyprus: Targeting Secondary Copper Deposits.
- Patten, C.G.C., Pitcairn, I.K., Teagle, D.A.H., 2017. Hydrothermal mobilisation of Au and other metals in supra-subduction oceanic crust: Insights from the Troodos ophiolite. *Ore Geology Reviews* 86, 487–508. <https://doi.org/10.1016/j.oregeorev.2017.02.019>
- Patten, C.G.C., Pitcairn, I.K., Teagle, D.A.H., Harris, M., 2016. Mobility of Au and related elements during the hydrothermal alteration of the oceanic crust: implications for the sources of metals in VMS deposits. *Miner Deposita* 51, 179–200. <https://doi.org/10.1007/s00126-015-0598-8>
- Pearce, J.A., Lippard, S.J., & Roberts, S. (1984). Characteristics and tectonic significance of supra-subduction zone ophiolites. P.p. 77-96. In: *Ophiolites and Oceanic Lithosphere* (Gass, I.G.; Lippard, S.J. & Shelton, A.W. eds.). Geological Society of London, No. 13
- Pearce, J.A., Robinson, P.T., 2010. The Troodos ophiolitic complex probably formed in a subduction initiation, slab edge setting. *Gondwana Research, A Tribute to Miyashiro* 18, 60–81. <https://doi.org/10.1016/j.gr.2009.12.003>
- Pedersen, L.-E.R., Staudigel, H., McLoughlin, N., Whitehouse, M.J., Strauss, H., 2017. A multiple sulfur isotope study through the volcanic section of the Troodos ophiolite. *Chem. Geol.* 468, 49–62. <https://doi.org/10.1016/j.chemgeo.2017.08.008>
- Peltonen, P., Kontinen, A., Huhma, H., Kuronen, U., 2008. Outokumpu revisited: New mineral deposit model for the mantle peridotite-associated Cu–Co–Zn–Ni–Ag–Au sulphide deposits. *Ore Geol. Rev.* 33, 559–617. <https://doi.org/10.1016/j.oregeorev.2007.07.002>
- Perkins, W.T., 2011. Extreme selenium and tellurium contamination in soils — An eighty year-old industrial legacy surrounding a Ni refinery in the Swansea Valley. *Sci. Total Environ.* 412–413, 162–169. <https://doi.org/10.1016/j.scitotenv.2011.09.056>
- Peters, M., Strauss, H., Farquhar, J., Ockert, C., Eickmann, B., Jost, C.L., 2010. Sulfur cycling at the Mid-Atlantic Ridge: A multiple sulfur isotope approach. *Chem. Geol.* 269, 180–196. <https://doi.org/10.1016/j.chemgeo.2009.09.016>
- Petersen, S., Herzig, P.M., Hannington, M.D., 2000. Third dimension of a presently forming VMS deposit: TAG hydrothermal mound, Mid-Atlantic Ridge, 26°N. *Miner. Deposita* 35, 233–259. <https://doi.org/10.1007/s001260050018>

- Pokrovski, G.S., Akinfiev, N.N., Borisova, A.Y., Zotov, A.V., Kouzmanov, K., 2014. Gold speciation and transport in geological fluids: insights from experiments and physical-chemical modeling. *Geol. Soc. Lond. Spec. Publ.* 402, 1–1. <https://doi.org/10.1144/SP402.4.Err>
- Prichard, H.M. and Maliotis, G., 1998. Gold mineralization associated with low-temperature, off-axis, fluid activity in the Troodos ophiolite, Cyprus. *Journal of the Geological Society*, 155(2), pp.223–231.
- Prichard, H.M., Knight, R.D., Fisher, P.C., McDonald, I., Zhou, M.-F., Wang, C.Y., 2013. Distribution of platinum-group elements in magmatic and altered ores in the Jinchuan intrusion, China: an example of selenium remobilization by postmagmatic fluids. *Miner Deposita* 48, 767–786. <https://doi.org/10.1007/s00126-013-0454-7>
- Pütke, C., Gerya, T., 2014. Dependence of mid-ocean ridge morphology on spreading rate in numerical 3-D models. *Gondwana Res.* 25, 270–283. <https://doi.org/10.1016/j.gr.2013.04.005>
- Qian, G., Brugger, J., Testemale, D., Skinner, W., Pring, A., 2013. Formation of As(II)-pyrite during experimental replacement of magnetite under hydrothermal conditions. *Geochimica et Cosmochimica Acta* 100, 1–10. <https://doi.org/10.1016/j.gca.2012.09.034>
- Rahm, M., Hoffmann, R., Ashcroft, N.W., 2016. Atomic and Ionic Radii of Elements 1–96. *Chem. – Eur. J.* 22, 14625–14632. <https://doi.org/10.1002/chem.201602949>
- Rautenschlein, M., Jenner, G.A., Hertogen, J., Hofmann, A.W., Kerrich, R., Schmincke, H.-U., White, W.M., 1985. Isotopic and trace element composition of volcanic glasses from the Akaki Canyon, Cyprus: implications for the origin of the Troodos ophiolite. *Earth Planet. Sci. Lett.* 75, 369–383. [https://doi.org/10.1016/0012-821X\(85\)90180-3](https://doi.org/10.1016/0012-821X(85)90180-3)
- Redlinger, M., Eggert, R., Woodhouse, M., 2015. Evaluating the availability of gallium, indium, and tellurium from recycled photovoltaic modules. *Sol. Energy Mater. Sol. Cells* 138, 58–71. <https://doi.org/10.1016/j.solmat.2015.02.027>
- Reed, M.H., Palandri, J., 2006. Sulfide Mineral Precipitation from Hydrothermal Fluids. *Reviews in Mineralogy and Geochemistry* 61, 609–631. <https://doi.org/10.2138/rmg.2006.61.11>
- Reeves, E., S. Seewald, J., Saccocia, P., Bach, W., Craddock, P., Shanks, W., Sylva, S., Walsh, E., Pichler, T., Rosner, M., 2013. Geochemistry of hydrothermal fluids from the PACMANUS, Northeast Pual and Vienna Woods hydrothermal fields, Manus Basin, Papua New Guinea. *Geochim. Cosmochim. Acta* 1088–1123. <https://doi.org/10.1016/j.gca.2010.11.008>
- Regelous, M., Haase, K.M., Freund, S., Keith, M., Weinzierl, C.G., Beier, C., Brandl, P.A., Endres, T., Schmidt, H., 2014. Formation of the Troodos Ophiolite at a triple junction: Evidence from trace elements in volcanic glass. *Chemical Geology* 386, 66–79. <https://doi.org/10.1016/j.chemgeo.2014.08.006>
- Reich, M., Chryssoulis, S.L., Deditius, A., Palacios, C., Zúñiga, A., Weldt, M., Alvear, M., 2010. “Invisible” silver and gold in supergene digenite (Cu<sub>1.8</sub>S). *Geochim. Cosmochim. Acta* 74, 6157–6173
- Reich, M., Deditius, A., Chryssoulis, S., Li, J.-W., Ma, C.-Q., Parada, M.A., Barra, F., Mittermayr, F., 2013. Pyrite as a record of hydrothermal fluid evolution in a porphyry copper system: A SIMS/EMPA trace element study. *Geochim. Cosmochim. Acta* 104, 42–62.

- Reich, M., Kesler, S.E., Utsunomiya, S., Palenik, C.S., Chryssoulis, S.L., Ewing, R.C., 2005. Solubility of gold in arsenian pyrite. *Geochim. Cosmochim. Acta* 69, 2781–2796.
- Revan, M.K., Genç, Y., Maslennikov, V.V., Maslennikova, S.P., Large, R.R., Danyushevsky, L.V., 2014. Mineralogy and trace-element geochemistry of sulfide minerals in hydrothermal chimneys from the Upper-Cretaceous VMS deposits of the eastern Pontide orogenic belt (NE Turkey). *Ore Geol. Rev.* 63, 129–149.  
<https://doi.org/10.1016/j.oregeorev.2014.05.006>
- Reyes, A.G., Massoth, G., De Ronde, C. and Wright, I.C., 2006. Hydrothermal mineralization in arc-type submarine volcanoes. *Geochimica et Cosmochimica Acta*, 70(18), p.A528.
- Richardson, C.J., Cann, J.R., Richards, H.G., Cowan, J.G., 1987. Metal-depleted root zones of the Troodos ore-forming hydrothermal systems, Cyprus. *Earth Planet. Sci. Lett.* 84, 243–253.
- Robb, J.L., 2005. Hydrothermal ore forming processes. Introduction to ore forming processes. Johannesburg, Black well Publishing Company, pp.129-214.
- Roberts, S., Bach, W., Binns, R.A., Vanko, D.A., Yeats, C.J., Teagle, D. a. H., Blacklock, K., Blusztajn, J.S., Boyce, A.J., Cooper, M.J., Holland, N., McDonald, B., 2003. Contrasting evolution of hydrothermal fluids in the PACMANUS system, Manus Basin: The Sr and S isotope evidence. *Geology* 31, 805–808. <https://doi.org/10.1130/G19716.1>
- Robertson, A., Xenophontos, C., 1993. Development of concepts concerning the Troodos ophiolite and adjacent units in Cyprus. *Geol. Soc. Lond. Spec. Publ.* 76, 85–119.  
<https://doi.org/10.1144/GSL.SP.1993.076.01.05>
- Robertson, A.H., Woodcock, N., 1980. Tectonic setting of the Troodos massif in the east Mediterranean, in: *Ophiolites, Proceedings: International Ophiolite Symposium, Cyprus 1979*. The Geological Survey Department, Ministry of Agriculture and Natural Resources, Nicosia, Cyprus, pp. 36–49.
- Robertson, A.H.F. and Woodcock, N.H., 1986. The role of the Kyrenia Range lineament, Cyprus, in the geological evolution of the Eastern Mediterranean area. *Philosophical Transactions of the Royal Society of London. Series A, Mathematical and Physical Sciences*, 317(1539), pp.141-177.
- Robertson, A.H.F., Hudson, J.D., 1973. Cyprus umbers: Chemical precipitates on a Tethyan ocean ridge. *Earth Planet. Sci. Lett.* 18, 93–101. [https://doi.org/10.1016/0012-821X\(73\)90039-3](https://doi.org/10.1016/0012-821X(73)90039-3)
- Robertson, A.H.F., 1975. Cyprus umbers: basalt-sediment relationships on a Mesozoic ocean ridge. *J. Geol. Soc.* 131, 511–531. <https://doi.org/10.1144/gsjgs.131.5.0511>
- Robertson, A.H.F., 1977. Tertiary uplift history of the Troodos massif, Cyprus. *GSA Bull.* 88, 1763–1772. [https://doi.org/10.1130/0016-7606\(1977\)88<1763:TUHOTT>2.0.CO;2](https://doi.org/10.1130/0016-7606(1977)88<1763:TUHOTT>2.0.CO;2)
- Robertson, A.H.F., 1990, October. Tectonic evolution of Cyprus. In *Ophiolites: Oceanic Crustal Analogues. Proc. Symp.* “Troodos (pp. 235-250).
- Robertson, A.H.F., 2002. Overview of the genesis and emplacement of Mesozoic ophiolites in the Eastern Mediterranean Tethyan region. *Lithos, Eastern Mediterranean Ophiolites: Magmatic Processes and Geodynamic Implications*, held at the 10th Meeting of the European Union of Geosciences, Strasbourg, France, 28 March-1 April, 1999 65, 1–67.  
[https://doi.org/10.1016/S0024-4937\(02\)00160-3](https://doi.org/10.1016/S0024-4937(02)00160-3)

- Robertson, A.H.F., 2006. Contrasting modes of ophiolite emplacement in the Eastern Mediterranean region. *Geological Society, London, Memoirs*, 32(1), pp.235-261.
- Robertson, A.H.F., Mountrakis, D., 2006. Tectonic development of the Eastern Mediterranean region: an introduction. *Geol. Soc. Lond. Spec. Publ.* 260, 1–9.  
<https://doi.org/10.1144/GSL.SP.2006.260.01.01>
- Robertson, A.H.F., Parlak, O., Ustaömer, T., 2012. Overview of the Palaeozoic–Neogene evolution of Neotethys in the Eastern Mediterranean region (southern Turkey, Cyprus, Syria). *Pet. Geosci.* 18, 381–404. <https://doi.org/10.1144/petgeo2011-091>
- Robinson, B.W., Kusakabe, M., 1975. Quantitative preparation of sulfur dioxide, for sulfur-34/sulfur-32 analyses, from sulfides by combustion with cuprous oxide. *Anal. Chem.* 47, 1179–1181. <https://doi.org/10.1021/ac60357a026>
- Robinson, P., Malpas, J., 1990. The Troodos ophiolite of Cyprus: New perspectives on its origin and emplacement, in: *OPHIOLITES Oceanic Crustal Analogues, Proceedings of the Symposium "Troodos 1987."* The Geological Survey Department, Ministry of Agriculture and Natural Resources, Nicosia, Cyprus.
- Robinson, P.T., Melson, W.G., O'Hearn, T. and Schmincke, H.U., 1983. Volcanic glass compositions of the Troodos ophiolite, Cyprus. *Geology*, 11(7), pp.400-404.
- Rona, P.A., Klinkhammer, G., Nelsen, T.A., Trefry, J.H. and Elderfield, H., 1986. Black smokers, massive sulphides and vent biota at the Mid-Atlantic Ridge. *Nature*, 321(6065), p.33.
- Rona, P.A., 2005. TAG hydrothermal field: a key to modern and ancient seafloor hydrothermal VMS ore-forming systems. In *Mineral Deposit Research: Meeting the Global Challenge*(pp. 687-690). Springer, Berlin, Heidelberg.
- Rouxel, O., Fouquet, Y., Ludden, J.N., 2004. Subsurface processes at the lucky strike hydrothermal field, Mid-Atlantic ridge: evidence from sulfur, selenium, and iron isotopes  
11Associate editor: S. Sheppard. *Geochim. Cosmochim. Acta* 68, 2295–2311.  
<https://doi.org/10.1016/j.gca.2003.11.029>
- Rouxel, O., Ono, S., Alt, J., Rumble, D. and Ludden, J., 2008. Sulfur isotope evidence for microbial sulfate reduction in altered oceanic basalts at ODP Site 801. *Earth and Planetary Science Letters*, 268(1-2), pp.110-123.
- Rovira, M., Giménez, J., Martínez, M., Martínez-Lladó, X., de Pablo, J., Martí, V., Duro, L., 2008. Sorption of selenium(IV) and selenium(VI) onto natural iron oxides: Goethite and hematite. *J. Hazard. Mater.* 150, 279–284. <https://doi.org/10.1016/j.jhazmat.2007.04.098>
- Ruaya, J.R., 1988. Estimation of instability constants of metal chloride complexes in hydrothermal solutions up to 300°C. *Geochim. Cosmochim. Acta* 52, 1983–1996.  
[https://doi.org/10.1016/0016-7037\(88\)90179-2](https://doi.org/10.1016/0016-7037(88)90179-2)
- Saal, A.E., Hauri, E.H., Langmuir, C.H., Perfit, M.R., 2002. Vapour undersaturation in primitive mid-ocean-ridge basalt and the volatile content of Earth's upper mantle. *Nature* 419, 451.  
<https://doi.org/10.1038/nature01073>
- Safina, N.P., Melekestseva, I.Y., Nimis, P., Ankusheva, N.N., Yuminov, A.M., Kotlyarov, V.A., Sadykov, S.A., 2016. Barite from the Saŷyanovka VMS deposit (Central Urals) and Semenov-1 and Semenov-3 hydrothermal sulfide fields (Mid-Atlantic Ridge): a

- comparative analysis of formation conditions. *Miner Deposita* 51, 491–507. <https://doi.org/10.1007/s00126-015-0617-9>
- Saunders, J.A., Schoenly, P.A., 1995. Boiling, colloid nucleation and aggregation, and the genesis of bonanza Au-Ag ores of the sleeper deposit, Nevada. *Miner. Deposita* 30, 199–210. <https://doi.org/10.1007/BF00196356>
- Schiffman, P., Smith, B.M., Varga, R.J., Moores, E.M., 1987. Geometry, conditions and timing of off-axis hydrothermal metamorphism and ore-deposition in the Solea graben. *Nature* 325, 423. <https://doi.org/10.1038/325423a0>
- Schiffman, P., Bettison, L.A., Smith, B., 1990. Epidiosites of the Solea graben, in: *OPHIOLITES Oceanic Crustal Analogues, Proceedings of the Symposium "Troodos 1987."* The Geological Survey Department, Ministry of Agriculture and Natural Resources, Nicosia, Cyprus, pp. 673–683.
- Schirmer, T., Koschinsky, A., Bau, M., 2014. The ratio of tellurium and selenium in geological material as a possible paleo-redox proxy. *Chem. Geol.* 376, 44–51. <https://doi.org/10.1016/j.chemgeo.2014.03.005>
- Schmidt, K., Garbe-Schönberg, D., Hannington, M.D., Anderson, M.O., Bühring, B., Haase, K., Haruel, C., Lupton, J., Koschinsky, A., 2017. Boiling vapour-type fluids from the Nifonea vent field (New Hebrides Back-Arc, Vanuatu, SW Pacific): Geochemistry of an early-stage, post-eruptive hydrothermal system. *Geochim. Cosmochim. Acta* 207, 185–209. <https://doi.org/10.1016/j.gca.2017.03.016>
- Schmidt, K., Koschinsky, A., Garbe-Schönberg, D., de Carvalho, L.M., Seifert, R., 2007. Geochemistry of hydrothermal fluids from the ultramafic-hosted Logatchev hydrothermal field, 15°N on the Mid-Atlantic Ridge: Temporal and spatial investigation. *Chemical Geology* 242, 1–21. <https://doi.org/10.1016/j.chemgeo.2007.01.023>
- Schmincke, H.-U., Rautenschlein, M., Robinson, P.T., Mehegan, J.M., 1983. Troodos extrusive series of Cyprus: A comparison with oceanic crust. *Geology* 11, 405–409. [https://doi.org/10.1130/0091-7613\(1983\)11<405:TESOCA>2.0.CO;2](https://doi.org/10.1130/0091-7613(1983)11<405:TESOCA>2.0.CO;2)
- Schouten, H., Kelemen, P.B., 2002. Melt viscosity, temperature and transport processes, Troodos ophiolite, Cyprus. *Earth Planet. Sci. Lett.* 201, 337–352.
- Scott, R.B., Rona, P.A., McGregor, B.A., Scott, M.R., 1974. The TAG hydrothermal field. *Nature* 251, 301. <https://doi.org/10.1038/251301a0>
- Seal, R.R., 2006. Sulfur isotope geochemistry of sulfide minerals. *Reviews in mineralogy and geochemistry*, 61(1), pp.633-677.
- Seewald, J.S., Seyfried Jr., W.E., 1990. The effect of temperature on metal mobility in subseafloor hydrothermal systems: constraints from basalt alteration experiments. *Earth and Planetary Science Letters* 101, 388–403. [https://doi.org/10.1016/0012-821X\(90\)90168-W](https://doi.org/10.1016/0012-821X(90)90168-W)
- Seyfried Jr., W.E., Ding, K., 1993. The effect of redox on the relative solubilities of copper and iron in Cl-bearing aqueous fluids at elevated temperatures and pressures: An experimental study with application to subseafloor hydrothermal systems. *Geochim. Cosmochim. Acta* 57, 1905–1917. [https://doi.org/10.1016/0016-7037\(93\)90083-9](https://doi.org/10.1016/0016-7037(93)90083-9)

- Seyfried Jr., W.E., Janecky, D.R., 1985. Heavy metal and sulfur transport during subcritical and supercritical hydrothermal alteration of basalt: Influence of fluid pressure and basalt composition and crystallinity. *Geochim. Cosmochim. Acta* 49, 2545–2560. [https://doi.org/10.1016/0016-7037\(85\)90123-1](https://doi.org/10.1016/0016-7037(85)90123-1)
- Seyfried Jr., W.E., Mottl, M.J., 1982. Hydrothermal alteration of basalt by seawater under seawater-dominated conditions. *Geochim. Cosmochim. Acta* 46, 985–1002. [https://doi.org/10.1016/0016-7037\(82\)90054-0](https://doi.org/10.1016/0016-7037(82)90054-0)
- Seyfried, W., Bischoff, J.L., 1977. Hydrothermal transport of heavy metals by seawater: The role of seawater/basalt ratio. *Earth Planet. Sci. Lett.* 34, 71–77. [https://doi.org/10.1016/0012-821X\(77\)90107-8](https://doi.org/10.1016/0012-821X(77)90107-8)
- Shanks III, W.C., 2001. Stable isotopes in seafloor hydrothermal systems: vent fluids, hydrothermal deposits, hydrothermal alteration, and microbial processes. *Reviews in Mineralogy and Geochemistry*, 43(1), pp.469-525.
- Shanks, W.C., Seyfried, W.E., 1987. Stable isotope studies of vent fluids and chimney minerals, southern Juan de Fuca Ridge: Sodium metasomatism and seawater sulfate reduction. *J. Geophys. Res. Solid Earth* 92, 11387–11399. <https://doi.org/10.1029/JB092iB11p11387>
- Sievert, T., Wolter, A., Singh, N.B., 2005. Hydration of anhydrite of gypsum (CaSO<sub>4</sub>.II) in a ball mill. *Cem. Concr. Res.* 35, 623–630. <https://doi.org/10.1016/j.cemconres.2004.02.010>
- Sillitoe, R.H., Hannington, M.D., Thompson, J.F.H., 1996. High sulfidation deposits in the volcanogenic massive sulfide environment. *Econ. Geol.* 91, 204–212. <https://doi.org/10.2113/gsecongeo.91.1.204>
- Simon, G., Huang, H., Penner-Hahn, J.E., Kesler, S.E., Kao, L.-S., 1999. Oxidation state of gold and arsenic in gold-bearing arsenian pyrite. *American Mineralogist* 84, 1071–1079. <https://doi.org/10.2138/am-1999-7-809>
- Simonian, K.O., and Gass, I.G., 1978, Arakapas fault belt, Cyprus: A fossil transform fault: *Geological Society of America Bulletin*, v. 89, p. 1220-1230.
- Skirrow, R., Coleman, M.L., 1982. Origin of sulphur and geothermometry of hydrothermal sulphides from the Galapagos Rift, 86 °W. *Nature* 299, 142–144. <https://doi.org/10.1038/299142a0>
- Smith, D.K., Cann, J.R., Escartín, J., 2006. Widespread active detachment faulting and core complex formation near 13° N on the Mid-Atlantic Ridge. *Nature* 442, 440–443. <https://doi.org/10.1038/nature04950>
- Smith, J.W., Holwell, D.A., McDonald, I., 2014. Precious and base metal geochemistry and mineralogy of the Grasvalley Norite–Pyroxenite–Anorthosite (GNPA) member, northern Bushveld Complex, South Africa: implications for a multistage emplacement. *Miner. Deposita* 49, 667–692. <https://doi.org/10.1007/s00126-014-0515-6>
- Smith, J.W., Holwell, D.A., McDonald, I., Boyce, A.J., 2016. The application of S isotopes and S/Se ratios in determining ore-forming processes of magmatic Ni–Cu–PGE sulfide deposits: A cautionary case study from the northern Bushveld Complex. *Ore Geol. Rev.* 73, Part 1, 148–174. <https://doi.org/10.1016/j.oregeorev.2015.10.022>
- Spiess, F.N., Macdonald, K.C., Atwater, T., Ballard, R., Carranza, A., Cordoba, D., Cox, C., Garcia, V.M.D., Francheteau, J., Guerrero, J., Hawkins, J., Haymon, R., Hessler, R., Juteau, T.,

- Kastner, M., Larson, R., Luyendyk, B., Macdougall, J.D., Miller, S., Normark, W., Orcutt, J., Rangin, C., 1980. East Pacific Rise: Hot Springs and Geophysical Experiments. *Science* 207, 1421–1433. <https://doi.org/10.1126/science.207.4438.1421>
- Spooner, E.T.C., 1977. Hydrodynamic model for the origin of the ophiolitic cupriferous pyrite ore deposits of Cyprus. *Geol. Soc. Lond. Spec. Publ.* 7, 58–71. <https://doi.org/10.1144/GSL.SP.1977.007.01.06>
- Staudigel, H., Tauxe, L., Gee, J.S., Bogaard, P., Haspels, J., Kale, G., Leenders, A., Meijer, P., Swaak, B., Tuin, M., Van Soest, M.C., Verdurmen, E.A.T., Zevenhuizen, A., 2000. Geochemistry and intrusive directions in sheeted dikes in the Troodos ophiolite: Implications for mid-ocean ridge spreading centers. *Geochem. Geophys. Geosystems* 1, n/a-n/a. <https://doi.org/10.1029/1999GC000001>
- Sun, W., Arculus, R.J., Kamenetsky, V.S., Binns, R.A., 2004. Release of gold-bearing fluids in convergent margin magmas prompted by magnetite crystallization. *Nature* 431, 975–978. <https://doi.org/10.1038/nature02972>
- Tardani, D., Reich, M., Deditius, A. P., Chryssoulis, S., Sánchez-Alfaro, P., Wrage, J., & Roberts, M. P. (2017). Copper–arsenic decoupling in an active geothermal system: A link between pyrite and fluid composition. *Geochim. Cosmochim. Acta*, 204, 179-204.
- Taylor, S.L. (2015). The effect of heap bioleach processes on VMS copper ores, MEdSci Thesis, Cardiff University, unpub
- Teagle, D. a. H., Alt, J.C., Chiba, H., Halliday, A.N., 1998. Dissecting an active hydrothermal deposit: the strontium and oxygen isotopic anatomy of the TAG hydrothermal mound - anhydrite. *Proc. Ocean Drill. Program Sci. Results* 158, 129–141.
- Thalhammer, O., Stumpfl, E.F., Panayiotou, A., 1986. Postmagmatic, hydrothermal origin of sulfide and arsenide mineralizations at Limassol Forest, Cyprus. *Miner. Deposita* 21, 95–105. <https://doi.org/10.1007/BF00204268>
- Thy, P., 1987. Petrogenetic implications of mineral crystallization trends of Troodos cumulates, Cyprus. *Geological Magazine* 124, 1–11. <https://doi.org/10.1017/S0016756800015739>
- Thy, P., Moores, E.M., 1988. Crustal accretion and tectonic setting of the Troodos ophiolite, Cyprus. *Tectonophysics* 147, 221–245. [https://doi.org/10.1016/0040-1951\(88\)90188-6](https://doi.org/10.1016/0040-1951(88)90188-6)
- Varga, R.J., Gee, J.S., Bettison-Varga, L., Anderson, R.S., Johnson, C.L., 1999. Early establishment of seafloor hydrothermal systems during structural extension: paleomagnetic evidence from the Troodos ophiolite, Cyprus. *Earth Planet. Sci. Lett.* 171, 221–235.
- Tivey, M.K., Humphris, S.E., Thompson, G., Hannington, M.D., Rona, P.A., 1995. Deducing patterns of fluid flow and mixing within the TAG active hydrothermal mound using mineralogical and geochemical data. *J. Geophys. Res. Solid Earth* 100, 12527–12555. <https://doi.org/10.1029/95JB00610>
- Tornos, F., 2006. Environment of formation and styles of volcanogenic massive sulfides: The Iberian Pyrite Belt. *Ore Geol. Rev.* 28, 259–307. <https://doi.org/10.1016/j.oregeorev.2004.12.005>

- Tornos, F., Peter, J.M., Allen, R., Conde, C., 2015. Controls on the siting and style of volcanogenic massive sulphide deposits. *Ore Geol. Rev.* 68, 142–163. <https://doi.org/10.1016/j.oregeorev.2015.01.003>
- Torró, L., Proenza, J.A., Espaillet, J., Belén-Manzeta, A.J., Román-Alday, M.C., Amarante, A., González, N., Espinoza, J., Román-Alpiste, M.J., Nelson, C.E., 2018. The Discovery of the Romero VMS Deposit and Its Bearing on the Metallogenic Evolution of Hispaniola during the Cretaceous. *Minerals* 8, 507. <https://doi.org/10.3390/min8110507>
- Trudinger, P.A., Chambers, L.A., Smith, J.W., 1985. Low-temperature sulphate reduction: biological versus abiological. *Can. J. Earth Sci.* 22, 1910–1918. <https://doi.org/10.1139/e85-207>
- Tyrrell, T., Zeebe, R.E., 2004. History of carbonate ion concentration over the last 100 million years. *Geochim. Cosmochim. Acta* 68, 3521–3530. <https://doi.org/10.1016/j.gca.2004.02.018>
- Urabe, T., Kusakabe, M., 1990. Barite silica chimneys from the Sumisu Rift, Izu-Bonin Arc: possible analog to hematitic chert associated with Kuroko deposits. *Earth Planet. Sci. Lett.* 100, 283–290. [https://doi.org/10.1016/0012-821X\(90\)90191-Y](https://doi.org/10.1016/0012-821X(90)90191-Y)
- Varga, R.J. and Moores, E.M., 1985. Spreading structure of the Troodos ophiolite, Cyprus. *Geology*, 13(12), pp.846-850.
- Varga, R.J., 1991. Modes of extension at oceanic spreading centers: evidence from the Solea graben, Troodos ophiolite, Cyprus. *J. Struct. Geol.* 13, 517–537. [https://doi.org/10.1016/0191-8141\(91\)90041-G](https://doi.org/10.1016/0191-8141(91)90041-G)
- Varga, R.J., Gee, J.S., Bettison-Varga, L., Anderson, R.S., Johnson, C.L., 1999. Early establishment of seafloor hydrothermal systems during structural extension: paleomagnetic evidence from the Troodos ophiolite, Cyprus. *Earth Planet. Sci. Lett.* 171, 221–235. [https://doi.org/10.1016/S0012-821X\(99\)00147-8](https://doi.org/10.1016/S0012-821X(99)00147-8)
- Varga, R.J., Moores, E.M., 1985. Spreading structure of the Troodos ophiolite, Cyprus. *Geology* 13, 846–850.
- Varga, R.J., Moores, E.M., 1990. Intermittent magmatic spreading and tectonic extension in the Troodos Ophiolite: implications for exploration for black smoker-type ore deposits, in: *OPHIOLITES Oceanic Crustal Analogues, Proceedings of the Symposium “Troodos 1987.”* The Geological Survey Department, Ministry of Agriculture and Natural Resources, Nicosia, Cyprus, pp. 53–64.
- Vear, A., Curtis, C., 1981. A quantitative evaluation of pyrite weathering. *Earth Surf. Process. Land.* 6, 191–198. <https://doi.org/10.1002/esp.3290060214>
- Vibetti, N.J., 1993. Chemical alteration trends, fluid inclusion patterns and stable isotope compositions in the plutonic sequence of the Troodos ophiolite, Cyprus. *J. Afr. Earth Sci. Middle East* 17, 193–202. [https://doi.org/10.1016/0899-5362\(93\)90035-O](https://doi.org/10.1016/0899-5362(93)90035-O)
- Vine, F.J., Matthews, D.H., 1963. Magnetic Anomalies Over Oceanic Ridges. *Nature* 199, 947–949. <https://doi.org/10.1038/199947a0>
- Vine, F.J. and Smith, G.C., 1990. Structure and physical properties of the Troodos crustal section at ICRDG drill holes CY1, 1a and 4. *Ophiolites—oceanic crustal analogues.*

- Geological Survey Department, Ministry of Agriculture and Natural Resources, Cyprus, pp.113-124.
- Von Damm, K.L. and Lilley, M.D., 2004. Diffuse flow hydrothermal fluids from 9 50' N East Pacific Rise: origin, evolution and biogeochemical controls. *The Subseafloor Biosphere at Mid-Ocean Ridges*, 144, pp.245-268.
- Von Damm, K.L., 1990. Seafloor Hydrothermal Activity: Black Smoker Chemistry and Chimneys. *Annual Review of Earth and Planetary Sciences* 18, 173–204.  
<https://doi.org/10.1146/annurev.ea.18.050190.001133>
- Von Damm, K.L., Buttermore, L.G., Oosting, S.E., Bray, A.M., Fornari, D.J., Lilley, M.D., Shanks, W.C., 1997. Direct observation of the evolution of a seafloor “black smoker” from vapor to brine. *Earth Planet. Sci. Lett.* 149, 101–111. [https://doi.org/10.1016/S0012-821X\(97\)00059-9](https://doi.org/10.1016/S0012-821X(97)00059-9)
- Von Damm, K.L., Edmond, J.M., Grant, B., Measures, C.I., Walden, B., Weiss, R.F., 1985. Chemistry of submarine hydrothermal solutions at 21 °N, East Pacific Rise. *Geochim. Cosmochim. Acta* 49, 2197–2220. [https://doi.org/10.1016/0016-7037\(85\)90222-4](https://doi.org/10.1016/0016-7037(85)90222-4)
- Wallace, P.J., 2005. Volatiles in subduction zone magmas: concentrations and fluxes based on melt inclusion and volcanic gas data. *J. Volcanol. Geotherm. Res., Energy and Mass Fluxes in Volcanic Arcs* 140, 217–240. <https://doi.org/10.1016/j.jvolgeores.2004.07.023>
- Webber, A.P., Roberts, S., Murton, B.J., Hodgkinson, M.R.S., 2015. Geology, sulfide geochemistry and supercritical venting at the Beebe Hydrothermal Vent Field, Cayman Trough. *Geochem. Geophys. Geosystems* 16, 2661–2678.  
<https://doi.org/10.1002/2015GC005879>
- Webber, A.P., Roberts, S., Murton, B.J., Mills, R.A., Hodgkinson, M.R.S., 2017. The formation of gold-rich seafloor sulfide deposits: Evidence from the Beebe hydrothermal vent field, Cayman Trough. *Geochem. Geophys. Geosystems* 18, 2011–2027.  
<https://doi.org/10.1002/2017GC006922>
- Webber, A.P., Roberts, S., Murton, B.J., Mills, R.A., Hodgkinson, M.R.S., 2017. The formation of gold-rich seafloor sulfide deposits: Evidence from the Beebe hydrothermal vent field, Cayman Trough. *Geochem. Geophys. Geosystems* 18, 2011–2027.  
<https://doi.org/10.1002/2017GC006922>
- White, N.C., Hedenquist, J.W., 1990. Epithermal environments and styles of mineralization: Variations and their causes, and guidelines for exploration. *Journal of Geochemical Exploration* 36, 445–474. [https://doi.org/10.1016/0375-6742\(90\)90063-G](https://doi.org/10.1016/0375-6742(90)90063-G)
- Williams-Jones, A.E., Bowtell, R.J., Migdisov, A.A., 2009. Gold in Solution. *Elements* 5, 281–287.  
<https://doi.org/10.2113/gselements.5.5.281>
- Williams-Jones, A.E., Heinrich, C.A., 2005. 100th Anniversary Special Paper: Vapor Transport of Metals and the Formation of Magmatic-Hydrothermal Ore Deposits. *Economic Geology* 100, 1287–1312. <https://doi.org/10.2113/gsecongeo.100.7.1287>
- Wilson, R.A.M. 1959. The geology of the Xeros-Troodos area, Cyprus. *Geol. Surv. Dep. Mem*, 1, pp.1-184.
- Wilson, R.A.M. and Ingham, F.T., 1959. The geology of the Xeros-Troodos area (No. 1). authority of the Government of Cyprus.

- Wohlgemuth-Ueberwasser, C.C., Viljoen, F., Petersen, S., Vorster, C., 2015. Distribution and solubility limits of trace elements in hydrothermal black smoker sulfides: An in-situ LA-ICP-MS study. *Geochimica et Cosmochimica Acta* 159, 16–41. <https://doi.org/10.1016/j.gca.2015.03.020>
- Woodruff, L.G., Shanks, W.C., 1988. Sulfur isotope study of chimney minerals and vent fluids from 21°N, East Pacific Rise: Hydrothermal sulfur sources and disequilibrium sulfate reduction. *J. Geophys. Res. Solid Earth* 93, 4562–4572. <https://doi.org/10.1029/JB093iB05p04562>
- Xiong, Y., 2003. Predicted equilibrium constants for solid and aqueous selenium species to 300 °C: applications to selenium-rich mineral deposits. *Ore Geol. Rev.* 23, 259–276. [https://doi.org/10.1016/S0169-1368\(03\)00038-6](https://doi.org/10.1016/S0169-1368(03)00038-6)
- Yamaoka, K., Matsukura, S., Ishikawa, T., Kawahata, H., 2015. Boron isotope systematics of a fossil hydrothermal system from the Troodos ophiolite, Cyprus: Water–rock interactions in the oceanic crust and seafloor ore deposits. *Chem. Geol.* 396, 61–73. <https://doi.org/10.1016/j.chemgeo.2014.12.023>
- Yang, K., Scott, S.D., 1996. Possible contribution of a metal-rich magmatic fluid to a sea-floor hydrothermal system. *Nature* 383, 420–423. <https://doi.org/10.1038/383420a0>
- Yang, K., Scott, S.D., 2002. Magmatic Degassing of Volatiles and Ore Metals into a Hydrothermal System on the Modern Sea Floor of the Eastern Manus Back-Arc Basin, Western Pacific. *Economic Geology* 97, 1079–1100. <https://doi.org/10.2113/gsecongeo.97.5.1079>
- Ye, L., Cook, N.J., Ciobanu, C.L., Yuping, L., Qian, Z., Tiegeng, L., Wei, G., Yulong, Y., Danyushevskiy, L., 2011. Trace and minor elements in sphalerite from base metal deposits in South China: A LA-ICPMS study. *Ore Geol. Rev.* 39, 188–217. <https://doi.org/10.1016/j.oregeorev.2011.03.001>
- Yeats, C.J., Hollis, S.P., Halfpenny, A., Corona, J.-C., LaFlamme, C., Southam, G., Fiorentini, M., Herrington, R.J., Spratt, J., 2017. Actively forming Kuroko-type volcanic-hosted massive sulfide (VHMS) mineralization at Iheya North, Okinawa Trough, Japan. *Ore Geol. Rev.* 84, 20–41. <https://doi.org/10.1016/j.oregeorev.2016.12.014>
- Yeats, C.J., Parr, J.M., Binns, R.A., Gemmell, J.B., Scott, S.D., 2014. The SuSu Knolls Hydrothermal Field, Eastern Manus Basin, Papua New Guinea: An Active Submarine High-Sulfidation Copper-Gold System. *Econ. Geol.* 109, 2207–2226. <https://doi.org/10.2113/econgeo.109.8.2207>
- Yıldırım, N., Dönmez, C., Kang, J., Lee, I., Pirajno, F., Yıldırım, E., Günay, K., Seo, J.H., Farquhar, J., Chang, S.W., 2016a. A magnetite-rich Cyprus-type VMS deposit in Ortaklar: A unique VMS style in the Tethyan metallogenic belt, Gaziantep, Turkey. *Ore Geol. Rev.* 79, 425–442. <https://doi.org/10.1016/j.oregeorev.2016.05.021>
- You, C.-F., Bickle, M.J., 1998. Evolution of an active sea-floor massive sulphide deposit. *Nature* 394, 668–671. <https://doi.org/10.1038/29279>
- Young, E.C., 2014. Volcanology of the Troodos Ophiolite (Cyprus) and mechanisms of accretion of the upper oceanic crust (Doctoral dissertation, Cardiff University).

- Zevin, D.Y., Migdisov, A.A., Williams-Jones, A.E., 2011. The solubility of gold in H<sub>2</sub>O–H<sub>2</sub>S vapour at elevated temperature and pressure. *Geochim. Cosmochim. Acta* 75, 5140–5153. <https://doi.org/10.1016/j.gca.2011.06.027>

# APPENDIX 3

**Field locality summaries from VMS and other referenced areas.**

**Appendix 3.1** provides a summary of field observations and **initial** interpretations from field locations across Troodos. VMS deposits and 'type' localities are summarised here.

Table A3.1: Summary of all localities visited during 2016/2017 field seasons (GR: WGS 1984).

<b>Locality name</b>	<b>Grid reference</b>	<b>Deposit classification</b>
Red Cap	<b>36S 053016/3874107</b>	Silicified umber/ oxidised pyrite
Theotokos	<b>36S 052465/3874094</b>	Silicified umber/umber
Dhrapia	<b>36S 052625/3851955</b>	Umbur
Asgata	<b>36S 052389/3848465</b>	Silicified umber/umber
Marki	<b>36S 052915/3875466</b>	Umbur/ Silicified umber
Pyrga	<b>36S 054098/3865323</b>	Umbur
Maghelani	<b>36S 051238/3846177</b>	VMS(?)/ umber
Three Hills	<b>36S 049088/3883189</b>	VMS Stockwork
Phoucassa	<b>36S 049018/3884032</b>	VMS
Phoenix	<b>36S 048993/3884050</b>	VMS Stockwork
Apliki	<b>36S 048575/3881758</b>	VMS
Kokkinopezula	<b>36S 051053/3877332</b>	VMS
Agrokippia	<b>36S 051330/3877964</b>	VMS
Kokkinoyia	<b>36S 050976/3877885</b>	VMS
Kampia	<b>36S 052493/3872969</b>	VMS
Kaphedes	<b>36S 052394/3871610</b>	VMS
Mathiatis North	<b>36S 053181/3870617</b>	VMS
Sha	<b>36S 053423/3867773</b>	VMS
Peristerka	<b>36S 052125/3872035</b>	VMS
Troulloi	<b>36S 055700/3876747</b>	VMS
Limni	<b>36S 045293/3877235</b>	VMS
Kynousa	<b>36S 045556/3876659</b>	VMS
Marla	<b>36S 047046/3864224</b>	VMS
Memi	<b>36S 050352/3877516</b>	VMS
Alestos	<b>36S 050232/3876999</b>	VMS/ low T
Kalavastos	<b>36S 052368/3850375</b>	VMS
Kokkinovounaros	<b>36S 052512/3872507</b>	"off axis"
Mathiatis South	<b>36S 053170/3867660</b>	Gossanised zone
Apliki West	<b>36S 048476/3881263</b>	Gossanised zone
Ay. Eftykhios	<b>36S 053325/3867902</b>	Gossanised zone
Strongyli	<b>36S 053449/3868864</b>	Disseminated sulfides
Mosfiloti	<b>36S 053983/3867565</b>	Disseminated sulfides
Lythrodontas	<b>36S 052411/3867924</b>	Disseminated sulfides
Almyras	<b>36S 053390/3870761</b>	Disseminated sulfides
Agia Ioannis	<b>36S 050245/3861864</b>	Massive sulfide veins
Sheeted dykes	<b>36S 051821/3866724</b>	Quartz shear zone
Alpen Rose	<b>36S 053305/3869950</b>	Quartz shear related
Marki seafloor contact	<b>36S 052909/3875824</b>	Oxidised pyrite/ Si umber
Alampra lava-sediment	<b>36S 053771/3871756</b>	Umbur/Ochre
Agrokippia 'B'	<b>36S 051333/3878543</b>	VMS (replacement ore)
Peraphedi	<b>36S 048966/3857435</b>	Umbur
Touronja	<b>36S 053242/3856579</b>	Epithermal Au (?)
Mathiatis umber	<b>36S 053214/3871363</b>	Umbur
Pevkos and Mavro	<b>N/A</b>	Hydro/magmatic

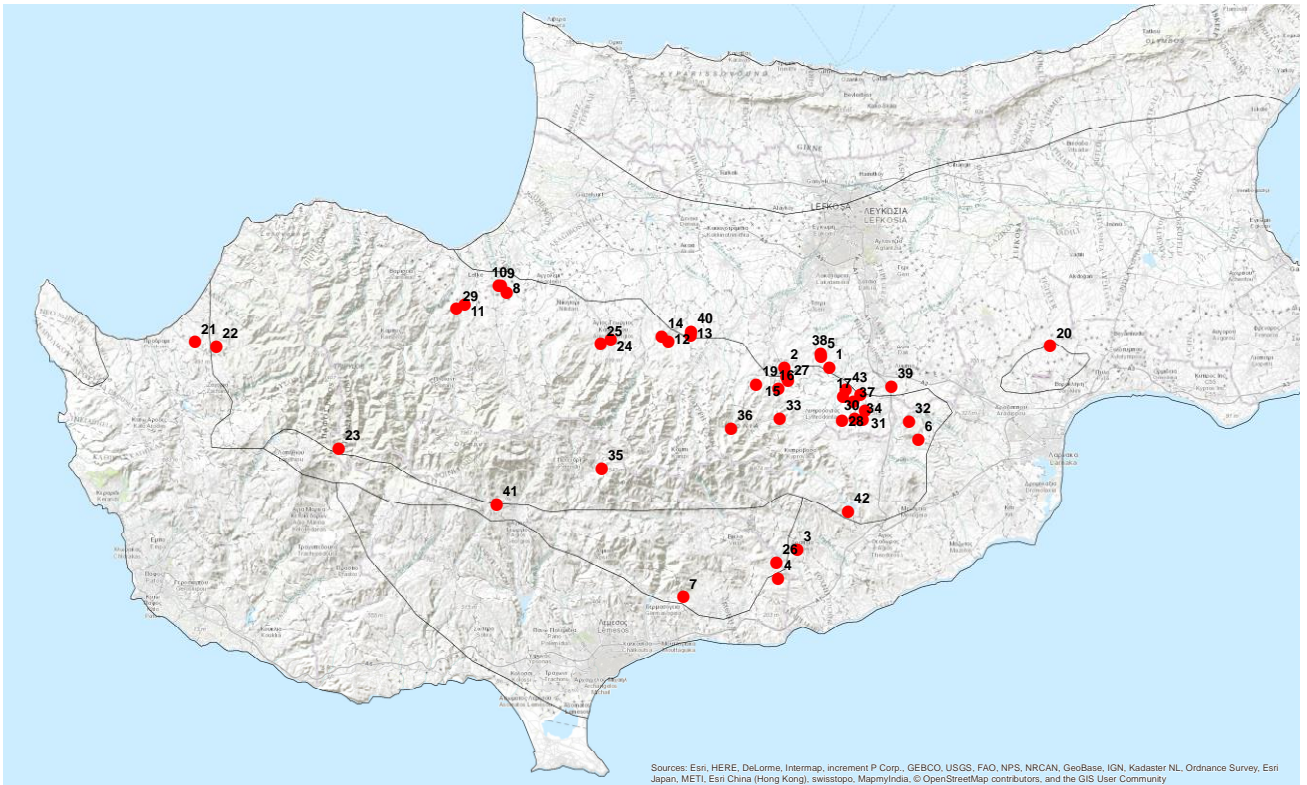


Figure A3.1: Overview map of main sample localities.

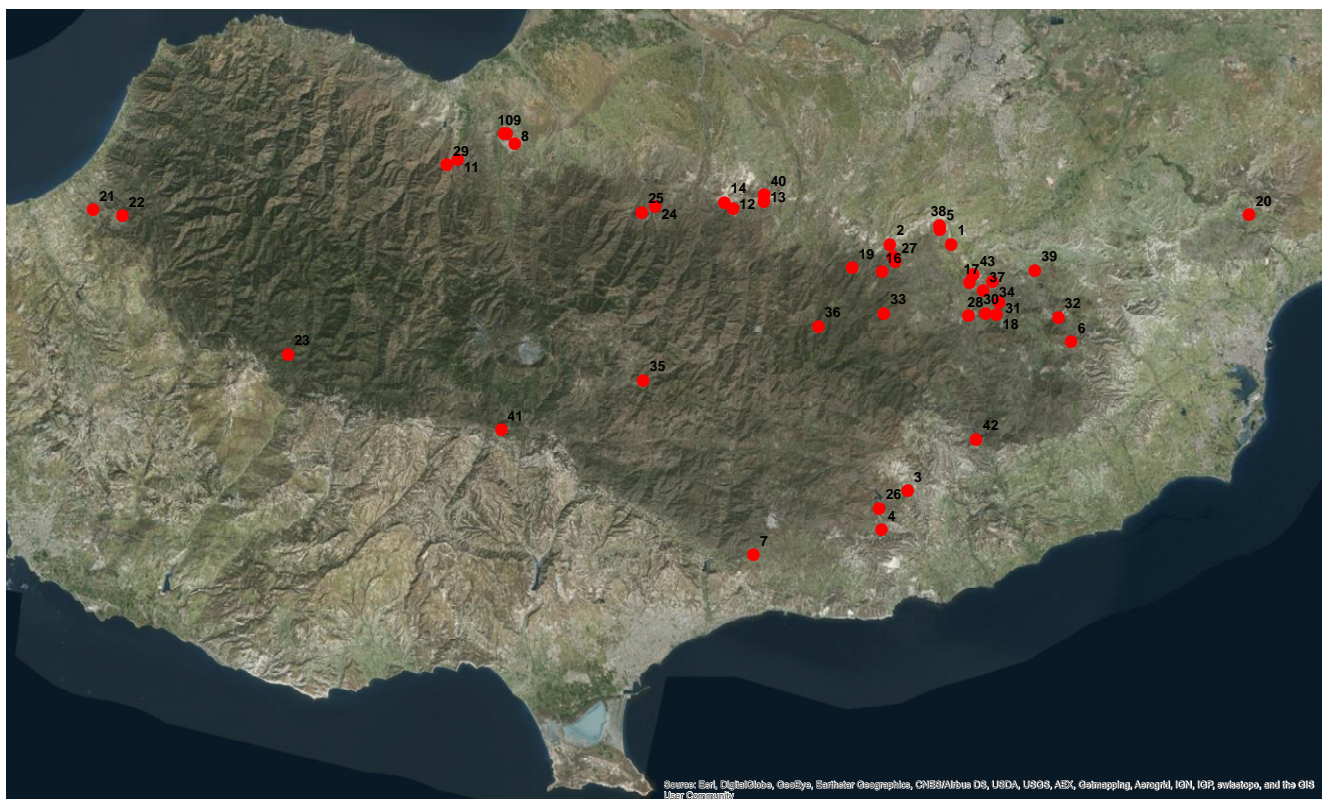


Figure A3.2: Landsat image showing sample locations.

# VMS deposits

- Skouriotissa
- Apliki
- Kokkinopezula
- Agrokipia
- Kokkinoyia
- Kambia
- Kaphedes
- Mathiatis North
- Sha
- Peristerka
- Troulloi
- Limni
- Kynousa
- Mala
- Memi
- Alestos
- Kalavasos

## Locality 1-2-3 Skouriotissa

### Introduction to Skouriotissa

Skouriotissa is located in northern Troodos 42 km ESE of Lefkosia. Skouriotissa is the only active mine on Cyprus extracting Cu via SX-EW using open pit methods. Mining has focused around three deposits: Phoenix, Phoucasa and Three Hills (Figure A3.3). Phoenix ceased production in 2012 and is now used for tailings storage. Phoucasa massive ore has been exhausted but HMC plan to start mining Phoucasa stockwork again next year (2016-17). Three Hills is currently the only producing pit at Skouriotissa (2016). Ore varies from 0.1-4.5 wt.% Cu. Unusually, most Cu at Skouriotissa is supergene in nature (e.g. chalcocite, covellite, native Cu), and only minor hypogene mineralisation exists in the form of chalcopyrite. Extracted ore totals around 6.7 Mt. Cyanide leaching of stock-piled Au-rich gossan commenced in 2017.

Phoenix and Three Hills are stockwork mineralisation whilst Phoucasa is massive. Faulting is well defined in the area with the Phoucasa and Skouriotissa faults cross-cutting the deposit. The mineralisation occurs at the UPL- seafloor boundary. Importantly one telluride was found by L. Taylor and historic Se grades are high (~3000 ppm). The most spectacular unbr situated directly overlying the VMS mound is also located at Skouriotissa allowing a complete cross-section through the VMS stratigraphy and sediments that overlie mineralisation to be analysed.



Figure A3.3: Aerial photograph of the Skouriotissa mine site. Green= Three Hills, Blue = Phoucasa, Red = Phoenix.

### 1A) The Three Hills deposit

Three Hills is the E most mine in Skouriotissa and the only active pit. Three Hills is a stockwork ore body and mineralisation is controlled by the phoucasa fault which strikes N-S. Mineralisation is developed extensively on the E side of the fault. Mineralogy is dominantly pyrite +/- chalcopyrite +/- covellite +/- chalcocite +/- bornite. The pit will be approximately 50 m deep when finished in the next two years. Grade distribution is variable ranging from 0.25-0.5 wt.%

Cu. Three Hills has not previously been the focus of any study. Stockwork samples have been collected (NE pit exposure) with a range of hypogene and supergene Cu minerals. Mineral paragenesis has been established for Phoenix and Phoucasa.

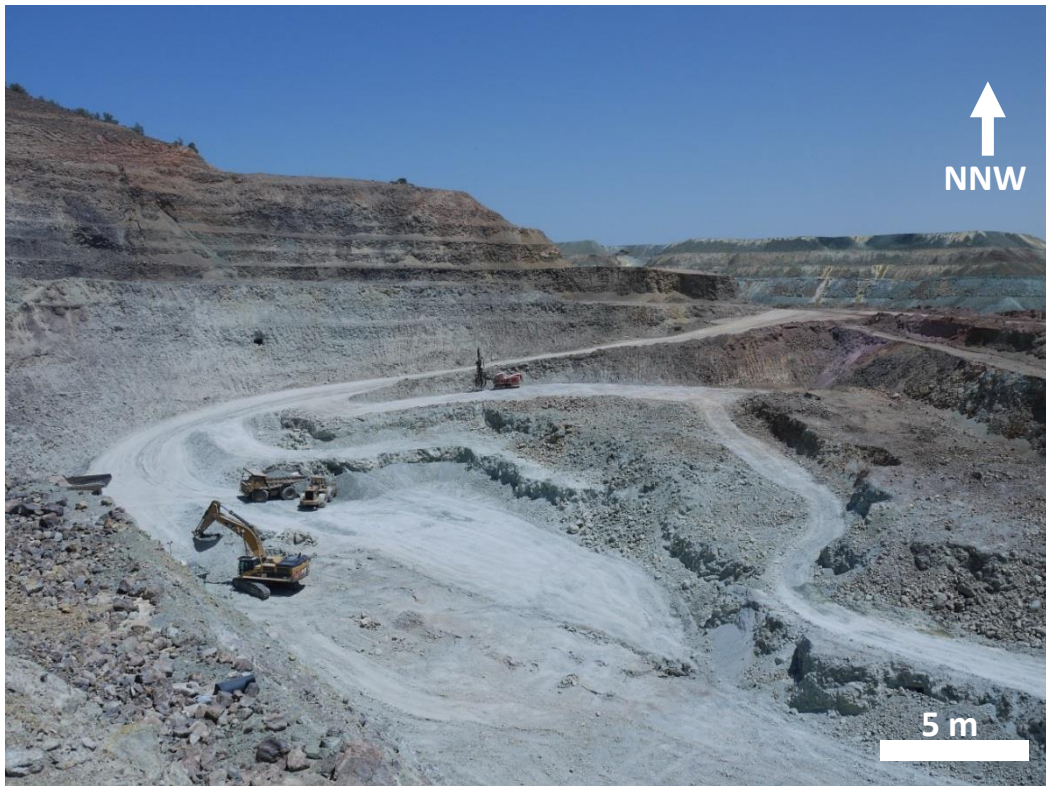


Figure A3.4: Extraction of low-grade Cu ore from the Three Hills pit.



Figure A3.5: Cut and blast operation at Three Hills.



Figure A3.6: Typical Three Hills ore. Basalts are LPL and have been extensively chloritized. Ore occurs infilling fractures. A thin veneer of chalcopyrite with covellite + chalcocite. Pyrite is coarse (up to 1.5 cm) and euhedral.

## 2A) Phoucasa deposit

Phoucasa is located just N of Phoenix and is the only 'traditional' massive sulfide deposit in the Skouriotissa camp; it comprises a massive cupriferous lens of pyrite +/- chalcopyrite underlain by a zone of high-grade Cu-rich stringers. It is clearly fault controlled with the NE-SW Phoucasa fault cross-cutting the deposit. It is situated at the top of the UPL and is overlain directly by umbers and ochre. It has not been buried by subsequent lava flows and is inferred (on this observation) to be one of the youngest VMS in Troodos. The massive sulfide has been historically extracted and is now nearly depleted, the pit is planned to be re-mined in 2017. Luckily samples of both the high-grade stockwork and massive sulfide have been obtained.

Massive sulfide ore is 95% pyrite with interstitial chalcopyrite. Stockwork ore consists of chalcopyrite stringers with chalcocite, covellite and pyrite. The gossanised zone E (uphill) of the Phoucasa and Phoenix ore bodies is interpreted to have formed as a result of seafloor weathering of the massive ore.

More significant at this locality is a spectacular umber. The umber is 30 m thick and infills a hollow directly overlying the VMS mound (Figure A3.8). The preserved sequence is outlined in Figure A3.8 below. Samples were collected throughout all layers underlying the umber and the massive sugary pyrite below to assess changes in trace geochemistry. Samples from the base and upper umber were also collected. Generally the umber looks homogenous with no ochre bands. This locality adds to the evidence that umber may be fault derived due to the proximity of umber to the Phoucasa fault.

Although Skouriotissa is undoubtedly the most studied and recognisable VMS on Cyprus in the author's opinion the abundance of supergene ore and lack of massive sulfide makes it atypical in terms of what is observed in other VMS in Troodos. The effect of supergene enrichment, especially change in oxidation state will have important implications for the mobility of Te and Se.





Figure A3.8: Ochre-volcanoclastic-sulfide package directly underlying umber. Bands dip 28SE/050. Sulfide horizons decrease in width to only a few cm as the umber interface is approached, they do however appear to be more Cu-rich.



Figure A3.9: Ochre package in centre of hollow. White bands are volcanoclastic, mottled grey-brown with white surface staining is sulfide, orange is ochre. Note Cu secondaries (e.g. chalcantite) commonly occur in the upper sulfide horizons directly below umber.

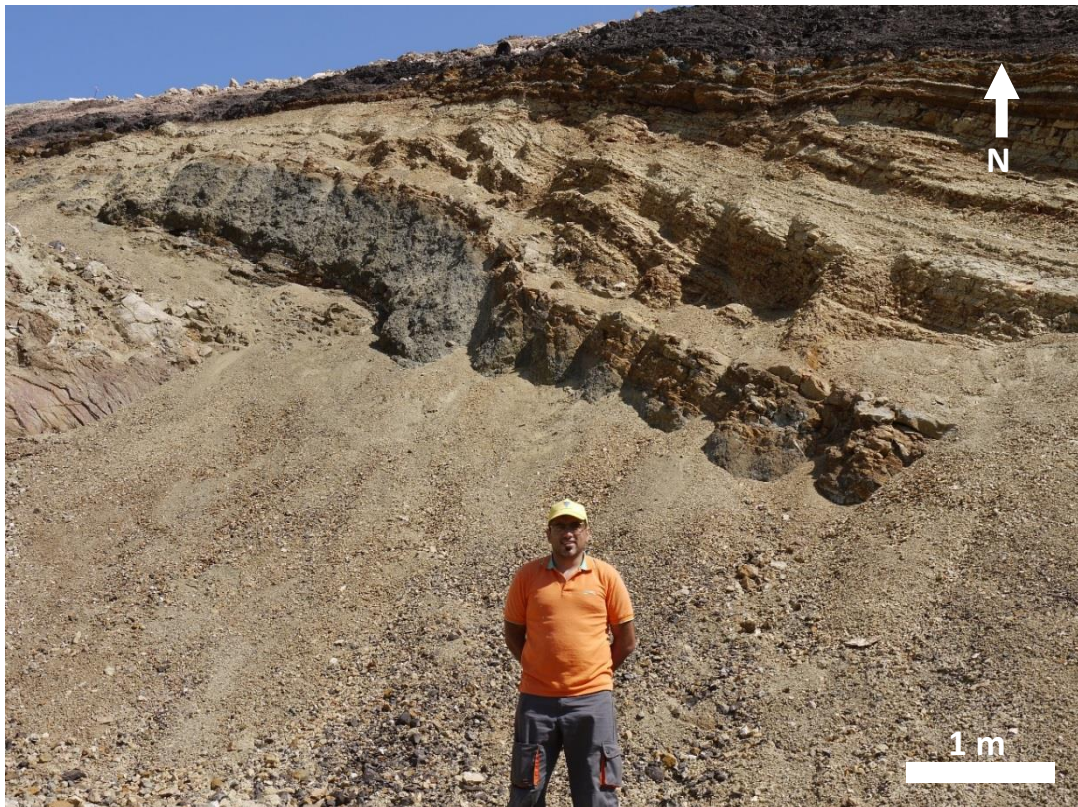


Figure A3.10: Basal sugary sulfide below umber marks the top of the Phoucasa mound and the last stages of sulfide deposition. Band is ~1 m thick and underlain by a volcanic horizon which in turn is underlain by a second ~2m sulfide horizon.



Figure A3.11: View from the Phoucasa massive sulfide mound (red line). Massive sulfide is covered by the ochre-umber-sulfide-lava layer that has been subsequently buried by limestones of the lower Lefkara group.

3A) Phoenix deposit

The Phoenix body is the largest of the three ore bodies (>3 Mt), it began producing in 1996 and reserves were exhausted in 2014. Like Three Hills, Phoenix is a stockwork ore body. Mineralogy is dominantly coarse pyrite with accessory chalcopyrite. Secondary enrichment at Phoenix is more prolific than Three Hills with covellite +/- chalcocite and rare native Cu. The mode of supergene enrichment is poorly constrained for Phoenix, the most widely accepted theory is that the Skouriotissa fault provided a permeability pathway from fluids to migrate from the Phoucasa deposit to the Phoenix pit. Again this deposit is not a typical Cyprus type VMS as there is no massive ore and abundant supergene enrichment.

This body was the focus of Manuel's (Keith et al., 2016a) study who found that deep stockwork pyrite was more enriched in Te-Se than shallow. Does this vary as a function of distance from the Skouriotissa fault and was the atypical setting factored into the equation? Both chalcopyrite and pyrite as well as Cu secondaries and native Cu were sampled from this location.

1-2-3B) Sample locations (all)

Sample	Grid reference	Brief description
16CA390	049018 3884032	Ochre horizon beneath massive sulfide
16CA391	049018 3884032	Massive sugary pyrite
16CA392	049018 3884032	Ochre band on top of massive sulfide
16CA393	049018 3884032	Altered basalt material slightly sheared
16CA394	049018 3884032	Cu stained ochre
16CA395	049018 3884032	Cu rich sulfide band
16CA396	049018 3884032	Non-stained ochre
16CA397	049018 3884032	Volcanoclastic horizon
16CA398	049018 3884032	Thin sulfate stained band
16CA399	049018 3884032	Brown finely laminated umber
16CA400	049018 3884032	Interbedded ochre umber
16CA401	049018 3884032	Base umber/ochre package contact
16CA397B	049018 3884032	Massive grey unit, no sulfide
16CA402	049018 3884032	Upper umber
16CA403	048993 3884050	White composite kaolin
16CA404	048993 3884050	Limonic gossan composite
16CA405	048993 3884050	Hematitic sample composite
16CA406	N/A	Gossan Au stockpile
16CA407	049088 3883189	Three hills sulfide/oxide ore
16CA408	049088 3883189	Three Hills disseminated ore
16CA409	049088 3883189	Phoucassa massive sulfide
16CA410	049088 3883189	Ochre-massive contact Phoucassa
16CA411	049088 3883189	Veined material from Three Hills
16CA412	048990 3883713	Jasper with qtz and pyrite
16CA413	048990 3883713	Disseminated blue grey basalt (LPL)
16CA414	048990 3883713	Cu rich material- secondary rich
16CA415	048990 3883713	Cu secondary S Phoenix
16CA416	048990 3883713	Cu secondary S Phoenix
16CA417	048990 3883713	Native Cu from N Phoenix
16CA418	048990 3883713	Phoucassa Stockwork (V high-grade)
16CA013	049018 3884032	Beds below umber (ochre horizons)
16CA014	048994 3884068	Au rich white areas (upper gossan)
16CA015	048990 3884074	Box-work material with relict pyrite



Figure A3.12: Typical ore textures from the Phoenix ore body. Euhedral coarse grained (up to 2 cm) pyrite stringer with occasional jasper vein with blue/grey lower pillow lavas.

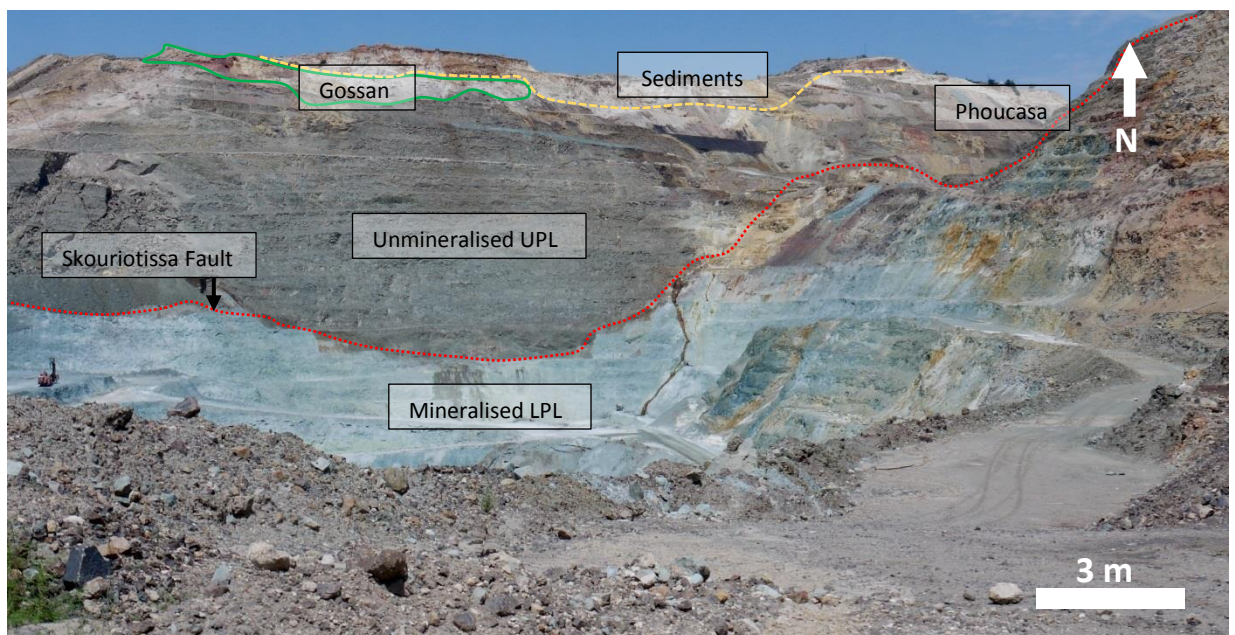


Figure A3.13: Classic view over the Phoenix pit. Contact between LPL and UPL is faulted by Skouriotissa fault (E-W). Phoucasa is located to the E of Phoenix. Note number on top of dark UPL and sediments/gossan formation at the upper levels.

4A) Apliki

Apliki mine is located in NW Troodos, 4.4 km SW of Skouriotissa. To get the mine follow the road past Skouriotissa and take the next major turning on your right, climb to the top of the hill and you will come to a sharp corner. There is a sign that says OSCAR 18, park the car here and walk N down the slope then head E opposite the small allotment (you are now in UN buffer territory!). Follow the winding road for 1 km and the mine will come into view. Apliki is a well preserved VMS with abundant sulfide, the structural controls are clearly visible and a good range of samples were obtained.

4B) Mineralisation

Apliki is a typical Cyprus-type VMS, it has a massive sulfide lens underlain by a stockwork. Country rock in the mineralised zone (between the two faults: Figure A3.15) Apliki is characterised by abundant fine (1-2 mm) disseminated pyrite. The host rock is LPL that are blue-green in colour and exhibit moderate silicification. The outcrop has clearly been brecciated and now appears cobbled (like Agrokippia). In this case the cobbled appearance is just an effect of weathering; weathering smooths an originally jagged profile. This silicified zone represents mineralisation that formed distally to the VMS mound within the effusive fluid flow zone between two faults.

Semi-massive to massive sulfide is preserved in the central S zone (between parallel faults). Evidence suggests that this is the margin of the mound, the periphery of the massive sulfide lens. The zone is characterised by massive pyrite proximal to the lake with abundant malachite and azurite staining that grades to silicified semi-massive ore to the S over approximately 4 m. At the margin of the outcrop, massive jasper was collected, jasper was extremely enriched in pyrite with occasional chalcopyrite. The pit wall is mineralised with disseminated pyrite. The box-work texture preserved in the distal silicified facies suggests dissolution of earlier mineral phases (chalcopyrite + anhydrite?) by later fluids.

In terms of Au, the silicified matrix between the faults possesses significant potential to host Au. Although it is not clear if this silicification is late or primary? The mini gossanised zone to the N (Figure A3.19) with bleached and hematized lavas that are similar in appearance to Kokkinovounaros and may also contain high Au.

4C) Structural data

Two main faults control mineralisation and ore formation at Apliki. The faults are clearly traceable and continuous across the pit separating dark LPL flows from mineralised, chloritized, silicified LPL. The first fault (to the W) measures 60 E/012. The second fault measures 50 E/022.

On the N side of the pit (A3.19) a small antithetic fault splays off the main W fault within the hanging wall locally controlling gossanisation in the upper part of the open pit face. The fault measures 60 W/020. Between the major fault and the minor antithetic fault is a zone of highly bleached supergene altered lavas. Once E of the fault plane material rapidly transitions (2 m) to hematitic and then back to 'unaltered' LPL.

4D) Samples collected

Sample	Grid reference	Brief description
16CA325	048575 3881758	Jasper silicified vein material
16CA326	048575 3881758	Disseminated sulfides in basalt
16CA327	048575 3881758	Qtz vein in basalt

16CA238D	048575 3881737	Silicified boxwork
16CA239D	048575 3881737	Silicified breccia
16CA240D	048571 3881806	Fault gauge Fe rich
16CA241D	048572 3881802	Semi kaolinised
16CA242D	048572 3881802	Haematitic material
16CA243D	048572 3881802	Jasper
16CA244D	048573 3881812	Silicified Fe vein
16CA245D	048573 3881812	Kaolinised basalt
16CA246D	048573 3881812	Upper kaolinised horizon
16CA247D	048573 3881812	Purple veined hematite
16CA248D	048573 3881812	Celadonite –kaolinite clast
16CA249D	048569 3881756	Basalt and sulfides
16CA250D	948567 3881708	Slag
16CA251D	048575 3881375	Cu rich secondary basalts
16CA252D	048574 3881375	Jasper and sulfide rich material
16CA253D	048572 3881376	Massive sulfide
16CA254D	048574 3881377	Semi-massive silica rich
16CA255D	048574 3881384	Azurite/malachite
16CA256D	048574 3881384	Silicified with disseminated pyrite
16CA257D	048574 3881384	Globular jasper horizon

## 11E) Photos



Figure A3.14: View S towards Troodos (standing on fault plane). Foreground is semi-silicified cobbled LPL with disseminated pyrite. In the distance (dark coloured) is non-mineralised LPL not pillowed but many small (<1m) flows.



Figure A3.15: View looking N from the base of the South Apliki Breccia Zone. White lines indicate dip of flows.



Figure A3.16: Silicified box-work texture with minor pyrite. Commonly found in the S pit area in distal mound areas. Voids suggest late dissolution (similar to Mathiatis N).



Figure A3.17: Oxidised massive to semi-massive sulfide (S) with prolific malachite and azurite, no fresh chalcopyrite was observed.



Figure A3.18: South Apliki Breccia zone mineralisation, hematite with disseminated pyrite, chalcopyrite and oxidised semi-massive ore.



Figure A3.19: Bleached silica-rich gossan at the top of the N margin of the Apliki open pit, small normal fault.



Figure A3.20: One of the main mineralising faults exposed at the top of the open pit (N side). Zone is highlighted by a breccia zone dipping 44E/002. The fault is responsible for the intense alteration of surrounding rocks in image above.



Figure A3.21: Brecciated, chloritised, silicified wall rock between two bounding normal faults at Apliki.



Figure A3.22: View of E pit wall. The boundary between the mineralised and non-mineralised LPL is distinct. The flows are ~1 m thick or less and dip at 40N/084.

## Locality 5 Kokkinopezula

### 5A) Location

Kokkinopezula is located 1 km SW of the village of Mitsero. Follow the main road past the village, there is a construction site with green mesh awning take the small dirt road to the mine. The deposit is classified as stockwork type on the GSD mineral resource map and forms part of the Tamsos district. Disseminated pyrite is prolific at Kokkinopezula, however unlike Apliki silicification is minimal. A small gossanised area is preserved N of Kokkinopezula and exhibits similar characteristics to Apliki.

### 5B) Mineralisation

Disseminated pyrite is abundant in all pit exposures. Pyrite occurs as perfect cubes or pentagons varying in size from >1 mm to 1 cm. The coarsest pyrite occurs proximal to faults. Pyrite is hosted within blue/green weakly chloritized LPL with occasional flows. With the exception of the dark black coloured lithology (highlighted in Figure A3.23) all material is characteristic of the LPL succession. Pillows are very similar in appearance to Apliki, they are brecciated and appear cobbled but chilled margins are visible around the margins of some clasts suggesting they have been brecciated and weathered not transported and deposited. No massive sulfide ore was sampled.

Jasper veins commonly occur in areas of patchy silicification and are generally associated with minor massive sulfide. Jasper veins represent localised fluid up-flow zones as they occur proximal to antithetic faults that cross-cut the main mineralising fault. They commonly occur parallel to faults. Silicification commonly occurs in veins and is not pervasive.

Gossan is not widely developed at Kokkinopezula with the exception of a 10 m<sup>2</sup> area to the N of the main pit. The gossan is fault controlled and is characterised by highly coloured supergene minerals including hematite and silica. Some areas are semi-silicified (Au potential). Fresh pyrite is commonly altered to jarosite +/- hematite.

### 5C) Structural data

The main structural control on the Kokkinopezula ore body is an E-W trending fault. The fault is poorly exposed but is inferred to be parallel to the strike of the pit. Alteration and fragmentation intensity increases in the W pit corner suggesting the presence of a fault. The fault is inferred to strike 266. Given the perpendicular nature of the fault to the Mitsero graben axis it seems highly likely it has a strike-slip motion. The main fault is cross-cut by a series of small (appx.) N-S faults which are ridge parallel with downthrow (generally) to the E towards the Mitsero axis (or E-W forming small graben structures). An example of this is the N pit face where three faults are observed one dipping W (318/52W) and two E (45E/008, 62E/350).

Antithetic faults control gossan formation and in this case look to be infilled by UPL that are dark in colour dark and un-mineralised on the N face in contact with mineralised LPL (Figure A3.23).

Previous models (e.g. Constainou, 1963) did not infer the E-W fault however this seems obvious as the main mineralising structure, the occurrence of just these small N-S faults, although ridge parallel do not seem large enough to account for such a large accumulation of sulfide.

## 5D) Samples collected

Sample	Grid reference	Brief description
16CA149	051057 3877374	Silicified gossan material
16CA150	051057 3877374	Soft red haematitic material
16CA151	051057 3877374	Yellow Fe limonitic semi silicified
16CA152	051053 3877332	Kaolinised fault gauge
16CA153	051053 3877332	Amygdaloidal brown basalt
16CA154	051053 3877332	Light matrix amygdaloidal basalt
16CA155	051048 3877320	Sulfide vein material (lower flow)
16CA156	051048 3877320	Pillow material with sulfides
16CA157	051048 3877320	Slag
16CA158	051043 3877296	White fault gauge material
16CA159	051043 3877296	Pillow clast with disseminated sulfides
16CA160	051039 3877260	Highly fragmented fault material
16CA161	051038 3877259	Silicified sulfide rich vein
16CA162	051038 3877259	Disseminated sulfide clast
16CA163	051036 3877241	Vein material (jasperitic)
16CA164	051036 3877201	Green sulfide fault material
16CA165	051037 3877121	Jasper rich with massive sulfide
16CA166	051038 3877110	Disseminated sulfide cobble
16CA167	051072 3877270	Disseminated sulfide in highly vesicular
16CA168	051060 3877294	Green vein material (Cu ?)
16CA169	051060 3877294	Black basalt (UPL?) material
16CA170	051060 3877294	Brecciated matrix material
16CA171	051070 3877295	Dark flow material
16CA172	051076 3877268	Bench floor- blue/grey with sulfides
16CA173	051076 3877268	Black and red upper lithology
16CA174	051075 3877186	Sulfide vein
16CA175	051064 3877125	Semi altered amygdaloidal
16CA176	051079 3877197	VMS material (exsitu)

## 5E) Photos



Figure A3.23: View of the Kokkinopezula pit. Note gossanised outcrop N. and wedge of darker UPL material in the central pit face. AMD is well developed.



Figure A3.24: View looking W over Kokkinopezula. Photo taken from standing on top of UPL (dark in colour). Outcrop is poor which makes delineating faults very difficult.

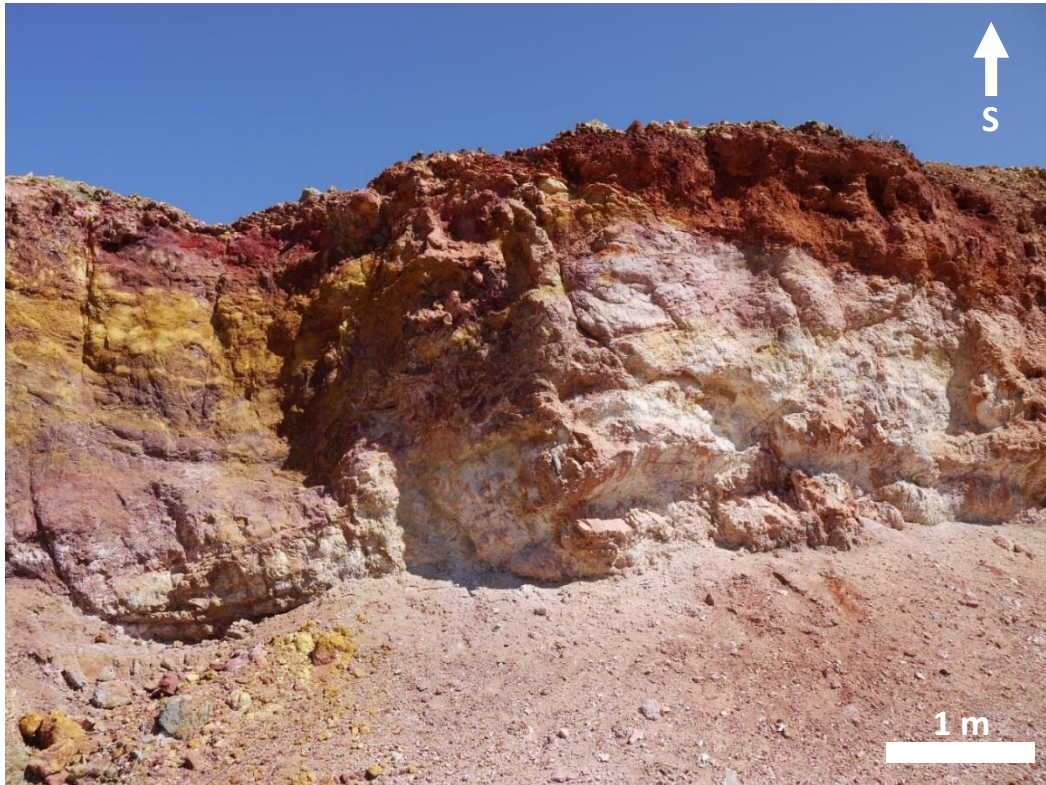


Figure A3.25: Gossan exposure NE pit wall. Interwoven facies of different Fe minerals. Hematite, and jarosite common. Some areas are semi-silicified with pyrite preserved, more commonly pyrite is oxidised.



Figure A3.26: View looking W over N pit wall. Different view of gossan highlighting the scale of alteration, the feeder fault is the same fault the separates the basal un-mineralised and LPL lithologies.



Figure A3.27: Small faults cross-cut typical outcrop. Fault dips steeply (62W/012) to the W and is associated with minor silicification surrounding (~50 cm).

Locality 6 Agrokipia A6A) Location

Agrokipia is located 800 m W of Agrokipia Village. Follow the main road through the village, the mine is clearly visible on the right. If you see Mitsero you've gone too far. The deposit consist of a small open pit (0.5 Mt) and a large underground (disseminated/stockwork) ore body (5.7 Mt). The site is also the location of the CY2A drill hole. Agrokipia A is a typical Cyprus type VMS with massive ore underlain by stockwork. Agrokipia B classified as a replacement type ore deposit.

6B) Mineralisation

Both in situ massive sulfide and disseminated ore is readily observed at Agrokipia. The deposit is situated at the UPL/LPL boundary (W face) with fault down-throw to the east leading to LPL being exposed on the S and E pit walls. Disseminated ore is prolific in the E pit wall; cubic pyrite, generally fine grained <4 mm is hosted in green/grey silicified LPL (Figure A 3.32). This unit is interpreted as being a tectonic unit that formed at the base of a seafloor fault scarp. The talus slope has then later been mineralised and silicified (see structure). On the W pit face a complete cross-section of seafloor topography is preserved.

At the N end of the pit, fresh sulfide is visible; pyrite exhibits a sugary texture indicative of the top of the VMS mound. This is in turn overlain by a gossan of variable thickness (up to > 3m), the gossan was produced by seafloor weathering of the VMS mound. This is overlain by a sequence of small (< 1m) sparsely phyrlic pillow lavas and lower Lefkara group limestones (Figure A 3.28/3.29).

The NE pit corner comprises of a series of semi-silicified highly altered UPL with faulted contacts with surrounding unaltered UPL.

6C) Structural data

The main fault direction is ~N-S (+/- 10°) (downthrow to the E), the main fault controlling pit mineralisation runs from the S corner (next to silicified cobbles) to the N end of the pit; it is not traceable to the football field and is likely truncated by an E-W fault (evidence is found near the metal gate of a fault). A series of approximately parallel faults control the variety of alteration facies in the E wall. These faults are probably continuous for the length of the pit but again are likely truncated to the N. Cross-cutting N-S trending faults are a series of E-W faults which explain the observed lithological distribution, the LPL on the S wall are bound on both margins by faults, to the E the main pit fault and the W a smaller cross-cutting fault that displaces the gossan. A similar scenario is envisaged for the N of the pit although this is very much inferred with only the E fault clearly visible

6D) Samples collected

Sample	Grid reference	Brief description
16CA133	051324 3877966	Silicified disseminated UPL
16CA134	051333 3877943	Fault breccia/bleached clast
16CA135	051336 3877999	White green vein
16CA136	051336 3877999	Grey host rock material
16CA137	051336 3878010	Bleached altered celadonite pillows
16CA138	051336 3878056	White yellow, tip of ridge
16CA139	051336 3878056	Banded pink with limonite
16CA140	051336 3878056	Qtz, chlorite, epidote?
16CA141	051336 3878056	Kaolinised with Fe banding
16CA142	051336 3878056	Semi silicified beige material
16CA143	051337 3878064	Highly altered kaolinised basalt
16CA144	051327 3878134	Massive sulfide
16CA145	N/A	Slag

16CA146	N/A	Silicified amygdaloidal basalt
16CA147	N/A	Gossan material
16CA148	N/A	Jasper, sulfide rich sample

6E) Photos

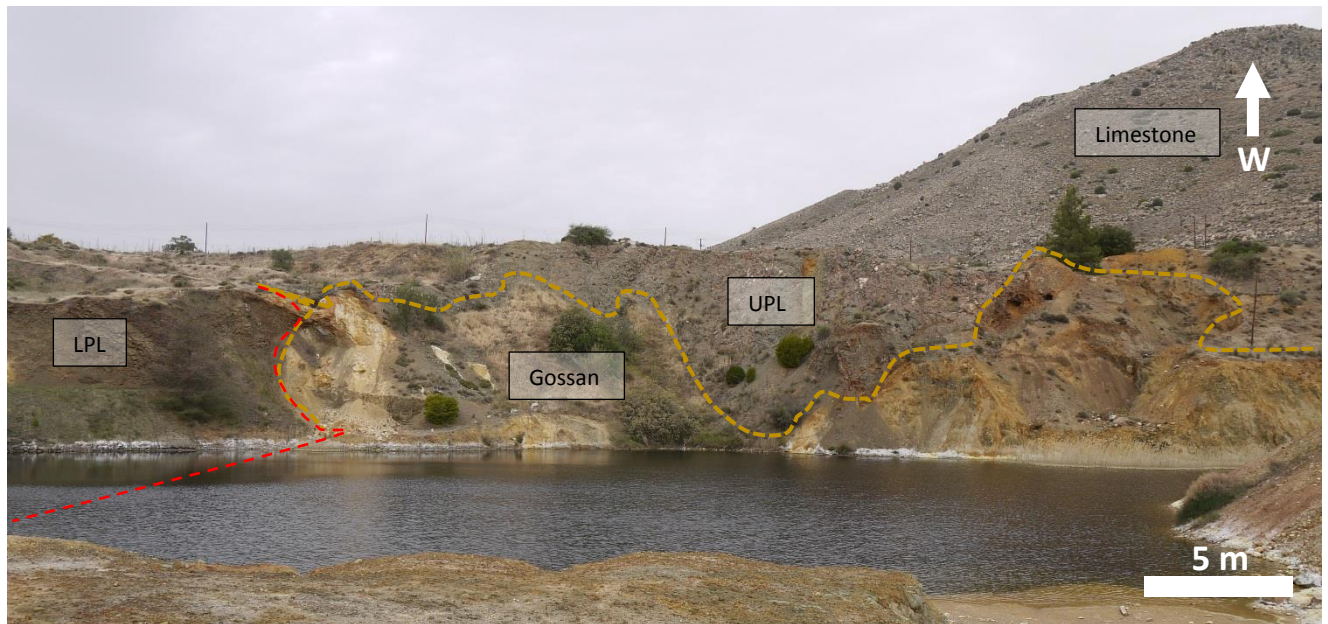


Figure A3.28: View WSW looking at the W pit wall. Note gossan is displaced in the left of the picture, the boundary is very sharp, fault is inferred. The gold line shows the limit of the gossan and paleo mound topography. UPL infill seafloor topography.

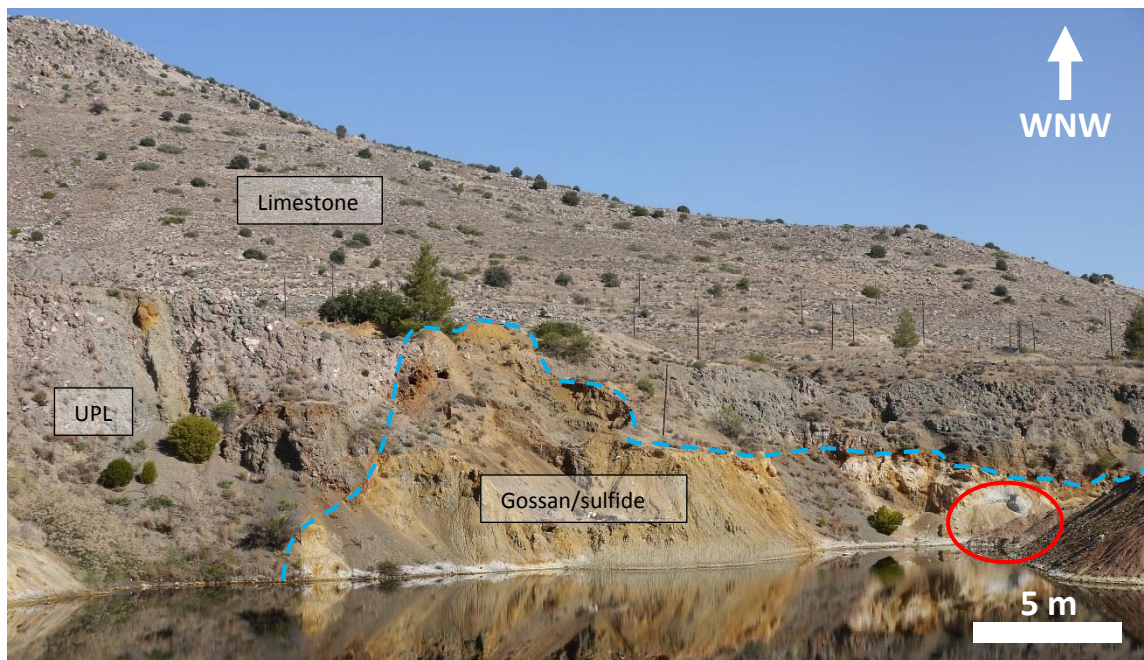


Figure A3.29: View of the W face. The gossan-UPL boundary is highlighted in blue. Massive sulfide is highlighted in red. UPL are commonly veined with calcite derived from above limestone. UPL are barren of mineralisation and thus formed significantly later post VMS formation.



Figure A3.29: Ridge of bleached pillows.



Figure A3.30: South pit wall. LPL outcrop comprised of flows, large pillows >1 m and lava domes. Celadonite staining is prolific. Pillows are not mineralised and likely up-thrown from a deeper higher temperature zone adjacent to VMS mound.



Figure A3.31: Breccia; highly angular with sulfide-rich matrix, clasts are variably altered basalt.



Figure A3.32: SE pit wall/corner. Cobbled, silicified boulders. Very highly silicified with disseminated pyrite. Cobbles are generally small (<30 cm) and highly spherical. They do not have chilled margins. Cobbled appearance is a function of preferential weathering of the exposed face.

## Locality 7 Kokkinoyia

### 7A) Location

Kokkinoyia is located 1.5 km E of Mitsero and 0.9 km NW of Kokkinopezula. Take the main road out of Mitsero, past the turning for Kokkinopezula. There is a small dirt road to the right with signs for a haulage/storage company, follow the road for 250 m past the old mine workings and the deposit is on your right. Kokkinoyia was mainly an underground operation although there is a small open pit. Total extraction was 1.6 Mt of sulfide ore. The deposit is classified as massive by the GSD mineral resource map; no massive sulfide was collected. The deposit is situated at the LPL-UPL transition which is clearly visible in the mine.

### 7B) Mineralisation

Kokkinoyia is located at the LPL-UPL transition zone; this is clearly evident in the pit especially in the N pit face. Through the narrow passage, dykes and flows are abundant, dykes dip uniformly between 50-30° N-NW. Strike is more variable from 260 to 070. Thickness also varies greatly with the majority of dykes around 0.8-1 m, some larger and countless small sinuous swarms. A large variation in dyke size is common in the lower LPL.

If massive sulfide was present it would have occurred in the central pit to the N; a clear transition is observed in Figure A3.36. The lower area is grey/orange indicative of pyrite oxidation and Fe-oxide formation. This is overlain by basalts with a very sharp contact between the limonite and UPL, similar to Agrokipia, the UPL above the gossan creates a very sharp contact. The contact is conformable throughout the pit.

Although there is no fresh sulfides, Cu secondaries are prolific (mainly azurite) which occurs to the N but is also visible along dyke margins to the S. It occurs as blebs coating the dyke surface and seems to be associated with gypsum, clearly azurite and gypsum is not hypogene in origin. The author favours a model of secondary remobilisation of Cu from massive ore that mixed with carbonate-rich groundwater leading to azurite precipitation. The gossan area to the E may be prospective for Au but as no silicification is observed in the area, Au prospectively is low.

### 7C) Structural data

Two main faults appear to control mineralisation at Kokkinoyia both trend approximately N-S but with slightly inverted strikes (they cross). F1 strikes 70E/018 and F2 68E/332, these faults are approximately parallel to the Mitsero graben axis and down thrown blocks are conformable. Several small E-W faults are observed cross-cutting the main fault trends (e.g. 52 NW/270). These faults are responsible for the juxtaposition of the basal group directly with the UPL. As previously mentioned the deposition of the UPL on top of the limonite-rich lower zone is conformable in the sense that it is not faulted.

## 7D) Samples collected

Sample	Grid reference	Brief description
16CA149	051057 3877374	Silicified gossan material
16CA150	051057 3877374	Soft red haematitic material
16CA151	051057 3877374	Yellow Fe limonitic semi silicified
16CA152	051053 3877332	Kaolinised fault gauge
16CA153	051053 3877332	Amygdaloidal brown basalt
16CA154	051053 3877332	Light matrix amygdaloidal basalt
16CA155	051048 3877320	Sulfide vein material (lower flow)
16CA156	051048 3877320	Pillow material with sulfides
16CA157	051048 3877320	Slag
16CA158	051043 3877296	White fault gauge material
16CA159	051043 3877296	Pillow clast with disseminated sulfides
16CA160	051039 3877260	Highly fragmented fault material
16CA161	051038 3877259	Silicified sulfide rich vein
16CA162	051038 3877259	Disseminated sulfide clast
16CA163	051036 3877241	Vein material (jasperitic)
16CA164	051036 3877201	Green sulfide fault material
16CA165	051037 3877121	Jasper rich with massive sulfide
16CA166	051038 3877110	Disseminated sulfide cobble
16CA167	051072 3877270	Disseminated sulfide in highly vesicular
16CA168	051060 3877294	Green vein material (Cu ?)
16CA169	051060 3877294	Black basalt (UPL?) material
16CA170	051060 3877294	Brecciated matrix material
16CA171	051070 3877295	Dark flow material
16CA172	051076 3877268	Bench floor- blue/grey with sulfides
16CA173	051076 3877268	Black and red upper lithology
16CA174	051075 3877186	Sulfide vein
16CA175	051064 3877125	Semi altered amygdaloidal
16CA176	051079 3877197	VMS material (exsitu)

## 7E) Photographs



Figure A3.33: View parallel to strike of major E fault at Kokkinoyia. Typically flows with occasional pillows are overlain by a 1-3 m thick gossan. To the NE mineralisation is more massive and overlain directly by lavas and limestone.



Figure A3.34: View along strike of major W fault. Foreground is “main” mineralisation with a pod of massive oxidised pyrite. The left wall is massive flows overlain by gossan. The area highlighted is the sharp transition from fragmented basalts with calcite matrix infill.

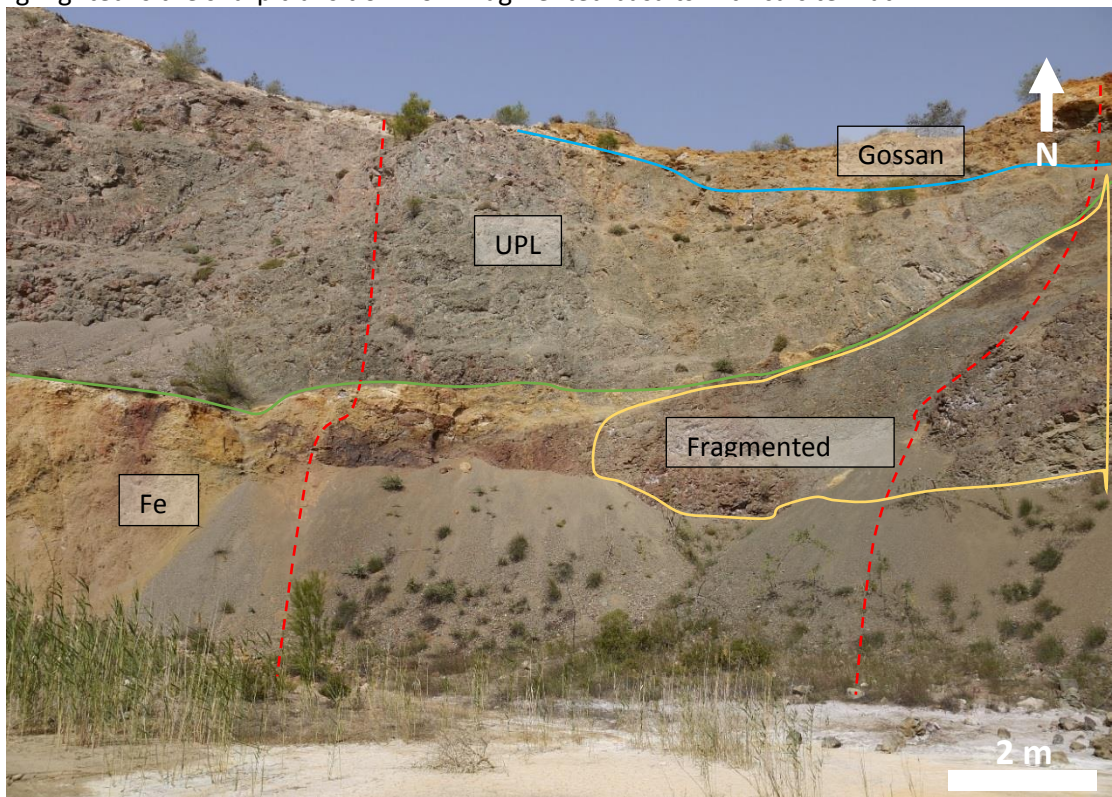


Figure A3.35: N pit wall. UPL/BG (mineralised) contact is clearly visible and marked by a distinct change in colour. UPL are dark and vesicular. To the E between the transition zone lava is a fragmented.



Figure A3.36: W pit wall. The limonitic mineralised horizon/UPL contact is clearly definable, it looks so sharp it could be erosional or seafloor topography covered by UPL? Gossan is well developed to the W. Note very sharp faulted boundary between LPL and UPL, downthrow to the N then infilling with UPL.



Figure A3.37: Typical exposure from "passage area" heading N toward main pit. Dykes make up the majority of the outcrop >70% is dykes, the remainder is pillows and sinuous dyke swarms.

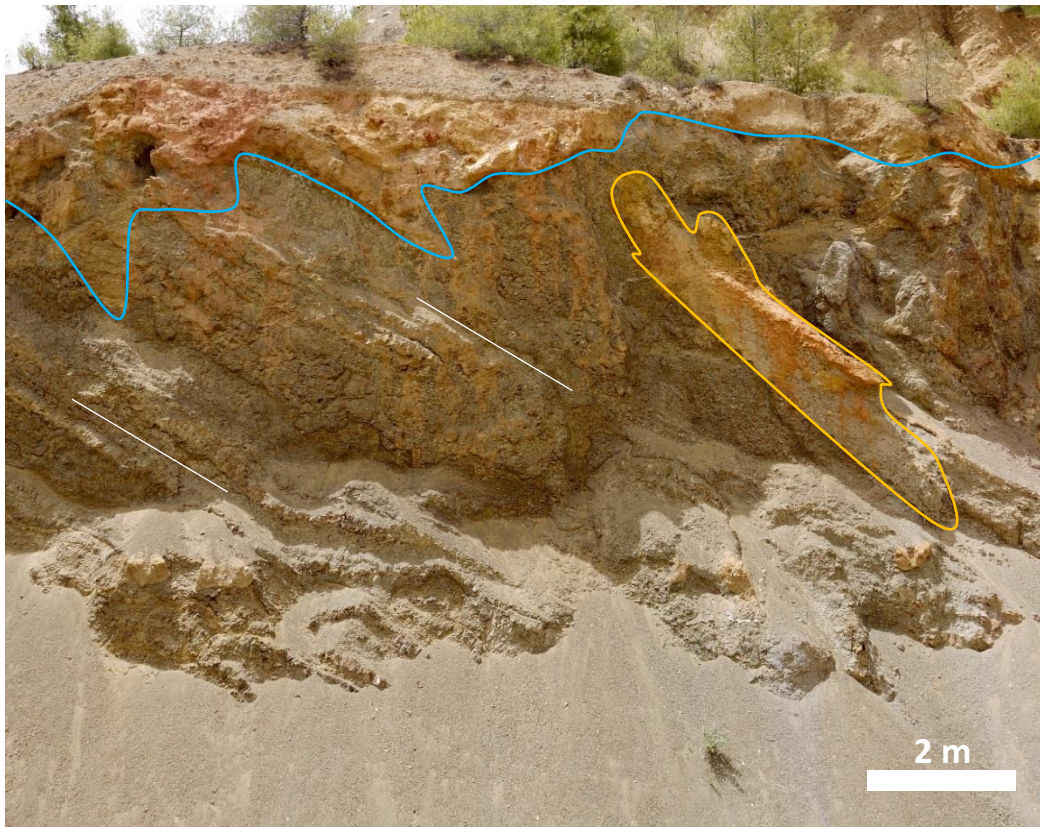


Figure A3.38: E wall “passage area”. Sinuous dykes intrude fragmented pillow screens. Gossan (blue line) is well developed. No notable sulfide mineralisation. Note the strange “xenolith” outlined in yellow, boundary is very well defined (see below).



Figure A3.39: Zoomed in image of sediment, possibly ochre. No clear baked margin. Clear horizontal bedding that is not parallel to the dip of surrounding dykes. Material ranges in grain size from clay to fine sand and is cyclically bedded.



Figure A3.40: Azurite and gypsum associated with the supergene remobilisation of Cu. Occurs in discrete veins.



Figure A3.41: Adsorption of Cu as malachite and minor azurite onto carbonite boulders, a common feature in many VMS.



Figure A3.42: Gossan above the Kokkinoyia mine site.

Locality 8 Kampia8A) Location

Kampia is located in E Troodos and lies on the UPL-LPL contact. Kampia mine is located 1.6 km SE of Kampia and 1.8 km SW of Analiontas. The mine is best accessed from Analiontas, take the 2<sup>nd</sup> turning on your left (approaching from Agia Varvara) just as you enter the village. The tarmac road stops and bends sharply right where a dirt track continues, follow to the mine. The mine is located at the UPL/LPL transition and is classified on the GSD resource map as stockwork type, barren ore body.

8B) Mineralisation

Mineralisation at Kampia is poorly preserved or largely inaccessible due to pit stability issues; only the upper benches were accessible. The E wall was readily accessible and comprised almost entirely of fragmented pillows with minor disseminated sulfides. Euhedral pyrite comprises approximately <3 wt.% and is <2mm in size and occurs as both disseminated and veined forms. As with Apliki, the appearance of the pit wall is cobbled, a similar mode of formation is inferred (weathering of breccia Figure A3.46). Host lithology is green-grey LPL.

To the N of the exposure (away from faults) “mega pillows” >1.5 m occur (typical of LPL). Pillows are in-tact with interstitial jasper. Jasper formed during fluid channelling around pillow margins (Figure A3.44), possibly a localised up flow zone. Jasper veins commonly contain pyrite.

To the W of the pit, just S of the slumped area could represent the relicts of a small massive sulfide lens (albeit now very highly weathered). The lens is 3 m wide and surrounded by bleached-hematized LPL; sulfide has been altered to green-grey clay minerals.

The massive area N of the pit (behind slump) is un-mineralised celadonite stained LPL. Pillows and flows exhibit minimal fragmentation. A range of jasperitic and massive samples were collected from the spoil heaps.

8C) Structural data

Faulting is complex and further complicated by the poor outcrop. At least three fault directions are noted in the area. Two faults are inferred to cross-cut originating from the NE pit corner (slumped area). F1 measures 42NE/318, F2 measures 58NNE/294; these faults are the major faults controlling mineralisation. Smaller faults are observed on the E pit wall forming meter scale graben structures (e.g. 44W/008 and 50E/332), throw on these faults is minor, approximately a meter. These smaller faults control local permeability and the abundance of pyrite in the surrounding area. A small parallel fault outside the pit was also recorded measuring 60 NNE/300.

The most important question is how these faults relate to Kokkinovounaros 600 m SE of Kampia? Is Kokkinovounaros linked along strike and therefore a possible failed VMS?

8D) Samples collected

Sample	Grid reference	Brief description
16CA101	052490 3872995	Jasperitic pillow infill material
16CA102	052490 3872967	Fe rich silicate matrix
16CA103	052491 3872904	Silicified pillow fragment
16CA104	052491 3872904	Jasper Fe matrix
16CA105	052473 3873019	Kaolinised altered pillows
16CA106	052473 3873019	Veined hematized pillows
16CA107	052473 3873019	Kaolinised white material
16CA108	052473 3873019	Massive sulfide
16CA109	052472 3872913	Silicified jasper with euhedral pyrite

16CA110	052501 38729676	Massive sulfide- layers?
16CA111	052501 38729676	Disseminated with jasper
16CA112	052501 38729676	Stock-box texture
16CA113	052501 38729676	Celadonite altered pillow

### 15E) Photos



Figure A3.43: The Kampia open pit.



Figure A3.44: Inter pillow jasper veining, jasper is pyrite-rich. In this instance jasper veins cross-cut pillows, more commonly they are confined to pillow margins.



Figure A3.45: Typical veined and disseminated LPL. Pyrite commonly forms mm scale veinlets crosscutting pillow. Pyrite infills vesicles and occurs as fine <1mm sized grains within silicified lava.



Figure A3.46: Typical pit wall exposure of highly brecciated “cobbled” looking pillows with disseminated sulfides.

Locality 9 Kaphedes9A) Location

Kaphedes mine is located 2.4 km SSE of Kambia and 1.5 km NW of Kaphedes. The mine is accessible by a dirt track and currently used as a site of waste disposal. From Agia Varvara take the road to Analiontas but instead of turning right to Analiontas turn left then immediately right. Follow this road for 2 km, the mine turning is 300 m past a small solar farm next to a small house on the right. The deposit is classified as massive on the GSD resource map.

9B) Mineralisation

In general, the outcrop at Kaphedes is poor, it is covered in a mountain of rubbish. To the very E of the pit a very nice slice of massive sulfide overlain by a thin gossan and lava is preserved. A lens structure 2-3 m wide is located in the E pit corner, very little fresh sulfide remains. Instead sulfide has been weathered to a white sulfate-rich clay like material (similar to Mala and Mathiatis South). This clay is the product of weathering and leaching of sulfides. In rare patches fist sized aggregates of pyrite were collected, no chalcopyrite was visible. Overlying the lens and dipping 15°N is a well-developed gossan zone approximately 1-1.2 m thick (Figure A3.48). It is comprised of massive Fe(oxy)hydroxide with a blocky texture.

On the W pit wall similar but more weathered green grey sulfate-rich clay is found, unlike the E which is stratigraphically controlled the W is faulted. The country rock which seems common throughout the mine is heavily celadonite stained flows and pillows indicative of the LPL/BG. To the N of the mine along the access road these flows are clearly visible. Flows commonly occur in clusters of 5-6 units and may exhibit internal brecciation.

The only visible disseminated sulfide was found in the W pit wall and was associated with a fault, the area surrounding the fault (58E/332) was brecciated with minor matrix silicification and associated disseminated sulfides.

9C) Structure

Flows at Kaphedes measure uniformly 50E/016. Faulting in the area occurs in two distinct orientations: 66W/058 and 58 E/332. The NE-SW 58 E/332 fault direction appears to have the most significant influence on mineralisation. The fault plane is best exposed on the W pit wall and is associated with disseminated pyrite in the wall rock. Other smaller faults striking approximately 90° (NW-SE) cross-cut the pit and are best exposed on the S wall.

9D) Samples collected

Sample	Grid reference	Brief description
16CA124	052394 3871610	Massive sulfide, upper mound
16CA125	052394 3871610	Gossan material
16CA126	052394 3871610	Gossan-sulfide contact
16CA127	052394 3871610	Amygdaloidal lava
16CA128	052389 3871581	Highly altered (S rich) clay material
16CA129	052387 3871564	Bleached brecciated material
16CA130	052383 3871566	Sulfide mud
16CA131	052378 3871587	Disseminated sulfide in blue/grey basalt
16CA132	052400 3871959	Slag from road leading to mine

9E) Photos



Figure A3.47: The Kaphedes open pit is now a waste disposal site.

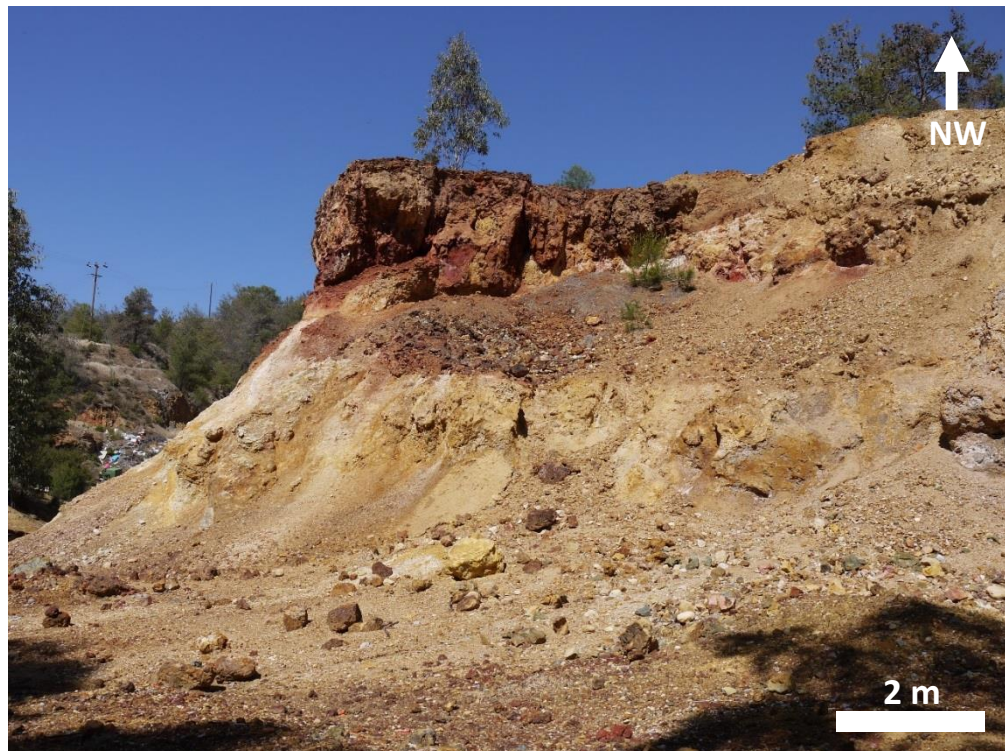


Figure A3.48: Gossan underlain by massive sulfide (mainly pyritic).

## Location 10 Mathiatis North

### 10A) Location

Mathiatis N is located on the main road between Agia Varvara and Mathiatis. It is approximately 1.6 km NE of Mathiatis and 2.7 km from Agia Varvara. Mathiatis is classified as a massive ore body by the GSD's resource map. The deposit has historically been mined for S with approximately 1 Mt extracted. Only the SE face remains accessible, conveniently this is where the sulfide is best exposed. Silicification is prolific at Mathiatis with secondary silicification textures common.

### 10B) Mineralisation

A clear progression is noted in mineralisation style as you transition from the base of the Mathiatis NE face towards upper horizons. The base is a typical stockwork texture; this does not infer it is a high temperature Cu-rich zone, instead it appears to be largely silica-rich. The stockwork is silicified within quartz veins cutting lavas containing disseminated pyrite. Progressing upwards, mineralisation becomes more massive and is classified as massive to semi-massive type mineralisation. This zone is characterised by massive sulfide with occasional semi-silicified LPL clast, again silicification is prolific within this zone occurring as quartz veins cross-cutting massive to semi-massive ore. The upper bench is characterised by highly silicified brecciated LPL that exhibit a cobbled appearance. This zone would have probably formed the marginal mound facies.

It should be noted that massive ore in the central bench area is heavily weathered to a goethitic clay (Figure A3.50) once chipped back this reveals grey/white clay with visible pyrite. In the lower stockwork zone a box-work texture is common and formed through the dissolution of hypogene mineral phases by late stage silica-rich fluids: could these silicifying fluids be rich in Au? Euhedral voids are also common contributing to the evidence of dissolution of sulfide phases.

### 10C) Structure

Two faults are clearly visible in Mathiatis N, one of which is clearly traceable across the pit, the other is less clear. The traceable fault (on the NE face) measures 60SSW/298 (F1), the second (inferred but possible visible in the top bench) measures 66SSW/300 (F2). Given the tectonics of the area I envisage that F1 is the original mineralising fault and F2 may be later, they both occur parallel to the Larnaca graben and have the correct geometry to infer downthrow to the NE/NNE (towards graben as expected).

## 10D) Samples collected

Sample	Grid reference	Brief description
16CA114	053182 3870619	Breccia with quartz/pyrite infill
16CA115	053182 3870619	Pyrite infill boxwork
16CA116	053182 3870619	Semi-massive sulfide
16CA117	053184 3870615	Semi-silicified sulfide rich clast
16CA118	053185 3870606	Massive infill material
16CA119	053185 3870606	Clast of "cobble" from upper horizon
16CA120	053185 3870606	Silicified matrix material
16CA121	053185 3870571	Fault breccia with pyrite
16CA122	053159 3870802	Mathiatis N slag heap (? In situ)
16CA123	053188 3870776	Massive sulfide ex situ

## 10E) Photos

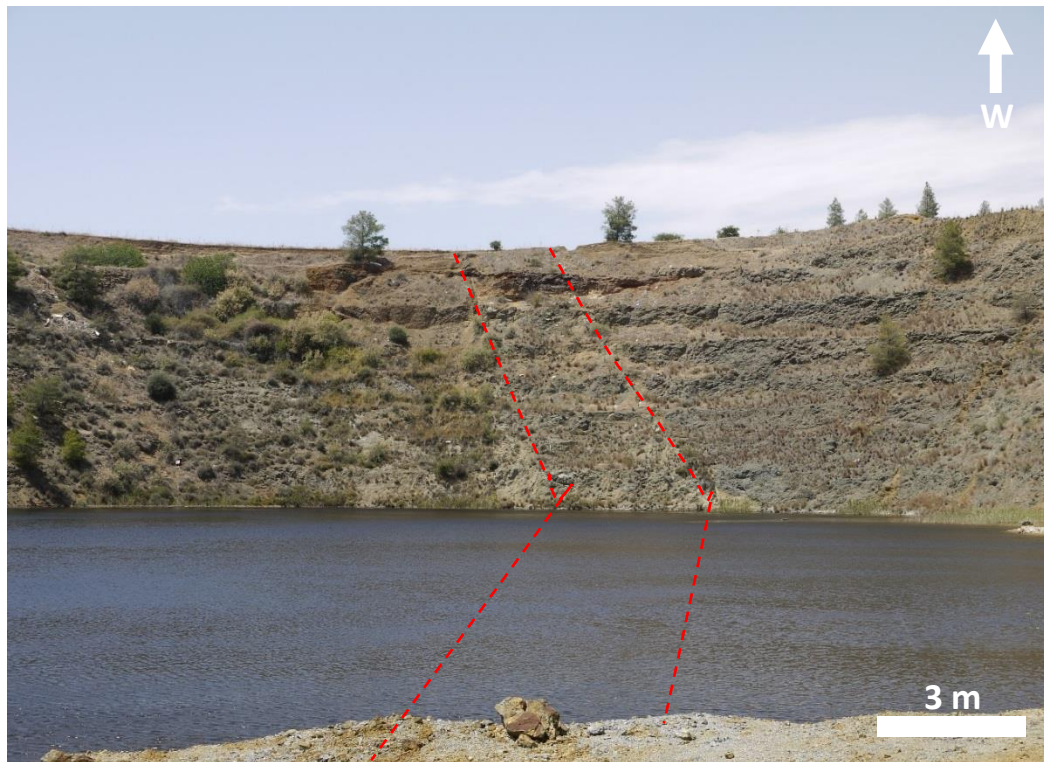


Figure A3.49: NW pit wall. Red lines indicate faults (60 SSW/ 300), faults are oblique strike-slip with downthrow to NE.

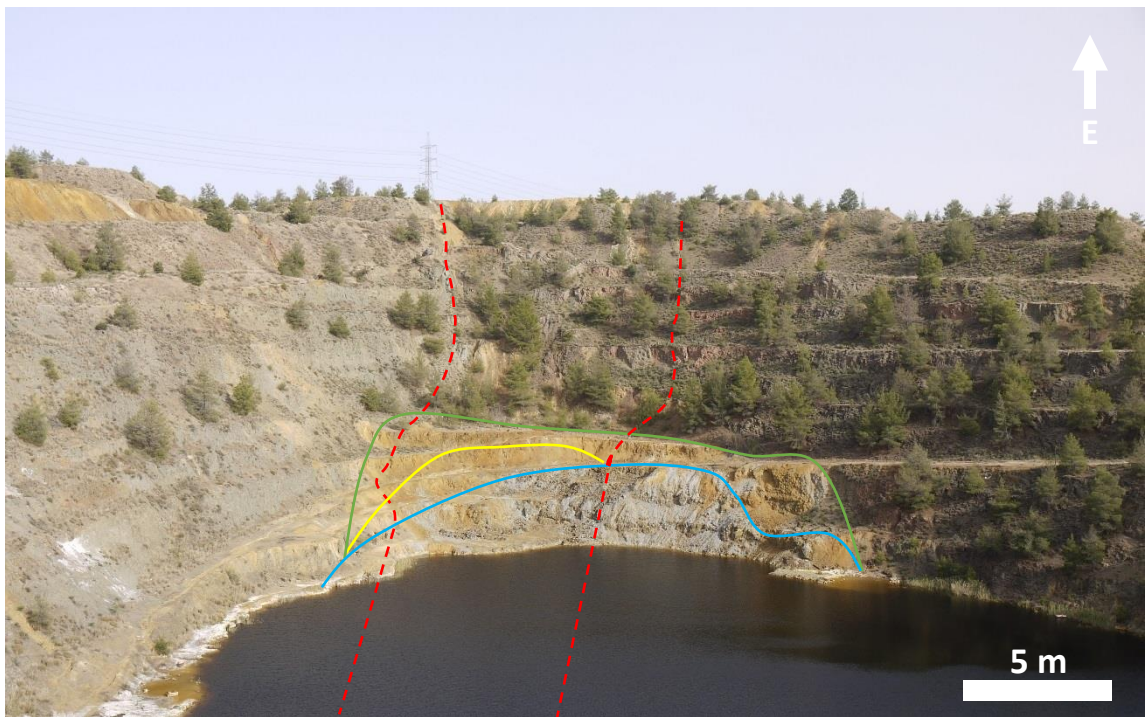


Figure A3.50: SE Pit wall. Blue line marks the extent of the semi silicified ore. Yellow line (highly Fe stained zone) is massive-semi-massive zone with sugary fresh pyrite. The upper (green) is silicified disseminated ore.



Figure A3.51: Stockwork veins of silica and pyrite in the base of the Mathiatis N open pit.



Figure A3.52: Fault plane and breccia in the lower Mathiatis N open pit.

## Location 11 Sha

### 11A) Location

Sha is located in the E part of Troodos. The mine is situated 1.4 km SW of Sha village and 3.6 km ESE of Mathiatis. The mine is easily visible from the main road to Sha from Mathiatis, make sure you go on a Sunday as you might get shot otherwise. The mine is classified as massive type on the GSD resource map and is situated at the LPL-UPL transition. In situ edge of mound sulfide and prolific jasper were sampled from Sha.

### 11B) Mineralisation

Preserved mineralisation at Sha is very good. The pit axis trends NE-SW. The NE end of the pit preserves in situ massive sulfide material. Sulfide ranges from massive to semi massive with abundant silica veining (Figure A3.56). Pyrite is the only visible ore mineral. Jasperitic veins generally <4 cm wide commonly cross-cut the area.

Massive-semi massive ore is enveloped by disseminated ore (several m thick). Pyrite is commonly found infilling vesicles or as mm scale euhedral crystals disseminated in green-grey LPL. The outcrop is typically highly Fe stained. As with the massive ore jasper veins commonly cross-cut the disseminated zone but do not transition into surrounding altered country rock. As with Mathiatis N the proportion of silicified areas at Sha is high. Is this coincidence I am seeing the exact same mound facies (the silica-rich margin), a common source rock, favourable tectonic position?

The zonation from massive to disseminated through to chloritised, silicified but not mineralised country rock appears consistent on all pit walls. On the SE pit wall unusual pipe like structures are observed (Figure A3.56). The origin of these is not clearly understood. Pipes are associated with semi-massive sulfide in otherwise un-mineralised bleached lavas (above) and semi-massive sulfide in the bench floor below. The pipes are typically wedge shaped and between 0.9 and 1.3 m wide. Pipes commonly have massive gypsum veins cross-cutting in a mesh texture.

### 11C) Structure

Two main trends are clearly evident within the Sha pit. The main mineralisation trend is NW-SE. Several faults on the NW pit wall trend 76 NNW/298, 62 ENE/330 and the SE pit wall measuring 40 NE/120, 66 ENE /142 and 60E/140 respectively. These faults are parallel to the Larnaca graben, downthrown direction is uniformly to the E toward the graben axis. Perpendicular to the main fault direction are numerous smaller faults (likely oblique normal or strike-slip). These faults strike NE-SW and occur readily on the N pit wall (e.g. Figure A3.53) measuring 76SSE/050, the high fault angle and oblique geometry to the main spreading ridge suggests a probable strike-slip motion.

A note on the continuation of Alpen Rose (Figure A3.55), there is no evidence for the continuation of Alpen Rose and the associated large quartz vein in Sha. Although the ridge does trend in a direction whereby it should intersect Sha the quartz vein is slightly oblique this trend and is pinched out half way along Alpen Rose (See Alpen Rose locality). The ridge immediately behind Sha was investigated but exhibits no silicification. It is clear that silicification is more prolific in this area than others warranting further investigation, especially for Au distribution.

11D) Samples collected

Sample	Grid reference	Brief description
16CA585	053411 3867860	Fault gauge
16CA584	053409 3867818	White bleached basalt
16CA585	053409 3867818	Hematite Fe stained gossan
16CA586	053412 3867853	Disseminated pyrite in basalt
16CA587	053414 3867843	Silica-sulfide rich material
16CA588	053419 3867869	Disseminated sulfide with jasper
16CA589	053423 3867874	White bleached basalts
16CA590	053423 3867874	Veined Fe fault material
16CA591	053423 3867874	Hematite fault related gossan
16CA592	053422 3867861	Upper sulfide horizon
16CA593	053422 3867845	Sulfide-gypsum pillowed material
16CA594	053421 3867790	Jasper with pyrite
16CA595	053423 3867799	Highly bleached vein

18E) Photos

Figure A3.53: View along pit strike. Pit is 190 m long and 70 m wide at its widest point. AMD is well developed. Massive sulfide is preserved at the base of the pit.



Figure A3.54: Outline of silica-rich ore that mantles the massive pyrite zone at Sha.



Figure A3.55: View W to neighbouring Alpen Rose and Mathiatis North.



Figure A3.56: Fault contact between massive sulfide zone at N pit face. Upper (hanging wall) is massive un-altered flows exhibiting minor brecciation whilst the footwall is kaolinised and Fe stained.



Figure A3.57: Massive jasper and pyrite boulder at the margin of Sha open pit.

Location 12 Peristerka12A) Location

Peristerka VMS is located 2.25 km NE of Kaphedes and 2.8 km SE of Kambia. The mine itself is private property and is located in a resort called "Angel Hills". Park the car at the gates and head right down the steep wooded bank, keep heading E and the mine will come into view. The mine itself is near inaccessible as the water level is so high. The waste tips are full of unusual mineralised samples. Peristerka is classified as massive on the GSD resource map and occurs at the BG-LPL transition.

12B) Mineralisation

Unable to comment as the mine is under water, a range of ore types are found within spoil suggesting a similar morphology as described above at Sha. Disseminated, massive and jasperitic ore were collected from waste. A series of dykes cross-cut pillow screens along both pit walls-typical of the basal-LPL transition. Dykes trend uniformly 030-040 dipping at 70-80° to the E. Faults are not clearly exposed however given the pit axis and the collapsed area in the E corner it seems reasonable to assume that this where the fault intersects the pit wall. The approximate strike of the fault is 234° dipping 48° NW (downthrown to NW). This orientation fits well with the overall tectonics of the area.

12C) Samples collected

Sample	Grid reference	Brief description
16CA283	052151 3872174	Slag
16CA284	052151 3872174	Jasper with pyrite
16CA285	052151 3872174	Massive sulfide
16CA286	052151 3872174	Silicified with disseminated pyrite
16CA287	052151 3872174	Silicified pillow
16CA288	052151 3872174	Disseminated pyrite in blue/grey

12E) Photos



Figure A3.58: Typical pit exposure, note abundant near-vertical dyke intrusions.



Figure A3.59: Fault zone in eastern pit margin. Increased leaching and oxidisation.

## Location 13 Troulloi

### 13A) Location

Troulloi is the furthest E VMS deposit in Troodos, it is the only VMS that lies E of the Larnaca graben axis. The deposit is located within the UN buffer zone 0.8 km SE of Troulloi village centre and is approximately 12 km N of Larnaca. Permission to visit the mine can be obtained from the UN peacekeeper Therapoulla Kalatha (+357 22 614421 or [kalatha@un.org](mailto:kalatha@un.org)). Head to the village church and take the street past the village council bear right and the mine is on you right next to abandoned mine buildings (200m). The deposit is classified by the GSD resource map as stockwork type ore. The deposit was most significant for its unusual umbers.

### 13B) Mineralisation and umbers

Mineralisation at Troulloi is mainly disseminated, brecciated mineralisation. Pyrite commonly occurs as fine <2mm cubic crystals within blue-grey UPL basalts, occasionally it forms aggregates within amygdaloidal lava. Pyrite also occurs in veins several cm thick, these veins in some cases look to contain trace chalcopyrite; this mineralisation is well developed on the E and S pit walls. Malachite is observed on the upper S pit wall within blue-grey UPL with a friable texture. Disseminated sulfides are common in the basalts up to 3-4 wt.%. Malachite occurs as a patchy surface coating. To the W of this locality Cu secondaries (as in Kokkinoyia) are associated with gypsum veins which measure 40 ENE/ 334 (NNW). Jasper was not readily observed in the pit but was found in waste as was more massive pyrite.

Umbers are very unusual at Troulloi; they occur infilling (or precipitated perhaps) along fault planes and infilling small hollows with later lava flows covering them (Figure A3.60). To the NE of the pit (behind massive red brecciated outcrop) lies a fault which measures 64 N/262. The fault zone is characterised by a zone of semi sheared umber, the zone is 'V' shaped and at its widest point 1.2 m. This could be interpreted in two ways; umber has precipitated along the fault plane and that the fault was feeding a Mn-Fe plume on the seafloor or that the fault "valley" was exposed on the seafloor and was filled in by VMS plume fallout. In this instance the first scenario is most likely. Field evidence suggests umber deposition was coeval with fault movement as the central zone of umber is clearly sheared. If it was simply a function of infill the umber would be bedded and not exhibit shearing.

There is plentiful evidence that in the Troulloi area that umber deposition was succeeded by magmatism, umbers are not commonly covered by lava flows. This occurs in two notable localities, firstly the NE corner, 5 m from the umber-rich fault gauge. The lower umber-lava contact is brecciated (as commonly seen at the umber-lava interface) and, as at Marki is silicified. UMBER grades to a massive non-silicified bedded unit no more than 1 m thick. This is then overlain by marginally altered UPL flows.

The second example is located on the upper SSW bench; a lens of umber is encapsulated in hematized basalt. At its thickest the umber lens is 1.2 m but pinches out in a sinuous horizon 50 cm thick. The lens morphology suggest umber deposition followed by magmatism and lava eruption and further umber deposition. Rocks surrounding the umber are oxidised to bright red colour a product of umber-lava interaction or fluid flow?

These localities are not entirely unique as a small umber outcrop at Theotokos is covered by later lava; the abundance and quality of outcrop makes them valuable. They show that umber may be precipitated away from the main VMS mound through faults and that umber deposition was coeval with magmatism not always the last depositional event.

13C) Structure

Fault directions at Troulli are complex, NW-SE faults appear to be the most common and are inferred as the main mineralising faults. Other smaller N-S and NE-SW faults commonly cross-cut the pit. Brecciation is very common throughout and is particularly prolific in the NW and SE corners of the pit. It remains unclear why N-S faults should occur in the area as they would not be active under either a strike-slip or normal geometry in relation to the Larnaca graben.

13D) Samples collected

Sample	Grid reference	Brief description
16CA616	055700 3876747	Bleached altered W zone
16CA617	055700 3876747	Limonitic veins
16CA618	055698 3876745	Fault gauge
16CA619	055697 3876745	Pyritic black matrix veins
16CA620	055697 3876745	Disseminated pyrite in basalt
16CA621	055693 3876769	Disseminate pyrite amygdaloidal basalt
16CA622	055697 3876759	Fault gauge with pyrite
16CA623	055699 3876774	Minor disseminated pyrite
16CA624	055697 3876729	Sulfide veins with gypsum
16CA625	055696 3876735	Cu secondary stained
16CA626	055696 3876735	Disseminated non- Cu stained
16CA627	055694 3876799	Gossanised veined basalt
16CA628	055693 3876820	Umber from fault plane
16CA629	055693 3876820	Green mineral S fault plane
16CA630	055692 3876839	Silicified basal umber
16CA631	055692 3876839	Non-silicified umber
16CA632	055691 3876764	Umber from main lens
16CA633	055697 3876711	Fine pyrite rich vein
16CA634	055696 3876698	Umber from faulted contact
16CA635	055691 3876713	Umber interstitial pillow material
16CA636	055696 3876785	Highly limonitic gossan material
16CA647	N/A	Jasper and pyrite from waste

13E) Photos

Figure A3.60: The Troulloi open pit.



Figure A3.61: Upper brecciated horizon 1 m from kaolinised fault plane above. Clasts as semi-angular Fe stained basalt with a limonitic-sulfate-rich matrix.



Figure A3.62: Umber infilling a fault plane surrounded by oxidised lava.



Figure A3.63: Typical breccia with hematite-pyrite matrix and sub-angular clasts.



Figure A3.64: Upper pillow lava 'tubes' exposed in the Troulloi pit.

Location 14 Limni14A) Location

Limni is the furthest W mine investigated in this study. Limni is located 3 km SSW of Argaka and 5 km NE of Polis. Heading from Pafos take the main road into Polis, just before the petrol station (left) there is a right hand turn (N). Follow the road for 4 km, you will come to a tree lined area just after the golf resort, take the dirt road on the right (past old buildings), continue for 1.5 km and the mine is on your left. Limni is classified as stockwork type on the GSD resource map. The pit is large (800 x 350 m) and now infilled with waste.

14B) Mineralisation

Mineralisation is hard to assess at Limni as very little exposure remains due to pit infilling. The south side of the mine is heavily gossanised. In this area lavas are commonly stained red to yellow, with hard silica-rich veins cross-cutting. Occasionally veins are dark brown and look to be sulfide-rich (commonly mm scale). Patchy jasper is also noted in these areas and is usually associated with faulting (and increase in temp and fluid flow etc.).

Continuing W along the S pit wall minor disseminated pyrite is noted. Pillows are fragmented and exhibit minor chloritisation. Pyrite is fine (1-2 mm) and cubic around 1 wt.%. Fracture intensity within the basalts increases heading N along the back wall and peaks in the centre of the pit (presumably where fault intersects).

The N pit wall is largely un-mineralised UPL, as the NE pit corner is approached mineralisation increases. This is the location of the main mineralising fault, the intensity of mineralisation is not that high with only disseminated pyrite observed, although this is probably a function of poor exposure as only the upper 10 m is exposed. At depth the mineralisation might be more prolific. Generally, the area is characterised by intense Fe oxide staining and prolific pillow fragmentation and minor disseminated pyrite.

14C) Structure

The main faulting direction of ESE (120/55SW) fits well with this hypothesis. There is no evidence to suggest that Limni is related to the Solea spreading axis; no N-S trending faults are observed in the pit. Small antithetic faults are observed on the E face leading to localised wall-rock kaolinisation (100/80SW). It is inferred these small antithetic faults would occur pit wide.

Locally in the N pit wall a small fault is noted measuring 60 NNE/284, these might be important in gossan formation with a well-developed gossan proximal to faults. They also locally control proportion of disseminated sulfides.

14D) Samples collected

Sample	Grid reference	Brief description
16CA289	045294 3877209	Vein material sulfide rich
16CA290	045293 3877235	Semi-silicified jasper
16CA291	045291 3877243	White altered lens
16CA292	045291 3877243	Hematite stock under lens
16CA293	045290 3877287	Vein material (Fe/hem/kaol)
16CA294	045288 3877778	Disseminated sulfides
16CA295	045316 3877636	Un-mineralised lava
16CA003	0452729 3877157	Disseminated chloritized basalt
16CA004	0452854 3877130	Coarse euhedral and agglomerate pyrite
16CA005	0453034 3877114	Covellite + pyrite veins
16CA006	0453303 3877169	Bleached basalt from fault zone

## 14E) Photos



Figure A3.65: View looking E of Limni open pit. The pit has been nearly completely back filled with VMS waste. The pit is underlain by a geomembrane to stop AMD production.



Figure A3.66: Main mineralising fault exposed in E pit corner. Footwall is heavily brecciated and Fe stained with disseminated sulfides.

Location 15 Kynousa15A) Location

Kynousa VMS is located in W Troodos. The mine is 0.4 km SE of Kynousa village and 1.9 km E of Limni mine. To access the mine take the coast road and take the turn just after Limni mine, you should climb parallel to Limni. Head through the village and just before the road turns to dirt the mine will be on the left. Kynousa and Uncle Charles are classified as massive on the GSD resource map, they are also Zn rich. They occur on the BG-UPL boundary. The pit is small only 100x60 m and outcrop is poor as it's covered in dyke scree. Good massive sulfide samples were obtained from waste.

15B) Mineralisation

It was clearly evident that Kynousa occurs within the basal group due to the abundance of scree and the lack of any pillow structures. The lack of any pillow material suggest Kynousa formed "deep" within the BG and not at the transition between the LPL and BG (e.g. Peristerka); in the more shallow deposits pillow screens are common. Massive sulfide in the NE corner was coarse grained >4-5 mm pyrite (no sphalerite or chalcopyrite) and very little disseminated pyrite mineralisation was observed.

15C) Structure

Structure was very hard to interpret in the Kynousa pit. The only sign of faulting was a breccia zone on the E wall, just above the open pit. A zone of 3 m of visible brecciation within the wall rock is noted, breccia is clast supported with fine quartz veins (up to 1.5 cm). BG dykes appear amygdaloidal with white (zeolite) minerals, distinctly different from the dense non vesicular scree from surrounding BG. The fault zone is inferred to trend E-W/280 and appears to control mineralisation. Given the pit morphology and the occurrence of quartz-pyrite breccia in the NE corner a minor fault is inferred trending NE-SW (040).

15D) Samples collected

Sample	Grid reference	Brief description
16CA523	045555 3876810	Spoil: Massive sulfide
16CA524	045555 3876810	Disseminated blue/grey
16CA525	045555 3876810	Disseminated within quartz
16CA526	045555 3876810	Quartz with tarnished CCP
16CA527	045555 3876810	Sulfide stringers in bleached basalt
16CA528	045555 3876677	Breccia with quartz veins
16CA529	045555 3876677	Amygdaloidal blue green basalt
16CA560	045560 3876644	Celadonite, qtz breccia
16CA561	045540 3876817	Mineralised fault breccia
16C1562	044540 3876820	Qtz vein in basal group
16CA563	045546 3876557	Slag
16CA564	045549 3877014	Orange-limonitic to white alteration
16CA565	045549 3877014	Hematite deep red
16CA566	045540 3877090	Gossanised zone

15E) Photos



Figure A3.67: Lysos/Kynousa pit exposure. Massive sulfide in NE corner of pit.



Figure A3.68: Gossan exposure uphill from main pit exposure.



Figure A3.69: Pyrite associated with quartz breccia to the N of Kynousa pit.

## Location 16 Mala

### 16A) Location

Mala VMS is located in the Pafos forest 3.8 km E of Pano Panagia or 30 km directly N of Aphroditis Rock. To get to Mala take the turning for Agia Varvara (Pafos district) and follow the road for 25 km through the mountains. It is a dirt road so if it's wet you would definitely need a 4WD. The mine is only accessible via one small road. GPS co-ordinates for satnav (34 55 108 N, 32 40 575 E). The deposit is classified as massive and Cu-Zn rich on the GSD resource map and occurs on the BG-LPL transition. Excellent in-situ massive ore was collected from Mala.

### 16B) Mineralisation

Lower pillow lavas appear highly vesicular, dark grey and in areas amygdaloidal (white zeolite mineral). They are aphyric and interestingly no celadonite is observed (unlike Agrokippia) this is surprising especially when considering the elevated geothermal gradient around the mound. The second basal group lithology is dyke material. This typically lacks vesicles, is finely crystalline <1 mm and occurs as massive flows and dykes. Quartz veins (a few mm wide) commonly occur at flow margins. Flow dip is variable towards the SE end of the pit measuring 30W/024. These observations are in agreement with the GSD resource map and place the deposit at the LPL-basal transition.

The NE pit face is highly brecciated and gossanised (Figure A3.72 - at least 20 m of exposure). Within the pit wall pods of much less altered material are noted. The distribution of gossanisation within a very limited area raises the possibility of a small graben crosscutting the main pit axis? The geometry of this seems unlikely. Within the gossan stringers of sulfide commonly cross-cut light coloured altered LPL, veins are typically pyritic and <2 cm thick.

Continuing N along the NE face a fault cross cuts the face, at this point two lenses of massive-semi-massive sulfide occur. The contact between the sulfide and surrounding dolerite is sharp and suggests the body was originally one but has been truncated by a later dyke. The dyke below has subsequently experienced some fluid flow and is weakly mineralised with disseminated pyrite. This looks as though it might have formed the margin of the mound and has been truncated in the late stages of VMS formation, probably by dykes feeding the UPL.

In front of the massive sulfide (on the "sulfide delta") disseminated sulfide is prolific, Coarse grained pyrite is abundant (5-10 wt.%), basalts are blue grey. Occasional lens of massive to semi-massive sulfide occurs. Jasper and quartz is found at the margin of massive and disseminated facies. The massive sulfide itself is characterised by pyrite with interstitial quartz (>10%) and secondary sulfate (gypsum; up to 100% in places). Samples were collected through the mound to ascertain variation in Te and Se with depth in the ore body (although higher samples are highly weathered). Interestingly throughout the body (clearly evident in Figure A3.71) are these waxy sulfate bands with no pyrite. Why the layered appearance? A function of mound growth? Each band is an influx of geochemically distinct fluid. Sulfate bands are bright white with a vitreous lustre. No chalcopyrite was observed.

The top of the mound is truncated by a flow. Behind the flow there appears to be a small sulfide horizon. Was this post formation? The VMS had completely finished forming and the dyke intrusion simply displaced the top of the mound or does this horizon represent a separate event as we see at Skouriotissa, sulfide then lava then repeat sulfide accumulation?

16C) Structure

Two fault directions control the distribution of mineralisation at Mala; the main direction is parallel to the pit axis trending NW-SE (no fault plane to measure). Given the extreme elongation of the pit (and thus mineralisation) it seems likely the fault strikes the same direction. The second fault is responsible for the bulb like pit morphology and the truncation of the small sulfide lodes as outlined previously, measures 42 ESE/016.

16D) Samples collected

Sample	Grid reference	Brief description
16CA567	047046 3864224	Amygdaloidal pillow
16CA568	047045 3864259	Veined bleached basalt
16CA569	047045 3864259	Hematite rich
16CA570	047045 3864259	Sheeted material with Cu staining
16CA571	047045 3864259	Kaolinised basalt
16CA572	047044 3864275	Cu stained dark pillow material
16CA573	047042 3864323	Massive semi-massive body A
16CA574	047042 3864323	Massive semi-massive body B
16CA575	047039 3864317	Blue-grey disseminated sulfide
16CA576	047039 3864317	Lower most massive sulfide
16CA577	047039 3864317	Jasper with quartz and pyrite
16CA578	047039 3864317	Mid VMS mound material
16CA579	047039 3864317	Top of VMS mound
16CA580	047039 3864317	Massive sulfate band
16CA581	047037 3864314	Ex-situ massive sulfide material
16CA582	N/A	Slag

16E) Photos

Figure A3.70: Overview of the open pit. Note elongate pit exposure.



Figure A3.71: Massive sulfide mound NW Mala pit wall. Mound is homogenous massive pyrite with interstitial sulfate (<10%).

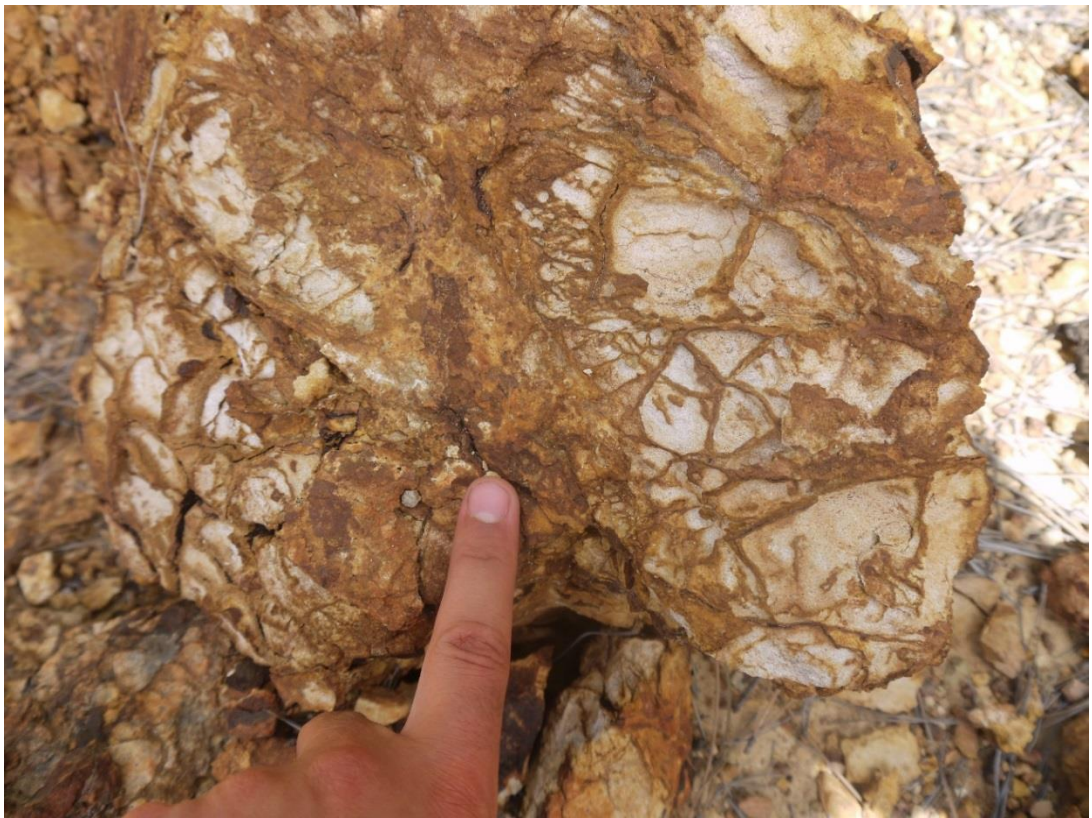


Figure A3.72: Stockwork veins in wall-rock. Oxidised pyrite.

Location 17 Memi17A) Location

The Memi VMS deposit is located 7 km W of Kokkinopezula, 1.4 km SW of Agia Marina and 0.7 km N of Xyliatos. The deposit is classified as massive on the GSD resource map with historic extraction of 1.5 Mt. The deposit is located 1 km NE of the 'unusual' Alestos deposit. The pit was challenging to access as the water table is very high. The faulted NE pit corner is accessible via the drainage ditch. To access the NW face, drive and park round the back of the spoil heaps and access this way as the pit walls are too unstable to navigate around the side.

17B) Mineralisation

Memi formed within the LPL, possibly, given the low abundance of vertical BG dykes towards the LPL/UPL transition. Pit walls are composed of sub horizontal flows up to 3 m thick often exhibiting columnar jointing and celadonite staining. Pillows are fragmented and again celadonite stained, celadonite commonly infills vesicles. Increased fragmentation correlates with celadonite abundance and thus increased permeability. The SE wall was inaccessible but from a distance appear darker in colour and less altered.

In general with the exception of a highly weathered 2x1 m zone within the NE corner (adjacent to fault zone) no massive sulfide (in situ) remains. The patchy highly weathered clay material is interpreted as weathered massive ore and is similar to that observed in Kaphedes. Massive ore, disseminated ore and jasperitic ore were collected from waste.

Samples collected from the waste pile exhibit evidence of multiple fluid phases (Figure A3.74), a box-work texture is common, similar to that observed at Mathiatis suggesting dissolution of early mineral phases, No real silicification is noted although quartz does occur in the SW corner within sulfide vein inter pillows.

17C) Structure

The fault zone in the NE corner is characterised by a zone 6 m wide of increased Fe staining (Figure A3.73), both footwall and hanging wall rocks are heavily gossanised. Kaolinisation is patchy and localised to the NW (footwall) of the fault. Bleached LPL are cross-cut by mm scale limonite-goethite stringers that are interpreted as weathered sulfide veins. Fine disseminated, cubic pyrite (<1 mm) is readily observed in the vicinity of the fault plane. Fault breccia is found only within a very narrow 1 m zone, matrix supported and poorly exposed. The fault looks to link with a zone of Fe stained degraded pit wall on the opposite pit face suggesting a trend of NE (040) with down-throw towards the SW. Need to ascertain how this deposit relates to Alestos, clearly this is older as its stratigraphically deeper (LPL) in comparison to Alestos which is UPL.

17D) Samples collected

Sample	Grid reference	Brief description
16CA212	050366 3877476	Slag
16CA213	050366 3877476	Disseminated sulfides
16CA214	050366 3877476	Sulfide with clay matrix
16CA215	050366 3877476	Kaolinised basalt
16CA216	050366 3877476	Hematite/ jarosite rich gossan
16CA217	050347 3877622	Silicified breccia (ex-situ)
16CA218	050336 3877421	Fe/Si matrix material
16CA219	050336 3877421	Non silicified matrix material
16CA220	050336 3877389	Jasper material from pillow margin
16CA221	050336 3877389	Purple pillow margin

24E) Photos



Figure A3.73: NE fault zone delineated by increased oxidation and brecciation.



Figure A3.74: Jasper-stockwork vein exhibiting a boxy dissolution texture



Figure A3.75: Massive euhedral pyrite (pyritohedrons).

Location 18 Alestos18A) Location

The Alestos deposit is located on the central N flank of Troodos. It lies 1.6 km WNW of Xyliatos and is 1.3 km SSW of Memi VMS. This deposit is located on a topographic high in the area (605 m), surrounding land and the Memi VMS deposit is at 355 m. Geologically the deposit lies within a small outcrop of UPL surrounded to the W by BG within LPL. To the W lies the Alestos Forest Fault (apparently an N-S trending ridge parallel fault). The relationship between Alestos and Memi and its mode of formation are debated: it is clearly not a typical VMS.

18B) Mineralisation

No massive mineralisation was evident at Alestos. Firstly it is important to note the unusual colour of the lake at Alestos, it is not the usual AMD red but instead a deep blue/green (Figure A3.75/76), this suggests that there is a greater abundance of Cu minerals than pyrite (hence the blue colour). Pipes surrounding the lake suggest it might have been used as a reservoir for hydrometallurgy processes? Cu sulfates are commonly found at the margin of the lake. A green lake is not observed at any other VMS.

No massive mineralisation is evident at Alestos, instead mineralisation is confined to bands of intense brecciation. No primary Cu sulfides were observed in hand specimen, only euhedral fine grained (<2-3 mm) pyrite. The occurrence of disseminated pyrite was limited to the SW pit wall.

Wall rock alteration is intense throughout Alestos, UPL are extensively chloritised (Figure A3.80). A patchy pink material is also noted and occurs readily (up to 50%) in chloritised areas. Chloritised areas are variably veined by small <3mm quartz stringers (with accessory pyrite). The rock itself may be variably silicified if the intensity of veins is high enough. Typically a box work texture is noted on all but the SE pit wall, indicating multiple fluid phases.

The SE pit wall was distinctly more altered than all others. Basalts over 6-8 m are intensely bleached and have been subsequently silicified (very hard and dense, unlike bleached material from Kokkinovounaros). The white grades to more typical green chloritized faces to the W. Within the most altered white areas blebs of Cu secondaries (most notably azurite) are noted; no primary chalcopryite was observed in the pit itself.

18C) Structure

The structure of Alestos was very hard to decipher as everything was so intensely brecciated, however clear fault planes were visible at a few localities. Fault planes (Figure A3.81) were typically mineralised with disseminated pyrite and had a much finer matrix supported breccia and were less intensely chloritized than surrounding rock. Faults measured e.g. 68E/004 to 62 W/342. Strike is relatively uniform however dip seems to vary, this suggest the deposit is situated within a small horst structure or that faults formed under different opposing stress regimes related to both Solea and Mitsero grabens.

18D) Samples collected

Sample	Grid reference	Brief description
16CA177	050232 3876999	Blue-grey veined lava
16CA178	050229 3876799	Massive jasper vein
16CA179	050231 3876957	Unusual silicified vein
16CA180	050228 3876941	Box-work
16CA181	050225 3876948	Highly bleached dense basalt
16CA182	050225 3876948	Cu 'nuggets' from surface

16CA183	050225 3876948	Minor veined green lava
16CA184	050225 3876948	Chloritized veined lava
16CA185	050225 3876948	Fault breccia, jasper with blue-grey
16CA186	050224 3876922	Blue-grey lava with minor veining
16CA187	050224 3876937	Black matrix breccia
16CA188	050224 3876937	Massive pyrite
16CA189	050219 3876830	Minor jasper in basalt
16CA190	050219 3876830	Sulfide vein
16CA191	050219 3876830	Box-work ore
16CA192	050219 3876830	Blue/grey breccia clast
16CA193	050219 3876830	Mystery massive black ore
16CA194	050220 3876948	Sulfide veins with jasper
16CA195	050226 3876936	Light coloured breccia

## 18E) Photos



Figure A3.76: View over Alestos pit looking towards “Alestos Hill”. Lower regions appear more heavily Fe stained, this is however a function of outcrop freshness (they are more weathered). Gossan is well developed (red hematite) to the W of Alestos Hill.



Figure A3.77: Highly bleached material with minor azurite and malachite.



Figure A3.78: Jasper interpillow material. Jasper infills between fragmented pillows and veins pinch out and boudinage. Note intense chloritisation of basalts.



Figure A3.79: Copper sulfate precipitate at lake margin, the lake is uncharacteristically green in colour compared to the traditional deep red colour of a 'normal' VMS AMD.



Figure A3.80: Quartz stringers with a chloritized quartz amygdaloidal basalt. Very common in almost all wall rock.



Figure A3.81: Hematite breccia with chloritised wall rock. Pyrite and hematite coexist- Similar to SABZ.



Figure A3.82: Typical wall-rock alteration. Hematite and chlorite with quartz veins.

Location 19 Kalavassos19A) Location

Kalavassos mining district is located 4 km NW of Kalavassos village and 1.5 km NE of Asgata. The mines are located within the STTZ. The district comprised several small mines, mining was mainly conducted via underground methods. Notably Kalavassos mines are enriched in Au, possibly a function of the increased boninitic/mafic lava? Does this have any implications for Te and Se? Indicated geology for the area is LPL-BG transition and the deposits are classified as stockwork and massive on the GSD resource map. Continue on road towards dam and take small dirt track on sharp hairpin corner past signs for active firing range.

19B) Mineralisation

In comparison to other VMS deposits, Kalavassos was comparatively sulfide poor, or at least sulfide was not present at the surface. Mineralisation was limited to the LPL and gossan. LPL's are characteristically green-grey, large vesicles and aphyric. Disseminated pyrite <2mm are common within the LPL, it should be noted that this was only observed in the W and SW pit corner, no disseminated sulfides were evident on the "main" NW pit wall. The SE pit exposure is now covered by a landslide (Kalavassos formation- chalky marls etc.).

The gossan where accessible was sampled and could possess potential to host Au mineralisation. There is also lots of kaolinisation and bleaching on the E part of the NW wall (as you enter mine to your immediate right).

19C) Structure

As you enter the main pit lithology changes, basalts become less fractured and intensity of BG dykes increases, this then rapidly grades into highly fractured basalts (over 10 m) to the SE. Small faults along road into mine trend 60 NE/314 whilst main mineralising fault trends 65E/340. Is the white plane a fault related feature, its linear and continuous across whole pit and strikes NNE? Faulting is also associated with Cu secondaries on the road into mine. Need to better understand the structure of Kalavassos and why the district is so closely spaced and confined to a very limited area.

19D) Samples collected

Sample	Grid reference	Brief description
16CA196	052368 3850398	White bleached fault gauge
16CA197	052368 3850398	Fe rich matrix material
16CA198	052368 3850375	Globular pyrite within quartz
16CA199	052369 3850324	Hematised fault gauge
16CA200	052371 3850315	Cu rich vein material
16CA201	052371 3850315	White heavily bleached material
16CA202	052371 3850315	Yellow stained upper
16CA203	052369 3850291	Kaolinised banded Fe scree
16CA204	052356 3850308	White bleached ridge material
16CA205	052356 3850319	Clay, possibly S rich?
16CA206	052354 3850311	Crust from fault plane
16CA207	052354 3850311	Ex-situ gossan
16CA208	052350 3850274	Fine breccia
16CA209	052349 3850277	Sulfide rich vein
16CA210	052350 3850226	Hematised clast
16CA211	052350 3850226	Disseminated sulfides- blue grey

## 19E) Photos



Figure A3.83: Typical pit exposure at Kalavassos. Well-developed bleached gossan underlain by flow and lavas cross-cut by ultramafic dykes.

# **Low temperature silica-rich deposits**

- Kokkinovounaros
- Mathiatis South
- Alpen Rose
- Touronjia
- Theotokos

## Location 20 Kokkinovounaros

### 20A) Location

Kokkinovounaros is an elongate (N-S) mineral prospect in the Analiontas-Kambia area of central-eastern Troodos. The deposit is best approached from the village of Analiontas (heading from Agia Varvara) take the turning just before you enter Analiontas, from Kambia drive through Analiontas). The deposit is 1.9 km SW of Analiontas and 0.5 km SE of the Kambia VMS deposit. The deposit is not a VMS as minimal sulfide mineralisation is present, it is instead Au-rich and was historically mined as an Au deposit.

### 20B) Mineralisation

Alteration at Kokkinovounaros is extremely intense and is clearly fault controlled. The deposit is split into three areas; Pit A (main) and Pit B (N of road) and the southern limb (S of main road). Due to time constraints the bulk of the study will be focused on pit A and B. Mineralisation can be broadly categorised into Au-rich (silica, hematite, jarosite etc.) and sulfide-rich (silicified and pyrite bearing). The two facies are spatially associated with different generations of faulting, clearly fluids had a very different redox/geochemistry.

The main pit is characterised by a large well exposed fault measuring 58 W/002, radiating laterally from the fault are zoned facies of alteration which signify decreasing alteration intensity with distance from the fault plane. The deposit is situated within the LPL. Most lithologies within a narrow 30-40 m zone surrounding the main fault are so intensely altered that they are unrecognisable as lava (Figure A3.85).

**Pit A:** Pit A or Main Pit is the most intensely altered zone, the pit has been historically mined for Au that is thought to occur within the most intensely altered bleached basalts. The pit measures approximately 30 x 60 m with a N-S (002) trending fault cutting through the middle. Figure A3.85 clearly highlights the zoned nature of the mineralisation at Kokkinovounaros. The fault plane is clearly the most intensely altered zone and is characterised by white, silica-rich, leached basalt (advanced argillic). Silica leached basalt lacks any relict igneous features and is very low density and highly porous. This zone is massive for 1-1.5 m both sides of the fault plane and then grades over 50 cm into goethite dominated facies. Intense silicification (leaching) boudinages along fault strike, it may be up to 4-5 m in some areas where smaller faults intersect the main mineralising structure. Bleaching of lava is also observed in patches and pockets several m away from the fault, this is interpreted as local permeability variations.

Grading laterally from the fault plane are banded facies of jarositic, goethite and hematitic alteration (broadly parallel to the fault plane). At the margin between alteration facies wall rock is often silica-rich but contains veins of goethite (relict sulfide stringers?). The alteration package is 30-50 m wide in total. The outer 10 m is characterised by purple coloured, weakly hematized lava that is cross-cut by a network of fine (<3mm) limonitic stringers. Alteration in these outer areas is not pervasive and limited to veins. Within these distal facies pyrite voids are commonly cubic, euhedral, and generally coarse grained.

To the W, near F2 (approximately 25 m W of F1) vein hosted silicification is noted; massive quartz veins occur within hematized LPL. Veins are typically 8-10 cm wide and orientated near vertical and are parallel to F1/F2. Pyrite occurs as globules within quartz. Is the pyrite from early fluids or associated with the same fluid as the silicification? It is interesting that silicification is associated with pyrite as this is not common in other deposits. It is clear from the distribution of silicification that it is associated with F2 not F1.

**Pit B:** Alteration is less extensive and highly bleached white leached lavas as observed surrounding F1 in Pit A are absent. Brecciation is well developed and typically angular, clast supported with an average clast size of 8-10 cm. Alteration is typically hematitic with patchy jarosite. The transition and variation in alteration along fault strike suggests fluid flow was focused in Pit A and then migrated laterally along strike, the source was seemingly focused. This could be a function of the density of cross-cutting faults (i.e. Pit A has more and is therefore more highly mineralised).

### 20C) Structure

Two main faults control the mineralisation and subsequent supergene alteration at Kokkinovounaros, they strike parallel approximately 40 m apart. The faults are normal with F1 occurring in the main pit measuring 78W/350, the fault is normal with downthrow to the W. The fault is traceable along strike for some 370 m, it is visible in pit B and on the S side of the main road that cuts through the mineralised zone. Alteration intensity decreases to the S.

F2 is not as clearly exposed but is visible as you follow the road down slope from the main Kokkinovounaros pit. F2 measures 58W/002 making it approximately parallel to F1. The fault plane exhibits only minor brecciation and in comparison to F1 only minor mineralisation.

F3 faults are rarely encountered with the exception of Figure A3.87 found within exploration trenches. These faults are believed to have an oblique normal-strike slip geometry. In pit A cross-cutting faults are inferred to be an important feature causing localised dilation and increasing permeability and thus mineralisation. It remains unclear, due to extensive brecciation the extent and influence of these small F3 faults.

It is clear from the scale and variety of breccia found at Kokkinovounaros that these faults are major features that show multiple periods of brecciation followed by mineralisation and then overprinting by further mineralisation (see alteration textures and veining textures). It is also clear that F1 and F2 have significantly different attributes in terms of alteration intensity and mineralogy. F1 exhibits the most intense alteration to silica dominated lithologies (advanced argillic), whilst F2 only minor sulfides and silicification.

### 20D) Samples collected

Sample	Grid reference	Brief description
16CA032	052523 3872643	Hematized pillows
16CA033	052523 3872643	Fe/Mn matrix material
16CA034	052523 3872643	Fe/Mn matrix material
16CA035	052523 3872643	Un altered pillow
16CA036	052523 3872547	Brecciated hematized pillows
16CA037	052523 3872547	Intensely altered fault zone
16CA038	052523 3872547	Orange yellow, jarosite-limonite zone
16CA039	052523 3872547	Hematized distal fault zone
16CA040	052523 3872547	Green mineral- Cu rich?
16CA041	052523 3872547	Kaolinised bleached
16CA042	052523 3872547	Interstitial Fe material
16CA043	052521 3872559	COMP brown yellow altered
16CA044	052521 3872434	COMP white/pink
16CA045	052521 3872542	COMP white and orange patches
16CA046	052521 3872529	COMP Red-White
16CA047	052521 3872516	COMP white alteration
16CA048	052521 3872511	White kaolinised breccia
16CA049	052521 3872525	COMP white fault zone
16CA050	052521 3872517	White coating orange
16CA051	052522 3872533	Red clast
16CA052	052522 3872370	Highly altered soft white
16CA053	052522 3872549	Red/yellow gypsum
16CA054	052524 3872560	Gypsum with green mineral and Fe
16CA055	052524 3872560	Baked margin- gypsum rich
16CA056	052524 3872560	Stained slumped gypsum
16CA057	INSIDE ADIT	Fault breccia
16CA058	INSIDE ADIT	White vein wall material

16CA059	052525 3872591	Silicified ochre
16CA060	052525 3872591	Silicified umber
16C1061	052524 3872584	Non silicified umber
16CA062	052524 3872584	Upper silicified ochre
16CA063	052518 3872556	Matrix material infilling basalt
16CA064	052518 3872556	Massive qtz vein material
16CA065	052518 3872556	Pillow interior material
16CA066	052517 3872550	Jasper rich matrix surrounding pillow
16CA067	052517 3872519	Purple altered pillow
16CA068	052517 3872520	Hematized red pillows
16CA069	052518 3872512	Kaolinised zone
16CA070	052519 3872510	Fault breccia from trench
16CA071	052519 3872511	Gossan
16CA072	052522 3872512	Bright green Cu? mineral
16CA073	052522 3872512	White hanging wall material
16CA074	052522 3872512	Fe/hematite sheared sample
16CA075	052522 3872512	Fe basalt matrix material
16CA076	052323 3872525	Veined white with interstitial Fe
16CA077	052323 3872525	Intense hematite veined
16CA078	052523 3872538	Highly bleached pillow
16CA079	052525 3872543	Jasper with pyrite dissolution
16CA080	052522 3872509	Sheared basalt hematite
16CA081	052521 3872449	Fault breccia Fe matrix
16CA082	052521 3872460	Massive hematized basalt
16CA083	052521 3872460	Silicified umber
16CA084	052521 3872460	Silicified ochre
16CA085	052521 3872460	Silicified jasper with pyrite
16CA086	052520 3872459	White composite W face
16CA087	052520 3872459	Orange composite W face
16CA088	052520 3872459	Red hematite W face
16CA089	052520 3872459	Orange composite E face
16CA090	052520 3872459	Silicified fault breccia
16CA091	052521 3872462	Composite white matrix
16CA092	052521 3872462	Clast material
16CA093	052520 3872459	White composite E face
16CA094	052524 387442	Silicified umber
16CA095	052524 387442	Silicified ochre
16CA096	052518 3872456	White with red pyrite rich veins
16CA097	052522 3872456	Non-silicified umber
16CA098	052530 3872342	Altered pillow with veins
16CA099	052543 3872387	Si ochre
16CA100	052543 3872387	Si Jasper with green staining

## 20E) Photos

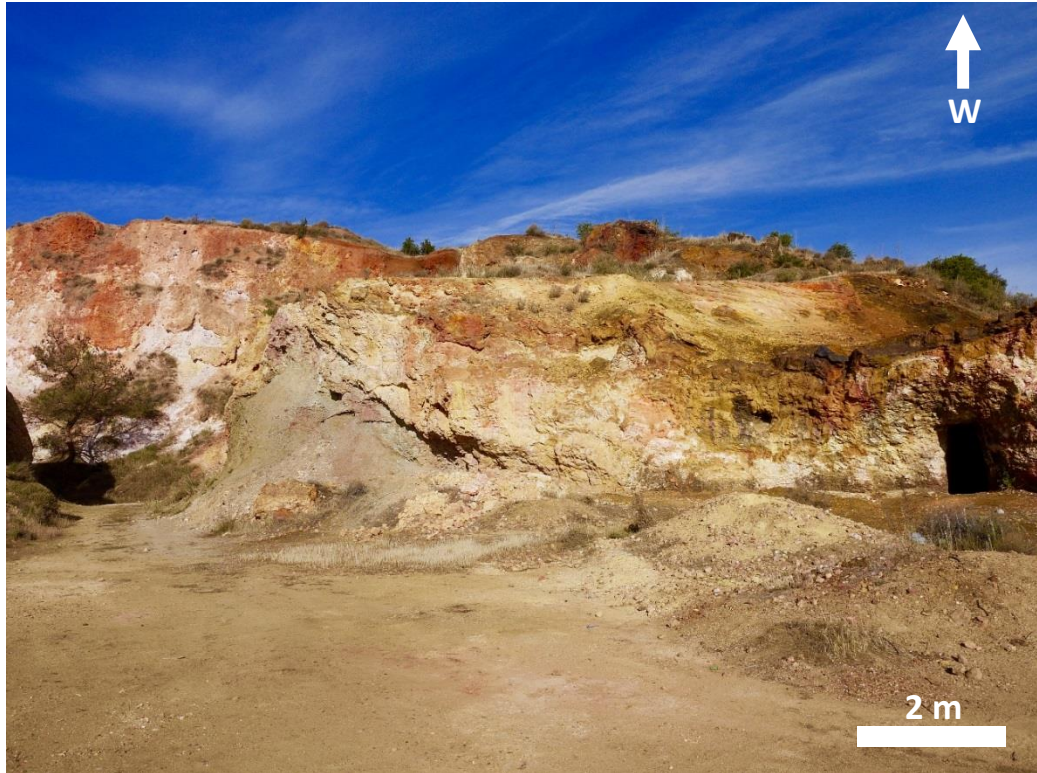


Figure A3.84: View looking W over Kokkinovounaros. Country rock is highly altered to a range of coloured facies: leached silica (white), goethite (yellow) and hematite (red). The deposit is formed at the seafloor as indicated by the presence of umber.



Figure A3.85: View looking N along strike of the main fault. Note extensive supergene alteration of lavas.



Figure A3.86: Veins cross-cutting hematised lava. Veins are jarosite-goethite, probably formed through pyrite oxidation.



Figure A3.87: Small fault crosscutting an exploration trench on the upper level of Kokkinovounaros.



Figure A3.88: Thin veneer of uranium above exploration adit that occurs in highly bleached brecciated lava.



Figure A3.89: Veined hand specimen. Goethite veins in a leached silica-rich matrix.



Figure A3.90: 'Unaltered' lava from lava dome with malachite and gypsum along contact.



Figure 3.91: Lava dome situated adjacent to main fault (bleached white area).



Figure A3.92: Un-silicified umber to the S of Kokkinovounaros.

## Location 21 Mathiatis South

### 21A) Location

Mathiatis South is located 1.8 km SE of Mathiatis village. To access the deposit head into the Mathiatis village centre and follow the main road to Sha. Follow for 350 m and turn right (you should see a pink house in the distance). Follow this road for 900 m and you will reach a dirt cross roads, turn left. If you hit the army barracks you have taken the wrong road. Follow the gravel track for 400 m and the deposit will be visible on your left, there is a house on the right side of the road. The deposit is an unusual gossanised zone, historically mined for Au and minor BMS. The deposit is complex and the structural features are very hard to distinguish due to the prolific brecciation.

### 21B) Mineralisation

Mathiatis South is a midpoint between mineralisation observed in a typical VMS and what we see at Kokkinovounaros. It exhibits both massive sulfide mineralisation as well as well-developed silica patches and gossanisation (Figure A3.93). Historically the prospect has been mined for BMS but today it is being investigated as a Au prospect.

The northern area of the deposit is now exhausted (20x40 m pit), presumably representing the main massive sulfide mound. The sulfide exposure is surrounded by variably altered banded to brecciated silicified and hematized zones. Jasper veins are common and cross-cut all alteration facies. The whole outcrop is highly brecciated but some zones appear more highly brecciated and are inferred to be fault planes. Behind to the N the gossan is well developed and consistently >2 m thick.

On the adjacent pit wall (SW) no evidence of massive sulfide is observed. The pit wall is characterised by two distinct lithologies; a soft Fe stained breccia cross-cut by hard jarosite veins (later silicification?). The second lithology (similar in retrospect to Touronjia) is a light-coloured silica-rich highly porous breccia; this infers dissolution of early mineral phases or an epithermal 'uggy silica' texture? It could contain significant Au.

To the SE there is a well exposed massive to semi-massive sulfide mound (approximately 5 m wide). Samples (252-255) appear to show zone refining with depth through the mound; the base is Cu-rich (secondaries not primary CCP) whilst the top is massive pyrite. The surrounding country rock is highly gossanised blocky and surrounded by Fe stained pillows.

The back (S) pit wall (Figure A3.94) is complex with no clear controls on mineralisation or distribution of alteration facies. The western exposure appears to exhibit a sub-horizontal banding in alteration facies; small 3-4 cm veins cross-cut brecciated white pillows. Towards the base veins become thicker (up to 10 cm) and are black in colour (Mn-rich?). The package is overlain by a 2.5 m patchy horizon, nodules of up to 60 cm appear white but when chipped are orange in colour. Both the lower layered and upper patchy horizons are cross-cut by a hematite band.

In the upper most S pit wall, alteration facies are interwoven, in general silicification (bleaching) is dominant. Near horizontal very hard limonitic (>10 cm wide) veins cross-cut the silicified wall-rock. Sporadic patchy silicification is common and is not obviously structurally controlled. Gossan is well developed and sporadic in distribution. In the uppermost SE corner some zonation is observed (similar to Kokkinovonaros) a central silicified 'pipe' grades to Fe facies then hematite.

It appears that multiple fluid phases are evident at Mathiatis South, an early high temperature phases which is responsible for massive sulfide formation which is then overprinted by Si-rich fluids that have laterally migrated into surrounding rock exploiting fault planes.

### 21C) Structure

The main fault direction is inferred from a colour change in the S pit wall, hematite facies is clearly visible on one side whilst silica and limonite on the other. Inferred strike is 320 (NW-SE), this is in agreement with the proposed Larnaca graben axis. Ultimately it remains unclear and speculative as alteration and brecciation is so intense no fault direction can be clearly established. It is inferred that where these two faults cross main VMS mineralisation occurs (W pit area).

### 21D) Samples collected

Sample	Grid reference	Brief description
16CA228	053168 3867685	Kaolinised
16CA229	053168 3867685	Fe veined
16CA230	053168 3867685	Massive jasper vein
16CA231	053168 3867692	Hematite breccia pipe
16CA232	053167 3867695	Sulfide rich- once massive sulfide?
16CA233	053168 3867704	Upper hematitic veins
16CA234	053168 3867704	Lower Cu veins
16CA235	053168 3867704	Western most stained material
16CA236	053168 3867704	Sulfate boulder
16CA237	053168 3867704	E most dipping Fe material
16CA238	053168 3867704	Green mineral (v dark green)
16CA239	053168 3867712	Gossan material
16CA240	053168 3867712	Kaolinised cap to sulfide zone
16CA241	053171 3867653	Unaltered fine breccia
16CA242	053171 3867653	Altered limonitic
16CA243	053172 3867666	Grey material with patchy oxidation
16CA244	053172 3867668	Sandy coloured clay
16CA245	053170 3867685	Hematite pod material
16CA246	053167 3867667	Hematitic matrix/fault gauge?
16CA247	053170 3867643	Brecciated kaolinised
16CA248	053171 3867642	Jasper vein
16CA249	053171 3867642	White (clast material)
16CA250 (47)	053171 3867642	Fe vein
16CA251	053172 3867645	Gossan material with strange texture
16CA252	053170 3867617	Cu rich lower sulfide
16CA253	053170 3867617	Massive sulfide with jasper
16CA254	053170 3867617	Nodular sulfide clast
16CA255	053170 3867617	Misc massive + disseminated ore
16CA256	053172 3867624	Top silicified rich layer
16CA257	053172 3867624	Directly under silicified cap
16CA258	053172 3867624	Infill breccia material
16CA259	053172 3867624	Non Si vein in lower horizon
16CA260	053174 3867633	White material from NE zone
16CA261	053174 3867633	Massive crudely banded fmn
16CA262	053174 3867633	Silicified gossan material
16CA263	053174 3867633	Silicified breccia
16CA264	053174 3867633	Fe boudinaged veins
16CA265	053174 3867633	Gossan material
16CA266	053174 3867633	Mn/Fe rich vein

16CA267	053173 3867614	Gossan material
16CA268	053173 3867614	Silicified white material
16CA269	053173 3867614	Jarosite veined silicified gossan
16CA270	053173 3867614	Sandy coloured basalt
16CA271	053174 3867614	Hematised basaltic pillow
16CA272	053174 3867614	Silicified vein
16CA273	053174 3867614	Slag

## 21E) Photos

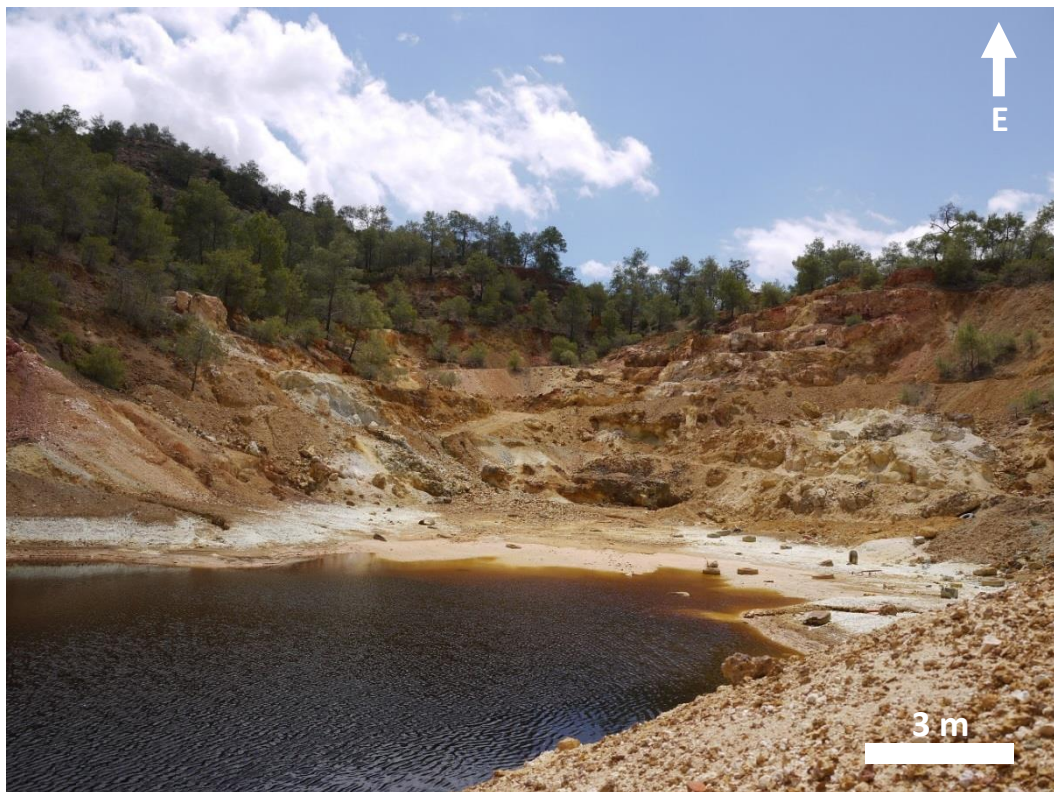


Figure A3.93: View over the Mathiatis open pit. Note the extensive gossan. AMD marks limit of historic mining for sulfide ore.



Figure A3.94: Foreground bleached light grey-white are is silica breccia. Note historic ancient workings.



Figure A3.95: Silica breccia exhibiting a vuggy texture suggesting mineral dissolution.



Figure A3.96: Typical gossan exposure. Multiple layers of Fe oxides and sulfates, predominantly jarosite, goethite and hematite.



Figure A3.97: Extensive chalcantinite developed in a small massive pyrite lens at the margin of the AMD lake.

## Location 22 Alpen Rose

### 22A) Location

Alpen Rose is located 1.6 km NE of Mathiatis and 700 m SE of Mathiatis North mine. The ridge creates a topographic high in the area and is clearly visible from the main road. To access the ridge take the main road from Agia Varvara to Mathiatis, just after the VMS mine there is a sharp corner. On this corner there is a small dirt track, take the track (car is fine). Follow for 200m or so and bear left and park in the field at the base of Alpen Rose. The area is thought to be anomalously high in Au.

### 22B) Mineralisation and structure

Alpen Rose is a large fault bound ridge where Au mineralisation is thought to be associated with quartz veining and sulfide mineralisation. The ridge trends NW-SE and measures approximately 1 km in length; it is narrow and less than 80 m wide. It creates a topographic high in the area rising from 369 m at its base to 470 m at its peak.

For ease of interpretation the ridge is divided into four areas; lower ridge (1<sup>st</sup> 350 m), Upper ridge and E and W surrounding areas.

The lower ridge is generally less mineralised than the upper-mid portion of Alpen Rose. Although ridge segmentation is noted (trending 022-NNE with a displacement to the E of 4 m) no mineralisation is associated with the initial offset. Heading up the outcrop (NW) the abundance of quartz slowly increases; quartz commonly occurs as small veinlets and as clasts within lava breccia. Quartz is milky white with minor Fe staining. The first major quartz occurrence with a clear vein morphology is noted at 053207/3869921. The ridge at this location strikes 312; the large quartz vein at is parallel to ridge strike.

Vein textures suggested repeated brecciation. Initially the vein would have formed with in-tact country rock but has subsequently been brecciated (multiple events) leading to the inclusion of vein derived quartz fragments in surrounding country rocks and a brecciated-silica-rich matrix (Figure A3.102). The vein at this point measures 80 cm wide and strikes 74S/106. The vein was extensively sampled. Is Au hosted in the matrix or the early silica that initially formed the vein? Quartz frequency decreases rapidly within 1-1.5 m either side of the vein.

The ridge to the W of the locality above is unbrecciated and thus thought to be a later intrusion however it is offset by a NE (046) trending fault. The quartz vein is not continuously traceable up slope towards the pylon (O/C is very poor).

Directly under the pylon quartz veins are not massive, they are sinuous in nature and a few cm wide. Country rock at this point is highly gossanised suggesting it was once sulfide-rich. Quartz veins are brecciated with fragments typically 3-4 cm wide they form discontinuous veins that strike 304. At this point the ridge topography becomes prominent; to the SW a brecciated unit marks the boundary of the main ridge structure (66SW/300). Breccia is clast supported and occurs in a band approximately 1.5 m wide and is surrounded to the SW by non-fragmented pillows. To the NE, flows are parallel to fault plane and highly gossanised, at this point quartz veins are parallel to the ridge/fault. Given the uniform sense of strike and apparent brecciation trend, it is inferred that the fault plane defines the ridge geomorphology and spatial extent of mineralisation.

Heading SW up Alpen Rose a subtle change in ridge attitude due to faulting is noted. Ridge strike migrates from 302 WNW through a rotated segment of ridge (336 NNW) back to 292 WNW. Within the rotated small block of ridge, quartz concentrations increase over an area 1.5 m<sup>2</sup>.

From this locality onwards (053221/3869847- Figure A3.103) the quartz vein becomes massive (50 cm wide) and continuous along strike for intervals of several m toward the SE.

A further area of dilation is noted (30 m from pylon) at this point, intersecting fault planes displace the ridge by 4 m to the NE. After this point the ridge and quartz vein appear to have sub parallel strikes (minor deviation); the ridge trends 78 SSW/286 whilst the vein trends 80 SSW/304. In this area the vein is still massive (30-50 cm) with internal layering, quartz breccia in surrounding country rock is well-developed.

Intersecting fault directions suggest the area is under the influence of two graben structures (Larnaca and Mitsero). The 'normal' network of ridge parallel and perpendicular faults is cross-cut by later faults formed under the stress field relating to the Mitsero graben, these faults then offset the ridge causing areas of low pressure and dilation causing the inward migration of silica rich fluid (hence quartz) which are then later brecciated by subsequent fault movement.

Moving further along the ridge (SE) the vein truncates against the SW striking fault plane, at this point the vein measures 88 WSW/328. A few metres further SE a vein (possibly the same or a new vein?) re-appears; the vein measures 0.8-1 m wide. Approximately 3 m further SE the vein is again truncated along the fault plane, on investigating the lower area where the vein deviates from the ridge, no trace of it was visible in the lower outcrop making it difficult to ascertain its continuity into the surrounding area.

Continuing SE, further ridge segmentation is noted (053241/3869712). At this point the whole ridge is shifted 2.5 m NE. Accompanying this dilation is a further change in ridge attitude from 68 SW/310 to 70 SW/302. The faults responsible for this offset and attitude change strike 78 ENE/340.

The upper ridge area is less intensely mineralised with quartz, instead sulfide (goethite-rich) lithologies are most abundant. Stringers are hematite/goethite rich, 1.5 cm wide and occur cross-cutting flows; the only quartz observed is interstitial in nature commonly coating joints. At this point the otherwise uniform sense of flow strike becomes more chaotic. Strike varies significantly from 66 NNE/300 to 72ESE/050.

To the NE (towards Agia Varvara) an Alpen Rose parallel swarm of dykes occur. Dykes exhibit well-developed columnar jointing. As with Alpen Rose, the ridge shows segmentation along its length. The dykes strike approximately NNW (330-340). The ridge is truncated numerous times along its length that approximately coincides with the offsets of strike-slip faults observed on Alpen Rose.

Major segmentation is observed at 053253 3869975, the ridge at this location is offset 10 m to the NE by two faults striking in opposite directions (N-S and E-W). This locality is the only place any clear vertical displacement is noted; the block is not just offset laterally but downthrown by several m suggesting an oblique strike-slip movement. Between the ridge segments are highly phytic undeformed UPL.

The area to the SE (the end of Alpen Rose) is UPL dominated however directly along strike of Alpen Rose in the base of the valley shear is observed within basalts suggesting the fault responsible for Alpen Rose formation continues.

### 22C) Structural overview

Alpen Rose ridge trends approximately NW-SE that is parallel to the Larnaca graben. The ridge is then truncated at intervals by N-S (approximate) trending faults that segment and offset portions of the main ridge. The SW side of Alpen Rose is bound by a normal fault that runs the

entirety of the ridge (downthrow to SW 4-8 m). Cross cutting faults are clearly later, strike-slip and related to different tectonic stresses. It seems likely these faults are related to the Mitsero graben; however if they are N-S and therefore ridge parallel they should in theory have a normal geometry and not strike-slip?

### 37D) Samples collected

Sample	Grid reference	Brief description
16CA419	053204 3869962	Lower ridge breccia
16CA420	053205 3869946	Fe stained vuggy silica
16CA421	053207 3869932	Qtz breccia fragments
16CA422	053207 3869932	Limonitic quartz material
16CA423	053207 3869921	Upper qtz vein
16CA424	053207 3869921	Lower qtz vein
16CA425	053207 3869921	Mid qtz vein
16CA426	053207 3869921	Ex-situ scree material
16CA427	053207 3869921	Fe basal vein material
16CA428	053207 3869921	Vein breccia margin
16CA429	053207 3869921	Upper Fe stained vein material
16CA430	053207 3869921	Sulfide rich stringer
16CA431	053210 3869911	Veined oxidised ridge material
16CA432	053210 3869911	Brecciated quartz clast
16CA433	053204 3869915	Interesting texture sulfide clast
16CA434	053211 3869900	Gossan material with qtz
16CA435	053213 3869907	NE gossan with fine breccia
16CA436	053218 3869924	Ex-situ gossanised material
16CA437	053216 3869879	Brecciated quartz vein
16CA438	053216 3869879	Gossanised boulder
16CA439	053217 3869875	Clast supported limonite rich
16CA440	053220 3869865	Vein margin
16CA441	053220 3869858	Sulfide rich vein
16CA442	053221 3869852	Quartz from ridge intersection
16CA443	053221 3869852	Qtz clast from vein
16CA444	053221 3869847	Qtz breccia/gossan material
16CA445	053222 3869845	Ridge material, highly Fe stained
16CA446	053224 3869824	Massive qtz vein
16CA447	053226 3869810	Limonite and qtz breccia
16CA448	053226 3869810	Qtz clast from vein
16CA449	053226 3869810	Matrix Fe with qtz
16CA450	053228 3869815	Fe vein material
16CA451	053229 3869042	Section of qtz vein
16CA452	053229 3869042	Hematite vein with minor sulfide
16CA453	053230 3867860	Massive qtz with blebby Fe
16CA454	053230 3867860	Qtz/country contact
16C1455	053232 3869770	Qtz from fault plane
16CA456	053232 3869773	End of vein material
16CA457	053234 3869758	Massive qtz ridge
16CA458	053236 3869144	Matrix supported breccia
16CA459	053238 3869726	Jasper sulfide
16CA460	053242 3869704	Vein + country rock
16CA461	053245 3869691	Qtz coating
16CA462	053245 3869685	Qtz coating
16CA463	053242 3869997	Magnetic flow material
16CA464	053248 3869994	Chloritised altered flow
16CA465	053255 3869930	Primitive protolith
16CA466	053271 3859734	Vein in basalt
16CA467	n/a	Interstitial qtz from pillow
16CA468	053224 3869730	Finely brecciated
16CA469	053227 3869689	Light basalt with qtz
16CA470	053227 3869689	Sulfide rich qtz vein
16CA471	053256 3869506	Chloritised flow
16CA472	053266 3869483	Inter pillow material
16CA473	053273 3869501	Quartz brecciated basalt
16CA474	053274 3869487	Inter pillow material
16CA475	053219 3870023	Ochre Fe pillow

22E) Photos



Figure A3.98: Prominent topographic high formed by Alpen Rose.



Figure A3.99: Prominent near vertical fault scarp to the S of Alpen Rose.



Figure A3.100: Brecciated quartz vein lower ridge segment.



Figure A3.101: Quartz breccia in a weathered lava from the lower ridge area.



Figure A3.102: Massive quartz breccia with silica cement and highly angular clasts from the upper Alpen Rose segment.



Figure A3.103: Vein offset by small strike slip fault.



Figure A3.104: 'Epithermal' type quartz rich breccia. Jarosite-goethite cement, probably once sulfide. Breccia clasts are sub angular.



Figure A3.105: Dyke swarm adjacent to Alpen Rose that is also truncated by small strike slip fault. In the distance are the Mathiatis North spoil heaps.

Location 23 Touronjia23A) Location

Touronjia is located on the margin of the Makheras domain in SE Troodos. The deposit is only accessible via 4x4 unless you fancy a hike. The deposit is located 2.9 km N of Skarinou and 50 m W of Dipotomas Reservoir. The deposit is best accessed via the B1. Take the exit for Skarinou (Alphamega) and follow the B1 E for 1.25 km. There will be a series of buildings/greenhouses on your left and Old Skarinou Station bar on your right, take the right turn and follow the road around, you will head under the motorway. Continue until you hit the dam.

23B) Mineralisation

Touronjia shares certain attributes with Mathiatis South and Red Cap (e.g. abundant silicification) but on a much larger scale. The outcrop is sub-divided into two main horizons, the lower, below the reservoir and upper horizons. The upper was investigated in this fieldwork (both appear similar). The area is characterised by massive silica-rich breccia with minor kaolinisation. The outcrop has previously been described as a good example of epithermal mineralisation or a 'volcanic' breccia. In general the outcrop is sulfide-poor with only minor disseminated pyrite found within silicified breccia (SW wall). Gold grades historically have been documented up to 50 ppm but no genetic model has been developed for the formation of Touronjia.

The deposit is located on the sediment contact and was once assumed to be BG. Now BG dykes and pillows are highly fragmented and silicified, they are bleached white with minor Fe staining on surface in areas. The unusual thing about Touronjia is that there is a volcanic horizon in the upper outcrop which is near continuous which is altered but not brecciated. This suggests an element of later flow/formation of the deposit, otherwise this horizon would also be brecciated (appears to be built in layers in a flow type morphology with lateral variation). Although there are several small faults cross cutting the extent of brecciation is greater than you would expect from such small faults. Silicification shows no correlation with faulting but is pervasive throughout all areas.

23D) Samples Collected

Sample	Grid reference	Brief description
16CA637	053242 3856597	Bleached silicified breccia
16CA638	053242 3856597	Upper Fe rich horizon
16CA639	053239 3856518	Sulfide within silicified breccia
16CA640	053240 3856524	Volcanic? Pepperite?
16CA641	053240 3856524	Non silicified kaolinised horizon
16CA642	053240 3856539	Fault breccia
16CA643	053241 3856553	Brecciated breccia
16CA644	053238 3856575	Lower kaolinised horizon
16CA645	053238 3856588	Silicified, kaolinised clast
16CA646	053238 3856588	Kaolinised area

## 23E) Photos



Figure A3.106: View from adjacent hillside over Touronjia mineralisation. Distant hills are Lefkara limestone. Photo courtesy of Michael Green.



Figure A3.107: Veined oxidised outcrop typical of the central Touronjia area.



Figure A3.108: Rock with a pepperitic texture in the upper Touronjia area. Also contained minor disseminated pyrite.



Figure A3.109: Silicified brecciated outcrop typical of Touronjia.

Location 24: Silicified umber at Theotokos24A) Location

Theotokos is located 1.8 km E of Analiontas. Follow the main road through Analiontas until you see Theotokos Monastery on your left, follow the road that runs behind the Monastery there is ample room to park and turn. Theotokos is located approximately 400 m due N of the Kampia VMS deposit on the UPL-sediment contact. Theotokos is the 'type' locality for silicification. Non-silicified umber, pillow lavas and radiolarites are common in the surrounding area.

24B) Mineralisation/Silicification

An area approximately 5 m<sup>2</sup> and 2-3 m thick is pervasively silicified. Silicified umbers at the main outcrop rest on non-silicified UPL suggesting that fluid has migrated laterally from a zone underlying the outcrop along focused fluid pathways and did not occur as effusive fluid flow through the lava pile. Silicified umbers are typically dark brown with mm scale quartz veins. Brecciation is patchy with clasts 1-2 cm and highly angular. Clasts are usually Fe-rich and possibly represent the brecciation of an early ochre layer?

Five metres S of the main silicified area (heading away from Monastery) is an area of patchy brecciation with a distinct green colour. As with the main umber outcrop breccia clasts are Fe rich; the matrix is believed to be celadonite (Figure A3.XXX). The inclusion of celadonite is unusual given the low temperature nature of fluids associated with silicified umbers. The location of celadonite occurs along the fault zone responsible for silicification.

24C) Structural data

Two main fault trends occur in the Theotokos area; 006 (N-S) and 048 (NE-SW). N-S faults form a series of small graben/half graben structures with a throw generally less than 3 m that form scarps and therefore clearly post-date umber deposition. Directly W of the main silicified outcrop is a continuous thin veneer of umber 50-80 cm thick with the lava contact visible. UMBER is massive and well-bedded; the nature of this ridge is thought to be fault controlled due to its prominent N-S strike- equally it could just be seafloor topography.

Silicification occurs in the area where the two faults sets obliquely intersect. This occurs at Theotokos directly under the silicified outcrop. Slickensides occur on the S most margin of the lower umber outcrop indicating a lateral movement. The eastern outcrop appears to be less structurally controlled, a complete stratigraphic succession from UPL through umbers (non-silicified) to massive radiolarite is preserved; no obvious faulting was visible.

24D) Samples collected

Sample	Grid reference	Brief description
16CA258	052465 3874094	Non silicified umber from upper graben
16CA259	052465 3874086	Green interstitial pillow mineral
16CA260	052465 3874086	Northern silicified umber
16CA261	052465 3874086	Directly below umber (Fe pillow)
16CA262	052463 3874065	Silicified green breccia
16CA263	052463 3874060	Silicified jasperitic vein
16CA264	052463 3874059	Large silicified breccia vein
16CA265	052463 3874065	W veined green breccia
16CA266	052463 3874065	Complete silicified vein network
16CA267	052463 3874065	Brecciated ochre
16CA268	052461 3874035	Lower-brecciated horizon
16CA269	052462 3874056	Fe rich vein, distal to fault
16CA270	052459 3874004	Patchy vein with pyrolusite
16CA271	052459 3874004	End of ridge (v. distal) vein
16CA272	052459 3874022	Non-silicified umber
16CA273	052469 3874010	E non-silicified umbers

16CA274	052482 3874124	Green veined material
16CA275	052478 3824084	Non silicified Mn umbers
16CA318	052477 3873833	Semi-silicified umber with celadonite
16CA319	052477 3873833	Silicified ochre
16CA320	052477 3873833	Non-silicified ochre

#### 24E) Photos



Figure A3.110: Fault scarp along N-S fault with non-silicified umber exposed. Throw is approximately 1-1.5m.



Figure A3.111: UMBER-pillow lava contact. A thin crust of finely laminated umber infilling pillow lavas.



Figure A3.112: Celadonite-rich breccia from outcrop S of Theotokos. Note prominent brecciated texture with Fe-rich orange clasts. Celadonite occurs as veins between pillows.



Figure A3.113: Pillow fragments in umber.



Figure A3.114: Perfect pillows with Fe-rich interstitial material.



Figure A3.115: Massive silicified ochre, near Kampia mine site E of Theotokos.

BLANK PAGE

# APPENDIX 4

**4.1:** P-XRF analytical setup

**D4.1:** P-XRF screening data – All samples

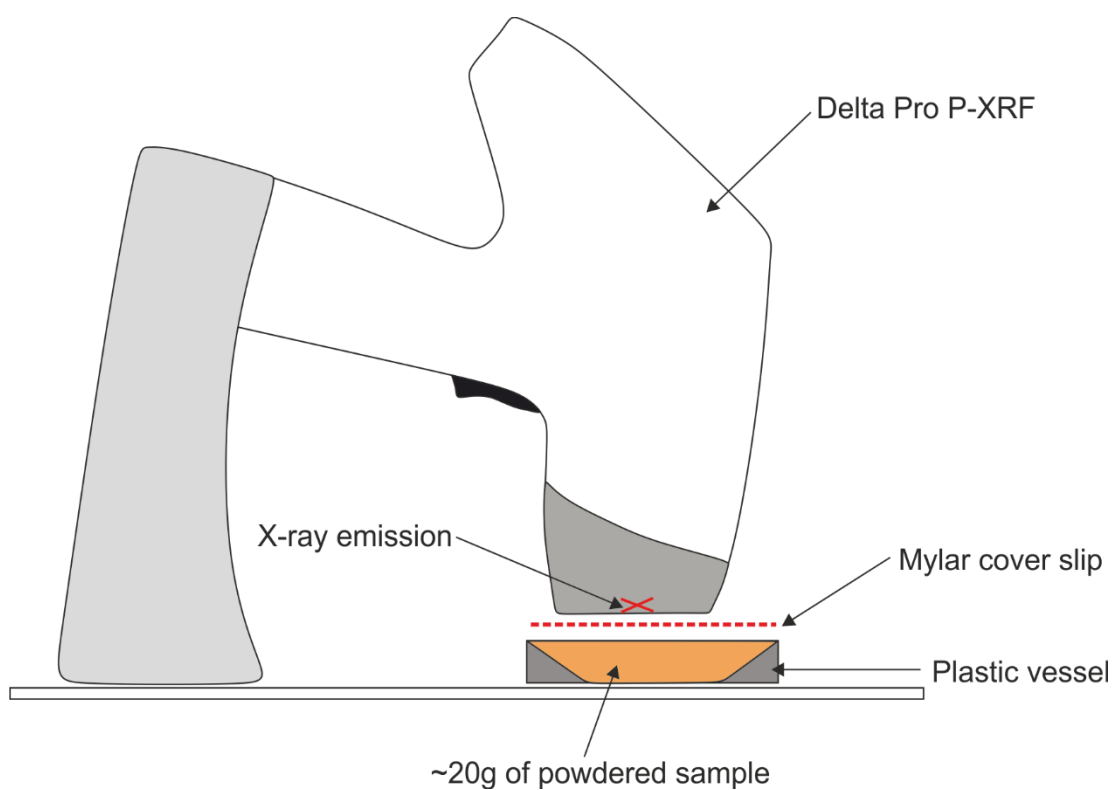
**4.2:** Detection limit- solution ICP-MS

**4.3:** Detection limit LA-ICP-MS

**4.4:** Standard information LA-ICP-MS

**4.5:** Standard information S isotopes

## 4.1 P-XRF analytical setup



**A4.1:** Portable X-ray Fluorescence analytical setup for the rapid screening of samples. The introduction of a Mylar cover slip improved detection limits.

## 4.2 Detection limits for solution ICP-MS analysis

Element	unit	LOD	LOQ
24Mg	ppm	0.2830	0.943
27Al	ppm	0.1875	0.624
29Si	ppm	0.4595	1.530
51V	ppm	0.0560	0.187
53Cr	ppm	0.0293	0.098
55Mn	ppm	0.0204	0.068
57Fe	ppm	0.3176	1.058
59Co	ppm	0.0071	0.024
60Ni	ppm	0.0132	0.044
65Cu	ppm	0.1146	0.382
66Zn	ppm	0.1481	0.493
75As	ppm	0.0283	0.094
<b>77Se</b>	<b>ppm</b>	<b>0.1486</b>	<b>0.495</b>
95Mo	ppm	0.0206	0.068
99Ru	ppm	0.0003	0.001
103Rh	ppm	0.0003	0.001
106Pd	ppm	0.0003	0.001
107Ag	ppm	0.0190	0.063
111Cd	ppm	0.0030	0.010
121Sb	ppm	0.0062	0.021
<b>125Te</b>	<b>ppm</b>	<b>0.0086</b>	<b>0.029</b>
185Re	ppm	0.0019	0.006
189Os	ppm	0.0007	0.002
193Ir	ppm	0.0002	0.001
195Pt	ppm	0.0006	0.002
197Au	ppm	0.0003	0.001
206Pb	ppm	0.0193	0.064
209Bi	ppm	0.0053	0.018

**Table A4.1:** Limit of detection (LOD and limit of quantification (LOQ) for aqua regia digest samples. Analyses were performed using a Thermo iCAP RQ ICP-MS at Cardiff University.

### 4.3 Detection limits for LA-ICP-MS analysis

Element	DL	Unit
59Co	1.9	ppm
61Ni	0.02	%
65Cu	0.01	%
66Zn	15	ppm
75As	2.1	ppm
77Se	12	ppm
95Mo	0.02	%
99Ru	0.10	ppm
101Ru	0.08	ppm
103 Rh	0.08	ppm
105Pd	0.09	ppm
106Pd	0.10	ppm
108Pd	0.10	ppm
109Ag	0.21	ppm
111Cd	0.9	ppm
121Sb	0.25	ppm
125Te	0.45	ppm
185Re	0.02	ppm
189Os	0.02	ppm
193Ir	0.02	ppm
195Pt	0.02	ppm
197Au	0.01	ppm
206Pb	0.001	%
209Bi	0.03	ppm

**Table A4.2:** Average detection limits for LA-ICP-MS across 6 laser runs analysed using a Thermo X-Series 2 ICP-MS and a Thermo iCAP-RQ ICP-MS.

## 4.4 Accuracy and precision measurements for LA-ICP-MS

### Accuracy

Results from different runs for standard reference material are summarised in Table A4.3. Percentage error of measured values compared with certified values are summarised for each element in Table 4.3 and are calculated using the following equation:

$$\% \text{ Error} = 100 - \left( \frac{\text{Certified value}}{\text{Measured value}} \right) \times 100$$

### Precision

The precision of element data is obtained using multiple analyses of external standards (UQAC-FeS1 and Mem Po724). The precision of standard samples relative to each other is expressed by the relative standard deviation (RSD). RSD values for elements considered are summarised in Table A4.3. RSD is calculated using the following equations:

$$x_a = \frac{\sum x}{n}$$

where  $x_a$  is the average element concentration,  $x$  is the element concentration and  $n$  is the number of analyses.

$$S = \frac{\sqrt{\sum (x - x_a)^2}}{n - 1}$$

where  $S$  is the standard deviation

$$RSD (\%) = \frac{100s}{x_a}$$

The standard error of the mean (SEM) is reported for repeat analyses of external standards in Table A4.3 and A4.4 and is calculated using the following equation:

$$SEM = \frac{\sigma}{\sqrt{n}}$$

*(The same equations are used in section A4.5 for S isotope analyses)*

Analytical Run		1	2	3	4	5	6	7	8	9	10	11	12	Mean	1 $\sigma$	RSD (%)	SEM	
<b>Element</b>																		
57Fe	%	46.7	46.6	47.1	47.2	44.8	44.4	42.8	44.6	45.2	44.4	44.1	44.7	45.2	1.4	3.06	0.4	
59Co	ppm	632.7	615.1	596.2	625.2	715.3	698.9	672.8	724.3	733.5	689.5	692.2	705.8	675.1	46.3	6.86	13.4	
61Ni	%	2.7	2.5	2.5	2.2	3.1	2.9	2.8	2.9	3.0	2.8	2.7	2.9	2.8	0.2	8.85	0.1	
65Cu	%	2.2	2.2	1.5	1.4	2.4	2.4	2.1	2.2	2.3	2.3	2.2	2.3	2.1	0.3	16.19	0.1	
66Zn	ppm	243.9	266.5	263.9	246.6	262.7	239.8	340.2	326.3	245.2	264.1	263.6	279.2	270.2	31.8	11.77	9.2	
75As	ppm	986.0	988.4	984.7	1009.6	1148.9	1168.3	1148.7	1283.1	1142.4	1200.7	1125.3	1101.8	1107.3	96.2	8.69	27.8	
77Se	ppm	297.5	305.2	284.5	283.5	276.0	284.9	295.9	314.6	251.3	339.4	278.7	319.5	294.2	23.2	7.90	6.7	
99Ru	ppm	63.4	68.0	68.2	67.3	73.6	71.7	70.1	72.2	76.0	70.4	72.1	71.0	70.3	3.3	4.68	0.9	
101Ru	ppm	63.7	67.9	67.5	65.3	70.8	69.9	67.6	70.8	74.2	68.7	69.5	70.9	68.9	2.8	4.04	0.8	
103Rh	ppm	67.9	70.5	64.4	64.4	70.3	67.9	68.7	70.9	77.0	71.3	70.6	71.5	69.6	3.4	4.86	1.0	
105Pd	ppm	56.5	53.3	57.2	55.5	57.6	54.1	54.4	56.7	60.6	57.7	53.0	55.2	56.0	2.2	3.88	0.6	
106Pd	ppm	56.5	54.4	57.4	55.5	53.8	59.6	53.9	56.8	59.5	58.3	53.8	57.4	56.4	2.1	3.77	0.6	
108Pd	ppm	56.7	53.7	58.1	54.0	53.5	55.5	54.8	63.1	58.6	60.0	53.8	59.5	56.8	3.1	5.45	0.9	
109Ag	ppm	158.2	143.2	144.9	155.8	167.9	152.0	158.9	165.5	169.8	153.3	161.4	154.8	157.2	8.3	5.28	2.4	
111Cd	ppm	1.2	1.2		1.1	1.9	2.1	2.4	2.2	1.9	2.2	2.2	2.2	1.9	0.5	26.15	0.1	
121Sb	ppm	79.1	91.9	78.2	83.2	55.4	61.0	64.8	68.1	54.5	72.6	51.3	67.2	68.9	12.5	18.13	3.6	
125Te	ppm	179.8	155.3	129.4	134.4	158.4	153.6	187.5	208.9	136.6	173.5	148.7	176.7	161.9	23.9	14.77	6.9	
185Re	ppm	67.1	66.7	47.2	46.9	73.3	72.2	66.3	76.9	82.6	69.1	75.6	74.1	68.2	10.9	16.04	3.2	
189Os	ppm	78.5	75.4	74.2	70.1	114.1	109.6	105.9	109.6	118.2	103.9	113.5	112.8	98.8	18.4	18.61	5.3	
193Ir	ppm	61.7	64.6	61.9	59.1	67.4	69.1	63.6	68.7	70.7	65.1	68.4	69.1	65.8	3.7	5.56	1.1	
195Pt	ppm	48.1	51.1	57.7	49.5	74.8	67.8	65.5	70.3	73.2	77.8	62.9	69.4	64.0	10.2	15.96	2.9	
197Au	ppm	59.7	71.1	58.9	61.2	78.1	72.2	78.0	88.0	78.8	78.4	66.6	73.5	72.0	9.0	12.48	2.6	
206Pb	ppm					49.8	44.2	43.5	46.6	47.0	44.3	52.6	46.2	46.8	3.1	6.64	1.1	
209Bi	ppm	114.9	113.3	113.4	111.5	118.4	129.8	120.1	119.1	124.7	125.3	117.9	124.5	119.4	5.70	4.78	1.6	

**Table A4.3:** Summary of repeat analyses for UQAC FeS-1 analysed via LA-ICP-MS.

## 4.5 Accuracy and precision measurements for S isotope analyses

Data quality was monitored through the repeat analysis of two standard reference materials and SUERC's internal standard CP1. Accuracy and precision measurements are summarised in Table 4.4.

Run	1	2	3	Certified value	% Error CRM	Mean	1 $\sigma$	RSD (%)	SEM
Standard									
CP1	-3.7	-4.6	-4.3	-4.6	6.8	-4.2	0.4	10.6	0.3
NBS123	16.0	15.5	17.4	17.1	4.9	16.3	0.8	5.9	0.6
S3	-34.1	-35.0	-32.2	-31.5	9.4	-33.8	1.2	4.2	0.8

Table A4.4: Summary of repeat analyses of CP1, NBS123 and S3 analysed via conventional sulfur extraction (See Chapter 4). All results are in standard notation relative to V-CDT in ‰.

BLANK PAGE

# APPENDIX 5

**D5.1: LA-ICP-MS trace element data for pyrite**

5.2: Sphalerite inclusions

**D5.3: LA-ICP-MS trace element data for chalcopyrite**

**D5.4: LA-ICP-MS trace element data for sphalerite**

5.5: Selenium/sulfur ratios

Appendix 5 provides supplementary material for Chapter 5.

## Appendix 5.2

### Mineral inclusions in pyrite

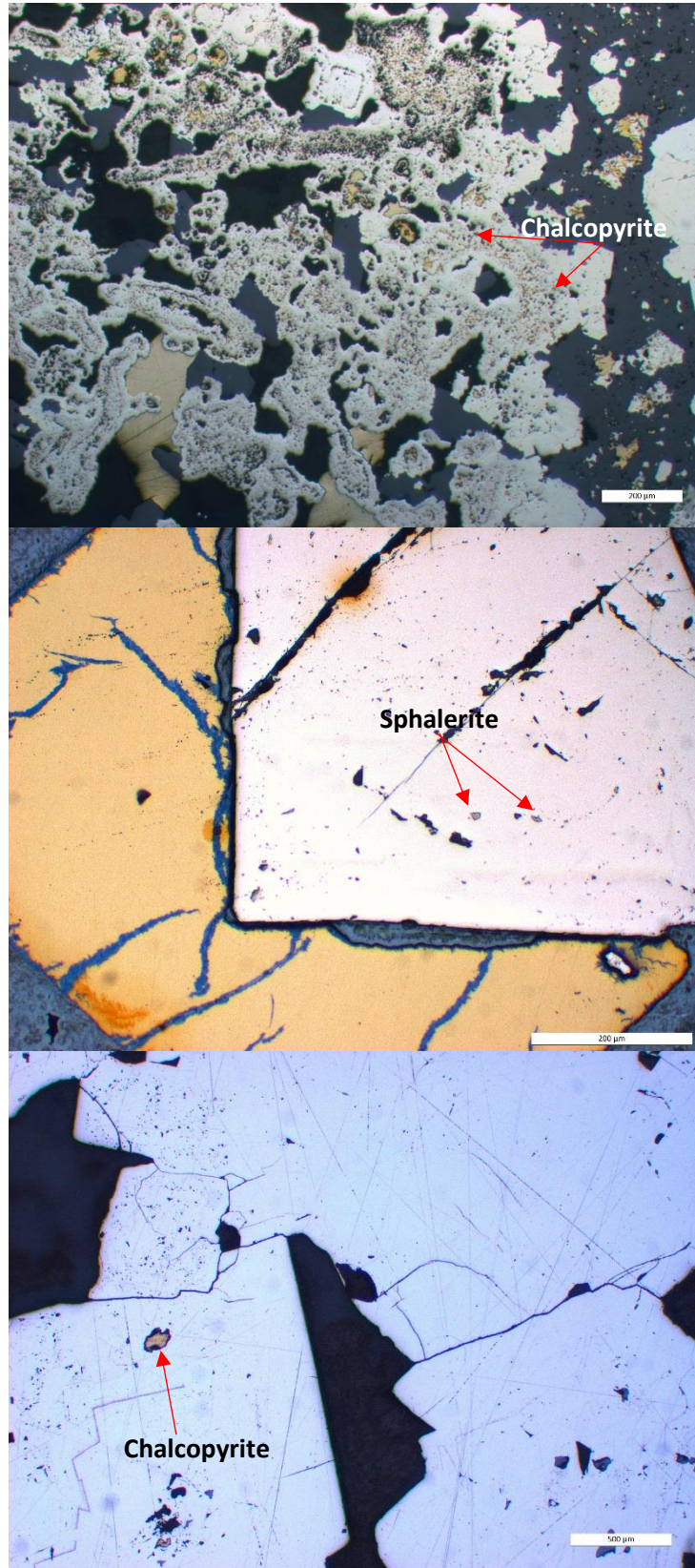


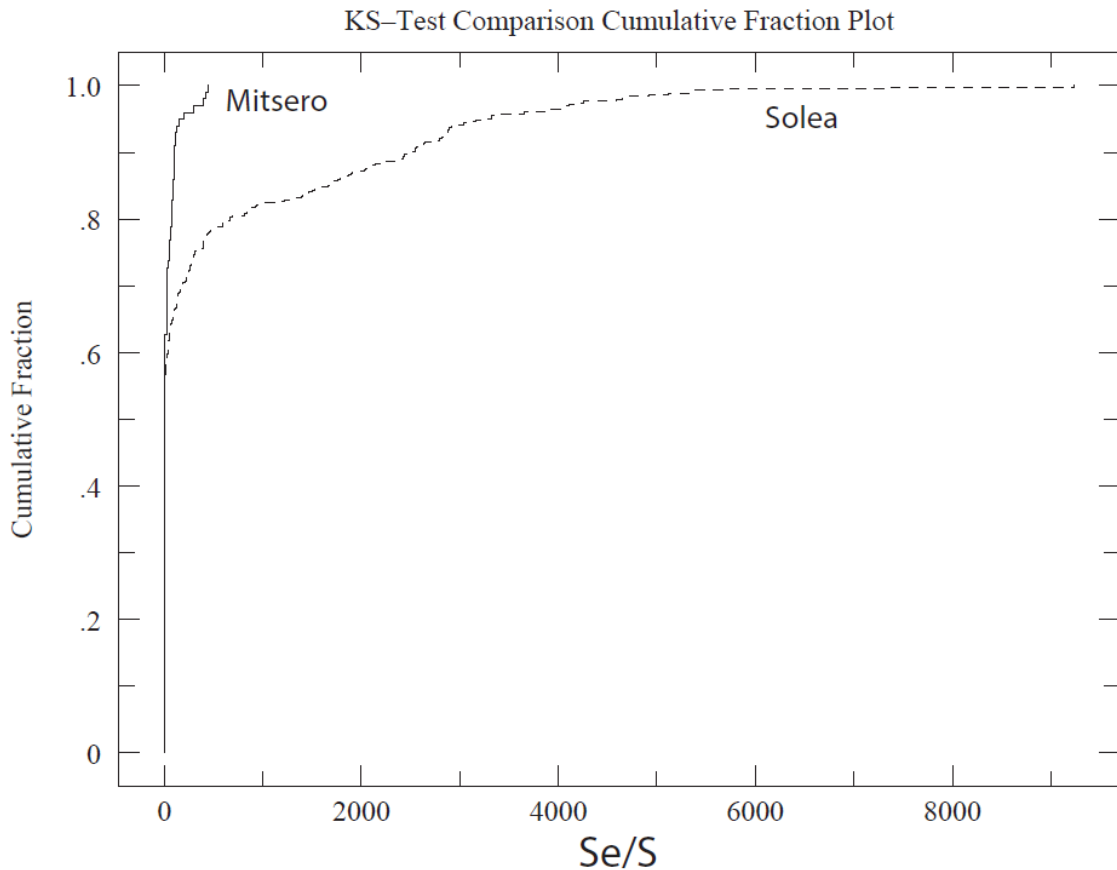
**Figure A5.1:** Examples of mineral inclusions in pyrite from Troodos VMS.

## Appendix 5.5 Se/S Statistical analysis

Comparison of the Solea and Mitsero grabens

### Kolmogorov-Smirnov Comparison of Two Data Sets

The maximum difference between the cumulative distributions,  $D$ , is: 0.2704 with a corresponding  $P$  of: 0.000 so the **distribution** of the two populations are significantly different.



Cumulative fraction plot from the Kolmogorov-Smirnov test showing the difference between the cumulative Se/S distributions of Solea (dashed line) and Mitsero (solid line). For a given Re concentration the cumulative fraction represents the fraction of the population which is below that value, showing that the Mitsero samples contain consistently lower Se/S than the Solea samples, however a large proportion of both are null results.

#### Data Set 1 (Mitsero):

99 data points were entered

Mean = 40.09

95% confidence interval for actual Mean: 23.34 thru 56.85

Standard Deviation = 84.0

High = 440. Low = 0.00

Third Quartile = 51.0 First Quartile = 0.00

Median = 0.000

Average Absolute Deviation from Median = 40.1

John Tukey defined data points as *outliers* if they are 1.5\*IQR above the third quartile or below the first quartile. Following Tukey, the following data points are outliers: 440. 424. 395. 299. 199. 154.

KS says it's unlikely this data is normally distributed:  $P= 0.00$  where the normal distribution has mean= 123.1 and sdev= 114.5

### Data Set 2 (Solea):

426 data points were entered

Mean = 582.0

95% confidence interval for actual Mean: 463.1 thru 701.0

Standard Deviation = 1.249E+03

High = 9.239E+03 Low = 0.00

Third Quartile = 320. First Quartile = 0.00

Median = 0.000

Average Absolute Deviation from Median = 582.

John Tukey defined data points as *outliers* if they are 1.5\*IQR above the third quartile or below the first quartile. Following Tukey, the following data points are outliers: 9.239E+03 7.307E+03 5.682E+03 5.330E+03 5.328E+03 5.118E+03 4.915E+03 4.693E+03 4.653E+03 4.595E+03 4.254E+03 4.168E+03 4.108E+03 4.057E+03 4.035E+03 3.918E+03 3.892E+03 3.650E+03 3.397E+03 3.326E+03 3.321E+03 3.235E+03 3.158E+03 3.093E+03 3.038E+03 2.914E+03 2.911E+03 2.892E+03 2.882E+03 2.876E+03 2.866E+03 2.848E+03 2.833E+03 2.820E+03 2.791E+03 2.734E+03 2.644E+03 2.636E+03 2.578E+03 2.555E+03 2.548E+03 2.545E+03 2.498E+03 2.459E+03 2.439E+03 2.429E+03 2.423E+03 2.399E+03 2.259E+03 2.187E+03 2.138E+03 2.112E+03 2.094E+03 2.044E+03 2.028E+03 1.915E+03 1.898E+03 1.866E+03 1.844E+03 1.789E+03 1.765E+03 1.706E+03 1.704E+03 1.699E+03 1.657E+03 1.552E+03 1.526E+03 1.496E+03 1.469E+03 1.468E+03 1.403E+03 1.398E+03 1.288E+03 1.218E+03 1.157E+03 994. 931. 925. 887. 869. 841. 841. 816.

**Mann-Whitney-Wilcoxon U test**

U =17400

Z score = 2.88139 (NB/ results approximately normal so Z value can be used).

*p* value = 0.00398 so the result is significant  $p < 0.01$

This is a statistically significant group difference (Mann-Whitney U=497.5,  $p = .004$ , sig.  $< .01$ , 2-tailed).

*Fagerland, M.W., 2012. t-tests, non-parametric tests, and large studies—a paradox of statistical practice? BMC Medical Research Methodology, v. 12(1), p. 78*

BLANK PAGE

# APPENDIX 6

6.1: P-XRF data for Apliki

6.2: XRD for SABZ

**D6.3: LA-ICP-MS trace element data for Apliki**

6.4: Trace element histogram plots

6.5: Additional TRA profiles

6.6: Element maps of SABZ samples

**Appendix 6** provides supplementary material for Chapter 6.

## Appendix 6.1

## P-XRF data

Sample	Grid Ref.	WGS 84	Cu	Cu +/-	Zn	Zn +/-	As	As +/-	Se	Se +/-	Mo	Mo +/-	Pb	Pb +/-
16CA274	<b>48574</b>	<b>3881389</b>	72	15	31	10								
16CA257	<b>48574</b>	<b>3881384</b>	255700	2700	1659	160	369	34	1071	40	75	11		
16CA253	<b>48572</b>	<b>3881376</b>	656	56			231	19	45	9	48	7		
16CA240	<b>48571</b>	<b>3881806</b>	779	65	239	32							135	33
16CA247	<b>48573</b>	<b>3881812</b>	19979	294	238	34	382	18	970	24	69	6		
16CA244	<b>48573</b>	<b>3881812</b>	54	15	65	12	180	10	22	4	58	5	41	9
16CA325	<b>48575</b>	<b>3881758</b>	185	19	45	12	18	4						
16CA239	<b>48575</b>	<b>3881737</b>	735	38	35	11	22	5						
16CA252	<b>48574</b>	<b>3881375</b>	60900	800			636	32	233	16	390	14		
16CA325	<b>48575</b>	<b>3881759</b>	1151	74			156	21	147	13				
16CA352	<b>48575</b>	<b>3881758</b>	6155	158			53	12			36	7	68	16
16CA255	<b>48574</b>	<b>3881384</b>	15333	200	108	24	24	5	36	4	57	5		
16CA254	<b>48574</b>	<b>3881377</b>	876	60	308	31	141	16	23	6	56	7	75	18
16CA256	<b>48574</b>	3881384	3028	81			38	8	161	9	55	5		
16CA245	<b>48573</b>	<b>3881812</b>	1817	51	41	11	27	5						
16CA249	<b>48569</b>	<b>3881756</b>			118	15								
16CA254D	<b>48574</b>	<b>3881377</b>	9543	185			138	12	29	8	86	7		
16CA326	<b>48575</b>	<b>3881758</b>	1471	53	228	19								
16CA241	<b>48572</b>	<b>3881802</b>	4117	74	399	20			113	5				
16CA254	<b>48574</b>	<b>3881377</b>	BDL	159	117	18	62	8						
16CA246	<b>48573</b>	<b>3881812</b>					51	5	47	4	93	4		
16CA244	<b>48573</b>	<b>3881812</b>	1054	62			351	23	269	15	43	7	132	23
16CA248	<b>48573</b>	<b>3881812</b>	11556	152	243	21			241	8	38	4		
16CA245	<b>48573</b>	<b>3881812</b>	12768	174	273	25	144	9	148	7	102	5		

**Table A6.1:** P-XRF data for selected elements from the Apliki VMS. All values are in ppm. Blank cells indicate values below detection limit.

## Appendix 6.2

### XRD spectra

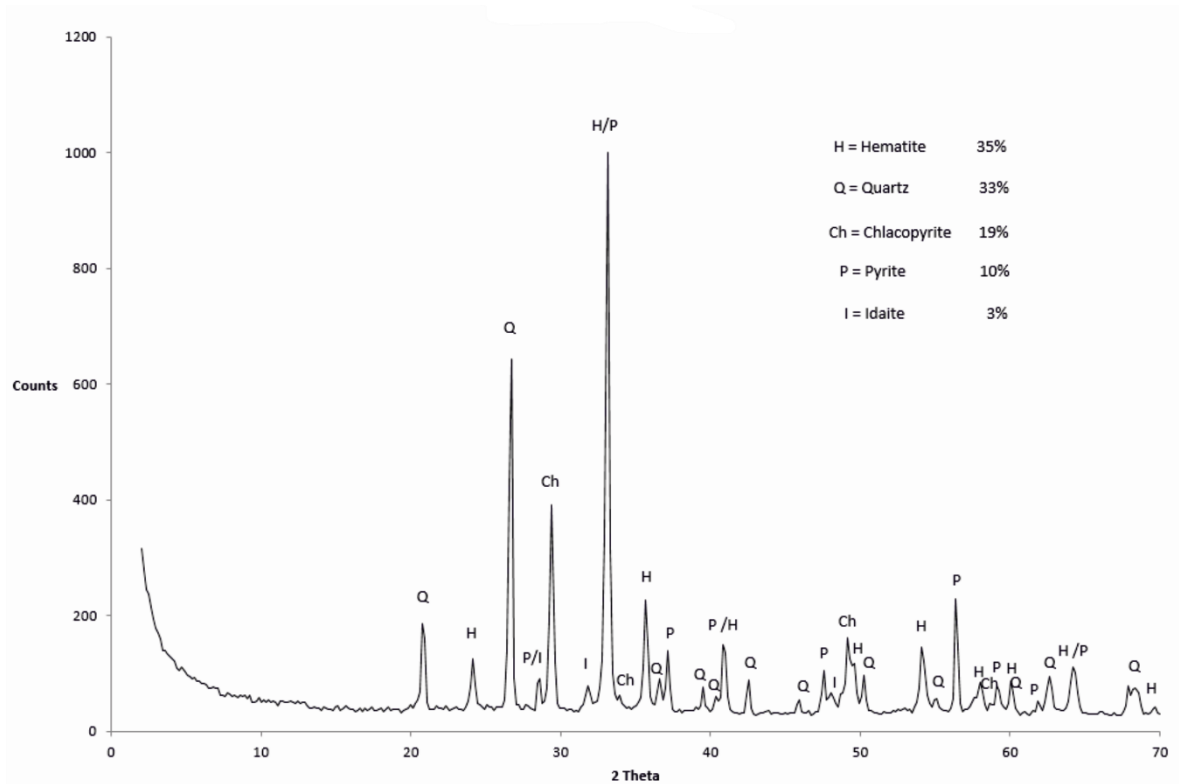


**Figure A6.2:** XRD diffractogram of SABZ samples showing that hematite is the dominant Fe phase identified.

### Appendix 6.4 Selenium distribution

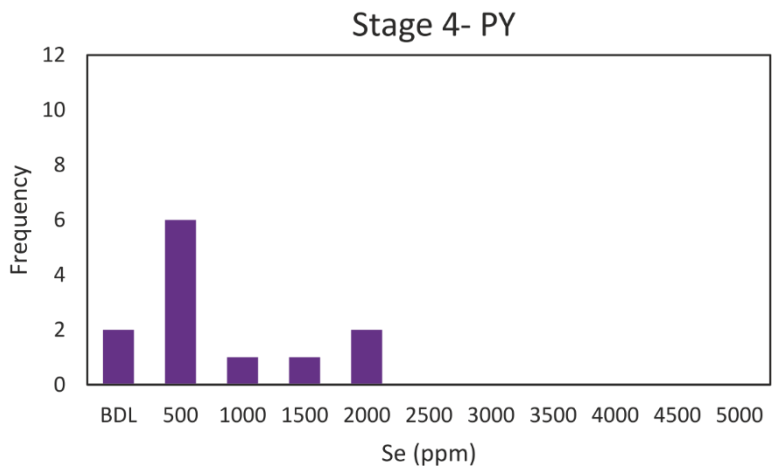
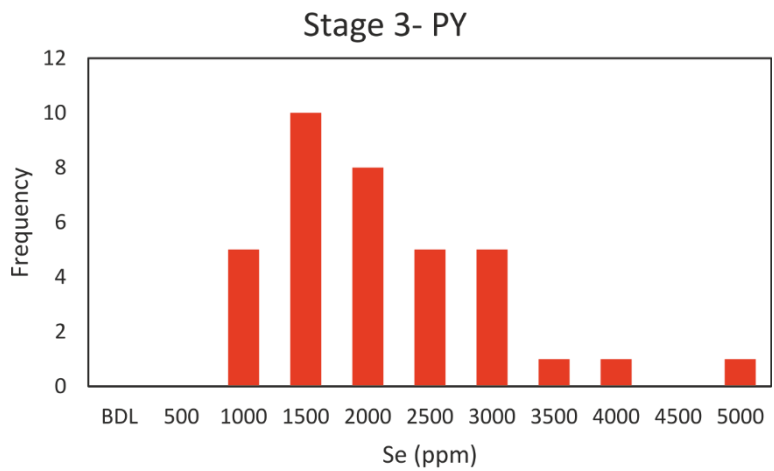
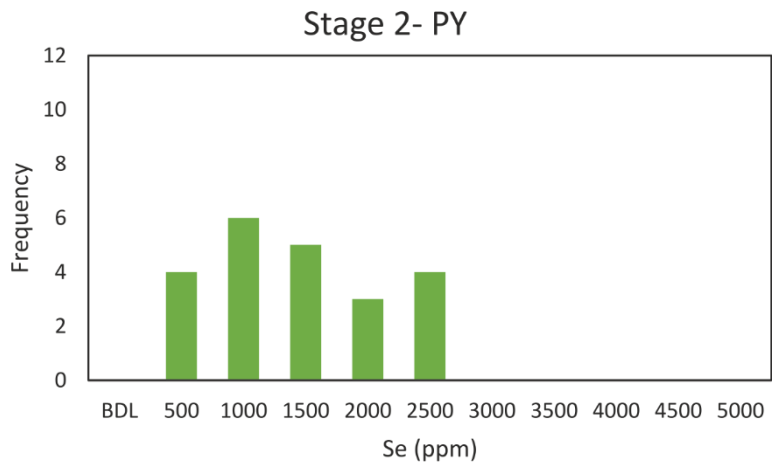
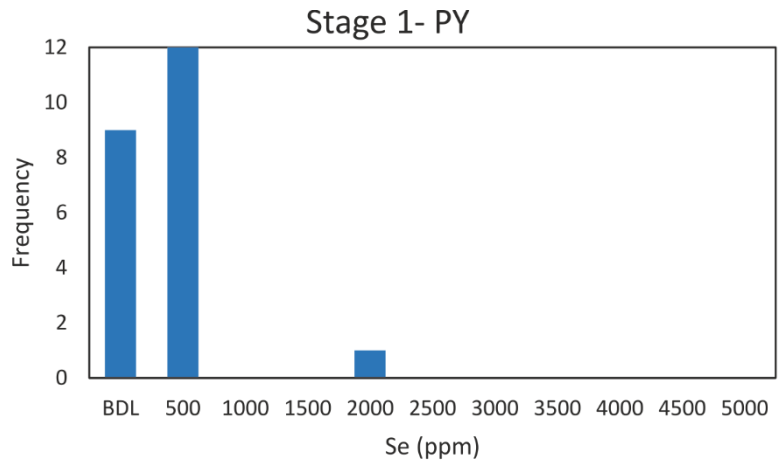
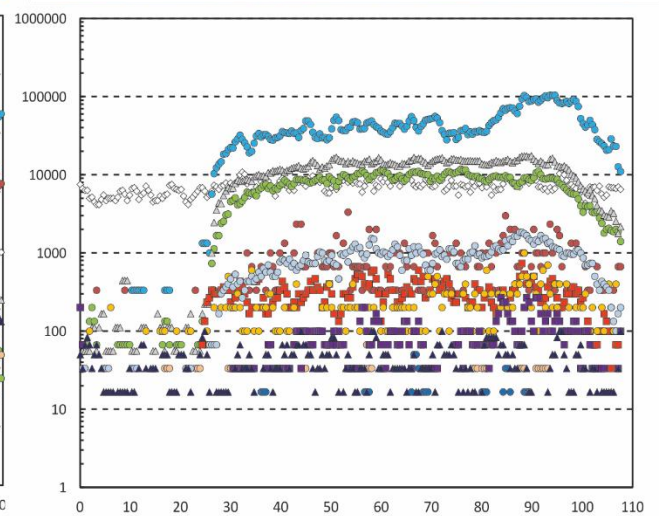
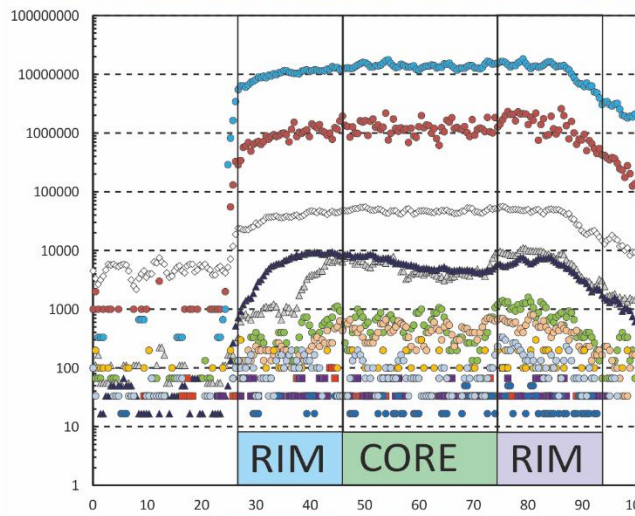
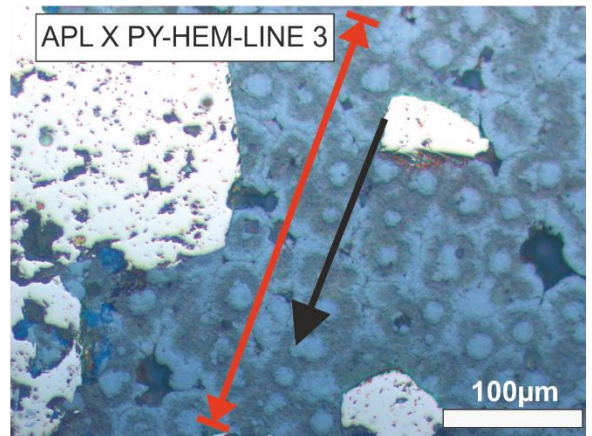
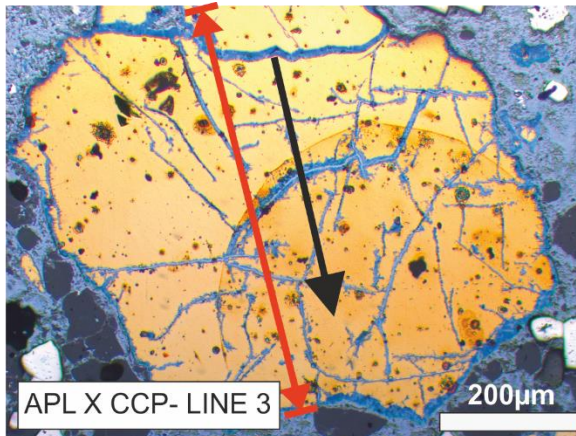


**Figure A6.4:** Histograms of Se concentration vs. paragenesis stage of pyrite for the South Apliki Breccia Zone. Detection limit (BDL) is approximately 12 ppm. Data from LA-

### Appendix 6.5

Additional TRA profiles

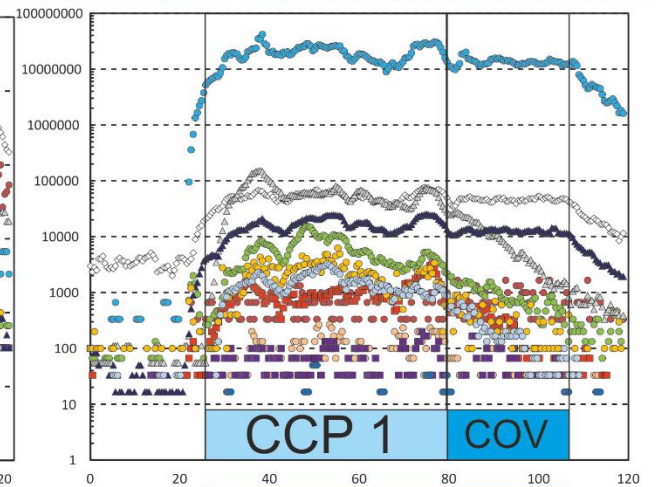
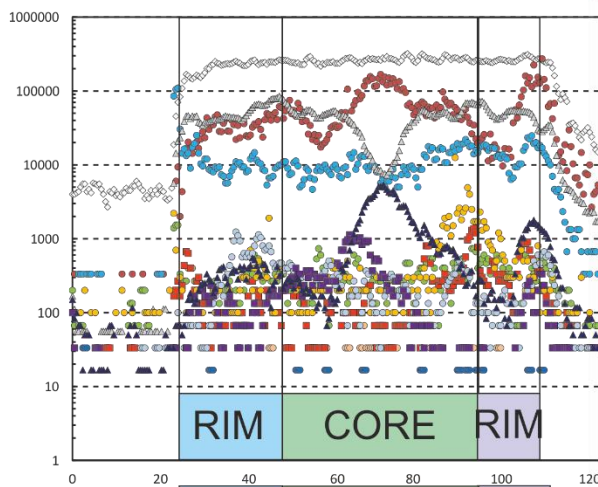
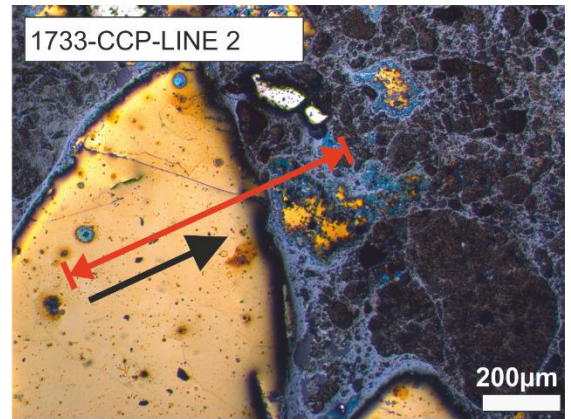
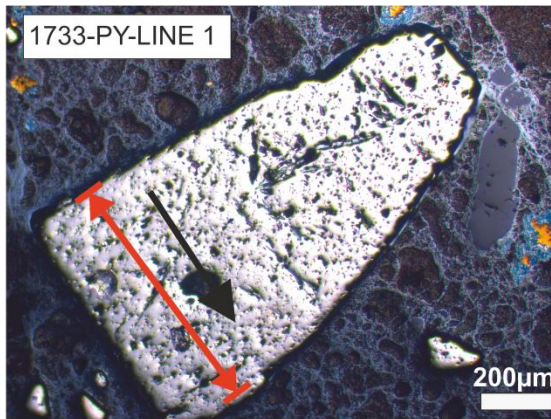


L4-CCP1	L4-CCP2	L4-CCP3
<1.9	<1.9	<1.9
27.17	28.22	23.11
133	143	221
109.7	131.1	199.7
2404	1634	1615
2.84	3.79	3.62
<0.9	<0.9	<0.9
<0.25	<0.25	<0.25
3.67	1.93	2.21
0.05	0.06	0.10
0.22	0.11	0.28

- ◇ S    ○ Ag
- Co    ■ Sb
- Cu    ■ Te
- Zn    ● Au
- △ As    ● Pb
- ▲ Se    ● Bi

All line analyses were analysed using a 55µm spot size at a frequency of 10Hz. Concentrations are in ppm and are summarised for the mineral phases analysed in tables below. For samples with no S (i.e. oxides) no data is available. However, the relative intensity of counts indicates the presence of absence of a phase. For example, Se in HEM-LINE 3 above.

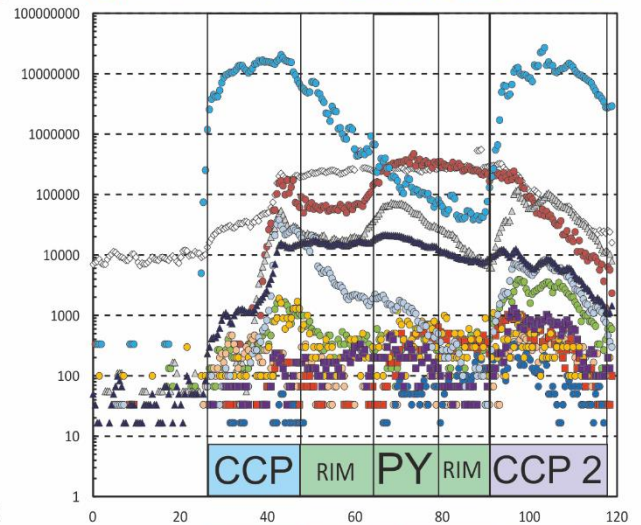
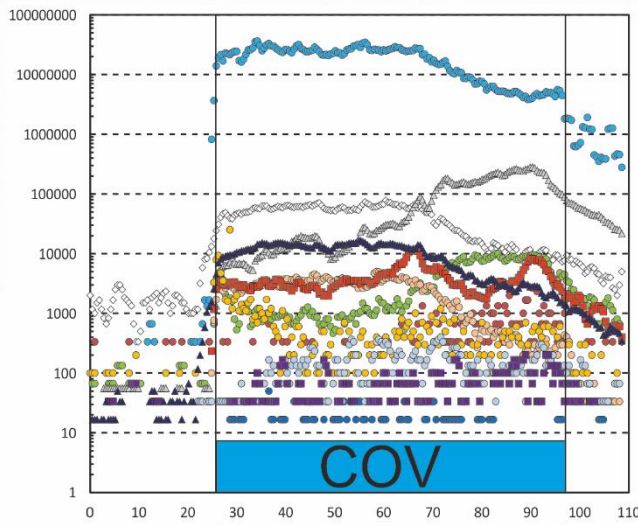
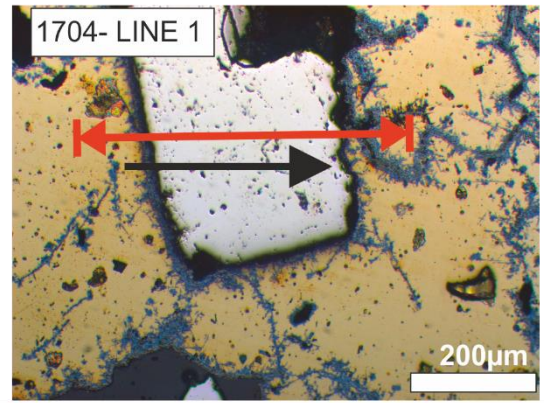
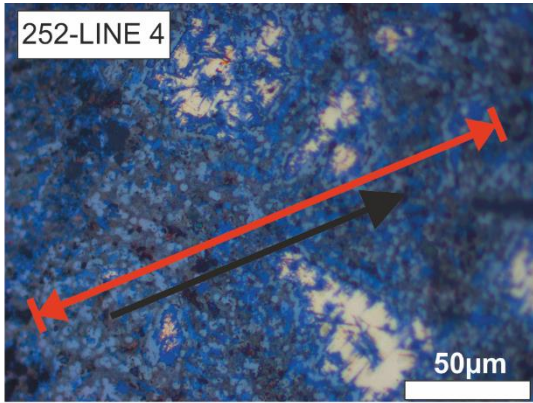
**PY= pyrite, HEM= hematite, CCP = chalcopyrite, COV = covellite**



Region	L1-PY1	L1-PY2	L1-PY3
59Co	26.3	62.2	41.1
65Cu	<0.01	<0.01	<0.01
66Zn	<15	<15	<15
75As	216.4	119.2	180.4
77Se	14	92	24
109Ag	<0.21	<0.21	<0.21
111Cd	<0.9	<0.9	<0.9
121Sb	<0.25	<0.25	0.46
125Te	2.21	4.49	0.71
185Re	0.13	0.28	0.19
197Au	<0.01	<0.01	<0.01
209Bi	0.14	<0.03	<0.03

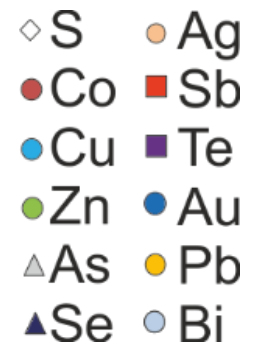
Region	L2 CCP 1	L2 COV
59Co	<1.9	<1.9
65Cu	27.34	28.79
66Zn	1193	583
75As	1270.2	836.2
77Se	3669	3902
109Ag	0.52	0.71
111Cd	2.1	1.8
121Sb	5.44	8.57
125Te	3.19	3.53
185Re	0.13	0.11
197Au	<0.01	0.05
209Bi	2.68	1.46

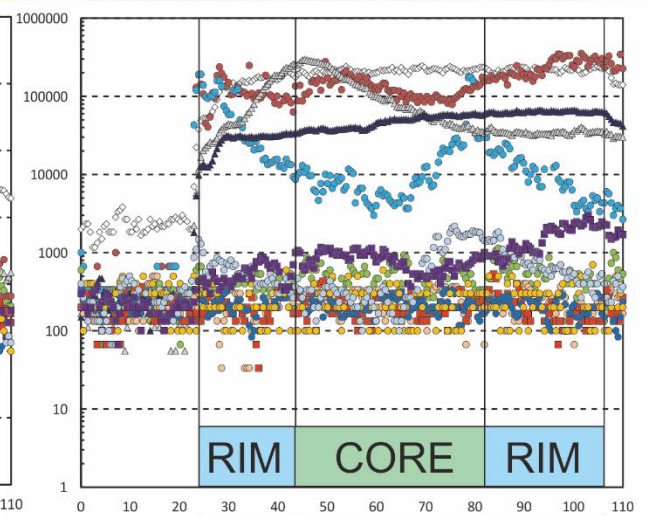
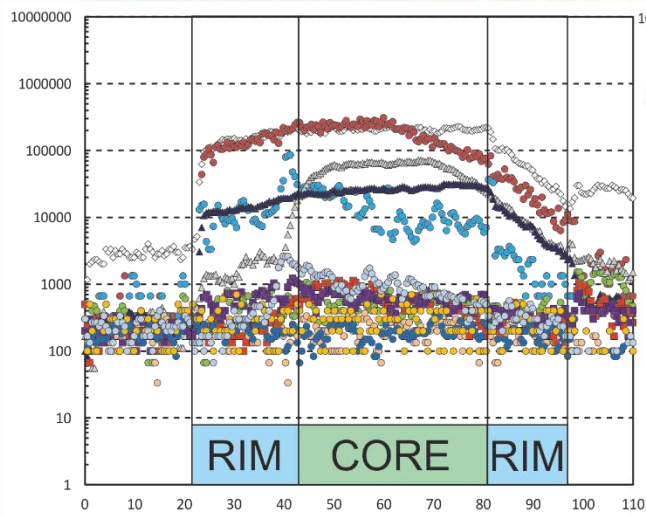
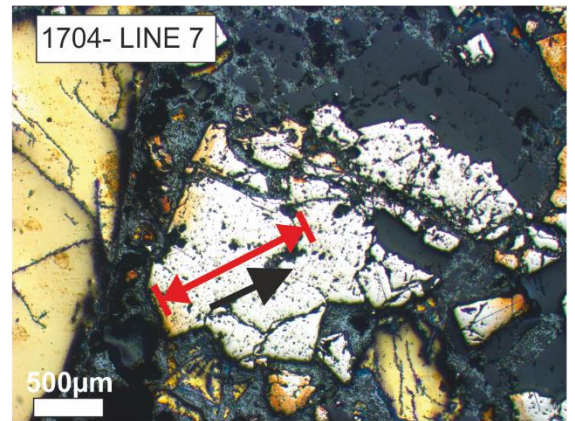
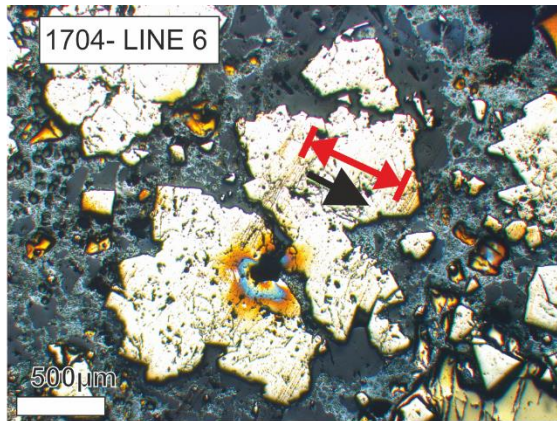
- ◇ S      ○ Ag
- Co     ■ Sb
- Cu     ■ Te
- Zn     ● Au
- ▲ As     ● Pb
- ▲ Se     ● Bi



Region	COV
59Co	<1.9
65Cu	52.81
66Zn	275
75As	439.0
77Se	4310
109Ag	29.42
111Cd	1.8
121Sb	29.22
125Te	2.72
197Au	0.09
209Bi	0.30

Region	CCP 1	RIM	CORE	RIM	CCP 2
59Co	28.1	44.8	152.2	129.4	60.9
61Ni	<0.01	0.02	0.02	<0.01	<0.01
65Cu	27.62	1.31	<0.01	0.45	6.43
66Zn	95	21	<15	28	189
75As	83.6	71.8	150	89.9	513.6
77Se	566	539	609	323	515
109Ag	3.24	<0.21	<0.21	<0.21	0.69
121Sb	<0.25	<0.25	<0.25	0.47	0.79
125Te	4.11	1.45	1.99	2.48	15.67
197Au	0.03	<0.01	0.02	0.09	0.15
209Bi	2.55	3.31	0.35	0.39	3.43





	RIM	CORE	RIM
<b>59Co</b>	197.4	239.9	96.6
<b>61Ni</b>	<0.01	<0.01	<0.01
<b>65Cu</b>	<0.01	<0.01	<0.01
<b>66Zn</b>	<0.01	<0.01	<0.01
<b>75As</b>	20	<15	<15
<b>77Se</b>	13.1	306.9	233.5
<b>109Ag</b>	1300	1605	1780
<b>121Sb</b>	<0.25	0.88	0.37
<b>197Au</b>	10.42	8.66	5.67
<b>209Bi</b>	0.07	0.51	0.15

	RIM	CORE	RIM
<b>59Co</b>	282.3	181.7	132.6
<b>61Ni</b>	0.06	0.05	0.06
<b>65Cu</b>	<0.01	<0.01	<0.01
<b>66Zn</b>	<0.01	<0.01	<0.01
<b>75As</b>	<15	16	<15
<b>77Se</b>	184.5	1151.0	387.6
<b>109Ag</b>	3774	2750	3060
<b>121Sb</b>	<0.25	<0.25	<0.25
<b>197Au</b>	32.49	10.57	10.32
<b>209Bi</b>	0.11	0.15	0.26

- ◇ S      ○ Ag
- Co     ■ Sb
- Cu     ■ Te
- Zn     ● Au
- ▲ As     ● Pb
- ▲ Se     ● Bi

## Appendix 6.6

Element maps of SABZ samples:

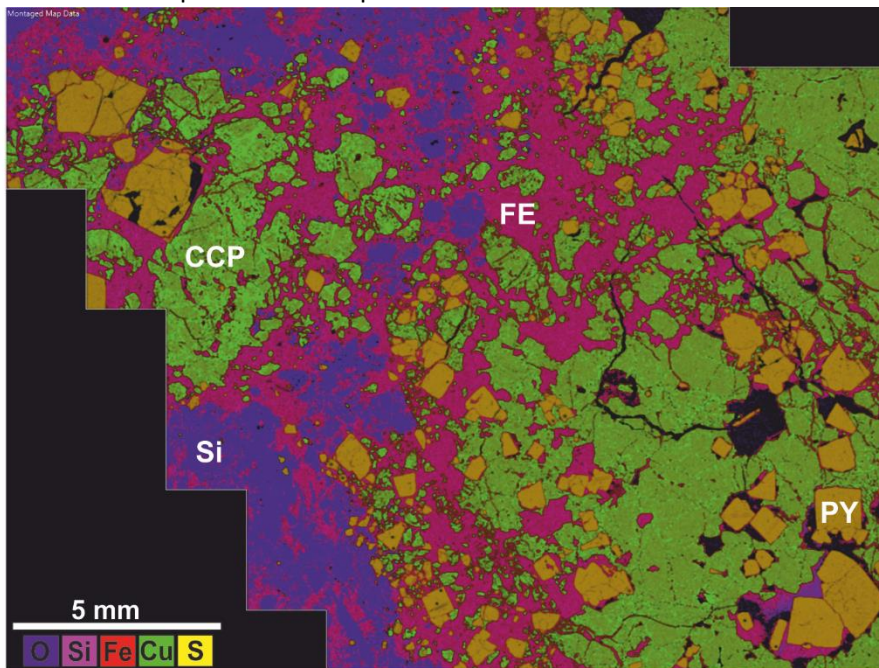
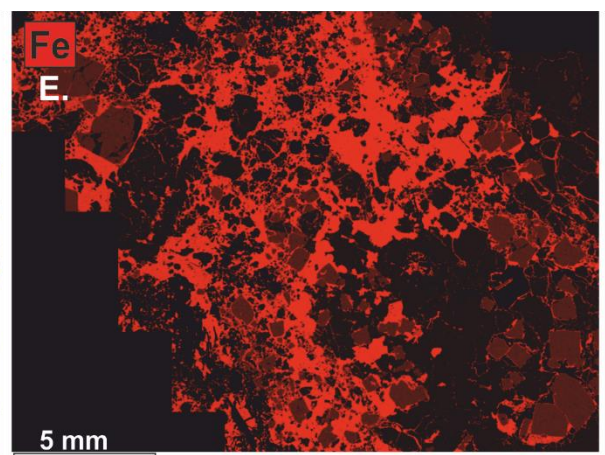
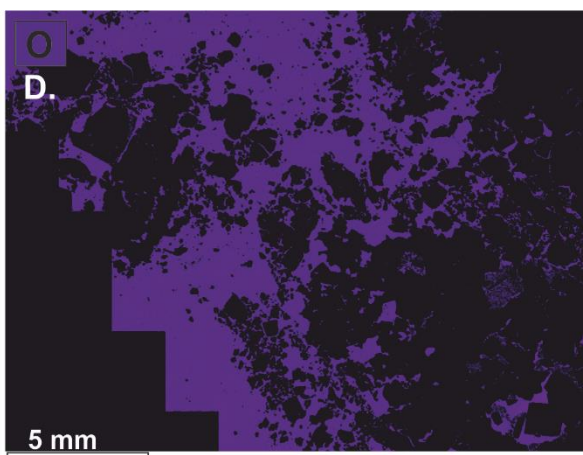
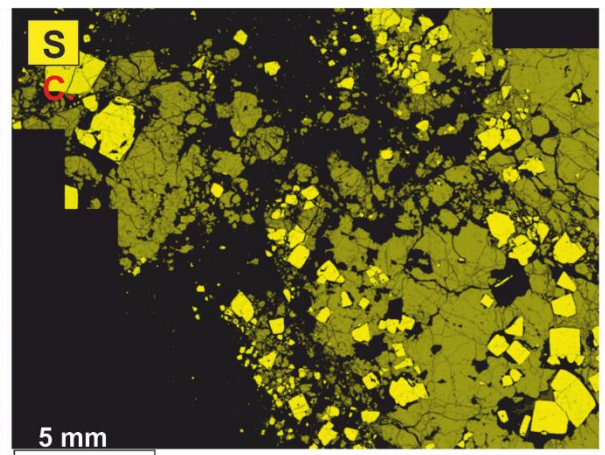
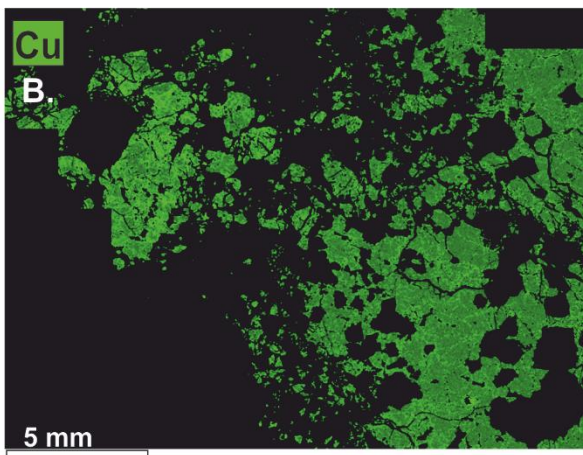


Figure A6.6C: Element maps of a SABZ sample. Figure A: element map highlighting the distribution of hematite, chalcopyrite, pyrite and jasper. B shows the distribution of chalcopyrite. C identifies the distribution of sulfide minerals (PY and CCP). Figure D and E highlight the extensive occurrence of secondary Fe phases and silicate material. PY = pyrite, CCP = chalcopyrite, FE = secondary Fe phase, Si = silicates/jasper.



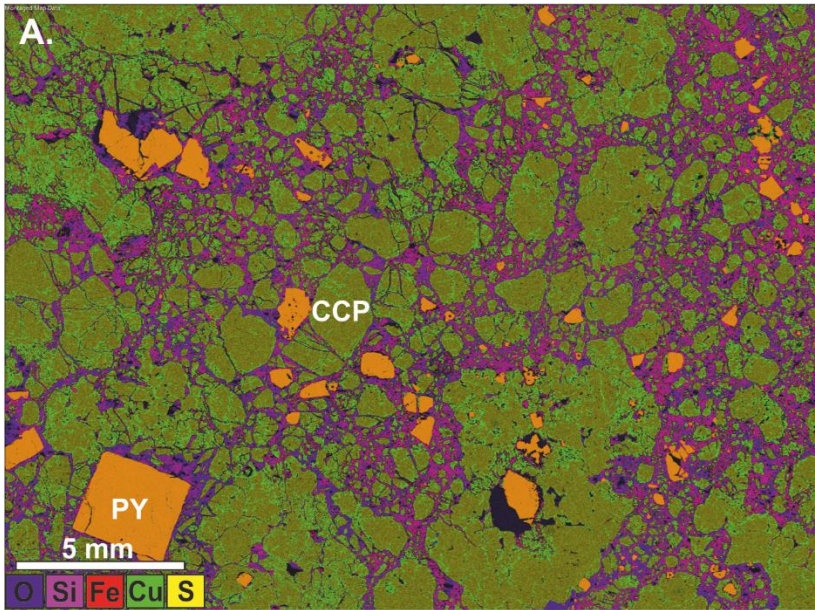
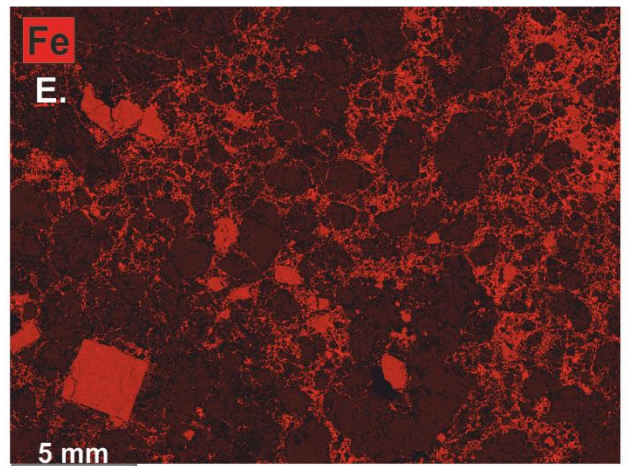
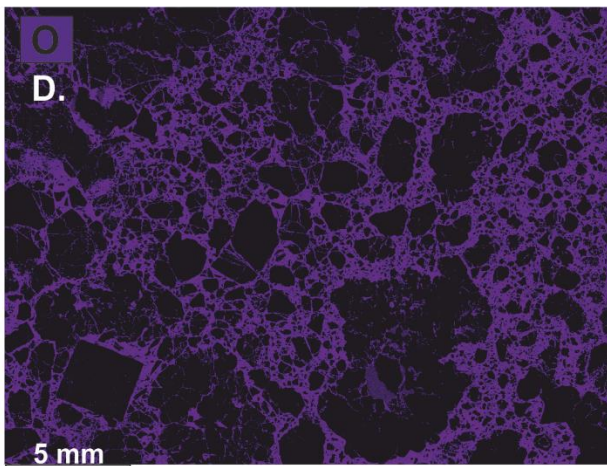
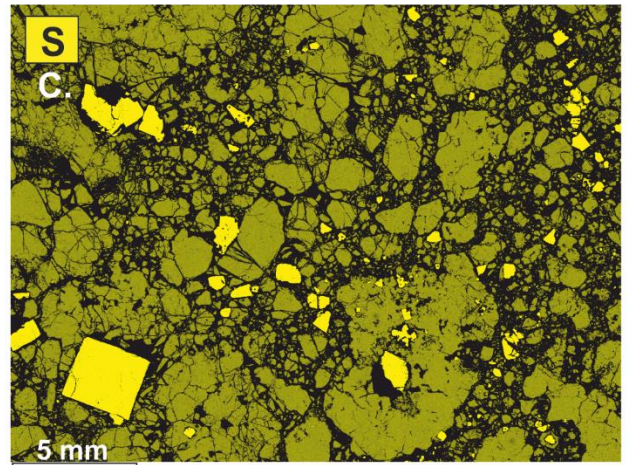
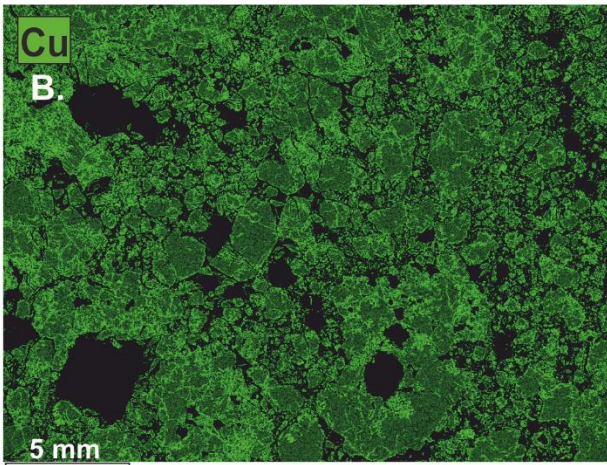


Figure A6.6B: Element map of a SABZ sample. Figure A highlights the distribution of pyrite (orange) and chalcopyrite (green). Secondary Fe phases are well-developed in the matrix (blue/purple). B shows the distribution of Cu, note that chalcopyrite grains are rimmed by bright green diginite and covellite. C shows the distribution of sulfur, primarily highlighting pyrite distribution. D and E show the distribution of secondary Fe phases, most likely jasper with minor goethite. PY = pyrite, CCP = chalcopyrite.



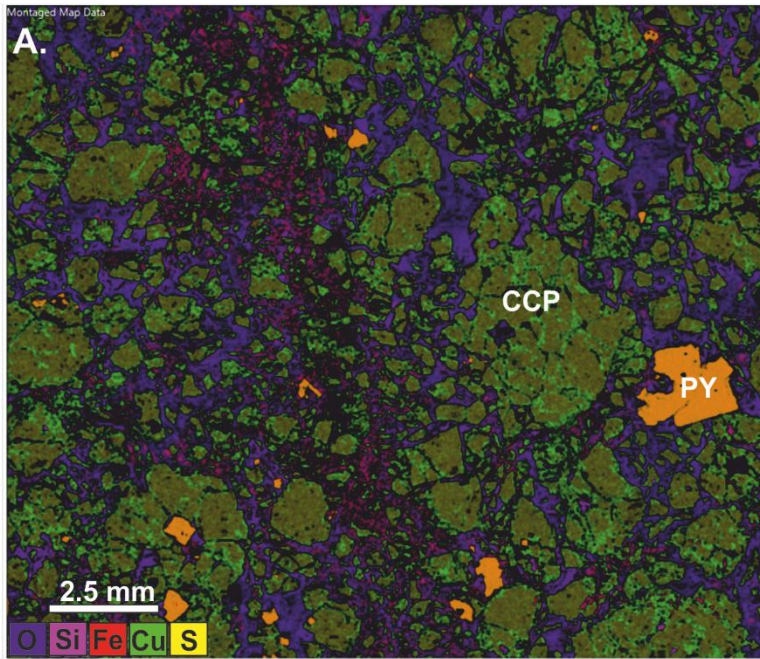
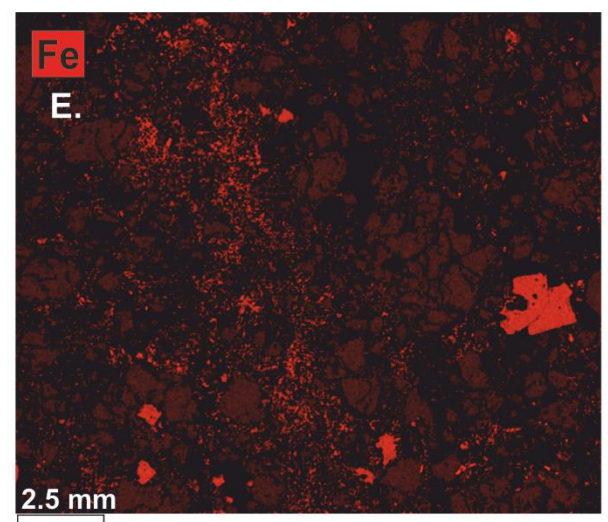
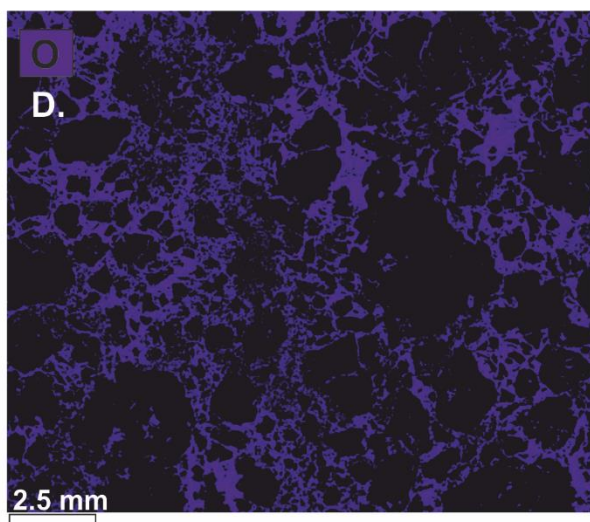
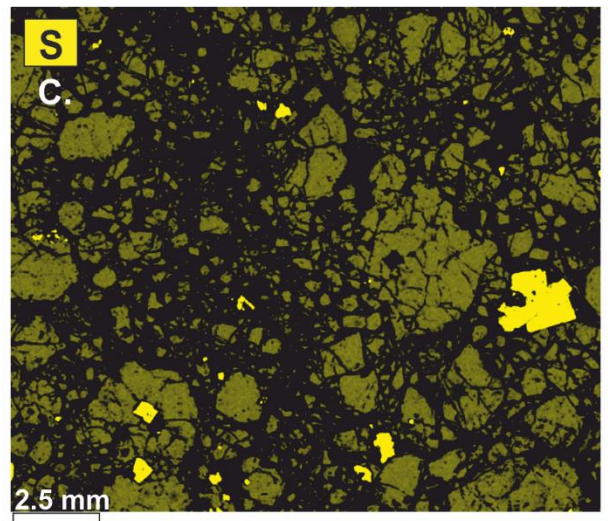
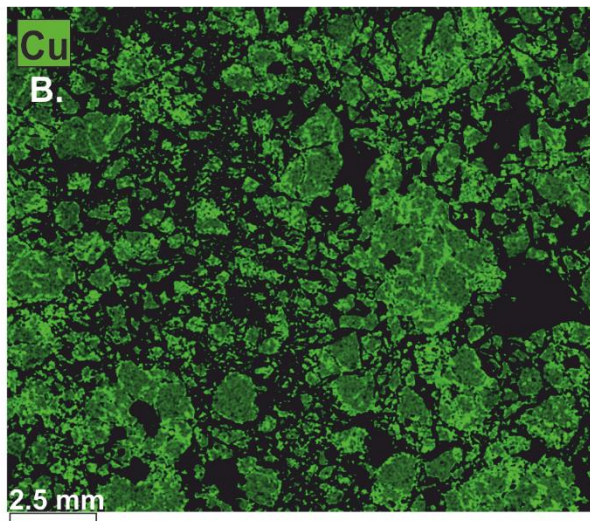


Figure A6.6: Element map of SABZ sample. Chalcopyrite is the dominant mineral phase with minor, euhedral to subhedral pyrite. Cu secondary minerals such as covellite and diginite are distinguishable in Figure B. Cu secondaries appear bright green in colour. Figure C highlights the distribution of chalcopyrite and pyrite. Figure D shows the distribution of O in samples which probably relates to interstitial silicate material. Figure E shows the distribution of Fe primarily distinguishing pyrite and interstitial hematite-goethite (bright red). PY = pyrite, CCP = chalcopyrite.



BLANK PAGE

# APPENDIX 7

7.1: XRD mineralogy summary

**D7.2: Whole rock geochemistry for Au deposits**

**D7.3: VMS whole rock geochemistry**

**D7.4: Correlation matrices**

Appendix 7 provides supplementary material for Chapter 7

## 7.1: XRD Mineral Summary

Additional XRD from Au localities

### Touronjia:

<b>16CA637</b>	<b>vol.%</b>	<b>16CA638</b>	<b>vol.%</b>	<b>16CA640</b>	<b>vol.%</b>
Quartz	86	Quartz	87	Quartz	91
Kaolinite	11	Kaolinite	13	Kaolinite	6
Natrojarosite	3			Calcite	3

<b>16CA646</b>	<b>vol.%</b>	<b>16CA642 (TJ1)</b>	<b>vol.%</b>	<b>16CA644 (TJ5)</b>	<b>vol.%</b>
Quartz	49	Calcite	3	Jarosite	2
Kaolinite	45	Quartz	84	Quartz	81
Goethite	4	Kaolinite	13	Hematite	1
Covellite	1			Kaolinite	8
Natrojarosite	1			Sergeevite	8

<b>16CA639 (TJ2)</b>	<b>vol.%</b>	<b>16CA641 (TJ6)</b>	<b>vol.%</b>
Calcite	1	Calcite	83
Quartz	96	Quartz	15
Kaolinite	3	Kaolinite	3

### Mathiatis South:

<b>16CA245 (MT24)</b>	<b>vol.%</b>	<b>16CA261 (MT13)</b>	<b>vol.%</b>	<b>16CA242 (MT31)</b>	<b>vol.%</b>
Goethite	57	Cristobalite	95	Illite	1
Hematite	37	Anatase	3	Quartz	95
Millosevichite	6	Quartz	2	Jarosite	2
				Hematite	2

<b>16CA254</b>	<b>vol.%</b>	<b>16CA263 (MT8)</b>	<b>vol.%</b>	<b>16CA228 (MT3)</b>	<b>vol.%</b>
Quartz	90	Quartz	97	Amorphous Si	77
Pyrite	3	Anatase	1	Quartz	16
Millosevichite	4	Hematite	1	Kaolinite	4
Cristobalite	3	Jarosite	1	Anatase	4
Sulfur	2				
Illite	1				

<b>16CA258</b>	<b>vol.%</b>	<b>16CA266 (MT 11)</b>	<b>vol.%</b>	<b>16CA229 (MT5)</b>	<b>vol.%</b>
Quartz	68	Goethite	69	Goethite	74
Clinocllore	23	Quartz	12	Jarosite	9
Albite	9	Jarosite	7	Kaolinite	17
		Kaolinite	12		

<b>16CA239 (MT42)</b>	<b>vol.%</b>	<b>16CA241 (MT3)</b>	<b>vol.%</b>	<b>16CA270 (MT 5)</b>	<b>vol.%</b>
Quartz	60	Quartz	100	Calcite	97
Goethite	23	Jarosite	0	Goethite	3
Hematite	11				
Natrojarosite	6				

16CA247 (MT36)	vol.%	16CA249 (MT33)	vol.%	16CA268 (MT39)	vol.%
Jarosite	39	Cristobalite	95	Carphosiderite	42
Carphosiderite	26	Kaolinite	3	Jarosite	49
Natroalunite	35	Jarosite	2	Quartz	5
				Natrolaunite	4

16CA270 (MT17)	vol.%
Carphosiderite	41
Jarosite	40
Quartz	14
Natrolaunite	5

**Kokkinovounaros:**

16CA035	vol.%	16CA036 (KN18)	vol.%
Goethite	40	Quartz	94
Jarosite	28	Natrojarosite	5
Montmorillonite	25	Hematite	1
Hematite	7		

16CA048	vol.%	16CA043 (KN57)	vol.%
Amorphous Si	52	Quartz	98
Quartz	46	Natrojarosite	1
Millosevichite	2	Hematite	1

16CA052	vol.%	16CA044 (KN51)	vol.%
Cristobalite	100	Quartz	99
		Hematite	1

16CA080	vol.%	16CA058 (KN52)	vol.%
Opal	62	Quartz	97
Jarosite	23	Jarosite	1
Hematite	15	Hematite	2

16CA088	vol.%	16CA097	vol.%
Jarosite	55	Goethite	73
Hematite	32	Hematite	13
Quartz	13	Quartz	11
		Jarosite	3

**Alpen Rose:**

<hr/>		<hr/>	
16CA434		16CA450	
Quartz	84	Quartz	82
Goethite	10	Goethite	16
Hematite	6	Hematite	2
<hr/>		<hr/>	
16CA436		16CA449	
Quartz	72	Quartz	95
Goethite	16	Kaolinite	5
Hematite	12	<hr/>	
<hr/>		<hr/>	
16CA443		16CA447	
Quartz	100	Quartz	99
<hr/>		Goethite	1
<hr/>		<hr/>	
16CA445			
Quartz	100	<hr/>	

# APPENDIX 8

**D8.1:** Sulfur isotope data

**D8.2:** Trace element data (LA-ICP-MS)

8.3: Sulfur isotope fractionation effects

## 8.3 Sulfur isotope fractionation effects

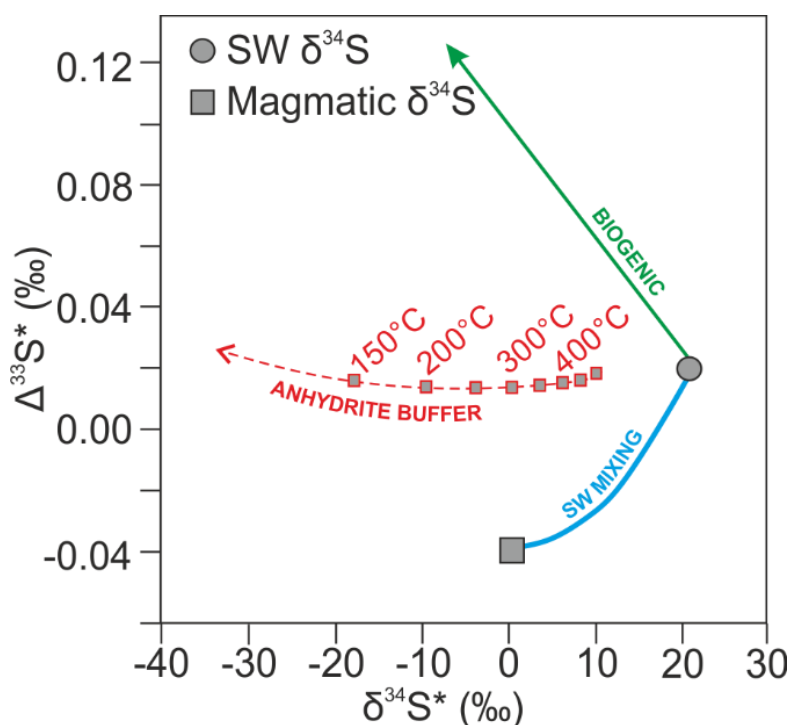


**Figure A8.1:** The effect of two phase seawater mixing and the anhydrite buffer model on multiple sulfur isotopes. In the two phase mixing model (blue line)  $\delta^{34}\text{S}$  of seawater (21-22‰) is expected to lie between seawater and magmatic values (0-1‰). In the anhydrite buffer values are strongly influenced by temperature with minimal fractionation in  $\Delta^{33}\text{S}$  (see table A8.1). Modern hydrothermal vent sulfide  $\delta^{34}\text{S}$  are best explained by the two phase mixing model (after Ono et al., 2007 and Ohmoto et al., 1983).

Temperature (°C)	$100 \ln(^{34}\alpha)$	$\Theta^{33}\text{S}$
0	78.4	0.5145
50	59.8	0.5147
100	46.9	0.5148
150	37.6	0.5150
200	30.7	0.5151
<b>250</b>	<b>25.5</b>	<b>0.5151</b>
<b>300</b>	<b>21.5</b>	<b>0.5152</b>
<b>350</b>	<b>18.3</b>	<b>0.5153</b>
<b>400</b>	<b>15.8</b>	<b>0.5153</b>
450	13.7	0.5154
500	12.0	0.5154
1000	4.4	0.5156

**Table A8.1:** The anhydrite buffer model. Theoretical multiple isotope response to changing temperature.  $100 \ln(^{34}\alpha)$  indicates the corresponding maximum fractionation factor between  $\text{SO}_2^{4-}$  and  $\text{H}_2\text{S}$  (after Ono et al., 2007).

# APPENDIX 9

9.1: XRD mineralogy summary

**D9.2: Mala LA-ICP-MS trace element data**

9.3: TAG anhydrite textures

9.4: XRD of sulfate bands

## Appendix 9.1

### XRD summary

Sample	Mineral	Vol. %	Sample	Mineral	Vol. %
16CA579	Quartz	63	16CA568	Quartz	72
	Jarosite	27		Illite	13
	Montmorillonite	5		Kaolinite	7
	Albite	3		Anorthite	8
	Wollastonite	2			
16CA572	Quartz	50	16CA571	Quartz	74
	Mordenite	46		Jarosite	26
	Montmorillonite	4			
16CA577	Quartz	92	16CA567	Albite	78
	Hematite	8		Quartz	14
				Montmorillonite	7
				Talc	1

**Table A9.1:** XRD summary for wall-rock samples from the Mala VMS

### Appendix 9.3

#### TAG anhydrite textures

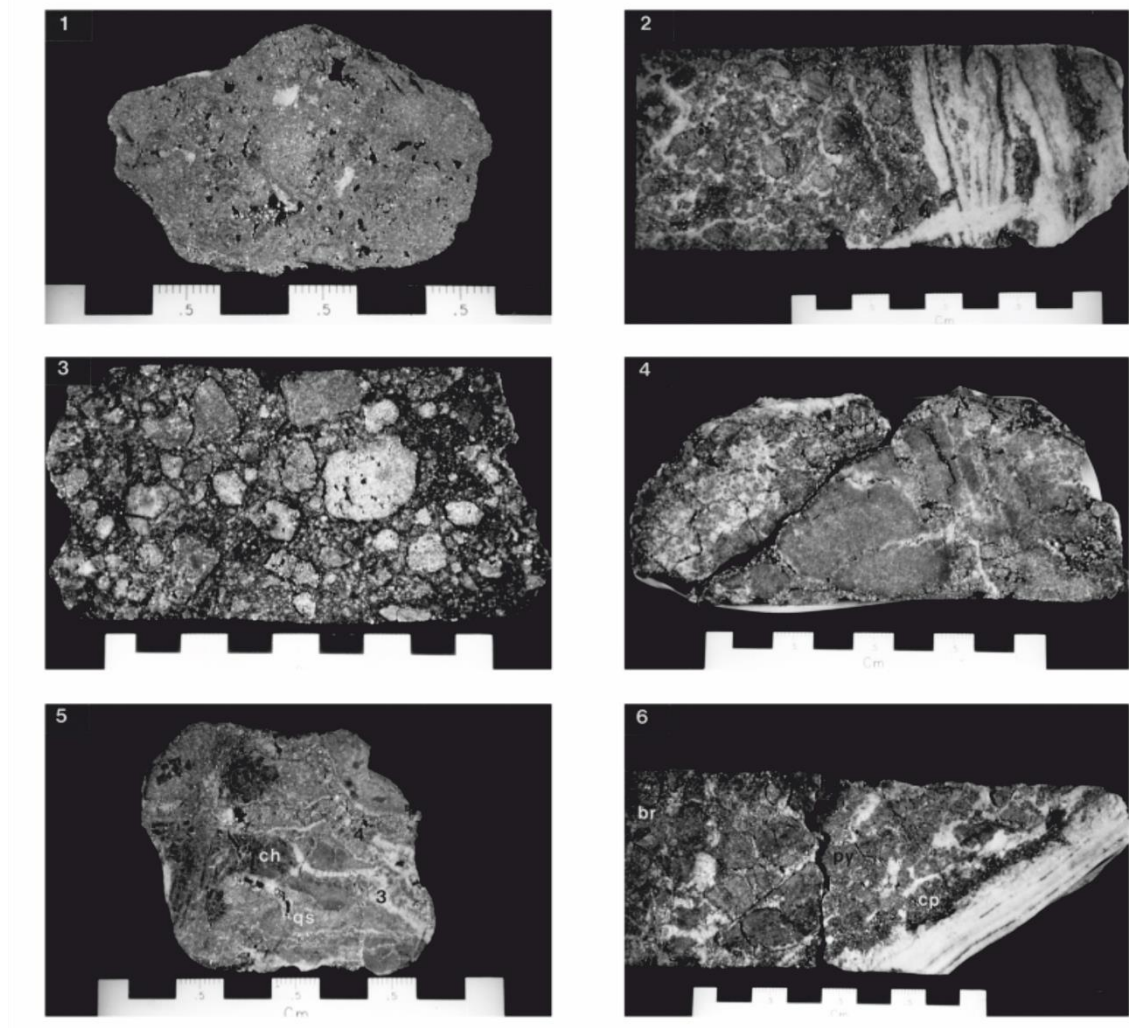


**Figure A9.3:** Examples of common anhydrite-sulfide relationships in the TAG mound (from Gemmell and Sharpe, 1998). Morphologies are similar to those observed in the Mala VMS in chapter 9.

## Appendix 9.4

### XRD analysis of sulfate from Mala

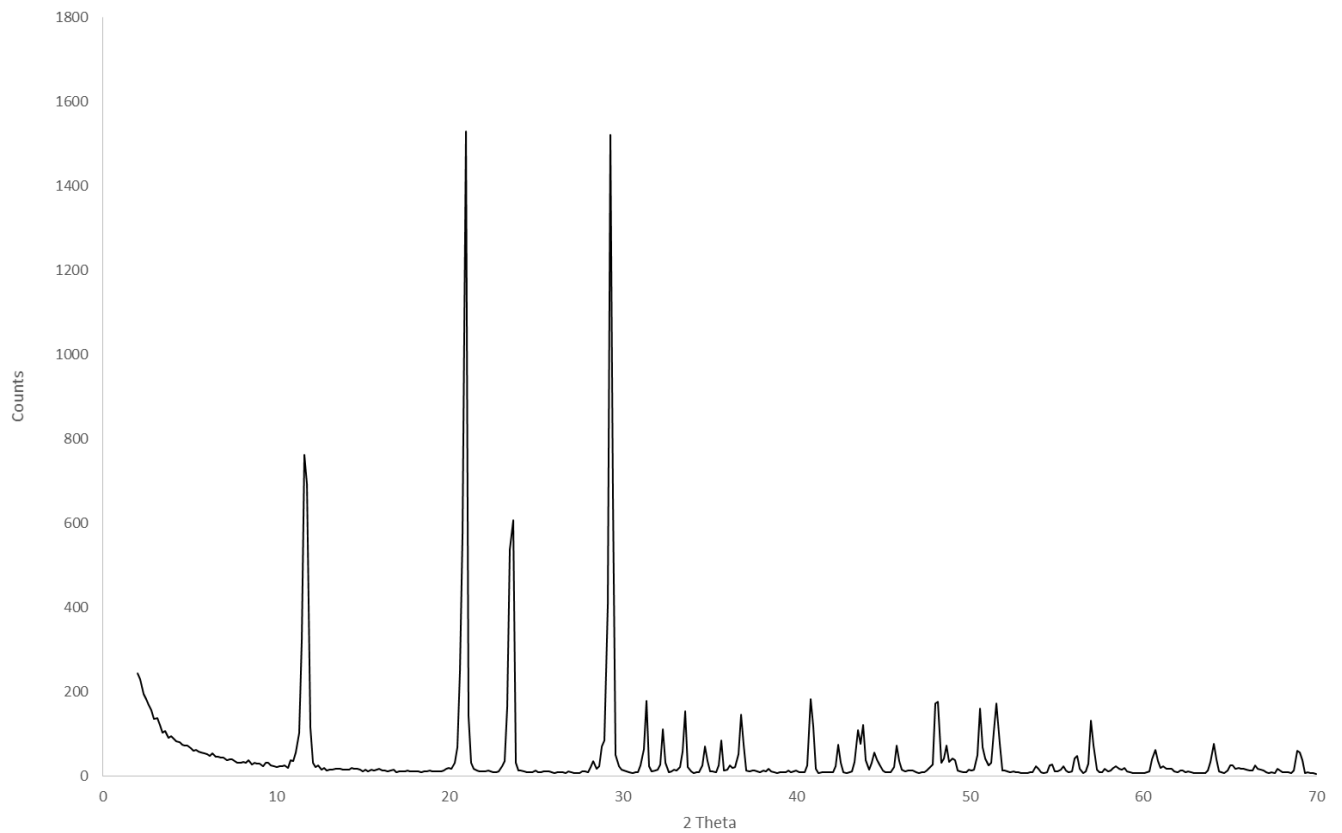


**Figure A9.4:** XRD trace of gypsum sample from Mala VMS. Characteristic peaks identified at a  $2\theta$  angle of 10.53, 20.77, 23.44 and 29.15 indicate the sample is >95% gypsum.

# DIGITAL APPENDIX

- **D4.1: Regional P-XRF data**
- **D5.1: Pyrite geochemistry (LA-ICP-MS)**
- **D5.3 Chalcopyrite geochemistry (LA-ICP-MS)**
- **D5.4 Sphalerite geochemistry (LA-ICP-MS)**
- **D6.3 Apliki geochemistry (LA-ICP-MS)**
- **D7.2 Whole rock geochemistry (Si-rich Au)**
- **D7.3 Whole rock geochemistry (VMS)**
- **D7.4 Whole rock correlation matrices**
- **D8.1 Sulfur isotope analysis**
- **D8.2 Trace element geochemistry (LA-ICP-MS/all)**
- **D9.2 Mala trace element geochemistry (LA-ICP-MS)**
- **A digital copy of this thesis**